# Contributions à la modélisation numérique des guides d'ondes élastiques

Fabien Treyssede

Le Mans Université

École doctorale UBL-SPI

# Contributions à la modélisation numérique des guides d'ondes élastiques

Mémoire

présenté pour l'obtention d'une

**Habilitation à diriger des recherches**

soutenue le 19 novembre 2019

par

Fabien Treyssède

**Composition du jury**

| | |
|---|---|
| *Présidente :* | Anne-Sophie Bonnet-BenDhia, Directrice de Recherche au CNRS, ENSTA |
| *Rapporteurs :* | Marc Deschamps, Directeur de Recherche au CNRS, Université de Bordeaux<br>André Nicolet, Professeur des Universités, Aix-Marseille Université<br>Vincent Pagneux, Directeur de Recherche au CNRS, Le Mans Université |
| *Examinateurs :* | Claire Prada, Directrice de recherche au CNRS, ESPCI<br>Patrice Cartraud, Professeur des Universités, Centrale Nantes<br>Laurent Laguerre, Directeur de Recherche, IFSTTAR |

**IFSTTAR/GERS/Laboratoire Géophysique et Évaluation Non Destructive**

# Sommaire

# 1

# Curriculum vitae détaillé

**Sommaire**



## 1.1 Curriculum vitae résumé

### 1.1.1 Informations générales

Fabien TREYSSÈDE, né le 7 février 1974 à Blois (41).

Affectation et carrière :

**Établissement :** IFSTTAR Nantes
**Affectation depuis le :** 1er sept. 2004
**Département :** GERS
**Travail à temps partiel :** 80% de 2012 à 2018

**Grade :** CR
**Discipline :** acoustique (60ème CNU)
**Laboratoire :** GeoEND

Adresse professionelle :

✉ : IFSTTAR Centre de Nantes
Allée des Ponts et Chaussées Route de
Bouaye - CS 5004
44344 Bouguenais Cedex
☎ : +33 (0)2 40 84 59 32
🖷 : +33 (0)2 40 84 59 97
@ : fabien.treyssede@ifsttar.fr

### 1.1.2 Formation initiale et complémentaire

**Formation initiale :**

- **2002 :** Doctorat en Sciences Mécaniques pour l'Ingénieur (Laboratoire Roberval, Université de Technologie de Compiègne, obtenu le 19 décembre 2002), mention : très honorable avec félicitations du jury
  Intitulé de thèse : *"Étude de la propagation acoustique en présence d'écoulement non uniforme par une méthode d'éléments finis mixtes basée sur l'équation de Galbrun"*, Jury : M. Ben Tahar, J.-C. Debus, Y. Gervais, P. Gatignol, G. Dhatt, M. Roger, B. Poirée
- **1997 :** DEA Sciences Mécaniques pour l'Ingénieur (Université de Technologie de Compiègne), mention : très bien
- **1997 :** Ingénieur Génie Mécanique (Université de Technologie de Compiègne), filière Acoustique et Vibrations

**Formations complémentaires (de type écoles d'été) :**

- VIPER Winter School "Wave propagation in periodic media", 6-8 février 2017, École Centrale Lyon (France)
- CISM, Advanced School, "New trends in vibration based structural health monitoring", 22-26 septembre 2008, Udine (Italy)
- CNRS, École thématique du GDR, "Interaction fluide-structure", 23-27 juin 2008, Villeneuve d'Ascq (France)
- CISM, Advanced School, "Waves in nonlinear pres-stressed materials", 4-8 septembre 2006, Udine (Italy)
- INRIA, écoles CEA-EDF-INRIA, "Acoustique dans les écoulements", 25-29 Septembre 2000, Rocquencourt (France)

### 1.1.3 Activités professionnelles et déroulement de carrière

- **Depuis 2010 :** Chargé de Recherche, IFSTTAR Nantes, Département GERS, Laboratoire GeoEND (Géophysique et Évaluation Non Destructive), ex-MACS/AI sur la période 2010-2013
- **2004-10 :** Chargé de Recherche, LCPC Nantes, Division Métrologie et Instrumentation, Groupe Structures et Instrumentation Intégrée
- **2003-04 :** Enseignant-chercheur contractuel, INSA (Rouen)
- **2001-03 :** Attaché Temporaire à l'Enseignement et à la Recherche, UTC (Compiègne)
- **1999-01 :** Doctorant, UTC (Compiègne)
- **1998-99 :** Ingénieur d'études acoustiques, Acouphen (Lyon)
- **1997-98 :** Service civil, DRIRE (Blois)

## 1.2 Enseignement, formation et évaluation

### 1.2.1 Activités d'enseignements et de formation

**Vacations dispensées en tant que CR à l'Ifsttar (et ex-LCPC) :**

| Année | Type | Niveau | Établissement | Intitulé | Volume (éq. TD) |
|---|---|---|---|---|---|
| 2018-19 | Cours | 2nd cycle | ITII (*) | Acoustique | 24h |
| 2017-18 | Cours | 2nd cycle | ITII (*) | Acoustique | 24h |
| 2016-17 | Cours | 2nd cycle | ITII | Acoustique | 24h |
| 2015-16 | Cours | 2nd cycle | ITII | Acoustique | 24h |
| 2014-15 | Cours | 2nd cycle | ITII | Acoustique | 24h |
| 2013-14 | Cours | 2nd cycle | ITII | Acoustique | 24h |
| 2012-13 | TD | 2nd cycle | ECN (**) | Dynamique et Vibrations | 16h |
| 2012-13 | TP | 2nd cycle | ECN | Dynamique et Vibrations | 16h |
| 2012-13 | Cours | 2nd cycle | ITII | Acoustique | 24h |
| 2011-12 | TD | 2nd cycle | ECN | Dynamique et Vibrations | 16h |
| 2011-12 | TP | 2nd cycle | ECN | Dynamique et Vibrations | 16h |
| 2011-12 | Cours | 2nd cycle | ITII | Acoustique | 24h |
| 2010-11 | TD | 2nd cycle | ECN | Dynamique et Vibrations | 16h |
| 2010-11 | TP | 2nd cycle | ECN | Dynamique et Vibrations | 16h |
| 2010-11 | Cours | 2nd cycle | ITII | Acoustique | 24h |

(*) ITII : Institut des Techniques d'Ingénieur de l'Industrie (Pays de Loire)
(**) ECN : École Centrale Nantes

**Enseignements dispensés en tant qu'enseignant contractuel à l'INSA de Rouen :**

| Année | Type | Niveau | Établissement | Intitulé | Volume (éq. TD) |
|---|---|---|---|---|---|
| 2003-04 | Cours | 2nd cycle | INSA Rouen | Interactions fluide-structure | 21h |
| 2003-04 | TD/TP | 2nd cycle | INSA Rouen | Interactions fluide-structure | 27h |
| 2003-04 | TD | 2nd cycle | INSA Rouen | Méthodes numériques | 75h |
| 2003-04 | TD | 2nd cycle | INSA Rouen | Mécanique générale | 67,5h |
| 2003-04 | TD | 2nd cycle | INSA Rouen | Transferts thermiques | 45h |
| 2003-04 | TD | 2nd cycle | INSA Rouen | Machines thermiques | 45h |
| 2003-04 | TD | 2nd cycle | INSA Rouen | Informatique | 60h |
| 2003-04 | TP | 2nd cycle | INSA Rouen | Vibrations | 30h |

**Enseignements dispensés en tant qu'attaché temporaire à l'enseignement et à la recherche (2001-03) à l'UTC (***) :**

| Année | Type | Niveau | Établissement | Intitulé | Volume (éq. TD) |
|---|---|---|---|---|---|
| 2002-03 | Cours | 2nd cycle | UTC (***) | Acoustique industrielle | 12h |
| 2002-03 | TD | 2nd cycle | UTC | Acoustique industrielle | 24h |
| 2002-03 | TP | 2nd cycle | UTC | Acoustique industrielle | 40h |
| 2002-03 | TD | 2nd cycle | UTC | Analyse modale | 34h |
| 2002-03 | TP | 2nd cycle | UTC | DESS Acoustique transports | 8h |
| 2002-03 | TD | 1er cycle | UTC | Mécanique physique | 68h |
| 2001-02 | TD | 2nd cycle | UTC | Acoustique industrielle | 16h |
| 2001-02 | TP | 2nd cycle | UTC | Acoustique industrielle | 22h |
| 2001-02 | TD | 2nd cycle | UTC | Analyse modale | 17h |
| 2001-02 | TP | 2nd cycle | UTC | DESS Acoustique transports | 3h |
| 2001-02 | TD | 1er cycle | UTC | Mécanique physique | 34h |

**Enseignements dispensés en tant que vacataire (1999-01) à l'UTC :**

| Année | Type | Niveau | Établissement | Intitulé | Volume (éq. TD) |
|---|---|---|---|---|---|
| 2000-01 | TD | 2nd cycle | UTC | Analyse modale | 46h |
| 2000-01 | TD/TP | 2nd cycle | UTC | Pratique expérimentale | 6h |
| 2000-01 | TD/TP | 2nd cycle | UTC | Mécanique des vibrations | 4h |
| 2000-01 | TP | 2nd cycle | UTC | Acoustique industrielle | 15h |
| 2000-01 | TD | 1er cycle | UTC | Algèbre linéaire | 32h |
| 1999-00 | TD | 2nd cycle | UTC | Analyse modale | 34h |
| 1999-00 | TP | 2nd cycle | UTC | Acoustique industrielle | 44h |
| 1999-00 | TP | 2nd cycle | UTC | Mécanique des vibrations | 29h |
| 1999-00 | TP | 2nd cycle | UTC | DESS Acoustique transports | 11h |

(***) UTC : Université de Technologie de Compiègne

### 1.2.2 Encadrements

**Doctorants (co-encadrements) :**

- Matthieu Gallezot (oct. 2015-sept. 2018), sujet : simulation numérique du contrôle non destructif des guides d'ondes enfouis, co-financement IFSTTAR/Région Pays de la Loire, Directeur : Laurent Laguerre (IFSTTAR/GeoEND), thèse soutenue le 22 novembre 2018, devenir : post-doctorant (Université de Nantes, 2018-2020)
- Khac Long Nguyen (oct. 2011-sept. 2014), sujet : modélisation numérique des guides d'ondes ouverts, financement IFSTTAR, Directeur : Laurent Laguerre (IFSTTAR/GeoEND), Codirectrice : Anne-Sophie Bonnet-BenDhia (ENSTA/POems), thèse soutenue le 27 novembre 2014, devenir : post-doctorant (POems UMR 7231 2014-15, CETHIL UMR 5008 2015-2017, LAMCOS UMR 5259 2017-2018)
- Ahmed Frikha (oct. 2007-sept. 2010), sujet : modélisation de la propagation des ondes élastiques dans les guides multi-brins hélicoïdaux précontraints, financement LCPC, Directeur : Patrice Cartraud (ECN/GeM), thèse soutenue le 13 décembre 2010, devenir : Ingénieur R&D chez ADR 2011-2015, maître assistant depuis 2016 (ENIS, Sfax, Tunisie)

**Post-doctorants :**

— Matthieu Gallezot (décembre 2018-mars 2020), sujet : modélisation des modes de galerie élastiques dans une sphère enfouie, financement projet Paris Scientifiques SMoG (Région PdL)
— Changwei Zhou (septembre 2017-décembre 2018), sujet : modélisation numérique de la propagation des ondes guidées mécaniques dans des structures multi-brins, financement projet RFI WeAMEC OMCEND, devenir : post-doctorante (IFSTTAR, 2019-2020)
— Mohamed Masmoudi (mai 2012-août 2013), sujet : développement d'outils pour l'analyse expérimentale de la propagation des ondes guidées, financement projet ANR FilameNDT, devenir : maître assistant depuis 2013 (ISSI Gabès, Tunisie)
— Farouk Benmeddour (oct. 2010-mai 2011), sujet : comparaison expérimentale-numérique de l'interaction ondes-défauts dans les guides, financement projet ANR FilameNDT, devenir : maître de conférence depuis 2011 (UVHC, Valenciennes)
— Farouk Benmeddour (nov. 2007-déc. 2008), sujet : modélisation numérique de l'interaction ondes-défauts dans les guides élastiques 3D, financement projet ANR ACTENA, devenir : voir-ci-dessus

**Stagiaires M2 :**
— Khac Lan Nguyen (mars. 2015-juillet 2015), sujet : méthode des éléments finis spectraux pour la propagation des ondes guidées par approche modale
— Amine Ihamouten (avr. 2008-août 2008), sujet : étude expérimentale des effets de température sur les modes de vibrations des câbles
— Mohamed Masmoudi (oct. 2007-fév. 2008), sujet : modélisation numérique du comportement dynamique des poutres 3D précontraintes
— Ahmed Frikha (nov. 2006-fév. 2007), sujet : modélisation numérique du comportement dynamique des poutres planes précontraintes basée sur une formulation Lagrangienne actualisée

### 1.2.3 Activités d'évaluation

**Membre de jury de thèse :**
— thèse de Matthieu Gallezot, soutenue le 22 novembre 2018 (voir §1.2.2)
— thèse de Khac Long Nguyen, soutenue le 27 novembre 2014 (voir §1.2.2)
— thèse de Miguel Moleron (thèse LAUM, 2009-2012, ED SPIGA), sujet : modélisation de la propagation acoustique en milieu urbain, soutenue le 30 novembre 2012
— thèse d'Ahmed Frikha, soutenue le 13 décembre 2010 (voir §1.2.2)

**Comité de suivi de thèse :**
— Miguel Moleron (thèse LAUM, 2009-2012, ED SPIGA), sujet : modélisation de la propagation acoustique en milieu urbain, président du comité de suivi

**Relecture pour revues internationales :**
— Journal of Sound and Vibration (12 articles)
— Ultrasonics (6 articles)
— Journal of the Acoustical Society of America (5 articles)
— Wave Motion (6 articles)
— International Journal of Solids and Structures (2 articles)
— Computer and Structures (1 article)
— Nonlinear Dynamics (1 article)

— Finite Elements in Analysis and Design (1 article)
— International Journal of Mechanical Sciences (1 article)
— Journal of Applied and Computational Mechanics (1 article)
— Proceedings of the Royal Society A (1 article)
— autres revues en langue anglaise (3 articles)

**Évaluation de projet :**
— 1 projet ANR expertisé

## 1.3 Activités d'administration de la recherche

### 1.3.1 Contrats de recherche

**Projets de recherche internationaux :**
— Projet DESDEMONA (2018-2021) "DEtection of Steel DEfects by Enhanced MONitoring and Automated procedure for self-inspection and maintenance", European Project (H2020), rôle : participant, montant : 1 320 531 €, partenaires : Universita Di Roma La Sapienza (Italy), Iniversida de Castilla (Spain), Universidade do Porto (Portugal), Universita di Pisa (Italy), IFSTTAR, Aiviewgroup Srl (Italy), Advitam (France), ECISA Compania General de Construcciones S.A. (Spain), descriptif : DESDEMONA objective is the development of novel design methods, systems, procedure and technical solution, to integrate sensing and automation technologies for the purpose of self-inspection and self-monitoring of steel structures
— Projet FilameNDT (2010-2013) "NDT for Need Based Maintenance of Civil Infrastructure", ANR Programme Inter Carnot Fraunhofer 2010, rôle : participant, montant : 1 499 281 €, partenaires : LCPC (coordinateur), IZFP (coordinateur), descriptif : outils d'aide à la maintenance d'infrastructures de génie civil à câbles au moyen de méthodologies d'évaluation non-destructives
— Programme européen DUCAT (1998-00) : "Duct acoustics and radiation", partenaires : DTU (Denmark), ISVR (England), UTC, ONERA (France), NUIG (Ireland), NLR (Netherlands), KTH (Sweden), partenaires industriels : EADS, Turbomeca, Rolls-Royce, rôle : participant, dont résultats publiés dans : M.J. Fisher, R.H. Self, "Aeroacoustics research in Europe : the CEAS-ASC report on 2001 highlights", Journal of Sound and Vibration 258 (1), 1-30 (2002)

**Projets de recherche nationaux :**
— Projet OMCEND (2016-2019) "Ondes Mécaniques dans les Câbles pour leur Évaluation Non Destructive : approche numérique et expérimentale", RFI Pays de le Loire WeAMEC, rôle : porteur, montant : 204 500 €, partenaires : GERS/GeoEND (IFSTTAR, coordinateur), GeM (Centrale Nantes), descriptif : modélisation numérique et validation expérimentale de la propagation des ondes guidées dans les câbles ombilicaux de transport d'électricité utilisés pour l'éolien off-shore
— Projet SMOG (2016-2020) "Sentinelle à MOdes de Gallerie", Paris Scientifiques Régionaux Pays de la Loire, rôle : participant, montant : 222 588 €, partenaires : GeM (Université de Nantes, coordinateur), GERS/GeoEND (IFSTTAR), COSYS/SII (IFSTTAR), descriptif : modes de galerie à la surface d'une sphère enfouie pour mesurer les composantes du tenseur de déformation en un point du matériau environnant

— Projet ANR ACTENA (2006-09) : "Auscultation des Câbles TEndus Non Accessibles", rôle : participant, montant : 531 944 €, partenaires : LCPC (coordinateur), Université Bordeaux I, CEA, Université Toulouse III, Université des Sciences et Technologies de Lille, UTC, INSA Lyon, Université d'Artois, Université de Méditerranée, ENPC, ARMINES, CETE Lyon, CEBTP, descriptif : développement de méthodes non destructives pour l'inspection des câbles du génie civil
— Projet national CONSTRUCTIF (2003-06) : "COuplage de coNcepts pour la Surveillance de sTRUCTures InFormatisées", rôle : participant, montant : 216 500 €, partenaires : IRISA, INRIA, Centrale Paris, LCPC, descriptif : couplage de méthodes d'inférence statistique et de modèles physiques pour la prise en compte intrinsèque des phénomènes de température dans la surveillance vibratoire des structures

### 1.3.2 Responsabilités dans l'animation de la communauté scientifique

**Codirection du Groupement de Recherche "MecaWave" (GDR CNRS) :**

Le GDR CNRS MecaWave porte sur les ondes mécaniques et a débuté le 1er janvier 2018 pour une durée de 5 ans. Sa gouvernance est assurée par un directeur et deux codirecteurs, dont les travaux de recherche respectifs portent sur l'acoustique physique, la mécanique théorique et le contrôle non destructif :

— Bruno Lombard (LMA, UPR 7051 CNRS), Marseille
— Kim Pham (IMSIA, CEA-EDF-ENSTA ParisTech, UMR 9219), Palaiseau
— Fabien Treyssède (GERS/GeoEND, IFSTTAR), Nantes

Le GDR MecaWave vise à rassembler la communauté scientifique française à l'interface de l'acoustique physique, de la mécanique théorique et des mathématiques appliquées, soit 21 laboratoires (LMA, I2M, LAUM, LMS, LTDS, Institut Langevin, POEMS, JADE, IMATH, ...) dont 2 côté Ifsttar (GeoEND, ISTerre). Il est organisé en 4 groupes de travail :

— dynamique effective des milieux microstructurés (couches fines, milieux continus généralisés, fondements des métamatériaux, etc.)
— ondes non linéaire dans les solides (ondes et fissures, dynamique lente dans les milieux endommagés, milieux "réglables", etc.)
— guides d'ondes mécaniques (modes piégés, guides ouverts, etc.)
— problèmes inverses (contrôle non destructif, optimisation de microstructure, etc.).

La principale action du GDR MecaWave est de promouvoir les échanges scientifiques, en organisant des journées thématiques et des colloques. Le budget annuel est évalué à 24 000 €. Pour cela, nous avons sollicité une aide financière de partenaires académiques, industriels, ainsi que de Labex (CNRS, IFSTTAR, INRIA, ONERA, CEA, Labex LaSIPS, Labex MEC, Labex Henri Lebesque, ...).

L'objectif premier du GDR MecaWave est de coordonner des recherches amont selon différents contextes applicatifs, dont l'évaluation non destructive (END) et la géophysique. Pour ne citer que quelques exemples, les applications phares intéressant l'Ifsttar en END sont les câbles, le béton, les matériaux composites... Par ailleurs, une attention particulière est accordée à l'implémentation et la validation des méthodes inverses et d'imagerie récentes sur des configurations réelles, impliquant théoriciens et expérimentateurs sur le même objet. Cet aspect représente de forts enjeux industriels et reste à l'heure actuelle un défi pour le transfert opérationnel des méthodes d'auscultation. Les applications qui en découleront intéressent donc d'autres départements et laboratoires de l'Ifsttar utilisateurs des méthodes END.

Cette création de GDR comble le vide laissé par les GDR et GDRI Ultrasons qui se sont

succédé de 2001 à 2014, et dans lesquels le LCPC puis Ifsttar se sont impliqués (2006-2009 puis 2011-2014). Ces groupements étaient résolument tournés vers les applications CND. Un renouvellement de GDRI avait été soumis en 2015 (voir §1.4) mais refusé par le CNRS, qui nous a incité à proposer un projet de taille plus modeste et un peu plus amont intégrant notamment la mécanique théorique. Les applications, sans être au cœur du projet, en sont les motivations, et ce nouveau GDR constituera une passerelle très importante pour le transfert opérationnel des méthodes d'auscultation et de CND. L'implication de l'Ifsttar dans ce nouveau GDR s'inscrit dans la lignée des précédents, qui ont permis d'identifier les principaux verrous scientifiques à lever.

Les actions réalisées en 2018 ont été les suivantes :

- 1er colloque du GdR MecaWave, 5-9 novembre 2018, Fréjus
- journée thématique "Propagation d'ondes dans les milieux dispersifs : application aux liquides à bulles et aux matériaux de second gradient", 5 octobre 2018, Marseille
- journée thématique "Méthodes inverses et imagerie : de la théorie aux applications", 29 juin 2018, Paris.

et les actions réalisées en 2019 :

- 4th Workshop on Seismic Metamaterials, April 15-17, 2019, Marseille (soutien financier)
- Summer School "Wave propagation in complex and microstructured media" sur les thèmes homogénéisation et ondes guidées, August 20-30, 2019, Cargèse (soutien financier)
- journée thématique "Modélisation du contact et de l'endommagement en dynamique", 10 octobre 2019, Bordeaux.

Site Web du GDR : http ://mecawave.cnrs.fr/

### 1.3.3 Activités d'expertise

- Étude "Simulation numérique de la propagation des ondes dans la section d'un cylindre tricouche aluminium-verre/epoxy-plexiglass" (2013-2014), client : PRECEND/CETIM, rôle : responsable du contrat, montant : 2 140,84 €, rapport de 9 pages

## 1.4 Rayonnement scientifique

### 1.4.1 Organisation de congrès et workshops

- 1er colloque du GdR MecaWave, 5-9 novembre 2018, Fréjus, co-organisateur (voir §1.3.2)
- ICMS Workshop "New mathematics for a safer world : wave propagation in heterogeneous materials", 12-15 juin 2017, Édinbourg (Écosse), co-organisateur, liste des organisateurs : Anthony Croxford (University of Bristol), Bruno Lombard (Laboratoire de Mécanique et Acoustique, CNRS), Anthony Mulholland (University of Strathclyde), Katy Tant (University of Strathclyde), Fabien Treyssède (GeoEND, IFSTTAR)
- Congrès international Acoustics 2012 Nantes (SFA/IoA), 1200 participants, membre du comité d'organisation (responsable publications)

### 1.4.2 Présentation de séminaires sur invitation

- Séminaire Institut Jean Le Rond d'Alembert (UMR CNRS 7190), Paris, mars 2019, "Propagation des ondes dans les milieux périodiques à symétries hélicoïdales"

— Séminaire Computational and Applied Mathematics Research Group, Brunel University, London (UK), juin 2015, "Modeling the free and forced high frequency response of cables : propagation and excitation of elastic guided waves in prestressed multi-wire helical structures"
— Séminaire Journée de Mécanique de l'IRMAR (UMR CNRS 6625), Rennes, juin 2014, "Numerical modeling of curved waveguides : computation of elastic propagation modes in prestressed multi-wire helical structures"
— Séminaire LAUM (UMR CNRS 6613), Le Mans, sept. 2012, "Modélisation numérique des guides d'ondes courbes, application à l'élastodynamique de structures hélicoïdales"
— Séminaire POEMS (UMR CNRS-INRIA-ENSTA), Paris, mars 2009, "Investigation numérique de la propagation des ondes dans les guides courbes - Application à l'élastodynamique"

### 1.4.3 Participation à des réseaux de recherche

— Membre et directeur adjoint du GDR CNRS MecaWave (2018-2022) - voir §1.3.2
— Membre du Groupement de Recherche Européen franco-anglais "Wave propagation in complex media for quantitative and non destructive evaluation" (GDRE US, 2011-2014)
— Membre du GDR 2501 "Étude de la propagation ultrasonore en milieux non homogènes en vue du contrôle non-destructif" (2006-2010)
— Contribution au GdR 2493 "Bruit des Transports" (2ème journées annuelles, 20-21 janvier 2004, Marseille)

### 1.4.4 Collaborations académiques

— POems (Propagation des Ondes : Étude Mathématique et Simulation), Palaiseau, UMR 7231 CNRS - ENSTA - INRIA
— GeM (Institut de Recherche en Génie Civil et Mécanique), Nantes, UMR 6183 CNRS - École Centrale de Nantes - Université de Nantes
— I2M (Institut de Mécanique et d'Ingénierie), Bordeaux, UMR 5295 CNRS - Université de Bordeaux - Bordeaux INP - ENSAM ParisTech

### 1.4.5 Affiliations

— Membre de la SFA (Société Française d'Acoustique)
— Membre de l'AFM (Association Française de Mécanique)

## 1.5 Publications

| | Code | Nombre total |
|---|---|---|
| Article dans revue à comité de lecture répertoriée dans les BDI JCR, Scopus, ERIH, HCRES | ACL | 33 |
| Conférence invitée dans un congrès international ou national (*) | INV | 1 |
| Communication avec actes dans un congrès international | ACTI | 27 |
| Communication avec actes dans un congrès national | ACTN | 9 |
| Communication orale sans actes dans un congrès international ou national | COM | 18 |
| Communication par affiche dans un congrès international ou national | AFF | 3 |

(*) conférences invitées au sens de frais d'inscription et de voyages offerts et/ou de conférences (semi)plénières

**ACL**

**Gallezot, M., F. Treyssède et L. Laguerre (2019) :** « Numerical modelling of wave scattering by local inhomogeneities in elastic waveguides embedded into infinite media », *Journal of Sound and Vibration*, 443, p. 310–327.

**Treyssède, F. (2019) :** « Free and forced response of three-dimensional waveguides with rotationally symmetric cross-sections », *Wave Motion*, 87, p. 75–91.

**Gallezot, M., F. Treyssède et L. Laguerre (2018a) :** « A modal approach based on perfectly matched layers for the forced response of elastic open waveguides », *Journal of Computational Physics*, 356, p. 391–409.

— **(2017b) :** « Contribution of leaky modes in the modal analysis of unbounded problems with perfectly matched layers », *Journal of the Acoustical Society of America*, 141, EL16–EL21.

**Treyssède, F. (2017a) :** « Finite element modeling of temperature load effects on the vibration of local modes in multi-cable structures », *Journal of Sound and Vibration*, 413, p. 191–204.

— **(2016a) :** « Dispersion curve veering of longitudinal guided waves propagating inside prestressed seven-wire strands », *Journal of Sound and Vibration*, 367, p. 56–68.

— **(2016b) :** « Investigation of the interwire energy transfer of elastic guided waves inside prestressed cables », *Journal of the Acoustical Society of America*, 140, p. 498–509.

— **(2016c) :** « Spectral element computation of high frequency leaky modes in three-dimensional solid waveguides », *Journal of Computational Physics*, 314, p. 341–354.

**Nguyen, K. L. et F. Treyssède (2015c) :** « Numerical investigation of leaky modes in helical structural waveguides embedded into a solid medium », *Ultrasonics*, 57, p. 125–134.

**Nguyen, K. L., F. Treyssède et C. Hazard (2015) :** « Numerical modeling of three-dimensional open elastic waveguides combining semi-analytical finite element and perfectly matched layer methods », *Journal of Sound and Vibration*, 344, p. 158–178.

**Treyssède, F. (2015b) :** « Three-dimensional modeling of elastic guided waves excited by arbitrary sources in viscoelastic multilayered plates », *Wave Motion*, 52, p. 33–53.

**Treyssède, F., K. L. Nguyen, A. S. Bonnet-BenDhia et C. Hazard (2014) :** « Finite element computation of trapped and leaky elastic waves in open stratified waveguides », *Wave Motion*, 51 (7), p. 1093–1107.

**Frikha, A., P. Cartraud et F. Treyssède (2013) :** « Mechanical modeling of helical structures accounting for translational invariance. Part 1 : Static behavior », *International Journal of Solids and Structures*, 50 (9), p. 1373–1382.

**Kurz, J., L. Laguerre, F. Niese, L. Gaillet, K. Szielasko, R. Tschuncky et F. Treyssède (2013) :** « NDT for need based maintenance of bridge cables, ropes and pre-stressed elements », *Journal of Civil Structural Health Monitoring*, 3, p. 285–295.

**Treyssède, F., A. Frikha et P. Cartraud (2013) :** « Mechanical modeling of helical structures accounting for translational invariance. Part 2 : Guided wave propagation under axial loads », *International Journal of Solids and Structures*, 50 (9), p. 1383–1393.

**Treyssède, F. et L. Laguerre (2013b) :** « Numerical and analytical calculation of modal excitability for elastic wave generation in lossy waveguides », *Journal of the Acoustical Society of America*, 133 (6), p. 3827–3837.

**Benmeddour, F., F. Treyssède et L. Laguerre (2011) :** « Numerical modeling of guided wave interaction with non-axisymmetric cracks in elastic cylinders », *International Journal of Solids and Structures*, 48 (5), p. 764–774.

**Frikha, A., F. Treyssède et P. Cartraud (2011) :** « Effect of axial load on the propagation of elastic waves in helical beams », *Wave Motion*, 48 (1), p. 83–92.

**Laguerre, L. et F. Treyssède (2011) :** « Non destructive evaluation of seven-wire strands using ultrasonic guided waves », *European Journal of Environmental and Civil Engineering*, 15 (4), p. 487–500.

**Treyssède, F. (2011) :** « Mode propagation in curved waveguides and scattering by inhomogeneities : Application to the elastodynamics of helical structures », *Journal of the Acoustical Society of America*, 129 (4), p. 1857–1868.

**Basseville, M., F. Bourquin, L. Mevel, H. Nasser et F. Treyssède (2010) :** « Handling the Temperature Effect in Vibration Monitoring : Two Subspace-Based Analytical Approaches », *Journal of Engineering Mechanics-ASCE*, 136 (3), p. 367–378.

**Treyssède, F. (2010b) :** « Vibration analysis of horizontal self-weighted beams and cables with bending stiffness subjected to thermal loads », *Journal of Sound and Vibration*, 329 (9), p. 1536–1552.

**Treyssède, F. et L. Laguerre (2010) :** « Investigation of elastic modes propagating in multi-wire helical waveguides », *Journal of Sound and Vibration*, 329 (10), p. 1702–1716.

**Treyssède, F. (2009) :** « Free linear vibrations of cables under thermal stress », *Journal of Sound and Vibration*, 327 (1-2), p. 1–8.

**Treyssède, F. et M. Ben Tahar (2009) :** « Jump conditions for unsteady small perturbations at fluid-solid interfaces in the presence of initial flow and prestress », *Wave Motion*, 46 (2), p. 155–167.

**Balmes, E., M. Basseville, F. Bourquin, L. Mevel, H. Nasser et F. Treyssède (2008) :** « Merging sensor data from multiple temperature scenarios for vibration monitoring of civil structures », *Structural Health Monitoring*, 7 (2), p. 129–142.

**Treyssède, F. (2008b) :** « Elastic waves in helical waveguides », *Wave Motion*, 45 (4), p. 457–470.

— **(2007a) :** « Numerical investigation of elastic modes of propagation in helical waveguides », *Journal of the Acoustical Society of America*, 121 (6), p. 3398–3408.

— **(2007c) :** « Prebending effects upon the vibrational modes of thermally prestressed planar beams », *Journal of Sound and Vibration*, 307 (1-2), p. 295–311.

**Gabard, G., F. Treyssède et M. Ben Tahar (2004) :** « A numerical method for vibro-acoustic problems with sheared mean flows », *Journal of Sound and Vibration*, 272 (3-5), p. 991–1011.

**Treyssède, F. et M. Ben Tahar (2004a) :** « Comparison of a finite element model with a multiple-scales solution for sound propagation in varying ducts with swirling flows », *Journal of the Acoustical Society of America*, 115 (6), p. 2716–2730.

— **(2004b) :** « Validation of a finite element method for sound propagation and vibro-acoustic problems with swirling flows », *Acta Acustica United with Acustica*, 90 (4), p. 731–745.

**Treyssède, F., G. Gabard et M. Ben Tahar (2003) :** « A mixed finite element method for acoustic wave propagation in moving fluids based on an Eulerian-Lagrangian description », *Journal of the Acoustical Society of America*, 113 (2), p. 705–716.

**INV**

**Treyssède, F., M. Gallezot et K. L. Nguyen (2017) :** « On the modeling of elastic waveguides coupled to infinite media », *ICMS Workshop, New mathematics for a safer world : wave propagation in heterogeneous materials, Edinburgh (Scotland).*

**ACTI**

**Gallezot, M., F. Treyssède et L. Laguerre (2017a) :** « A numerical method for the scattering by defects in axisymmetrical open elastic waveguides », *X International Conference on Structural Dynamics (EURODYN 2017, Rome, 10-13 septembre 2017), In Procedia Engineering*, 199, p. 1527–1532.

— **(2017c) :** « Modal expansion in elastic open waveguides with perfectly matched layers », *13th International Conference on Mathematical and Numerical Aspects of Wave Propagation, Minneapolis (USA)*, 2 pages.

**Treyssède, F. (2017b) :** « Numerical modeling of waveguides accounting for translational invariance and rotational symmetry », *X International Conference on Structural Dynamics (EURODYN 2017, Rome, 10-13 septembre 2017), In Procedia Engineering*, 199, p. 1562–1567.

**Nguyen, K. L. et F. Treyssède (2015a) :** « Computation of modes in embedded helical structures with the SAFE-PML method », *12th International Conference on Mathematical and Numerical Aspects of Wave Propagation, Karlsruhe (Germany)*, 2 pages.

**Treysséde, F. (2015) :** « Veering of dispersion curves and prestress effects in multi-wire helical waveguides », *9th GDR Conference on Wave Propagation in Complex Media for Quantitative and Non Destructive Evaluation, Aussois (France)*, 4 pages.

**Nguyen, K. L., F. Treysséde, A.-S. Bonnet-BenDhia et C. Hazard (2014a) :** « Finite element computation of leaky modes in straight and helical elastic waveguides », *8th GDR Conference on Wave Propagation in Complex Media for Quantitative and Non Destructive Evaluation, Gregynog (Wales)*, 4 pages.

**Treysséde, F. et L. Laguerre (2014) :** « Excitation of prestressed multi-wire helical waveguides », *8th GDR Conference on Wave Propagation in Complex Media for Quantitative and Non Destructive Evaluation, Gregynog (Wales)*, 4 pages.

**Treyssède, F. et L. Laguerre (2014) :** « Wave propagation in helical multi-wire cables », *7th European Workshop on Structural Health Monitoring, Nantes*, 8 pages.

**Nguyen, K. L., F. Treysséde, A.-S. Bonnet-BenDhia et C. Hazard (2013a) :** « Computation of dispersion curves in elastic waveguides of arbitrary cross-section embedded in infinite solid media », *13th International Symposium on Nondestructive Characterization of Materials, Le Mans*, 8 pages.

— **(2013b) :** « Computation of leaky modes in three-dimensional open elastic waveguides », *11th International Conference on Mathematical and Numerical Aspects of Wave Propagation, Tunis*, 2 pages.

**Benmeddour, F., L. Laguerre et F. Treyssède (2012) :** « Scattering of guided waves from discontinuities in cylinders : numerical and experimental analysis », *International Congress on Ultrasonics, Gdansk (Poland), AIP Conference Proceedings*, 1433, p. 435–438.

**Kurz, J., L. Laguerre, F. Niese, L. Gaillet, K. Szielasko et F. Treyssède (2012) :** « NDT for need based maintenance of civil infrastructure – FilameNDT a Franco-German project for monitoring and inspection of bridge cables, ropes and pre-stressed elements », *Workshop on Civil Structural Health Monitoring, Berlin*, 8 pages.

**Treyssséde, F., K. L. Nguyen, A.-S. Bonnet-BenDhia et C. Hazard (2012) :** « On the use of a SAFE-PML technique for modeling two-dimensional open elastic waveguides », *Acoustics 2012, Nantes*, p. 667–672.

**Frikha, A., F. Treyssède et P. Cartraud (2010b) :** « Numerical modeling of elastic wave propagation in prestressed helical waveguides with the safe method », *5th International Conference on Advances in Mechanical Engineering and Mechanics, Hammamet (Tunisia)*, 6 pages.

**Leparoux, D., L. Laguerre, F. Treyssède, P. Côte et V. Ferber (2010) :** « Seismic dispersion analysis feasibility for the subgrade investigation : measurement, experimental and numerical modeling », *Near Surface 2010, 16th European Meeting of Environmental and Engineering Geophysics, Zurich*, 5 pages.

**Benmeddour, F., F. Treyssède et L. Laguerre (2009) :** « Numerical prediction of guided waves interaction with non-axisymmetric cracks in elastic cylinders », *7th International Symposium on Non-Destructive Testing in Civil Engineering, Nantes*, p. 73–78.

**Frikha, A., F. Treyssède et P. Cartraud (2009) :** « Modelling of elastic wave propagation in prestressed helical waveguides », *9th International Conference on Mathematical and Numerical Aspects of Wave Propagation, Pau*, 2 pages.

**Laguerre, L. et F. Treyssède (2009) :** « Some advances towards a better understanding of wave propagation in civil engineering multi-wire strands », *Ultrasonic Wave Propagation in Non Homogeneous Media, Springer Proceedings in Physics*, 128, p. 123–135.

**Treyssède, F. (2008a) :** « Vibroacoustics interface conditions between prestressed structures and moving fluids », *Acoustics'08, Paris*, 6 pages.

**Treyssède, F. et A. Frikha (2008) :** « A semi-analytical finite element method for elastic guided waves propagating in helical structures », *Acoustics'08, Paris*, 5 pages.

**Bériot, H., F. F. Treyssède et M. Ben Tahar (2007) :** « Ducted propagation in the presence of vortical flows using an Eulerian-Lagrangian description », *13th AIAA/CEAS Aeroacoustics Conference, Roma*, 11 pages.

**Basseville, M., F. Bourquin, L. Mevel, H. Nasser et F. Treyssède (2006a) :** « A statistical nuisance rejection approach to handle the temperature effect for monitoring civil structures », *Fourth World Conference on Structural Control and Monitoring, San Diego*, 8 pages.

— **(2006b) :** « Handling the temperature effect in SHM : Combining a subspace-based statistical test and a temperature-adjusted null space », *Proceedings of the Third European Workshop Structural Health Monitoring 2006, Granada (Spain)*, p. 499–506.

— **(2006c) :** « Merging sensor data from multiple temperature scenarios for vibration-based monitoring of civil structures », *Proceedings of the Third European Workshop Structural Health Monitoring 2006, Granada (Spain)*, p. 759–766.

**Treyssède, F. (2006) :** « Numerical and experimental study of the vibrational modes of thermally prestressed and prebent beams », *13th International Congress on Sound and Vibration, Vienna*, 8 pages.

**Ben Tahar, M., G. Gabard et F. Treyssède (2002) :** « A numerical method for vibro-acoustic problems with sheared non-uniform mean flows », *9th International Congress on Sound and Vibration, Orlando*, 8 pages.

**Ben Tahar, M., F. Treyssède et G. Gabard (2002) :** « Sound wave propagation in non-uniform flow using an Eulerian-Lagrangian description », *Theoretical and Computational Acoustics 2001, Beijing (China)*, p. 265–273.

**ACTN**

**Gallezot, M., F. Treyssède et L. Laguerre (2016) :** « Calcul numérique de la réponse élastodynamique forcée des guides d'onde cylindriques ouverts par approche modale », *13ème Congrès Français d'Acoustique, Le Mans*, 6 pages.

**Nguyen, K. L., F. Treysséde, A.-S. Bonnet-BenDhia et C. Hazard (2014b) :** « Modélisation numérique des guides d'onde ouverts : cas des structures élastiques courbes », *12ème Congrès Français d'Acoustique, Poitiers*, 7 pages.

**Frikha, A., F. Treyssède et P. Cartraud (2010a) :** « Modélisation de la propagation des ondes élastiques dans des guides hélicoïdaux soumis à un chargement axial », *10ème Congrès Français d'Acoustique, Lyon*, 4 pages.

**Frikha, A. et F. Treyssède (2008) :** « Propagation d'ondes élastiques dans un guide hélicoïdal par la méthode SAFE », *COTUME'2008, Hammamet (Tunisie)*, 2 pages.

**Treyssède, F. (2007b) :** « Obtention numérique des modes de propagation élastiques dans un guide d'onde hélicoïdal », *18ème Congrès de Mécanique, Grenoble*, 6 pages.

**Ben Tahar, M., G. Gabard et F. Treyssède (2004) :** « FEM method for vibro-acoustic problems with non-potential mean flow », *2nd International Conference on Advances in Mechanical Engineering, Sousse (Tunisie).*

**Treyssède, F. et A. Elhami (2004) :** « Une méthode couplée de sous-structuration dynamique/sous-domaines acoustiques pour des problèmes d'interaction fluide-structure de grandes tailles », *XIVème Colloque de Vibrations, Chocs et Bruit, Écully*, 13 pages.

**Gabard, G., F. Treyssède et M. Ben Tahar (2002) :** « Couplage vibro-acoustique en présence d'un écoulement non uniforme », *6ème Congrès Français d'Acoustique, Lille*, p. 153–157.

**Treyssède, F., G. Gabard et M. Ben Tahar (2002) :** « Présentation et validation numérique d'une méthode d'éléments finis mixtes pour la propagation acoustique en présence d'écoulement non uniforme », *6ème Congrès Français d'Acoustique, Lille*, p. 149–152.

**COM**

**Gallezot, M., F. Treyssède et L. Laguerre (2018b) :** « Imagerie par gradient de défauts abrupts dans les barres enfouies », *Journée thématique GdR MecaWave, Méthodes inverses et imagerie : de la théorie aux applications, Paris.*

— **(2018c) :** « Imagerie rapide de guides d'ondes cylindriques d'accès restreint basée sur un formalisme modal », *1er colloque du GDR MecaWave, Fréjus.*

— **(2018d) :** « Modélisation numérique par approche modale de la propagation et de la diffraction des ondes dans un guide élastique ouvert et localement endommagé », *14ème Congrès Français d'Acoustique, Le Havre.*

**Treyssède, F. (2018) :** « Modélisation numérique des guides d'onde tridimensionnels à section symétrique par rotation », *14ème Congrès Français d'Acoustique, Le Havre.*

**Zhou, C., F. Treyssède et P. Cartraud (2018a) :** « Modélisation numérique de la propagation des ondes guidées dans des milieux périodiques multi-hélicoïdaux », *14ème Congrès Français d'Acoustique, Le Havre.*

— **(2018b) :** « Numerical modeling of elastic guided wave propagation in bi-helical periodic media », *2nd Franco-Chinese Acoustic Conference (FCAC), Le Mans.*

**Nguyen, K. L. et F. Treyssède (2015b) :** « Leaky modes in open elastic waveguides », *1st Leaky Days Workshop, Palaiseau.*

**Treyssède, F. (2015a) :** « Modélisation numérique de la propagation des ondes élastiques guidées dans les câbles hélicoïdaux précontraints », *Journées Techniques Acoustique et Vibrations, Nantes.*

**Masmoudi, M., L. Laguerre et F. Treyssède (2013) :** « Dispersion compensation method for the experimental study of the propagation of elastic guided waves in a cylinder », *12th Anglo French Physical Acoustics Conference, Fréjus.*

**Treyssède, F. (2013) :** « Modèles rapides pour la propagation des ondes mécaniques guidées : vers une application à la prévision des vibrations », *Journées Techniques Acoustique et Vibrations, Blois.*

**Treyssède, F. et L. Laguerre (2013a) :** « Investigation of guided modes in helical structures : understanding wave propagation in civil engineering cables », *12th Anglo French Physical Acoustics Conference, Fréjus.*

**Treyssède, F., K. L. Nguyen, A.-S. Bonnet-BenDhia et C. Hazard (2012) :** « Finite element computation of elastic propagation modes in open stratified waveguides », *7th Meeting of the GDR on Wave Propagation in Complex Media for Quantitative and Non Destructive Evaluation, Saint Pierre d'Oléron.*

**Treyssède, F. et L. Laguerre (2011) :** « Recent progress in modeling the propagation of elastic guided waves in civil engineering cables », *International Symposium in Non Destructive Testing and Evaluation : Physics, Sensors, Materials and Information, Nantes.*

**Frikha, A., F. Treyssède et P. Cartraud (2010c) :** « SAFE modelling of elastic wave propagation in helical waveguides under axial preload », *6th Conference of the GDR 2501 Research on Ultrasound Propagation for NDT jointly with the 10th Anglo French Conference on Physical Acoustics Conference, Lake District (UK).*

**Treyssède, F. (2010a) :** « Hybrid FE-SAFE modelling of elastic wave scattering in curved waveguides », *6th Conference of the GDR 2501 Research on Ultrasound Propagation for NDT jointly with the 10th Anglo French Conference on Physical Acoustics Conference, Lake District (UK).*

**Benmeddour, F., F. Treyssède et L. Laguerre (2008) :** « Numerical study of guided modes scattering by non-axisymmetric cracks in cylinders », *8th Anglo French Physical Acoustics Conference, Arcachon.*

**Ben Tahar, M., F. Treyssède et G. Gabard (2003) :** « Résolution numérique de l'équation de Galbrun », *Troisièmes Journées sur l'Acoustique de Galbrun, La Rochelle.*

**Treyssède, F., G. Gabard et M. Ben Tahar (2001) :** « Validation d'une méthode FEM pour la résolution de l'équation de Galbrun avec des cas semi-analytiques », *Deuxièmes Journées sur l'Acoustique de Galbrun, Arcachon.*

**AFF**

**Gallezot, M., F. Treyssède et O. Abraham (2019) :** « Calcul numérique des modes de galerie d'une sphère solide incluse dans une matrice élastique », *JJCAP 2019 (Journées Jeunes Chercheurs en Acoustique Physique), Paris.*

**Zhou, C., F. Treyssède et P. Cartraud (2018c) :** « Propagation des ondes mécaniques dans des milieux périodiques multi-hélicoïdaux », *Journées du GdR Ondes, Advanced theoretical and numerical methods for waves in structured media, Paris.*

— **(2017) :** « Modélisation numérique de la propagation des ondes guidées dans des câbles multibrins », *JJCAB 2017 (Journées Jeunes Chercheurs en Vibrations, Acoustique et Bruit), Paris.*

# 2

# Activités de recherche

## Sommaire

*Note : pour éviter une redondance avec les articles relatifs à chaque section, j'ai fait le choix de ne pas réintroduire de repères bibliographiques dans le texte. Certaines références seront parfois précisées en note de bas de page, pour une lecture plus facile ou lorsqu'elles n'ont pas été citées dans les articles.*

## 2.1 Introduction

### 2.1.1 Contexte

Les domaines d'applications impliquant des ondes élastiques se propageant dans des structures élancées (plaques, barres, tubes, ...) sont nombreux. On peut citer par exemple l'END (Évaluation Non Destructive), la réduction du bruit et des vibrations, les métamatériaux, l'analyse statistique énergétique (SEA), ... La compréhension des mécanismes de propagation de ces ondes est capitale, en particulier dans les moyennes ou hautes fréquences, lorsque la taille de la structure devient grande par rapport à la longueur d'onde. Une structure élancée peut être considérée comme un guide d'onde, infini dans une ou plusieurs directions. Les ondes guidées ont la particularité de se propager sur de longues distances avec peu de perte d'énergie, ce qui peut constituer un avantage ou bien un inconvénient suivant l'application visée.

Une difficulté liée aux ondes guidées est qu'elles sont de nature multimodale (à une fréquence donnée, plusieurs modes peuvent coexister, chacun se propageant à une vitesse différente) et dispersive (la vitesse de propagation d'un mode donné dépend de la fréquence). Typiquement, ce sont les courbes de dispersion qui permettent d'identifier les modes d'onde qui se propagent dans une plage de fréquences donnée, ou au contraire ne se propagent pas (cas des bandes interdites dans les guides périodiques, par exemple). Ces courbes fournissent la vitesse de phase, la vitesse de groupe ou encore l'atténuation des modes en fonction de la fréquence. Pour les déterminer, des outils de modélisation sont indispensables.

Les travaux de recherche exposés dans ce manuscrit concernent essentiellement le développement de modèles dédiés aux ondes guidées élastiques. Les applications visées concernent principalement l'END pour le génie civil. Elles s'inscrivent dans un contexte où le parc d'ouvrages national est vieillissant, l'urbanisation est en forte évolution et la société aspire à plus de sécurité et de confort. Le développement de méthodes non-destructives pour évaluer l'état de santé des structures devient alors incontournable. L'application phare de mes activités concerne les câbles du génie civil (ponts en particulier). Les câbles ont une géométrie complexe, généralement multi-brins et hélicoïdale, si bien que la modélisation de leur comportement mécanique soulève diverses difficultés.

Rappelons que les méthodes d'END ont pour finalité de caractériser l'état de structures ou de matériaux sans les dégrader, soit au cours de la production, soit en cours d'utilisation, soit dans le cadre d'opérations de maintenance. Les objectifs sont de détecter, localiser et dimensionner d'éventuelles anomalies (fissures, corrosion, ...). Outre le génie civil, de nombreuses industries y font donc appel : aéronautique, aérospatiale, transport, énergie... Les travaux présentés dans

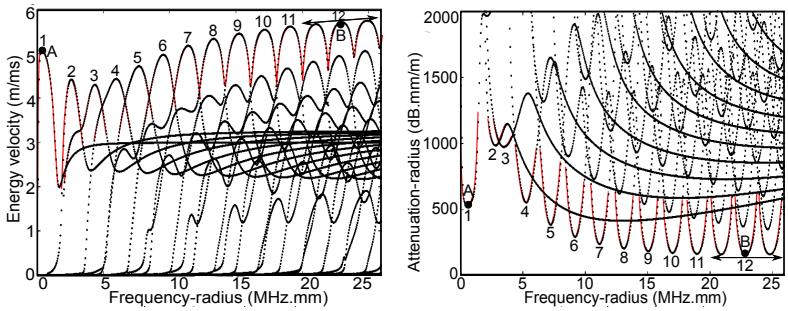


(a) (b)

FIGURE 2.1 – Exemple de courbes de dispersion calculées pour une barre cylindrique enfouie dans un coulis de ciment : (a) vitesse d'énergie, (b) atténuation en fonction de la fréquence.

ce manuscrit sont ainsi susceptibles de trouver des applications dans des secteurs autres que le génie civil. Précisons également que nous utiliserons le terme END pour englober à la fois le CND (Contrôle Non Destrictif) et le SHM (Structural Health Monitoring). Pour faire simple, les objectifs du CND et du SHM tels que nous les définissons ici sont les mêmes, mais les moyens pour y parvenir sont différents : le CND exploite des mesures plutôt ponctuelles dans le temps et nécessite l'intervention d'un opérateur, le SHM exploite des mesures en continu et nécessite des capteurs à demeure.

En génie civil, les structures sont généralement de très grande taille, ce qui limite ou rend coûteuse la mise en œuvre de méthodes pour les ausculter. Les longues distances de propagation des ondes guidées leur confèrent donc un fort potentiel applicatif. Toutefois, l'interprétation et l'exploitation des signaux mesurés se révèlent complexes. Pour faciliter cette tâche et optimiser les techniques d'END, il faut d'abord calculer les courbes de dispersion afin d'identifier les modes "utiles", c'est-à-dire les modes les moins atténués, les moins dispersifs et si possible les plus rapides (voir Figure 2.1). Il est également utile de connaître la sensibilité des modes à une inhomogénéité locale donnée (un type de défaut, par exemple). Pour cela, il est nécessaire de développer des outils de modélisation capables de traiter l'interaction, ou diffraction, des ondes avec cette inhomogénéité.

Pour déterminer les courbes de dispersion, on peut utiliser une approche analytique ou numérique. Une approche analytique ne permet de considérer que des géométries canoniques (plaques, cylindres ou tubes). Mes travaux se sont orientés vers le développement d'outils plus généraux, capables de traiter des géométries de guides complexes, ce qui nécessite la mise en œuvre de méthodes numériques.

Les outils exposés dans ce manuscrit sont principalement basés sur une méthode d'éléments finis permettant le calcul des modes d'onde. Cette méthode consiste à discrétiser uniquement la section du guide tout en décrivant analytiquement la direction de propagation de l'onde dans l'axe. Le maillage éléments finis est donc 2D pour un problème 3D (1D pour un problème 2D), ce qui permet des calculs rapides et hautes fréquences. Elle permet d'étudier des guides ayant une section de forme arbitraire. Cette méthode a été appliquée sous diverses appellations dans la littérature (voir par exemple l'introduction de GALLEZOT, TREYSSÈDE et LAGUERRE 2018 pour une liste non-exhaustive de ces appellations). Dans ce manuscrit, on appellera cette méthode SAFE (Semi-Analytical Finite Element).

La méthode SAFE n'est applicable qu'aux guides d'ondes uniformes. Lorsque les guides sont périodiques, une autre technique d'éléments finis doit être utilisée. Elle consiste à appliquer des

conditions aux limites de type Bloch-Floquet sur la cellule unitaire du problème périodique. Cette seconde approche est souvent appelée WFEM (Wave Finite Element Method) dans la littérature. Elle conduit à un problème aux valeurs propres à résoudre sur un maillage 3D, mais réduit à une seule cellule. J'ai eu parfois recours à cette méthode dans le cadre de mes travaux.

Les développements résumés dans ce manuscrit, théoriques et numériques, tiennent compte de diverses spécificités : courbure du guide, excitation, présence d'une inhomogénéité, pertes par fuite ou viscoélastiques, géométrie multi-brins. Ces cinq aspects sont déclinés tour à tour en différentes sections et forment le plan de ce manuscrit. Pour chacune des sections, j'ai essayé de donner un aperçu synthétique de mes travaux, parfois complémentaire aux publications, ainsi que des perspectives que je souhaiterais explorer dans les années à venir. D'une certaine manière, l'objectif commun à ces sections est de tirer parti du formalisme modal, que ce soit pour l'obtention des courbes de dispersion (réponses libres), le calcul de solutions sous excitation (réponses forcées) ou pour la résolution de problèmes de diffraction (interaction entre ondes et inhomogénéité locale).

Pour clore ce manuscrit, une dernière section résume brièvement les autres activités de recherche que j'ai abordées avant de me focaliser sur les guides élastiques : acoustique en présence d'écoulement, conditions générales de saut, vibrations des structures précontraintes.

### 2.1.2 Formulation SAFE et notations

On rappelle ici brièvement les grandes lignes de l'établissement d'une formulation SAFE. Ceci permet d'introduire la plupart des notations qui seront utilisées dans la suite de ce manuscrit. Pour plus de détails, on pourra consulter les références citées en introduction du papier Treyssède et Laguerre 2013 par exemple.

Soit un guide élastique d'axe droit $z$ et de plan transverse $(x, y)$ (voir Figure 2.2a). La section $S$ du guide dans ce plan peut avoir une forme quelconque. On fait l'hypothèse de petites déformations et petits déplacements. Pour la dépendance harmonique en temps des champs ondulatoires, on adoptera une convention en $\mathrm{e}^{-\mathrm{i}\omega t}$, $\omega$ désignant la pulsation. Les équations d'équilibre de l'élastodynamique s'écrivent :

$$\nabla \cdot \sigma(\mathbf{u}) + \rho\omega^2 \mathbf{u} = \mathbf{f}, \tag{2.1}$$

où $\mathbf{u}$ est le vecteur déplacement, $\sigma(\mathbf{u})$ est le tenseur des contraintes, $\rho$ est la masse volumique et $\mathbf{f}$ est le vecteur des sources volumiques. La relation contrainte-déformation est donnée par : $\sigma(\mathbf{u}) = C : \epsilon(\mathbf{u})$, où $C$ est le tenseur d'ordre 4 des constantes élastiques (complexes pour des matériaux viscoélastiques). La relation déformation-déplacement s'écrit : $\epsilon(\mathbf{u}) = (\nabla\mathbf{u} + \nabla\mathbf{u}^{\mathrm{T}})/2$, où l'exposant T désigne le transposé. On réécrit la relation déformation-déplacement sous la forme suivante :

$$\boldsymbol{\epsilon} = \left(\mathbf{L}_\perp + \mathbf{L}_z \frac{\partial}{\partial z}\right) \mathbf{u}, \tag{2.2}$$

où $\boldsymbol{\epsilon} = [\epsilon_{xx}\ \epsilon_{yy}\ \epsilon_{zz}\ 2\epsilon_{xy}\ 2\epsilon_{xz}\ 2\epsilon_{yz}]^{\mathrm{T}}$ désigne le vecteur déformation. L'opérateur $\mathbf{L}_z$ s'applique uniquement aux termes de dérivées en $z$, tandis que l'opérateur $\mathbf{L}_\perp$ contient tous les autres termes (dont les dérivées selon $x$ et $y$). À titre indicatif, l'expression des opérateurs en coordonnées

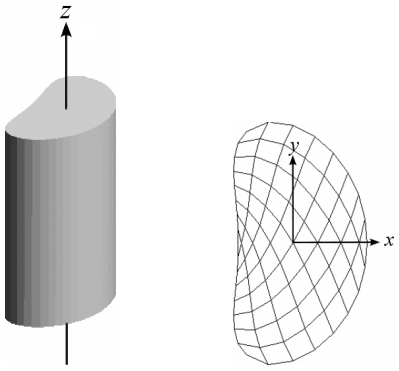


(a) (b)

FIGURE 2.2 – (a) Guide d'onde 3D de section arbitraire, (b) maillage SAFE de la section.

cartésiennes est donnée par :

$$\mathbf{L}_x = \begin{bmatrix} 1 & 0 & 0 \\ 0 & 0 & 0 \\ 0 & 0 & 0 \\ 0 & 1 & 0 \\ 0 & 0 & 1 \\ 0 & 0 & 0 \end{bmatrix}, \ \mathbf{L}_y = \begin{bmatrix} 0 & 0 & 0 \\ 0 & 1 & 0 \\ 0 & 0 & 0 \\ 1 & 0 & 0 \\ 0 & 0 & 0 \\ 0 & 0 & 1 \end{bmatrix}, \ \mathbf{L}_z = \begin{bmatrix} 0 & 0 & 0 \\ 0 & 0 & 0 \\ 0 & 0 & 1 \\ 0 & 0 & 0 \\ 1 & 0 & 0 \\ 0 & 1 & 0 \end{bmatrix}, \tag{2.3}$$

avec $\mathbf{L}_\perp = \mathbf{L}_x \frac{\partial}{\partial x} + \mathbf{L}_y \frac{\partial}{\partial y}$.

La section du guide est discrétisée par éléments finis (voir Figure 2.2b). Le déplacement sur chaque élément s'écrit : $\mathbf{u}^e(x, y, z, \omega) = \mathbf{N}^e(x, y)\mathbf{U}^e(z, \omega)$, où $\mathbf{N}^e(x, y)$ est la matrice des fonctions d'interpolation et $\mathbf{U}^e(z, \omega)$ est le vecteur des déplacements aux nœuds. La discrétisation de la formulation faible associée à l'Équation (2.1) aboutit au système matriciel global suivant :

$$(\mathbf{K}_1 - \omega^2\mathbf{M})\mathbf{U} + (\mathbf{K}_2 - \mathbf{K}_2^{\mathrm{T}})\mathbf{U}_{,z} - \mathbf{K}_3\mathbf{U}_{,zz} = \mathbf{F}, \tag{2.4}$$

avec les matrices élémentaires :

$$\mathbf{K}_1^e = \int_{S^e} (\mathbf{L}_\perp \mathbf{N}^e)^{\mathrm{T}} \mathbf{C} \mathbf{L}_\perp \mathbf{N}^e \mathrm{d}S, \quad \mathbf{K}_2^e = \int_{S^e} (\mathbf{L}_\perp \mathbf{N}^e)^{\mathrm{T}} \mathbf{C} \mathbf{L}_z \mathbf{N}^e \mathrm{d}S, \quad \mathbf{K}_3^e = \int_{S^e} (\mathbf{L}_z \mathbf{N}^e)^{\mathrm{T}} \mathbf{C} \mathbf{L}_z \mathbf{N}^e \mathrm{d}S,$$
$$\mathbf{M}^e = \int_{S^e} \rho \mathbf{N}^{e\mathrm{T}} \mathbf{N}^e \mathrm{d}S, \quad \mathbf{F}^e = \int_{S^e} \mathbf{N}^{e\mathrm{T}} \mathbf{f} \mathrm{d}S. \tag{2.5}$$

La matrice $\mathbf{C}$ est la matrice des constantes élastiques correspondant à la notation de Voigt du tenseur $C$. Selon cette notation, le vecteur des contraintes s'écrit $\boldsymbol{\sigma} = [\sigma_{xx}\ \sigma_{yy}\ \sigma_{zz}\ \sigma_{xy}\ \sigma_{xz}\ \sigma_{yz}]^{\mathrm{T}}$ et est donné par le produit matriciel $\boldsymbol{\sigma} = \mathbf{C}\boldsymbol{\epsilon}$.

L'application d'une transformée de Fourier spatiale dans la direction $z$ à l'Équation (2.4) donne :

$$\left(\mathbf{K}_1 - \omega^2\mathbf{M} + \mathrm{j}k(\mathbf{K}_2 - \mathbf{K}_2^{\mathrm{T}}) + k^2\mathbf{K}_3\right)\hat{\mathbf{U}} = \hat{\mathbf{F}}. \tag{2.6}$$

Ci-dessus, la notation $\hat{(\cdot)}$ désigne la transformée de Fourier définie selon la convention suivante, pour une fonction $g(z)$ donnée :

$$\hat{g}(k) = \int_{-\infty}^{+\infty} g(z)\mathrm{e}^{-\mathrm{j}kz}\mathrm{d}z, \tag{2.7}$$

où $k$ désigne le nombre d'onde axial (dans la direction $z$). Dans l'Équation (2.6), les vecteurs déplacement et force ont donc une dépendance implicite en $k$ et $\omega$ : $\hat{\mathbf{U}} = \hat{\mathbf{U}}(k,\omega)$, $\hat{\mathbf{F}} = \hat{\mathbf{F}}(k,\omega)$.

Le système donné par l'Équation (2.6), quadratique en $k$, peut se transformer sous la forme linéaire :

$$(\mathbf{A} - k\mathbf{B})\mathbf{x} = \mathbf{b}, \tag{2.8}$$

dont un choix possible de vecteurs et matrices est le suivant :

$$\mathbf{A} = \begin{bmatrix} \mathbf{0} & \mathbf{I} \\ -(\mathbf{K}_1 - \omega^2\mathbf{M}) & -\mathrm{j}(\mathbf{K}_2 - \mathbf{K}_2^{\mathrm{T}}) \end{bmatrix}, \quad \mathbf{B} = \begin{bmatrix} \mathbf{I} & \mathbf{0} \\ \mathbf{0} & \mathbf{K}_3 \end{bmatrix}, \quad \mathbf{x} = \begin{bmatrix} \hat{\mathbf{U}} \\ k\hat{\mathbf{U}} \end{bmatrix}, \quad \mathbf{b} = \begin{bmatrix} \mathbf{0} \\ -\hat{\mathbf{F}} \end{bmatrix}. \tag{2.9}$$

La réponse libre (*i.e.* pour $\hat{\mathbf{F}} = 0$) correspond à un problème aux valeurs propres, où $k$ est la valeur propre et la fréquence $\omega$ un paramètre réel (ce problème doit être résolu pour chaque fréquence). Comparé à la forme quadratique donnée par l'Équation (2.6), une forme linéaire en $k$ telle que celle ci-dessus est plus adaptée à une résolution par des solveurs aux valeurs propres. Dans le cadre des travaux exposés dans ce manuscrit, j'ai utilisé la librairie ARPACK, basée sur une méthode d'Arnoldi à redémarrage implicite. Avec cette méthode, l'utilisateur spécifie un nombre de valeurs propres à déterminer ainsi qu'un shift autour duquel ces valeurs propres sont calculées.

On peut remarquer que les matrices $\mathbf{K}_1$, $\mathbf{K}_3$ et $\mathbf{M}$ sont symétriques. De ces symétries résulte la propriété importante suivante : les solutions propres apparaissent en couples de valeurs propres opposées. On notera ces couples $\{k_m, \mathbf{U}_m\}$ et $\{k_{-m}, \mathbf{U}_{-m}\}$ (où $k_{-m} = -k_m$). Dans ce manuscrit, on utilisera l'indice $+m$ (ou $m$ sans signe pour simplifier les notations) pour désigner les modes voyageant dans le sens des $z$ positifs et l'indice $-m$ pour désigner les modes voyageant dans le sens des $z$ négatifs.

Pour des raisons qui seront expliquées ultérieurement, il s'avère important d'introduire à ce stade les vecteurs forces modaux, notés $\mathbf{F}_m$, associés aux vecteurs déplacement modaux $\mathbf{U}_m$. Ces vecteurs sont définis par la relation suivante :

$$\int_S \delta\mathbf{u}^{\mathrm{T}}\mathbf{t}_m \mathrm{d}S = \delta\mathbf{U}^{\mathrm{T}}\mathbf{F}_m, \tag{2.10}$$

où $\mathbf{t}_m = [\sigma_{zx}\, \sigma_{zy}\, \sigma_{zz}]^{\mathrm{T}}$ désigne l'effort imposé sur la section $S$ du guide (de normale unitaire $\mathbf{e}_z$). À partir de cette définition, on peut montrer que la relation qui unit les vecteurs forces aux vecteurs déplacements est la suivante (Treyssède 2011) :

$$\mathbf{F}_m = (\mathbf{K}_2^{\mathrm{T}} + \mathrm{i}k_m\mathbf{K}_3)\mathbf{U}_m. \tag{2.11}$$

Notons qu'une autre façon de considérer le problème aux valeurs propres pourrait être de choisir $\omega$ comme valeur propre et $k$ comme paramètre réel. L'avantage est que le problème est alors directement linéaire (en $\omega^2$), donc plus facile à résoudre. L'inconvénient est que ce point de vue est vibratoire : les modes sont des modes de vibration (au lieu de modes d'onde), plutôt destinés à l'étude de structures finies en régime entretenu. Les informations que contiennent ces modes sont plus difficilement exploitables pour des problèmes de nature ondulatoire (régime transitoire, structures infinies). À titre d'exemple, on voit pas mal comment les modes de vibration pourraient être exploités pour établir des conditions transparentes à un guide d'onde (voir §2.4). Nous laisserons donc de côté le point de vue vibratoire.

## Articles relatifs à cette section

**Gallezot, M., F. Treyssède et L. Laguerre (2018) :** « A modal approach based on perfectly matched layers for the forced response of elastic open waveguides », *Journal of Computational Physics*, 356, p. 391–409.

**Treyssède, F. et L. Laguerre (2013) :** « Numerical and analytical calculation of modal excitability for elastic wave generation in lossy waveguides », *Journal of the Acoustical Society of America*, 133 (6), p. 3827–3837.

**Treyssède, F. (2011) :** « Mode propagation in curved waveguides and scattering by inhomogeneities : Application to the elastodynamics of helical structures », *Journal of the Acoustical Society of America*, 129 (4), p. 1857–1868.

## 2.2 Guides courbes

### 2.2.1 Motivations

Les applications susceptibles d'impliquer structures courbes et propagation d'ondes sont nombreuses. Comme exemple, on peut citer : les plaques circulaires, les tubes toroïdaux, les pneus, les coques cylindriques et sphériques, les barres torsadées, les ressorts, les fibres optiques – et bien sûr les câbles, déjà évoqués en introduction. La littérature concernant la théorie des guides d'ondes élastiques courbes est relativement peu fournie comparée à celle des guides droits.

L'objectif de mes travaux sur les guides courbes est d'étendre les méthodes numériques dédiées au calcul des modes d'onde (*i.e.* SAFE et WFEM), plutôt initialement établies pour les structures droites. En amont de cet objectif, des questions de nature théorique peuvent se poser :

— quels types de structures courbes autorisent l'existence de modes d'onde (c'est-à-dire d'ondes capables de voyager à l'infini sans aucune réflexion) ?
— l'existence de ces ondes dépend-elle de la physique considérée (acoustique, optique, élasticité,...) ?

La réponse à ces questions apparaît triviale dans le cas le plus simple : celui des structures à géométrie circulaire, puisque l'on sait – au moins par expérience – que l'utilisation d'un système de coordonnées cylindriques ou polaires permet une décomposition des solutions aux équations d'ondes en série de Fourier selon la variable azimutale. D'une certaine manière, la réponse apparaît triviale aussi dans le cas le plus compliqué : celui d'une structure dont l'axe décrirait une courbe arbitraire de l'espace (dans ce dernier cas, on sent intuitivement que les ondes tentant de voyager dans une direction donnée seraient partiellement réfléchies dans l'autre direction en raison de la variation arbitraire de la courbure du guide). En revanche, la réponse à ces questions peut sembler moins triviale dans d'autres cas, du moins pour les non-mathématiciens (dont je fais partie), en particulier dans le cas des structures à géométrie hélicoïdale.

*Note : pour expliciter la courbure d'un guide, nous introduisons dans cette section un changement de notation. Un axe courbe sera désigné par la variable $s$ (au lieu de $z$ pour un axe droit).*

### 2.2.2 Invariance

Considérons pour commencer le cas d'un guide uniforme, c'est-à-dire dont la géométrie ne varie pas selon un axe donné. Par définition, les modes d'onde sont des ondes se propageant sans réflexion le long de l'axe de guides infinis (on suppose ici que les guides sont homogènes

selon l'axe). L'évolution axiale de tels modes doit donc être harmonique. En d'autres termes, la dépendance des champs ondulatoires selon la variable $s$ doit être de la forme $e^{\mathrm{i}ks}$.

D'un point de vue mathématique, cette dépendance en $e^{\mathrm{i}ks}$ découle d'une séparation de variables qui est applicable si la propriété fondamentale suivante est vérifiée : les coefficients des équations d'équilibre, y compris les conditions aux limites, ne doivent pas dépendre de $s$. Dans la suite, on qualifiera cette propriété d'*invariance continue*. Techniquement, l'application d'une transformée de Fourier spatiale en $s$ permet alors de remplacer toutes les dérivées $\partial(\cdot)/\partial s$ par des produits $\mathrm{i}k(\cdot)$ dans les équations d'équilibre (sans faire apparaître de produits de convolution).

On montre assez simplement que cette propriété d'*invariance continue* est satisfaite sous trois conditions (Treyssède 2011) :

1. la section transversale du guide n'évolue pas selon l'axe $s$ (condition liée à la géométrie du guide) ;
2. les propriétés physiques du problème (*e.g.* masse volumique, module d'Young, ...) ne dépendent pas $s$ (condition liée à la physique du problème considéré) ;
3. le tenseur métrique ne dépend pas de $s$ (condition liée au système de coordonnées).

Les conditions 1 et 2 sont évidentes. La condition 3 est systématiquement satisfaite pour les guides droits (le tenseur métrique est égal au tenseur identité).

L'ajout de la condition 3 s'avère nécessaire dans le cas des guides courbes, pour lesquels les conditions 1 et 2 ne sont plus suffisantes (pour s'en convaincre, il suffit de penser au cas d'une structure remplissant les conditions 1 et 2 mais dont l'axe décrirait une courbe arbitraire de l'espace, comme évoqué en §2.2.1).

En effet, pour concevoir des modes dans des guides courbes, il faut considérer les équations d'équilibre du problème dans un système de coordonnées curvilignes capable de suivre la géométrie du guide (de manière à ce que la condition 1 puisse être satisfaite). La conséquence de ce changement de système de coordonnées est que les coefficients des équations aux dérivées partielles deviennent fonctions des symboles dits de Christoffel, intrinsèques au système de coordonnées choisi (et dépendants de la courbure de la géométrie). Les symboles de Christoffel, notés $\Gamma^k_{ij}$, sont définis par :

$$\Gamma^k_{ij} = \mathbf{g}_{i,j} \cdot \mathbf{g}^k, \tag{2.12}$$

où les $\mathbf{g}_i$ et $\mathbf{g}^k$ désignent respectivement les vecteurs des bases covariantes et contravariantes du système de coordonnées.

En guise d'exemple, prenons les équations d'équilibre de l'élastodynamique (Équation (2.1)). La courbure de la géométrie nous incite à exprimer les équations d'équilibre selon un système de coordonnées curviligne qui "suit" la géométrie du guide. Sous une forme tensorielle générale, ces équations sont (voir par exemple Treyssède 2008 ; Treyssède et Ben Tahar 2009) :

$$\sigma^{ij}_{,j} + \Gamma^i_{mj}\sigma^{mj} + \Gamma^j_{mj}\sigma^{im} + \rho\omega^2 g^{ij} u_j = f^i, \quad \sigma^{ij} = C^{ijkl}\epsilon_{kl}, \quad \epsilon_{kl} = \frac{1}{2}(u_{k,l} + u_{l,k} - \Gamma^m_{kl}u_m), \tag{2.13}$$

où la convention de sommation d'Einstein a été utilisée et les $i, j = 1, 2, 3$ sont associés aux trois directions curvilignes (la direction axiale $s$ du guide étant la direction 3). Les indices et exposants désignent les composantes covariantes et contravariantes respectivement. L'Équation (2.13) montrent clairement que les coefficients des équations aux dérivées partielles, lorsqu'elles sont exprimées dans un système de coordonnées courbe, dépendent des symboles de Christoffel (en plus des propriétés physiques $\rho$ et $C^{ijkl}$). Ainsi, si les $\Gamma^k_{ij}$ ne dépendent pas de la direction courbe $s$ (la direction 3) alors l'*invariance continue*, et par suite l'existence des modes d'onde, sera préservée dans cette direction. Pour les mathématiciens spécialistes des groupes de symétrie, cette

justification *a posteriori* de l'existence de modes d'onde semblera heuristique[1], mais elle aura peut-être le mérite d'être plus accessible aux non-initiés.

Les symboles de Christoffel peuvent être exprimés uniquement en fonction du tenseur métrique, selon :

$$\Gamma_{ij}^{k} = \frac{1}{2} g^{kl} \left( \frac{\partial g_{jl}}{\partial x^i} + \frac{\partial g_{il}}{\partial x^j} - \frac{\partial g_{ij}}{\partial x^l} \right), \tag{2.14}$$

où $g_{ij} = \mathbf{g}_i \cdot \mathbf{g}_j$ et $g^{ij} = \mathbf{g}^i \cdot \mathbf{g}^j$ désignent les tenseurs métriques covariant et contravariant respectivement. Ce dernier est égal à l'inverse du tenseur métrique covariant. Par conséquent, si $g_{ij}$ ne dépend pas de la variable axiale $s$ (condition 3), alors l'Équation (2.14) montre que les symboles de Christoffel non plus.

À partir de ce cadre théorique relativement général, intéressons-nous au cas hélicoïdal. On peut construire simplement un système hélicoïdal à partir de l'équation paramétrique d'une hélice, dont le vecteur position d'un point est notée $\mathbf{R}(s)$, et de sa base de Serret-Frenet associée, notée $(\mathbf{N}(s), \mathbf{B}(s), \mathbf{T}(s))$ – voir Figure 2.3. Le vecteur position $\mathbf{OM}$ d'un point quelconque de l'espace s'écrit alors (Treyssède 2008) :

$$\mathbf{OM}(x, y, s) = \mathbf{R}(s) + x\mathbf{N}(s) + y\mathbf{B}(s). \tag{2.15}$$

Par définition, les vecteurs de la base covariante sont donnés par :

$$\begin{cases} \mathbf{g}_1 = \frac{\partial \mathbf{OM}}{\partial x} \\ \mathbf{g}_2 = \frac{\partial \mathbf{OM}}{\partial y} \\ \mathbf{g}_3 = \frac{\partial \mathbf{OM}}{\partial s} \end{cases}. \tag{2.16}$$

Le calcul du tenseur métrique conduit alors au résultat suivant (Treyssède 2008 ; Treyssède 2011) :

$$\mathbf{g} = \begin{bmatrix} 1 & 0 & -\tau y \\ 0 & 1 & \tau x \\ -\tau y & \tau x & \tau^2(x^2 + y^2) + (1 + \kappa x)^2 \end{bmatrix}, \tag{2.17}$$

avec la notation $(\mathbf{g})_{ij} = g_{ij}$ et où $\kappa$ et $\tau$ désignent respectivement la courbure et la torsion, toutes deux constantes pour une hélice. Le tenseur métrique $\mathbf{g}$ ne dépend donc pas de $s$. Ceci montre que tout guide hélicoïdal possèdent des modes d'onde (sous réserve que les conditions 1 et 2 soient vérifiées bien entendu), et ce, quelle que soit la physique considérée puisque la condition 3 est de nature purement géométrique (indépendante de la physique).

Quant au calcul numérique de ces modes, il peut être fait par la méthode SAFE (Treyssède 2008) ou la WFEM (Treyssède 2007). Contrairement à la WFEM (voir §2.2.3), la méthode SAFE nécessite toutefois de réécrire les équations d'équilibre dans le système hélicoïdal et les bases associées (covariantes, contravariantes ou Serret-Frenet). On peut cependant remarquer que la méthode SAFE est issue d'une formulation faible si bien que l'effort calculatoire se restreint à l'expression de la relation deformation-déplacement. Une forme forte aurait nécessité des calculs plus lourds, impliquant la divergence d'un tenseur d'ordre deux (celui des contraintes). À titre indicatif, l'expression des opérateurs $\mathbf{L}_\perp$ et $\mathbf{L}_s$ dans l'Équation (2.2) est donnée par (Treyssède

1. La classe de problèmes qui nous intéresse finalement ici est celle des problèmes à *symétrie continue*. Aussi, la définition d'*invariance continue* pourra sembler quelque peu artificielle.

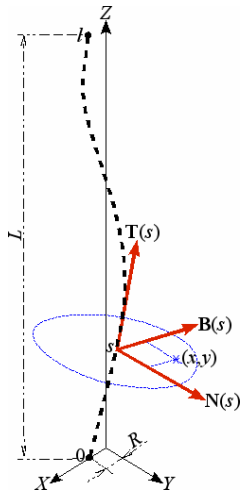


FIGURE 2.3 – Construction d'un système de coordonnées hélicoïdal $(x, y, s)$. Le système cartésien est noté $(X, Y, Z)$. Les paramètres $L = \frac{2\pi\tau}{\kappa^2+\tau^2}$ et $R = \frac{\kappa}{\kappa^2+\tau^2}$ désignent respectivement le pas droit et le rayon de l'hélice. On définit aussi l'angle d'hélice, $\phi = \tan^{-1}(2\pi R/L)$, et le pas selon la direction courbe $s$, $l = \sqrt{L^2 + 4\pi^2 R^2}$.

2011) :

$$\mathbf{L}_\perp = \frac{1}{1+\kappa x}\begin{bmatrix} (1+\kappa x)\partial/\partial x & 0 & 0 \\ 0 & (1+\kappa x)\partial/\partial y & 0 \\ \kappa & 0 & \tau y\partial/\partial x - \tau x\partial/\partial y \\ (1+\kappa x)\partial/\partial y & (1+\kappa x)\partial/\partial x & 0 \\ \tau y\partial/\partial x - \tau x\partial/\partial y & -\tau & -\kappa + (1+\kappa x)\partial/\partial x \\ \tau & \tau y\partial/\partial x - \tau x\partial/\partial y & (1+\kappa x)\partial/\partial y \end{bmatrix}, \quad \mathbf{L}_s = \frac{1}{1+\kappa x}\begin{bmatrix} 0 & 0 & 0 \\ 0 & 0 & 0 \\ 0 & 0 & 1 \\ 0 & 0 & 0 \\ 1 & 0 & 0 \\ 0 & 1 & 0 \end{bmatrix}, \tag{2.18}$$

et l'élément de surface $\mathrm{d}S$ impliqué dans les Eqs. (2.5) est donnée par $\mathrm{d}S = (1+\kappa x)\mathrm{d}x\mathrm{d}y$.

### 2.2.3 Extension au cas périodique

L'approche utilisée précédemment pour des guides uniformes (*invariance continue*) s'étend assez directement aux guides périodiques, pour lesquels la périodicité opère selon une direction courbe.

Considérons un problème régi par un ensemble d'équations aux dérivées partielles dont les coefficients, concaténés sous la forme d'un vecteur $\mathbf{a}(x, y, s)$, sont $\Delta l$-périodiques selon la direction $s$ : $\mathbf{a}(x, y, s + n\Delta l) = \mathbf{a}(x, y, s)$ pour tout entier $n$. Pour faire écho à l'*invariance continue* précédemment définie, on qualifiera cette propriété d'*invariance discrète*[2]. Le théorème de Bloch stipule alors qu'il existe des modes d'onde (ondes de Bloch), c'est-à-dire des solutions de la forme $\psi(x, y, s) = \mathrm{e}^{\mathrm{i}ks}u(x, y, s; k)$ où $k$ est le nombre d'onde et $u(x, y, s; k)$ est une fonction $\Delta l$-périodique selon $s$.

Comme expliqué précédemment, les coefficients $\mathbf{a}$ des équations d'équilibre deviennent dépendants des symboles de Christoffel lorsque la direction $s$ est courbe. Par conséquent, si le tenseur métrique est indépendant de $s$ alors les symboles de Christoffel le seront aussi, ce qui permet de préserver la périodicité des coefficients. On peut donc écrire que la propriété d'*invariance*

2. Bien que, là encore, cette définition d'*invariance discrète* pourra sembler artificielle, puisqu'on devrait plutôt parler de *symétrie discrète*.

*discrète* est satisfaite, et donc l'existence des ondes de Bloch justifiée, sous les trois conditions suivantes :

1. la géométrie de la cellule unitaire est $\Delta l$-périodique selon l'axe $s$ ;
2. les propriétés physiques du problème sont $\Delta l$-périodiques en $s$ ;
3. le tenseur métrique ne dépend pas de $s$.

Remarquons que l'on pourrait aussi considérer le cas d'un tenseur métrique $\Delta l$-périodique en $s$ (plutôt qu'indépendant de $s$) : ce cas ne semble toutefois pas intéressant à première vue puisqu'il correspondrait à un système de coordonnées défini par morceaux de taille $\Delta l$, c'est-à-dire de pas identique à la cellule elle-même (d'une certaine manière, la condition 3 deviendrait donc redondante avec la condition 1).

Intéressons-nous maintenant au cas particulier d'un système de coordonnées permettant de combiner une symétrie hélicoïdale continue et une symétrie de rotation discrète. Cette configuration à double symétrie est fréquemment rencontrée dans les câbles. Un tel système de coordonnées s'obtient à partir de l'Équation (2.15) en opérant le changement de variable polaire $(x, y) = (\rho\cos\theta, \rho\sin\theta)$, ce qui donne :

$$\mathbf{OM}(\rho, \theta, s) = \mathbf{R}(s) + \rho\cos\theta\mathbf{N}(s) + \rho\sin\theta\mathbf{B}(s). \tag{2.19}$$

Par définition, les vecteurs de la base covariante sont :

$$\begin{cases} \mathbf{g}_1 = \frac{\partial \mathbf{OM}}{\partial \rho} \\ \mathbf{g}_2 = \frac{\partial \mathbf{OM}}{\partial \theta} \\ \mathbf{g}_3 = \frac{\partial \mathbf{OM}}{\partial s} \end{cases}. \tag{2.20}$$

Le calcul du tenseur métrique conduit alors au résultat suivant :

$$\mathbf{g} = \begin{bmatrix} 1 & 0 & 0 \\ 0 & \rho^2 & \tau\rho^2 \\ 0 & \tau\rho^2 & \tau^2\rho^2 + (1 + \kappa\rho\cos\theta)^2 \end{bmatrix}. \tag{2.21}$$

On peut constater que $\mathbf{g}$ ne dépend pas de $s$ (l'axe du guide) mais dépend de $\theta$ : la justification de l'existence des ondes de Bloch n'est pas possible dans la direction $\theta$... sauf si l'on annule la courbure ! Le système de coordonnées ainsi défini, $(\rho, \theta, s)$ avec $\kappa = 0$ (mais torsion $\tau$ non nulle), permet d'exploiter la double symétrie, hélicoïdale dans l'axe et de rotation dans la section, présente dans de nombreuses architectures de câbles multi-brins (Treyssède 2019) – voir aussi §2.6.

Enfin, l'extension de ce qui précède aux ondes de Bloch selon deux directions courbes différentes, notées $s_1$ et $s_2$, est immédiate : si $\mathbf{g}$ ne dépend pas des directions courbes $s_1$ et $s_2$, l'existence des ondes de Bloch est justifiée dans ces directions – sous réserve bien entendu que la géométrie de la cellule unitaire et les propriétés physiques du problème soient $(\Delta l_1, \Delta l_2)$-périodiques selon $(s_1, s_2)$. On peut définir un système de coordonnées, dit bi-hélicoïdal, satisfaisant cette propriété. Un tel système se construit en définissant deux directions hélicoïdales $s_1$ et $s_2$, combinaison linéaire des coordonnées $\theta$ et $z$ (voir Figure 2.4), auxquelles on ajoute une troisième direction, la direction radiale $r$ :

$$\begin{cases} r = r \\ \theta = \frac{2\pi}{l_1} s_1 + \frac{2\pi}{l_2} s_2 \\ z = \frac{L_1}{l_1} s_1 + \frac{L_2}{l_2} s_2 \end{cases}, \tag{2.22}$$

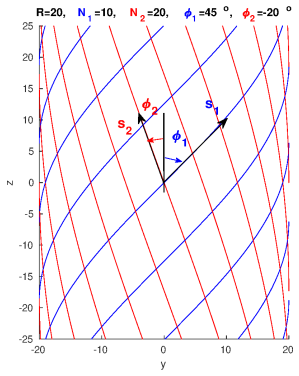


FIGURE 2.4 – Découpage d'une structure cylindrique d'axe $z$ contenant un motif périodique dans deux directions hélicoïcales, notées $s_1$ et $s_2$ (vue 2D).

où $(r, \theta, z)$ désignent les coordonnées cylindriques classiques. Les paramètres $L_1$ et $l_1$ désignent les pas d'hélice selon la direction droite $z$ et la direction courbe $s_1$ respectivement (idem pour $L_2$ et $l_2$, dans la seconde direction hélicoïdale). Le vecteur position d'un point de l'espace s'écrit dans le système cylindrique : $\mathbf{OM} = r\mathbf{e}_r(\theta) + z\mathbf{e}_z$ (avec $\mathbf{e}_r = \mathbf{e}_x \cos\theta + \mathbf{e}_y \sin\theta$). En utilisant l'Équation (2.22), le vecteur position s'expriment en fonction des nouvelles coordonnées $(s_1, s_2, r)$ :

$$\mathbf{OM} = r\cos\left(\frac{2\pi}{l_1}s_1 + \frac{2\pi}{l_2}s_2\right)\mathbf{e}_x + r\sin\left(\frac{2\pi}{l_1}s_1 + \frac{2\pi}{l_2}s_2\right)\mathbf{e}_y + \left(\frac{L_1}{l_1}s_1 + \frac{L_2}{l_2}s_2\right)\mathbf{e}_z. \tag{2.23}$$

Les vecteurs de la base covariante sont donnés par :

$$\begin{cases} \mathbf{g}_1 = \frac{\partial \mathbf{OM}}{\partial s_1} \\ \mathbf{g}_2 = \frac{\partial \mathbf{OM}}{\partial s_2} \\ \mathbf{g}_3 = \frac{\partial \mathbf{OM}}{\partial r} \end{cases}, \tag{2.24}$$

et le calcul du tenseur métrique associé aux nouvelles coordonnées $(s_1, s_2, r)$ aboutit au résultat suivant :

$$\mathbf{g} = \begin{bmatrix} \frac{4\pi^2 r^2 + L_1^2}{l_1^2} & \frac{4\pi^2 r^2 + L_1 L_2}{l_1 l_2} & 0 \\ \frac{4\pi^2 r^2 + L_1 L_2}{l_1 l_2} & \frac{4\pi^2 r^2 + L_2^2}{l_2^2} & 0 \\ 0 & 0 & 1 \end{bmatrix}. \tag{2.25}$$

Ce tenseur métrique est bien indépendant des coordonnées $(s_1, s_2)$. Un tel système de coordonnées permet de traiter des structures de type double armure dans les câbles (voir §2.6.6) ou encore des nanotubes. Ceci fait l'objet d'un article en cours de soumission [3].

Quant au calcul numérique des ondes de Bloch, il peut être effectué par la WFEM, qui consiste à appliquer des conditions de périodicité en déplacement et en force aux frontières de la cellule unitaire. Pour simplifier, prenons le cas où il n'y a qu'une seule direction de périodicité. Les conditions de périodicité relient la frontière "droite" $(s = s_R)$ à la frontière "gauche" $(s = s_L)$ par :

$$u_j|_{s=s_R} = \lambda\, u_j|_{s=s_L}, \quad f^i\big|_{s=s_R} = \lambda f^i\big|_{s=s_L}, \tag{2.26}$$

3. C. Zhou, and F. Treyssède, "Bloch waves in two-directional helical periodic structures," en cours de soumission à International Journal of Solids and Structures

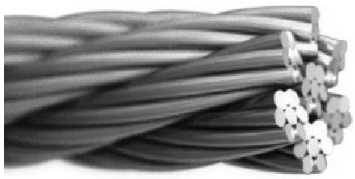

FIGURE 2.5 – Câble constitué d'un ensemble de torons enroulés autour d'une âme centrale.

où $\lambda = \mathrm{e}^{\mathrm{i}k\Delta l}$ définit le nombre d'onde $k$ dans la direction $s$, appartenant à la première zone de Brillouin ($k \in [-\pi/\Delta l, +\pi/\Delta l]$, $\Delta l = s_R - s_L$). Dans le cas où il y a deux directions de périodicité, on ajoute des conditions similaires dans la seconde direction plus un traitement particulier aux "coins" de la cellule (comme fait classiquement avec la WFEM bi-directionnelle lorsque les directions sont droites [4]).

Contrairement à la méthode SAFE, la WFEM ne nécessite pas de réécrire toutes les équations d'équilibre dans le système de coordonnées courbe. Seules les conditions de périodicité nécessitent une attention particulière, ce qui simplifie considérablement l'implémentation numérique de la méthode. Pour exprimer ces conditions, il suffit de veiller à projeter les composantes des vecteurs déplacement et force dans les bases du système courbe (TREYSSÈDE 2007) : typiquement, les bases covariantes et contravariantes, comme indiqué par l'Équation (2.26). En effet, il faut garder en tête que les équations aux dérivées partielles qui vérifient l'*invariance* sont celles exprimées selon des coordonnées curvilignes. Or, ces équations mettent en jeu des tenseurs dont les composantes sont elles-mêmes exprimées dans les bases associées au système courbe (voir Équation (2.13)).

### 2.2.4 Perspectives

Dans la continuité des travaux exposés dans cette section, on pourra s'intéresser à d'autres géométries courbes, parmi lesquelles il faut noter :

— les géométries sphériques ;
— les géométries en double hélice (*i.e.* à hélice autour d'une autre hélice).

Concernant le premier item, je travaille actuellement sur le développement d'un modèle numérique de guide d'onde sphérique (encadrement en cours d'un post-doctorant). L'objectif est d'étudier le comportement des modes de gallerie lorsqu'une sphère est enfouie dans une matrice solide, puis à terme, d'exploiter ces modes pour mesurer les déformations d'un matériau.

Quant au second item, il est motivé par sa quasi-omniprésence dans les câbles. En effet, ceux-ci sont souvent constitués par un ensemble de torons enroulés autour d'une âme centrale. Or, ces torons sont eux-mêmes des assemblages de brins métalliques enroulés hélicoïdalement autour d'un brin central (voir Figure 2.5). Ainsi, la géométrie de ce dernier est à simple hélice tandis que celles des brins périphériques est à double hélice. L'objectif est ainsi d'aller progressivement vers des architectures de câbles de plus en plus complexes (voir aussi §2.6.6). Soulignons toutefois que le tenseur métrique d'un système de coordonnées associé à une double hélice doit *a priori* dépendre de la coordonnée axiale $s$ : dans l'Équation (2.17), il faut imaginer que $\kappa$ et $\tau$ ne seront plus constants mais dépendront de $s$. Il n'existerait donc pas à proprement parler de modes d'onde dans une telle structure. Le traitement de cette configuration géométrique nécessitera sans doute une adaptation des outils de modélisation, voire certaines approximations.

4. R. S. Langley, "A Note On The Force Boundary Conditions For Two-Dimensional Periodic Structures With Corner Freedoms," Journal of Sound and Vibration, vol. 167, pp. 377–381, 1993.

**Tirés à part :**

— Treyssède 2011 (voir page 78) ;
— Treyssède 2019 (voir page 168).

## Articles relatifs à cette section

**Treyssède, F. (2019) :** « Free and forced response of three-dimensional waveguides with rotationally symmetric cross-sections », *Wave Motion*, 87, p. 75–91.

**Treyssède, F. (2011) :** « Mode propagation in curved waveguides and scattering by inhomogeneities : Application to the elastodynamics of helical structures », *Journal of the Acoustical Society of America*, 129 (4), p. 1857–1868.

**Treyssède, F. et M. Ben Tahar (2009) :** « Jump conditions for unsteady small perturbations at fluid-solid interfaces in the presence of initial flow and prestress », *Wave Motion*, 46 (2), p. 155–167.

**Treyssède, F. (2008) :** « Elastic waves in helical waveguides », *Wave Motion*, 45 (4), p. 457–470.

— **(2007) :** « Numerical investigation of elastic modes of propagation in helical waveguides », *Journal of the Acoustical Society of America*, 121 (6), p. 3398–3408.

## 2.3 Guides excités

### 2.3.1 Motivations

Le calcul des modes à chaque fréquence aboutit au tracé des courbes de dispersion, c'est-à-dire au tracé des propriétés modales (vitesse de phase, de groupe, atténuation...) en fonction de la fréquence. Ces courbes permettent d'identifier les modes qui se propagent dans une plage de fréquences donnée avec une faible dispersion et une faible atténuation. Elles représentent la réponse libre du système, indépendante de l'excitation. Cependant, il est aussi nécessaire de déterminer et de contrôler les amplitudes de chaque mode excité par une source donnée (réponse forcée). Une telle information permet de déterminer les modes les plus excitables et d'optimiser le type et l'emplacement des capteurs à utiliser.

L'amplitude des modes peut être élégamment calculée en tirant parti de relations d'orthogonalité (plus précisément, de biorthogonalité dans le cas de l'élasticité). Pour les guides élastiques, on peut trouver plusieurs formes de relations de biorthogonalité. Celles-ci seront brièvement discutées en §2.3.3. L'une des plus utilisées dans les problèmes d'excitation est peut-être la relation de Auld *complexe*, bien que son domaine d'application soit limité aux nombres d'onde réels uniquement (modes purement propagatifs, non atténués axialement). Or, l'atténuation axiale, que représente la partie imaginaire du nombre d'onde, constitue une propriété modale essentielle. Dans le contexte de l'END, elle permet d'identifier les modes susceptibles de voyager le plus loin.

Pour obtenir les atténuations modales, il est nécessaire de prendre en compte les pertes se produisant dans un guide. On peut distinguer deux grands types de pertes :

— les pertes intrinsèques aux matériaux constitutifs du guide (pertes viscoélastiques) ;
— les pertes se produisant dans un guide ouvert, c'est-à-dire plongé dans un milieu environnant non borné (pertes par rayonnement ou fuite).

L'objectif principal de mes travaux sur l'excitation des guides élastiques pourrait se résumer ainsi : identifier, ou du moins clarifier, la relation de biorthogonalité "générale" de laquelle peut découler toutes les autres. Par "générale", on entend en particulier :

— applicable en présence de constantes élastiques complexes ;
— applicable en présence de couches parfaitement adaptées (PML) ;
— applicable en anisotropie complète.

Le premier item autorise les pertes viscoélastiques, le second les pertes par rayonnement (voir §2.5). Quant au troisième, il est motivé par l'analyse des guides hélicoïdaux, dont la courbure induit une forme d'anisotropie de nature géométrique (voir 2.3.4).

### 2.3.2 Biorthogonalité générale

Comme point de départ, on peut exploiter la forme discrète des équations d'équilibre plutôt que leur forme continue. Cette forme discrète est typiquement obtenue par une méthode numérique (SAFE en l'occurrence). Ceci permet de calculer sans difficulté la réponse forcée d'un guide dans un cas très général. La relation d'orthogonalité obtenue, discrète mais "générale", fait intervenir les vecteurs propres à droite et à gauche du système aux valeurs propres. Les vecteurs à gauches sont différents de ceux à droite, d'où le terme de biorthogonalité.

Moyennant quelques manipulations, on montre que la relation de biorthogonalité discrète peut s'écrire sous la forme suivante (Treyssède et Laguerre 2013) :

$$\frac{\mathrm{i}\omega}{4}(\mathbf{U}_m^{\mathrm{T}}\mathbf{F}_{-n} - \mathbf{U}_{-n}^{\mathrm{T}}\mathbf{F}_m) = Q_{m,-m}\delta_{mn}, \tag{2.27}$$

et que la réponse forcée dans la direction des $z$ positifs peut s'exprimer ainsi :

$$\mathbf{U} = \sum_{m=1}^{M} \mathbf{E}_m \hat{\mathbf{F}}(k_m) e^{\mathrm{i}k_m z}, \tag{2.28}$$

où la matrice $\mathbf{E}_m$ est donnée par :

$$\mathbf{E}_m = \frac{\mathrm{i}\omega}{4Q_{m,-m}} \mathbf{U}_m \mathbf{U}_{-m}^{\mathrm{T}}. \tag{2.29}$$

La matrice $\mathbf{E}_m$ peut s'interpréter comme la matrice d'excitabilité du mode $m$. En effet, $(\mathbf{E}_m)_{ij}$ représente l'amplitude de déplacement du mode $m$ à son degré de liberté $i$ lorsqu'une force unitaire agit au degré de liberté $j$. Dans les Équations (2.28) et (2.29), $z$ est supposé supérieur à la position de la source (on suppose que l'excitation $\mathbf{F}$ est nulle en dehors d'un intervalle de $z$ fini) et la somme ne retient que les modes voyageant dans la direction des $z$ positifs (les $m$ sont en fait des $+m$, mais on a supprimé les $+$ pour ne pas alourdir les notations). La solution vers les $z$ négatifs s'obtient en intervertissant les indices $m$ et $-m$ dans les Équations (2.28) et (2.29) et en remplaçant i par $-$i dans l'Équation (2.29).

L'introduction du vecteur force modal $\mathbf{F}_m$, défini par l'Équation (2.10), permet une réécriture immédiate de ces résultats sous forme continue. Ainsi, l'Équation (2.27) correspond en fait à la version discrète de la relation de biorthogonalité suivante :

$$Q_{m,-n} = \frac{\mathrm{i}\omega}{4} \int_S (\mathbf{u}_m \cdot \mathbf{t}_{-n} - \mathbf{u}_{-n} \cdot \mathbf{t}_m) \mathrm{d}S = 0 \text{ si } m \neq n. \tag{2.30}$$

L'Équation (2.28) s'expriment sous la forme continue :

$$\mathbf{u} = \sum_{m=1}^{M} \frac{\mathrm{i}\omega \int_S \mathbf{u}_{-m} \cdot \hat{\mathbf{f}}(k_m) \mathrm{d}S}{4Q_{m,-m}} \mathbf{u}_m e^{\mathrm{i}k_m z}, \tag{2.31}$$

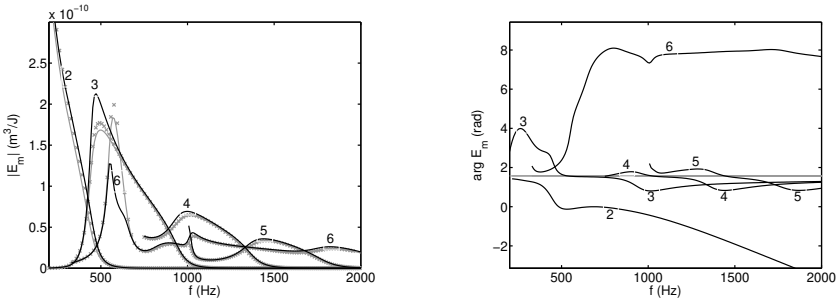


(a) (b)

FIGURE 2.6 – Courbes d'excitabilité calculées pour un milieu stratifié à perte : (a) module, (b) argument. Traits noirs : excitabilité basée sur Auld *réelle*, traits gris : approximation basée sur Auld *complexe* (croix grises : résultats analytiques calculés par le logiciel DISPERSE).

et la matrice d'excitabilité $\mathbf{E}_m$ donne lieu au tenseur d'ordre 2 suivant :

$$\mathbf{e}_m = \frac{\mathrm{i}\omega}{4Q_{m,-m}} \mathbf{u}_m \otimes \mathbf{u}_{-m}. \tag{2.32}$$

L'Équation (2.30) n'est autre qu'une réécriture sous une forme légèrement différente de la relation de Auld *réelle* : $Q_{m,n} = 0$ si $m \neq -n$. De manière surprenante, la relation de Auld *réelle* a parfois été utilisée pour résoudre des problèmes de diffraction, mais pas pour résoudre des problèmes d'excitation (à ma connaissance du moins).

Soulignons qu'aucune hypothèse particulière sur le milieu n'a été formulée pour aboutir à ces résultats. Les expressions restent donc valables pour des modes non propagatifs, des guides à pertes, en anisotropie complète. En particulier, les équations demeurent applicables si l'on introduit une PML, ce qui permet de calculer numériquement la réponse forcée de guides ouverts (GALLEZOT, TREYSSÈDE et LAGUERRE 2018) – voir §2.5. Notons aussi que les Équations (2.29) et (2.32) généralisent les expressions de l'excitabilité modale, initialement définies pour des guides sans perte. Un exemple de résultat est donné en Figure 2.6.

La seule propriété sous-jacente utilisée pour aboutir aux formules ci-dessus est que les solutions propres doivent apparaître en couples ayant des nombres d'onde opposés, $\{k_m, \mathbf{u}_m\}$ et $\{-k_m, \mathbf{u}_{-m}\}$. Cette propriété découle de la symétrie de la matrice des constantes élastiques $\mathbf{C}$, toujours satisfaite, qui se traduit par la symétrie des matrices $\mathbf{K}_1$ et $\mathbf{K}_3$ avec une méthode SAFE (symétrie déjà évoquée en §2.1.2).

Lorsqu'une symétrie de rotation dans la section du guide est prise en compte – qu'elle soit continue (axisymétrie) ou discrète (périodicité circulaire) – les couples opposés sont de la forme : $\{k_m^{(n)}, \mathbf{u}_m^{(n)}\}$ et $\{-k_m^{(n)}, \mathbf{u}_{-m}^{(-n)}\}$, où les exposants $(\pm n)$ désignent l'ordre circonférentiel des modes. Les modes doivent donc être appariés en considérant à la fois des directions axiales opposées et des sens de rotation opposés (TREYSSÈDE 2019).

### 2.3.3 Dégénérescence aux relations de biorthogonalité usuelles

#### Relation de Auld *complexe*

Considérons d'abord le cas particulier des modes propagatifs dans des guides sans perte, c'est-à-dire à nombres d'onde réels. Dans ce cas, les égalités suivantes s'appliquent (TREYSSÈDE et LAGUERRE 2013) :

$$\mathbf{u}_{-m} = \mathbf{u}_m^*, \quad \mathbf{t}_{-m} = \mathbf{t}_m^*, \tag{2.33}$$

où, dans l'ensemble de ce manuscrit, le $*$ désignera le conjugué non transposé. L'Équation (2.30) dégénère ainsi à la relation de Auld *complexe* :

$$\frac{i\omega}{4}\int_S (\mathbf{u}_m \cdot \mathbf{t}_n^* - \mathbf{u}_n^* \cdot \mathbf{t}_m) dS = 0 \text{ si } m \neq n. \tag{2.34}$$

Dans ce cas, on a $Q_{m,-m} = P_{m,m}$, c'est-à-dire que le facteur de normalisation $Q_{m,-m}$ est égale à la puissance $P_{m,m}$ du mode $m$. Dans le cas de modes non propagatifs (évanescents ou inhomogènes), la puissance $P_{m,m}$ est nulle. Une normalisation de ces modes basée sur Auld *complexe* n'est donc pas applicable. À l'inverse, le facteur de normalisation $Q_{m,-m}$ tel que défini par l'Équation (2.30) reste toujours non nul.

### Relation de Fraser

Considérons maintenant le cas de matériaux orthotropes, dont les normales aux plans de symétrie coïncident avec les axes du système de coordonnées. Dans ce cas, on peut montrer les égalités suivantes (voir §2.3.4) :

$$\mathbf{u}_{-m_\perp} = -\mathbf{u}_{m_\perp}, \quad u_{-m_z} = u_{m_z}, \tag{2.35}$$

et :

$$\mathbf{t}_{-m_\perp} = \mathbf{t}_{m_\perp}, \quad t_{-m_z} = -t_{m_z}, \tag{2.36}$$

où l'indice $\perp$ désigne ici les composantes perpendiculaires à l'axe $z$ du guide.

Par ailleurs, on peut écrire l'Équation (2.30) sous la forme : $Q_{m,-n} + Q_{m,n} = 0$ si $m \neq \pm n$. Cette dernière conduit, en tenant compte des Équations (2.35) et (2.36), à la relation suivante (Treyssède 2015) :

$$\int_S (\mathbf{u}_{n_\perp} \cdot \mathbf{t}_{m_\perp} - u_{m_z} t_{n_z}) dS = 0 \text{ si } m \neq \pm n. \tag{2.37}$$

Cette relation correspond à la relation de biorthogonalité de Fraser [5], initialement obtenue pour les ondes de Lamb. Cette relation reste applicable pour un milieu à perte mais ne l'est plus dès lors que l'axe d'isotropie est incliné (fibres non parallèles ni perpendiculaires à $z$). Cette limitation peut être incompatible dans le cas des guides courbes pour lesquels une forme d'anisotropie de nature géométrique est induite.

### Relation de Herrera

Considérons enfin le cas particulier des ondes de surface se propageant dans un milieu stratifié semi-infini. L'intégrale impliquée dans l'Équation (2.30) devient alors une intégrale de la forme $\int_0^\infty (\cdot) dx$ où $x$ désigne la profondeur du milieu ($x = 0$ étant la surface libre). Par ondes de surface, on entend ici ondes décroissantes dans la direction de la profondeur (ondes piégées), ce qui exclut les modes à fuite et les modes de rayonnement (sinon les champs ne seraient pas intégrables en l'état – voir §2.5). La relation correspondante est celle de Herrera [6], relativement connue dans le milieu de la géophysique semble-t-il. Cette relation permet de calculer explicitement les contributions des ondes de Love et de Rayleigh aux fonctions de Green de milieux stratifiés.

5. W. B. Fraser, "Orthogonality relation for the Rayleigh-Lamb modes of vibration of a plate," J. Acoust. Soc. Am., vol. 59, no. 1, pp. 215–216, 1976.

6. I. Herrera, "On a method to obtain a Green's function for a multi-layered half-space," Bull. Seismol. Soc. Am., vol. 54, pp. 1087–1096, 1964.

Remarquons toutefois que la relation de Herrera est généralement appliquée dans le cas de milieux isotropes, pour lesquels finalement la relation de Fraser s'applique aussi.

Pour terminer, soulignons que la relation de biorthogonalité "générale" donnée par l'Équation (2.30) est clairement moins commode d'utilisation que ses congénères (Auld *complexe* et Fraser) car elle nécessite d'apparier les modes opposés, ce qui d'un point de vue numérique nécessite une implémentation plus lourde (sachant que l'utilisation seule de la propriété $k_{-m} = -k_m$ n'est pas satisfaisante en raison de l'imprécision numérique des solutions). Ceci explique peut-être aussi pourquoi cette relation est assez peu utilisée dans la littérature.

### 2.3.4 Anisotropie et courbure

Tout d'abord, montrons les égalités données par les Eqs. (2.35). On considère un guide droit et un milieu orthotrope. Un matériau orthotrope a trois plans de symétrie, orthogonaux. Le système de coordonnées, orthonormé, est tel que les trois axes coïncident avec les normales des trois plans de symétrie, si bien que la matrice $\mathbf{C}$ s'écrit :

$$\mathbf{C} = \begin{bmatrix} C_{11} & C_{12} & C_{13} & 0 & 0 & 0 \\ C_{12} & C_{22} & C_{23} & 0 & 0 & 0 \\ C_{13} & C_{23} & C_{33} & 0 & 0 & 0 \\ 0 & 0 & 0 & C_{44} & 0 & 0 \\ 0 & 0 & 0 & 0 & C_{55} & 0 \\ 0 & 0 & 0 & 0 & 0 & C_{66} \end{bmatrix}. \tag{2.38}$$

Partitionnons le vecteur déplacement $\mathbf{U}$ impliqué dans le système aux valeurs propres correspondant à l'Équation (2.6), ainsi que le vecteur déformation impliqué dans l'Équation (2.2), selon :

$$\mathbf{U} = \begin{bmatrix} \mathbf{U}_\perp \\ \mathbf{U}_z \end{bmatrix}, \quad \boldsymbol{\epsilon} = \begin{bmatrix} \boldsymbol{\epsilon}_1 \\ 2\epsilon_{xy} \\ \boldsymbol{\epsilon}_3 \end{bmatrix}, \tag{2.39}$$

où $\mathbf{U}_z$ contient l'ensemble des composantes de déplacement selon $z$ aux nœuds, $\mathbf{U}_\perp$ contient toutes les autres composantes (celles selon $x$ et $y$), et avec les notations $\boldsymbol{\epsilon}_1 = [\epsilon_{xx}\, \epsilon_{yy}\, \epsilon_{zz}]^{\mathrm{T}}$, $\boldsymbol{\epsilon}_3 = [2\epsilon_{xz}\, 2\epsilon_{yz}]^{\mathrm{T}}$.

Selon ce partitionnement, $\mathbf{L}_\perp$, $\mathbf{L}_z$, $\mathbf{C}$ et la matrice des fonction d'interpolation $\mathbf{N}^e$ ont les structures creuses suivantes :

$$\mathbf{L}_\perp = \begin{bmatrix} \times & 0 \\ \times & 0 \\ 0 & \times \end{bmatrix}, \quad \mathbf{L}_z = \begin{bmatrix} 0 & \times \\ 0 & 0 \\ \times & 0 \end{bmatrix}, \quad \mathbf{C} = \begin{bmatrix} \times & 0 & 0 \\ 0 & \times & 0 \\ 0 & 0 & \times \end{bmatrix}, \quad \mathbf{N}^e = \begin{bmatrix} \times & 0 \\ 0 & \times \end{bmatrix}. \tag{2.40}$$

À partir de ces expressions et en effectuant les produits impliqués dans les Eqs. (2.5), on peut vérifier que :

$$\mathbf{K}_1 - \omega^2\mathbf{M} + k^2\mathbf{K}_3 = \begin{bmatrix} \times & 0 \\ 0 & \times \end{bmatrix}, \quad \mathbf{K}_2 - \mathbf{K}_2^{\mathrm{T}} = \begin{bmatrix} 0 & \times \\ \times & 0 \end{bmatrix}. \tag{2.41}$$

Soit $\{k_m, \mathbf{U}_m\}$ une solution propre du problème, ce que l'on peut écrire :

$$\left( \begin{bmatrix} \times & 0 \\ 0 & \times \end{bmatrix} + \mathrm{i}k_m \begin{bmatrix} 0 & \times \\ \times & 0 \end{bmatrix} \right) \begin{bmatrix} \mathbf{U}_{m_\perp} \\ \mathbf{U}_{m_z} \end{bmatrix} = \begin{bmatrix} \mathbf{0} \\ \mathbf{0} \end{bmatrix}. \tag{2.42}$$

Alors, la structure particulière des matrices ci-dessus permet aussi d'écrire :

$$\left( \begin{bmatrix} \times & 0 \\ 0 & \times \end{bmatrix} - \mathrm{i}k_m \begin{bmatrix} 0 & \times \\ \times & 0 \end{bmatrix} \right) \begin{bmatrix} -\mathbf{U}_{m_\perp} \\ \mathbf{U}_{m_z} \end{bmatrix} = \begin{bmatrix} \mathbf{0} \\ \mathbf{0} \end{bmatrix}, \tag{2.43}$$

ce qui montre que $[-\mathbf{U}_{m_\perp}\ \mathbf{U}_{m_z}]^{\mathrm{T}}$ est le vecteur propre associé à la valeur propre $-k_m$, et donc les égalités de l'Équation (2.35). L'Équation (2.36) découle ensuite de ces égalités, introduites dans la loi de comportement $\boldsymbol{\sigma} = \mathbf{C}\boldsymbol{\epsilon}$. En anisotropie complète, ces propriétés ne sont plus vérifiées car la matrice $\mathbf{C}$ devient dense (la forme de $\mathbf{C}$ dans l'Équation (2.40) ne s'applique plus).

Dans un guide courbe, isotrope ou non, c'est aussi l'opérateur $\mathbf{L}_\perp$ qui est susceptible de devenir dense. Si l'on considère par exemple un guide hélicoïdal (voir Équation (2.18)), alors $\mathbf{L}_\perp$ a la structure suivante, qui diffère de celle de l'Équation (2.40) :

$$\mathbf{L}_\perp = \begin{bmatrix} \times & \times \\ \times & 0 \\ \times & \times \end{bmatrix}, \tag{2.44}$$

si bien que les égalités des Équations (2.35) et (2.36) ne sont pas satisfaites non plus. La relation de Fraser ne s'applique donc pas dans les guides hélicoïdaux même lorsque les matériaux sont isotropes (Treyssède 2019).

En revanche, la relation de Fraser reste applicable dans le cas de guides d'axe circulaire (guides toroïdaux). Pour cela, il suffit de considérer l'Équation (2.18) pour $\tau = 0$ : même s'il est modifié par l'introduction de la courbure ($\kappa \neq 0$), l'opérateur $\mathbf{L}_\perp$ garde la même structure que celui supposé dans l'Équation (2.40).

### 2.3.5 Excitation d'une plaque 3D

Les résultats présentés jusque-là s'appliquent à des guides d'ondes uniaxiaux. Si l'on considère des plaques, cela signifie que ces résultats ne sont applicables que pour une modélisation plane, c'est-à-dire pour des sources qui s'étendent infiniment dans la direction hors plan. Dans ce cas, les ondes guidées ne sont pas atténuées géométriquement lorsqu'elles se propagent.

Une modélisation 3D de plaque nécessite de prendre en compte la dimension finie de l'excitation. Une telle modélisation s'avère plus complexe car l'on doit faire face à une transformée de Fourier inverse bidimensionelle (pour les deux dimensions dans le plan de la plaque). Ceci rend plus difficile l'application de techniques modales et la littérature est moins fournie à ce sujet. On peut trouver des résultats basés sur des hypothèses variant d'un auteur à l'autre (source ponctuelle, isotropie, guides sans perte, champ lointain...) – voir l'article Treyssède 2015 pour davantage de détails.

Je me suis intéressé à l'obtention d'une solution modale permettant la gestion d'une excitation 3D de forme arbitraire, valable pour des guides à perte, en champ lointain comme en champ proche (le champ proche impliquant notamment la contribution des modes évanescents et inhomogènes). La seule hypothèse restrictive adoptée a été celle d'isotropie transverse (axe d'isotropie dirigée selon la normale au plan de la plaque), de manière à ce que les modes ne dépendent pas de l'angle de propagation.

Les développements théoriques ont été conduits sur la base d'une méthode SAFE, pour laquelle les calculs sont rapides puisque seule l'épaisseur de la plaque nécessite d'être discrétisée (éléments finis 1D). Ceci permet aussi de manipuler facilement des matériaux hétérogènes dans l'épaisseur (multi-couches, variation continue, etc.).

La procédure mise en place pour mener à bien les développements conduit à des calculs assez fastidieux, combinaison de plusieurs techniques : changements de base, biorthogonalité de Fraser (puisque l'on est en isotropie transverse), transformées de Hankel inverses d'ordres multiples, puis calcul des résidus correspondant. Au final, la transformée de Fourier inverse bidimensionelle est ainsi remplacée par une double somme de modes : une somme pour les ordres circonférentielles

(selon un angle $\theta$, défini ci-après) et une somme pour les modes de SH-Lamb (indépendant de $\theta$ en raison de l'isotropie).

À titre indicatif, mais pour illustrer la complexité des solutions, prenons le cas particulier d'une source ponctuelle dans le plan $(x, y)$, localisée en $r = 0$ (pour une excitation répartie dans le plan, consulter Treyssède 2015). Le vecteur force discrétisé est alors de la forme suivante :

$$\begin{Bmatrix} \mathbf{F}_x(x,y) \\ \mathbf{F}_y(x,y) \\ \mathbf{F}_z(x,y) \end{Bmatrix} = \delta(x)\delta(y) \begin{Bmatrix} \mathbf{F}_x \\ \mathbf{F}_y \\ \mathbf{F}_z \end{Bmatrix}, \tag{2.45}$$

où l'on a défini les systèmes de coordonnées suivants (voir Figure 2.7) :

— $(x, y, z)$, où $(x, y)$ désignent les coordonnées dans le plan de la plaque (les deux axes de propagation guidée) et $z$ est la direction normale à la plaque (notons ici le changement de convention choisie par rapport à l'ensemble du manuscrit, puisque $z$ ne désigne plus ici l'axe du guide) ;

— $(r, \theta, z)$, où $r$ et $\theta$ sont les coordonnées polaires dans le plan ($x = r\cos\theta$ et $y = r\sin\theta$).

La solution pour ce cas particulier de source est alors donnée par :

$$\begin{Bmatrix} \mathbf{U}_r \\ \mathbf{U}_\theta \\ \mathbf{U}_z \end{Bmatrix} = \left( \sum_{m=1}^{M^L} \begin{bmatrix} \frac{k_m}{2}\mathbf{E}_{m_{x'x'}} \hat{H}_0^{(1)}(k_m r)\cos\theta & \frac{k_m}{2}\mathbf{E}_{m_{x'x'}} \hat{H}_0^{(1)}(k_m r)\sin\theta & \mathrm{i}\frac{k_m}{2}\mathbf{E}_{m_{x'z}} H_1^{(1)}(k_m r) \\ -\frac{k_m}{2}\mathbf{E}_{m_{x'x'}} \frac{H_1^{(1)}(k_m r)}{k_m r}\sin\theta & \frac{k_m}{2}\mathbf{E}_{m_{x'x'}} \frac{H_1^{(1)}(k_m r)}{k_m r}\cos\theta & \mathbf{0} \\ \mathrm{i}\frac{k_m}{2}\mathbf{E}_{m_{zx'}} H_1^{(1)}(k_m r)\cos\theta & \mathrm{i}\frac{k_m}{2}\mathbf{E}_{m_{zx'}} H_1^{(1)}(k_m r)\sin\theta & \frac{k_m}{2}\mathbf{E}_{m_{zz}} H_0^{(1)}(k_m r) \end{bmatrix} \right.$$
$$\left. + \sum_{m=1}^{M^{SH}} \begin{bmatrix} \frac{l_m}{2}\mathbf{E}_{m_{y'y'}} \frac{H_1^{(1)}(l_m r)}{l_m r}\cos\theta & \frac{l_m}{2}\mathbf{E}_{m_{y'y'}} \frac{H_1^{(1)}(l_m r)}{l_m r}\sin\theta & \mathbf{0} \\ -\frac{l_m}{2}\mathbf{E}_{m_{y'y'}} \hat{H}_0^{(1)}(l_m r)\sin\theta & \frac{l_m}{2}\mathbf{E}_{m_{y'y'}} \hat{H}_0^{(1)}(l_m r)\cos\theta & \mathbf{0} \\ \mathbf{0} & \mathbf{0} & \mathbf{0} \end{bmatrix} \right) \begin{Bmatrix} \mathbf{F}_x \\ \mathbf{F}_y \\ \mathbf{F}_z \end{Bmatrix}, \tag{2.46}$$

avec la notation $\hat{H}_0^{(1)}(\cdot) = H_0^{(1)}(\cdot) - \frac{H_1^{(1)}(\cdot)}{(\cdot)}$ et où $k_m$ and $l_m$ désignent les nombres d'onde des modes de Lamb et des modes SH respectivement. Les fonctions $H_0^{(1)}(\cdot)$ et $H_1^{(1)}(\cdot)$ sont les fonctions de Hankel du premier type, respectivement d'ordre 0 et 1. Chacune des composantes des matrices de l'Équation (2.46) implique un produit de trois termes :

— le permier terme, donné par le produit entre $\mathbf{E}_{m_{i'j'}}$ et $\pm\frac{k_m}{2}$ ou $\pm\frac{l_m}{2}$ (éventuellement $\times\mathrm{i}$), peut être interprété comme l'excitabilité à un point source ;

— le deuxième terme, donné par $\hat{H}_0^{(1)}(k_m r)$ ou $\frac{H_1^{(1)}(k_m r)}{k_m r}$, représente le terme propagateur (la dépendance radiale des champs), incluant des effets de champ proche en $1/k_m r$ ;

— le troisième terme représente la directivité du champ (en 1, $\sin\theta$ ou $\cos\theta$).

La matrice $\mathbf{E}_{m_{i'j'}}$ est la matrice d'excitabilité calculée pour une modélisation plane (plaque 2D, d'axe $x'$ et d'épaisseur $z$), donc donnée par l'Équation (2.29). La solution donnée par l'Équation (2.46) fournit ainsi des formules pratiques, faciles à utiliser, permettant d'obtenir les excitabilités d'un modèle 3D de plaque à partir des excitabilités 2D. Dans l'Équation (2.46), la somme se décompose en une somme sur les modes de Lamb (qui satisfont $\mathbf{E}_{m_{y'y'}} = \mathbf{0}$) et une somme sur les modes SH (pour lesquels seule la composante $\mathbf{E}_{m_{y'y'}}$ est non nulle).

L'ensemble des développements et résultats, bien que menés sur la base d'une approche numérique, s'applique bien entendu à une approche purement analytique. Le lien entre forme discrète et forme continue est explicité dans l'article Treyssède 2015.

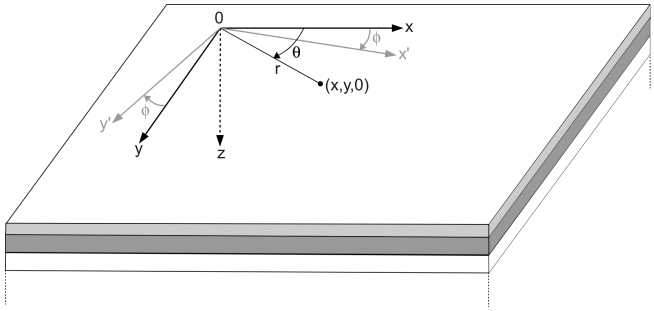


FIGURE 2.7 – Systèmes de coordonnées nécessaires à la modélisation d'une plaque 3D ($z$ désigne ici la direction dans l'épaisseur, $x'$ est la direction de propagation dans le domaine des nombres d'onde).

**Comparaison avec d'autres résultats de la littérature.** Si l'on considère le cas d'un déplacement et d'une force ponctuelle tous deux orientés selon $z$, l'excitabilité issue de l'Équation (2.46) nous donne $\frac{k_m}{2}\mathbf{E}_{m_{zz}}$ pour les modes Lamb (le propagateur étant $H_0^{(1)}(k_m r)$) et $\mathbf{0}$ pour les modes SH. Ce résultat se vérifie si l'on compare la solution de Viktorov [7] (obtenue en modélisation plane) avec celle de Ditri [8].

Si l'on approxime la solution donnée par l'Équation (2.46) en champ lointain, c'est-à-dire avec des propagateurs en $e^{ik_m r}/\sqrt{r}$, on retrouve les excitabilités modales obtenus par Velichko et Wilcox en isotropie transverse [9], à la différence près suivante : nos résultats restent applicables dans le cas de guides à perte et pour n'importe quel type de modes, propagatifs ou non (puisque comme expliqué en §2.3.2, l'excitabilité définie par l'Équation (2.29) ne se limite pas aux modes propagatifs dans les guides sans perte).

Enfin, la solution donnée par l'Équation (2.46) est dans sa totalité en accord avec la solution analytique obtenue par Achenbach dans le cas isotrope [10]. D'une certaine manière, ceci valide nos résultats... mais réciproquement, ceci permet aussi de justifier *a posteriori* la méthode atypique de calcul suivie par Achenbach, qui écrivait lui-même en conclusion de l'un de ses articles [11] : *"As a final note, and in response to comments by a reviewer, I will admit that the methods presented in this paper have not been justified by rigorous mathematical considerations. I would be delighted if a reader of this paper would provide a rigorous methodology to show that the approach is mathematically justifiable, or, alternatively, represents an approximation for which error estimates can be given. Until such a time, I will not totally discard the possibility, perish the thought, that there is no rigorous mathematical justification, even though for some specific cases it has been shown by direct comparison that the correct results are obtained".*

### 2.3.6 Perspectives

Les travaux menés sur la réponse forcée des guides élastiques ouvrent une perspective indirecte dans laquelle je compte m'investir dans les années à venir : le développement de techniques

7. I. A. Viktorov, "Rayleigh and Lamb Waves," Plenum, New York, 1967.
8. J. J. Ditri, "Utilization of guided waves for the characterization of circumferential cracks in hollow cylinders," J. Acoust. Soc. Am., vol. 96, pp. 3769-3775, 1994.
9. A. Velichko and P. D. Wilcox, "Modeling the excitation of guided waves in generally anisotropic multilayered media," J. Acoust. Soc. Am., vol. 121, pp. 60-69, 2007.
10. J. D. Achenbach, "Reciprocity in elastodynamics," Cambridge University Press, Cambridge, 2003.
11. J. D. Achenbach, "Simplifications for the calculation of surface wave pulses generated by laser-irradiation," J. Acoust. Soc. Am., vol. 116, pp. 1481-1487, 2004.

d'imagerie dans les guides d'ondes par méthodes de sensibilité. L'idée est d'exploiter la puissance du formalisme modale pour calculer rapidement des solutions à une excitation donnée. Cette idée a notamment été appliquée pour l'imagerie topologique de plaques [12]. L'imagerie par méthodes de sensibilité s'inscrit dans le cadre des problèmes inverses en élastodynamique. Ce nouvel axe de recherche constituera pour moi une évolution notable de mes activités. Des travaux à ce sujet ont déjà été initiés, lors de l'encadrement de la thèse de Matthieu Gallezot soutenue en 2018 (et dont un chapitre est consacrée à l'imagerie des guides). Ci-dessous, un court paragraphe est consacré à cet axe de recherche pour en expliquer le principe. D'un point de vue stratégique, le développement de méthodes opérationnelles d'imagerie dans les guides représente des enjeux industriels considérables pour l'END dans tous les secteurs : aéronautique, automobile, énergie, industries maritimes...

En marge de ce qui précède, des perspectives plus spécifiques pourraient concerner la modélisation des plaques 3D exposée en §2.3.5. La solution générale obtenue pourrait être exploitée pour traiter des problèmes de diffraction par une inhomogénéité locale (en utilisant un principe de superposition, par exemple). On pourrait aussi s'intéresser à lever l'hypothèse d'isotropie transverse. Toutefois, une généralisation en anisotropie complète nécessitera des calculs de modes fonction de l'angle de propagation, plus lourds d'un point de vue numérique. La réponse impliquera le calcul d'une intégrale complète suivant l'angle de propagation, à approximer par une méthode de quadrature (ou par la méthode de la phase stationnaire si l'on se restreint au champ lointain [13]).

**Imagerie rapide des guides par méthodes de sensibilité (principe)**

L'objectif est de localiser et de caractériser un ou plusieurs défauts présents dans un guide à partir d'une mesure du champ diffracté. Le point de départ consiste à chercher à minimiser la fonctionnelle de coût :

$$j(\mathbf{m}) = \mathrm{J}(\mathbf{u}(\mathbf{m}), \mathbf{m}) = \frac{1}{2} \int_{\mathbb{R}^+} \int_{S_{\mathrm{obs}}} |\mathbf{u}(\mathbf{x}, \mathbf{m}, \omega) - \mathbf{u}_{\mathrm{obs}}(\mathbf{x}, \omega)|^2 \mathrm{d}S_{\mathrm{obs}} \mathrm{d}\omega, \tag{2.47}$$

où $\mathbf{u}_{\mathrm{obs}}$ est le champ mesuré sur une surface d'observation $S_{\mathrm{obs}}$ dans le milieu réel incluant des défauts, $\mathbf{u}(\mathbf{x}, \mathbf{m}, \omega)$ est le champ calculé dans un milieu fictif incluant une répartition arbitraire de défauts caractérisée par un ensemble de paramètres $\mathbf{m}$. La fonctionnelle $j(\mathbf{m})$ traduit donc l'écart entre les deux milieux. Le gradient de la fonctionnelle par rapport à $\mathbf{m}$, $\frac{\delta j}{\delta \mathbf{m}}(\mathbf{x})$, caractérise la sensibilité de la fonctionnelle à l'introduction d'un défaut infinitésimal en un point donné $\mathbf{x}$ du milieu de référence. Si l'on considère ce milieu de référence comme étant l'état sain (sans défaut), le gradient est censé prendre des valeurs importantes à l'emplacement des défauts présents dans le milieu réel. Évalué en chaque point du milieu fictif sain, le gradient peut alors être utilisé comme une fonction d'imagerie dont la représentation spatiale forme une image révélatrice de la position des défauts réels.

La minimisation de la fonctionnelle correspond à un problème d'optimisation sous contraintes (celles de satisfaire les équations d'équilibre du problème, c'est-à-dire ici les équations de l'élastodynamique), si bien que le gradient de la fonctionnelle peut s'exprimer en fonction des champs direct et adjoint. L'obtention du champ direct consiste à simuler la propagation des ondes émises par la source expérimentale dans le milieu sain. L'obtention du champ adjoint consiste à simuler

12. S. Rodriguez, M. Deschamps, M. Castaings, and E. Ducasse, "Guided wave topological imaging of isotropic plates," Ultrasonics, vol. 54, no. 7, pp. 1880–1890, 2014.

13. B. Chapuis, N. Terrien, and D. Royer, "Excitation and focusing of Lamb waves in a multilayered anisotropic plate.," J. Acoust. Soc. Am., vol. 127, no. 1, pp. 198–203, 2010.

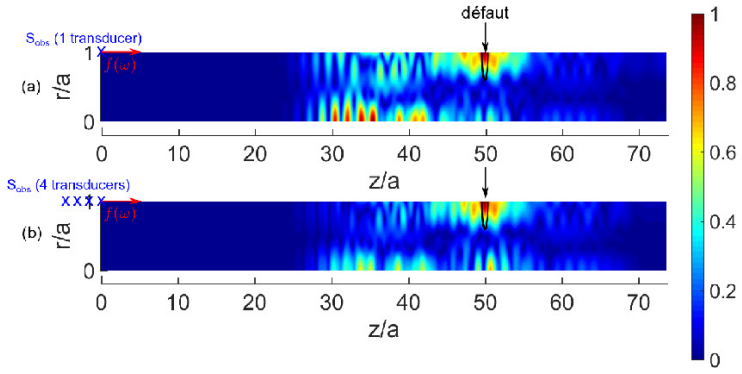


FIGURE 2.8 – Exemple d'image obtenue pour un défaut à la surface d'un guide d'onde cylindrique en backscattering sous excitation multimodale ($a$ désigne le rayon du cylindre), avec un seul récepteur (haut) et quatre récepteurs (bas). Les mesures sont ici synthétiques, calculées grâce à la méthode décrite en §2.4.2.

la propagation des ondes dans ce même milieu mais avec une source en $S_{\text{obs}}$ correspondant au résidu $(\mathbf{u} - \mathbf{u}_{\text{obs}})$ retourné temporellement. Le processus est non-itératif, puisque le calcul du gradient n'est réalisé qu'une fois, à partir de l'état sain. Dans un guide d'onde, ceci permet d'exploiter l'expression donnée par l'Équation (2.28), dont le calcul est très rapide, aussi bien pour le champ direct que le champ adjoint. Un exemple d'image obtenue par cette approche, issue de la thèse de Matthieu Gallezot [14], est donné en Figure 2.8. L'exploitation du formalisme modal nécessite bien sûr de calculer au préalable les modes. Ce calcul peut prendre un certain temps mais il faut garder à l'esprit qu'il n'est réalisé qu'une fois pour toutes (par essence, les modes ne dépendent pas de l'excitation).

**Tirés à part :**

— TREYSSÈDE et LAGUERRE 2013 (voir page 90) ;
— GALLEZOT, TREYSSÈDE et LAGUERRE 2018 (voir page 149) ;
— TREYSSÈDE 2019 (voir page 168).

## Articles relatifs à cette section

**Treyssède, F. (2019) :** « Free and forced response of three-dimensional waveguides with rotationally symmetric cross-sections », *Wave Motion*, 87, p. 75–91.

**Gallezot, M., F. Treyssède et L. Laguerre (2018) :** « A modal approach based on perfectly matched layers for the forced response of elastic open waveguides », *Journal of Computational Physics*, 356, p. 391–409.

**Treyssède, F. (2015) :** « Three-dimensional modeling of elastic guided waves excited by arbitrary sources in viscoelastic multilayered plates », *Wave Motion*, 52, p. 33–53.

**Treyssède, F. et L. Laguerre (2013) :** « Numerical and analytical calculation of modal excitability for elastic wave generation in lossy waveguides », *Journal of the Acoustical Society of America*, 133 (6), p. 3827–3837.

14. Matthieu Gallezot, "Simulation numérique du contrôle non-destructif des guides d'ondes enfouis", Thèse de doctorat de l'École Centrale de Nantes, 2018, 125 p.

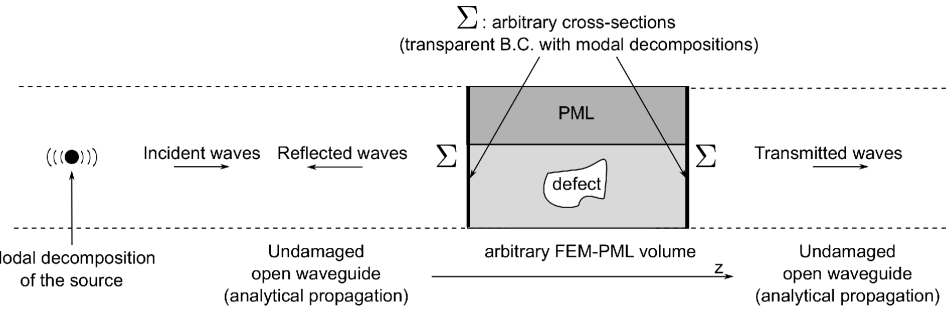


FIGURE 2.9 – Description de l'approche "hybride" (ici, pour un guide ouvert borné par une PML). L'onde incidente est décomposée sur la somme des modes entrants dans le domaine discrétisé par éléments finis, grisé sur le schéma. Les ondes réfléchies et transmises sont décomposées sur la somme des modes sortants de part et d'autre. Les ondes incidentes peuvent éventuellement correspondre à une source localisée à une distance arbitraire de l'inhomogénéité, grâce à la technique de calcul exposée précédemment en §2.3.2.

## 2.4 Guides inhomogènes

### 2.4.1 Motivations

Les travaux évoqués dans les sections précédentes concernaient les guides uniformes, sans inhomogénéités ("défaut"). On s'intéresse dans cette section aux guides présentant une inhomogénéité locale (par exemple, un trou). L'analyse de la diffraction des ondes par une inhomogénéité permet d'évaluer la sensibilité de chaque mode à la présence d'un défaut donné. Du point de vue de la modélisation, des techniques numériques particulières doivent être mise en place, dédiées aux guides d'ondes, en raison du caractère non borné du problème. En effet, une structure uniaxiale infinie comportant une inhomogénéité implique deux guides semi-infinis, de part et d'autre de l'inhomogénéité.

Diverses approches numériques ont été proposées dans la littérature (on pourra consulter BENMEDDOUR, TREYSSÈDE et LAGUERRE 2011 pour un état de l'art non-exhaustif). L'approche que nous avons retenue est une approche dite "hybride", combinant une modélisation aux éléments finis standard autour de l'inhomogénéité (ce qui permet de traiter des formes complexes) et des raccords modaux à chaque extrémité du domaine maillé – voir Figure 2.9. L'objectif est de reproduire des conditions transparentes, c'est-à-dire des conditions aux limites capables de faire sortir les ondes sans réflexion du domaine incluant le défaut. Ceci implique de déterminer d'abord les modes d'onde à chaque extrémité du domaine, modes que nous choisirons de calculer par une méthode numérique (de manière à traiter des sections de forme arbitraire). En cohérence avec les sections précédentes, la méthode numérique retenue pour le calcul des modes sera la méthode SAFE.

Pour les mêmes raisons que celles évoquées dans §2.3.1, j'ai cherché à orienter mes travaux vers une approche qui soit suffisamment "générale", c'est-à-dire restant applicable :

— pour des guides à perte (*i.e.* impliquant des constantes élastiques complexes et/ou des PML) ;
— en configuration anisotrope (ce qui implique en particulier une applicabilité aux guides courbes).

### 2.4.2 Méthode hybride

Pour commencer, donnons le principe de base de la méthode. Un raccordement modal de la solution aux extrémités du domaine, notées $\Sigma$ (voir Figure 2.9), implique d'y décomposer le vecteur déplacement sous la forme de la somme des modes d'onde :

$$\mathbf{u}|_\Sigma = \sum_{n=1}^{\infty} \alpha_n^- \mathbf{u}_n^- + \sum_{n=1}^{\infty} \alpha_n^+ \mathbf{u}_n^+, \tag{2.48}$$

où l'on a distingué les modes entrants des modes sortants du domaine par des exposants $-$ et $+$ respectivement et où les $\alpha_n^\pm$ sont les coefficients modaux associés [15]. En pratique, les sommes infinies sont tronquées. On désignera par $N$ le nombre de modes retenus. Dans un problème de diffraction, les modes entrants $(-)$ sont les modes incidents, dont on connaît l'amplitude : les coefficients $\alpha_n^-$ sont donc supposés connus. En revanche, les modes sortants $(+)$ sont les modes diffractés par l'inhomogénéité : les coefficients $\alpha_n^+$ sont inconnus et doivent être calculés.

Une condition aux limites du domaine qui serait donnée uniquement par l'Équation (2.48) ne serait pas suffisante : une manière quelque peu simpliste d'expliquer les choses (désolé pour les puristes...) serait de dire que l'Équation (2.48) n'impose qu'une "demi-condition" aux limites car seule la moitié des coefficients y est imposée. Il faut donc lui ajouter une autre "moitié" de condition, qui de manière assez intuitive, consiste à effectuer la décomposition modale pour le vecteur contrainte exercée sur l'extrémité :

$$\mathbf{t}|_\Sigma = \sum_{n=1}^{\infty} \alpha_n^- \mathbf{t}_n^- + \sum_{n=1}^{\infty} \alpha_n^+ \mathbf{t}_n^+. \tag{2.49}$$

D'un point de vue numérique, on part du système matriciel usuel correspondant à la discrétisation par éléments finis du domaine (noté $\Omega$) restreint autour de l'inhomogénéité, soit :

$$(\mathbf{K} - \omega^2 \mathbf{M})\mathbf{U} = \mathbf{F}, \tag{2.50}$$

où $\mathbf{K}$ and $\mathbf{M}$ sont les matrices de raideur et masse. $\mathbf{U}$ est le vecteur des degrés de liberté en déplacement du domaine $\Omega$. Partitionnons ce système selon les degrés de liberté placés aux extrémités $\Sigma$ et les degrés de liberté restants (dits "internes") :

$$\mathbf{U} = \begin{Bmatrix} \mathbf{U}_\Sigma \\ \mathbf{U}_I \end{Bmatrix}, \quad \mathbf{F} = \begin{Bmatrix} \mathbf{F}_\Sigma \\ \mathbf{F}_I \end{Bmatrix}, \tag{2.51}$$

où $I = \Omega \backslash \Sigma$. Le vecteur $\mathbf{F}_I$, connu, représente d'éventuelles sources acoustiques situées à l'intérieur du domaine $\Omega$. Les conditions de raccordement, données par les Équations (2.48) et (2.49), prennent alors la forme discrète suivante :

$$\mathbf{U}_\Sigma = \sum_{n=1}^{N} \alpha_n^- \mathbf{U}_n^- + \sum_{n=1}^{N} \alpha_n^+ \mathbf{U}_n^+, \quad \mathbf{F}_\Sigma = \sum_{n=1}^{N} \alpha_n^- \mathbf{F}_n^- + \sum_{n=1}^{N} \alpha_n^+ \mathbf{F}_n^+. \tag{2.52}$$

Au final, on montre que le problème décrit par les Équations (2.50) et (2.52) peut se mettre sous la forme condensée suivante (Treyssède 2011) :

$$\mathbf{G}_u^{+\mathrm{T}}(\mathbf{D}\mathbf{G}_u^+ - \mathbf{G}_f^+)\mathbf{U}^+ = \mathbf{G}_u^{+\mathrm{T}}(\mathbf{G}_f^- - \mathbf{D}\mathbf{G}_u^-)\mathbf{U}^-, \tag{2.53}$$

15. Cette notation des $\pm$ en exposant pour les modes sortants/entrants est à distinguer de celle des $\pm m$ en indice, utilisée pour différencier les modes voyageant vers les $z$ positifs/négatifs.

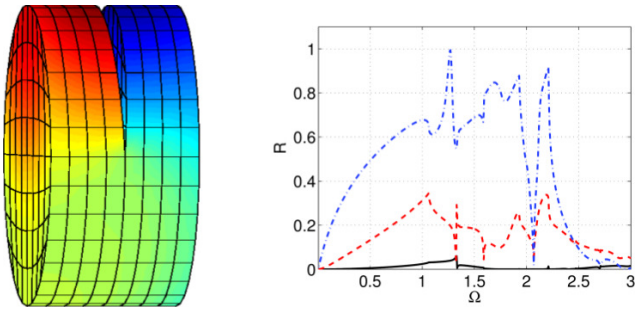


FIGURE 2.10 – À gauche : maillage aux éléments finis utilisé par l'approche hybride (les extrémités à gauche et à droite sont des conditions transparentes) et champ total correspondant à la diffraction du mode longitudinal fondamental (L(0,1)) par un défaut de type fissure dans un cylindre. À droite : coefficients de réflexion en puissance du mode L(0,1) sur lui-même en fonction de la fréquence normalisée et pour différentes profondeurs de défaut (profondeur croissante de la courbe noire à la courbe bleue).

où $\mathbf{D} = \mathbf{K} - \omega^2\mathbf{M}$ et avec les notations :

$$\mathbf{U}^- = \begin{Bmatrix} \boldsymbol{\alpha}^- \\ \mathbf{F}_I \end{Bmatrix}, \mathbf{U}^+ = \begin{Bmatrix} \boldsymbol{\alpha}^+ \\ \mathbf{U}_I \end{Bmatrix}, \mathbf{G}_u^- = \begin{bmatrix} \mathbf{B}_u^- & \mathbf{0} \\ \mathbf{0} & \mathbf{0} \end{bmatrix}, \mathbf{G}_u^+ = \begin{bmatrix} \mathbf{B}_u^+ & \mathbf{0} \\ \mathbf{0} & \mathbf{I} \end{bmatrix}, \mathbf{G}_f^- = \begin{bmatrix} \mathbf{B}_f^- & \mathbf{0} \\ \mathbf{0} & \mathbf{I} \end{bmatrix}, \mathbf{G}_f^+ = \begin{bmatrix} \mathbf{B}_f^+ & \mathbf{0} \\ \mathbf{0} & \mathbf{0} \end{bmatrix}. \tag{2.54}$$

Les vecteurs $\boldsymbol{\alpha}^\pm$ contiennent les coefficients modaux. Les matrices $\mathbf{B}_u^\pm$ and $\mathbf{B}_f^\pm$ contiennent les bases modales en déplacements et forces stockés en colonnes :

$$\mathbf{B}_u^\pm = [\mathbf{U}_1^\pm | \mathbf{U}_2^\pm | ... | \mathbf{U}_N^\pm], \quad \mathbf{B}_f^\pm = [\mathbf{F}_1^\pm | \mathbf{F}_2^\pm | ... | \mathbf{F}_N^\pm]. \tag{2.55}$$

Le système donné par l'Équation (2.53) représente un système linéaire à résoudre pour $\mathbf{U}^+$ à chaque fréquence $\omega$. Ce vecteur solution inclut explicitement les coefficients modaux diffractés, qui ne nécessitent donc aucun post-traitement supplémentaire. Soulignons qu'aucune hypothèse particulière n'a été formulée quant à la nature du guide ou des modes. Ainsi, les décompositions modales peuvent inclure tous les types de modes, y compris non-propagatifs ou atténués, ce qui permet de placer les frontières $\Sigma$ à proximité de l'inhomogénéité : la taille du domaine $\Omega$ à mailler est en pratique relativement petite. La méthode hybride FE-SAFE ainsi présentée s'avère donc à la fois simple à mettre en œuvre et relativement peu coûteuse numériquement. Elle a pu être appliquée à des guides droits comportant des défauts 3D (BENMEDDOUR, TREYSSÈDE et LAGUERRE 2011), des guides courbes (TREYSSÈDE 2011) et des guides à perte (GALLEZOT, TREYSSÈDE et LAGUERRE 2019). Des exemples de résultats sont donnés en Figures 2.10 et 2.11.

### 2.4.3 Discussion

#### Consistance

Le principe de base, qu'il y a dans l'application des Eqs. (2.52) aux extrémités d'un modèle éléments finis, n'est pas novatrice. On peut trouver un certain nombre d'articles, parus dans les années 90 et 2000, qui exploitent cette idée pour résoudre numériquement des problèmes de diffraction dans des guides de type plaque et cylindre (consulter BENMEDDOUR, TREYSSÈDE et LAGUERRE 2011 pour une liste non-exhaustive). Même si ces articles ne fournissent souvent que peu de détails quant à l'implémentation numérique, on peut distinguer deux types : ceux qui utilisent des modes issus d'un calcul analytique, et ceux qui utilisent des modes issus d'un calcul

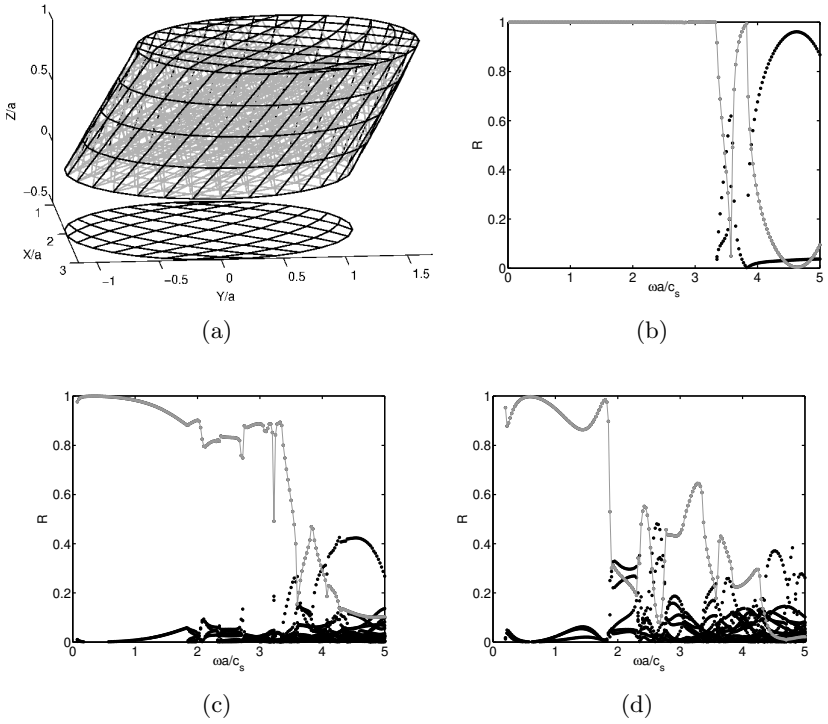


(a) (b)

(c) (d)

FIGURE 2.11 – (a) Maillage d'un guide hélicoïdal d'angle d'hélice $\phi = 30°$ (l'extrémité inférieure représente la condition transparente, l'extrémité supérieure est une condition libre). Coefficients de réflexion en puissance en fonction de la fréquence normalisée obtenus pour le mode L(0,1) incident, réfléchi par l'extrémité libre d'un guide hélicoïdal d'angle d'hélice : (b) $\phi = 0°$, (c) $\phi = 15°$, (d) $\phi = 30°$. La courbe grise correspond à la réflexion du mode sur lui-même, les points noirs représentent les conversions vers d'autres modes.

numérique (type SAFE). Dans le premier cas, les contraintes modales $\mathbf{t}_n^{\pm}$ sont calculées analytiquement puis réintroduite dans le modèle aux éléments finis. Dans le second cas, les contraintes doivent être post-traitées, ce qui peut générer des approximations numériques supplémentaires si l'on n'y prend garde (les contraintes impliquent des dérivées premières du déplacement, et sont donc discontinues d'un élément à l'autre).

Dans les deux cas, se pose la question de la *consistance* des approximations modales du point de vue des éléments finis. Or, il faut souligner ici que les forces modales $\mathbf{F}_n^{\pm}$ impliquées dans l'Équation (2.52) s'obtiennent de manière *consistante* à partir du vecteur déplacement grâce à la formule donnée par l'Équation (2.11). Le terme *consistant* signifie que l'on n'introduit aucune erreur numérique supplémentaire outre celle de l'erreur sur le déplacement lui-même (qui dépend du maillage et de l'ordre de l'interpolation des éléments). Par ailleurs, le maillage SAFE et le type d'éléments utilisés pour le calcul des modes sont choisis comme identiques à ceux de la frontière du domaine $\Omega$ : l'approximation liée au calcul SAFE des déplacements modaux est elle-même *consistante* avec celle des déplacements calculés dans le domaine $\Omega$. Ces remarques ne sont peut-être pas étrangères au fait que la méthode hybride telle que présentée en §2.4.2 fournisse des systèmes matriciels qui semblent bien conditionnés, et ce, quel que soit le nombre de modes retenus dans les décompositions (ceci n'est toutefois qu'un constat empirique, dressé sur les problèmes que j'ai été amené à traiter avec cette méthode).

**Troncature**

La seule erreur non *consistante* introduite par la méthode hybride est celle liée à la troncature des bases modales. Une idée simple pour évaluer *a priori* la contribution d'un mode donnée dans la solution consiste à calculer son atténuation intrinsèque sur une longueur $d$ égale à la distance entre l'inhomogénéité et les extrémités du domaine, c'est-à-dire à calculer l'expression $\mathrm{e}^{-|\mathrm{Im}(k_m^{\pm})d|}$. En dessous d'un seuil (fixé par l'utilisateur), on peut alors décider de négliger ce mode. Cependant, une telle idée ne tient pas compte de l'amplitude effective du mode dans la solution (*i.e.* son coefficient $\alpha_m^{\pm}$). Ceci pose particulièrement problème dans le cas des guides ouverts en raison des modes de rayonnement (voir §2.4.4 et §2.5). Pour évaluer les erreurs de troncature, il semble plus approprié de tirer parti d'un bilan d'énergie *a posteriori* sur la "boîte" correspondant au domaine $\Omega$. Si l'on considère le cas d'un guide fermé élastique (sans perte viscoélastique), alors l'erreur sur le bilan d'énergie peut se calculer simplement (Treyssède 2011) :

$$e = \frac{\mathrm{Re}(\Pi^-) + \mathrm{Re}(\Pi^+)}{\mathrm{Re}(\Pi^-)}, \tag{2.56}$$

où $\Pi^{\pm} = -\mathrm{i}\omega(\mathbf{G}_u^{\pm}\mathbf{U}^{\pm})^{\mathrm{T}*}(\mathbf{G}_f^{\pm}\mathbf{U}^{\pm})/2$ est égal à la puissance complexe totale entrante $(-)$ ou sortante $(+)$, et où le $*$ désigne le conjugué (non transposé). Ces puissances dépendent du nombre de modes retenus. Dans le cas des guides à pertes, le bilan d'énergie est plus compliqué à formuler et quelques développements sont à prévoir (voir §2.4.4).

**Lien avec la biorthogonalité**

L'approche proposée n'utilise *a priori* aucune relation de biorthogonalité, contrairement à une approche de type DtN (Dirichlet-to-Neumann). Cependant, il faut noter que la relation de biorthogonalité de Auld *réelle* intervient *a posteriori* dans l'Équation (2.53) car elle rend symétrique le système à résoudre. En effet, l'Équation (2.27) donne l'égalité suivante pour deux modes sortants $m$ et $n$ (qui voyagent donc dans la même direction) :

$$\mathbf{U}_m^{+\mathrm{T}}\mathbf{F}_n^{+} = \mathbf{U}_n^{+\mathrm{T}}\mathbf{F}_m^{+}, \tag{2.57}$$

ce qui montre que la matrice $\mathbf{B}_u^{+\mathrm{T}}\mathbf{B}_f^{+}$ est symétrique. Par conséquent, la matrice $\mathbf{G}_u^{+\mathrm{T}}(\mathbf{D}\mathbf{G}_u^{+} - \mathbf{G}_f^{+})$ est aussi symétrique. Il faut préciser que cette symétrie découle du choix du champ test suivant (Benmeddour, Treyssède et Laguerre 2011) :

$$\delta\mathbf{U}_\Sigma = \sum_{n=1}^{N} \delta\alpha_n \mathbf{U}_n^{+}. \tag{2.58}$$

D'autres choix seraient possibles, moins judicieux à première vue. Le choix $\delta\mathbf{U}_\Sigma = \sum \delta\alpha_n \mathbf{U}_n^{+*}$ conduirait à une matrice à inverser de la forme $\mathbf{G}_u^{+\mathrm{T}*}(\mathbf{D}\mathbf{G}_u^{+} - \mathbf{G}_f^{+})$. Cette matrice est hermitienne dans le cas sans perte ($\mathbf{D}$ réelle) et à condition de ne garder que les modes propagatifs dans les décompositions (la relation de Auld *complexe* permet de montrer que $\mathbf{B}_u^{+\mathrm{T}*}\mathbf{B}_f^{+}$ est hermitienne). Elle n'a plus aucune propriété de symétrie dès lors que l'on inclut des modes non propagatifs ou que $\mathbf{D}$ devient non hermitienne (cas des guides à pertes).

Un choix de champ test en $\delta\mathbf{U}_\Sigma = \sum \delta\alpha_n \mathbf{U}_n^{-}$ impliquerait une matrice à inverser de la forme $\mathbf{G}_u^{-\mathrm{T}}(\mathbf{D}\mathbf{G}_u^{+} - \mathbf{G}_f^{+})$ [16]. En utilisant l'Équation (2.35), c'est-à-dire sous hypothèse d'orthotropie,

16. $\mathbf{G}_u^{-}$ serait alors défini comme dans l'Équation (2.54) mais en remplacant le $\mathbf{0}$ de la diagonale par la matrice identité.

on peut écrire :

$$\mathbf{U}_m^{-\mathrm{T}}\mathbf{F}_n^{+} = \mathbf{U}_{m_z}^{+\mathrm{T}}\mathbf{F}_{n_z}^{+} - \mathbf{U}_{m_\perp}^{+\mathrm{T}}\mathbf{F}_{n_\perp}^{+}. \tag{2.59}$$

La relation de Fraser (Équation (2.37)) permet de montrer que les termes non diagonaux de $\mathbf{B}_u^{-\mathrm{T}}\mathbf{B}_f^{+}$ (et donc de $\mathbf{G}_u^{-\mathrm{T}}\mathbf{G}_f^{+}$) sont de type antisymétrique. Toutefois, les termes diagonaux sont non nuls. De plus, le terme en $\mathbf{G}_u^{-\mathrm{T}}\mathbf{D}\mathbf{G}_u^{+}$ apparaît sans propriété de symétrie particulière.

#### Puissances croisées

En aparté, précisons que la relation de biorthogonalité de Auld *réelle* ne constitue pas une orthogonalité en terme de puissance. En effet, soit $\Pi = -\frac{\mathrm{i}\omega}{2}\mathbf{U}^{\mathrm{T}*}\mathbf{F}$, la puissance complexe totale associée à un champ solution en déplacement $\mathbf{U} = \sum \alpha_m \mathbf{U}_m$ et en force $\mathbf{F} = \sum \alpha_m \mathbf{F}_m$ (les sommes allant de $-N$ à $N$). Alors, on peut montrer que (Gallezot, Treyssède et Laguerre 2019) :

$$\mathrm{Re}(\Pi) = \sum_{m=-N}^{N} |\alpha_m|^2 P_{m,m} + \sum_{m=-N}^{N}\sum_{n\neq m} \alpha_n^* \alpha_m P_{m,n}, \tag{2.60}$$

où $P_{m,n} = \frac{\mathrm{i}\omega}{4}(\mathbf{F}_n^{\mathrm{T}*}\mathbf{U}_m - \mathbf{U}_n^{\mathrm{T}*}\mathbf{F}_m)$ correspond à la puissance croisée des modes $m$ and $n$. Pour $m = n$, on a $P_{m,m} = \frac{\omega}{2}\mathrm{Im}(\mathbf{U}_m^{\mathrm{T}*}\mathbf{F}_m)$, qui est la puissance réelle du mode $m$. L'expression ci-dessus signifie qu'il n'y a orthogonalité de puissance que si la puissance totale est égale à la somme des puissances individuelles de chaque mode, c'est-à-dire si $P_{m,n} = 0\ \forall m \neq n$. Or, les puissances croisées $P_{m,n}$ sont non nulles sauf lorsque la relation de Auld *complexe* s'applique, c'est-à-dire pour des modes purement propagatifs car dans ce cas : $Q_{m,-n} = P_{m,n} = P_{m,m}\delta_{mn}$ (voir §2.3.3). Dans les guides d'ondes à perte, il n'y a pas d'orthogonalité de puissance car les modes ne sont plus purement propagatifs : $P_{m,n} \neq Q_{m,-n}$ (du moins si l'on excepte le cas particulier des ondes de surface). Il faut donc garder en tête que les puissances croisées sont généralement non nulles. Lorsque ces dernières deviennent significatives, l'interprétation des résultats de l'analyse modale d'un problème de diffraction se complique quelque peu (on parle parfois de *mode coupling*, un exemple est donné dans Gallezot, Treyssède et Laguerre 2019).

### 2.4.4 Perspectives

Avec la méthode hybride proposée, une question essentielle concerne le lien que l'on pourrait établir avec une approche plus rigoureuse de type DtN. Montrer une forme d'équivalence entre les deux approches permettrait de justifier les fondements de cette méthode hybride dans un cadre plus mathématique. À l'inverse, la mise en évidence de différences en montrerait les éventuelles limitations.

Un autre travail consistera à écrire proprement les bilans d'énergie sur la "boîte" représentée par le domaine maillé autour de l'inhomogénéité. Si ce bilan apparaît relativement simple à écrire dans un guide fermé, il l'est peut-être un peu moins dans un guide ouvert traité par des PMLs (les coordonnées deviennent complexes). Comme mentionné précédemment, l'intérêt de calculer ces bilans peut résider dans l'évaluation des erreurs liées aux troncatures modales. Si ces troncatures peuvent être évaluées par un critère *a priori* dans un guide fermé (grâce à la partie imaginaire du nombre d'onde), ce critère n'est plus exploitable en guide ouvert en raison des continua, qui émanent de l'axe réel et donne ainsi naissance à des modes de rayonnement dont l'atténuation peut être très faible mais la contribution négligeable (voir §2.5.4 pour des détails à ce sujet).

Enfin, disposer d'un outil fiable de modélisation des guides inhomogènes s'avère très utile, si ce n'est indispensable, au développement de méthodes d'imagerie (évoquées en §2.3.6). D'une

part, un tel outil permettra de tester la robustesse des méthodes sur des mesures synthétiques, avant application sur des expérimentations réelles. D'autre part, il pourra permettre de tenir compte d'inhomogénéités connues dans les modèles directs (par exemple, des jonctions de guides).

**Tiré à part :** Treyssède 2011 (voir page 78).

## Articles relatifs à cette section

**Gallezot, M., F. Treyssède et L. Laguerre (2019) :** « Numerical modelling of wave scattering by local inhomogeneities in elastic waveguides embedded into infinite media », *Journal of Sound and Vibration*, 443, p. 310–327.

**Benmeddour, F., F. Treyssède et L. Laguerre (2011) :** « Numerical modeling of guided wave interaction with non-axisymmetric cracks in elastic cylinders », *International Journal of Solids and Structures*, 48 (5), p. 764–774.

**Treyssède, F. (2011) :** « Mode propagation in curved waveguides and scattering by inhomogeneities : Application to the elastodynamics of helical structures », *Journal of the Acoustical Society of America*, 129 (4), p. 1857–1868.

## 2.5 Guides ouverts

### 2.5.1 Motivations

Dans le secteur du génie civil, les structures sont souvent enfouies ou noyées, partiellement ou totalement, dans une grande matrice solide (matériau naturel, ciment, ...). À titre indicatif, on peut citer les exemples suivants : tirants d'ancrage, pieux de fondation, câbles de ponts... Ces structures peuvent être vues comme des guides d'ondes élastiques ouverts, c'est-à-dire dont la direction transverse à l'axe du guide est non bornée. Or, comparé aux guides fermés (*i.e.* de section bornée) :

— la distance de propagation des ondes selon l'axe du guide peut être considérablement réduite en raison du rayonnement de l'énergie dans le milieu environnant (on parle de pertes par rayonnement, ou pertes par fuite) ;
— la physique sous-jacente est profondément modifiée.

Dans un guide fermé, on peut distinguer trois catégories de modes : les modes propagatifs, les modes non propagatifs évanescents et les modes non propagatifs inhomogènes. Dans un guide ouvert, les modes sont aussi divisés en trois catégories mais de nature différente : les modes piégés, les modes de rayonnement et les modes à fuite. Les caractéristiques de ces modes seront brièvement rappelées un peu plus loin.

La difficulté majeure de la modélisation numérique des guides ouverts provient du caractère non borné de la section. Cette difficulté est d'autant plus sévère que les modes à fuite ont la particularité de croître à l'infini dans la direction transverse. Pour pallier cette difficulté, plusieurs stratégies sont possibles (consulter par exemple Gallezot, Treyssède et Laguerre 2018 pour une revue des différentes méthodes). Celle que nous avons retenue consiste à remplacer le milieu environnant, supposé homogène, par une couche artificielle absorbante parfaitement adaptée (PML en anglais, pour Perfectly Matched Layer). Cette couche est d'épaisseur finie dans la direction transverse (voir Figure 2.12). La section du guide, désormais bornée, peut alors être traitée par une méthode SAFE (que l'on pourra ainsi désigner SAFE-PML).

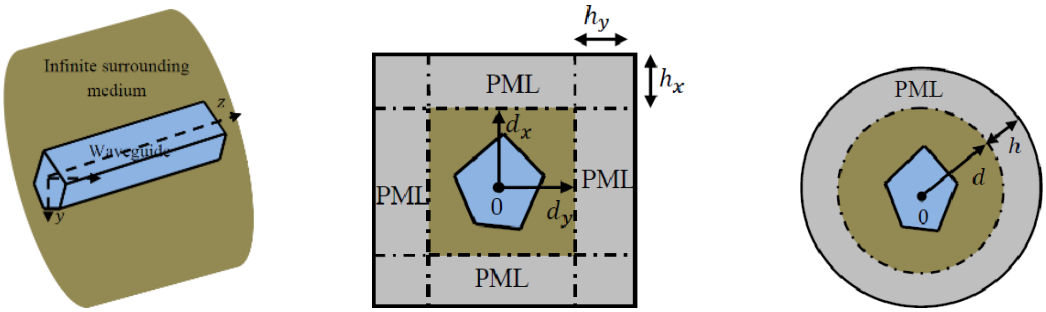


(a) (b) (c)

FIGURE 2.12 – (a) Guide enfoui dans un milieu infini (vue 3D), (b) section du guide avec PML cartésienne tronquée, (c) idem avec PML radiale.

Cette section est de nature moins méthodologique que les précédentes (elle utilise notamment des développements présentées en §2.2, §2.3 et §2.4), si bien qu'une part plus importante est consacrée à la synthèse de résultats de calcul.

Une partie des travaux exposés dans cette section a été réalisée en étroite collaboration avec Anne-Sophie Bonnet-BenDhia et Christophe Hazard du laboratoire POEMS, lors de l'encadrement de la thèse de Khac Long Nguyen (2011-2014) – voir §2.5.2 et §2.5.4. Une autre partie s'est effectuée en collaboration avec Laurent Laguerre de l'Ifsttar, via l'encadrement de la thèse de Matthieu Gallezot (2015-2018) – voir §2.5.3 et 2.5.5.

### 2.5.2 Rappels sur le spectre d'un problème non borné

Nous rappelons ici les caractéristiques des différents modes se produisant dans un guide ouvert en l'absence de PML. L'effet d'une PML sur le spectre sera discuté en §2.5.3.

Le problème posé par les guides ouverts appartient à une famille plus large, celle des problèmes spectraux non bornés. Comme autre exemple de cette famille, on peut citer celui des résonances de cavités ouvertes (dans ce dernier cas, la valeur propre est alors la fréquence). Passons en revue les trois catégories de modes qui se produisent dans un problème non borné, en considérant le cas des guides.

Soient les relations de dispersion : $k^2 + k_{l/s}^2 = \omega^2/c_{l/s}^2$, où $c_l$ et $c_s$ sont respectivement les célérités des ondes de compression et de cisaillement du milieu non borné. Les nombres d'onde $k_l$ et $k_s$ désignent les nombres d'onde transverses de compression et de cisaillement. Pour simplifier, nous supposerons dans ce paragraphe que $c_l$ et $c_s$ sont réelles (le matériau n'est pas viscoélastique).

Les modes de rayonnement ont les caractéristiques suivantes. Ils sont de nature oscillante dans les directions transversales (*i.e.* $k_{l/s} \in \mathbb{R}$). Ils peuvent être oscillants ou évanescents dans la direction axiale du guide ($k$ réel ou bien imaginaire pur). Ces modes constituent un continuum appelé spectre essentiel. Ce continuum est intrinsèque à la nature non bornée de la section et permet de représenter l'ensemble des phénomènes de rayonnement dans le milieu enrobant. Vis-à-vis de l'END, ces modes ne présentent qu'un intérêt très limité car ils "vivent" principalement dans le milieu enrobant.

À l'inverse, les modes piégés sont particulièrement intéressants car ils se propagent suivant l'axe du guide sans s'atténuer ($k \in \mathbb{R}$). Ils décroissent exponentiellement dans la direction transverse ($k_{l/s} \in i\mathbb{R}$). Ces modes sont donc confinés dans la structure guidante (le cœur) ou à l'interface avec le milieu environnant. Les modes piégés constituent un spectre discret, qui peut

être vide. Dans le cas scalaire, les modes piégés existent uniquement si la célérité des ondes dans le cœur est inférieure à celle du milieu environnant. Dans le cas élastique, la situation est plus compliquée. Pour faire simple : à moins que des ondes de Stoneley n'existent à l'interface entre les matériaux, aucun mode piégé n'existe lorsque la vitesse de cisaillement est plus rapide dans le cœur. Une telle configuration est malheureusement fréquente : le matériau constituant le cœur est bien souvent plus raide que le matériau environnant (c'est quasiment toujours le cas pour les structures du génie civil).

Quant aux modes à fuite (leaky en anglais), ils existent quelles que soient les configurations. Leur définition est néanmoins plus délicate. Les modes à fuite constituent un spectre discret, tout comme les modes piégés. Mais ils prennent aussi en compte le rayonnement dans le milieu enrobant, à la manière des modes de rayonnement. Ceci se traduit par une décroissance de type exponentiel selon l'axe du guide... et une croissance exponentielle dans les directions transverses ! Ce comportement inusuel est relativement bien connu en optique, peut-être un peu moins en mécanique. Précisons que les modes à fuite sont bien des solutions des équations d'équilibre de départ. En ce sens, ils sont intrinsèques à la physique. En outre, ces modes donnent accès directement aux informations clés suivantes : l'atténuation et la vitesse des paquets d'onde. Or, ces informations sont "cachées" dans le continuum initial. Une détermination précise des modes à fuite s'avère donc capitale pour l'END des guides ouverts.

En élasticité, on peut aussi distinguer une quatrième classe de modes : les modes à fuite rétrogrades (leaky backward). Ceux-ci ont une vitesse de phase opposée à leur direction de propagation. Contrairement aux modes à fuite, ils s'atténuent à la fois axialement et transversalement. Leur atténuation axiale est généralement importante.

### 2.5.3 Spectre avec PML infinie

Discutons maintenant de la contribution de chaque type de modes à la réponse forcée d'un guide ouvert. L'objectif est de comprendre/clarifier comment les bases modales sont construites, en particulier lorsqu'une PML est introduite. Ceci a été l'objet de l'étude analytique exposée dans Gallezot, Treyssède et Laguerre 2017, dont on rappelle ici les grandes lignes.

Rappelons tout d'abord la situation du problème sans PML. D'un point de vue théorique, l'analyse modale des guides ouverts est relativement bien connue dans la littérature. Leur réponse $u(\mathbf{x},\omega)$ à une excitation peut être décomposée seulement sur les modes piégés et les modes de rayonnement :

$$u(\mathbf{x},\omega) = \sum \text{modes piégés} + \int \text{modes de rayonnement}. \tag{2.61}$$

Les modes à fuite n'apparaissent donc pas dans cette décomposition. Rappelons maintenant l'origine de cette décomposition. Pour simplifier, considérons d'abord le cas de l'équation de Helmholtz 2D avec terme source (équation scalaire). Dans le domaine des nombres d'onde $k$, la solution au problème est une fonction multivaluée dépendant du nombre d'onde transverse $k_\infty$ dans le milieu environnant. En effet, le nombre d'onde transverse est la racine carrée d'un nombre complexe (il vérifie $k_\infty^2 = \omega^2/c_\infty^2 - k^2$, où $c_\infty$ est la célérité des ondes dans le milieu non borné), définie sur deux feuillets de Riemann séparés par une branche de coupure (voir Figure 2.13a). Celle-ci sépare le feuillet de Riemann propre (auquel appartiennent les modes piégés, bornés transversalement) du feuillet de Riemann impropre (auquel appartiennent les modes à fuite, non bornés transversalement), tels que $\mathrm{Im}k_\infty > 0$ et $\mathrm{Im}k_\infty < 0$ respectivement. La transformée de Fourier inverse est intégrée ce qui, après application du théorème des résidus et du lemme de Jordan, fait apparaître la somme discrète de modes piégés et une intégrale contournant la branche de coupure. Pour cela, il faut au préalable choisir un chemin d'intégration dans le plan

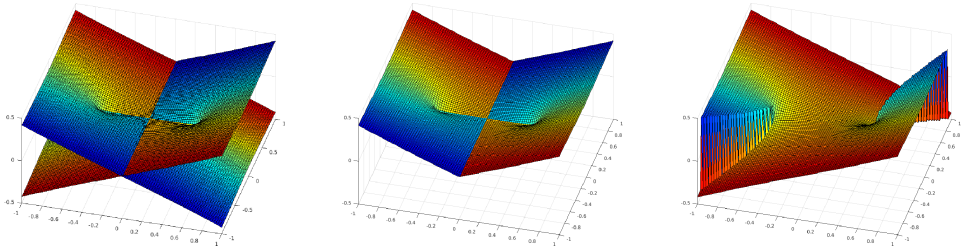

(a) (b) (c)

FIGURE 2.13 – (a) Feuillets de Riemann de la racine carrée $k_\infty$, (b) feuillet propre sans PML ($\operatorname{Im} k_\infty > 0$), (c) feuillet propre avec PML ($\operatorname{Im}(\gamma k_\infty) > 0$). Le plan horizontal est le plan ($\operatorname{Re} k, \operatorname{Im} k$). L'axe vertical correspond à $\operatorname{Im} k_\infty$. Les couleurs correspondent à $\operatorname{Re} k_\infty$ (de bleu à rouge : de négatif à positif).

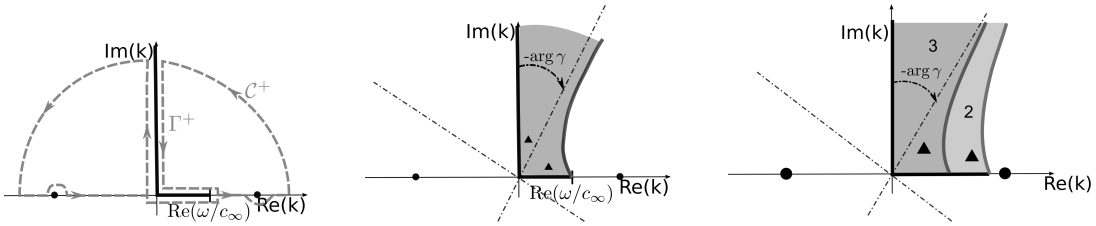


(a) (b) (c)

FIGURE 2.14 – (a) Chemin d'intégration initial (sans PML), (b) rotation de la branche de coupure en présence d'une PML, (c) cas de l'élasticité. Ronds : modes piégés, triangles : modes à fuite.

complexe fermé par un demi-cercle le long duquel l'intégrale doit s'annuler pour un rayon grand (voir Figure 2.14a) : ceci implique en particulier de choisir une intégration sur le feuillet de Riemann propre (voir Figure 2.13b) afin que les termes de l'intégrande, en $\mathrm{e}^{\mathrm{i}kz}$ et $\mathrm{e}^{\mathrm{i}k_\infty x}$, tendent vers zéro sur le demi-cercle d'intégration. L'intégrale de la branche de coupure représente une somme continue, qui s'interprète comme le continuum des modes de rayonnement. Cette intégrale, propre au caractère non borné du problème, est difficile à manipuler mathématiquement et physiquement. Elle peut être approximée analytiquement par une somme discrète sur les modes à fuite, par exemple en utilisant la méthode du col, mais une telle approximation reste fastidieuse.

Considérons maintenant le problème avec une PML, et pour commencer, rappelons le principe de fonctionnement d'une PML en mettant les modes de côté. Le principe de base peut se comprendre facilement dans le cas unidimensionnel. Considérons le cas d'une onde longitudinale se propageant dans la direction $\tilde{x}$ positive. Une telle onde s'exprime sous la forme d'une fonction exponentielle $\exp(\mathrm{i}k_l\tilde{x})$. Cette fonction se prolonge analytiquement à des valeurs complexes de $\tilde{x}$. Au lieu de considérer $x$ réel, on peut choisir un chemin particulier $\tilde{x}(x)$ dans le plan complexe, paramétré par la variable réelle $x$, tel que $\exp(\mathrm{i}k_l\tilde{x})$ décroît exponentiellement lorsque $x$ tend vers $+\infty$. L'application d'une PML consiste donc à prolonger analytiquement les équations d'équilibre initiales du problème à des coordonnées complexes, paramétrées de manière à atténuer les ondes.

Pour simplifier, nous supposons une PML d'épaisseur infinie obéissant au prolongement analytique $\tilde{x} = \gamma x$, où $\gamma$ est une constante complexe. Une tel paramétrage correspond à une fonction

d'absorption constante et une interface avec le milieu physique positionnée en $x = 0$. On peut montrer que le terme de l'intégrande s'écrit alors en $e^{i\gamma k_\infty x}$ (au lieu de $e^{ik_\infty x}$, sans PML). La définition des feuillets de Riemman initiaux est ainsi modifiée en deux feuillets tels que $\mathrm{Im}(\gamma k_\infty) > 0$ (voir Figure 2.13c) et $\mathrm{Im}(\gamma k_\infty) < 0$. Graphiquement dans le plan des nombre d'onde $k$, ceci se traduit par la rotation d'angle $-\arg\gamma$ des branches de coupure (voir Figure 2.14b). Cette rotation permet d'avoir accès à une partie du feuillet de Riemann impropre initial, contenant les modes à fuite. On peut donc dire de manière élégante que la rotation du continuum des modes de rayonnement "dévoile" les modes à fuite [17]. Ainsi, avec une PML d'épaisseur infinie, une somme discrète de modes à fuite apparaît naturellement dans la base modale. Les modes piégés, quant à eux, ne sont pas modifiés par l'introduction de la PML. Par conséquent, la réponse d'un guide ouvert avec une PML infinie s'écrit sous la forme suivante :

$$u(\mathbf{x},\omega) = \sum \text{modes piégés} + \sum \text{modes à fuite dévoilés} + \int \text{modes de rayonnement dans la PML}. \tag{2.62}$$

Ce résultat permet de justifier que les trois types de modes calculés avec une PML infinie forment une base modale. La solution n'est toutefois valable que dans le domaine physique : la décomposition donnée par l'Équation (2.62) ne coïncide avec celle de l'Équation (2.61) qu'à l'extérieur de la PML.

Pour terminer, considérons le cas élastique. Deux continua apparaissent car il y a deux nombres d'onde transverses à considérer dans le milieu non borné : $k_{l/s}$ ($k_{l/s}^2 = \omega^2/c_{l/s}^2 - k^2$). Ceci donne naissance à deux branches de coupure et à quatre feuillets de Riemmann, dont seul l'un constitue le feuillet propre (celui tel que $\mathrm{Im}(\gamma k_l) > 0$ et $\mathrm{Im}(\gamma k_s) > 0$) – voir Figure 2.14c. La décomposition modale des solutions met ainsi en jeu deux continua de modes de rayonnement au lieu d'un seul. Parmi les "bizarreries" que l'on peut constater : l'un des quatre feuillets devient inaccessible par une PML lorsque les célérités des ondes sont réelles ; un autre feuillet, accessible quant à lui, contient les modes à fuite à nombres d'onde transverse longitudinal rentrants (donc dirigés vers le cœur)... Notons que les modes à fuite rétrogrades, mentionnés en fin de §2.5.2, sont situés sur le feuillet propre initial : ces modes particuliers sont donc à inclure dans les sommes discrètes des Équations (2.61) et (2.62).

Pour résumer, les modes à fuite n'appartiennent pas à la base modale initiale du problème, donnée par l'Équation (2.61). L'introduction d'une PML permet de réécrire le continuum des modes de rayonnement comme une somme discrète de modes à fuite dévoilés par la rotation des branches coupures et une somme continue modifiée par cette même rotation. Si l'on néglige cette somme continue, alors on obtient une approximation du continuum des modes de rayonnement par une somme discrète uniquement. En raison de la croissance transverse des modes à fuite, cette approximation n'est valable que sur une région restreinte de l'espace, proche du cœur.

### 2.5.4 Calcul numérique des modes (PML finie)

#### Formulation SAFE-PML

On peut distinguer deux grandes familles de PMLs : les PMLs cartésiennes (voir Figure 2.12b) et les PMLs radiales (voir Figure 2.12c). Soient $(x, y, z)$ et $(r, \theta, z)$ les systèmes de coordonnées cartésien et cylindrique, où $x = r\cos\theta$, $y = r\sin\theta$ ($z$ désigne, comme d'habitude, l'axe du guide). L'application d'une PML cartésienne consiste à prolonger les coordonnées transversales réelles

17. B. Goursaud, Étude mathématique et numérique de guides d'ondes ouverts non uniformes, par approche modale, thèse de doctorat, École Polytechnique X, 2010

$x$ et $y$ en coordonnées complexes $\tilde{x}$ et $\tilde{y}$ selon les changements de variables suivants :

$$\tilde{x}(x) = \int_0^x \gamma_x(\xi)\mathrm{d}\xi, \quad \tilde{y}(y) = \int_0^y \gamma_y(\xi)\mathrm{d}\xi, \tag{2.63}$$

où $\gamma_x(x)$ et $\gamma_y(y)$ sont des fonctions complexes telles que :
— $\gamma_x(x) = 1$ si $|x| \leq d_x$ ; $\gamma_y(y) = 1$ si $|y| \leq d_y$ ;
— $\mathrm{Im}\,\gamma_x > 0$ si $|x| > d_x$ ; $\mathrm{Im}\,\gamma_y > 0$ si $|y| > d_y$.
$d_x$ et $d_y$ sont les positions des interfaces de la PML avec le milieu physique. Du point de vue de la modélisation numérique, il est nécessaire de tronquer la PML à une épaisseur finie. La section du guide dans le plan $(x, y)$, PML tronquée incluse, est alors un rectangle de largeur $L_x = d_x + h_x$ et $L_y = d_y + h_y$, $h_x$ et $h_y$ étant les épaisseurs de la PML selon les directions $x$ et $y$ (voir Figure 2.12b). L'application d'une PML radiale consiste à prolonger la coordonnée radiale réelle $r$ en coordonnée complexe $\tilde{r}$, soit :

$$\tilde{r}(r) = \int_0^r \gamma(\xi)\mathrm{d}\xi, \tag{2.64}$$

où $\gamma(r) = 1$ si $r \leq d$ et $\mathrm{Im}\,\gamma > 0$ si $r > d$. Le paramètre $d$ correspond au rayon de l'interface de la PML avec le milieu physique. La section dans le plan $(x, y)$, PML incluse, correspond à un disque de rayon $R = d + h$, $h$ étant l'épaisseur de la PML (voir Figure 2.12c). Les fonctions d'absorption des PML $(\gamma_x(x), \gamma_y(y))$ ou $\gamma(r)$ sont choisies selon un profil utilisateur – parabolique dans nos travaux – qui dépend de trois paramètres (utilisateurs aussi) : la position de l'interface de la PML $(d_x, d_y)$ ou $d$, l'épaisseur de la PML $(h_x, h_y)$ ou $h$, la moyenne de la fonction d'absorption dans la PML $(\hat{\gamma}_x, \hat{\gamma}_y)$ ou $\hat{\gamma}$.

Les deux types de PMLs ont été implémentés dans des formulations SAFE (Nguyen et Treyssède 2015). À titre d'exemple, prenons le cas d'une PML radiale. Son implémentation dans une formulation variationnelle exprimée en coordonnées cartésiennes nécessite une série de transformations entre différentes coordonnées, qui peut être schématisée comme suit :

$$(\tilde{x}, \tilde{y}, z) \to (\tilde{r}, \theta, z) \to (r, \theta, z) \to (x, y, z). \tag{2.65}$$

Au final, on montre que le système matriciel obtenu garde la même forme que celui d'une formulation SAFE classique (voir §2.1.2), mais où l'expression de l'opérateur $\mathbf{L}_\perp$ dans l'Équation (2.2) est donnée par :

$$\mathbf{L}_\perp = \mathbf{L}_x \left[ \left( \frac{x^2}{\gamma r^2} + \frac{y^2}{\tilde{r} r} \right) \frac{\partial}{\partial x} + \left( \frac{1}{\gamma r^2} - \frac{1}{\tilde{r} r} \right) xy \frac{\partial}{\partial y} \right] + \mathbf{L}_y \left[ \left( \frac{1}{\gamma r^2} - \frac{1}{\tilde{r} r} \right) xy \frac{\partial}{\partial x} + \left( \frac{y^2}{\gamma r^2} + \frac{x^2}{\tilde{r} r} \right) \frac{\partial}{\partial y} \right], \tag{2.66}$$

et l'élément de surface impliqué dans les Eqs. (2.5) est donné par : $\mathrm{d}S = \frac{\tilde{r}\gamma}{r}\mathrm{d}x\mathrm{d}y$.

En présence de PML, les matrices SAFE définies par les Eqs. (2.5) deviennent complexes. Le système aux valeurs propres n'est intrinsèquement plus hermitien. D'un point de vue numérique, la résolution peut donner lieu à des valeurs propres parasites (associées à des grandes valeurs de la norme de la résolvante). Le placement de la PML proche du cœur permet en pratique de limiter ce problème (d'une façon plus intuitive, placer l'interface de la PML proche du cœur permet de limiter la croissance transverse naturelle des modes à fuite). Notons aussi que nous avons fait le choix de fonctions d'absorption indépendantes de la fréquence de manière à éviter un réassemblage des matrices à chaque fréquence.

Par rapport à d'autres stratégies, l'utilisation de PML a plusieurs avantages. Premièrement, la structure du problème aux valeurs propres est préservée. Celui-ci reste de nature linéaire, donc relativement facile à résoudre par des solveurs aux valeurs propres. Deuxièmement, le

calcul des modes à fuite par une PML bénéficie d'une assise mathématique solide dans le cas des problèmes scalaires. Ensuite, une PML permet d'atténuer fortement les ondes sans créer de réflexions artificielles à l'interface (par rapport à d'autres types de couches absorbantes, cette technique permet notamment de réduire l'épaisseur de la couche artificielle). Enfin, la technique est assez simple à implémenter dans un code. Elle est aussi relativement versatile, malgré une limitation qu'il convient de souligner : les PMLs échouent dans le cas où des ondes rétrogrades existent [18]. De telles ondes sont susceptibles de se produire dans des cas anisotropes. Pour éviter ces situations, nous supposerons donc que le milieu où l'on applique la PML, c'est-à-dire l'enrobant, est isotrope (en plus d'être homogène).

Les modes calculés numériquement, avec une PML finie, peuvent être classés en trois grandes familles : les modes piégés, les modes à fuites et les modes de PML (ou modes de Berenger). Ces derniers, comme leur nom l'indique, oscille principalement dans la PML. Les effets d'une PML finie sur ces différentes familles sont discutés plus loin.

#### Principe de fonctionnement d'une PML finie sur les modes piégés et à fuite

On rappelle que les modes à fuites croissent dans la direction transversale ($\operatorname{Im} k_{l/s} < 0$). Ces modes sont donc tels que $\arg k_{l/s} < 0$ (où arg désigne la détermination principale de l'argument, comprise dans l'intervalle $]-\pi, +\pi]$). Reprenons le cas unidimensionel. Dans une PML finie, les modes à fuite seront atténués si $\exp(\mathrm{i}k_l\tilde{x})$ décroît lorsque $x$ augmente. La valeur de cette exponentielle en bout de PML est donnée par $\exp(\mathrm{i}k_l\tilde{L}_x)$, où $\tilde{L}_x$ définit l'épaisseur complexe de la PML :

$$\tilde{L}_x = \int_0^{L_x} \gamma_x(\xi)\mathrm{d}\xi, \tag{2.67}$$

soit $\tilde{L}_x = d_x + h_x\hat{\gamma}_x$. Il y aura donc décroissance en bout de PML si $\arg(k_{l/s}\tilde{L}_x) > 0$, c'est-à-dire $\arg k_{l/s} > -\arg \tilde{L}_x$. Ainsi, augmenter $\arg \tilde{L}_x$ élargira la région du plan complexe où les modes à fuites peuvent être calculés. En notant que $\arg \tilde{L}_x \xrightarrow{h_x\to\infty} \arg \hat{\gamma}_x$, ceci est cohérent avec le résultat obtenu en PML infinie (§2.5.3). L'augmentation de $|\tilde{L}_x|$ n'élargit pas la région de dévoilement mais accroît l'absorption de la PML dans cette région : à partir d'une certaine distance, le champ exponentiellement décroissant devient négligeable si bien que la troncature de la PML n'altère plus significativement le calcul des modes à fuite dévoilés.

Quant aux modes piégés, on rappelle qu'ils décroissent exponentiellement dans la direction transverse ($\operatorname{Re} k_{l/s} = 0$ et $\operatorname{Im} k_{l/s} > 0$). Ces modes sont donc tels que $\arg k_{l/s} = \pi/2$. En présence de PML, les modes piégés resteront donc décroissants transversalement si $\arg \tilde{L}_x < \pi/2$. La PML permettra même d'amplifier artificiellement la décroissance naturelle des modes piégés si $\operatorname{Im}(k_{l/s}\tilde{L}_x) > \operatorname{Im}(k_{l/s}L_x)$, c'est-à-dire $\operatorname{Re}\tilde{L}_x > L_x$ : pour calculer les modes piégés, il est ainsi conseillé d'augmenter la partie réelle de la fonction d'absorption. Ceci n'est pas usuel dans la littérature traitant des PMLs en général (la partie réelle est souvent maintenue à 1). Ceci n'a rien de surprenant non plus, puisqu'augmenter la partie réelle est équivalent à étirer la coordonnée $x$ et donc l'épaisseur réelle de la PML.

#### Résultats principaux

L'influence des paramètres de PMLs finies sur le spectre numérique des modes a été étudiée dans le détail dans les articles Treyssède, Nguyen, Bonnet-BenDhia et Hazard 2014 et

18. Attention à une confusion possible : dans notre cas de figure, le terme rétrograde s'entend dans la direction transverse, et non axiale

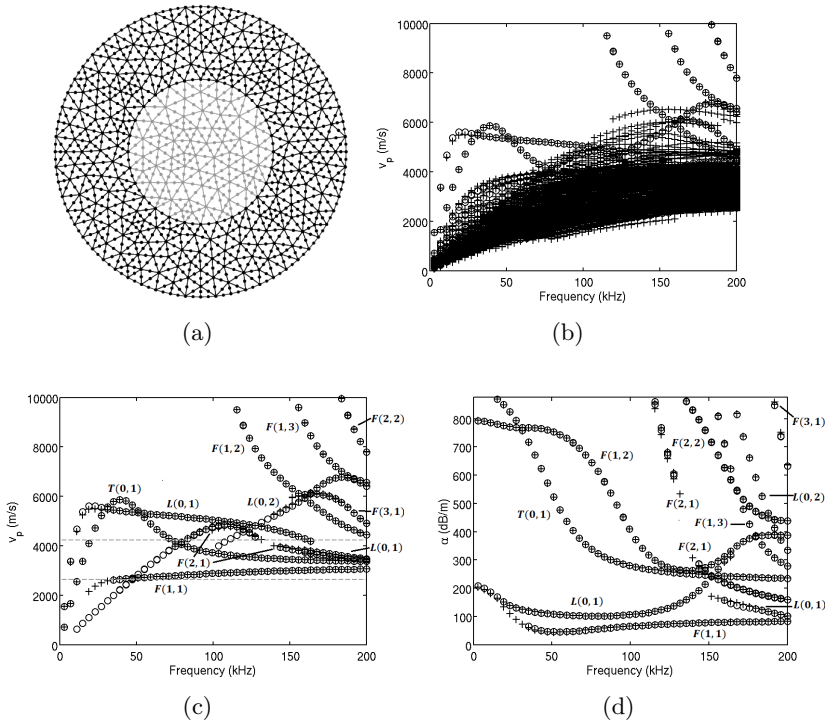


FIGURE 2.15 – Courbes de dispersion calculées pour une barre cylindrique acier enfouie dans du béton. (a) Maillage SAFE avec PML radiale, (b) vitesse de phase sans filtrage, (c) vitesse de phase et (d) atténuation après filtrage des modes de PML. Ronds : PML radiale, croix : PML cartésienne.

NGUYEN, TREYSSÈDE et HAZARD 2015. Diverses expériences numériques ont été réalisées, pour certaines confrontées à des solutions analytiques.

Les résultats obtenus pour les modes à fuite et piégés sont en bon accord avec des résultats de référence issus de la littérature, avec les remarques suivantes :

— une fonction d'absorption parabolique dans la PML donne en général de meilleurs résultats qu'une fonction constante ;
— les PMLs cartésiennes et radiales donnent des résultats ayant une précision du même ordre ;
— un filtrage basé sur l'énergie cinétique s'avère efficace pour éliminer les modes de PML dans la visualisation des courbes de dispersion (voir Figure 2.15).

Concernant les modes de PML :

— ceux-ci appartiennent à deux continua, au lieu d'un seul pour un problème scalaire ;
— ces deux continua sont bien ceux précédemment mentionnés dans le cas d'un milieu élastique (cf. fin de §2.5.3) ;
— la troncature de la section a pour effet de discrétiser ces continua et l'introduction de la PML les fait tourner d'un même angle dans le plan complexe ;
— au-delà d'un certain ordre qui dépend du maillage, les modes de PML d'ordre supérieur divergent des continua en raison de l'approximation éléments finis ;
— la densité modale des continua discrétisés augmente avec le module des épaisseurs complexes, c'est-à-dire ($\tilde{L}_x = d_x + \hat{\gamma}_x h_x, \tilde{L}_y = d_y + \hat{\gamma}_y h_y$) pour une PML cartésienne et $\tilde{R} = d + \hat{\gamma} h$ pour une PML radiale ;

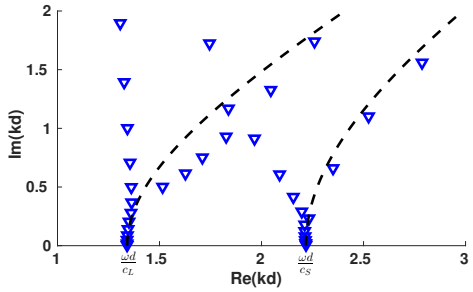


FIGURE 2.16 – Exemple typique de spectre obtenu numériquement pour les modes de PML. Traits pointillés : branches de coupure théoriques, tournées d'un angle égal à l'argument de l'épaisseur complexe de la PML.

— l'angle de rotation des continua s'avère indépendant du profil de la fonction d'absorption.

Ces conclusions sont pour la plupart cohérentes avec les résultats de la littérature traitant des problèmes scalaires (optique, acoustique). Un exemple de spectre est donné en Figure 2.16.

Attardons-nous sur la rotation des continua dans le plan complexe en $\lambda = -k^2$. Dans le cas d'un guide 2D (problème modal 1D, cas des plaques par exemple), chacun des deux continua tend alors asymptotiquement vers une demi-droite. Les deux demi-droites ont des origines différentes, situées en $-\omega^2/c_{l/s}^2$, mais des angles identiques, égaux à $-2\arg\tilde{L}_x$. Le comportement du spectre des modes de PML obtenus pour des guides 3D (problème modal 2D) est sensiblement différent. Avec une PML cartésienne, chaque continuum ne tend plus vers une demi-droite mais vers un secteur angulaire, délimité par deux demi-droites d'angles $-2\arg\tilde{L}_x$ et $-2\arg\tilde{L}_y$ (lorsque les épaisseurs complexes $\tilde{L}_x$ et $\tilde{L}_y$ sont égales, chaque secteur dégénère alors à une demi-droite, comme pour les guides 2D). Avec une PML radiale, chaque continuum s'inscrit dans un secteur angulaire délimité par deux demi-droites d'angles $-2\arg\tilde{R}$ et $-2\arg(\tilde{R}-a)$ où $a$ est le rayon du cœur. Ces caractéristiques, via un examen visuel des spectres, peuvent aider à discriminer les modes physiques des modes de PML. Toutefois, cette discrimination est en pratique plutôt automatisée grâce au filtrage basé sur l'énergie cinétique sus-mentionné.

### Courbure

La méthode SAFE-PML a également été appliquée à des guides élastiques hélicoïdaux (NGUYEN et TREYSSÈDE 2015). La motivation de ce travail était d'étudier l'influence de la courbure sur les pertes par rayonnement.

Une PML de type radial a été implémentée. L'implémentation d'une telle PML nécessite de réécrire la formulation variationnelle de l'élastodynamique selon la même série de transformations que celles décrites par l'Équation (2.65), mais où les coordonnées $(x, y, z)$ désignent dorénavant des coordonnées tournantes (ces coordonnées sont décrites dans §2.6.2), ce qui nécessite une transformation supplémentaire au préalable... Du coup, les coordonnées $(r, \theta, z)$ désignent des coordonnées polaires tournantes. Celles-ci sont définies par :

$$\begin{cases} x - x_0 = r\cos\theta \\ y = r\sin\theta \\ z = z \end{cases} . \tag{2.68}$$

Dans le plan $(x, y)$, le point de coordonnées $(x_0, 0)$ est le centre du système polaire. Si $x_0 \neq 0$, ce point décrit une hélice quand il se déplace le long de l'axe $z$. Cette hélice représente l'axe du

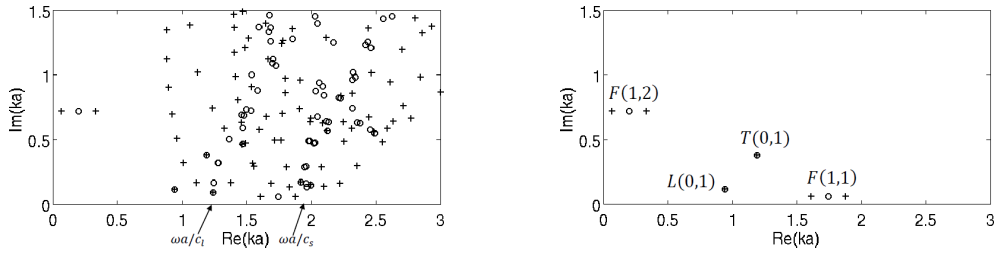


(a) (b)

FIGURE 2.17 – Spectre calculé par SAFE-PML pour un guide cylindrique acier-béton. (a) Avant filtrage, (b) après filrage. Croix : résultats pour un système tournant ($\tau \neq 0$), ronds : résultats de référence ($\tau = 0$).

système de coordonnées, alors appelé système décentré. Le cas particulier $x_0 = 0$ correspond à un système centré, dont l'axe est droit et coïncide avec l'axe $z$.

Dans un système de coordonnées tournant, l'atténuation des ondes par une PML se justifie analytiquement, sur la base de fonctions de Hankel, lorsque la PML est centrée (NGUYEN et TREYSSÈDE 2015). Selon la configuration de guide traité, l'utilisation d'une PML décentrée permet de réduire considérablement la taille du domaine de calcul, mais la justification théorique de l'absorption des ondes apparaît plus difficile dans ce cas. Nous nous sommes donc contentés de tests numériques, permettant de vérifier que les résultats obtenus par PML décentrée et PML centrée étaient en accord.

En considérant le cas test d'une barre cylindre, on montre que l'introduction d'un système de coordonnées tournant translate le spectre des nombres d'onde de $\pm\tau n$ ($\tau$ désigne la torsion et $n$ est l'ordre circonférentiel des modes). Ce phénomène se traduit par un évasement significatif des continua qui tend à "noyer" les modes à fuites, mais que l'on peut toujours filtrer efficacement par post-traitement via le critère basé sur l'énergie cinétique – voir Figure 2.17. Enfin, les résultats obtenus montrent que l'atténuation axiale des modes à fuite dans un guide hélicoïdal augmente sensiblement par rapport à un guide droit. Ce phénomène a notamment été identifié en optique et se confirme donc pour l'élasticité.

### 2.5.5 Exploitation des modes

Ayant calculé les modes, l'objectif suivant est de construire des solutions, par superposition modale, à des problèmes avec sources. Techniquement, le caractère général des méthodes présentées en §2.3 et §2.4 pour modéliser l'excitation et la diffraction des ondes les rend directement applicables en présence d'une PML. Cependant, le rôle des modes est à clarifier, en particulier celui des modes de PML. L'importance de leur prise en compte ou non dans les décompositions modales doit être éclaircie. Ceci a fait l'objet de deux papiers : GALLEZOT, TREYSSÈDE et LAGUERRE 2018 pour les problèmes d'excitation, GALLEZOT, TREYSSÈDE et LAGUERRE 2019 pour les problèmes de diffraction.

#### Guides ouverts excités

D'après ce qui précède, la troncature de la PML à une épaisseur finie a pour effet de discrétiser les continua des modes de rayonnement liés aux branches de coupures. D'un point de vue formel, on peut donc avancer que la somme continue est transformée en une somme discrète de modes

de PML, soit :

$$u(\mathbf{x},\omega) = \sum \text{modes piégés} + \sum \text{modes à fuite dévoilés} + \sum \text{modes de PML}. \tag{2.69}$$

Toutefois, se pose la question de l'utilité ou non de considérer les modes de PML dans la décomposition, étant donné que ceux-ci ne sont pas intrinsèques à la physique (ils dépendent fortement des paramètres utilisateurs de la PML).

On rappelle que l'Équation (2.27) fournit une relation de biorthogonalité générale, qui reste en particulier applicable pour des matrices complexes. Cette relation, et par suite l'ensemble des résultats présentés en §2.3.2, sont donc applicables en bloc pour des guides comportant une PML. Il faut observer que la relation d'orthogonalité implique la section complète du guide, PML incluse. Elle s'applique à n'importe quel type de modes sans distinction : piégés, à fuite ou de PML. Ceci permet notamment de calculer des excitabilités pour des modes leaky, alors que ceci est impossible sans PML en raison de la croissance transverse de ces modes (ceci n'est d'ailleurs pas sans poser quelques questions qui seront évoquées en §2.5.6).

Afin de valider la démarche et de clarifier le rôle des modes de PML, il s'avère instructif de considérer le cas d'un milieu homogène excité par une force ponctuelle. Un milieu homogène peut être vu comme un cas limite de guide d'onde ouvert, constitué d'une seule couche donc sans contraste d'impédance. Dans ce cas, il n'y a ni modes piégés ni modes à fuite, mais seulement des modes de PML. La solution obtenue peut-être comparée à une solution exacte. On fait varier deux paramètres : le nombre de modes retenus dans la décomposition modale, ainsi que l'épaisseur complexe de la PML. Les résultats numériques montrent qu'une bonne précision peut être obtenue dans un intervalle donné de distances à la source (plus l'épaisseur complexe est grande, plus cette distance pourra être éloignée). Ceci signifie qu'il est possible de reconstruire le comportement des ondes de volume, à décroissance géométrique, à partir de modes de PML (alors que ceux-ci décroissent exponentiellement selon l'axe, par nature). Ces résultats confirment des développements mathématiques obtenus dans le cas de guides scalaires [19]. Ainsi, on peut dire que la contribution du spectre discret des modes de PML est intrinsèque à la physique (ce spectre discret représente une approximation de la somme continue de l'Équation (2.62)), bien que les modes de PML considérés indépendamment les uns des autres ne le soient pas !

Ensuite, le cas d'une barre cylindrique (acier) enfouie dans un milieu souple (ciment) a été considéré, également excité par une source ponctuelle. Dans cette configuration, il n'existe aucun mode piégé si bien que seuls des modes à fuite et de PML y sont autorisés. Très loin de la source, les résultats obtenus montrent que la contribution des modes de PML à la réponse forcée devient prédominante (voir Figure 2.18). À cette distance, la majeure partie de l'énergie a fui du cœur du guide vers le milieu environnant. Le comportement du champ devient alors proche de celui des ondes de volume (sa décroissance est géométrique). Plus proche de la source, la réponse forcée est dominée par les modes à fuite, à décroissance exponentielle. Dans cet intervalle de distance – qui est en fait celui qui est intéressant pour l'END – les modes à fuite sont suffisants pour obtenir une bonne approximation de la solution et les modes de PML peuvent être négligés. Ceci permet de réduire l'épaisseur complexe de la PML et donc le coût de calcul, ce qui est indispensable pour pouvoir traiter des problèmes hautes fréquences et/ou 3D (impliquant, en particulier, un grand nombre de modes).

Pour illustrer les potentialités de la méthode, la réponse forcée de guides 2D et 3D en régime haute fréquence a été résolue par superposition sur les modes à fuite uniquement. Précisons que les modes à fuite longitudinaux d'ordre élevé, qui se propagent en régime haute fréquence,

19. F. Olyslager, "Discretization of continuous spectra based on perfectly matched layers," Siam J. Appl. Math., vol. 64, no. 4, pp. 1408–1433, 2004.

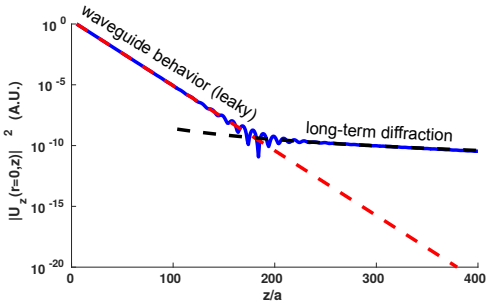


FIGURE 2.18 – Décroissance en énergie du champ en fonction de la distance le long de l'axe du guide. Courbe bleue : solution obtenue avec un grand nombre de modes, courbe rouge : solution obtenue avec un seul mode à fuite (décroissance exponentielle). La courbe noire représente une décroissance de type géométrique. Les résultats sont ici obtenus en basse fréquence, si bien qu'un seul mode à fuite contribue de manière significative à la réponse.

sont particulièrement intéressant pour l'END en raison de leur faible atténuation par fuite (les courbes de dispersion de ces modes sont représentés par les traits rouges de la Figure 2.1).

### Guides ouverts inhomogènes

Intéressons-nous maintenant à la modélisation de la diffraction des ondes par une inhomogénéité locale. À partir des modes calculés par méthode SAFE-PML, nous appliquons la méthode hybride présentée en §2.4.2 pour reproduire des conditions transparentes dans des guides ouverts. Des questions se posent quant à l'influence des modes de PML sur les solutions.

Les modes de PML appartiennent à des continua qui émanent de l'axe réel (les points de branchement sont situés en $\omega/c_{l/s}$ – voir Figure 2.16). Ceux proches de cet axe ont une atténuation axiale faible, si bien que leurs contributions aux conditions transparentes (qui sont en champ proche) pourraient *a priori* être significatives. D'un autre côté, les modes de PML oscillent principalement à l'intérieur de la PML, ce qui réduit considérablement leurs contributions dans le cœur. Mais ces contributions sont-elles négligeables pour autant ?

Soulignons que l'influence des modes de PML en champ lointain, évoquée précédemment, n'est pas d'un intérêt central ici. En effet, il faudrait que les frontières transparentes soient très éloignées de l'inhomogénéité pour que le comportement du champ rayonnant, à décroissance géométrique, devienne prédominant. Ceci est en contradiction avec l'objectif de la méthode hybride, qui est de réduire le domaine à mailler autour d'une région proche du défaut.

Reste donc à explorer une autre facette des modes de PML : leur influence en champ (très) proche. Diverses configurations ont été étudiées : 2D ou 3D, inhomogénéité de type jonction ou entaille... Les résultats montrent que le poids des modes de PML (leurs coefficients $\alpha_m$) tend à augmenter avec leur atténuation axiale ($\mathrm{Im}\, k$). Ceci se traduit par le fait que les modes de PML améliorent la précision des résultats lorsque les frontières transparentes sont "très" proches de l'inhomogénéité (on parle ici de distances inférieures au rayon moyen de la section) - voir l'exemple donné en Figure 2.19. Leur contribution diminue rapidement, jusqu'à devenir négligeable, à mesure que l'on augmente la distance des frontières transparentes.

Ainsi, la précision des résultats obtenus doit être soigneusement vérifiée en guide ouvert en faisant varier la distance entre l'inhomogénéité et les frontières transparentes, ainsi que le nombre de modes retenus dans les décompositions modales aux frontières. Ceci est particulièrement critique pour les problèmes 3D, pour lesquels il est nécessaire de réduire le nombre de modes à

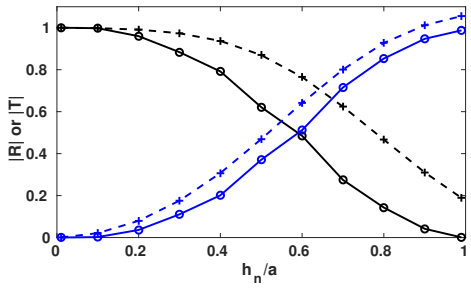


FIGURE 2.19 – Coefficients de réflexion et transmission du mode L(0,12) sur lui-même dans un guide cylindrique acier-ciment en fonction de la profondeur $h_n$ d'un défaut de type entaille. Les frontières transparentes sont positionnées à une distance de $0.25a$ du défaut ($a$ : rayon du guide). Lignes pointillées : résultats de calcul ne retenant que les modes à fuite dans les décompositions. Lignes continues : résultats incluant plusieurs modes de PML (ainsi que des modes à fuite rétrogrades).

calculer afin de maintenir un coût de calcul raisonnable. Les frontières transparentes doivent alors être positionnées à une distance qui ne soit pas trop proche de l'inhomogénéité pour permettre de négliger les modes de PML (et éviter leur calcul).

Par ailleurs, l'analyse modale de la diffraction des ondes dans les guides ouverts peut soulever d'autres difficultés, autour de certaines fréquences, liées à la non-orthogonalité des puissances modales (voir §2.4.3, Équation (2.60)). La puissance croisée entre deux modes, c'est-à-dire la puissance résultant du couplage de deux modes, est généralement non nulle dans un guide à perte. Celle-ci peut devenir significative lorsque les modes interagissent fortement entre eux (lors de croisement de vitesses de phase, typiquement). Les coefficients modaux individuels sont alors susceptibles d'évoluer de manière contre-intuitive (augmentation à la fois en réflexion et transmission par exemple).

Enfin, notons que l'application de la méthode en régime haute fréquence a aussi permis de montrer que le mode à fuite longitudinal le moins atténué exhibait un coefficient de réflexion élevé et qu'il était peu converti vers d'autres modes (du moins, pour des défauts de type entaille). Ceci confirme l'intérêt des modes longitudinaux hautes fréquences pour l'END.

### 2.5.6 Perspectives

En résumé, les modes de PML sont susceptibles de contribuer au champ très proche ainsi qu'au champ très lointain. En dehors de ces zones particulières (peu intéressantes vis-à-vis de l'END), les solutions peuvent être approximées par la contribution des modes à fuite seulement. Une telle approximation est indispensable du point de vue numérique, car elle permet de réduire l'épaisseur de la PML et le nombre de modes à calculer, et donc le coût des calculs.

Ceci étant dit, il n'en reste pas moins que le principal inconvénient de l'approche demeure l'augmentation du temps de calcul liée à la présence des modes de PML, bien plus nombreux que les modes à fuite. Or, l'emplacement des modes de PML dans le spectre les rend difficiles à séparer des modes à fuite. Cette difficulté est particulièrement marquée en élasticité (deux continua à séparer au lieu d'un seul en acoustique scalaire). Si les temps de calculs restent relativement rapides pour des guides 2D (problèmes modaux 1D), cet inconvénient devient vite rédhibitoire pour des guides 3D (problèmes modaux 2D). L'utilisation d'éléments finis spectraux peut permettre de réduire sensiblement le coût de calcul, mais à condition de centrer les

recherches de valeurs propres sur des modes particuliers (Treyssède 2016). La démocratisation des méthodes de type SAFE-PML pour des guides 3D passe sans doute par la mise en place de stratégies destinées à éviter le calcul des modes de PML, ou du moins à en diminuer le nombre. Ceci constitue une première piste de travail.

Une autre piste de travail, plus théorique, concerne la normalisation des modes à fuite. Observons tout d'abord que c'est l'idée même du prolongement analytique (mis en œuvre dans une PML) qui permet de résoudre la délicate question de la normalisation des modes à fuite : sans prolongement analytique, la normalisation diverge en raison de la croissance transverse des modes à fuite. Le facteur de normalisation $Q_{m,-m}$, qui intervient notamment dans la notion d'excitabilité, repose sur la relation de biorthogonalité introduite en §2.3.2. Or, celle-ci dépend des paramètres de la PML. Si l'on extrapole certaines conclusions issues de l'optique [20], alors on doit pouvoir montrer l'indépendance de la normalisation des modes à fuite aux paramètres de la PML, soit en d'autres termes : l'unicité de la normalisation. En particulier, il apparaît important de vérifier que l'excitabilité des modes à fuite, pour qu'elle ait un sens physique, ne dépend pas de la PML.

En marge des pistes qui précèdent, il serait intéressant (au moins par curiosité) de comparer les performances d'une méthode de type hybride, dont les décompositions modales sont écrites sur des sections éloignées de celle de l'inhomogénéité, avec une méthode de type mode-matching, dont les décompositions modales sont écrites sur la même section que celle de l'inhomogénéité. La convergence en mode-matching devrait nécessiter, à première vue, la prise en compte d'un très grand nombre de modes de PML (étant donné leurs contributions non négligeables en champ très proche), potentiellement rédhibitoire.

Dernier point : les travaux menés sur les guides ouverts permettent d'envisager directement des applications aux ondes de surface dans le domaine géophysique (milieux stratifiés, sols, chaussées, digues, ...). À ce titre, il apparaît que l'approche numérique que nous avons suivie ne soit pas si répandue en géophysique. Comme semble le sous-entendre Kausel dans la conclusion d'un papier dont il est co-auteur [21], à propos d'une approche combinant TLM (c'est-à-dire SAFE) et PML appliquée à des milieux stratifiés (problème modal 1D) : *"Moreover, the results are vastly superior to those of the conventional approach which relies on paraxial boundaries, and accomplishes this improvement with fewer degrees of freedom. Thus, this approach is likely to become the method of choice for this class of problems..."*

**Tirés à part :**


— Nguyen, Treyssède et Hazard 2015 (voir page 122) ;
— Gallezot, Treyssède et Laguerre 2017 (voir page 143) ;
— Gallezot, Treyssède et Laguerre 2018 (voir page 149).


## Articles relatifs à cette section

**Gallezot, M., F. Treyssède et L. Laguerre (2019) :** « Numerical modelling of wave scattering by local inhomogeneities in elastic waveguides embedded into infinite media », *Journal of Sound and Vibration*, 443, p. 310–327.

20. P. Lalanne, W. Yan, K. Vynck, C. Sauvan, and J. Hugonin, "Light Interaction with Photonic and Plasmonic Resonances," Nanophotonics, vol. 12, p. 1700113, 2018.

21. J. M. de O. Barbosa, J. Park, and E. Kausel, "Perfectly matched layers in the thin layer method," Comput. Methods Appl. Mech. Eng., vol. 217–220, pp. 262–274, Apr. 2012.

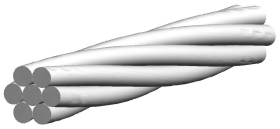

FIGURE 2.20 – Schéma d'un toron à sept brins.

**Gallezot, M., F. Treyssède et L. Laguerre (2018) :** « A modal approach based on perfectly matched layers for the forced response of elastic open waveguides », *Journal of Computational Physics*, 356, p. 391–409.

— **(2017) :** « Contribution of leaky modes in the modal analysis of unbounded problems with perfectly matched layers », *Journal of the Acoustical Society of America*, 141, EL16–EL21.

**Treyssède, F. (2016) :** « Spectral element computation of high frequency leaky modes in three-dimensional solid waveguides », *Journal of Computational Physics*, 314, p. 341–354.

**Nguyen, K. L. et F. Treyssède (2015) :** « Numerical investigation of leaky modes in helical structural waveguides embedded into a solid medium », *Ultrasonics*, 57, p. 125–134.

**Nguyen, K. L., F. Treyssède et C. Hazard (2015) :** « Numerical modeling of three-dimensional open elastic waveguides combining semi-analytical finite element and perfectly matched layer methods », *Journal of Sound and Vibration*, 344, p. 158–178.

**Treyssède, F., K. L. Nguyen, A. S. Bonnet-BenDhia et C. Hazard (2014) :** « Finite element computation of trapped and leaky elastic waves in open stratified waveguides », *Wave Motion*, 51 (7), p. 1093–1107.

## 2.6 Application aux câbles

### 2.6.1 Motivations

Les développements théoriques et numériques que j'ai exposés dans les sections précédentes ont été motivés par une application particulièrement complexe : les câbles. En ce qui concerne les ponts, ces éléments sont soumis à des sollicitations axiales importantes. Ceci peut engendrer la dégradation du matériau et sa fissuration liées au développement de la corrosion et de la fatigue mécanique, qui menacent l'intégrité de l'ouvrage (et donc la sécurité des usagers). Il est donc primordial de disposer de méthodes d'END permettant l'auscultation des câbles, et en amont, de modèles permettant d'identifier les ondes qui s'y propagent.

La structure des câbles est généralement hélicoïdale et multi-brins. Un des éléments le plus fréquent est le toron à sept brins (d'acier), constitué d'un brin cylindrique droit entouré d'une couche de six brins hélicoïdaux (voir Figure 2.20). Mes travaux sur les câbles se sont focalisés sur cette architecture. Suivant les configurations, ces torons peuvent être noyés dans un coulis de ciment pour retarder la corrosion.

Ainsi, les difficultés auxquelles doit faire face la modélisation sont les suivantes :

1. la structure considérée couple des brins hélicoïdaux avec un brin droit ;
2. ces brins sont couplés par contact mécanique ;
3. la structure est soumis à un chargement axial très important (en tension), qu'il est difficile de négliger *a priori* ;
4. en configuration noyée, les brins périphériques sont en contact avec une matrice solide.

Le point 1 pose la question de l'existence des ondes guidées d'un point de vue géométrique et sera abordée en §2.6.2. Le point 2 pose la question de la linéarité du problème. Pour préserver

la linéarité, nous supposerons un contact parfaitement collant (*i.e.* sans décollement, sans glissement et donc sans frottement). Le point 3 pose la question des effets acoustoélastiques (effet de la précontrainte statique sur la propagation des ondes élastiques). Le point 2 et le point 3 sont intimement liés : sous un chargement en traction, les brins hélicoïdaux compriment radialement le brin central, ce qui provoque un accroissement de la largeur de contact inter-brins. Les points 2 et 3 seront traités en §2.6.3. Le point 4 rend le problème non borné transversalement (guide ouvert) et sera évoqué en §2.6.4.

Cette section, comme la précédente, est de nature moins méthodologique que les premières. Elle utilise les développements présentées en §2.2, §2.3 et §2.5. Une part importante est donc consacrée à la synthèse des résultats de simulation obtenus.

Dans l'ensemble des simulations réalisées, nous avons supposé qu'il n'y avait aucun contact mécanique entre les brins périphériques. Cette supposition est liée à un critère de conception destiné à limiter les phénomènes de frottement. Il n'y a *a priori* aucune limitation, dans l'approche numérique proposée, qui empêche de prendre en compte ces contacts (à condition qu'ils soient collants).

Une partie des travaux exposés dans cette section a été réalisée en collaboration avec Patrice Cartraud du GeM, lors de l'encadrement de la thèse d'Ahmed Frikha (2007-2010) – voir §2.6.3 et 2.6.5).

### 2.6.2 Système de coordonnées tournant

Si l'on considère la propagation des ondes dans chaque brin indépendamment les uns des autres, on peut distinguer naturellement sept systèmes de coordonnées : un système droit pour le brin central, un système hélicoïdal pour chaque brin périphérique (ces systèmes hélicoïdaux étant définis sur six hélices différentes). Pour résoudre la question de l'existence des ondes guidées dans un toron à sept brins, il faut donc chercher un système de coordonnées capable d'unifier les différentes géométries de brins mises en jeu.

On peut montrer qu'un système de coordonnées tournant permet de résoudre le problème (Treyssède et Laguerre 2010). Un système tournant correspond à un cas particulier de système hélicoïdal dont la courbure est nulle ($\kappa = 0$), mais dont la torsion est non nulle et donnée par : $\tau = 2\pi/L$ où $L$ est le pas d'hélice, commun à tous les brins périphériques. Avec un tel système, l'axe $s$ reste droit ($s = z$) mais les coordonnées de section $(x, y)$ tournent autour de l'axe $z$ en suivant les brins périphériques au fur et à mesure que l'on se déplace sur cet axe (voir Figure 2.21a). Concernant le brin central, celui-ci a une section circulaire : sa section ne varie donc pas non plus dans le repère tournant puisque celui-ci est centré sur l'axe du brin central. Conclusion : l'ensemble de la section du toron n'évolue donc pas selon l'axe $z$ dans le système tournant ainsi défini. Par ailleurs, puisqu'un système tournant n'est qu'un cas particulier de système hélicoïdal, le tenseur métrique reste indépendant de $z$ (il suffit de considérer l'Équation (2.17) avec $\kappa = 0$). Les conditions 1 à 3 de l'*invariance continue* définie en §2.2.2 sont ainsi vérifiés, ce qui justifie l'existence des modes d'onde dans un toron à sept brins.

À partir des résultats évoqués en §2.2, l'application d'une méthode SAFE est alors relativement simple : il suffit de prendre l'expression des opérateurs $\mathbf{L}_\perp$ et $\mathbf{L}_s$, donnée par l'Équation (2.18), particularisée à $\kappa = 0$. Il faut toutefois veiller au paramétrage géométrique des sections des brins périphériques. En effet, la section d'un brin donné n'est circulaire que dans un plan de coupe perpendiculaire à l'axe hélicoïdal du brin en question. Or, le plan de coupe du système tournant est perpendiculaire à l'axe droit $z$ : les sections des brins périphériques n'y sont donc plus circulaires, mais déformées selon un paramétrage précis défini dans Treyssède et Laguerre 2010. Par ailleurs, le maillage doit être raffiné aux zones de contact (voir

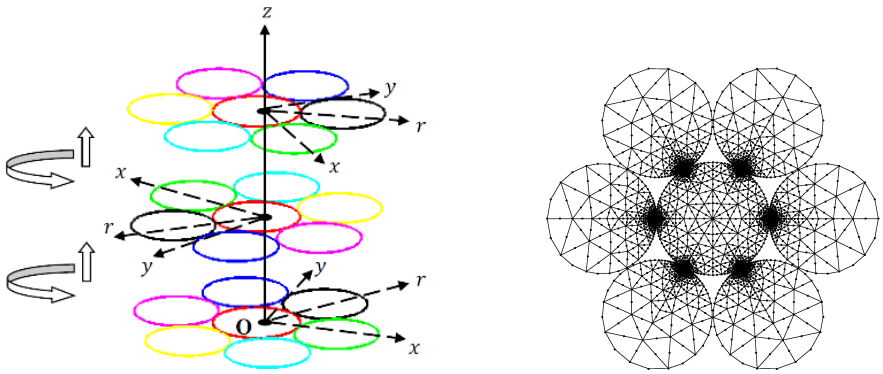


(a) (b)

FIGURE 2.21 – (a) Système de coordonnées tournant $(x, y, z)$ associé à un toron à sept brins, (b) maillage SAFE de la section dans le plan $(x, y)$.

Figure 2.21b).

Les résultats numériques obtenus dans TREYSSÈDE et LAGUERRE 2010 ont montré l'existence d'une multitude de courbes de dispersion, distinctes les unes des autres en raison d'un couplage inter-brins significatif. Dans le régime de fréquence considéré, le mode le plus rapide s'avère être un mode de compression. Le comportement de ce mode est très similaire à celui du premier mode de compression se propageant dans une barre cylindrique (souvent noté L(0,1)), sauf autour d'une fréquence particulière pour laquelle une chute rapide de la vitesse d'énergie se produit. Cette chute est liée à un phénomène de répulsion entre deux modes ("curve veering"). L'origine de ce phénomène réside dans le couplage élongation/flexion résultant de la rupture de symétrie de rotation des brins périphériques, liée au déplacement radial contraint par la zone de contact (TREYSSÈDE 2016a).

**Comparaison avec des résultats expérimentaux.** Cette chute de la vitesse s'observe expérimentalement. Elle se traduit par une bande de fréquence manquante dans les résultats de mesure, dont la fréquence centrale a initialement été appelée "notch frequency" [22]. Dans TREYSSÈDE et LAGUERRE 2010, les résultats de modélisation donnent une fréquence assez proche des résultats expérimentaux obtenus par dispositif magnétostrictif (sans contact). Toutefois, les effets de chargement ne sont pas pris en compte dans cet article préliminaire, si bien que le contact reste de nature ponctuel (le terme ponctuel s'entend ici dans le plan de la section). La convergence des résultats numériques en fonction du chargement est discutée dans un papier postérieur (TREYSSÈDE 2016a).

En aparté, des tests numériques ont été effectués avec hypothèse de contact glissant : les résultats obtenus apparaissent alors peu réalistes par rapport aux observations expérimentales, ce qui milite en faveur d'un contact plutôt collant (TREYSSÈDE 2016a).

22. H. Kwun, K. A. Bartels, and J. J. Hanley, "Effects of tensile loading on the properties of elastic-wave propagation in a strand," J. Acoust. Soc. Am., vol. 103, pp. 3370–3375, 1998.

### 2.6.3 Acoustoélasticité

#### Dynamique des structures précontraintes

L'acoustoélasticité étudie l'effet des précontraintes statiques sur la propagation des ondes élastiques. Du point de vue de la modélisation, il nous faut donc choisir des équations qui permettent de révéler ces effets, ce qui requiert une théorie non-linéaire à la base. Dans les problèmes d'élasticité, on peut distinguer deux grands types de non-linéarités : les non-linéarités géométriques (liées à des grands déplacements, voire grandes déformations) et les non-linéarités matérielles (dues aux lois de comportement des matériaux).

Dans la littérature, ce dernier type de non-linéarité est généralement pris en compte en considérant des constantes élastiques du troisième ordre dans la loi de comportement (constantes de Murnaghan). Ce type de non-linéarité ne provoque que de faibles variations de vitesse sur des matériaux métalliques, de l'ordre du pourcent. Or, les expérimentations menées sur les torons montrent des effets significatifs de la précontrainte. On négligera donc les non-linéarités matérielles (les déformations élastiques restent petites, aussi bien en dynamique qu'en statique).

Enfin, on considérera aussi de petits déplacements dynamiques autour de l'état statique précontraint (dynamique linéarisée, "small-on-large"). Le problème peut ainsi se décomposer en un problème statique, résolu indépendamment, et un problème de dynamique autour de cet état précontraint. Trois configurations doivent donc être distinguées : la configuration initiale (sans contrainte initiale), la configuration de la précontrainte statique et la configuration finale (incluant la dynamique). Les indices $i$ et 0 seront utilisés pour distinguer les variables dans la configuration initiale et dans la configuration précontrainte, respectivement.

Si l'on choisit d'exprimer le problème dans la configuration précontrainte (indice 0), les équations d'équilibre de l'élastodynamique linéarisée sont données par :

$$\nabla_0 \cdot (\sigma(\mathbf{u}) + \nabla_0 \mathbf{u} \cdot \sigma_0) + \rho_0 \omega^2 \mathbf{u} = \mathbf{f}, \tag{2.70}$$

avec $\sigma = C_0 : \epsilon$ et $\epsilon = (\nabla_0 \mathbf{u} + \nabla_0 \mathbf{u}^{\mathrm{T}})/2$. Le vecteur $\mathbf{u}$ représente la petite perturbation ondulatoire de déplacement autour de l'état précontraint. Dans ces expressions, $C_0$ et $\rho_0$ désignent le tenseur des propriétés élastiques et la masse volumique du matériau dans l'état précontraint. Le tenseur $\sigma_0$ est le tenseur des contraintes de Cauchy dans l'état précontraint. L'opérateur $\nabla_0$ désigne le gradient exprimé selon la configuration précontrainte. Précisons que sous l'hypothèse de petites déformations, les propriétés des matériaux peuvent être considérées comme indépendantes de la déformation appliquée, si bien que les égalités suivantes s'appliquent : $C_0 \simeq C_i$ and $\rho_0 \simeq \rho_i$.

#### Formulation SAFE précontrainte

Par rapport à l'Équation (2.1), la forme forte donnée par l'Équation (2.70) fait intervenir un terme supplémentaire, qui dépend de $\sigma_0$, et est écrite selon les coordonnées de la configuration précontrainte. Ces équations correspondent à une formulation Lagrangienne actualisée, bien connue en analyse non-linéaire des structures.

Pour le problème qui nous intéresse, la formulation variationnelle associée à cette forme forte doit être réécrite dans le système de coordonnées tournant. Les tenseurs sont exprimés dans la base de Serret-Frenet. Par ailleurs, cette formulation variationnelle est exprimée dans la configuration précontrainte : ceci signifie que la section à mailler est la section déformée $S_0$ (la section dans son état précontraint). De même, la torsion du système est celle correspondant à l'état précontraint, soit : $\tau_0 = 2\pi/L_0$, où $L_0$ est le pas d'hélice actualisé sous l'effet de la précontrainte.

Au final, on montre que l'application d'une méthode SAFE à l'Équation (2.70) conduit à un problème qui garde la même forme que l'Équation (2.4) :

$$(\mathbf{K}_{1\sigma} - \omega^2\mathbf{M})\mathbf{U} + (\mathbf{K}_{2\sigma} - \mathbf{K}_{2\sigma}^{\mathrm{T}})\mathbf{U}_{,z} - \mathbf{K}_{3\sigma}\mathbf{U}_{,zz} = \mathbf{F}, \tag{2.71}$$

mais où les matrices, indicées $\sigma$, dépendent dorénavant de la précontrainte de Cauchy $\sigma_0$. Pour plus de détails, on pourra consulter Treyssède, Frikha et Cartraud 2013.

La formulation SAFE nécessite donc trois paramètres d'entrée liés à la précontrainte : $\sigma_0$, $\tau_0$ et $S_0$. Ces paramètres doivent être déterminés par un calcul préalable de l'état précontraint. Pour la détermination de cet état, nous avons développé une méthode d'homogénéisation particulière, à laquelle la section §2.6.5 est consacrée.

L'ensemble de l'approche proposée, combinant calculs statiques et calculs SAFE en système tournant, a été validé sur des ressorts ($\tau$ élévé) et soumis à un chargement en extension important (Treyssède, Frikha et Cartraud 2013). Les résultats numériques obtenus sont en accord avec ceux d'une approche analytique, elle-même issue d'un autre papier (Frikha, Treyssède et Cartraud 2011).

#### Résultats numériques vs. expérimentaux

Les tests numériques montrent qu'un modèle de toron chargé mais négligeant les effets de contact, c'est-à-dire dont le contact reste ponctuel, laisse quasiment inchangée la "notch frequency" (Treyssède, Frikha et Cartraud 2013). Ceci est en contradiction avec les résultats expérimentaux, qui montrent une évolution significative en fonction du chargement. Les effets de non-linéarité géométrique, liés à la précontrainte $\sigma_0$, restent donc négligeables – du moins pour le phénomène qui nous intéresse (car ces effets peuvent devenir significatifs en très basse fréquence).

L'évolution observée de la "notch frequency" est en fait provoquée par l'accroissement de la largeur de contact au fur et à mesure du chargement. Outre les effets de courbure et de précontrainte, la modélisation du toron conduit donc à une complexité supplémentaire : la prise en compte de la mécanique du contact inter-brins. Celle-ci correspond à une troisième forme de non-linéarité. Le modèle statique présenté en §2.6.5 utilise une procédure itérative qui permet de tenir compte de ce contact. Les résultats numériques obtenus donnent alors une "notch frequency" qui évolue de l'ordre de 60 kHz non chargé à 80 kHz sous extension de 0.6% (voir Figure 2.22), en accord avec les résultats expérimentaux.

Ainsi l'augmentation de la "notch frequency" est principalement causée par l'augmentation de la largeur de contact inter-brins, plutôt que par la précontrainte (mais qui, elle, est bien à l'origine de l'augmentation de la largeur de contact...). En marge de cela, on constate aussi un décalage vers les hautes fréquences de l'ensemble des courbes de dispersion du toron, également lié à cette augmentation de la largeur de contact (voir Figure 2.22).

### 2.6.4 Transferts d'énergie

#### Fuite de l'énergie dans un milieu environnant

En configuration noyée, les torons sont en contact avec une matrice solide. Cette matrice peut être considérée de taille suffisamment grande pour être supposée infinie, si bien que le toron peut être vu comme un guide ouvert. Cette matrice est constituée d'un matériau, typiquement un coulis de ciment ou du béton, qui est plus souple que celui des brins (acier). Une telle configuration de matériau n'autorise pas l'existence de modes piégés. Ceci signifie que l'énergie

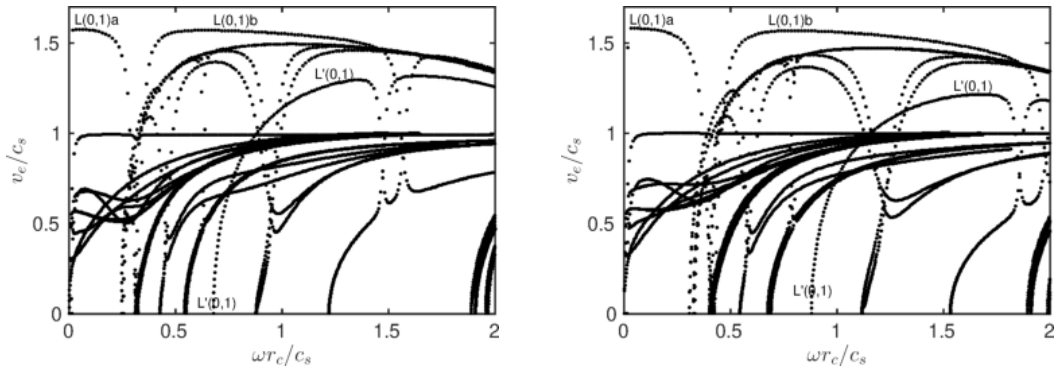


(a) (b)

FIGURE 2.22 – Courbes de dispersion normalisées pour la vitesse d'énergie en fonction de la fréquence dans un toron : (a) non chargé ($E^E = 0$) et (b) chargé ($E^E = 0.6\%$).

fuit dans le milieu environnant quelles que soient les conditions de propagation (seuls des modes à fuite et de rayonnement existent).

La modélisation d'un toron ouvert nécessite l'utilisation d'un outil présenté en §2.5.4, à savoir une PML en coordonnées tournantes. L'application de cet outil ne pose pas de difficultés particulières dans le cas du toron, si ce n'est des difficultés liées à la résolution numérique du problème aux valeurs propres : augmentation de la taille du problème (la PML constitue un domaine supplémentaire à mailler), cumulée avec la présence d'une multitude de modes de PML dans le spectre (ayant peu, voire aucun, intérêt sur le plan physique). Notons que la PML utilisée pour un toron est une PML centrée. Comme mentionné en §2.5.4, l'atténuation des ondes y est théoriquement justifiée.

Nous négligeons ici les effets de précontrainte (en particulier, les contacts inter-brins sont de nature ponctuelle). Les résultats numériques obtenus (NGUYEN et TREYSSÈDE 2015) montrent une différence significative des courbes de dispersion comparé au cas du toron dans le vide. On observe toujours une chute de vitesse d'énergie du mode de compression (mode global), moins marquée, décalée vers les hautes fréquences et entièrement décrite par une seule courbe (il n'y a donc plus de répulsion entre deux courbes). En plus de rendre le guide ouvert, il faut signaler que l'introduction du milieu enrobant à un autre effet : celui de mettre quasiment en contact les brins périphériques. Ceci accentue probablement les différences entre les configurations fermée et ouverte.

Dans le régime fréquentiel étudié, les résultats numériques montrent que les modes les moins atténués sont les deux modes de flexion fondamentaux (modes globaux) et un autre mode, local et propre à la structure du toron lui-même. Il s'agit d'un mode de compression dont le mouvement est essentiellement confiné dans le brin central, ce qui explique donc sa faible fuite d'énergie dans le milieu environnant.

### Transfert d'énergie entre les brins

Un second type de transfert d'énergie a été étudié. Il s'agit du transfert d'énergie qui s'opère d'un brin à l'autre lorsque seul l'un d'entre eux est excité (le brin actif). L'objectif est d'identifier les conditions d'excitation, s'il y en a, qui permettent à l'énergie de rester confinée dans le brin excitée. Pour simplifier l'analyse et limiter les paramètres mis en jeu, on considère un toron sans pertes viscoélastiques, ni pertes par fuite (*i.e.* en configuration fermée, sans enrobant). Étant

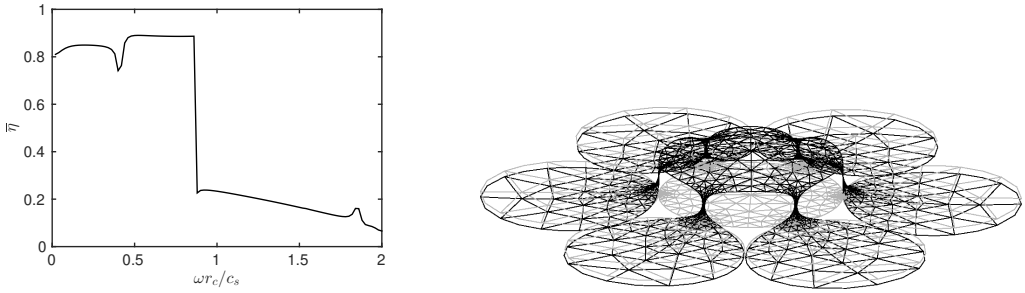


(a) (b)

FIGURE 2.23 – (a) Évolution du paramètre de transfert d'énergie, noté $\bar{\eta}$, en fonction de la fréquence pour une excitation axiale du brin central (toron chargé), (b) déformée modale du mode de compression local (labellisé L(0,1)' sur la Figure 2.22).

donné que le transfert d'énergie inter-brins doit être influencé par la largeur de contact, les effets de précontraintes sont pris en compte.

L'outil utilisé ici est donc différent du paragraphe précédent : nul besoin de PML mais il faut prendre en compte l'excitation. On utilise pour cela les développements présentés en §2.3, en simplifiant l'analyse au cas des modes purement propagatifs. Techniquement, ceci permet aussi de recourir à la relation d'orthogonalité de Auld complexe, plus simple à utiliser que Auld réelle. Rappelons que la torsion du système de coordonnées modifie la structure de l'opérateur $\mathbf{L}_\perp$, ce qui induit une forme d'anisotropie dans les équations d'équilibre. Comme expliqué dans §2.3.4, la relation de Fraser n'est *a priori* pas applicable dans ce cas.

Afin d'identifier la répartition de l'énergie dans le toron, un paramètre énergétique a été défini (TREYSSÈDE 2016b). Ce paramètre est égal au rapport de la puissance des six brins passifs (non excités), moyennée dans la direction $z$, sur la puissance totale (celle des sept brins).

Pour la plupart des cas d'excitation, les résultats montrent que l'énergie ne reste pas confinée dans le brin actif lorsque les ondes se propagent suivant l'axe et que la répartition de l'énergie entre les brins dépend généralement de la distance de propagation depuis la source. En raison du caractère multimodal de la propagation, l'énergie à l'intérieur d'un brin donné peut osciller fortement le long de l'axe du guide d'onde. Ainsi suivant la distance à la source, la réponse peut s'avérer localisée dans le brin actif, ou répartie sur plusieurs brins, ou bien même être localisée dans un brin passif. Vis-à-vis de l'END, un tel phénomène est susceptible de compliquer l'interprétation des mesures...

Pour une source polarisée dans l'axe et localisée dans le brin central, le paramètre énergétique défini plus haut chute brutalement à partir d'une certaine fréquence, indiquant un confinement de l'énergie (voir Figure 2.23a). Cette fréquence correspond à la fréquence de coupure d'un mode de compression, très excitable et confiné au brin central (voir Figure 2.23b). Il s'agit en fait du même type de mode que celui identifié auparavant dans le cas de pertes par fuite. Un phénomène similaire se produit en torsion, mais pas en flexion, dans le brin central (existence d'un mode de torsion local et facilement excitable). En revanche, aucun phénomène de localisation ne semble se produire dans le cas où le brin actif est périphérique, et ce, quelle que soit la polarisation de la source (du moins dans la gamme de fréquence considérée).

En marge de ces investigations, on peut noter que l'analyse de la réponse forcée suivant différentes polarisations et différents brins actifs aident à identifier la nature des nombreux modes se propageant dans un toron (longitudinal/flexion/torsion, local/global, ...).

### 2.6.5 Modélisation du comportement statique

Pour déterminer l'état précontraint statique, nécessaire à la résolution du problème d'acoustoélasticité, nous avons développé une méthode d'homogénéisation spécifique utilisant les coordonnées tournantes (Frikha, Cartraud et Treyssède 2013). Cela permet d'exploiter pleinement la symétrie hélicoïdale continue du problème, et par conséquent, de réduire le problème à un maillage 2D de la section du câble (à la manière de la méthode SAFE). Ce travail est un peu à part dans le contexte de ce manuscrit, focalisé sur la propagation des ondes guidées. Néanmoins, il constitue une relative originalité au regard de l'état de l'art sur la modélisation du comportement statique des câbles.

On rappelle que les non-linéarités matérielles ont été négligées (voir §2.6.3). On supposera également que les non-linéarités géométriques de l'état précontraint sont négligeables. À première vue, ceci peut sembler en contradiction avec le point de vue "small-on-large" adopté en acoustoélasticité. L'influence de ces non-linéarités statiques sur les ondes peut toutefois être raisonnablement négligée en pratique (voir Frikha, Treyssède et Cartraud 2011 pour des résultats sur des ressorts soumis à forte extension).

Nous suivons la méthode des développements asymptotiques appliquée à des structures élancées. Pour cela, le point de départ consiste à écrire la solution du problème sous la forme du développement asymptotique suivant :

$$\mathbf{u}_0 = \mathbf{u}^0(z) + \epsilon \mathbf{u}^1\left(\frac{x}{\epsilon}, \frac{y}{\epsilon}, \frac{z}{\epsilon}, z\right) + \epsilon^2 \mathbf{u}^2\left(\frac{x}{\epsilon}, \frac{y}{\epsilon}, \frac{z}{\epsilon}, z\right), \tag{2.72}$$

où les coordonnées $(x, y, z)$ désignent les coordonnées associées au système tournant et sont les variables lentes (ou macroscopiques). Les variables $(x/\epsilon, y/\epsilon, z/\epsilon)$ sont les variables rapides (ou microscopiques). Le terme d'ordre 0 du développement, qui ne dépend pas des variables microscopiques, ne comprend pas de composante axiale. Celle-ci apparaît à l'ordre suivant ce qui traduit que la structure à l'échelle macroscopique est plus souple en flexion qu'en traction-compression. Dans le cadre de ce travail, on s'intéresse exclusivement à des précontraintes issues d'un chargement axial (traction-torsion), donc sans flexion globale. Ceci entraîne la nullité du terme d'ordre 0 ($\mathbf{u}^0 = \mathbf{0}$). Par ailleurs, on peut supprimer les dépendances en $z/\epsilon$ dans l'Équation (2.72), en vertu de la symétrie hélicoïdale continue du problème (on se restreint ici au cas d'un chargement homogène, constant selon l'axe).

On montre que le déplacement au premier ordre $\mathbf{u}^1$ s'interprète comme le déplacement macroscopique, caractérisé par les déformations macroscopiques de l'extension $E^E = \partial U/\partial z$ et de la torsion $E^T = \partial \Phi/\partial z$ (les données d'entrée du problème), et s'écrit sous la forme suivante :

$$\mathbf{u}^1(x, y, z) = U(z)\mathbf{e}_z + \Phi(z)(x\mathbf{e}_y - y\mathbf{e}_x). \tag{2.73}$$

Le déplacement au second ordre $\mathbf{u}^2$ correspond au déplacement microscopique. Il est solution d'un système linéaire de la forme : $\mathbf{K}_0\mathbf{U}_0 = \mathbf{F}_0$, où $\mathbf{U}_0$ est le vecteur des déplacements microscopiques aux nœuds et $\mathbf{F}_0$ est le vecteur des efforts extérieurs exprimés en fonction des déformations imposées $E^E$ et $E^T$. Les matrices et vecteurs élémentaires sont donnés par :

$$\mathbf{K}_0^e = \int_{S_i^e} (\mathbf{L}_\perp \mathbf{N}^e)^{\mathrm{T}} \mathbf{C}_i \mathbf{L}_\perp \mathbf{N}^e \mathrm{d}x\mathrm{d}y, \quad \mathbf{F}_0^e = -\int_{S_i^e} (\mathbf{L}_\perp \mathbf{N}^e)^{\mathrm{T}} \mathbf{C}_i \boldsymbol{\epsilon}_0 \mathrm{d}x\mathrm{d}y, \tag{2.74}$$

où $\boldsymbol{\epsilon}_0 = [0\ 0\ E^E\ 0\ -yE^T\ xE^T]^{\mathrm{T}}$. Notons que $\mathbf{K}_0$ et $\mathbf{F}_0$ sont intégrés sur $S_i$ (section initiale, non déformée) et que dans ces expressions, l'opérateur $\mathbf{L}_\perp$ correspond à l'expression donnée par l'Équation (2.18) en remplaçant $\tau$ par $\tau_i$ (la torsion dans l'état initial). Pour plus de détails, on pourra consulter Frikha, Cartraud et Treyssède 2013.

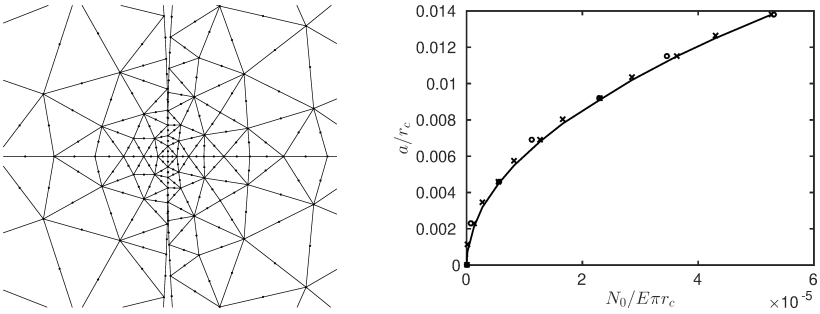


(a) (b)

FIGURE 2.24 – (a) Zoom du maillage SAFE sur la zone de contact inter-brins, (b) évolution de la demi-largeur de contact $a$ en fonction de l'effort de contact normal $N_0$ (ronds : résultats numériques obtenus avec un maillage initial, croix : avec maillage raffiné, traits continus : expression analytique de Hertz pour un contact cylindre-cylindre).

À partir de la solution, la précontrainte de Cauchy $\sigma_0$ est ensuite post-traitée. Le maillage éléments finis est actualisé sur la géométrie déformée $S_0$ par déplacement des nœuds. La torsion $\tau_0$ est obtenue à partir de la torsion initial $\tau_i$ via la relation suivante : $\tau_0 = \tau_i/(1 + E^E)$. Les matrices SAFE impliquées dans l'Équation (2.71) peuvent ensuite être calculées.

Lorsque le problème statique linéaire $\mathbf{K}_0\mathbf{U}_0 = \mathbf{F}_0$ est résolu en une seule étape, la mécanique du contact inter-brins est négligée. Or, comme expliqué précédemment, la géométrie hélicoïdale des brins périphériques engendre une compression radiale du brin central lorsqu'un chargement en traction est appliqué, et ainsi une augmentation de la largeur de contact. La prise en compte de ce phénomène, non-linéaire par essence, nécessite une procédure itérative. Pour cela, une procédure de contact nœud à nœud a été utilisée. Celle-ci nécessite des maillages conformes dans la zone de contact (voir Figure 2.24a). Le calcul, sur la section du câble, commence par un contact ponctuel (un seul nœud de contact entre les brins). Ensuite, des paires de nœuds en contact sont formées au fur et à mesure que le chargement est incrémenté : une fois que l'espace entre une paire de nœuds s'est refermé, la continuité du déplacement est imposée entre ces nœuds. Cette continuité, dans les trois directions selon l'hypothèse de contact collant, est appliquée par condensation des degrés de liberté. La procédure itérative peut être résumée par le système suivant, à résoudre pour chaque pas de chargement $j$ (TREYSSÈDE 2016a) :

$$\mathbf{K}_0^j \Delta\mathbf{U} = \frac{\Delta\epsilon}{\epsilon}\mathbf{P}^{j\mathrm{T}}\mathbf{F}_0, \quad \mathbf{K}_0^j = \mathbf{P}^{j\mathrm{T}}\mathbf{K}_0\mathbf{P}^j, \tag{2.75}$$

où $\mathbf{P}^j$ désigne la matrice de projection qui condense les degrés de liberté de déplacement en contact à l'incrément $j$, $\Delta\mathbf{U}$ et $\Delta\epsilon/\epsilon$ sont respectivement l'incrément de déplacement et de chargement. Le déplacement statique $\mathbf{U}_0$ pour le chargement total $\epsilon = \sum\Delta\epsilon$ est obtenu en faisant la somme des incréments de déplacement.

La méthode d'homogénéisation proposée a été validée dans l'article FRIKHA, CARTRAUD et TREYSSÈDE 2013 par comparaison du comportement global avec des résultats de référence issus de la littérature, pour des ressorts et des torons à sept brins. La prise en compte du contact dans les torons a été validée dans TREYSSÈDE 2016a en comparant l'évolution de la largeur de contact inter-brins en fonction du chargement appliqué avec une théorie de Hertz (voir Figure 2.24b).

### 2.6.6 Perspectives

La modélisation numérique de la propagation des ondes dans un toron à sept brins a permis d'éclaircir les phénomènes physiques observés dans certains résultats expérimentaux pour le mode longitudinal fondamental (donc dans un régime relativement bas en fréquence). Ce travail de compréhension des mécanismes de propagation dans le toron doit néanmoins se poursuivre. À court terme, on envisage de :

— poursuivre les simulations dans un régime plus haute fréquence (notamment pour continuer à y étudier les transferts d'énergie) ;
— poursuivre les validations expérimentales, en considérant d'autres modes.

Le premier point mentionné est motivé par la recherche de nouveaux modes locaux. Les simulations haute fréquence sont devenues plus accessibles grâce à la prise en compte de la symétrie de rotation de la section dans les modèles, qui permet de réduire la taille des problèmes (cette prise en compte de symétrie, évoquée en §2.2.3, est détaillée dans Treyssède 2019). Le second point est motivé par deux aspects. D'une part, l'idée est de vérifier expérimentalement l'existence des modes locaux identifiés numériquement en §2.6.4. L'utilisation de ces modes, confinés dans le brin central, pourrait trouver des applications en END intéressantes. D'autre part, il s'agit d'évaluer le bien-fondé de certaines hypothèses utilisées dans le modèle, en particulier celle du contact collant (sans frottement).

Attardons-nous justement sur l'hypothèse de contact collant. Pour une amplitude de déplacement donnée, la contrainte acoustique tend à augmenter avec la fréquence. Dans les zones de contact, une augmentation de la contrainte de cisaillement peut conduire à un contact imparfait impliquant des phénomènes de glissement et de frottement. L'hypothèse de contact collant implique que la contrainte de cisaillement acoustique soit suffisamment petite dans la largeur de contact, c'est-à-dire inférieure à la contrainte normale multipliée par le coefficient de frottement de la loi de Coulomb. En pratique, le chargement statique en traction d'un toron (jusqu'à 60% de la résistance à la rupture) est tel qu'il entraîne de très fortes contraintes de contact dans la direction normale. On peut supposer que ces contraintes de contact statique sont bien supérieures aux contraintes de cisaillement acoustiques (au moins jusqu'à une certaine fréquence limite ?) de sorte que supposer un contact collant apparaît raisonnable en première approximation. Les résultats expérimentaux devront confirmer ou infirmer cette supposition.

À ces perspectives à court terme, on pourrait aussi ajouter une analyse (simulations et expériences) de l'interaction ondes-défaut dans un toron, comportant une rupture totale de section ou d'un seul brin. Cette analyse permettrait en particulier de mieux comprendre les phénomènes de conversions modales dans les structures multi-brins (et d'en déduire les implications que cela comporte pour l'END).

Au-delà du toron à sept brins, une perspective plus globale qui se dégage de ce travail est de compliquer progressivement les architectures de câbles modélisées. Une géométrie, très fréquente dans les câbles, est celle de la double hélice déjà évoquée en §2.2.4. Par ailleurs, dans le cadre d'un projet en cours, nous nous intéressons actuellement aux armures des câbles ombilicaux de transport d'électricité des éoliennes. L'objectif du projet est de développer et valider expérimentalement des modèles de propagation dans ces armures. On distingue deux types d'armure. Les armures simples sont constituées d'une seule couche de brins hélicoïdaux (voir Figure 2.25a). Ces armures peuvent donc être modélisées par une méthode SAFE en coordonnées tournantes. Toutefois, le nombre de brins étant important (de l'ordre de 50), il est indispensable de réduire la taille du problème en prenant en compte la symétrie de rotation. C'est d'ailleurs ce qui a motivé l'article Treyssède 2019 (cet article montre, en guise de première étape, une validation numérique des développements sur un toron à sept brins ; des résultats obtenus sur une armure de

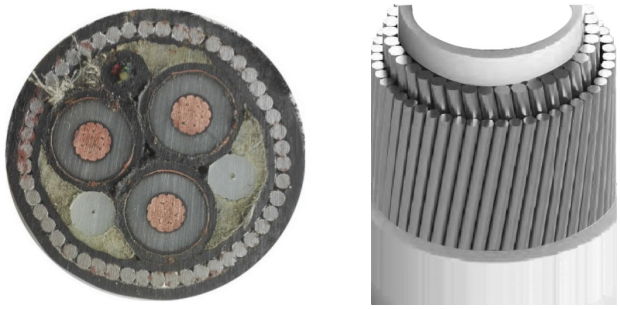

(a) (b)

FIGURE 2.25 – (a) Section d'un câble à armure simple, (b) structure d'une armure double.

câble ombilical devraient être soumis à publication prochainement). Deuxième type d'armure : les armures doubles, constituées de deux couches de brins hélicoïdaux (voir Figure 2.25b). Dans cette configuration, l'*invariance continue* est brisée car les deux couches de brins tournent dans des sens opposés. Ceci exclut l'utilisation d'une méthode SAFE, au profit d'une méthode de type WFEM, qui a été brièvement exposée en §2.2.3.

Un dernier axe de travail concerne la modélisation du comportement statique des câbles. L'idée est de tirer parti des systèmes de coordonnées hélicoïdaux pour reformuler les problèmes et réduire ainsi leur taille. Considérons l'exemple du toron à sept brins : l'exploitation du système de coordonnées tournant a permis de restreindre le problème à résoudre à la section du câble. Toutefois, l'approche proposée est actuellement limitée à des déformations macroscopiques imposées en extension et en torsion. Son application à des déformations en flexion, imposées sous la forme de courbure, est restée en suspens : contrairement aux déformations en extension et torsion, les courbures changent d'expression dans le système tournant, ce qui soulève certaines interrogations. La prise en compte de la flexion dans les modèles statiques revêt des enjeux importants pour l'évaluation de la fatigue des câbles.

Pour clore ce résumé de mes activités de recherche sur les guides élastiques, insistons sur la complexité et la richesse des problématiques abordées dans les câbles. Leur modélisation mécanique met potentiellement en jeu : des effets non-linéaires, de l'homogénéisation, des ondes guidées, des structures périodiques. Si l'on y inclut de l'imagerie de défauts dans le futur (voir §2.3.6), on retrouve les quatre thèmes du GDR CNRS Mecawave (débuté le 1er janvier 2018). Le cadre scientifique est donné...

**Tirés à part :**

- FRIKHA, CARTRAUD et TREYSSÈDE 2013 (voir page 101) ;
- TREYSSÈDE, FRIKHA et CARTRAUD 2013 (voir page 111) ;
- TREYSSÈDE 2019 (voir page 168).

## Articles relatifs à cette section

**Treyssède, F. (2019) :** « Free and forced response of three-dimensional waveguides with rotationally symmetric cross-sections », *Wave Motion*, 87, p. 75–91.

— **(2016a) :** « Dispersion curve veering of longitudinal guided waves propagating inside prestressed seven-wire strands », *Journal of Sound and Vibration*, 367, p. 56–68.

— **(2016b) :** « Investigation of the interwire energy transfer of elastic guided waves inside prestressed cables », *Journal of the Acoustical Society of America*, 140, p. 498–509.

**Nguyen, K. L. et F. Treyssède (2015) :** « Numerical investigation of leaky modes in helical structural waveguides embedded into a solid medium », *Ultrasonics*, 57, p. 125–134.

**Frikha, A., P. Cartraud et F. Treyssède (2013) :** « Mechanical modeling of helical structures accounting for translational invariance. Part 1 : Static behavior », *International Journal of Solids and Structures*, 50 (9), p. 1373–1382.

**Treyssède, F., A. Frikha et P. Cartraud (2013) :** « Mechanical modeling of helical structures accounting for translational invariance. Part 2 : Guided wave propagation under axial loads », *International Journal of Solids and Structures*, 50 (9), p. 1383–1393.

**Frikha, A., F. Treyssède et P. Cartraud (2011) :** « Effect of axial load on the propagation of elastic waves in helical beams », *Wave Motion*, 48 (1), p. 83–92.

**Treyssède, F. et L. Laguerre (2010) :** « Investigation of elastic modes propagating in multi-wire helical waveguides », *Journal of Sound and Vibration*, 329 (10), p. 1702–1716.

## 2.7 Autres activités de recherche

Cette section résume les autres thématiques auxquelles je me suis intéressé avant de commencer à travailler sur les guides d'ondes élastiques. Elles se décomposent en deux axes. Le premier porte sur la propagation acoustique en présence d'écoulement et était, sous la direction de Mabrouk Ben Tahar du laboratoire Roberval, le sujet de ma thèse de doctorat à l'UTC et de mes postes d'ATER. Mes travaux sur cet axe se sont déroulés entre 1999 et 2004 (voir §2.7.1). Le second porte sur les vibrations des structures précontraintes et a constitué mon principal sujet de recherche dans les années qui ont suivi mon recrutement au LCPC, de 2004 à environ 2010 (voir §2.7.3).

Dans cette section, on distinguera une autre thématique, consacrée aux conditions de saut. Il s'agit d'une thématique particulière, qui a assuré une transition entre les deux axes précédents et qui a joué un rôle indirect dans mes travaux sur les guides courbes. Ce travail sur les conditions de saut a été réalisé en collaboration avec Mabrouk Ben Tahar (voir §2.7.2).

### 2.7.1 Acoustique en présence d'écoulement

Dans de nombreuses applications industrielles, en particulier dans le domaine des transports, la propagation acoustique se fait à travers un écoulement. Mes travaux sur cet axe ont consisté à modéliser numériquement la propagation des ondes en présence d'un écoulement subsonique non uniforme, en particulier rotationnel afin de prendre en compte les effets de couche limite ou d'écoulement tournant.

La prise en compte de ces effets oblige à résoudre les équations d'Euler linéarisées. Cette linéarisation est effectuée selon des perturbations eulériennes. Il existe toutefois une alternative : l'équation dite de Galbrun (obtenue par l'auteur du même nom en 1931). Cette équation, établie dans une représentation mixte eulérienne-lagrangienne, représente le même phénomène physique que les équations d'Euler linéarisées mais possède la particularité de n'être écrite qu'en terme de la perturbation lagrangienne du déplacement. Ceci lui confère certaines propriétés physiques intéressantes : existence d'un lagrangien donnant accès à des expressions exactes de densité et de flux d'énergie, écriture simple des conditions aux limites aux parois.

Pour résoudre numériquement cette équation par une méthode d'éléments finis, une formulation mixte en déplacement-pression a été proposée. Ce type de formulation permet de pallier

le phénomène de blocage inhérent à toute formulation en déplacement, bien connu en mécanique des milieux déformables incompressibles.

La même approche a ensuite été appliquée aux équations de Navier-Stokes afin de tenir compte de l'influence des effets de la dissipation visqueuse et thermique. Ces effets deviennent typiquement non négligeables dans des problèmes mettant en jeu des cavités ou tubes de petites tailles. La perturbation des équations de Navier-Stokes en représentation mixte conduit alors à une formulation mixte en déplacement-pression-température.

Par ailleurs, la formulation mixte en déplacement-pression a été couplée à un solide élastique pour permettre l'étude des effets d'un écoulement non-uniforme sur le comportement vibroacoustique d'une structure. La formulation mixte retenue permet une prise en compte simple des conditions de couplage entre le fluide et la structure.

Les méthodes proposées ont été validées par comparaison avec divers modèles semi-analytiques. Elles ont donné lieu aux articles suivants : Treyssède, Gabard et Ben Tahar 2003 ; Gabard, Treyssède et Ben Tahar 2004 ; Treyssède et Ben Tahar 2004b ; Treyssède et Ben Tahar 2004a

Dans le cadre de ces travaux, je me suis également intéressé aux problèmes de réflexion-transmission dans les conduits. Pour cela, j'ai pu développer une technique de décomposition modale permettant de simuler des conditions de non-réflexion multimodales (autrement dit, des conditions transparentes...). Sur le principe, l'approche est en fait assez similaire à celle utilisée dans §2.4 pour les guides élastiques.

### 2.7.2 Conditions générales de saut

Durant mes années de thèse, j'ai commencé à m'intéresser aux conditions de couplage qui s'appliquent à des petites perturbations entre deux milieux continus non initialement au repos. Mes activités sur cette thématique se sont poursuivies après mon recrutement au LCPC et ont donné lieu à un (long) travail de nature théorique publié dans un article (Treyssède et Ben Tahar 2009).

La motivation initiale était d'identifier quelle condition cinématique appliquer à l'interface, de nature "glissante", entre une structure et un fluide parfait. Si le fluide est initialement au repos, il n'y a aucune ambiguité : la continuité de la vitesse normale équivaut à celle du déplacement normal. En revanche, si le fluide est en écoulement, ce n'est plus le cas. Se pose aussi la question du choix des perturbations mises en jeu : eulériennes ou lagrangiennes ? La problématique est identique pour la condition dynamique. Pour une structure initialement au repos, c'est la continuité du vecteur contrainte normale à l'interface qui s'applique. En revanche, si la structure est précontrainte, l'expression des conditions de couplage devient plus délicate.

Nous avons proposé une obtention rigoureuse des conditions de couplage pour des petites perturbations entre deux milieux continus non initialement au repos. L'interface, supposée imperméable, est non-plane. L'approche suivie est directement inspirée des travaux en interface plane de Bernard Poirée [23] : elle fait appel à une description mixte eulérienne-lagrangienne ainsi qu'au concept des fonctions généralisées en théorie des distributions. La démarche suivie est générale si bien que les résultats obtenus s'appliquent à toute perturbation linéaire satisfaisant une équation de conservation. Ainsi, des conditions générales de saut, associées respectivement aux équations de conservation de la masse, de la quantité de mouvement, de l'énergie et de l'entropie, ont pu être établies pour les perturbations lagrangiennes de déplacement, de contrainte, de flux de chaleur et de température.

23. B. Poirée, "Les équations de l'acoustique linéaire et non-linéaire dans les fluides en mouvement", Thèse d'état, Université Pierre et Marie Curie, Paris VI, 1982

Les conditions ainsi obtenues en représentation mixte ont été validées par comparaison avec des conditions exprimées en représentation eulérienne. En particulier, nous avons montré que la condition dite de Myers établie en description eulérienne découlait de la condition de continuité du déplacement normal lagrangien. L'examen des représentations montre qu'il apparaît difficile – voire impossible – d'établir une condition de passage générale écrite uniquement en terme de perturbations eulériennes (sauf dans les cas particuliers où les perturbations de déplacement eulérienne et lagrangienne sont confondues). En effet, une variable supplémentaire correspondant au déplacement normal de la surface doit être introduite en représentation eulérienne. Ce constat légitimise en quelque sorte l'utilisation d'une représentation mixte.

Par ailleurs, la description mixte eulérienne-lagrangienne permet une unification intéressante entre les formulations fluide et solide, qui sont alors écrites en terme du déplacement lagrangien seulement. Pour un solide, la perturbation des équations selon cette description aboutit à une formulation lagrangienne actualisée linéarisée, bien connue en mécanique non-linéaire (voir Équation (2.70)). Pour un fluide parfait, elle aboutit à l'équation de Galbrun.

Soulignons que la validation des conditions de saut a nécessité leur transformation dans un système de coordonnées associé à l'interface courbe, impliquant donc quelques notions de géométrie différentielle et calcul tensoriel. La familiarisation avec ce type d'outils a été particulièrement appréciable pour appréhender la propagation des ondes dans les structures courbes (cf. §2.2 et §2.6)... Ce travail a également nécessité, en parallèle, de se familiariser avec la dynamique des structures précontraintes, thématique dont l'activité est décrite ci-après.

### 2.7.3 Vibrations des structures précontraintes

L'analyse modale vibratoire constitue un outil potentiellement intéressant pour le SHM. Elle repose sur une mesure du comportement global de la structure. Cette mesure peut permettre d'identifier la présence de dysfonctionnements. Dans le domaine du génie civil, le SHM des ponts constitue un exemple typique d'application. Cependant, les variations de température ambiante (et plus généralement, des conditions environnementales) sont susceptibles de modifier les paramètres modaux : fréquences propres, déformées et amortissements. Vis-à-vis de l'identification (détection, localisation,...), ces variations de température sont considérées comme des nuisances car il peut devenir impossible de distinguer les effets d'un dysfonctionnement mécanique des effets thermiques naturels. Le développement de modèles peut alors aider à comprendre, voire compenser, ces effets sur les vibrations.

Partant d'une analyse non-linéaire, mes travaux sur cette thématique ont d'abord consisté à clarifier l'obtention des équations de la dynamique des structures précontraintes en y incluant les effets thermiques. Divers modèles de poutres et câbles, à la fois analytiques et numériques, ont été développés.

Dans Treyssède 2007, les vibrations de poutres thermiquement précontraintes ont été étudiées sur la base de modèles éléments finis de poutre 2D établis en formulations lagrangiennes totale et actualisée. Les modèles ont été corroborés par des résultats expérimentaux en chambre climatique. Les résultats ont montré l'importance des effets de prédéformation liée à la préflexion d'origine thermique et aux imperfections initiales.

Dans Treyssède 2009, un modèle analytique de câble 3D sous contrainte thermique a été proposé. Ce modèle néglige les effets de rigidité à la flexion. Il étend la théorie d'Irvine sur les vibrations de câbles au cas thermoélastique. Ce modèle simple a l'avantage de n'introduire que deux paramètres adimensionnels : le paramètre d'Irvine classique ("sag-extensibility"), qui dépend des caractéristiques du câble, et un nouveau paramètre lié au changement de température.

L'article Treyssède 2010 propose un modèle analytique de poutre 2D précontrainte, soumis

à son poids propre et des sollicitations thermiques. Les non-linéarités géométriques sont prises en compte sur la base de grands déplacements et petites rotations. Les fréquences propres sont obtenues à partir d'une linéarisation des équations d'équilibre. Le modèle ainsi obtenu a notamment permis de prendre en compte les effets combinés de température et de rigidité à la flexion d'un câble.

Un article plus récent (Treyssède 2017) a finalement clôturé mes travaux sur cet axe. Cet article propose une procédure numérique générale permettant la modélisation par éléments finis des effets thermiques sur la statique (non-linéaire) et les vibrations (linéarisées) de structures 3D impliquant des câbles multiples. La principale difficulté du problème réside dans la modification par changement de température de la tension dans chacun des câbles de la structure, tension qui devient alors indéterminée. La procédure proposée repose sur des conditions particulières à appliquer aux extrémités de chaque câble et autorise une discrétisation par des éléments non-linéaires de poutre (généralement disponibles dans les codes de calcul). La convergence et la précision des résultats ont pu être évaluées sur un câble seul, grâce aux modèles analytiques évoqués plus haut. La méthode a ensuite été appliquée à des ponts à câbles. Les résultats montrent l'importance de modéliser la structure globale pour une analyse quantitative des effets de la température sur la dynamique locale des câbles (en d'autres termes, les câbles ne peuvent pas être isolés du reste de la structure dans les modélisations).

Mes travaux sur cet axe m'ont en particulier familiarisé avec les formulations classiques de l'analyse non-linéaire des structures (formulations lagrangienne actualisée vs. lagrangienne totale). Une familiarisation exploitée, un peu plus tard, dans la modélisation des effets acoustoélastiques dans les guides d'onde (voir §2.6.3)...

## Articles relatifs à cette section

**Treyssède, F. (2017) :** « Finite element modeling of temperature load effects on the vibration of local modes in multi-cable structures », *Journal of Sound and Vibration*, 413, p. 191–204.

**Treyssède, F. (2010) :** « Vibration analysis of horizontal self-weighted beams and cables with bending stiffness subjected to thermal loads », *Journal of Sound and Vibration*, 329 (9), p. 1536–1552.

— **(2009) :** « Free linear vibrations of cables under thermal stress », *Journal of Sound and Vibration*, 327 (1-2), p. 1–8.

**Treyssède, F. et M. Ben Tahar (2009) :** « Jump conditions for unsteady small perturbations at fluid-solid interfaces in the presence of initial flow and prestress », *Wave Motion*, 46 (2), p. 155–167.

**Treyssède, F. (2007) :** « Prebending effects upon the vibrational modes of thermally prestressed planar beams », *Journal of Sound and Vibration*, 307 (1-2), p. 295–311.

**Gabard, G., F. Treyssède et M. Ben Tahar (2004) :** « A numerical method for vibro-acoustic problems with sheared mean flows », *Journal of Sound and Vibration*, 272 (3-5), p. 991–1011.

**Treyssède, F. et M. Ben Tahar (2004a) :** « Comparison of a finite element model with a multiple-scales solution for sound propagation in varying ducts with swirling flows », *Journal of the Acoustical Society of America*, 115 (6), p. 2716–2730.

— **(2004b) :** « Validation of a finite element method for sound propagation and vibro-acoustic problems with swirling flows », *Acta Acustica United with Acustica*, 90 (4), p. 731–745.

**Treyssède, F., G. Gabard et M. Ben Tahar (2003) :** « A mixed finite element method for acoustic wave propagation in moving fluids based on an Eulerian-Lagrangian description », *Journal of the Acoustical Society of America*, 113 (2), p. 705–716.

# 3

# Tirés à part

Les tirés à part sont donnés dans l'ordre chronologique (année de publication).

# Mode propagation in curved waveguides and scattering by inhomogeneities: Application to the elastodynamics of helical structures

Fabien Treyssède[a)]
*Institut franýais des sciences et technologies des transports, de l'amýnagement et des rýseaux, Centre de Nantes, BP4129, 44341 Bouguenais Cedex, France*

(Received 2 April 2010; revised 26 January 2011; accepted 2 February 2011)

This paper reports on an investigation into the propagation of guided modes in curved waveguides and their scattering by inhomogeneities. In a general framework, the existence of propagation modes traveling in curved waveguides is discussed. The concept of translational invariance, intuitively used for the analysis of straight waveguides, is highlighted for curvilinear coordinate systems. Provided that the cross-section shape and medium properties do not vary along the waveguide axis, it is shown that a sufficient condition for invariance is the independence on the axial coordinate of the metric tensor. Such a condition is indeed checked by helical coordinate systems. This study then focuses on the elastodynamics of helical waveguides. Given the difficulty in achieving analytical solutions, a purely numerical approach is chosen based on the so-called semi-analytical finite element method. This method allows the computation of eigenmodes propagating in infinite waveguides. For the investigation of modal scattering by inhomogeneities, a hybrid finite element method is developed for curved waveguides. The technique consists in applying modal expansions at cross-section boundaries of the finite element model, yielding transparent boundary conditions. The final part of this paper deals with scattering results obtained in free-end helical waveguides. Two validation tests are also performed.
 [DOI: 10.1121/1.3559682]

PACS number(s): 43.35.Cg, 43.20.Mv, 43.20.Bi [JJM] Pages: 1857–1868

## I. INTRODUCTION

Many applications are likely to involve guided wave propagation inside curved structures. However, the literature concerning the theory of curved waveguides is rather scarce compared to straight waveguides. For instance, some references can be found on elastic waves propagating in circular plates,[1–3] toroidal pipes,[4] tyres,[5] spherical plates,[6,7] circular waveguides of arbitrary cross-section,[8] twisted bars,[9] helical springs,[10–12] multi-wire helical strands,[13] as well as electromagnetic waves in optical fibers.[14–16]

The goal of this paper is to highlight the propagation of modes in curved waveguides as well as their scattering by inhomogeneities. The existence of propagation modes traveling in infinite curved waveguides is first discussed in a general framework (Sec. II), valid for any type of waves (elastic, acoustic, electromagnetic, etc.).

Then, the remainder of the paper focuses on the elastodynamics of helical waveguides. In the context of non-destructive testing and structural health monitoring of cables,[17–21] one of the motivations is to develop modeling tools for progress in the understanding of wave-damage interaction in helical structures. The basic element of civil-engineering cables is usually a seven-wire strand, consisting of one straight cylindrical core wire surrounded by one layer of six helical wires. The results of this paper will only concern single wires, inter-wire contact effects being left for further investigations.

Given the difficulty in achieving analytical solutions, a purely numerical approach is chosen. The formulation is fully three-dimensional (3D). For the computation of guided modes, the so-called semi-analytical finite element (SAFE) technique is employed. This technique has been extensively used in elasticity for uniform straight waveguides—see for instance Refs. 22–27. It has also been proposed in duct acoustics[28,29] and electromagnetics.[15,30] The advantage of SAFE methods is their capacity to handle complex waveguides of arbitrary cross-section, together with material anisotropy and transverse heterogeneity. An axial dependence $e^{iks}$ is assumed before finite element (FE) discretization ($k$ and $s$ are the wavenumber and distance along the waveguide axis, respectively)—hence reducing the problem from three to two dimensions—so that only the cross-section needs to be meshed. Recently, the author has proposed a SAFE method for helical elastic waveguides.[13,31] This method is briefly recalled in this paper (Sec. III) and some dispersion curves are shown for helical waveguides of circular cross-sections with different helix lay angles.

For modal scattering by inhomogeneities, the present paper proposes a hybrid FE-based method (Sec. IV). It consists of applying modal expansions at cross-section boundaries of an usual FE model, where semi-infinite waveguides are connected, yielding transparent boundary conditions. The FE model can then be limited to a small region surrounding the inhomogeneity, which in turn might be of complex shape (cracks, discontinuities, local bends, etc.). The modal expansions require the knowledge of guided modes, which can be obtained from analytical solutions

[a)]Author to whom correspondence should be addressed. Electronic mail: fabien.treyssede@ifsttar.fr

when available, or from the SAFE method as done in this paper. The solution of the hybrid system directly yields the coefficients of scattered modes. In the literature, hybrid methods have already been proposed for elastic guided waves in two-dimensional straight waveguides (plates[32–37] and cylinders[38]) as well as acoustic waves in ducts[39,40] for instance. A close relationship between hybrid and Dirichlet-to-Neumann approaches can be demonstrated, as done in Ref. 40 for acoustic problems. Hybrid methods are a powerful alternative to usual numerical approaches, transient[41,42] or time-harmonic,[43,44] which requires longer FE meshes as well as modal post-processing steps of results.

In this paper, useful expressions are presented in order to calculate modal forces and power flows and to efficiently separate ingoing from outgoing modes. These expressions may greatly simplify the development of hybrid methods inside commercial codes, as well as the post-process of power coefficients for the interpretation of results.

As illustrative examples, some results are finally shown on the scattering of the first extensional mode in free-end helical waveguides of different lay angles. Two validation tests are also performed in order to check the accuracy of the proposed approach. Though applied to elastic waves, the overall approach of this paper is rather general and may be applied or extended to other physics.

## II. ON THE EXISTENCE OF GUIDED MODES IN CURVED WAVEGUIDES

### A. Translational invariance

By definition, guided modes (or propagation modes) are waves traveling without reflection along the axis of infinite waveguides. The time and axial evolution of such modes is hence harmonic. In other words, an $e^{i(ks-\omega t)}$ dependence can be assumed and separated from all field components. In this paper, $k$ denotes the axial wavenumber, $s$ the axial coordinate, and $\omega$ the angular frequency.

This axial dependence can only be applied if the considered waveguide is translationally invariant along its axis. Intuitively for straight waveguides, translational invariance means that both the cross-section shape and the material do not vary with respect to $s$. This intuitive definition is yet no longer accurate for curved waveguides. For instance, one may think of an axis corresponding to an arbitrary curve: waves can generally not travel without reflection because of the curvature variation, even though the section and the material remain invariant along $s$. Indeed, a third condition should be added in that case: the curvature of the axis should also remain constant.

From a mathematical point of view, the $e^{iks}$ axial dependence indeed comes from a separation of variables that is applicable if the following fundamental property holds: the coefficients of equilibrium equations, including boundary conditions, must not depend on $s$. With this property, performing an axial Fourier transform do not give any convolution products but yields the same equilibrium equations as assuming an $e^{iks}$ dependence: one can truly speak of propagation modes. This fundamental property is checked under the following three conditions:

(1) the cross-section shape do not vary along the $s$-axis;
(2) the material properties remain constant along $s$;
(3) the coefficients associated with the partial derivatives of the differential operators that are involved in the physics under consideration (gradient, divergence, Laplacian, etc.) are independent on $s$.

These conditions somewhat extend the concept of translational invariance for curved waveguides. Condition 1 is geometric and necessary for the invariance of boundary conditions. Condition 2 is material. Both conditions are obvious and implicitly assumed in straight waveguide analyses. Condition 3 is non-trivial and closely related to the curvilinear coordinate system considered.

### B. Metric tensor

Condition 3 may be highlighted, thanks to the calculation of the metric tensor associated with the coordinate system. For a fundamental introduction to the use of general curvilinear coordinate systems, the reader may refer to Chap. 2 of Ref. 45 for instance.

Let us consider a curvilinear coordinate system denoted $(x, y, s)$, $x$ and $y$ being the transverse coordinates. Let $(X, Y, Z)$ and $(\mathbf{e}_X, \mathbf{e}_Y, \mathbf{e}_Z)$ be the Cartesian coordinates and the Cartesian basis, respectively. Any position vector $(X, Y, Z)$ is uniquely related to $(x, y, s)$ through a mapping denoted $\Phi$ as follows:

$$X\mathbf{e}_X + Y\mathbf{e}_Y + Z\mathbf{e}_Z = \Phi(x, y, s). \tag{1}$$

In the following, the notation $(x, y, s)$ may be changed to $(x^1, x^2, x^3)$ for simplicity. The covariant basis is given by $(\mathbf{g}_1, \mathbf{g}_2, \mathbf{g}_3)$, where $\mathbf{g}_i = \partial\Phi/\partial x^i$ $(i = 1, 2, 3)$. The contravariant basis, denoted $(\mathbf{g}^1, \mathbf{g}^2, \mathbf{g}^3)$, is defined from $\mathbf{g}^i \cdot \mathbf{g}_j = \delta^i_j$.

Then, the covariant metric tensor $\mathbf{g}$ is given by

$$g_{ij} = \mathbf{g}_i \cdot \mathbf{g}_j. \tag{2}$$

A fundamental point is that, when $\mathbf{g}$ does not depend on $s$ $(\mathbf{g} = \mathbf{g}(x, y))$, condition 3 is automatically satisfied for any differential operator and hence any physics. This can be explained by the fact that the coefficients of any differential operators are given by Christoffel symbols, which only depend on the $g_{ij}$'s. For clarity, the Christoffel symbols $\Gamma^k_{ij} = \mathbf{g}_{i,j} \cdot \mathbf{g}^k$ are expressed as a function of the metric tensor as follows:

$$\Gamma^k_{ij} = \frac{1}{2} g^{kl} \left( \frac{\partial g_{jl}}{\partial x^i} + \frac{\partial g_{il}}{\partial x^j} - \frac{\partial g_{ij}}{\partial x^l} \right), \tag{3}$$

where $g^{ij} = \mathbf{g}^i \cdot \mathbf{g}^j$ is the contravariant metric tensor, equal to the inverse of the covariant metric tensor $(g^{ij} = (\mathbf{g}^{-1})_{ij})$.

### C. Standard coordinate systems revisited

For clarity, we first consider the cylindrical coordinate system $(x^1, x^2, x^3) = (r, \theta, z)$, obtained from the mapping $(X, Y, Z) = (r\cos\theta, r\sin\theta, z)$. Its metric tensor is

$$\mathbf{g} = \begin{bmatrix} 1 & 0 & 0 \\ 0 & r^2 & 0 \\ 0 & 0 & 1 \end{bmatrix}. \tag{4}$$

As expected, **g** does not depend on $z$ (obvious existence of guided waves traveling in the $z$-direction). It does not depend on $\theta$ either (azimuthal direction), which also proves the existence of guided modes inside circular waveguides for any physics.

The spherical coordinate system $(x^1, x^2, x^3) = (r, \theta, \phi)$ is obtained from the mapping $(X, Y, Z) = (r\cos\theta\sin\phi, r\sin\theta\sin\phi, r\cos\phi)$. $\theta$ and $\phi$ are the azimuthal and zenith angles, respectively. The corresponding metric tensor is

$$\mathbf{g} = \begin{bmatrix} 1 & 0 & 0 \\ 0 & r^2\sin^2\phi & 0 \\ 0 & 0 & r^2 \end{bmatrix}. \tag{5}$$

**g** does not depend on $\theta$, which means that we can also speak of guided waves in the azimuthal direction for spherical waveguides (and any physics).

As mentioned in the introduction, analyses of circular and spherical waveguides have already been conducted (in elastodynamics). Yet, the existence of guided waves also occurs in some other coordinate systems. For instance, the metric tensor of spheroidal coordinate systems (oblate or prolate) does not depend on the azimuthal coordinate either. Also, helical coordinate systems are invariant along the helix axis, as shown in the next subsection.

### D. Helical coordinate system

A helical coordinate system is now built. One starts by defining the helix centerline curve, described by the following position vector in the Cartesian orthonormal basis

$$\mathbf{R}(s) = R\cos\frac{2\pi}{l}s\mathbf{e}_X + R\sin\frac{2\pi}{l}s\mathbf{e}_Y + \frac{L}{l}s\mathbf{e}_Z, \tag{6}$$

where $l = \sqrt{L^2 + 4\pi^2R^2}$ is the curvilinear length of one helix step. $R$ and $L$ are, respectively, the radius of the centerline in the $(X, Y)$ Cartesian plane and the helix step along the $Z$ axis (see Fig. 1). The helix lay angle $\phi$ is defined from $\tan\phi = 2\pi R/L$. The unit tangent, normal and binormal vectors to the centerline are, respectively, obtained from $\mathbf{T} = d\mathbf{R}/ds$ and the Serret–Frenet formula:[46] $d\mathbf{T}/ds = -\kappa\mathbf{N}$, $d\mathbf{N}/ds = \tau\mathbf{B} + \kappa\mathbf{T}$, and $d\mathbf{B}/ds = -\tau\mathbf{N}$ (one has $\mathbf{B} = \mathbf{T} \wedge \mathbf{N}$). Note that **N** is oriented outward the curvature in this paper. For a helix, both the curvature $\kappa = 4\pi^2R/l^2$ and torsion $\tau = 2\pi L/l^2$ are constant.

For clarity, **N**, **B,** and **T** are expressed in the Cartesian basis as

$$\begin{aligned}
\mathbf{N}(s) &= \cos\frac{2\pi s}{l}\mathbf{e}_X + \sin\frac{2\pi s}{l}\mathbf{e}_Y, \\
\mathbf{B}(s) &= -\frac{L}{l}\sin\frac{2\pi s}{l}\mathbf{e}_X + \frac{L}{l}\cos\frac{2\pi s}{l}\mathbf{e}_Y - \frac{2\pi R}{l}\mathbf{e}_Z, \\
\mathbf{T}(s) &= -\frac{2\pi R}{l}\sin\frac{2\pi s}{l}\mathbf{e}_X + \frac{2\pi R}{l}\cos\frac{2\pi s}{l}\mathbf{e}_Y + \frac{L}{l}\mathbf{e}_Z.
\end{aligned} \tag{7}$$

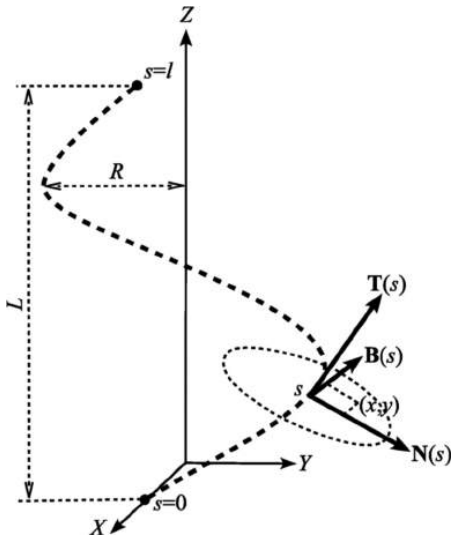


FIG. 1. Helix centerline curve (one step) with its associated Serret–Frenet basis and $(x, y, s)$ helical coordinate system.

A helical coordinate system can be built from the orthonormal basis (**N**, **B**, **T**), with the following mapping $\Phi$:

$$\Phi(x, y, s) = \mathbf{R}(s) + x\mathbf{N}(s) + y\mathbf{B}(s). \tag{8}$$

Using Serret–Frenet formula, one obtains the covariant basis (non-orthogonal)

$$\begin{aligned}
&\mathbf{g}_1 = \mathbf{N}(s), \qquad \mathbf{g}_2 = \mathbf{B}(s), \\
&\mathbf{g}_3 = -\tau y\mathbf{N}(s) + \tau x\mathbf{B}(s) + (1 + \kappa x)\mathbf{T}(s),
\end{aligned} \tag{9}$$

and the calculation of the covariant metric tensor finally gives

$$\mathbf{g} = \begin{bmatrix} 1 & 0 & -\tau y \\ 0 & 1 & \tau x \\ -\tau y & \tau x & \tau^2(x^2 + y^2) + (1 + \kappa x)^2 \end{bmatrix}. \tag{10}$$

**g** does not depend on $s$. As a consequence, the coefficients of any partial differential operators expressed in the so-defined coordinate system are independent on $s$ too. This coordinate system can hence be used for the analysis of helical waveguides.

As a side remark, note that the following relations hold:

$$R = \frac{\kappa}{\kappa^2 + \tau^2}, \quad L = \frac{2\pi\tau}{\kappa^2 + \tau^2}, \quad \frac{2\pi}{l} = \sqrt{\kappa^2 + \tau^2}. \tag{11}$$

Then from Eqs. (6) and (7), it can be checked that the particular case $\tau = 0$ degenerates into a circular coordinate system whose circular axis of radius $1/\kappa$ lies into the $(X, Y)$ plane. The case $\kappa = 0$ degenerates into a twisting system, as detailed in the next subsection.

### E. Note on the twisting coordinate system

A useful twisting coordinate system can be obtained from $\kappa = 0$ and $\tau = 2\pi/L$. It corresponds to a system for which the $(x, y)$ plane (cross-section plane) rotates around and along the $Z$ axis ($s \equiv Z$) with an axial periodicity $L$ (rotation rate of $\tau = 2\pi/L$). The cross-section plane remains parallel to $(X, Y)$. Indeed, such a coordinate system also allows the analysis of a helical waveguide; in the local rotating $(x, y)$ plane, the cross-section of a helical waveguide do not change along $Z$ either (condition 1 is still satisfied).

Such a system is particularly interesting. It also allows the consideration of cylindrical waveguides of axis $Z$ for any value of $\tau$ ("a twisted cylinder remains a cylinder"). And as a consequence, a twisting system is suitable for the analysis of multi-wire waveguides (see Ref. 13). This system will be chosen for the results obtained in the present paper. Note that this kind of system coincides with the one proposed in Ref. 9 for the analysis of pretwisted waveguides or in Refs. 15 and 16 for electromagnetics.

Yet, the cross-section shape must be carefully considered because it is usually provided in the cutting plane normal to the helix centerline. With a twisting system, the shape must be determined in a plane parallel to the $(X, Y)$ plane. Let us find the cross-section cut by the plane $Z = 0$. In the helical system, Eq. (8) yields

$$\begin{cases} X = (R + x)\cos\frac{2\pi s}{l} - y\frac{L}{l}\sin\frac{2\pi s}{l} \\ Y = (R + x)\sin\frac{2\pi s}{l} + y\frac{L}{l}\cos\frac{2\pi s}{l}, \\ Z = \frac{L}{l}s - \frac{2\pi R}{l}y \end{cases} \tag{12}$$

so that $s = 2\pi yR/L$ at $Z = 0$. Let $(x, y) = (x(t), y(t))$ be a curve parametrization of the cross-section normal to the helix centerline, $t$ denoting the curve parameter. Then, the cross-section cut by $Z = 0$ can be parametrized as follows:

$$\begin{cases} X(t) = (R + x(t))\cos(\alpha y(t)) - y(t)\frac{L}{l}\sin(\alpha y(t)) \\ Y(t) = (R + x(t))\sin(\alpha y(t)) + y(t)\frac{L}{l}\cos(\alpha y(t)) \end{cases}, \tag{13}$$

where $\alpha = 4\pi^2 R/lL$. The above parametrization yields the adequate cross-section that must be used with a twisting coordinate system.

For a helical waveguide of circular section of radius $a$, one has $(x(t), y(t)) = (a\cos t, a\sin t)$ with $t \in [0; 2\pi]$. Figure 2 exhibits cross-section shapes obtained for $\phi = 0°$, 15°, and 30° with $R = 2a$.

## III. ELASTIC GUIDED MODES IN HELICAL WAVEGUIDES

In this section, elastic guided modes in helical waveguides are solved numerically. One assumes a linearly elastic material, small strains, and displacements, with a time-harmonic $e^{-i\omega t}$ dependence. The general approach is based on a SAFE technique, which is briefly recalled. No special assumption is required on waveguide properties: arbitrary cross-sections, heterogeneous or anisotropic materials are allowed (but with invariance along the axis).

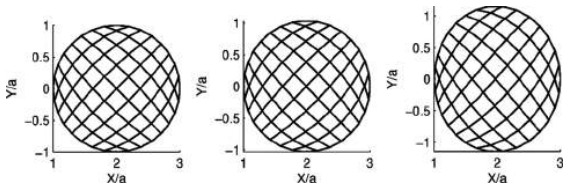


FIG. 2. $Z = 0$ plane-cut of a helical waveguide $R = 2a$ having a circular cross-section of radius $a$ for the following lay angles: $\phi = 0°$ (cylinder), 15°, and 30° (from left to right). The SAFE mesh used for the computations is also shown.

First, one recalls the variational formulation of elastodynamics for clarity,

$$\int_\Omega \delta\boldsymbol{\epsilon}^T\boldsymbol{\sigma}dV - \omega^2\int_\Omega \rho\delta\mathbf{u}^T\mathbf{u}dV = \int_\Omega \delta\mathbf{u}^T\mathbf{q}dV + \int_{\delta\Omega}\delta\mathbf{u}^T\mathbf{f}dV, \tag{14}$$

where $\mathbf{u}$, $\boldsymbol{\epsilon}$, and $\boldsymbol{\sigma}$ are the displacement, strain and stress vectors. $\delta$ denotes virtual fields. $\mathbf{f}$ is the traction vector on the surface $\delta\Omega$. $\rho$ is the material density and $\mathbf{q}$ represents some known acoustic sources inside the structural volume $\Omega$.

### A. Strain–displacement and stress–strain relations

In a general non-orthogonal curvilinear coordinate system, the strain–displacement relationship is expressed as

$$\epsilon_{ij} = 1/2(u_{i,j} + u_{j,i}) - \Gamma^k_{ij}u_k, \tag{15}$$

where subscripts denote covariant components with respect to the contravariant basis. The notation $(\cdot)_{,i}$ $(i = 1, 2, 3)$ is used for derivatives with respect to $x$, $y$, and $s$, respectively. Note that covariant components generally have non-physical units and the contravariant basis is non-orthogonal. In the remainder, physical components with respect to the orthonormal Serret–Frenet basis $(\mathbf{N}, \mathbf{B}, \mathbf{T})$ will be preferred.

The strain–displacement relation can be rewritten as follows:

$$\boldsymbol{\epsilon} = (\mathbf{L}_{xy} + \mathbf{L}_s\partial/\partial s)\mathbf{u}, \tag{16}$$

where $\mathbf{L}_{xy}$ is the operator containing all terms except the derivatives with respect to the $s$-axis. $\mathbf{u} = [u_n\ u_b\ u_t]^T$ is the displacement field, where the superscript $T$ denotes the matrix transpose. $\boldsymbol{\epsilon}$ denotes the strain vector $[\epsilon_{nn}\ \epsilon_{bb}\ \epsilon_{tt}\ 2\epsilon_{nb}\ 2\epsilon_{nt}\ 2\epsilon_{bt}]^T$. The stress–strain relation is then expressed as

$$\boldsymbol{\sigma} = \mathbf{C}\boldsymbol{\epsilon}, \tag{17}$$

where $\boldsymbol{\sigma} = [\sigma_{nn}\ \sigma_{bb}\ \sigma_{tt}\ \sigma_{nb}\ \sigma_{nt}\ \sigma_{bt}]^T$ is the stress vector and $\mathbf{C}$ is the matrix of material properties, expressed in the orthonormal Serret–Frenet basis. $\mathbf{C}$ might be complex (as it is the case for viscoelastic materials).

With the helical coordinate system of Sec. II D, the expression of $\mathbf{L}_{xy}$ and $\mathbf{L}_s$ are given by

$$\mathbf{L}_{xy} = \frac{1}{1+\kappa x}\begin{bmatrix} (1+\kappa x)\partial/\partial x & 0 & 0 \\ 0 & (1+\kappa x)\partial/\partial y & 0 \\ \kappa & 0 & \tau y\partial/\partial x - \tau x\partial/\partial y \\ (1+\kappa x)\partial/\partial y & (1+\kappa x)\partial/\partial x & 0 \\ \tau y\partial/\partial x - \tau x\partial/\partial y & -\tau & -\kappa + (1+\kappa x)\partial/\partial x \\ \tau & \tau y\partial/\partial x - \tau x\partial/\partial y & (1+\kappa x)\partial/\partial y \end{bmatrix}, \quad \mathbf{L}_s = \frac{1}{1+\kappa x}\begin{bmatrix} 0 & 0 & 0 \\ 0 & 0 & 0 \\ 0 & 0 & 1 \\ 0 & 0 & 0 \\ 1 & 0 & 0 \\ 0 & 1 & 0 \end{bmatrix}. \tag{18}$$

Details of calculations can be found in Refs. 13 and 31. As expected, note that both operators do not depend on $s$ so that we can truly assume and separate the axial $e^{iks}$ dependence.

### B. SAFE formulation

There is no external force for the purpose of studying propagation modes. The SAFE technique consist in assuming an $e^{iks}$ dependence for $\mathbf{u}$ ($e^{iks}$ for $\delta\mathbf{u}$) in the variational formulation (14) before FE discretization. Then, $\partial/\partial s$ can be replaced by $ik$ and the exponential separated from all field components. The dimensionality of the problem is hence reduced to the two dimensions of the cross-section.

From Eqs. (14), (16), and (17), this leads to the following eigenvalue problem for the determination of guided modes:[13,31]

$$\{\mathbf{K}_1 - \omega^2\mathbf{M}_S + ik(\mathbf{K}_2 - \mathbf{K}_2^T) + k^2\mathbf{K}_3\}\mathbf{U} = \mathbf{0}, \tag{19}$$

with the following elementary matrices:

$$\begin{aligned} \mathbf{K}_1^e &= \textstyle\int_{S^e} \mathbf{N}^{eT}\mathbf{L}_{xy}^T\mathbf{C}\mathbf{L}_{xy}\mathbf{N}^e\sqrt{g}dS, \\ \mathbf{K}_2^e &= \textstyle\int_{S^e} \mathbf{N}^{eT}\mathbf{L}_{xy}^T\mathbf{C}\mathbf{L}_s\mathbf{N}^e\sqrt{g}dS, \\ \mathbf{K}_3^e &= \textstyle\int_{S^e} \mathbf{N}^{eT}\mathbf{L}_s^T\mathbf{C}\mathbf{L}_s\mathbf{N}^e\sqrt{g}dS, \\ \mathbf{M}_S^e &= \textstyle\int_{S^e} \rho\mathbf{N}^{eT}\mathbf{N}^e\sqrt{g}dS. \end{aligned} \tag{20}$$

$\mathbf{U}$ is the column vector containing nodal displacements expressed in the orthonormal Serret–Frenet basis. $\rho$ is the material density. $\mathbf{N}^e$ is a matrix of nodal interpolating functions of displacement on the element, $dS = dxdy$ and $g$ is the determinant of the metric tensor ($g = \det \mathbf{g}$).

Due to the symmetry of $\mathbf{K}_1$, $\mathbf{K}_3$, and $\mathbf{M}_S$, the eigenproblem has two sets of eigensolutions $(k_n^+, \mathbf{U}_n^+)$ and $(-k_n^+, \mathbf{U}_n^-)$ ($n = 1, \ldots, N$), representing $N$ positive-going and $N$ negative-going wave types [$N$ being the number of degrees of freedom (dofs)].

Given $\omega$ and finding $k$, this eigenproblem is quadratic. It is recast into a generalized linear eigensystem written for $[\mathbf{U}^T\ k\mathbf{U}^T]^T$ in order to be solved by standard numerical solvers[31]—see Ref. 47 for details.

### C. Mode properties

Once the eigenproblem has been solved, the calculation of modal properties is crucial for the analysis and interpretation of solutions.

Let $(k_n, \mathbf{U}_n)$ be a given eigenmode, positive or negative-going (the $\pm$ sign is dropped for conciseness of notations). The phase velocity $v_{p_n}$ and the attenuation $\beta_n$ are simply given by $v_{p_n} = \omega/\Re(k_n)$ and $\beta_n = \Im(k_n)$, respectively.

The kinetic and potential energies are respectively defined as $E_k = \frac{1}{2}\rho v_\alpha v_\alpha$ and $E_p = \frac{1}{2}\epsilon_{\alpha\beta}\sigma_{\alpha\beta}$ ($\alpha = n, b, t$), where $v_\alpha = \dot{u}_\alpha$ is the velocity vector. The cross-section and time averaged energies of mode $n$ can be obtained from

$$\begin{aligned} \int_S \bar{E}_{k_n} dS &= \frac{\omega^2}{4}\Re(\mathbf{U}_n^{T*}\mathbf{M}_S\mathbf{U}_n), \\ \int_S \bar{E}_{p_n} dS &= \frac{1}{4}\Re\{\mathbf{U}_n^{T*}(\mathbf{K}_1 + ik_n(\mathbf{K}_2 - \mathbf{K}_2^T) + k_n^2\mathbf{K}_3)\mathbf{U}_n\}, \end{aligned} \tag{21}$$

where bars denote time averaging and the superscript * refers to the complex conjugate. From Eq. (19), note that each mode $n$ satisfies the equality $\int_S \bar{E}_{k_n} dS = \int_S \bar{E}_{p_n} dS$.

The post-process of modal power flow and energy velocity is less straightforward. This paper gives some explicit formula, derived below.

The complex Poynting vector[48] $\mathbf{P}$, defined in analogy with the electromagnetic case, is given by: $P_\beta = -\frac{1}{2}v_\alpha^*\sigma_{\alpha\beta}$. The complex power flow (cross-section averaged) is $\Pi = \int_S \mathbf{P}\cdot\mathbf{n}dS$, where $\mathbf{n}$ is the unit vector along the propagation direction (normal to the cross-section). Provided that $\mathbf{v} = -i\omega\mathbf{u}$ and $\mathbf{n} = \mathbf{T}$, one has

$$\mathbf{P}\cdot\mathbf{n}dS = -\frac{i\omega}{2}u_\alpha^*\sigma_{\alpha t}dS. \tag{22}$$

Then, it can be checked that $u_\alpha^*\sigma_{\alpha t} = \mathbf{u}^{T*}\mathbf{L}_s^T\sigma(1+\kappa x) = \mathbf{u}^{T*}\mathbf{L}_s^T\mathbf{C}(\mathbf{L}_{xy} + ik\mathbf{L}_s)\mathbf{u}(1+\kappa x)$, so that the following useful expression holds for the complex power flow of mode $n$ (cross-section averaged):

$$\Pi_n = -\frac{i\omega}{2}\mathbf{U}_n^{T*}(\mathbf{K}_2^T + ik_n\mathbf{K}_3)\mathbf{U}_n. \tag{23}$$

The real part $\Re(\Pi_n)$ coincides with the cross-section and time averaged power flow.

Then, the cross-section and time averaged energy velocity in waveguides is defined as follows:[49]

$$v_{e_n} = \frac{\Re(\Pi_n)}{\int_S (\bar{E}_{k_n} + \bar{E}_{p_n})dS}. \tag{24}$$

Expressions (21) and (23) allow a direct computation of the energy velocity. The energy velocity is an important wave property that remains appropriate even for damped media[50]

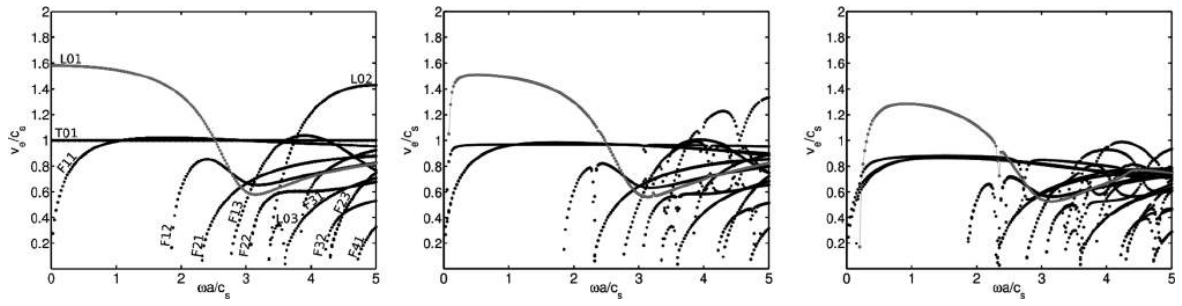


FIG. 3. From left to right: dimensionless energy velocity vs frequency for $\phi = 0°$ (cylinder), 15°, and 30°. The first compressional-like mode is colored gray.

(as opposed to the group velocity definition $v_{g_n} = \partial\omega/\partial k_n$, which is generally not valid for damped waveguides).

Modes can be normalized with respect to the mass matrix, yielding $\mathbf{U}_n^{T*}\mathbf{M}_S\mathbf{U}_n = 1$. Since the eigenvectors may be multiplied by any complex scalar of unit modulus, such a normalization is not unique, which might be not convenient in practice (for instance, when we want to track modes by visual inspection of their modeshapes). The above normalization can be made unique with the additional requirement: for a given $n$, $\mathbf{U}_n$ is multiplied by a complex scalar of unit modulus, such that its dof of maximum modulus is made real and positive.

### D. Results

We consider waveguides of circular cross-section of radius $a$ (in the plane normal to the helix centerline). For conciseness, we briefly give results for helical waveguides of helix radius $R = 2a$ and the following three lay angles $\phi = 0°$ (cylinder), 15°, and 30°. These three cases will also be considered in Sec. IV. For more detailed physical interpretations and parametric studies on helical waveguides, the reader can refer to Refs. 12 and 31. The validation of the proposed SAFE method has been performed in Ref. 31 with a helical coordinate system and in Ref. 13 with a twisting system.

Without loss of generality, no material damping is considered and the material is assumed to be isotropic. The Poisson coefficient is $\nu = 0.25$. The shear velocity is defined as $v_s = \sqrt{E/2\rho(1+\nu)}$, where $E$ denotes Young modulus. Variables are made dimensionless with characteristic length and time, chosen as $a$ and $a/c_s$, respectively. The dimensionless frequency is then given by $\omega a/c_s$. As already mentioned, a twisting system is used and the SAFE meshes are given by Fig. 2. The geometry is meshed with eight-node quadrangles (quadratic elements are used), yielding 675 dofs. SAFE computations are held at fixed dimensionless frequency $\omega a/c_s \in [0; 5]$, discretized into 250 equal steps.

Figure 3 shows the dimensionless energy velocity vs frequency plots. The results obtained for $\phi = 0°$ corresponds to a straight cylindrical waveguide, for which solutions are well-known in the literature. For that case, modes have been labeled accordingly to the convention used by Meitzler.[51] The fastest mode in the low frequency range ($\omega a/c_s \leq 2$), which is colored gray on the plots, corresponds to the first compressional-like mode [referred to as the $L(0, 1)$ mode in cylinders]. Though somewhat subjective, a visual inspection of modeshapes has been done in order to identify the evolution of this mode on a wider frequency range.

As expected, differences between cylinder and helical waveguides become greater as the lay angle increases. The energy velocity of the $L(0, 1)$-like mode decays as the lay angle increases, which is essentially due to the lengthening of the path covered by waves (waves travels along the helix axis but the wavenumber and velocity are measured along the $Z$ axis). In helical waveguides, note that this mode has a low but non-zero cut-off frequency that increases with the angle.[13,31]

Unlike in the cylindrical case, helical waveguides may exhibit sharp changes in dispersion curves at certain frequencies—see for instance the $F(1, 2)$-like mode for $\phi = 15°$ near $\omega a/c_s = 2.3$. These changes usually correspond to curve veering or branch connection between different modes.[13,31]

## IV. MODE SCATTERING BY INHOMOGENEITIES

Based on the previously obtained eigensolutions, a 3D hybrid FE-SAFE method is developed for the analysis of mode scattering by inhomogeneities inside helical waveguides. Inhomogeneities are assumed to be local (restricted to a small portion of the waveguide) but can be of complex shape. The usual FE method is applied to a region of the waveguide including the inhomogeneity (a crack for instance). Then, SAFE modal expansions are applied at cross-section boundaries of the 3D FE model, where semi-infinite waveguides are to be connected. This technique yields transparent conditions.

For simplicity, Fig. 4 depicts the FE portion, denoted $\Omega$, of a free-end waveguide. The free-end is on the top. The reflection of waves inside a free-end waveguide is a typical scattering problem. A free-end boundary can also be viewed as a complete crack of the wire. Incident waves travel from the bottom to the top, reflected waves by the free-end travel in the opposite direction. The bottom cross-section, denoted $\Sigma$, corresponds to the boundary where a semi-infinite waveguide is to be connected. The boundary condition on $\Sigma$ should be such that modes reflected by the free-end go out from $\Omega$ without reflecting on $\Sigma$ (transparent boundary).

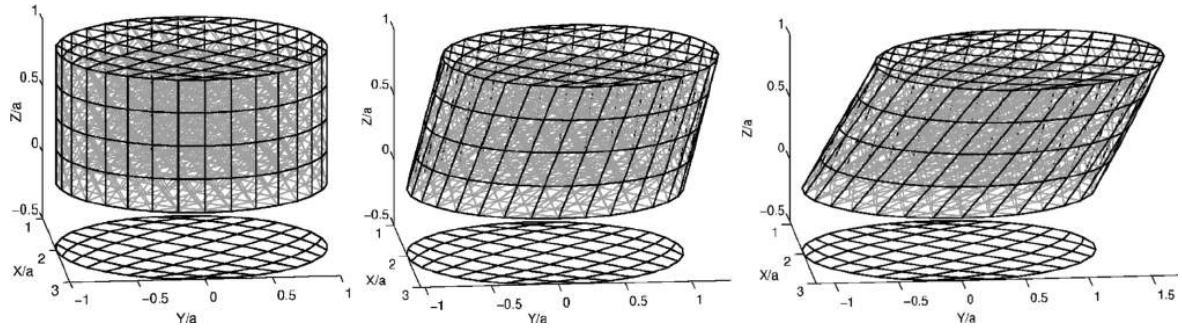


FIG. 4. Geometry and FE mesh used for the computations with the hybrid method for a free-end helical waveguide with $R = 2a$ and the following lay angles: $\phi = 0°$ (cylinder), 15°, and 30° (from left to right). The bottom cross-section, here duplicated in the plane $Z/a = -0.5$, corresponds to $\Sigma$ (transparent conditionz). The remaining boundaries of the FE model are free, including the top cross-section representing the free-end.

### A. Hybrid FE-SAFE formulation

We start from the FE model of the region $\Omega$. The discretization of the variational formulation (14) leads to the usual FE system for 3D elastodynamics

$$(\mathbf{K} - \omega^2\mathbf{M})\mathbf{U} = \mathbf{F}, \tag{25}$$

where $\mathbf{K}$ and $\mathbf{M}$ are the stiffness and mass matrices. $\mathbf{U}$ is the vector of displacement dofs of the whole FE region.

This system is partitioned into dofs associated with the cross-section $\Sigma$ and the remaining dofs as follows:

$$\mathbf{U} = \begin{Bmatrix} \mathbf{U}_\Sigma \\ \mathbf{U}_{\bar{\Sigma}} \end{Bmatrix}, \quad \mathbf{F} = \begin{Bmatrix} \mathbf{F}_\Sigma \\ \mathbf{F}_{\bar{\Sigma}} \end{Bmatrix}, \tag{26}$$

with $\bar{\Sigma} = \Omega \backslash \Sigma$.

The basic idea of hybrid methods consists in expanding both $\mathbf{U}_\Sigma$ and $\mathbf{F}_\Sigma$ on the guided modes associated with the cross-section $\Sigma$

$$\begin{aligned} \mathbf{U}_\Sigma &= \sum_{n=1}^{N} \alpha_n^- \mathbf{U}_n^- + \sum_{n=1}^{N} \alpha_n^+ \mathbf{U}_n^+, \\ \mathbf{F}_\Sigma &= \sum_{n=1}^{N} \alpha_n^- \mathbf{F}_n^- + \sum_{n=1}^{N} \alpha_n^+ \mathbf{F}_n^+. \end{aligned} \tag{27}$$

$\mathbf{U}_n^\pm$ denotes the displacement modeshape of mode $n$ obtained from SAFE analysis. $\mathbf{F}_n^\pm$ is the associated modal force (calculation detailed in the next subsection). The $\alpha_n^\pm$ 's are modal coefficients. Ingoing modes are differentiated from outgoing modes, thanks to the superscripts – and +, respectively. In the present example, ingoing modes are incident modes while outgoing modes are reflected modes. $N$ now denotes the number of modes retained in the expansion, and after truncation, is lower than the number of dof.

The incident coefficients $\alpha_n^-$ 's are known. The scattered coefficients $\alpha_n^+$ 's are unknowns and must be solved. A convenient way of rewriting the expansions (27) is to use global matrix forms. First, we separate and gather the unknown variables into a single global vector $\mathbf{U}^+$ as well as the known variables into a vector $\mathbf{U}^-$, defined as follows:

$$\mathbf{U}^- = \begin{Bmatrix} \alpha^- \\ \mathbf{F}_{\bar{\Sigma}} \end{Bmatrix}, \qquad \mathbf{U}^+ = \begin{Bmatrix} \alpha^+ \\ \mathbf{U}_{\bar{\Sigma}} \end{Bmatrix}, \tag{28}$$

where $\boldsymbol{\alpha}^\pm$ are the modal coefficients stored in column vectors. Note that $\mathbf{F}_{\bar{\Sigma}}$ is known and may represent acoustic sources located inside the FE region (but outside $\Sigma$).

Then, the eigenmode expansions (27) can be rewritten into the following global forms:

$$\mathbf{U} = \mathbf{G}_u^- \mathbf{U}^- + \mathbf{G}_u^+ \mathbf{U}^+, \quad \mathbf{F} = \mathbf{G}_f^- \mathbf{U}^- + \mathbf{G}_f^+ \mathbf{U}^+, \tag{29}$$

with the following notations:

$$\begin{aligned} \mathbf{G}_u^- &= \begin{bmatrix} \mathbf{B}_u^- & \mathbf{0} \\ \mathbf{0} & \mathbf{0} \end{bmatrix}, & \mathbf{G}_u^+ &= \begin{bmatrix} \mathbf{B}_u^+ & \mathbf{0} \\ \mathbf{0} & \mathbf{I} \end{bmatrix}, \\ \mathbf{G}_f^- &= \begin{bmatrix} \mathbf{B}_f^- & \mathbf{0} \\ \mathbf{0} & \mathbf{I} \end{bmatrix}, & \mathbf{G}_f^+ &= \begin{bmatrix} \mathbf{B}_f^+ & \mathbf{0} \\ \mathbf{0} & \mathbf{0} \end{bmatrix}, \end{aligned} \tag{30}$$

where $\mathbf{B}_u^\pm$ and $\mathbf{B}_f^\pm$ denote the modal basis of eigendisplacements and eigenforces, stored in column

$$\mathbf{B}_u^\pm = [\mathbf{U}_1^\pm | \mathbf{U}_2^\pm | \ldots | \mathbf{U}_N^\pm], \quad \mathbf{B}_f^\pm = [\mathbf{F}_1^\pm | \mathbf{F}_2^\pm | \ldots | \mathbf{F}_N^\pm]. \tag{31}$$

Finally, using Eq. (29) into Eq. (25) yields a linear matrix system for $\mathbf{U}^+$, which is inverted at each frequency $\omega$

$$\mathbf{G}_u^{+T}(\mathbf{D}\mathbf{G}_u^+ - \mathbf{G}_f^+)\mathbf{U}^+ = \mathbf{G}_u^{+T}(\mathbf{G}_f^- - \mathbf{D}\mathbf{G}_u^-)\mathbf{U}^-. \tag{32}$$

$\mathbf{D} = \mathbf{K} - \omega^2\mathbf{M}$ is the initial dynamic stiffness of the FE problem. Physical solutions can be reconstructed from Eq. (29). The procedure can be readily extended to the case of two transparent boundaries (or more), as it is the case for reflection–transmission problems in infinite waveguides (see Sec. IV E 1).

Note that the solution vector of the above system includes the scattered modal coefficients, which might be advantageous compared to other methods requiring additional post-processing steps.[43,52] Besides, $\mathbf{U}_{\bar{\Sigma}}$ is not condensed out in order to avoid the inversion of the dynamic stiffness (computationally expensive for 3D problems).

### B. Modal forces

With standard SAFE methods, the calculation of the modal forces $\mathbf{F}_n^{\pm}$ from the modal displacements $\mathbf{U}_n^{\pm}$ is a crucial point. Ideally, this calculation should be consistent with the FE approximation used. Nodal forces can be obtained by post-processing load vectors from displacement derivatives[35,38] associated to each mode, but this procedure might be tedious and time-consuming in practice. An explicit formula can indeed […], as shown in this subsection.

$\mathbf{F}_\Sigma$ is the left-hand side of Eq. (25) restricted to $S=\Sigma$ and comes from the variational form $\int_\Sigma \delta\mathbf{u}^T\mathbf{f}dS = \delta\mathbf{U}_\Sigma^T\mathbf{F}_\Sigma$, where $f_\alpha = \sigma_{\alpha\beta}n_\beta$ is the external traction ($\mathbf{n}$ is the outward unit normal). The normal mode expansion gives $\delta\mathbf{U}_\Sigma^T\mathbf{F}_\Sigma = \sum_{n=1}^N \alpha_n^- \delta\mathbf{U}_\Sigma^T\mathbf{F}_n^- + \sum_{n=1}^N \alpha_n^+ \delta\mathbf{U}_\Sigma^T\mathbf{F}_n^+$, where the $\mathbf{F}_n^{\pm}$'s can be defined from

$$\delta\mathbf{U}_\Sigma^T\mathbf{F}_n^{\pm} = \int_\Sigma \delta\mathbf{u}\cdot\mathbf{f}_n^{\pm}dS. \tag{33}$$

Note that $\mathbf{n}=\mathbf{T}$ on $\Sigma$. Similarly to the power flow in Sec. III C, we can write $\mathbf{f}_n^{\pm} = \mathbf{L}_s^T\boldsymbol{\sigma}_n^{\pm}(1+\kappa x) = \mathbf{L}_s^T\mathbf{C}(\mathbf{L}_{xy}+ik_n^{\pm}\mathbf{L}_s)\mathbf{u}_n^{\pm}(1+\kappa x)$. From this expression and Eq. (33), it can be checked that the modal forces are explicitly given by

$$\mathbf{F}_n^{\pm} = (\mathbf{K}_2^T + ik_n^{\pm}\mathbf{K}_3)\mathbf{U}_n^{\pm}. \tag{34}$$

As a side remark, it should be noted that the system (32) is in fact symmetric. This is due to the following property:

$$(k_n+k_m)(\mathbf{U}_m^T\mathbf{F}_n - \mathbf{U}_n^T\mathbf{F}_m) = 0, \tag{35}$$

which could be viewed as the discretized form of the real biorthogonality relationship.[53] This relation is obtained by subtracting the SAFE system (19) written for $\mathbf{U}_n$ and pre-multiplied by $\mathbf{U}_m^T$, from the transpose of the system written for $\mathbf{U}_m$ and pre-multiplied by $\mathbf{U}_n^T$. Note that the $\pm$ signs have been dropped because the traveling direction is not considered in the above relation. Let us consider outgoing modes only. Then, $k_n^+ + k_m^+ \neq 0$ so that $\mathbf{U}_m^{+T}\mathbf{F}_n^+ = \mathbf{U}_n^{+T}\mathbf{F}_m^+$ $(\forall m,n)$, which proves that $\mathbf{B}_u^{+T}\mathbf{B}_f^+$ is symmetric. As a consequence, the matrix $\mathbf{G}_u^{+T}(\mathbf{D}\mathbf{G}_u^+ - \mathbf{G}_f^+)$ is also symmetric. Note that this property still holds in the damped case, if $\mathbf{C}$ is complex (case of viscoelastic material).

### C. Traveling direction

Another difficulty concerns the determination of traveling direction for each mode. In undamped waveguides ($\mathbf{C}$ is real), eigensolutions for which $k_n$ is purely real, purely imaginary, and fully complex represent propagating waves, evanescent waves, and inhomogeneous waves (decaying but oscillatory), respectively. Furthermore, backward modes might occur in elastic waveguides (the energy and phase velocities of such modes have opposite signs).

Consequently, positive-going modes should be separated from negative-going ones by the criterion $v_{e_n} > 0$ when propagating and by $\Im(k_n) > 0$ when non-propagating. The problem consists in distinguishing propagating from non-propagating modes.

In undamped waveguides, propagating and non-propagating modes, respectively, satisfy $\Im(\Pi_n) = 0$ and $\Re(\Pi_n) = 0$. Hence in practice, the condition $|\Re(\Pi_n)| > |\Im(\Pi_n)|$ can be proposed as an efficient criterion for finding propagating modes. In damped waveguides, $\Pi_n$ usually becomes fully complex. Nevertheless, quasi-propagating modes are expected to have a small imaginary part so that the criterion can still be applicable.

### D. Results for free-end elastic helical waveguides

As illustrative examples, we analyze modal scattering occurring in semi-infinite waveguides terminated by a free-end. The same helix parameters as in Sec. III D are considered ($R=2a$, $\phi = 0°$, 15°, and 30°). A single mode is incident, corresponding to the $L(0,1)$-like mode previously identified on the dispersion curves (Fig. 3).

It is noteworthy that the modal expansion on $\Sigma$ also accounts for non-propagating modes, which allows to set the free-end boundary relatively close to the boundary $\Sigma$. In the present paper, the latter is set at $Z=0$ while the former is set at $Z=a$. Hybrid FE-SAFE meshes are shown in Fig. 4 (for clarity, $\Sigma$ is duplicated at $Z=-a/2$, but must be understood at $Z=a$). 20-node quadratic brick elements have been used, yielding 4347 dofs.

As already mentioned, guided modes are computed with a twisted system. This has the advantage of avoiding any transformation between Cartesian and Serret–Frenet components because the $\Sigma$ plane coincides with the Cartesian $(X,Y)$ plane.

In the following computations, modal bases are truncated by retaining modes satisfying $|\Im(ka)| \leq 5$. A good accuracy is expected because the amplitudes of non-propagating modes reflected from the free-end, but not taken into account in the expansion, would then be divided by at least $e^5 \simeq 148$ at the transparent boundary $\Sigma$. In practice, the error on the power balance has been checked at each frequency and for the three waveguides. This error can be defined as

$$e = \frac{\Re(\Pi^-) + \Re(\Pi^+)}{\Re(\Pi^-)}, \tag{36}$$

where $\Pi^{\pm} = -i\omega(\mathbf{G}_u^{\pm}\mathbf{U}^{\pm})^{T*}(\mathbf{G}_f^{\pm}\mathbf{U}^{\pm})/2$ is the total complex power flow of $-/+$ modes (ingoing/outgoing). In the following results, the worst error has been found to be less than 0.8%, which is quite satisfying. This tends to confirm that the proposed truncation does not yield any significant loss of accuracy.

Figure 5 shows the power reflection coefficients vs frequency plots obtained for the three waveguides, where the power reflection coefficient is defined as

$$R_n = \frac{\Re(\Pi_n^+)}{\Re(\Pi_i^-)}, \tag{37}$$

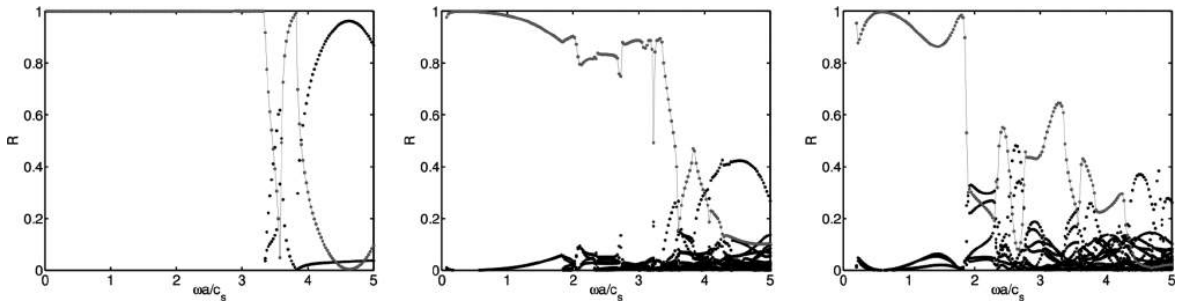


FIG. 5. From left to right: power reflection coefficient vs frequency for $\phi = 0°$ (cylinder), 15°, and 30°. The first compressional-like mode is colored gray.

where the index $i$ denotes the incident mode. In the cylinder case ($\phi = 0°$), the $L(0, 1)$ mode is fully reflected until $\omega a/c_s \simeq 3.3$. This frequency is indeed the first cut-off frequency of higher compressional modes, corresponding to $L(0, 2)$ and $L(0, 3)$. Above that frequency, the sudden drop of the $L(0, 1)$ reflection indicates that this mode is partially converted to $L(0, 2)$ and $L(0, 3)$. A full conversion might even occur at certain frequencies. The free-end cylinder case is further considered in Sec. IV E 2, where a comparison with literature results is given.

The geometry of a free-end cylinder is fully axisymmetric. Besides, compressional $L(0, n)$ modes are axisymmetric, unlike flexural modes $F(m, n)$. As a consequence, there is no conversion of the $L(0, 1)$ to $F(m, n)$ modes. In the case of helical waveguides ($\phi \neq 0°$), this symmetry is broken and conversion to flexural or torsional modes occurs. This causes a decrease of the power reflection coefficient of the $L(0, 1)$-like mode in the lowest frequency range, far below the first cut-off frequencies of $L(0, n)$-like modes. As usual with modal scattering in waveguides,[35,38] the sharp changes of the reflection coefficient generally coincide with cut-off frequencies (compare Figs. 3 and 5).

For the angle of 15°, some rough similarities may still be found with the cylinder case. For instance, a strong reflection drop is also observed near 3.3, which is the cut-off frequencies of the $L(0, 2)$ and $L(0, 3)$-like mode. However for 30°, results becomes quite different. A strong reflection drop is found near 1.9, corresponding to the cut-off of the $F(1, 2)$-like mode. Figure 6 shows the color plot of the axial displacement ($u_t = u_Z$) computed at $\omega a/c_s = 2$. The global motion observed at this frequency is clearly not purely extensional, indicating significant conversions into non-compressional modes.

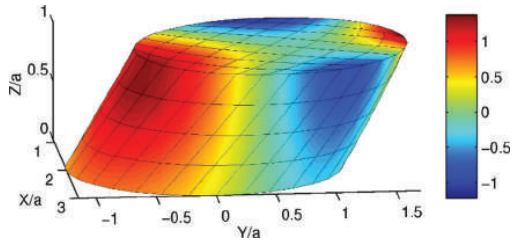


FIG. 6. (Color online) Reflection of the first compressional-like mode by a free-end in a helical waveguide of angle $\phi = 30°$, real part of the axial displacement at $\omega a/c_s = 2$.

### E. Validation tests

Though the power balance is well-satisfied in the previous simulations, this criterion is surely not sufficient to fully validate the proposed hybrid method and check the accuracy of results. In the following, two validation tests are performed.

#### 1. Infinite helical waveguide

A first test-case consists in checking that a single incident mode travels without conversion or reflection in an infinite helical waveguide. The larger angle ($\phi = 30°$) is considered. Figure 7 shows the hybrid FE-SAFE mesh. In that case, the transparent boundary $\Sigma$ is given by $\Sigma_1 \cup \Sigma_2$, respectively, corresponding to the bottom and top cross-sections. SAFE computations must be then performed on both $\Sigma_1$ and $\Sigma_2$. For clarity, $\mathbf{B}_u^{\pm}$ and $\mathbf{B}_f^{\pm}$ should now be understood as:

$$\mathbf{B}_u^{\pm} = \begin{bmatrix} {}_1\mathbf{B}_u^{\pm} & 0 \\ 0 & {}_2\mathbf{B}_u^{\pm} \end{bmatrix}, \qquad \mathbf{B}_f^{\pm} = \begin{bmatrix} {}_1\mathbf{B}_f^{\pm} & 0 \\ 0 & {}_2\mathbf{B}_f^{\pm} \end{bmatrix}, \quad (38)$$

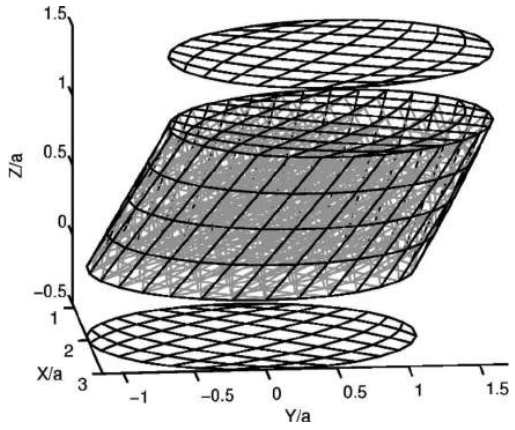


FIG. 7. Mesh of the infinite helical waveguide ($R = 2a$, $\phi = 30°$). Bottom and top boundaries are both transparent.

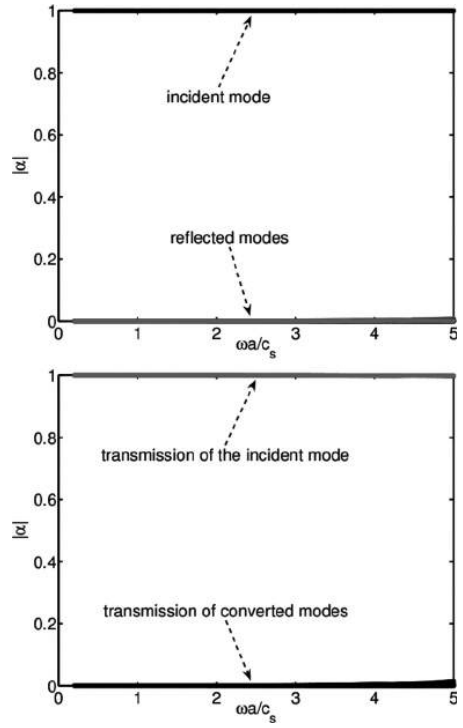


FIG. 8. Modal coefficient vs frequency for $\phi = 30°$. Top: reflection, bottom: transmission.

where ${}_i\mathbf{B}^{\pm}_{u,f}$ denotes modal bases associated with $\Sigma_i$.

Figure 8 gives the absolute value of the modal amplitudes of displacement, obtained in reflection (on $\Sigma_1$) and transmission (on $\Sigma_2$). The incident mode is still the $L(0, 1)$-like mode, launched with a unit modal amplitude for all frequencies. As can be observed, this mode is almost fully transmitted, without reflection nor conversion, for the whole frequency range [0;5]. Note that this test might also be viewed as a numerical way of checking that guided modes truly exist inside helical structures.

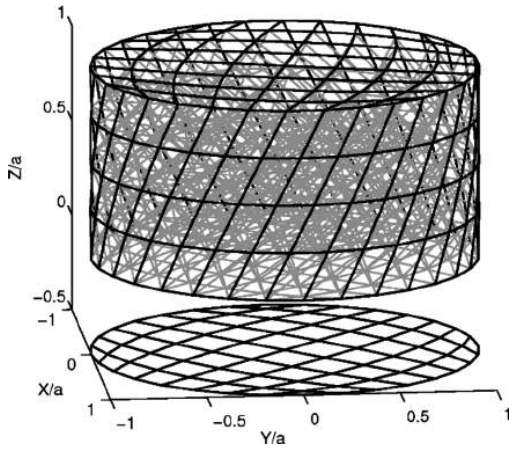


FIG. 9. Mesh used for the free-end twisted cylinder test.

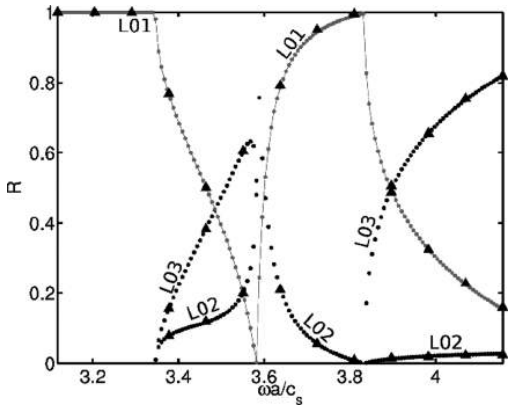


FIG. 10. Power reflection coefficient vs frequency. The $L(0, 1)$ mode is colored gray. Triangles: results of Gregory and Gladwell.[54]

It could be observed that the coefficients associated with reflected or transmitted converted modes tend to increase for highest frequencies. This is an expected result with FE techniques (the FE size should be diminished as the frequencies increases). The worst power balance error was 0.3% for that test.

### 2. Free-end twisted cylinder

The second validation test concerns the free-end cylinder, for which reference results are available in the literature.[54] This example has already been analyzed in Sec. IV D, where guided modes were computed for a straight waveguides ($\kappa = \tau = 0$). Here, the main difference is that guided modes are computed with an arbitrary twisted coordinate system, which allows to fully validate the hybrid approach proposed in this paper for helical waveguides.

As explained in Sec. II E, $\tau$ can be any value. We choose a high torsion value, $\tau a = 0.5$. Figure 9 shows the FE mesh used for the test. In order to harden the test, the mesh of the FE portion is also twisted instead of being straight. The dispersion curves computed on $\Sigma$ are identical to Fig. 3 in the cylinder case and are not shown for conciseness.

Figure 10 exhibits the power reflection coefficients computed for the dimensionless frequency range [3.1;4.2], divided into 150 equal steps, with the $L(0, 1)$ mode as incident. This frequency range focuses on the band where the $L(0, 1)$ mode becomes converted to $L(0, 2)$ and $L(0, 3)$. For comparison, the results of Gregory and Gladwell.,[54] obtained by means of analytical and least-square techniques, are superposed and all modes are explicitly labeled. Our numerical result are in quite good agreement, both qualitatively and quantitatively (note that the cylinder case in Fig. 5 also coincides with these results).

## V. CONCLUSION

In this paper, the propagation of guided modes in curved waveguides and their scattering by inhomogeneities have been investigated. First, the existence of propagation modes traveling in curved waveguides has been highlighted in a

general framework. Provided that the cross-section shape and medium properties do not vary along the waveguide axis, it has been proved that a sufficient condition for translational invariance is the independence on the axial coordinate of the metric tensor.

Then, the study has been focused on the elastodynamics of helical waveguides. Guided modes have been calculated, thanks to a SAFE method. For their scattering by inhomogeneities, a hybrid FE method has been proposed. The technique is based on modal expansions at boundaries of the FE model, yielding transparent conditions. Some results have been shown for the scattering of the first extensional mode in free-end helical waveguides. Two validation tests have successfully been performed, demonstrating a good accuracy of the approach with acceptable computational cost. The present work paves the way for studies of wave-damage interaction in helical multi-wire strands.

Regardless of waveguide curvature, 3D numerical tools are becoming essential to study guided wave scattering in complex-shaped waveguides and defects. The proposed 3D hybrid FE-SAFE method, relatively simple to implement and computationally little expensive, offers an interesting technique for defect classification and sizing by guided waves.


[1]D. Gridin, R. V. Craster, J. Fong, M. J. S. Lowe, and M. Beard, "The high-frequency asymptotic analysis of guided waves in a circular elastic annulus," Wave Motion **38**, 67–90 (2003).

[2]J. Qu, Y. Berthelot, and Z. Li, "Dispersion of guided circumferential waves in a circular annulus," in *Review of Progress in Quantitative NDE*, edited by D. O. Thompson and D. E. Chimenti (Plenum Press, New York, 1998), vol. 15, pp. 169–176.

[3]G. Liu and J. Qu, "Transient wave propagation in a circular annulus subjected to transient excitation on its outer surface," J. Acoust. Soc. Am. **104**, 1210–1220 (1998).

[4]A. Demma, P. Cawley, and M. Lowe, "The effect of bends on the propagation of guided waves in pipes," J. Pressure Vessel Technol. **127**, 328–335 (2005).

[5]S. Finneveden and M. Fraggstedt, "Waveguide finite element for curved structures," J. Sound Vib. **312**, 644–671 (2008).

[6]S. Towfighi and T. Kundu, "Elastic wave propagation in anisotropic spherical curved plates," Int. J. Solids Struct. **40**, 5495–5510 (2003).

[7]Y. Jiangong, W. Bin, H. Hongli, and H. Cunfu, "Characteristics of guided waves in anisotropic spherical curved plates," Wave Motion **44**, 271–281 (2007).

[8]A.-C. Hladky-Hennion, "Finite element analysis of the propagation of acoustic waves in waveguides," J. Sound Vib. **194**, 119–136 (1996).

[9]O. Onipede and S. B. Dong, "Propagating waves and end modes in pretwisted beams," J. Sound Vib. **195**, 313–330 (1996).

[10]W. H. Wittrick, "On elastic wave propagation in helical springs," Int. J. Mech. Sci. **8**, 25–47 (1966).

[11]J. Lee and D. J. Thompson, "Dynamic stiffness formulation, free vibration and wave motion of helical springs," J. Sound Vib. **239**, 297–320 (2001).

[12]F. Treyssède, "Numerical investigation of elastic modes of propagation in helical waveguides," J. Acoust. Soc. Am. **121**, 3398–3408 (2007).

[13]F. Treyssède and L. Laguerre, "Investigation of elastic modes propagating in multi-wire helical waveguides," J. Sound Vib. **329**, 1702–1716 (2010).

[14]W. Sollfrey, "Wave propagation on helical wires," J. Appl. Phys. **22**, 905–910 (1951).

[15]A. Nicolet, F. Zola, and S. Guenneau, "Modeling of twisted optical waveguides with edge elements," Eur. Phys. J. Appl. Phys. **28**, 153–157 (2004).

[16]A. Nicolet and F. Zola, "Finite element analysis of helicoidal waveguides," IET Sci. Meas. Technol. **28**, 67–70 (2007).

[17]H. Kwun, K. A. Bartels, and J. J. Hanley, "Effects of tensile loading on the properties of elastic-wave propagation in a strand," J. Acoust. Soc. Am. **103**, 3370–3375 (1998).

[18]L. Laguerre, M. Brissaud, and J.-C. Aime, "Magnetostrictive pulse-echo device for non-destructive evaluation of cylindrical steel materials using longitudinal guided waves," Ultrasonics **39**, 503–514 (2002).

[19]M. D. Beard, M. J. S. Lowe, and P. Cawley, "Ultrasonic guided waves for inspection of grouted tendons and bolts," J. Mater. Civ. Eng. **15**, 212–218 (2003).

[20]P. Rizzo and F. L. di Scalea, "Load measurement and health monitoring in cable stays via guided wave magnetostrictive ultrasonics," Mater. Eval. **62**, 1057–1065 (2004).

[21]S. Chaki and G. Bourse, "Guided ultrasonic waves for non-destructive monitoring of the stress levels in prestressed steel strands," Ultrasonics **49**, 162–171 (2009).;

[22]L. Gavrić, "Computation of propagative waves in free rail using a finite element technique," J. Sound Vib. **185**, 531–543 (1995).

[23]T. Hayashi, W.-J. Song, and J. L. Rose, "Guided wave dispersion curves for a bar with an arbitrary cross-section, a rod and rail example," Ultrasonics **41**, 175–183 (2003).

[24]V. Damljanovic and R. L. Weaver, "Propagating and evanescent elastic waves in cylindrical waveguides of arbitrary cross-section," J. Acoust. Soc. Am. **115**, 1572–1581 (2004).

[25]I. Bartoli, A. Marzani, F. L. di Scalea, and E. Viola, "Modeling wave propagation in damped waveguides of arbitrary cross-section," J. Sound Vib. **295**, 685–707 (2006).

[26]P. E. Lagasse, "Higher-order finite-element analysis of topographic guides supporting elastic surface waves," J. Acoust. Soc. Am. **53**, 1116–1122 (1973).

[27]S. K. Datta, A. H. Shah, R. L. Bratton, and T. Chakraborty, "Wave propagation in laminated composite plates," J. Acoust. Soc. Am. **83**, 2020–2026 (1988).

[28]R. J. Astley and A. Cummings, "A finite element scheme for attenuation in ducts lined with porous material: Comparison with experiment," J. Sound Vib. **116**, 239–263 (1987).

[29]R. Kirby, "Transmission loss predictions for dissipative silencers of arbitrary cross-section in the presence of mean flow," J. Acoust. Soc. Am. **114**, 200–209 (2003).

[30]S. Guenneau, A. Nicolet, F. Zolla, and S. Lasquellec, "Modeling of photonic crystal optical fibers with finite elements," IEEE Trans. Magn. **38**, 1261–1264 (2002).

[31]F. Treyssède, "Elastic waves in helical waveguides," Wave Motion **45**, 457–470 (2008).

[32]Y. Al-Nassar, S. K. Datta, and A. H. Shah, "Scattering of Lamb waves by a normal rectangular strip weldment," Ultrasonics **29**, 125–132 (1991).

[33]W. Karunasena, A. H. Shah, and S. K. Datta, "Plane-strain-wave scattering by cracks in laminated composite plates," J. Eng. Mech. **117**, 1738–1754 (1991).

[34]A. Mal and Z. Chang, "A semi-numerical method for elastic wave scattering calculations," Geophys. J. Int. **143**, 328–334 (2000).

[35]W. M. Karunasena, K. M. Liew, and S. Kitipornchai, "Hybrid analysis of Lamb wave reflection by a crack at the fixed edge of a composite plate," Comput. Methods Appl. Mech. Eng. **125**, 221–233 (1995).

[36]J. M. Galan and R. Abascal, "Lamb mode conversion at edges. A hybrid boundary element–finite-element solution," J. Acoust. Soc. Am. **117**, 1777–1784 (2005).

[37]Y. Cho and J. L. Rose, "A boundary element solution for a mode conversion study on the edge reflection of Lamb waves," J. Acoust. Soc. Am. **99**, 2097–2109 (1996).

[38]N. Rattanawangcharoen, W. Zhuang, A. H Shah, and S. K. Datta, "Axisymmetric guided waves in jointed laminated cylinders," J. Eng. Mech. **123**, 1020–1026 (1997).

[39]R. Kirby, "Modeling sound propagation in acoustic waveguides using a hybrid numerical method," J. Acoust. Soc. Am. **124**, 1930–1940 (2008).

[40]R. J. Astley, "FE mode-matching schemes for the exterior Helmholtz problem and their relationship to the FE-DtN approach," Commun. Numer. Methods Eng. **12**, 257–267 (1996).

[41]M. J. S. Lowe, D. N. Alleyne, and P. Cawley, "Defect detection in pipes using guided waves," Ultrasonics **36**, 147–154 (1998).

[42]J. Ma, F. Simonetti, and M. Lowe, "Scattering of the fundamental torsional mode by an axisymmetric layer inside a pipe," J. Acoust. Soc. Am. **120**, 1871–1880 (2006).

[43]L. Moreau, M. Castaings, B. Hosten, and M. Predoi, "An orthogonality relation-based technique for post-processing finite element predictions of waves scattering in solid waveguides," J. Acoust. Soc. Am. **120**, 611–620 (2006).

[44]M. V. Predoi, M. Castaings, and L. Moreau, "Influence of material viscoelasticity on the scattering of guided waves by defects," J. Acoust. Soc. Am. **124**, 2883–2894 (2008).

[45]D. Chapelle and K. J. Bathe, *The Finite Element Analysis of Shells—Fundamentals* (Springer-Verlag, Berlin, Germany, 2003), 330 p.
[46]A. Gray, E. Abbena, and S. Salamon, *Modern Differential Geometry of Curves and Surfaces with Mathematica*, 3rd ed. (Chapman & Hall, Boca Raton, FL, 2006), 984 p.
[47]F. Tisseur and K. Meerbergen, "The quadratic eigenvalue problem," SIAM Rev. **43**, 235–286 (2001).
[48]B. Auld, *Acoustic Fields and Waves in Solids*, vol. I, 2nd ed. (Krieger, Malabar, FL, 1990), p. 446.
[49]J. D. Achenbach, *Wave Propagation in Elastic Solids* (North-Holland, Amsterdam, the Netherlands, 1973), p. 425.
[50]A. Bernard, M. J. S. Lowe, and M. Deschamps, "Guided waves energy velocity in absorbing and non-absorbing plates," J. Acoust. Soc. Am. **110**, 186–196 (2001).
[51]A. H. Meitzler, "Mode coupling occurring in the propagation of elastic pulses in wires," J. Acoust. Soc. Am. **33**, 435–445 (1961).
[52]A. Gunawan and S. Hirose, "Mode-exciting method for Lamb wave-scattering analysis," J. Acoust. Soc. Am. **115**, 996–1005 (2004).
[53]B. Auld, *Acoustic Fields and Waves in Solids*, vol. II, 2nd ed. (Krieger, Malabar, FL, 1990), 432 p..
[54]R. D. Gregory and I. Gladwell, "Axisymmetric waves in a semi-infinite elastic rod," Q. J. Mech. Appl. Math. **42**, 327–337 (1989).

# Numerical and analytical calculation of modal excitability for elastic wave generation in lossy waveguides

Fabien Treyssède[a] and Laurent Laguerre
*LUNAM Université, IFSTTAR, route de Bouaye, 44344 Bouguenais, France*

(Received 28 September 2012; revised 22 March 2013; accepted 28 March 2013)

In the analysis of elastic waveguides, the excitability of a given mode is an important feature defined by the displacement-force ratio. Useful analytical expressions have been provided in the literature for modes with real wavenumbers (propagating modes in lossless waveguides). The central result of this paper consists in deriving a generalized expression for the modal excitability valid for modes with complex wavenumbers (lossy waveguides or non-propagating modes). The analysis starts from a semi-analytical finite element method and avoids solving the left eigenproblem. Analytical expressions of modal excitability are then deduced. It is shown that the fundamental orthogonality property to be used indeed corresponds to a form of Auld's real orthogonality relation, involving both positive- and negative-going modes. Finally, some results obtained from the generalized excitability are compared to the approximate lossless expression. © *2013 Acoustical Society of America*. [http://dx.doi.org/10.1121/1.4802651]

PACS number(s): 43.35.Cg, 43.20.Mv, 43.20.Bi [JBL] Pages: 3827–3837

## I. INTRODUCTION

Elastic guided waves are of great interest in the context of non-destructive testing of elongated structures. Such waves are dispersive and multimodal, which complicates their practical use. Dispersion curves of phase and group velocities as functions of frequency are useful to identify modes that propagate in a frequency range with low dispersion and low attenuation.[1] Such curves represent modal properties obtained regardless excitation. Yet for a practical inspection system, it is also essential to determine and control the amplitudes of each guided modes excited by a given source. Such information typically allows to optimize the type and location of sensors to be used.

Two approaches can mainly be distinguished in order to calculate the response of waveguides under excitation. A first approach consists of using integral transform techniques.[2–5] With this method, the response is obtained by a contour integration in the complex plane or numerical integration of the analytical solution explicitly derived in the wavenumber domain.

An alternative approach is based on modal analysis, which consists of expanding the excited field as a sum of guided modes.[6–8] The contribution of each mode is obtained in terms of the associated power flow from an orthogonality relation between eigenmodes. This second method appears to be more suitable to achieve a better interpretation and optimization of signals, as it directly provides the contribution of each mode as a function of the excitation. In particular, this method has allowed to introduce the modal excitability.[9–11] For a given frequency, the excitability of a particular mode can be defined as the ratio of the displacement of that mode to a point force applied in a given direction.

In practice, many applications involve lossy structures (e.g., made of viscoelastic materials). While the first approach has readily been applied to lossy waveguides,[12,13] analytical derivations of modal expansions use the so-called Auld's complex orthogonality relation, limited to real wavenumbers only[6] (propagating modes in lossless waveguides). Hence, neither non-propagating modes nor viscoelastic materials can be considered, although Auld's relation is sometimes applied as a first approximation.[14–16]

In addition to the above mentioned results, which are essentially analytical, the modal approach has also been applied on the basis of a numerical method referred to as the semi-analytical finite element (SAFE) method. The SAFE method is particularly efficient from a computational point of view because the axial dependence $e^{ikz}$ is assumed before finite element (FE) discretization ($k$ and $z$ denote the wavenumber and distance along the waveguide axis, respectively). As a consequence, only the transverse dimensions need to be discretized and meshed, see, for instance, Refs. 17–19. The waveguide response can be computed thanks to FE eigenvectors orthogonality resulting from properties of the matrix eigensystem.[20,21] The advantage of SAFE methods is their capacity to handle complex waveguides of arbitrary cross-section, together with material anisotropy and transversely inhomogeneous properties. Interestingly, viscoelastic materials can also be handled with the introduction of left eigenvectors of the matrix eigensystem.[22,23]

In this paper, one shows how to simply compute the modal excitability from the numerical SAFE method and highlights the direct link with analytical expressions. In particular, the central result of this paper provides a generalized expression for the modal excitability, which remains valid for lossy waveguides as well as non-propagating modes in lossless waveguides. Due to its relative simplicity, the approach adopted in this work consists in starting from the SAFE method and then deducing the analytical expressions from the FE ones.

Section II briefly recalls the SAFE formulation, as standardly presented in the literature. The concept of eigenforces is introduced, which will greatly simplify the interpretation of

[a]Author to whom correspondence should be addressed. Electronic mail: fabien.treyssede@ifsttar.fr

SAFE equations and their link with the analytical results in subsequent sections. In Sec. III, a SAFE version of the lossless analytical excitability is derived for lossless waveguides, which highlights the direct link between numerical and analytical approaches. In Sec. IV, the excitability expression is modified and generalized to non-propagating modes and lossy waveguides. Section V finally gives illustrative examples. Results obtained with the lossless and the generalized excitabilities are compared.

## II. SAFE FORMULATION

One assumes a linearly elastic material, small strains, and displacements with a time harmonic $e^{-i\omega t}$ dependence. For clarity, the variational formulation of elastodynamics in the frequency domain is given by

$$\int_V \delta\boldsymbol{\epsilon}^T\boldsymbol{\sigma}dV - \omega^2\int_V \rho\delta\mathbf{u}^T\mathbf{u}dV = \int_V \delta\mathbf{u}^T\mathbf{f}dV + \int_{\partial V}\delta\mathbf{u}^T\mathbf{t}d\partial V, \tag{1}$$

where $\mathbf{u}$, $\boldsymbol{\epsilon}$, and $\boldsymbol{\sigma}$ are the displacement, strain, and stress vectors. $\rho$ is the material density. $\delta$ denotes virtual fields. The stress-strain relation is $\boldsymbol{\sigma} = \mathbf{C}\boldsymbol{\epsilon}$, where $\mathbf{C}$ is the matrix of material properties. $\mathbf{C}$ is complex in the case of viscoelastic materials. $\mathbf{f}$ represents acoustic sources inside the structural volume $V$. $\mathbf{t}$ is the traction vector applied on the surface $\partial V$. In index notations, $\mathbf{t}$ is related to the stress tensor by $t_i = \sigma_{ij}n_j$, where $n_j$ is the outward normal to the boundary $\partial V$. For clarity, the strain and stress vectors for three-dimensional problems are $\boldsymbol{\epsilon} = [\epsilon_{xx}\ \epsilon_{yy}\ \epsilon_{zz}\ 2\epsilon_{xy}\ 2\epsilon_{xz}\ 2\epsilon_{yz}]^T$ and $\boldsymbol{\sigma} = [\sigma_{xx}\ \sigma_{yy}\ \sigma_{zz}\ \sigma_{xy}\ \sigma_{xz}\ \sigma_{yz}]^T$.

In this section, the SAFE technique is briefly recalled. For more details on this method, the reader can refer to Refs. 17–19 and 22–25, for instance.

Also, the concept of eigenforces is introduced. Eigenforces are defined as modal forces associated with displacement mode shapes.

### A. Governing equations

Let us denote $z$ the axis of the waveguide, and $x$ and $y$ the transverse coordinates. Separating transverse from axial derivatives, the strain-displacement relation can be rewritten as $\boldsymbol{\epsilon} = (\mathbf{L}_{xy} + \mathbf{L}_z\partial/\partial z)\mathbf{u}$, where $\mathbf{L}_{xy}$ is the operator containing all terms except derivatives with respect to $z$.

The SAFE technique consists in starting from a variational formulation integrated on the cross-section $S$, instead of the formulation (1) integrated on the volume $V$ ($dV = dSdz$). After FE discretization, the SAFE approach yields the matrix system

$$\mathbf{K}_1\mathbf{U} - \omega^2\mathbf{M}\mathbf{U} + (\mathbf{K}_2 - \mathbf{K}_2^T)\mathbf{U}_{,z} - \mathbf{K}_3\mathbf{U}_{,zz} = \mathbf{F}, \tag{2}$$

with the following elementary matrices:

$$\mathbf{K}_1^e = \int_{S^e}\mathbf{N}^{eT}\mathbf{L}_{xy}^T\mathbf{C}\mathbf{L}_{xy}\mathbf{N}^e dS, \quad \mathbf{K}_2^e = \int_{S^e}\mathbf{N}^{eT}\mathbf{L}_{xy}^T\mathbf{C}\mathbf{L}_z\mathbf{N}^e dS,$$
$$\mathbf{K}_3^e = \int_{S^e}\mathbf{N}^{eT}\mathbf{L}_z^T\mathbf{C}\mathbf{L}_z\mathbf{N}^e dS, \quad \mathbf{M}^e = \int_{S^e}\rho\mathbf{N}^{eT}\mathbf{N}^e dS. \tag{3}$$

On one element $S^e$ of the cross-section, the displacement is interpolated as $\mathbf{u} = \mathbf{N}^e\mathbf{U}^e$, where $\mathbf{N}^e$ is the matrix of nodal interpolating functions on the element. Note that $\mathbf{K}_1$, $\mathbf{K}_3$, and $\mathbf{M}$ are symmetric.

For clarity, $\mathbf{U} = \mathbf{U}(z,\omega)$ is the column vector containing cross-section nodal displacements in the space-frequency domain. $\mathbf{F} = \mathbf{F}(z,\omega)$ represents the excitation vector in the space-frequency domain, gathering both contributions of volume sources $\mathbf{f}$ and surface sources $\mathbf{t}$.

In the wavenumber-frequency domain, Eq. (2) becomes

$$\{\mathbf{K}_1 - \omega^2\mathbf{M} + ik(\mathbf{K}_2 - \mathbf{K}_2^T) + k^2\mathbf{K}_3\}\tilde{\mathbf{U}} = \tilde{\mathbf{F}}, \tag{4}$$

where $\tilde{\mathbf{U}} = \tilde{\mathbf{U}}(k,\omega)$ and $\tilde{\mathbf{F}} = \tilde{\mathbf{F}}(k,\omega)$. The following Fourier spatial transform has been introduced: $\tilde{f}(k) = \int_{-\infty}^{+\infty} f(z)e^{-ikz}dz$.

As standardly done in the SAFE literature, Eq. (4) can be recast into a linear form, for instance,

$$(\mathbf{A} - k\mathbf{B})\hat{\mathbf{U}} = \hat{\mathbf{F}}, \tag{5}$$

with

$$\mathbf{A} = \begin{bmatrix} \mathbf{0} & \mathbf{K}_1 - \omega^2\mathbf{M} \\ \mathbf{K}_1 - \omega^2\mathbf{M} & i(\mathbf{K}_2 - \mathbf{K}_2^T) \end{bmatrix},$$
$$\mathbf{B} = \begin{bmatrix} \mathbf{K}_1 - \omega^2\mathbf{M} & \mathbf{0} \\ \mathbf{0} & -\mathbf{K}_3 \end{bmatrix}, \tag{6}$$

and

$$\hat{\mathbf{U}} = \begin{Bmatrix} \tilde{\mathbf{U}} \\ k\tilde{\mathbf{U}} \end{Bmatrix}, \quad \hat{\mathbf{F}} = \begin{Bmatrix} \mathbf{0} \\ \tilde{\mathbf{F}} \end{Bmatrix}. \tag{7}$$

### B. Eigenvectors

Given $\omega$ and suppressing excitation, Eq. (5) corresponds to a generalized linear eigenvalue problem for finding the wavenumbers

$$\{\mathbf{A} - k_m\mathbf{B}\}\hat{\mathbf{U}}_m = \mathbf{0}, \tag{8}$$

where $\hat{\mathbf{U}}_m^T = [\mathbf{U}_m^T\ k_m\mathbf{U}_m^T]^T$. Such an eigenproblem can be solved by standard numerical solvers,[26] as opposed to the quadratic one that would be obtained from the formulation (4). The eigensolutions $(k_m, \mathbf{U}_m)$ represent the wavenumber and the displacement vector associated with the guided mode $m$ (note that the tilde on the $\mathbf{U}_m$'s can be dropped for conciseness of notations).

From a mathematical point of view, the $\hat{\mathbf{U}}_m$'s are right eigenvectors. Because the eigenproblem (8) is generally unsymmetric, left eigenvectors are also needed.[27] By definition, the left eigenvectors $\hat{\mathbf{V}}_n$ satisfy the following eigenproblem:

$$\hat{\mathbf{V}}_n^T\{\mathbf{A} - k_n\mathbf{B}\} = \mathbf{0}. \tag{9}$$

Pre-multiplying Eq. (8) by $\hat{\mathbf{V}}_n^T$, post-multipying Eq. (9) by $\hat{\mathbf{U}}_m$, and subtracting both equations yields the following bi-orthogonality relations:

$$\hat{\mathbf{V}}_n^T \mathbf{B} \hat{\mathbf{U}}_m = b_m \delta_{mn}, \quad \hat{\mathbf{V}}_n^T \mathbf{A} \hat{\mathbf{U}}_m = k_m b_m \delta_{mn}, \tag{10}$$

where $b_m$ is a normalization factor and $\delta_{mn}$ denotes Kronecker's symbol. The above relations are biorthogonal in the sense that both right and left eigenvectors are involved in the expressions.

### C. Forced response

The solution to Eq. (5), which is the forced response under the excitation $\hat{\mathbf{F}}$, is now expanded as a sum of guided modes: $\hat{\mathbf{U}} = \sum_{m=1}^{2M} \alpha_m \hat{\mathbf{U}}_m$. $2M$ is the number of modes, theoretically equal to twice the number of degrees of freedom (dofs) involved in the system [Eq. (4)], but truncated in practice.

Using this eigenmode expansion into Eq. (5) and taking advantage of biorthogonality relations (10), the $\alpha_m$'s are determined.[18,23–25] The displacement response in the wavenumber-frequency domain is

$$\tilde{\mathbf{U}} = \sum_{m=1}^{2M} \frac{\hat{\mathbf{V}}_m^T \hat{\mathbf{F}}}{b_m (k_m - k)} \mathbf{U}_m. \tag{11}$$

Then, one applies the inverse Fourier spatial transform, defined by $f(z) = 1/2\pi \int_{-\infty}^{+\infty} \tilde{f}(k) e^{ikz} dk$. Under the assumption that $\tilde{\mathbf{F}}$ is holomorphic (no pole), Cauchy residue theorem yields the response $\mathbf{U}$ in the space-frequency domain

$$\mathbf{U} = -i \sum_{m=1}^{M} \frac{\hat{\mathbf{V}}_m^{+T} \hat{\mathbf{F}}(k_m^+) e^{ik_m^+ z}}{b_m^+} \mathbf{U}_m^+, \tag{12}$$

for the positive-going wave and for $z$ outside the source region (one assumes that the excitation $\mathbf{F}$ is zero outside a finite interval along $z$). If one is interested in the response at a location $z$ inside the source region, the application of residue theorem could still be performed by splitting the integrand into two parts.[28]

As opposed to Eq. (11), note that the summation in Eq. (12) is performed over positive-going modes $(k_m^+, \mathbf{U}_m^+)$ only $(m = 1,\ldots,M)$. The expression for the negative-going wave is obtained by replacing the superscripts $+$ with $-$ and the $-i$ factor with $+i$ in Eq. (12).

In practice, modal bases can be truncated by retaining modes satisfying $|\mathrm{Im}(k_m^+ z)| < \gamma$, where $\gamma$ is a user-defined parameter and $z$ is the position at which the response is calculated. The amplitudes of non-propagating modes not included in the expansion are then attenuated by a factor $e^{\gamma}$ at least.

Finally, the response in the space-time $(z, t)$ domain can be obtained from the inverse time Fourier transform of $\mathbf{U}$, given by $(1/2\pi) \int_{-\infty}^{+\infty} \mathbf{U} e^{-i\omega t} d\omega$.

For conciseness, one will consider positive-going waves only and drop the $+$ superscripts in the remainder of the paper.

As a side remark, it is noteworthy that backward modes sometimes occur in elastic waveguides (energy and phase velocities then have opposite signs). Hence, the traveling direction of a mode must be determined from the sign of its energy velocity when propagating, and from the sign of $\mathrm{Im}(k_m)$ when non-propagating.

### D. Definition of eigenforces

The definition of eigenforces is now briefly introduced. The eigenforce concept has recently been used by the authors in Refs. 29 and 30 in the context of scattering of guided waves by inhomogeneities.

The eigenforce vector $\mathbf{F}_m$, associated with the displacement mode shape $\mathbf{U}_m$, can be defined from

$$\int_S \delta \mathbf{u}^T \mathbf{t}_m dS = \delta \mathbf{U}^T \mathbf{F}_m, \tag{13}$$

where $\mathbf{t}_m$ is the traction vector applied on the cross-section $S$, whose unit normal is $\mathbf{e}_z$. Then, it can be checked that $\mathbf{t}_m = \mathbf{L}_z^T \boldsymbol{\sigma}_m = \mathbf{L}_z^T \mathbf{C} (\mathbf{L}_{xy} + ik_m \mathbf{L}_z) \mathbf{u}_m$, so that modal forces can be explicitly calculated from displacements by

$$\mathbf{F}_m = (\mathbf{K}_2^T + ik_m \mathbf{K}_3) \mathbf{U}_m. \tag{14}$$

As shown in the present paper, the introduction of modal forces will greatly simplify the interpretation of SAFE equations and their link with analytical results of the literature.

## III. LOSSLESS EXCITABILITY FOR PROPAGATING MODES

In lossless waveguides, eigensolutions for which the wavenumber is pure real, pure imaginary, and fully complex represent propagating waves, evanescent waves, and inhomogeneous waves (decaying but oscillatory), respectively. Note that this section is focused on propagating modes in lossless waveguides.

Based on the SAFE method, a matrix expression of the excitability is proposed. This expression is shown to be the counterpart of the excitability tensor found in the literature by analytical approaches.

### A. Properties of propagating modes in lossless waveguides

For lossless waveguides, the matrix of material properties $\mathbf{C}$ is real so that $\mathbf{K}_1$, $\mathbf{K}_2$, $\mathbf{K}_3$, and $\mathbf{M}$ are also real. $\mathbf{A}$ and $\mathbf{B}$ are thus Hermitian: $\mathbf{A}^{*T} = \mathbf{A}$ and $\mathbf{B}^{*T} = \mathbf{B}$ ($*$ denotes the complex conjugate). Besides, for propagating modes, wavenumbers are purely real and $k_m = k_m^*$. Then, taking the transpose conjugate of Eq. (9), it is straightforward to prove that the left eigenvectors are related to the right ones by

$$\hat{\mathbf{V}}_m = \hat{\mathbf{U}}_m^*. \tag{15}$$

This property has been used in Ref. 31 for analyzing the elastodynamic response of anisotropic plates.

The general biorthogonality relations (10) can now be rewritten in an interesting manner. From Eqs. (6), (7), and (15), the development of the expression $\hat{\mathbf{V}}_n^T \mathbf{B} \hat{\mathbf{U}}_m = b_m \delta_{mn}$ yields

$$\mathbf{U}_n^{*T}(\mathbf{K}_1 - \omega^2\mathbf{M})\mathbf{U}_m - k_n k_m \mathbf{U}_n^{*T}\mathbf{K}_3\mathbf{U}_m = b_m\delta_{mn}. \quad (16)$$

Thanks to Eq. (4) written for mode $m$ (with $\tilde{\mathbf{F}} = \mathbf{0}$), one has $(\mathbf{K}_1 - \omega^2\mathbf{M})\mathbf{U}_m = -ik_m(\mathbf{K}_2 - \mathbf{K}_2^T)\mathbf{U}_m - k_m^2\mathbf{K}_3\mathbf{U}_m$. Then after rearrangement, Eq. (16) can be rewritten as

$$ik_m\mathbf{U}_n^{*T}(\mathbf{K}_2^T + ik_m\mathbf{K}_3)\mathbf{U}_m - ik_m\mathbf{U}_n^{*T}(\mathbf{K}_2 - ik_n\mathbf{K}_3)\mathbf{U}_m = b_m\delta_{mn}. \quad (17)$$

Finally using Eq. (14), the biorthogonality relation becomes

$$\frac{i\omega}{4}(\mathbf{U}_m^T\mathbf{F}_n^* - \mathbf{U}_n^{*T}\mathbf{F}_m) = P_{mm}\delta_{mn}, \quad (18)$$

with the notation (justified later)

$$P_{mm} = -\omega b_m/4k_m. \quad (19)$$

### B. Excitability matrix

Using Eqs. (15) and (19), the expansion (12) can be rewritten as

$$\mathbf{U} = \sum_{m=1}^{M}\mathbf{E}_m\tilde{\mathbf{F}}(k_m)e^{ik_m z}, \quad (20)$$

where

$$\mathbf{E}_m = \frac{i\omega}{4P_{mm}}\mathbf{U}_m\mathbf{U}_m^{*T}. \quad (21)$$

$\mathbf{E}_m$ is a $N \times N$ matrix, $N$ denoting the number of dofs involved in the system (4).

In the above expansion, the contribution of non-propagating modes has been neglected ($M$ should be here understood as the number of propagating modes, excluding non-propagating). Hence, the expansion (20) together with Eq. (21) constitutes a far-field approximation, not applicable in the near-field region where non-propagating modes may have a significant contribution in the excited field.

It can be seen from Eq. (20) that $(\mathbf{E}_m)_{ij}$ represents the displacement amplitude of the single wavemode $m$ at dof $i$ when a unit force acts at dof $j$. In particular, diagonal terms are ratios of modal displacement to applied force when both quantities are measured at the same location and direction in the cross-section. As a consequence, the matrix $\mathbf{E}_m$ can be viewed as the FE version of the excitability function given in Refs. 9 and 10. $\mathbf{E}_m$ will be referred to as the excitability matrix in the remainder of this paper.

### C. Interpretation based on analytical Auld's approach

With the analytical approach of Auld,[6,8] the starting point for obtaining the modal expansion of the excited field is the reciprocity relation associated with the equations of elastodynamics. Details can be found elsewhere and calculations yield the following final result:

$$\mathbf{u}(\mathbf{x}, z) = \sum_{m=1}^{M}\mathbf{e}_m(\mathbf{x}) \cdot \tilde{\mathbf{f}}(k_m)e^{ik_m z}, \quad (22)$$

where the applied force $\tilde{\mathbf{f}}$ is supposed to be concentrated at point $\mathbf{x}_s$ in the cross-section. In the above expression, $\tilde{\mathbf{f}}$ should be understood as $\tilde{\mathbf{t}}$ when the excitation source is a traction vector applied on the circumference $\delta S$ of the waveguide. $\mathbf{e}_m$ denotes the excitability tensor. Under the assumption of propagating modes in lossless waveguides, its expression is[8,11]

$$\mathbf{e}_m(\mathbf{x}) = \frac{i\omega}{4P_{mm}}\mathbf{u}_m(\mathbf{x}) \otimes \mathbf{u}_m^*(\mathbf{x}_s), \quad (23)$$

where $\mathbf{x} = (x,y)$ denotes transverse variables (in the cross-section). $\mathbf{x}_s = (x_s, y_s)$ denotes the source position.

It can be observed that Eqs. (20) and (21) are the numerical counterparts of Eqs. (22) and (23). The reason of this direct analogy is explained below.

Indeed, the fundamental property that is used to derive Eq. (23) is the so-called Auld's complex orthogonality relation for propagating modes in lossless waveguides,[6] written as

$$P_{mn} = \frac{i\omega}{4}\int_S(\mathbf{u}_m \cdot \mathbf{t}_n^* - \mathbf{u}_n^* \cdot \mathbf{t}_m)dS = 0 \quad \text{if} \quad m \neq n. \quad (24)$$

Such a relation indeed derives from the elastodynamic reciprocity theorem.[32]

With the SAFE approach, the fundamental property used to obtain Eq. (21) is the discrete biorthogonality relation (10). There is no obvious link between relations (10) and (24). However, in the particular case of propagating modes in lossless waveguides, one has shown that Eq. (10) can be rewritten as Eq. (18). Recalling the eigenforce definition (13), it is straightforward to see that the SAFE relation (18) is in fact the FE form of Auld's complex orthogonality relation.

As a consequence, if one restricts the analysis to propagating modes in lossless waveguides, the procedure standardly followed with the SAFE method is in fact quite analogous to Auld's analytical approach.

Note that Eq. (24) is a biorthogonality relation in the sense that both displacement and stress components are involved. From a physical point of view, $P_{mm}$ is equal to the averaged power flow[6] (cross-section and time averaged). $P_{mm}$ vanishes for non-propagating modes (evanescent or inhomogeneous), so that Eq. (23) is obviously not applicable for cut-off modes.

In the remainder of this paper, expressions (21) or (23) will be referred to as the lossless excitability

## IV. GENERALIZED EXCITABILITY

The SAFE expression given by Eq. (12) is general and not restricted to propagating modes in lossless waveguides. Starting from that result, this section proposes a generalized expression of the excitability, valid for non-propagating modes and lossy waveguides.

### A. General properties of the eigenproblem

From a computational point of view, the general response given by Eq. (12) has the drawback of requiring the

computation of both right and left eigenvectors. From a physical point of view, it is difficult to have a clear interpretation of left eigenvectors.

For isotropic materials, matrices $\mathbf{A}$ and $\mathbf{B}$ can be symmetrized by replacing the axial displacement $u_z$ with $iu_z$—as done in Refs. 20 and 21—so that the left and right eigenvectors become equal. In this paper, a simple relation between eigenvectors is obtained in the general case of anisotropic materials.

First, one recalls that if $k_m$ is an eigenvalue of the quadratic formulation (4), then $-k_m$ is also an eigenvalue. This is due to the symmetry of $\mathbf{K}_1$, $\mathbf{K}_3$, and $\mathbf{M}$ and the property $\det \mathbf{D}^T = \det \mathbf{D}$ ($\mathbf{D}$ is any matrix). Hence, the eigenproblem has two sets of eigensolutions $(k_m^+, \mathbf{U}_m^+)$ and $(k_m^-, \mathbf{U}_m^-)$, where $k_m^- = -k_m^+$ ($m = 1,\ldots, M$), representing $M$ positive-going and $M$ negative-going wave modes.

Let us redenote $(-k_m, \mathbf{U}_{-m})$ the opposite-going mode associated with the eigensolution $(k_m, \mathbf{U}_m)$. From Eq. (9) and the symmetry of $\mathbf{B}$, the left eigenvector $\hat{\mathbf{V}}_m$ of mode $m$, associated with the eigenvalue $k_m$, satisfies

$$\{\mathbf{A}^T - k_m\mathbf{B}\}\hat{\mathbf{V}}_m = \mathbf{0}. \tag{25}$$

Then, it can be readily checked that the above eigenvalue problem is satisfied by the following vector:

$$\hat{\mathbf{V}}_m = \begin{Bmatrix} \mathbf{U}_{-m} \\ k_m\mathbf{U}_{-m} \end{Bmatrix}, \tag{26}$$

which allows to get the left eigenvectors directly from the right ones (i.e., the guided modes). Note that thanks to this expression, solving the left eigenproblem is not needed.

Following Sec. III A, let us develop the general biorthogonality relation $\hat{\mathbf{V}}_n^T\mathbf{B}\hat{\mathbf{U}}_m = b_m\delta_{mn}$. Using Eqs. (14) and (26), one finally gets after rearrangement

$$\frac{i\omega}{4}(\mathbf{U}_m^T\mathbf{F}_{-n} - \mathbf{U}_{-n}^T\mathbf{F}_m) = Q_{m,-m}\delta_{mn}, \tag{27}$$

with the notation

$$Q_{m,-m} = -\omega b_m/4k_m. \tag{28}$$

One emphasizes that no specific assumption has been made. In particular, $\mathbf{C}$ can be complex, as in the viscoelastic case. Hence, properties (26) and (27) are general and still hold for non-propagating modes and lossy waveguides.

### B. Generalized excitability matrix

Using Eq. (26), one has: $\hat{\mathbf{V}}_m^T\hat{\mathbf{F}} = k_m\mathbf{U}_{-m}^T\mathbf{F}$. With notation (28), the expansion (12) can still be rewritten in the form of Eq. (20), but with the new modal excitability matrix

$$\mathbf{E}_m = \frac{i\omega}{4Q_{m,-m}}\mathbf{U}_m\mathbf{U}_{-m}^T. \tag{29}$$

The interpretation of $(\mathbf{E}_m)_{ij}$ does not change from Sec. III B. Yet, the above expression is general and not restricted to propagating modes in lossless waveguides. The expansion (20) together with Eq. (29) is valid in the far-field as well as in the near-field region ($z$ must yet lie outside the source region, as recalled in Sec. II).

The excitability defined by Eq. (29) will be referred to as the generalized excitability matrix in the remainder of the paper.

For propagating modes in lossless waveguides, Eqs. (15), (26), and (14) allow to get the following equalities:

$$\mathbf{U}_{-m} = \mathbf{U}_m^*, \quad \mathbf{F}_{-m} = \mathbf{F}_m^*. \tag{30}$$

From Eq. (27), one has $Q_{m,-m} = P_{mm}$, and the generalized excitability (29) reduces to the lossless excitability (21).

### C. Link with an analytical approach

Provided the straightforward analogy established between the analytical and numerical approaches in Sec. III C, it can be deduced from Eq. (29) that the analytical expression of the generalized excitability is

$$\mathbf{e}_m(\mathbf{x}) = \frac{i\omega}{4Q_{m,-m}}\mathbf{u}_m(\mathbf{x}) \otimes \mathbf{u}_{-m}(\mathbf{x}_s), \tag{31}$$

and the analytical form associated with the numerical biorthogonality relation (27) is

$$Q_{m,-n} = \frac{i\omega}{4}\int_S (\mathbf{u}_m \cdot \mathbf{t}_{-n} - \mathbf{u}_{-n} \cdot \mathbf{t}_m)dS = 0 \quad \text{if} \quad m \neq n. \tag{32}$$

The relation (32) is encountered in the literature, under the following slightly different form: $Q_{m,n} = 0$ if $m \neq -n$, which is usually referred to as the real biorthogonality relation.[6] Unlike the averaged power flow $P_{mm}$, note that the normalization factor $Q_{m,-m}$ remains non-zero for all modes including non-propagating ones.[33]

In fact, the analytical derivation of Eq. (31) can be obtained from the real reciprocity relation of Auld[6] (instead of the complex relation). It could be checked that writing the real reciprocity expression for two different wave fields, one corresponding to a given $-m$ mode and the other to the excited field, and applying the real biorthogonality relation (32) yields the generalized excitability result given by Eq. (31).

Surprisingly, the real orthogonality relation has been considered in scattering analysis,[6,33,34] but not for waveguide excitation problems for which the complex orthogonality relation has generally been preferred.[6,8,11,14,15]

### D. Green's matrix

The Green's matrix can be conveniently expressed in terms of modal excitabilities.

By definition, the response $\mathbf{u}(\mathbf{x}, z)$ is given by the convolution product between the Green's tensor $\mathbf{G}(\mathbf{x}, z)$ and the excitation $\mathbf{f}(z)$ in the $(z, \omega)$ domain, or equivalently in the wavenumber domain: $\tilde{\mathbf{u}}(\mathbf{x}, k) = \tilde{\mathbf{G}}(\mathbf{x}, k) \cdot \tilde{\mathbf{f}}(k)$. Applying the inverse spatial Fourier transform and the Cauchy residue theorem, one has[5,35]

$$\mathbf{u}(\mathbf{x},z)=\sum_{m=1}^{M} i\mathrm{Res}(\tilde{\mathbf{G}}(\mathbf{x},k);k=k_m)\cdot\tilde{\mathbf{f}}(k_m)e^{ik_m z}, \quad (33)$$

where Res($f$; $k$) denotes the residue of $f$ at $k$. Identifying the above expression with Eq. (22), one has the equality: $i\mathrm{Res}(\tilde{\mathbf{G}}(\mathbf{x},k);k=k_m)=\mathbf{e}_m(\mathbf{x})$.

The inverse spatial Fourier transform of $\tilde{\mathbf{G}}(\mathbf{x},k)$ yields after application of the Cauchy residue theorem: $\mathbf{G}(\mathbf{x},z)=\sum_{m=1}^{M} i\mathrm{Res}(\tilde{\mathbf{G}}(\mathbf{x},k);k=k_m)e^{ik_m z}$.

Hence, the expression of Green's tensor can be expressed in terms of the excitability, as follows:[11]

$$\mathbf{G}(\mathbf{x},z)=\sum_{m=1}^{M}\mathbf{e}_m(\mathbf{x})e^{ik_m z}. \quad (34)$$

## V. RESULTS

For three test cases, this section briefly compares results obtained from the lossless excitability (21) with the generalized one (29). As already mentioned in Sec. I, the excitability in lossy waveguides is sometimes approximated with the lossless expression. The error made from the standard formula approximation is highlighted. For simplicity, the examples are two-dimensional and correspond to layered plates excited by line sources. For clarity, $\mathbf{L}_{xy}=\mathbf{L}_x$ and $\mathbf{L}_z$ are the operators of two-dimensional plane strain given by

$$\mathbf{L}_x=\begin{bmatrix}\partial/\partial x & 0\\ 0 & 0\\ 0 & \partial/\partial x\end{bmatrix},\quad \mathbf{L}_z=\begin{bmatrix}0 & 0\\ 0 & 1\\ 1 & 0\end{bmatrix}. \quad (35)$$

Throughout this section, the excitabilities will be computed from displacement-force ratios measured at the free surface in the normal direction (i.e., $x$-direction). The SAFE method will be employed. One will also present the lossless excitability calculated analytically from the software DISPERSE[36] in order to check the accuracy of numerical models.

### A. Viscoelastic waveguide

This first test case compares the excitabilities calculated for a bilayered plate, with and without viscoelasticity. This test case is taken from the work of Simonetti.[37] The relevant material parameters are summarized in Table I.

First, let us consider the non-viscoelastic case. Figure 1 gives the SAFE dispersion curves in phase velocity for two modes of interest, denoted $M_0$ and $M_1$, in agreement with the results calculated in Ref. 37 from the software DISPERSE. Figure 2 shows the SAFE modal excitabilities, as well as DISPERSE lossless excitability. As expected, the lossless excitabilities are equal to the generalized ones because both $M_0$ and $M_1$ modes are propagating modes in a lossless waveguide.

TABLE I. Characteristics of the bilayered plate.

| | $c_s$ (m/s) | $c_l$ (m/s) | $\rho$ (kg/m$^3$) | Thickness (mm) |
|---|---|---|---|---|
| Layer 1 (elastic) | 900 | 1700 | 1250 | 9 |
| Layer 2 (metallic) | 3260 | 5960 | 7930 | 8 |

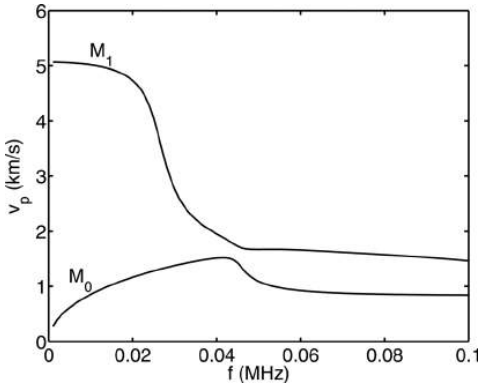


FIG. 1. Dispersion curves in phase velocity for modes $M_0$ and $M_1$ computed from the SAFE method.

Next, let us consider the viscoelastic case when a large material attenuation is considered. The metallic layer is still lossless but $\alpha_s=\alpha_l=1$ is set for the viscoelastic layer (Layer 1), $\alpha_s$ and $\alpha_l$ denoting the shear and longitudinal bulk wave attenuations (in Neper per wavelength). Complex bulk wave velocities are defined from

$$\tilde{c}_{s,l}=\frac{c_s}{1+\mathrm{i}\dfrac{\alpha_{s,l}}{2\pi}}. \quad (36)$$

The matrix of elasticity coefficients $\mathbf{C}$ becomes complex. The lossless excitability expression is not valid in that case and becomes approximate.

Figure 3 shows the SAFE dispersion curves in phase velocity and attenuation for the first two less attenuated modes, denoted $M_0'$ and $M_1'$ (also in agreement with Ref. 37).

Figure 4 exhibits the modal lossless and generalized excitabilities. In this example, it is remarkable that although the material attenuation is high and the viscoelasticity strongly modifies velocity curve patterns (compare Figs. 1

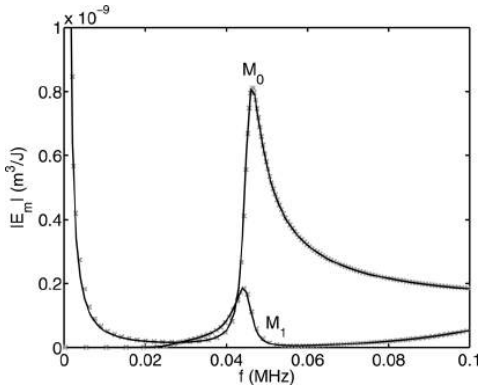


FIG. 2. $M_0$ and $M_1$ excitabilities computed from the SAFE method (black) and calculated from DISPERSE (crosses).

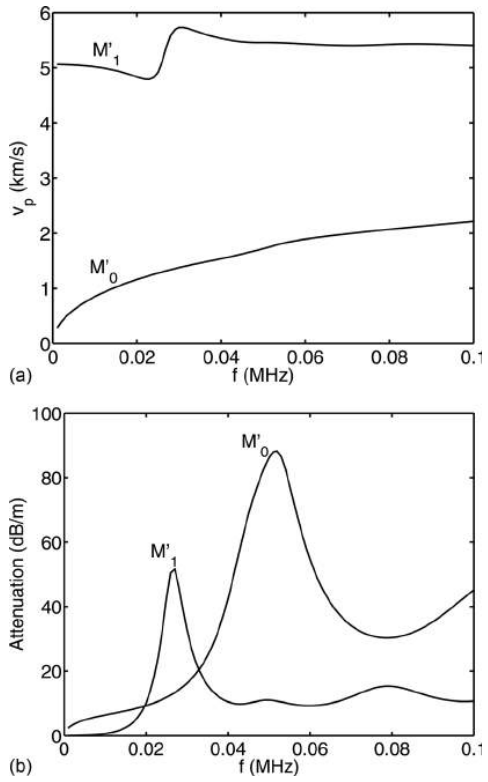


FIG. 3. Dispersion curves in phase velocity (top) and attenuation (bottom) for modes $M_0'$ and $M_1'$ computed from the SAFE method.

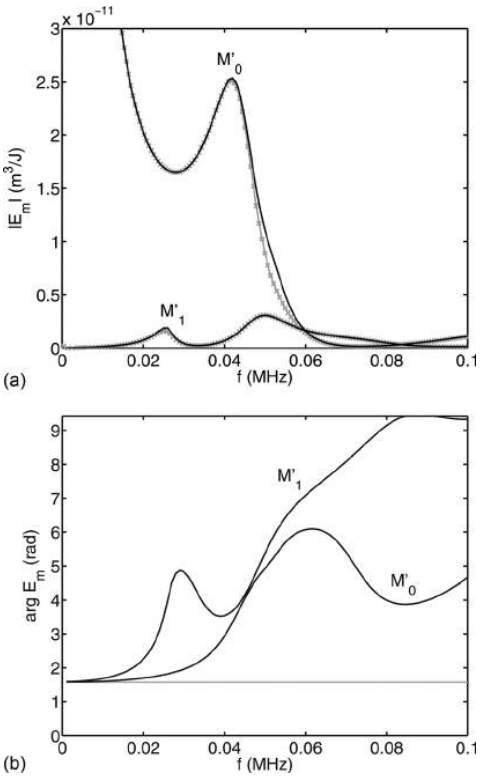


FIG. 4. $M_0'$ and $M_1'$ excitabilities, lossless (gray) and generalized (black), in modulus (top) and phase (bottom) computed from the SAFE method. Crosses: Lossless excitability calculated from DISPERSE. Horizontal gray line at $+\pi/2$: Phase of lossless excitability.

and 3), the lossless excitability still yields good modulus approximation.

For a given mode, it can be observed that the largest amplitude difference between the lossless and the generalized formula occurs at a frequency for which the modal attenuation is maximum (roughly 0.05 MHz for $M_0'$, 0.025 MHz for $M_1'$): As expected, the deviation of the approximate lossless excitability is increasing with loss.

As shown in Fig. 4 (bottom), the phase strongly differs. The generalized excitability is fully complex, with frequency varying phase. The lossless excitability remains constant and pure imaginary [the diagonal terms of Eq. (21) are always pure positive imaginary], yielding a constant $+\pi/2$ phase.

### B. Excitation of non-propagating modes

This second test deals with a numerical experiment simulating a zero group velocity (ZGV) resonance. A ZGV resonance is a local resonance occurring at a frequency of Lamb modes where the group velocity vanishes while the phase velocity remains non-zero.[38–40] Below the ZGV frequency, the modes contributing to the resonance are cut-off. Hence, the contribution of non-propagating modes is expected to be significant.

A steel plate of thickness $a = 1$ cm is considered, with Young modulus $E = 210$ GPa, Poisson ratio $\nu = 0.3$ and density $\rho = 7800$ kg/m$^3$. The first ZGV frequency can be obtained from the empirical formula:[41,42] $f_0 = \beta c_l/2a \simeq 280$ kHz, where $\beta$ is a correction factor that depends on $\nu$ ($\beta \simeq 0.93$ for $\nu = 0.3$—see Ref. 42). As already proved from theory and experiment,[38,42] the resonance is caused by the interference between the two symmetric $S_1$ and $S_{2b}$ modes propagating with opposite phase velocities and generated with comparable amplitudes (the subscript $b$ means that $S_{2b}$ is a backward mode near the resonance).

Figure 5 (top) shows the dimensionless wavenumber-frequency dispersion curves computed from the SAFE method. The first ZGV resonance is observed at the zero slope point of $S_1$ and $S_{2b}$ curves $(k_0a, \omega_0a/c_s) = (1.68, 5.47)$, giving a dimensional frequency of 280 kHz in agreement with the empirical formula.

Near the resonance, the contribution of $S_1$ and $S_2$ modes is expected to be significantly greater than the other modes.[41,42] This is confirmed by looking at the excitabilities shown in Fig. 5 (bottom).

Let us recall that lossless excitability curves cannot be calculated for non-propagating modes (due to zero power flow), and stop at cut-off frequencies. Such curves hence coincide with black lines in Fig. 5 (excluding gray ones).

Now, the plate is excited by a line force (along $y$) located at the surface $x = 0$ and oriented along the $x$ direction (normal to the plate). The time excitation is a Hanning-windowed

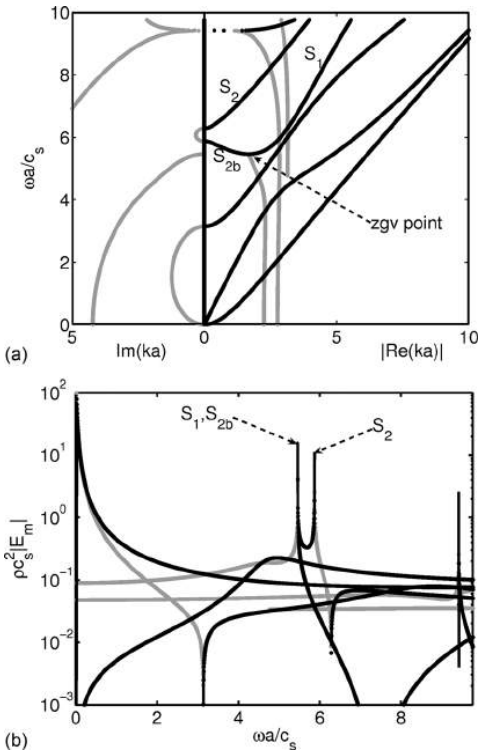


FIG. 5. Dimensionless dispersion curves (top) and excitabilities (bottom) computed from the SAFE method. Black: Propagating modes; gray: Non-propagating modes. DISPERSE lossless excitabilities are superimposed to black lines (excluding non-propagating modes).

5 cycles sinusoidal tone burst centered at 250 kHz, close to the first ZGV frequency. Its spectrum is given by Fig. 6.

Figure 7 gives the response spectrum for the $x$-displacement computed with the SAFE approach from Eq. (20), with the lossless excitability (21) as well as the generalized one (29), at a distance close to the source $z = 5$ mm. In order to avoid interfence nodes,[38,42] this distance has been chosen as less than a quarter wavelength of the $S_1$ and $S_{2b}$ modes ($\lambda = 2\pi/k_0 = 3.74$ cm). In the modal expansions, one has computed and kept the less attenuated modes satisfying

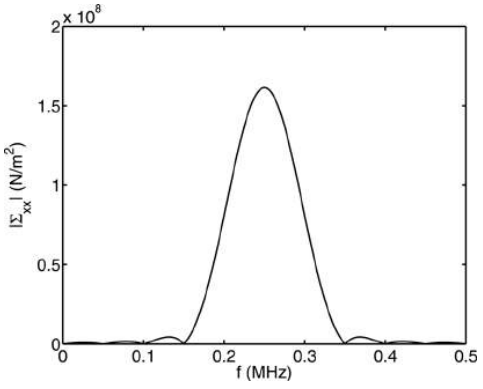


FIG. 6. Frequency spectrum of the excitation.

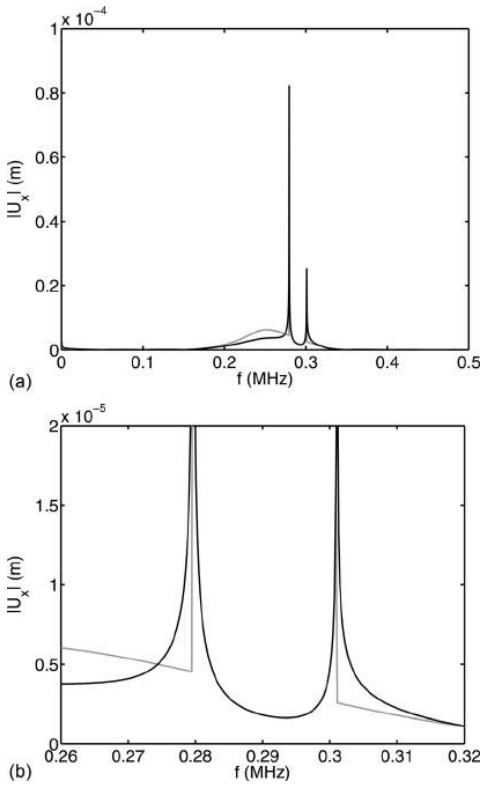


FIG. 7. SAFE computation of the frequency spectrum of the $x$-displacement response obtained from the generalized excitability (black lines) and from the lossless excitability (gray lines). Bottom: Zoom between 260 and 320 kHz.

$|\mathrm{Im}(k)| \leqslant 1\ \mathrm{mm}^{-1}$. This ensures that the contribution of higher order modes is negligible at the position $z = 5$ mm (less than $e^{-1\times 5} \simeq 0.007$).

As expected, the maximum response occurs at the ZGV frequency $f_0$. Although the spectrum seems to be almost identical between the lossless and the generalized formula, a zoom in the range [260 to 320 kHz] reveals differences—see Fig. 7 (bottom). Between 280 and 300 kHz, the $S_1$ and $S_{2b}$ modes are both propagating and the lossless excitability gives exactly the same results as the generalized one. Yet, both modes are inhomogeneous below 280 kHz and the $S_{2b}$ mode is evanescent in a narrow frequency range starting from 300 kHz [i.e., $\omega a/c_s \simeq 5.86$ in Fig. 5 (top)]. Then the lossless excitability, not applicable to non-propagating modes, gives erroneous abrupt changes near the cut-off frequencies 280 and 300 kHz.

Figure 8 (top) gives the time signal obtained from the inverse Fourier transform of the generalized formula, up to time $t = 5$ ms. One can observe the typical behavior of a zero-group velocity wave, oscillating with a very slow exponential decay.[38] As shown by Fig. 8 (bottom), this phenomenon cannot be recovered with the lossless formula. Indeed, neglecting the contribution of non-propagating modes acts as non-causal modal filters (high- or bandpass), yielding erroneous time waveforms (artificial growth at the end of the signal in the figure).

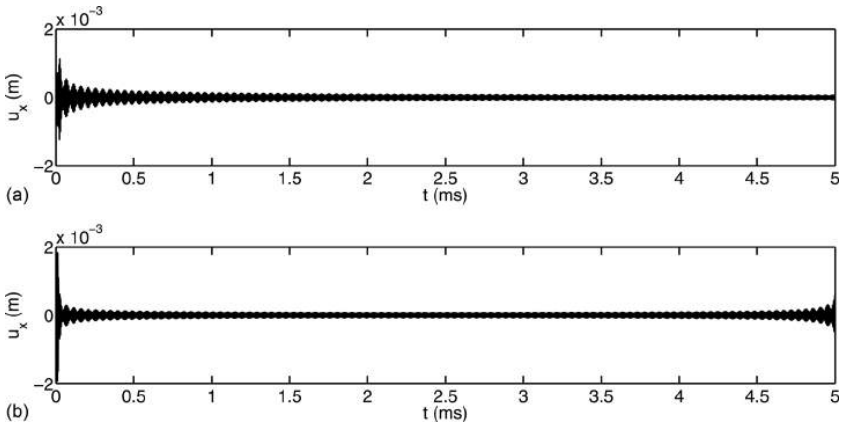


FIG. 8. SAFE $x$-displacement time response obtained from the generalized excitability (top) and the lossless excitability (bottom).

As already mentioned in Sec. II C, one recalls that only modes traveling in the proper direction (here, the positive direction) must be selected into the modal expansion. It has to be noticed that Fig. 5 (top) actually shows the dispersion curves of every mode included in the expansion (positive-going modes). The negative slope observed for the backward mode ($S_{2b}$) is due to the fact that Fig. 5 plots the absolute value of Re($ka$): Dropping the absolute value, the slope becomes properly positive because the wavenumber of a positive-going backward mode has a negative real part.

### C. Excitation of a layered half-space

In this last test case, a layered half space made of three layers is considered with characteristics given by Table II. This example is taken from Ref. 16 and represents a pavement construction. Layer 3 is a half-space, soft compared to the first two layers. No material attenuation is included in this model. Nevertheless, modes are attenuated in the axial direction [Im($k$) $> 0$] due to the loss of energy into the half-space. Such modes are called leaky modes.

In the numerical SAFE model, the presence of a semi-infinite layer is simulated thanks to an absorbing layer, which consists in truncating the unbounded layer (Layer 3) and adding an artificial growing viscoelasticity to the material properties. The open problem is hence transformed into a closed one and the numerical approach proposed in the present paper can be applied without difficulty (the problem becomes similar to a closed viscoelastic waveguide).

Following Ref. 43, the law adopted for the absorbing layer is

$$C'_{ij} = C_{ij}\left\{1 - is\left(\frac{x-d}{h}\right)^3\right\}, \tag{37}$$

where $d$ and $h$ denote the position and thickness of Layer 3 and $s$ is a user-defined parameter. In the simulation, one has set $h = 0.6$ m. A parametric study has been conducted leading to $s = 10$. Figure 9 shows the SAFE dispersion curves in phase velocity and attenuation. In order to validate the parameters of the absorbing layer, DISPERSE results are also shown for this test case. A good agreement is found.

TABLE II. Characteristics of the three-layer model.

| | $c_s$ (m/s) | $c_l$ (m/s) | $\rho$ (kg/m$^3$) | Thickness (m) |
|---|---|---|---|---|
| Layer 1 | 1400 | 2914 | 2000 | 0.2 |
| Layer 2 | 500 | 1041 | 2000 | 0.6 |
| Layer 3 | 100 | 208 | 2000 | $\infty$ |

Figure 10 compares the lossless and the generalized excitabilities calculated from the SAFE approach. As already mentioned in Sec. V A, the error in modulus made with the lossless excitability is greater at frequencies of highest modal attenuation. In this example, these frequencies also coincide with highest excitabilities. The amplitudes of modes 3 and 6 are particularly affected at 500 and 570 Hz, respectively. While the excitability of mode 3 is higher with

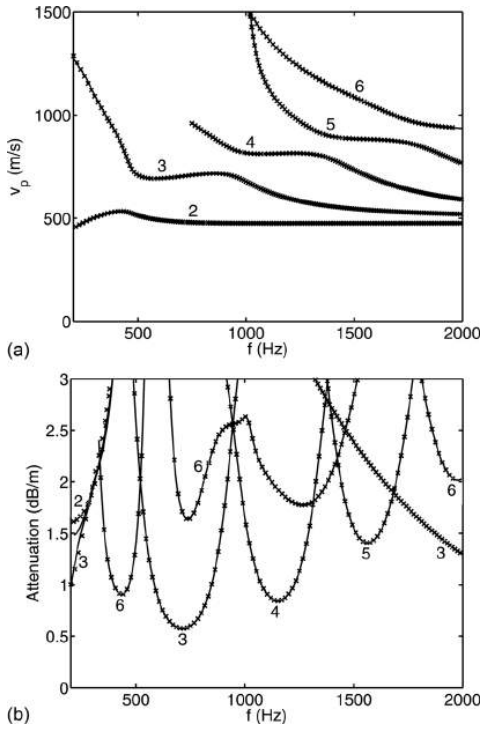


FIG. 9. Dispersion curves in phase velocity (top) and attenuation (bottom) computed from the SAFE method. Crosses: DISPERSE results.

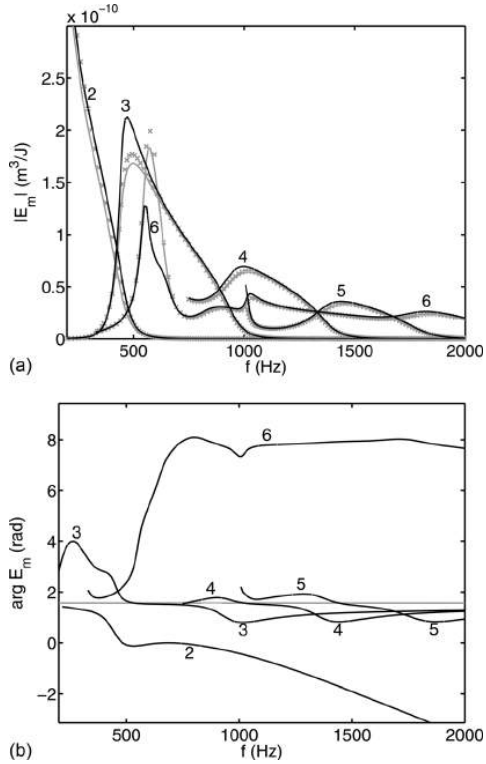


FIG. 10. Excitabilities in modulus (top) and phase (bottom). Same legend as Fig. 4.

the generalized formula, the excitability of mode 6 becomes substantially lower. In particular, the highest excitability is actually given by mode 3 (instead of mode 6 with the lossless formula approximation).

Figure 10 (bottom) shows the phase of excitabilities. As already observed in Sec. V A, the phase is strongly dependent on the modes and frequency (while the phase of the lossless excitability remains equal to $+\pi/2$).

It could be argued that the results of Fig. 10 may be dependent of the parameters of the absorbing layers with the SAFE method. However, one has checked that increasing the thickness $h$ yields negligible differences.

Furthermore, in Fig. 10 (top) the lossless excitability calculated with DISPERSE has also been plotted. From a theoretical point of view, the proof of orthogonality of leaky modes is still an open question (beyond the scope of this paper) because the wave fields of such modes do not vanish at infinity in the half-space. As a consequence, an orthogonality relation written with an integral including the whole half-space may be divergent, as noticed in Ref. 33. To circumvent this problem, these authors have proposed to use the integral restricted over the finite area excluding the half-space layer and have checked that such an approximation yields a small error in modal orthogonality. This explains why small discrepancies with the SAFE lossless excitabilities are observed in Fig. 10 (top) near the maxima of modes 3 and 6: The half-space (i.e., Layer 3) is not included in the power integral of DISPERSE.[36] This has been checked by a numerical test consisting of keeping only the dofs of Layers 1 and 2 in the SAFE computation of the power flow given by Eq. (18), yielding the same results as DISPERSE (curves not shown for clarity of figure).

Finally, one must emphasize that open waveguides could be efficiently modeled by perfectly matched layers (PMLs), as recently proposed in Ref. 44. With a PML method, SAFE matrices are complex but their symmetry is still preserved (as in the viscoelastic case) so that the numerical approach presented in this paper still applies.

## VI. CONCLUSION

A generalized expression has been proposed for the modal excitability of elastic waveguides. This expression remains applicable for lossy waveguides as well as non-propagating modes. It has been derived for analytical and SAFE approaches. For both approaches, the proper orthogonality relation is shown to be a form of Auld's real orthogonality relation, involving opposite-going modes.

From a computational point of view, only the right eigensolutions are needed in the SAFE method. Solving the left eigenproblem is avoided for response computations.

Differences between the lossless and the generalized excitabilities have been highlighted for viscoelastic materials, near-field, and local phenomena for which the contribution of non-propagating modes is significant, as well as leaky modes in open waveguides. In these three cases, the lossless excitability might yield acceptable response approximations in modulus in the frequency domain, but not in phase leading to inaccurate time results.

[1]P. D. Wilcox, M. J. S. Lowe, and P. Cawley, "Mode and transducer selection for long range Lamb wave inspection," J. Intell. Mater. Syst. Struct. **12**, 553–565 (2001).
[2]I. A. Viktorov, *Rayleigh and Lamb Waves* (Plenum, New York, 1967), 154 p.
[3]W. A. Green and E. R. Green, "Elastic waves in fiber composite laminates," Ultrasonics **38**, 228–231 (2000).
[4]A. Cheng, T. W. Murray, and J. D. Achenbach, "Simulation of laser-generated ultrasonic waves in layered plates," J. Acoust. Soc. Am. **110**, 2902–2913 (2001).
[5]E. V. Glushkov, N. V. Glushkova, W. Seemann, and O. V. Kvasha, "Elastic wave excitation in a layer by piezoceramic patch actuators," Acoust. Phys. **52**, 398–407 (2006).
[6]B. A. Auld, *Acoustic Fields and Waves in Solids*, 2nd ed. (Krieger, Malabar, FL, 1990), Vol. II, 432 p.
[7]J. J. Ditri and J. L. Rose, "Excitation of guided elastic wave modes in hollow cylinders by applied surface tractions," J. Appl. Phys. **72**, 2589–2597 (1992).
[8]I. Nunez, R. K. Ing, C. Negreira, and M. Fink, "Transfer and green functions based on modal analysis for Lamb waves generation," J. Acoust. Soc. Am. **107**, 2370–2378 (2000).
[9]P. D. Wilcox, "Lamb wave inspection of large structures using permanently attached transducers," Ph.D. thesis, Imperial College of Science, Technology and Medicine, University of London (1998).
[10]P. Wilcox, M. Evans, O. Diligent, and P. Cawley, "Dispersion and excitability of guided acoustic waves in isotropic beams with arbitrary cross-section," in *Review of Progress in Quantitative NDE*, edited by D. O. Thompson and D. E. Chimenti (AIP Conference Proceedings, New York, 2002), Vol. 615, pp. 203–210.
[11]A. Velichko and P. D. Wilcox, "Modeling the excitation of guided waves in generally anisotropic multilayered media," J. Acoust. Soc. Am. **121**, 60–69 (2007).

[12]S. Guilbaud and B. Audoin, "Measurement of the stiffness coefficients of a viscoelastic composite material with laser-generated and detected ultrasound," J. Acoust. Soc. Am. **105**, 2226–2235 (1999).
[13]A. Mal, "Elastic waves from localized sources in composite laminates," Int. J. Solids Struct. **39**, 5481–5494 (2002).
[14]X. Jia, "Modal analysis of Lamb wave generation in elastic plates by liquid wedge transducers," J. Acoust. Soc. Am. **101**, 834–841 (1997).
[15]L. Duquenne, E. Moulin, J. Assaad, and S. Grondel, "Transient modeling of Lamb waves generated in viscoelastic materials by surface bonded piezoelectric transducers," J. Acoust. Soc. Am. **116**, 133–141 (2004).
[16]N. Ryden and M. J. S. Lowe, "Guided wave propagation in three-layer pavement structures," J. Acoust. Soc. Am. **116**, 2902–2913 (2004).
[17]L. Gavric, "Computation of propagative waves in free rail using a finite element technique," J. Sound Vib. **185**, 531–543 (1995).
[18]T. Hayashi, W.-J. Song, and J. L. Rose, "Guided wave dispersion curves for a bar with an arbitrary cross-section, a rod and rail example," Ultrasonics **41**, 175–183 (2003).
[19]V. Damljanovic and R. L. Weaver, "Propagating and evanescent elastic waves in cylindrical waveguides of arbitrary cross-section," J. Acoust. Soc. Am. **115**, 1572–1581 (2004).
[20]V. Damljanovic and R. L. Weaver, "Forced response of a cylindrical waveguide with simulation of the wavenumber extraction problem," J. Acoust. Soc. Am. **115**, 1582–1591 (2004).
[21]P. W. Loveday, "Simulation of piezoelectric excitation of guided waves using waveguide finite elements," IEEE Trans. Ultrason. Ferroelectr. Freq. Control **55**, 2038–2045 (2008).
[22]I. Bartoli, A. Marzani, F. L. di Scalea, and E. Viola, "Modeling wave propagation in damped waveguides of arbitrary cross-section," J. Sound Vib. **295**, 685–707 (2006).
[23]A. Marzani, "Time-transient response for ultrasonic guided waves propagating in damped cylinders," Int. J. Solids Struct. **45**, 6347–6368 (2008).
[24]G. R. Liu and J. D. Achenbach, "Strip element method to analyze wave scattering by cracks in anisotropic laminated plates," J. Appl. Mech. **62**, 607–613 (1995).
[25]J. Zhu and A. H. Shah, "A hybrid method for transient wave scattering by flaws in composite plates," Int. J. Solids Struct. **34**, 1719–1734 (1997).
[26]F. Tisseur and K. Meerbergen, "The quadratic eigenvalue problem," SIAM Rev. **43**, 235–286 (2001).
[27]S. Adhikari and M. I. Friswell, "Eigenderivative analysis of asymmetric non-conservative systems," Int. J. Numer. Methods Eng. **51**, 709–733 (2001).
[28]J. M. Renno and B. R. Mace, "On the forced response of waveguides using the wave and finite element method," J. Sound Vib. **329**, 5474–5488 (2010).
[29]F. Treyssede, "Mode propagation in curved waveguides and scattering by inhomogeneities: Application to the elastodynamics of helical structures," J. Acoust. Soc. Am. **129**, 1857–1868 (2011).
[30]F. Benmeddour, F. Treyssede, and L. Laguerre, "Numerical modeling of guided waves interaction with non-axisymmetric cracks in elastic cylinders," Int. J. Solids Struct. **48**, 764–774 (2011).
[31]G. R. Liu, K. Y. Lam, and Y. Ohyoshi, "A technique for analyzing elastodynamic responses of anisotropic laminated plates to line loads," Composites, Part B **28**, 667–677 (1997).
[32]J. D. Achenbach, *Reciprocity in Elastodynamics* (Cambridge University Press, Cambridge, UK, 2003), 255 p.
[33]T. Vogt, M. Lowe, and P. Cawley, "The scattering of guided waves in partly embedded cylindrical structures," J. Acoust. Soc. Am. **113**, 1258–1272 (2003).
[34]J. J. Ditri, "Utilization of guided waves for the characterization of circumferential cracks in hollow cylinders," J. Acoust. Soc. Am. **96**, 3769–3775 (1994).
[35]W. Seemann, A. Ekhlakov, E. Glushkov, N. Glushkova, and O. Kvasha, "The modeling of piezoelectrically excited waves in beams and layered substructures," J. Sound Vib. **301**, 1007–1022 (2007).
[36]B. Pavlakovic and M. Lowe, "Disperse user's manual," Version 2.0.11, p. 131 (2001).
[37]F. Simonetti, "Sound propagation in lossless waveguides coated with attenuative materials," Ph.D. thesis, Imperial College of Science, Technology and Medicine, University of London (2003).
[38]D. Clorennec, C. Prada, and D. Royer, "Laser impulse generation and interferometer detection of zero group velocity Lamb mode resonance," Appl. Phys. Lett. **89**, 024101 (2006).
[39]M. F. Werby and H. Uberall, "The analysis and interpretation of some special properties of higher order symmetric Lamb waves: The case for plates," J. Acoust. Soc. Am. **111**, 2686–2691 (2002).
[40]A. L. Shuvalov and O. Poncelet, "On the backward Lamb waves near thickness resonances in anisotropic plates," Int. J. Solids Struct. **45**, 3430–3448 (2008).
[41]A. Gibson and J. S. Popovics, "Lamb wave basis for impact-echo method analysis," J. Eng. Mech. **131**, 438–443 (2005).
[42]C. Prada, D. Clorennec, and D. Royer, "Local vibration of an elastic plate and zero-group velocity Lamb modes," J. Acoust. Soc. Am. **124**, 203–212 (2008).
[43]M. Castaings and M. Lowe, "Finite element model for waves guided along solid systems of arbitrary section coupled to infinite solid media," J. Acoust. Soc. Am. **123**, 696–708 (2008).
[44]F. Treyssede, K. L. Nguyen, A. S. Bonnet-BenDhia, and C. Hazard, "On the use of a safe-pml technique for modeling two-dimensional open elastic waveguides," in *Proceedings of Acoustics*, Nantes, France (April 23–27, 2012), pp. 667–672.

International Journal of Solids and Structures 50 (2013) 1373–1382

Contents lists available at SciVerse ScienceDirect

International Journal of Solids and Structures

journal homepage: www.elsevier.com/locate/ijsolstr

# Mechanical modeling of helical structures accounting for translational invariance. Part 1: Static behavior

Ahmed Frikha [a], Patrice Cartraud [b], Fabien Treyssède [a,*]

[a] LUNAM Université, IFSTTAR, MACS, F-44344 Bouguenais, France
[b] LUNAM Université, GeM, UMR CNRS 6183, Ecole Centrale de Nantes, 1 rue de la Noë, 44 321 Nantes Cédex 3, France

ARTICLE INFO

*Article history:*
Available online 31 January 2013

*Keywords:*
Homogenization
Helical coordinates
Finite element method
Helical springs
Seven-wire strands
Axial load

ABSTRACT

The purpose of this paper is to investigate the static behavior of helical structures under axial loads. Taking into account their translational invariance, the homogenization theory is applied. This approach, based on asymptotic expansion, gives the first-order approximation of the 3D elasticity problem from the solution of a 2D microscopic problem posed on the cross-section and a 1D macroscopic problem, which turns out to be a Navier–Bernoulli–Saint-Venant beam problem. By contrast with earlier references in which a reduced 3D model was built on a slice of the helical structure, the contribution of this paper is to propose a 2D microscopic model. Homogenization is first applied to helical single wire structures, i.e. helical springs. Next, axial elastic properties of a seven-wire strand are computed. The approach is validated through comparison with reference results: analytical solution for helical single wire structures and 3D detailed finite element solution for seven-wire strands.



## 1. Introduction

Helical structures are widely used in mechanical and civil engineering applications. These structures are usually subjected to large loads which can lead to the material degradation and cracks associated with corrosion and mechanical fatigue. This threatens the structural strength. In this framework, non-destructive testing is a crucial tool for detection, localization and measurement of material discontinuities. The choice of the appropriate technique depends on dimensions and accessibility of the structure. Particularly, ultrasonics allow to control large components, such as plates and tubes, by analyzing their elastic guided waves. The purpose of this study, which is composed of two parts, is to develop a numerical model for the analysis of the elastic wave propagation phenomenon in prestressed helical structures. This problem requires the computation of the static prestress state. Therefore, a first model will be developed in Part 1 of this paper, to compute this static state. Taking into account this prestress state, a second model will be developed in Part 2, in order to analyze the wave propagation in these prestressed structures. The goal of this first part of this paper is thus to develop an approach that allows the computation of the prestress state in helical structures subjected to axial load.

Numerous works have been devoted to the modeling of the static behavior of helical structures as springs and multi-wire cables under axial loads. For helical springs, an analytical model was proposed among others in Ancker and Goodier (1958) and Wahl (1963) considering the spring as an Euler–Bernoulli beam with pitch and curvature corrections. Numerical approaches describing the static behavior of helical springs have been also developed. Among these works, a finite element model of half of a spring slice has been proposed in Jiang and Henshall (2000).

The static behavior of seven-wire strands has been widely studied in literature. Various analytical models based on different assumptions have been proposed, such as the model of Costello (1977) which is one of the most popular. These models are reviewed in Jolicoeur and Cardou (1991) and compared in Jolicoeur and Cardou (1991) and Ghoreishi et al. (2007). Besides, numerical models relying on the finite element method were developed. Some of them are based on beam elements (Durville, 1998; Nawrocki and Labrosse, 2000; Páczelt and Beleznai, 2011), see also Nemov et al. (2010) and Bajas et al. (2010) in which ITER superconducting cables composed of a large number of strands are studied. But most of the time, 3D models are used, see e.g. Boso et al. (2006), Ghoreishi et al. (2007), İmrak and Erdönmez (2010), Nemov et al. (2010), Stanova et al. (2011a,b) and Erdönmez and İmrak (2011). In order to obtain a good representation of the geometry as well as the displacement solution, which may involve bending phenomena, quadratic elements are employed. This leads to models which can be computationally expensive, when the model axial length is about the pitch length. Therefore, as soon as the loading fulfills helical symmetry, one can take benefit of this property to reduce the model size. This has been achieved in Jiang et al.

* Corresponding author. Tel.: +33 0240845932.
*E-mail address:* fabien.treyssede@ifsttar.fr (F. Treyssède).

0020-7683/$ - see front matter © 2013 Elsevier Ltd. All rights reserved.
http://dx.doi.org/10.1016/j.ijsolstr.2013.01.010

(1999) and Jiang et al. (2008) in which the computational domain is restricted to a basic sector of a helical slice. Helical symmetry may also be accounted for within the framework of homogenization theory. This has been proposed first in Cartraud and Messager (2006) using axial periodicity, and then improved in Messager and Cartraud (2008), in which helical symmetry enables to consider one slice of a strand. The derivation of the slice model is different in Jiang et al. (1999), Jiang et al. (2008) and Messager and Cartraud (2008). However, in both cases, helical symmetry yields displacement constraints between the two faces of the slice, with a loading under the form of an axial strain and a twist rate.

This work further advances Cartraud and Messager (2006) and Messager and Cartraud (2008), taking advantage of the translational invariance. Helical symmetry can be actually considered more efficiently. Thus the model can be reduced to a 2D one, i.e. a cross-section model. This requires to formulate the homogenization theory in a twisted coordinate system. This technique then allows the computation of the static prestressed state of helical structures (single wire and multi-wire) from the solution of a 2D problem. Let us mention that an advanced analytical 2D model has been recently proposed in Argatov (2011). This model takes into account Poisson's effect, contact deformation and allows to obtain the overall strand stiffness as well as local contact stresses. In this reference, plane strain was assumed to formulate the 2D problem while in the present work helical symmetry is used.

The method developed in this paper is restricted to multi-wire helical structures composed of a stack of helical wires wrapped with the same twisting rate around a straight axis. As explained in Section 3, this excludes the case of double helical structures (such as independent wire rope core for instance) and cross-lay strands.

This paper is organized as follows. First, in Section 2, the curvilinear coordinate system is introduced. Then in Section 3 the translational invariance is defined, which is a necessary condition for the helical homogenization approach. Based on the asymptotic expansion method and exploiting the translational invariance property, the homogenization procedure is presented in Section 4. Its finite element solution is detailed in Section 5. The helical homogenization approach is validated for helical single wire and seven-wire structures by comparison with analytical or numerical models in Section 6.

## 2. Curvilinear coordinate system

A helical structure is considered (see Fig. 1). Let $(\mathbf{e}_X, \mathbf{e}_Y, \mathbf{e}_Z)$ its Cartesian orthonormal basis. The helix centreline is defined by its helix radius $R$ in the Cartesian plane $(\mathbf{e}_X, \mathbf{e}_Y)$ and the length of one helix pitch along the $Z$-axis denoted by $L$. This helix centerline can be described by the following position vector:

$$\mathbf{r}(s) = R\cos\left(\frac{2\pi}{l}s+\theta\right)\mathbf{e}_X + R\sin\left(\frac{2\pi}{l}s+\theta\right)\mathbf{e}_Y + \frac{L}{l}s\mathbf{e}_Z, \tag{1}$$

where $l = \sqrt{L^2+4\pi^2R^2}$ is the curvilinear length of one helix pitch and $\theta$ is the helix phase angle in the $Z=0$ plane. For a seven-wire strand, $\theta$ is equal to $(N-1)\pi/3$, where $N = 1,..,6$ refers to the number of the helical wire. $\theta$ is equal to zero for a single wire helical structure. The helix lay angle $\Phi$ is defined by $\tan\Phi = 2\pi R/L$. A complete helix is described by the parameter $s$ varying from 0 to $l$.

### 2.1. Serret–Frenet basis

A Serret–Frenet basis $(\mathbf{e}_n, \mathbf{e}_b, \mathbf{e}_t)$ associated to the helix can be defined (see e.g. Gray et al. (2006)), where the unit vectors $\mathbf{e}_n, \mathbf{e}_b, \mathbf{e}_t$ are given by $\mathbf{e}_t = d\mathbf{r}/ds, d\mathbf{e}_n/ds = \tau\mathbf{e}_b - \kappa\mathbf{e}_t$ and $d\mathbf{e}_b/ds = -\tau\mathbf{e}_n$. For helical curves, the curvature $\kappa = 4\pi^2R/l^2$ and the torsion $\tau = 2\pi L/l^2$ are constant. In the Cartesian basis, $\mathbf{e}_n, \mathbf{e}_b$ and $\mathbf{e}_t$ are expressed by:

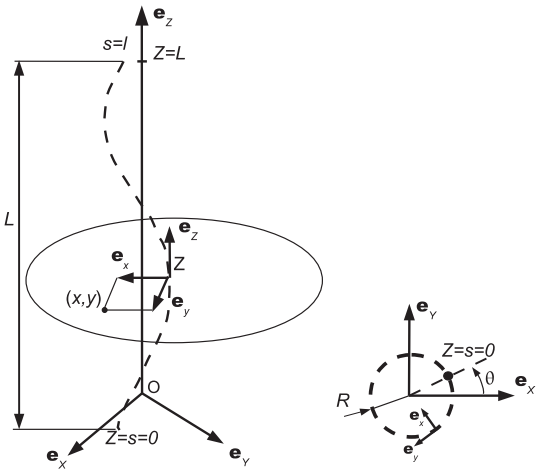


**Fig. 1.** Left: One helix pitch and its twisted basis associated to the twisted coordinate system $(x,y,Z)$. Right: view normal to the $Z$-axis. The point $Z = s = 0$ lies in the $(\mathbf{e}_X, \mathbf{e}_Y)$ plane.

$$\begin{aligned}
\mathbf{e}_n &= -\cos\left(\frac{2\pi}{l}s+\theta\right)\mathbf{e}_X - \sin\left(\frac{2\pi}{l}s+\theta\right)\mathbf{e}_Y,\\
\mathbf{e}_b &= \frac{L}{l}\sin\left(\frac{2\pi}{l}s+\theta\right)\mathbf{e}_X - \frac{L}{l}\cos\left(\frac{2\pi}{l}s+\theta\right)\mathbf{e}_Y + \frac{2\pi}{l}R\mathbf{e}_Z,\\
\mathbf{e}_t &= -\frac{2\pi R}{l}\sin\left(\frac{2\pi}{l}s+\theta\right)\mathbf{e}_X + \frac{2\pi R}{l}\cos\left(\frac{2\pi}{l}s+\theta\right)\mathbf{e}_Y + \frac{L}{l}\mathbf{e}_Z.
\end{aligned} \tag{2}$$

The normal vector $\mathbf{e}_n$ remains parallel to the $(\mathbf{e}_X, \mathbf{e}_Y)$ plane while $\mathbf{e}_b$ and $\mathbf{e}_t$ move in the three directions of the Cartesian basis as $s$ and $\theta$ vary.

### 2.2. Twisted basis

A special case of the Serret–Frenet basis denoted by $(\mathbf{e}_x, \mathbf{e}_y, \mathbf{e}_Z)$ corresponding to $\kappa = 0$ and $\tau = 2\pi/L$ can be considered. It corresponds to a twisted coordinate system along the $Z$-axis $(s \equiv Z)$ with axial periodicity $L$. The unit vectors $\mathbf{e}_x$ and $\mathbf{e}_y$ rotate around the $Z$-axis and remain parallel to the $(\mathbf{e}_X, \mathbf{e}_Y)$ plane (see Fig. 1). In the Cartesian basis, $\mathbf{e}_x$ and $\mathbf{e}_y$ are expressed as:

$$\begin{aligned}
\mathbf{e}_x &= -\cos\left(\frac{2\pi}{L}Z+\theta\right)\mathbf{e}_X - \sin\left(\frac{2\pi}{L}Z+\theta\right)\mathbf{e}_Y,\\
\mathbf{e}_y &= \sin\left(\frac{2\pi}{L}Z+\theta\right)\mathbf{e}_X - \cos\left(\frac{2\pi}{L}Z+\theta\right)\mathbf{e}_Y.
\end{aligned} \tag{3}$$

It should also be noted that this twisted coordinate system coincides with the one proposed in Onipede and Dong (1996), Nicolet et al. (2004) and Nicolet and Zola (2007) for the analysis of twisted and helical structures.

### 2.3. Covariant and contravariant bases

Differential operators can not be expressed directly in the Serret–Frenet or twisted bases. They have first to be expressed in the covariant and contravariant bases. The reader can find an in-depth treatment of curvilinear coordinate systems in Chapelle and Bathe (2003); Synge and Schild (1978); Wempner (1981) for instance.

From the twisted basis $(\mathbf{e}_x, \mathbf{e}_y, \mathbf{e}_Z)$, a new coordinate system $(x,y,Z)$ is built, for which any position vector can be expressed as:

$$\mathbf{X}(x,y,Z) = x\mathbf{e}_x(Z) + y\mathbf{e}_y(Z) + Z\mathbf{e}_Z. \tag{4}$$

The covariant basis $(\mathbf{g}_1,\mathbf{g}_2,\mathbf{g}_3)$ is obtained from the position vector by $(\mathbf{g}_1,\mathbf{g}_2,\mathbf{g}_3) = (\partial\mathbf{X}/\partial x, \partial\mathbf{X}/\partial y, \partial\mathbf{X}/\partial Z)$, which yields in the twisted basis:

$$\begin{aligned} &\mathbf{g}_1 = \mathbf{e}_x(Z), \quad \mathbf{g}_2 = \mathbf{e}_y(Z),\\ &\mathbf{g}_3 = -\tau y\mathbf{e}_x(Z) + \tau x\mathbf{e}_y(Z) + \mathbf{e}_Z. \end{aligned} \tag{5}$$

Note that the covariant basis is not orthogonal.

The covariant metric tensor, defined by $g_{mn} = \mathbf{g}_m \cdot \mathbf{g}_n$, is then given by:

$$\mathbf{g} = \begin{bmatrix} 1 & 0 & -\tau y \\ 0 & 1 & \tau x \\ -\tau y & \tau x & \tau^2(x^2+y^2)+1 \end{bmatrix}. \tag{6}$$

The covariant basis gives rise to the contravariant one $(\mathbf{g}^1,\mathbf{g}^2,\mathbf{g}^3)$, defined from $\mathbf{g}_i \cdot \mathbf{g}^j = \delta_i^j$. Superscripts and subscripts refer to the covariant and contravariant vectors, respectively. $\mathbf{g}^1,\mathbf{g}^2$ and $\mathbf{g}^3$ are expressed in the twisted basis as:

$$\mathbf{g}^1 = \mathbf{e}_x(Z) + \tau y\mathbf{e}_Z, \mathbf{g}^2 = \mathbf{e}_y(Z) - \tau x\mathbf{e}_Z, \quad \mathbf{g}^3 = \mathbf{e}_Z. \tag{7}$$

The Christoffel symbol of the second kind $\Gamma_{ij}^k$, defined by $\Gamma_{ij}^k = \mathbf{g}_{i,j} \cdot \mathbf{g}^k$, can be calculated from the covariant and contravariant bases, which leads to:

$$\begin{aligned} &\Gamma_{11}^k = \Gamma_{12}^k = \Gamma_{21}^k = \Gamma_{22}^k = 0,\\ &\Gamma_{13}^1 = \Gamma_{31}^1 = 0, \quad \Gamma_{23}^1 = \Gamma_{32}^1 = -\tau, \quad \Gamma_{33}^1 = -\tau^2 x,\\ &\Gamma_{23}^2 = \Gamma_{32}^2 = 0, \quad \Gamma_{33}^2 = -\tau^2 y, \quad \Gamma_{13}^2 = \Gamma_{31}^2 = \tau,\\ &\Gamma_{13}^3 = \Gamma_{31}^3 = \Gamma_{23}^3 = \Gamma_{32}^3 = \Gamma_{33}^3 = 0. \end{aligned} \tag{8}$$

It is noteworthy that the coefficients $\Gamma_{ij}^k$ do not depend on the axial variable $Z$. As shown in the next section, this is a necessary condition for translational invariance.

### 2.4. Strain tensor

The strain tensor is now rewritten in the curvilinear coordinate system. In the contravariant basis, the strain–displacement relation is Chapelle and Bathe, 2003:

$$\boldsymbol{\epsilon} = \epsilon_{ij}\mathbf{g}^i \otimes \mathbf{g}^j, \quad \epsilon_{ij} = \frac{1}{2}(u_{i,j} + u_{j,i}) - \Gamma_{ij}^k u_k, \tag{9}$$

where the $u_i$'s denote the displacement covariant components.

Using the relation (7) between the contravariant and the twisted bases, the strain vector can then be expressed in the twisted basis as follows:

$$\{\epsilon\} = \left(\mathbf{L}_{xy} + \mathbf{L}_Z\frac{\partial}{\partial Z}\right)\{u\},$$

$$\mathbf{L}_{xy} = \begin{bmatrix} \partial/\partial x & 0 & 0 \\ 0 & \partial/\partial y & 0 \\ 0 & 0 & \Lambda \\ \partial/\partial y & \partial/\partial x & 0 \\ \Lambda & -\tau & \partial/\partial x \\ \tau & \Lambda & \partial/\partial y \end{bmatrix}, \quad \mathbf{L}_Z = \begin{bmatrix} 0 & 0 & 0 \\ 0 & 0 & 0 \\ 0 & 0 & 1 \\ 0 & 0 & 0 \\ 1 & 0 & 0 \\ 0 & 1 & 0 \end{bmatrix}, \tag{10}$$

where $\Lambda = \tau(y\partial/\partial x - x\partial/\partial y)$. The column vectors $\{u\} = [u_x\, u_y\, u_Z]^T$ and $\{\epsilon\} = [\epsilon_{xx}\, \epsilon_{yy}\, \epsilon_{ZZ}\, 2\epsilon_{xy}\, 2\epsilon_{xZ}\, 2\epsilon_{yZ}]^T$ are the displacement vector and the strain vector respectively, both written in the orthonormal twisted basis $(\mathbf{e}_x,\mathbf{e}_y,\mathbf{e}_Z)$.

### 2.5. Constitutive law

For an isotropic material, the elasticity tensor is given in the covariant basis by Chapelle and Bathe, 2003:

$$\begin{aligned} &\mathbf{C} = C^{ijkl}\mathbf{g}_i \otimes \mathbf{g}_j \otimes \mathbf{g}_k \otimes \mathbf{g}_l,\\ &C^{ijkl} = \frac{\nu E}{(1+\nu)(1-2\nu)}g^{ij}g^{kl} + \frac{E}{2(1+\nu)}(g^{ik}g^{jl} + g^{il}g^{jk}), \end{aligned} \tag{11}$$

where $E$ and $\nu$ are the Young modulus and the Poisson's ratio, respectively. Using the relation between the covariant and the twisted bases and after simplifications, it can be checked that the elasticity tensor components in the twisted basis are given by:

$$C_{\alpha\beta\delta\gamma} = \frac{\nu E}{(1+\nu)(1-2\nu)}\delta_{\alpha\beta}\delta_{\delta\gamma} + \frac{E}{2(1+\nu)}(\delta_{\alpha\delta}\delta_{\beta\gamma} + \delta_{\alpha\gamma}\delta_{\beta\delta}), \tag{12}$$

where greek subscripts $\{\alpha,\beta,\gamma,\delta\}$ denote components $x,y,Z$ in the twisted basis. The above expression coincides with the one obtained in the Cartesian basis, as the twisted basis is orthonormal.

## 3. Translational invariance

Translational invariance is a key property for applying the homogenization theory. For cylindrical structures, translational invariance means that both the cross-section and the material properties do not vary along the axis. For curved structures, there is another condition which states that the differential operator coefficients must not depend on the axial variable (Treyssède, 2011). As a consequence, for helical structures, the translational invariance requires the following three conditions (Treyssède, 2008; Treyssède and Laguerre, 2010):

1. The material properties do not vary along the $Z$-axis in the twisted coordinate system;
2. The coefficients of the differential operators (gradient, divergence, Laplacian, ...) are independent on the axial variable $Z$;
3. The cross-section does not vary along the $Z$-axis in the twisted coordinate system.

Throughout this work, the material is assumed to be homogeneous and isotropic. In this case, the first condition is verified. To satisfy the second condition, it is sufficient to prove that the Christoffel symbols do not depend on the axial variable $Z$, which has been verified in the last section (see Eq. 8). Thus it remains only to verify the third condition.

Let us consider a helical single wire structure. The cross-section shape in the $(\mathbf{e}_X,\mathbf{e}_Y)$ plane at the axial position $Z_1$ is similar to that given at the position $Z_2$: there only exists a rotation of angle $2\pi(Z_2 - Z_1)/L$ around the $Z$-axis between these two cross-section shapes. Moreover, because the twisted basis plane $(\mathbf{e}_x,\mathbf{e}_y)$ also rotates around $Z$, the cross-section indeed remains fixed in this plane. Therefore, the translational invariance is checked for helical single wire structures. Fig. 2 shows the cross-section of four helical single wires with $R = 2a$ and different helical angles in the $(\mathbf{e}_X,\mathbf{e}_Y)$ plane. $a$ is the radius of the circular cross-section (the cross-section being circular in the plane normal to the helical curve). Note that for small angle $\Phi$, the cross-section shape in this plane is nearly circular because the structure is close to a cylinder (Fig. 2a). However the cross-section shape deviates from the circular one as $\Phi$ increases.

Let us now consider multi-wire helical structures. They are composed of a stack of helical wires, wrapped around a straight wire. A seven-wire strand is a special case of helical multi-wire structures containing one layer of six helical wires wrapped around the central wire. In the twisted basis, a cylindrical structure of axis $Z$ with isotropic material is translationally invariant for any value

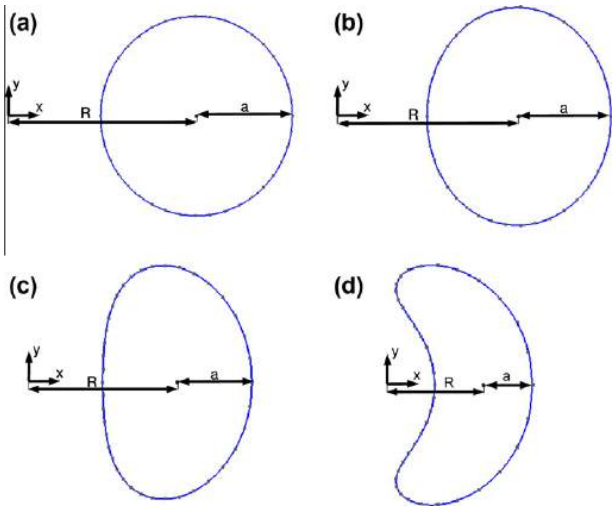


**Fig. 2.** Cross-section of helical wires, $R/a = 2$ and (a) $\Phi = 10^\circ$, (b) $\Phi = 30^\circ$, (c) $\Phi = 50^\circ$, (d) $\Phi = 70^\circ$.

of the torsion $\tau$ (see Treyssède and Laguerre (2010)). It therefore remains fixed in the Cartesian as in the twisted coordinate systems. The central wire is hence translationally invariant. As shown for helical single wire, the peripheral helical wires, which have the same helix parameters are also translationally invariant in the twisted coordinate system. The geometric invariance is then verified for the seven-wire strand in the twisted coordinate system and the problem is translationally invariant.

Let us briefly examine more complex structures. In multi-layer wire ropes, more than one layer of helical wires is present. Translational invariance in such structures is still satisfied if the torsion of each wire remains identical. This implies that translational invariance is not fulfilled in case of cross-lay strands because the torsion can be positive or negative. This loss of invariance is obvious if one thinks of contact discontinuities between two layers of opposite torsion. Contact discontinuities also necessarily occur in double helical structures, composed of one central strand wrapped by several peripheral strands. Such double helical structures, sometimes referred to as IWRC (independent wire rope core), hence cannot fulfill translational invariance.

To conclude this section, let us define the cross-section boundary in the plane $Z = 0$. The surface boundary of a helical single wire with circular cross-section is described in the Serret–Frenet basis by the following position vector:

$$\mathbf{X}(x, y, s) = \mathbf{r}(s) + a\cos t\mathbf{e}_n(s) + a\sin t\mathbf{e}_b(s), \tag{13}$$

where $t \in [0; 2\pi]$. Substituting Eq. (2) into Eq. (13), the cross-section shape parameterization in the $(\mathbf{e}_X, \mathbf{e}_Y)$ plane is:

$$\begin{cases} X(t) = (R - a\cos t)\cos(\eta a\sin t + \theta) + \frac{L}{l}a\sin t\sin(\eta a\sin t + \theta), \\ Y(t) = (R - a\cos t)\sin(\eta a\sin t + \theta) + \frac{L}{l}a\sin t\cos(\eta a\sin t + \theta), \end{cases} \tag{14}$$

where $\eta = -4\pi^2 R/lL$. This curve has been used to plot the cross-sections on Fig. 2. It has also been used for the FE mesh generation in Section 6.

## 4. Helical homogenization procedure

In this work, helical structures are supposed to be subjected to external loads at its end sections. Moreover, only axial loads (traction and torsion) are considered. Targeted helical structures are helical springs and seven-wire strands.

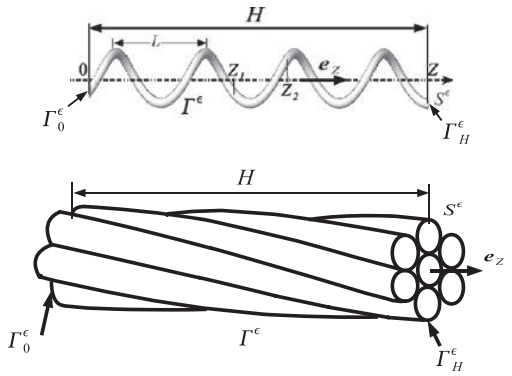


**Fig. 3.** 3D helical structures. (a) single wire, (b) seven-wire strand.

As explained in introduction, the purpose of this paper is to propose an approach for obtaining the static stress state, which will be used in the second part of this paper as a prestress state, for a wave propagation analysis. This can be achieved efficiently using an homogenization method. This approach, based on the asymptotic expansion method, exploits the translational invariance property. Homogenization splits the initial 3D elasticity problem into 2D problems posed on the cross-section, and a 1D straight beam problem. The overall beam behavior is computed thanks to the solution of the 2D problems. This solution, combined with the solution of the beam problem, provides also the local stress state.

For the present work, let us consider a slender helical structure of axial length $H$ (see Fig. 3), with a cross-section denoted $S^\varepsilon$. This structure occupies the configuration $\Omega^\varepsilon = S^\varepsilon \times [0, H]$. The boundary of $\Omega^\varepsilon$ is defined by $\partial\Omega^\varepsilon = \Gamma^\varepsilon \cup \Gamma^\varepsilon_0 \cup \Gamma^\varepsilon_H$, with $\Gamma^\varepsilon_0 = S^\varepsilon \times \{0\}$ and $\Gamma^\varepsilon_H = S^\varepsilon \times \{H\}$ the two end cross-sections of the helical structure and $\Gamma^\varepsilon$ the cross-section boundary. This structure exhibits a small parameter $\varepsilon$, corresponding to the inverse of the slenderness ratio, i.e. the ratio between the diameter of the cross-section $S^\varepsilon$ and the length $H$.

### 4.1. The initial problem

The linear elasticity problem consists in finding the fields $\boldsymbol{\sigma}^\varepsilon, \boldsymbol{\epsilon}^\varepsilon$ and $\mathbf{u}^\varepsilon$, solution of:

$$\begin{cases} \nabla \cdot \boldsymbol{\sigma}^\varepsilon = \mathbf{0}, \\ \boldsymbol{\sigma}^\varepsilon = \mathbf{C} : \boldsymbol{\epsilon}^\varepsilon(\mathbf{u}^\varepsilon), \\ \boldsymbol{\epsilon}^\varepsilon(\mathbf{u}^\varepsilon) = \nabla^s(\mathbf{u}^\varepsilon), \\ \boldsymbol{\sigma}^\varepsilon \cdot \mathbf{n} = \mathbf{0} \text{ on } \Gamma^\varepsilon, \end{cases} \tag{15}$$

where $\mathbf{C}$ is the elasticity tensor, which is supposed to be constant under the assumption of small displacements. $\nabla^s(\cdot)$ and $\nabla \cdot (\cdot)$ denote respectively the symmetric gradient (strain) and divergence operators. The solution must also verify the boundary conditions at the end sections. They are supposed to be under the form of stress data: $\boldsymbol{\sigma}^\varepsilon \cdot (-\mathbf{e}_Z) = \mathbf{t}^0$ on $\Gamma_0^\varepsilon$ and $\boldsymbol{\sigma}^\varepsilon \cdot \mathbf{e}_Z = \mathbf{t}^H$ on $\Gamma_H^\varepsilon$, where $\mathbf{t}^0$ and $\mathbf{t}^H$ are the tractions at the end sections located at $Z = 0$ and $Z = H$. Moreover $\mathbf{t}^0$ and $\mathbf{t}^H$ are such that the overall structure equilibrium is fulfilled, which is a necessary condition for problem (15) to have a solution.

For seven-wire strand, the solution must verify Eq. (15) on each wire as well as contact equations, on the contact line between the central wire and each helical wire. This raises the problem of contact assumptions. In Ghoreishi et al., 2007, stick and slip conditions have been studied for computing the overall behavior. In Gnanavel and Parthasarathy (2011), an analytical model with frictional contact was developed. Overall stiffness as well as maximum normal contact stresses were calculated from the authors's model and the Costello's model which assumes stick contact. In Argatov (2011) hypothesis of slip contact is made and maximum contact pressures (core-wire and wire-wire) were compared to FE computations performed with frictional contact in Jiang et al. (2008). All of these previous works have shown that the overall stiffness and contact stresses are very little sensitive to contact conditions. Therefore in this work, for simplicity, the contact is assumed to be stick. This amounts to perfect bonding conditions between wires: $\mathbf{u}_c = \mathbf{u}_p$ and $(\boldsymbol{\sigma} \cdot \mathbf{n})_c^+ + (\boldsymbol{\sigma} \cdot \mathbf{n})_p^- = 0$, where the subscripts $c$ and $p$ are related to the central and peripheral wires.

The solution of this problem (15) with boundary conditions and contact equations for multi-wire strand provides the prestress state. As mentioned previously, this problem may be computationally expensive to solve under this form, and the homogenization method aims to simplify it.

### 4.2. Asymptotic expansion method

To our knowledge very few works have been devoted to the asymptotic analysis of helical structures starting from a 3D formulation. We just mention Nicolet et al., 2007 in the framework of electrostatics. Therefore, the approach presented in this paper is based on Buannic and Cartraud (2000) and Buannic and Cartraud (2001a) developed for axially invariant and periodic beam-like structures respectively. More about asymptotic expansion method for slender structures may be found in some books (Sanchez-Hubert and Sanchez-Palencia, 1992; Kalamkarov and Kolpakov, 1997; Trabucho and Viaño, 1996).

The first step of the method consists in defining a problem equivalent to problem (15), but posed on a fixed domain that does not depend on the small parameter $\varepsilon$. A change of variables is thus introduced which takes into account the structure slenderness, in the twisted coordinates system: $(x, y, \zeta) = (x, y, \varepsilon Z)$. $\zeta = \varepsilon Z$ denotes the slow scale or macroscopic 1D-variable and $\{x, y\}$ denote the fast scale or microscopic 2D-variables. According to this change of variables, the differential operators become

$$\begin{aligned} \nabla^s(.) &= \nabla^s_{xy}(.) + \varepsilon \nabla^s_\zeta(.), \\ \nabla \cdot (.) &= \nabla_{xy} \cdot (.) + \varepsilon \nabla_\zeta \cdot (.), \end{aligned} \tag{16}$$

where $\nabla^s_\zeta(.)$ and $\nabla_\zeta \cdot (.)$ correspond to partial differentiations with respect to the macroscopic variable $\zeta$. $\nabla^s_{xy}(.)$ and $\nabla^s_{xy} \cdot (.)$ denote the differential operators with respect to the microscopic variables $x$ and $y$.

Next, the displacement solution is searched under an asymptotic expansion form:

$$\mathbf{u}(\mathbf{x}) = u_x^0(\zeta)\mathbf{e}_x + u_y^0(\zeta)\mathbf{e}_y + \varepsilon \mathbf{u}^1(x, y, \zeta) + \varepsilon^2 \mathbf{u}^2(x, y, \zeta) + \ldots \tag{17}$$

In this expression, the translational invariance is taken into account since the $k$th order displacement $\mathbf{u}^k(x, y, \zeta)$ does not depend on the microscopic axial coordinate $Z$. Moreover, it is usually considered that the 0th order displacement has no axial component, which results from the property that for slender structures, the bending stiffness is much lower than axial stiffness. So 0th order displacement corresponds to a transverse deflection. Note that a proof of this result may be found in Trabucho and Viaño (1996) for homogeneous beams, and in Kolpakov (1991) for beams with periodic structure. As axial loads are considered in this work, and under the assumption that bending is not coupled with tension and torsion, this 0th order term vanishes.

Reporting expansion (17) in problem (15) with the use of (16), and considering $\zeta$ and $\{x, y\}$ as independent coordinates, one is led to a sequence of problems. On one hand 2D microscopic problems posed on the cross-section $S$, which will be denoted $P^m_{2D}$, where $m$ denotes the order of $\varepsilon$ in the equilibrium equation. On the other hand a sequence of 1D macroscopic problems will be also obtained, but only the lowest order macroscopic problem will be considered in the following.

### 4.3. Microscopic problems

The lowest order 2D microscopic problem posed on the cross-section $S$ is $P^1_{2D}$ with the following equations:

$$\begin{cases} \nabla_{xy} \cdot \boldsymbol{\sigma}^1 = 0, \\ \boldsymbol{\sigma}^1 = \mathbf{C} : \boldsymbol{\epsilon}^1, \\ \boldsymbol{\epsilon}^1 = \nabla^s_{xy}(\mathbf{u}^1), \\ \boldsymbol{\sigma}^1 \cdot \mathbf{n} = 0 \text{ on } \partial S. \end{cases} \tag{18}$$

It is important to notice that though this problem is 2D, the displacement $\mathbf{u}^1$ has three components. This results from the property than in a matrix form, from Eq. (10), one has:

$$\{\nabla^s_{xy}(\mathbf{u}^1)\} = \mathbf{L}_{xy}\{u^1\} = \mathbf{L}_{xy} \begin{Bmatrix} u_x^1 \\ u_y^1 \\ u_\zeta^1 \end{Bmatrix}. \tag{19}$$

Problem $P^1_{2D}$ is well-posed and has a unique solution up to a rigid body motion (Sanchez-Hubert and Sanchez-Palencia, 1992; Buannic and Cartraud, 2000). The stress solution is obviously equal to zero. The displacement is thus a rigid body motion solution of $\nabla^s_{xy}(\mathbf{u}^1) = \mathbf{0}$, its expression in the twisted basis is:

$$\mathbf{u}^1 = u_\zeta^1(\zeta)\mathbf{e}_Z + \varphi^1(\zeta)[x\mathbf{e}_y - y\mathbf{e}_x], \tag{20}$$

corresponding to an overall translation $u_\zeta^1$ and rotation $\varphi^1$ around the $Z$-axis. The solution of problem (18) is then given by $\mathbf{u}^1$ with at this step arbitrary $u_\zeta^1(\zeta)$ and $\varphi^1(\zeta)$ and $\boldsymbol{\epsilon}^1 = \boldsymbol{\sigma}^1 = \mathbf{0}$.

The next order microscopic problem $P^2_{2D}$ involves $\boldsymbol{\sigma}^2, \boldsymbol{\epsilon}^2$ and $\mathbf{u}^2$ solution of:

$$\begin{cases} \nabla_{xy} \cdot \boldsymbol{\sigma}^2 = 0, \\ \boldsymbol{\sigma}^2 = \mathbf{C} : \boldsymbol{\epsilon}^2, \\ \boldsymbol{\epsilon}^2 = \nabla^s_{xy}(\mathbf{u}^2) + \nabla^s_{\zeta}(\mathbf{u}^1), \\ \boldsymbol{\sigma}^2 \cdot \mathbf{n} = 0 \text{ on } \partial S. \end{cases} \tag{21}$$

Note that the displacement vector $\mathbf{u}^1$, obtained from the solution of the problem $P^1_{2D}$, appears through $\nabla^s_{\zeta}(\mathbf{u}^1)$ in $P^2_{2D}$. From Eq. (20), it can be seen that the components of this strain tensor are, under a matrix form:

$$\{\nabla^s_{\zeta}(\mathbf{u}^1)\} = \begin{bmatrix} 0 & 0 & E^E & 0 & -yE^T & xE^T \end{bmatrix}^T, \tag{22}$$

where $E^E = \partial u^1_{\zeta}/\partial\zeta$ and $E^T = \partial\varphi^1/\partial\zeta$ and thus can be identified as macroscopic strains, i.e. extension and torsion respectively. Therefore, the other part of the strain $\nabla^s_{xy}(\mathbf{u}^2)$ is a microscopic strain.

Thanks to the problem linearity, its solution is a linear function of the macroscopic strains, up to a rigid body displacement which is of the form (20). So one has:

$$\begin{aligned} \mathbf{u}^2 &= \boldsymbol{\chi}^E(x,y)E^E(\zeta) + \boldsymbol{\chi}^T(x,y)E^T(\zeta) + u^2_{\zeta}(\zeta)\mathbf{e}_Z + \varphi^2(\zeta)[x\mathbf{e}_y - y\mathbf{e}_x], \\ \boldsymbol{\sigma}^2 &= \boldsymbol{\sigma}^E(x,y)E^E + \boldsymbol{\sigma}^T(x,y)E^T. \end{aligned} \tag{23}$$

As it will be shown in the next section, the lowest order macroscopic problem is a 1D beam problem, with extension and torsion. It thus involves macroscopic beam stresses which are simply defined from the integration over the cross-section $S$ of the local or microscopic stresses $\boldsymbol{\sigma}^1$. Consequently the axial force $T$ and the torque $M$ take the form:

$$\begin{aligned} T(\zeta) &= \int_S \sigma^2_{\zeta\zeta} dS, \\ M(\zeta) &= \int_S (-y\sigma^2_{x\zeta} + x\sigma^2_{y\zeta}) dS \end{aligned} \tag{24}$$

and from the solution of problem (21), one can define the overall beam behavior such that:

$$\begin{Bmatrix} T \\ M \end{Bmatrix} = [k^{hom}] \begin{Bmatrix} E^E \\ E^T \end{Bmatrix}, \tag{25}$$

where $[k^{hom}]$ is the stiffness matrix, which is symmetric.

### 4.4. Macroscopic problem

The lowest order macroscopic problem can be derived from compatibility conditions which express that problem (21) admits a solution, see e.g. Buannic and Cartraud (2000); Buannic and Cartraud (2001a). It amounts to integrate equilibrium equations of problem (21) over the cross-section. This yields:

$$\begin{cases} dT/d\zeta = 0, \\ dM/d\zeta = 0, \\ \begin{Bmatrix} T \\ M \end{Bmatrix} = [k^{hom}] \begin{Bmatrix} E^E \\ E^T \end{Bmatrix}, \\ E^E = \partial u^1_{\zeta}/\partial\zeta, \\ E^T = \partial\varphi^1/\partial\zeta, \end{cases} \tag{26}$$

with boundary conditions at $\zeta = 0$ and $\zeta = \varepsilon H$. Since we have stress data for the 3D initial problem, and taking into account the overall equilibrium, these boundary conditions can be written as:

$$\begin{cases} T(0) = \int_S \mathbf{t}^0 \cdot (-\mathbf{e}_Z) dS, \\ M(0) = \int_S (y\mathbf{t}^0 \cdot \mathbf{e}_x - x\mathbf{t}^0 \cdot \mathbf{e}_y) dS, \\ T(\varepsilon H) = T(0), \\ M(\varepsilon H) = M(0), \end{cases} \tag{27}$$

which corresponds to the application of the Saint-Venant principle, rigorously justified in the framework of asymptotic analysis of beams in Buannic and Cartraud, 2001b.

The solution of this 1D macroscopic problem (26) and (27) is thus straightforward with a uniform macroscopic state: $T = T(0), M = M(0)$, with the macroscopic strains $E^E$ and $E^T$ obtained from the inversion of (25) and $u^1_{\zeta}$ and $\varphi^1$ calculated thanks to $(26)_{4-5}$ and defined up to a constant.

### 4.5. Summary

One can summarize the results of the asymptotic expansion method with the following expressions:

$$\begin{aligned} \mathbf{u}(\mathbf{x}) &= \varepsilon(u^1_{\zeta}(\zeta)\mathbf{e}_Z + \varphi^1(\zeta)[x\mathbf{e}_y - y\mathbf{e}_x]) + \varepsilon^2(\boldsymbol{\chi}^E(x,y)E^E + \boldsymbol{\chi}^T(x,y)E^T \\ &\quad + u^2_{\zeta}(\zeta)\mathbf{e}_Z + \varphi^2(\zeta)[x\mathbf{e}_y - y\mathbf{e}_x]) + O(\varepsilon^3), \\ \boldsymbol{\sigma} &= \varepsilon(\boldsymbol{\sigma}^E(x,y)E^E + \boldsymbol{\sigma}^T(x,y)E^T) + O(\varepsilon^2). \end{aligned} \tag{28}$$

It is recalled that microscopic fields $\boldsymbol{\chi}^E(x,y), \boldsymbol{\chi}^T(x,y), \boldsymbol{\sigma}^E(x,y)$ $\boldsymbol{\sigma}^T(x,y)$ are provided by the solution of the 2D microscopic problem (21) posed on the cross-section. Then, the expansions given in (28) can be easily computed up to the second-order rigid body motion, combining the previous solution of the 1D macroscopic problem with these microscopic fields.

## 5. Finite element solution

The variational formulation of the 2D microscopic problem (21) in the twisted coordinate system takes the form:

$$\forall \delta\mathbf{u}^2(x,y), \quad \int_S \nabla^s_{xy}(\delta\mathbf{u}^2) : \boldsymbol{\sigma}^2 dxdy = 0 \tag{29}$$

and from Eq. $(21)_3$:

$$\boldsymbol{\sigma}^2 = \mathbf{C} : (\nabla^s_{xy}(\mathbf{u}^2) + \boldsymbol{\epsilon}_{macro}), \tag{30}$$

with $\boldsymbol{\epsilon}_{macro} = \nabla^s_{\zeta}(\mathbf{u}^1)$. Hence one has:

$$\begin{aligned} \forall \delta\mathbf{u}^2(x,y), \quad \int_S \nabla^s_{xy}(\delta\mathbf{u}^2) : \mathbf{C} : \nabla^s_{xy}(\mathbf{u}^2) dxdy &= -\int_S \nabla^s_{xy}(\delta\mathbf{u}^2) \\ &\quad : \mathbf{C} : \boldsymbol{\epsilon}_{macro} dxdy. \end{aligned} \tag{31}$$

We recall that $\{\nabla^s_{xy}(\mathbf{u}^2)\} = \mathbf{L}_{xy}\{u^2\}$, see (19). Then a finite element approximation of the form $\{u^2\} = [N^e]\{U^e\}$ is introduced, where $[N^e]$ is the matrix of shape functions, and $\{U^e\}$ the nodal displacements, with three degrees of freedom at each node. The variational formulation yields:

$$\begin{aligned} &[K]\{U\} = \{F\}, \\ &[K^e] = \int_{S^e} [N^e]^T \mathbf{L}^T_{xy} [C] \mathbf{L}_{xy} [N^e] dxdy, \\ &\{F^e\} = -\int_{S^e} [N^e]^T \mathbf{L}^T_{xy} [C] \{\epsilon_{macro}\} dxdy, \end{aligned} \tag{32}$$

with $[K]$ the stiffness matrix obtained from the assembly of element stiffness matrices $[K^e]$.

Note that in (32) the external load is given under the form of a macroscopic strain $\{\epsilon_{macro}\}$.

Once this system is solved, the stresses are computed thanks to (30) and after integration over the cross-section, the macroscopic beam stresses, i.e. the axial force and the torque are computed, thus providing the overall behavior $[k^{hom}]$.

## 6. Validation of the homogenization approach

In this section, the microscopic response is computed for helical springs and seven-wire strands under axial loading. The 2D FE

model based on helical homogenization has been implemented in an in-house code. This model is first validated for helical springs by comparison with an analytical solution. Another validation is also presented for seven-wire strands with a reference solution obtained from a 3D FE model.

For helical single wire or multi-wire structures subjected to a given macroscopic extension $E^E$ ($E^T = 0$), first the 2D model is generated. The cross-section is meshed, with six-node triangle elements to improve the geometrical description as well as results accuracy. The solution of the microscopic 2D problem is defined up to a rigid body displacement in the twisted coordinate system, see Eq. (20), which can be fixed by prescribing the axial displacement $u_Z$ of an arbitrary node and the binormal displacement $u_y$ of a node on the line $y = 0$. Then Eq. (32) is solved, and in the post-processing step, the computation of the axial force $T$ and moment $M$ are performed as well as the overall behavior.

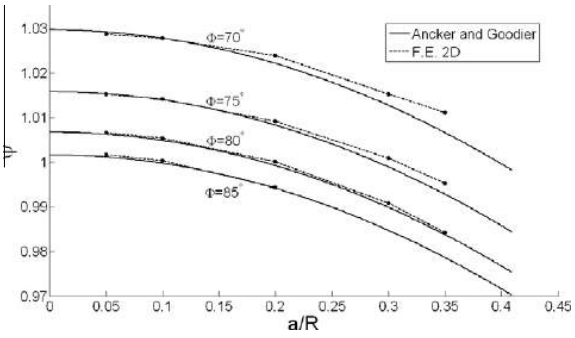


**Fig. 4.** Correction factor $\Psi$ vs. $a/R$ for $\Phi = 70^\circ, 75^\circ, 80^\circ, 85^\circ$.

### 6.1. Helical single wire structures

A helical single wire structure with circular cross-section is studied. $R, \Phi, n$ and $a$ denote the helix radius, helix angle, number of helix pitches and the wire radius, respectively. Two types of structures can be distinguished: helical springs (large helix angle $\Phi$ and ratio $R/a$) and civil engineering cable (small angle $\Phi$). The homogenization approach proposed in this paper is valid for any type of helical structures. However, in the literature, analytical solution is available only in the case of helical spring. Therefore, the validation of the homogenization approach is performed in that case.

The analytical solution may be found in Ancker and Goodier, 1958. When one end-section is clamped while the other is subjected to axial load $T$ with a fixed rotation, the axial deflection $\delta$ at its end is given by:

$$\delta = \frac{4TR^3 n}{Ga^4}\Psi,$$
$$\Psi = 1 - \frac{3}{16}\left(\frac{a}{R}\right)^2 + \frac{1}{(1+\nu)\tan^2\Phi}\left(\frac{1-\nu}{2} - \frac{\nu^2}{1+\frac{3-7\nu-20\nu^2-8\nu^3}{48(1+\nu)}\left(\frac{a}{R}\right)^2 + \frac{1+\nu}{\tan^2\Phi}}\right) + \cdots, \tag{33}$$

where $\Psi$ is a pitch and curvature correction factor.

The inputs of the analytical solution are the ratio $a/R$, the helix angle $\Phi$ and the Poisson coefficient $\nu$. For given geometric and material parameters, Eq. (33) is used to compute the correction factor $\Psi$.

The numerical results provided by the homogenization approach are compared with the analytical solutions for helical springs as follows. For a given $\delta$, the macroscopic strain $E^E = \delta/nL, E^T = 0$ is imposed as the loading in (32) on the 2D FE model. Then the axial force $T$ is computed. This leads to a numerical value of $\Psi$ according to Eq. $(33)_1$, which is compared to the analytical solution given by Eq. $(33)_2$. For $\nu = 0.3$, Fig. 4 shows the variation of the correction factor $\Psi$ as a function of $a/R$ for helix angle $\Phi = 70^\circ, 75^\circ$ , $80^\circ$ and $85^\circ$. Only small differences between numerical and analytical results can be seen for $a/R \leqslant 0.2$. This difference increases with $a/R$ and as $\Phi$ decreases but remains less than 0.7% for $\Phi = 70^\circ$ and $a/R = 0.35$, which is small.

The same evolution of the differences between the numerical results and the analytical solution was observed in Jiang et al., 2008, using a 3D FE model, with a free rotation. They are due to the non validity of the analytical model for large $a/R$ and small helix angle $\Phi$. However, our numerical results are in good agreement with those obtained from the analytical model providing a first validation of the computational homogenization approach.

Now, the 2D FE model is used to highlight the 3D microscopic displacements under extension. Fig. 5 shows the microscopic displacements $\mathbf{u}^2$ of helical spring with helix parameters $R/a = 10$ and $\Phi = 75^\circ$ subjected to axial extension $E^E = 40\%$. Note that this example corresponds to an extreme situation, where a large load is applied on helical spring with a small helix angle $\Phi$. The mesh is made of 4327 dofs. It can be seen that axial displacement in Fig. 5(b) exhibits a linear evolution over the cross-section, which indicates the local bending response. For the geometrical and material properties $a = 2.7$ mm, $\nu = 0.3$ and $E = 2e11$ Pa, the computed axial force and torque are $T = 930.9$ N and $M = -1.83$ N.m. This example will be used, in Part 2 of this paper, for the wave propagation analysis in prestressed elastic helical springs.

### 6.2. Seven-wire strands

Multi-wire cables form a large class of civil engineering components. Seven-wire strands, composed of one layer of helical wires wrapped around a central wire, are the basic element of these cables. The major advantage of the twisted structure is its ability to carry large loads.

The static behavior of seven-wire strands was studied among others in Ghoreishi et al. (2007) using a 3D FE model. In that paper the overall strand stiffness was identified from computations performed on a model of two pitch length, and these results are considered as reference results in the following.

The static behavior is computed using the computational homogenization approach and the 2D FE model. The 2D mesh is generated as follows: an independent mesh for each wire of the seven-wire strand is first considered. As mentioned before, the contact condition between the central and peripheral wires are assumed stick. Linear relations are then imposed at the contact point between the central and the peripheral wires, expressing the displacement continuity ($\mathbf{u}_c = \mathbf{u}_p$), where the subscripts $c$ and $p$ correspond to the central and peripheral wires, respectively. In practice, the system (32) is condensed to take into account these conditions.

As an example, Fig. 6 shows the mesh of the cross-section of a strand with the following parameters: central wire with radius $a$ and helical wires with helix radius $R/a = 1.967$ and angle $\Phi = 7.9^\circ$. The cross-section of the central straight wire is circular. As for the previous helical single wire structure, the cross-section of helical wires is no longer circular in the $(\mathbf{e}_X, \mathbf{e}_Y)$ plane. Note that the helix radius $R$ must be smaller than $2a$, otherwise the adjacent helical wires would overlap each other. This example will be considered later in this section as well as in Part 2.

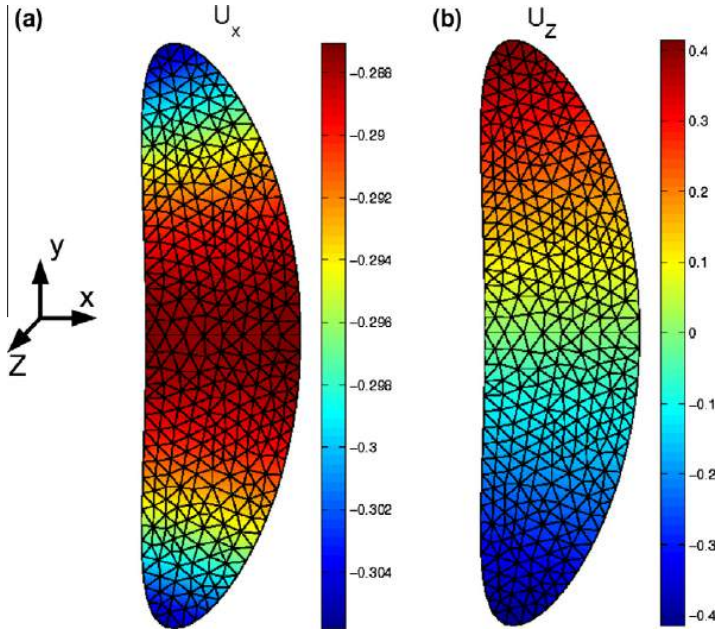


**Fig. 5.** Dimensionless microscopic displacements in the cross-section of a helical spring ($R/a = 10, \Phi = 75^\circ$) under axial deformation $E^E = 40\%$. (a) $u_x^2/a$, (b) $u_z^2/a$.

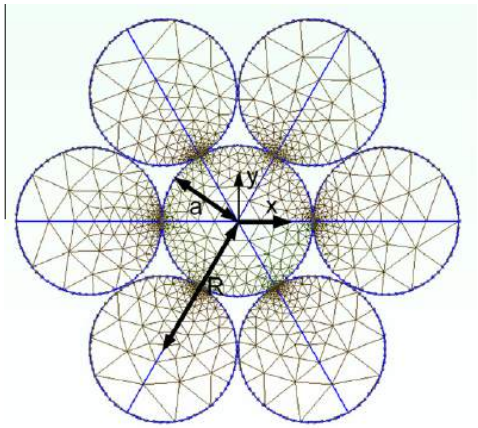


**Fig. 6.** Mesh of seven-wire strand ($R/a = 1.967, \Phi = 7.9^\circ, a$ is the radius of the central wire).

Now, the overall behavior of seven-wire strand is computed. The stiffness components studied are the axial stiffness and the coupling between extension and torsion, i.e. the 11 and 21 components of the matrix $[k^{hom}]$ introduced in (25). In order to compare results obtained from the 2D FE model with the reference solution of Ghoreishi et al., 2007, we set $R/a = 2, \nu = 0.3$ and the stiffness components are written in the dimensionless form: $\overline{k}_{11} = k_{11}^{hom}/(E\pi R^2), \overline{k}_{21} = k_{21}^{hom}/(E\pi R^3)$.

Fig. 7 displays the variation of the axial stiffness $\overline{k}_{11}$ as a function of the helix angle $\Phi$, which varies between 2.5° and 35°. For $\Phi \leqslant 25^\circ$, the difference between the two results is below 2%. This difference increases with $\Phi$ and reaches 10% for $\Phi = 35^\circ$.

The variation of the coupling term $\overline{k}_{21}$ as a function of the helix angle $\Phi$ is shown in Fig. 8. For $\Phi \leqslant 8^\circ$, the coupling term obtained by the two FE models are very close. For large helix angle, the difference between the two solutions is below 4%.

The difference between the 2D and the reference 3D FE solutions can be explained by the use of a different mesh in the 2D model compared to the reference model. Indeed, the 2D mesh of a seven-wire strand with $\Phi = 5^\circ$ use 1122 triangular elements and 2514 nodes, while the cross-section in the reference 3D model is made of 72 elements and 210 nodes. Both the 2D and 3D FE models use quadratic elements. Moreover, an elliptical approximation of the cross-section shape was used in the 3D model, while the geometry is rigorously represented in the 2D model, according to Eq. (14). However as can be seen from Fig. (2), this approximation seems to be justified for examples studied with $\Phi \leqslant 35^\circ$.

Overall the macroscopic behavior of the seven-wire strand computed by the 2D FE model according to the homogenization approach is in good agreement with that obtained from the 3D model. This provides a second validation of the helical computational homogenization approach.

Lastly, microscopic displacements computed using the 2D FE model are analyzed. From the symmetry between the six helical wires, the displacements of only one peripheral wire is discussed. Fig. 9 shows the microscopic displacements in the cross-section of the seven-wire strand considered in Fig. 6 ($R/a = 1.967, \Phi = 7.9^\circ$), subjected to $E^E = 0.6\%$. The in plane component $u_x^2$ of the central and the peripheral wire are shown in Fig. 9(a) and (c), respectively. One can observe the Poisson effect, with a linear evolution over the cross-section of $u_x^2$ in the central wire, and an affine evolution in the peripheral wire, which is maintained in contact with the central wire. The axial displacement is presented in Fig. 9(b) and (d) for the central and the peripheral wire, respectively. One can notice that for the central wire the microscopic axial displacement is close to zero except in the vicinity of contact points where small variations occur. In the helical wire, a linear evolution of the microscopic axial displacement over the cross-section is found, due to local bending. For this example, the core wire radius is $a = 2.7$ mm (the helical wire radius being 0.967 a). Material properties are: $\nu = 0.28$ and $E = 2.17e11$ Pa. The computed axial force and torque are $T = 190.3$ kN and $M = 118.1$ N.m. This example will used in Part 2 of this paper, for wave propagation analysis in prestressed strands.

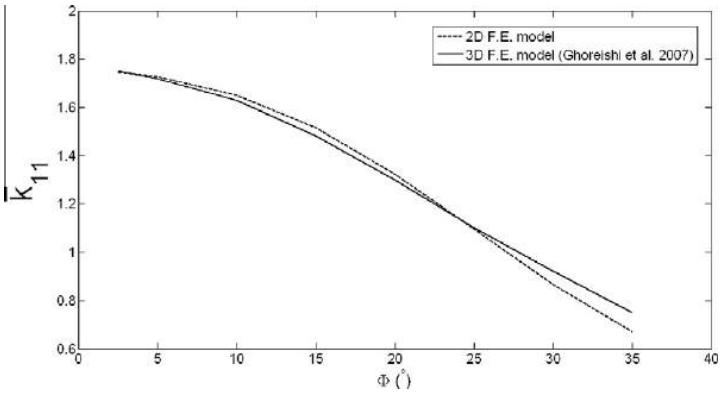


**Fig. 7.** Dimensionless axial stiffness of seven-wire strand. $\overline{k}_{11}$ vs. Φ. $R/a = 2$.

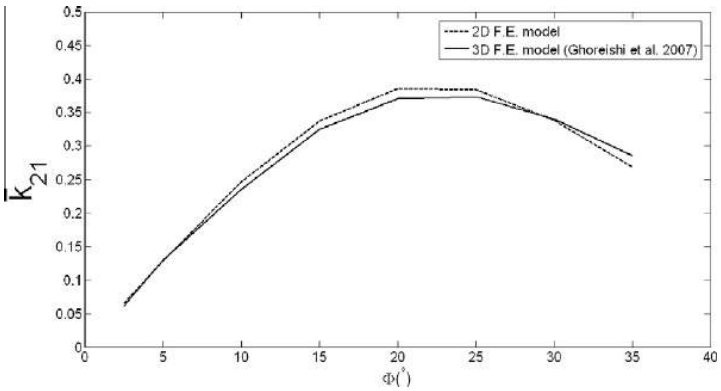


**Fig. 8.** Dimensionless stiffness coupling term of seven-wire strand. $\overline{k}_{21}$ vs. Φ. $R/a = 2$.

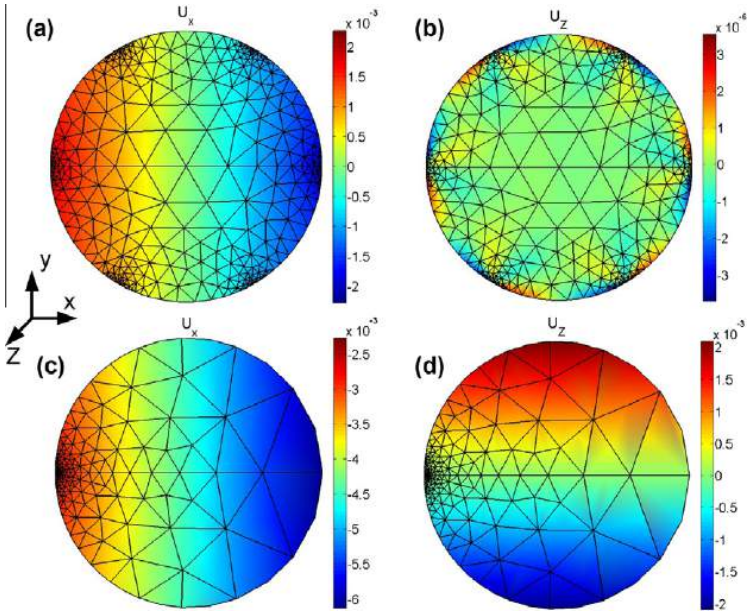


**Fig. 9.** Dimensionless microscopic displacements of a seven-wire strand under axial deformation $E^E = 0.6\%$. (a) $u_x^2/a$ and (b) $u_\zeta^2/a$ in the central wire (c) $u_x^2/a$ and (d) $u_\zeta^2/a$ in the peripheral wire.

## 7. Conclusions

In this paper, the asymptotic expansion method has been applied to helical structures subjected to axial loads (traction and torsion) at its end sections. Thanks to the use of a twisted coordinate system, the 3D elastic problem has been reduced to a 2D microscopic problem posed on the cross-section and a 1D macroscopic beam problem, which has an analytical solution. Therefore the main contribution of this work is the derivation of the 2D microscopic problem, which fully exploits the translational invariance of the problem. The solution of this problem enables the computation of the overall beam stiffness as well as microscopic stresses corresponding to a given macroscopic loading. The proposed approach has been validated for helical single wire structures and seven-wire strands and compares favorably with reference analytical results or 3D FE computations.

In Part 2 of this paper, the solution of the microscopic problem is used in order to take into account effects of prestress and geometry deformation on wave propagation.

## References


Ancker, C.J., Goodier, J.N., 1958. Pitch and curvature corrections for helical springs. Journal of Applied Mechanics 25, 466–470.

Argatov, I., 2011. Response of a wire rope strand to axial and torsional loads: asymptotic modeling of the effect of interwire contact deformations. International Journal of Solids and Structures 48, 1413–1423.

Bajas, H., Durville, D., Ciazynski, D., Devred, A., 2010. Numerical simulation of the mechanical behavior of iter cable-in-conduit conductors. IEEE Transactions on Applied Superconductivity 20, 1467–1470.

Boso, D.P., Lefik, M., Schrefler, B.A., 2006. Homogenisation methods for the thermo-mechanical analysis of nb3sn strand. Cryogenics 46, 569–580.

Buannic, N., Cartraud, P., 2000. Higher-order asymptotic model for a heterogeneous beam, including corrections due to end effects. In: Proc. of 41st AIAA/ASME/ASCE/AHS/ASC Structures, Structural Dynamics, and Materials Conference.

Buannic, N., Cartraud, P., 2001a. Higher-order effective modelling of periodic heterogeneous beams – Part 1: Asymptotic expansion method. International Journal of Solids and Structures 38, 7139–7161.

Buannic, N., Cartraud, P., 2001b. Higher-order effective modelling of periodic heterogeneous beams – Part 2: Derivation of the proper boundary conditions for the interior asymptotic solution. International Journal of Solids and Structures 38, 7163–7180.

Cartraud, P., Messager, T., 2006. Computational homogenization of periodic beam-like structures. International Journal of Solids and Structures 43, 686–696.

Chapelle, D., Bathe, K.J., 2003. The Finite Element Analysis of Shells-Fundamentals. Springer.

Costello, G.A., 1977. Theory of Wire Rope. Springer.

Durville, D., 1998. Modélisation du comportement mécanique de câbles métalliques. Revue Européenne des Eléments Finis 7, 9–22.

Erdönmez, C., İmrak, C.E., 2011. New approaches for model generation and analysis for wire rope. In: Murgante, B., Gervasi, O., Iglesias, A., Taniar, D., Apduhan, B. (Eds.), Computational Science and Its Applications - ICCSA 2011, Lecture Notes in Computer Science. Springer, pp. 103–111.

Ghoreishi, S.R., Messager, T., Cartraud, P., Davies, P., 2007. Validity and limitations of linear analytical models for steel wire strands under axial loading, using a 3d fe model. International Journal of Mechanical Sciences 49, 1251–1261.

Gnanavel, B., Parthasarathy, N., 2011. Effect of interfacial contact forces in radial contact wire strand. Archive of Applied Mechanics 81, 303–317.

Gray, A., Abbena, E., Salamon, S., 2006. Modern Differential Geometry of Curves and Surfaces with Mathmatica, third ed. Chapman and hall, Boca Raton.

İmrak, C.E., Erdönmez, C., 2010. On the problem of wire rope model generation with axial loading. Mathematical and Computational Applications 15, 259–268.

Jiang, W.G., Henshall, J.L., 2000. A novel finite element model for helical springs. Finite Elements in Analysis and Design 35, 363–377.

Jiang, W.G., Warby, M.K., Henshall, J.L., 2008. Statically indeterminate contacts in axially loaded wire strand. European Journal of Mechanics A/Solids 27, 69–78.

Jiang, W.G., Yao, M.S., Walton, J.M., 1999. A concise finite element model for simple straight wire rope strand. International Journal of Mechanical Sciences 41, 143–161.

Jolicoeur, C., Cardou, A., 1991. A numerical comparison of current mathematical models of twisted wire cables under axisymmetric loads. Journal of Energy Resources Technology 113, 241–249.

Kalamkarov, A.L., Kolpakov, A.G., 1997. Analysis, Design and Optimization of Composite Structures. Wiley.

Kolpakov, A.G., 1991. Calculation of the characteristics of thin elastic rods with a periodic structure. J. Appl. Math. Mech. 55, 358–365.

Messager, T., Cartraud, P., 2008. Homogenization of helical beam-like structures: application to single-walled carbon nanotubes. Computational Mechanics 41, 335–346.

Nawrocki, A., Labrosse, M., 2000. A finite element model for simple straight wire rope strands. Computers and Structures 77, 345–359.

Nemov, A.S., Boso, D.P., Voynov, I.B., Borovkov, A.I., Schrefler, B.A., 2010. Generalized stiffness coefficients for iter superconducting cables, direct fe modeling and initial configuration. Cryogenics 50, 304–313.

Nicolet, A., Movchan, A.B., Geuzaine, C., Zolla, F., Guenneau, S., 2007. High order asymptotic analysis of twisted electrostatic problems. Physica B: Condensed Matter 394, 335–338.

Nicolet, A., Zola, F., 2007. Finite element analysis of helicoidal waveguides. Measurement and Technology 28, 67–70.

Nicolet, A., Zola, F., Guenneau, S., 2004. Modeling of twisted optical waveguides with edge elements. The European Physical Journal Applied Physics 28, 153–157.

Onipede, O., Dong, S.B., 1996. Propagating waves and end modes in pretwisted beams. Journal of Sound and Vibration 195, 313–330.

Páczelt, I., Beleznai, R., 2011. Nonlinear contact-theory for analysis of wire rope strand using high-order approximation in the fem. Computers and Structures 89, 1004–1025.

Sanchez-Hubert, J., Sanchez-Palencia, E., 1992. Introduction Aux Méthodes Asymptotiques et L'homogénéisation. Masson, Paris.

Stanova, E., Fedorko, G., Fabian, M., Kmet, S., 2011a. Computer modelling of wire strands and ropes part i: theory and computer implementation. Advances in Engineering Software 42, 305–315.

Stanova, E., Fedorko, G., Fabian, M., Kmet, S., 2011b. Computer modelling of wire strands and ropes part ii: finite element-based applications. Advances in Engineering Software 42, 322–331.

Synge, J.L., Schild, A., 1978. Tensor Calculus. Dover.

Trabucho, L., Viaño, J.M., 1996. Mathematical modelling of rods. In: Ciarlet, P.G., Lions, J.L. (Eds.), Handbook of Numerical Analysis, vol. IV. North-Holland.

Treyssède, F., 2008. Elastic waves in helical waveguides. Wave Motion 45, 457–470.

Treyssède, F., 2011. Mode propagation in curved waveguides and scattering by inhomogeneities: application to the elastodynamics of helical structures. Journal of the Acoustical Society of America 129, 1857–1868.

Treyssède, F., Laguerre, L., 2010. Investigation of elastic modes propagating in multi-wire helical waveguides. Journal of Sound and Vibration 329, 1702–1716.

Wahl, A.M., 1963. Mechanical Springs, second ed. Mc Graw-Hill, Inc., New York.

Wempner, G., 1981. Mechanics of Solids with Applications to Thin Bodies. Sijthoff and Noordhoff, The Netherlands.

International Journal of Solids and Structures 50 (2013) 1383–1393

Contents lists available at SciVerse ScienceDirect

International Journal of Solids and Structures

journal homepage: www.elsevier.com/locate/ijsolstr

# Mechanical modeling of helical structures accounting for translational invariance. Part 2 : Guided wave propagation under axial loads

Fabien Treyssède [a,*], Ahmed Frikha [a], Patrice Cartraud [b]

[a] LUNAM Université, IFSTTAR, MACS, F-44344 Bouguenais, France
[b] LUNAM Université, GeM, UMR CNRS 6183, Ecole Centrale de Nantes, 1 rue de la Noë, 44 321 Nantes Cédex 3, France

ARTICLE INFO

*Article history:*
Available online 21 January 2013

*Keywords:*
Waveguide
Prestress
Helical coordinates
Finite element
Strands
Springs

ABSTRACT

This paper corresponds to the second part of a study that aims at modeling helical structures accounting for translational invariance. In the Part 1 of this paper, the static behavior has been addressed using a helical homogenization approach which provides the stress state corresponding to axial loads. The latter is considered as a prestressed state, for elastic wave propagation analysis in helical waveguides, which is the subject of the Part 2 of this paper. Non destructive testing of springs and multi-wire strands is a potential application of the proposed model. Accounting for translational invariance, the elastodynamic equations of prestressed helical structures yield a 2D problem posed on the cross-section, corresponding to a so-called semi-analytical finite element (SAFE) formulation. For helical springs, the numerical model is validated with an analytical solution corresponding to a Timoshenko beam approximation. It is shown that the influence of the prestressed state is significant at low frequencies. Finally, a seven-wire strand subjected to axial loads is considered. The computed dispersion curves are compared to experimental data. Good agreement is obtained for the first compressional-like modes and their veering central frequency.



## 1. Introduction

This paper is the second part of a study that aims at modeling helical structures accounting for translational invariance. In Part 1, the static state in the case of axial loads has been addressed. Taking into account the effects of prestress and geometry deformation due to these static loads, the objective of Part 2 is the computation of wave modes guided by the helical structures.

Inspection methods based on elastic guided waves are among the most popular techniques of non destructive testing. Due to the complexity of signals, this technique is often restricted to simple geometries such as plates and pipes. The computation of modes of propagation in more complex geometries (arbitrary cross-section, curved axis,...) requires appropriate simulation tools, typically based on finite element methods.

A first method based on the Floquet conditions, applicable to periodic structures, has been used for straight structures (Gry and Gontier, 1997; Duhamel et al., 2006; Mencik and Ichchou, 2007) and for helical waveguides (Treyssède, 2007). A more efficient method, valid for translationally invariant structures and often referred to as the semi-analytical finite element (SAFE) method, has also been developed. This technique has been proposed in early works in Dong and Nelson (1972). With this method, the problem is reduced on the cross-section, which decreases the computation time. More recently, the SAFE method has been used for straight waveguides with arbitrary cross-section (Gavric, 1995; Damljanovic and Weaver, 2004; Hayashi et al., 2006; Jezzine, 2006) or material complexity (Rattanawangcharoen et al., 1992; Zhuang et al., 1999; Bartoli et al., 2006; Marzani, 2008). This approach has also been applied to curved waveguides: twisted in Onipede and Dong (1996), toroidal in Demma et al. (2005) and Finnveden and Fraggstedt (2008) and helical in Treyssède (2008). Finally, a SAFE method modeling the propagation of elastic waves in seven-wire strands has been developed in Treyssède and Laguerre (2010).

Helical structures such as springs and strands are generally subjected to axial loads. The above-mentioned works are restricted to the propagation of guided waves in unloaded structures. Only few studies have extended the SAFE method to loaded waveguides. Straight waveguides under axial loads have been considered in Chen and Wilcox (2007) and Loveday (2009). To the authors knowledge, there is no general model in the literature that allows to determine guided modes propagating in prestressed curved waveguides.

Therefore the goal of this paper is to propose a numerical model for the propagation of guided waves in helical structures subjected to axial loads, particularly in prestressed multi-wire strands. This

* Corresponding author.
*E-mail address:* fabien.treyssede@ifsttar.fr (F. Treyssède).

0020-7683/$ - see front matter © 2013 Elsevier Ltd. All rights reserved.
http://dx.doi.org/10.1016/j.ijsolstr.2013.01.006

study is limited to linear elastic materials. The SAFE method is adopted, which allows to solve the 3D elastodynamic equations of motion thanks to a 2D model and without beam approximation.

The method developed in this paper is restricted to multi-wire helical structures composed of a stack of helical wires wrapped with the same twisting rate around a straight axis. As explained in Section 3 of Part 1, this excludes the case of double helical structures (such as independent wire rope core for instance) and cross-lay strands.

The paper is organized as follows. Considering the static state computed in Part 1 as the prestressed state, the variational formulation associated with the superimposed linear dynamics is first described in Section 2. The twisting coordinate system is then introduced and differential operators are expressed in this system in Section 3. Exploiting the translational invariance property, the 3D variational formulation is then reduced in Section 4 to a 2D problem posed on the cross-section, which is classical in the framework of SAFE methods. In Section 5, an energy velocity expression is derived for prestressed waveguides. Using SAFE matrices, the equality between group and energy velocities is proved for undamped materials. Then for helical springs, numerical results are compared in Section 6 to those of a beam model proposed in Frikha et al. (2011). For seven-wire strands subjected to axial loads, using stick contact conditions between the core and peripheral wires, numerical results are compared to experimental data in Section 7.

## 2. Dynamic motion of prestressed structures

The analysis of the dynamics of prestressed structures can be decomposed into a static problem, solved in Part 1 of this paper, and the motion superimposed on this prestressed state, which is the aim of Part 2. Therefore, three configurations must be distinguished: the initial configuration (without initial stress), the prestressed static configuration (which is denoted $V_0$) and the final configuration including dynamics. An updated Lagrangian formulation is used, the variables being expressed in the prestressed static configuration.

One assumes a linear and elastic material behavior and a time-harmonic $e^{-i\omega t}$ evolution of the solution. Considering small-amplitude waves as perturbations onto the prestressed static state, the 3D variational formulation governing elastodynamics is given by (see e.g. Bathe (1996) and Yang and Kuo (1994)):

$$\forall \delta\mathbf{u}, \quad \int_{V_0} \delta\boldsymbol{\epsilon} : \mathbf{C}_0 : \boldsymbol{\epsilon}\, dV_0 + \int_{V_0} \mathrm{tr}(\nabla_0 \delta\mathbf{u} \cdot \boldsymbol{\sigma}_0 \cdot \nabla_0 \mathbf{u}^T) dV_0 - \omega^2 \int_{V_0} \rho_0 \delta\mathbf{u} \cdot \mathbf{u}\, dV_0 = 0, \tag{1}$$

with $\delta\mathbf{u}$ kinematically admissible and where $\mathbf{u}$ and $\boldsymbol{\epsilon} = 1/2(\nabla_0\mathbf{u} + \nabla_0\mathbf{u}^T)$ denote the displacement and the strain tensor, respectively. The subscript 0 refer to the prestressed static configuration: $\mathbf{C}_0, \rho_0$ and $V_0$ denote the elasticity tensor, the material density and the structural volume in the prestressed configuration. $\mathrm{tr}(\cdot)$ is the trace and $\nabla_0$ is the gradient operator with respect to the prestressed configuration. $\boldsymbol{\sigma}_0$ is the Cauchy prestress, i.e. the stress tensor associated with the prestressed state. The second term of the formulation, related to $\boldsymbol{\sigma}_0$, is sometimes referred to as the geometric stiffness in the literature.

In the context of non-linear mechanics, Eq. (1) is the so-called linearized updated Lagrangian formulation, representing the motion of small perturbations superimposed on a given state. Its derivation requires a non-linear geometrical analysis (large displacement or strain). This implies that the prestressed configuration should correspond to a non-linear geometrical state. Yet in this paper, one will assume that the effects of non-linearity of the prestressed state can be neglected on dynamics, and the linear computations of Part 1 will be used for simplicity.

## 3. Formulation in the curvilinear coordinate system

For the wave propagation analysis in curved waveguides, the variational formulation described in Section 2 must be expressed in an appropriate curvilinear coordinate system. In this paper, a coordinate system that satisfies translational invariance both for helical single-wire and multi-wire waveguides is required. Therefore, the twisted basis is chosen. The translational invariance property will be checked in Section 4. The reader may refer to Part 1 of this paper for more details.

### 3.1. Twisted basis

One considers a helical single-wire waveguide (see Fig. 1 in Part 1). Let $(\mathbf{e}_X, \mathbf{e}_Y, \mathbf{e}_Z)$ denotes the Cartesian orthonormal basis. The centreline is defined by a helix of radius $R$ in the Cartesian plane $(\mathbf{e}_X, \mathbf{e}_Y)$ and pitch $L$ along the $Z$-axis. The helix lay angle $\Phi$ is defined by $\tan\Phi = 2\pi R/L$.

The twisted basis $(\mathbf{e}_x, \mathbf{e}_y, \mathbf{e}_Z)$ has been defined in Part 1, as an orthonormal basis rotating around the $Z$-axis. It corresponds to a particular case of helical system with $\kappa = 0$ and $\tau = 2\pi/L$, where $\kappa$ and $\tau$ denote the curvature and the torsion respectively. The unit vectors $\mathbf{e}_x$ and $\mathbf{e}_y$ are expressed in the Cartesian basis by Eq. (3) of Part 1.

However throughout Part 2, geometrical parameters $R, L, \Phi, \kappa$ and $\tau$ are now associated with the prestressed configuration, i.e. the deformed helix under the action of the static axial load. Rigorously, these parameters should be denoted with subscripts 0, omitted for brevity's sake of notations throughout Part 2. When needed, we will use subscripts $i$ ($R_i$ or $\Phi_i$ for instance) to refer to the initial geometrical parameters, i.e. parameters associated with the initial configuration (without initial stress).

In order to express differential operators in the twisted basis, one has to develop them in the covariant and contravariant bases, $(\mathbf{g}_1, \mathbf{g}_2, \mathbf{g}_3)$ and $(\mathbf{g}^1, \mathbf{g}^2, \mathbf{g}^3)$, which have been defined by Eqs. (5) and (7) in Part 1.

One recalls that the Christoffel symbol of the second kind $\Gamma^k_{ij}$ can be calculated from $\Gamma^k_{ij} = \mathbf{g}_{i,j} \cdot \mathbf{g}^k$, where $\mathbf{g}_{i,j}$ corresponds to the derivatives of the covariant basis. Its expression in the twisted basis has been obtained in Eq. (8) of Part 1.

As a side remark, note that twisting coordinates have also been used for elastic wave propagation in pretwisted beams (Onipede and Dong, 1996), for electromagnetic waves in optical helical waveguides (Nicolet et al., 2004; Nicolet and Zola, 2007) and for twisted electrostatic problems (Nicolet et al., 2007).

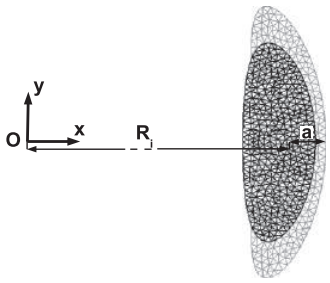


**Fig. 1.** Cross-section FE mesh of a helical waveguide with $R_i/a = 10$ and $\Phi_i = 75°$. Grey: initial mesh ($E^E = 0$), black: updated mesh ($E^E = 40\%$), plotted in the initial and updated twisting coordinate system respectively.

### 3.2. Differential operators

The differential operators involved in the variational formulation (1) are the gradient and the strain operators. As explained in Part 1 of this study, they have first to be expressed in the covariant and contravariant bases (see e.g. Chapelle and Bathe (2003); Synge and Schild (1978); Wempner (1981)).

The gradient tensor $\nabla_0$ is defined in the contravariant basis as:

$$\nabla_0 \mathbf{u} = \gamma_{ij} \mathbf{g}^i \otimes \mathbf{g}^j, \quad \gamma_{ij} = u_{i,j} - \Gamma^k_{ij} u_k, \tag{2}$$

where $u_i$ denotes the covariant displacement.

Using the relation between the contravariant and the twisted vectors (Eq. (7) of Part 1), the gradient tensor can be expressed in the twisted basis under the following vector form:

$$\{\gamma\} = \left( \mathbf{G}_{xy} + \mathbf{G}_Z \frac{\partial}{\partial Z} \right) \{u\}, \tag{3}$$

with:

$$\mathbf{G}_{xy} = \begin{bmatrix} \partial/\partial x & 0 & 0 \\ \partial/\partial y & 0 & 0 \\ \Lambda & -\tau & 0 \\ 0 & \partial/\partial x & 0 \\ 0 & \partial/\partial y & 0 \\ \tau & \Lambda & 0 \\ 0 & 0 & \partial/\partial x \\ 0 & 0 & \partial/\partial y \\ 0 & 0 & \Lambda \end{bmatrix}, \quad \mathbf{G}_Z = \begin{bmatrix} 0 & 0 & 0 \\ 0 & 0 & 0 \\ 1 & 0 & 0 \\ 0 & 0 & 0 \\ 0 & 0 & 0 \\ 0 & 1 & 0 \\ 0 & 0 & 0 \\ 0 & 0 & 0 \\ 0 & 0 & 1 \end{bmatrix}, \tag{4}$$

where $\Lambda = \tau(y\partial/\partial x - x\partial/\partial y)$. The column vectors $\{u\} = [u_x\, u_y\, u_z]^T$ and $\{\gamma\} = [\gamma_{xx}\, \gamma_{xy}\, \gamma_{xz}\, \gamma_{yx}\, \gamma_{yy}\, \gamma_{yz}\, \gamma_{zx}\, \gamma_{zy}\, \gamma_{zz}]^T$ are the displacement and gradient components respectively.

Following Part 1, the strain vector is related to the displacement vector in the twisted basis through: $\{\epsilon\} = (\mathbf{L}_{xy} + \mathbf{L}_Z \frac{\partial}{\partial Z})\{u\}$, where $\{\epsilon\} = [\epsilon_{xx}\, \epsilon_{yy}\, \epsilon_{ZZ}\, 2\epsilon_{xy}\, 2\epsilon_{xZ}\, 2\epsilon_{yZ}]^T$ is the strain vector. $\mathbf{L}_{xy}$ and $\mathbf{L}_Z$ have the expression given by Eq. (10) of Part 1, recalling that this time the geometrical parameter $\tau$ corresponds the torsion of the geometry in the prestressed state.

### 3.3. Material properties

Mechanical properties are strain-dependent but under the small strain assumption, which is used in this paper, the elasticity tensor is the same in the reference and prestressed configurations, hence $\mathbf{C}_0 = \mathbf{C}$ (Bathe, 1996; Yang and Kuo, 1994). Its expression in the twisted basis, which is orthonormal, has been given in Eq. (12) of Part 1.

Besides the change of material density between the reference and prestressed states can also be neglected ($\rho_0 = \rho$).

### 3.4. Variational formulation

The variational formulation given by Eq. (1), is now rewritten in a suitable matrix form based on the displacement, strain and gradient vectors previously defined. It can be shown that one has:

$$\mathrm{tr}(\nabla_0 \delta\mathbf{u} \cdot \boldsymbol{\sigma}_0 \cdot \nabla_0 \mathbf{u}^T) = \{\delta\gamma\}^T [\Sigma_0] \{\gamma\}, \tag{5}$$

where the matrix $[\Sigma_0]$ is defined as follows:

$$[\Sigma_0] = \begin{bmatrix} [\sigma_0] & 0 & 0 \\ 0 & [\sigma_0] & 0 \\ 0 & 0 & [\sigma_0] \end{bmatrix}, \quad [\sigma_0] = \begin{bmatrix} \sigma_{0_{xx}} & \sigma_{0_{xy}} & \sigma_{0_{xZ}} \\ \sigma_{0_{yx}} & \sigma_{0_{yy}} & \sigma_{0_{yz}} \\ \sigma_{0_{Zx}} & \sigma_{0_{Zy}} & \sigma_{0_{ZZ}} \end{bmatrix}. \tag{6}$$

Note that the components of $[\sigma_0]$ must be expressed in the twisted basis associated with the prestressed configuration.

Finally, the variational formulation of the elastodynamics of prestressed structures (1) becomes:

$$\forall \delta u, \quad \int_{V_0} \{\delta\epsilon\}^T [C_0] \{\epsilon\} dx dy dZ + \int_{V_0} \{\delta\gamma\}^T [\Sigma_0] \{\gamma\} dx dy dZ - \omega^2 \int_{V_0} \rho_0 \{\delta u\}^T \{u\} dx dy dZ = 0. \tag{7}$$

## 4. SAFE method

In this section, a SAFE method is applied starting from the formulation (7). This method consists in assuming wave fields with a harmonic axial dependence. The displacement field is thus of the form:

$$\mathbf{u} = \mathbf{u}(x, y) e^{i(kZ - \omega t)}. \tag{8}$$

The first term represents the displacement field in the cross-section. The second corresponds to an exponential $e^{ikZ}$ representing wave traveling along the axis, $k$ being the axial wavenumber, and to the time-harmonic dependence as already mentioned in Section 2. SAFE methods only require finite element (FE) discretization of the cross-section, which is advantageous since it reduces the problem from three to two dimensions.

The SAFE method has been thoroughly presented for straight waveguides in the literature (see for instance Gavric (1995); Hayashi et al. (2006); Bartoli et al. (2006)). For details on the extension of the SAFE method to helical waveguides, the reader may refer to Treyssède (2008) or Treyssède and Laguerre (2010).

### 4.1. Translational invariance

Assuming an $e^{ikZ}$ dependence implies that axial and transverse variables must be separable in the governing equations of motion. This requires that the problem must be translationally invariant along the $Z$-axis in the twisted coordinate system.

As proved in Treyssède (2011), three conditions are sufficient for translational invariance of curved waveguides. These conditions, checked in Part 1 for the statics of springs and seven-wire strands, are recalled here for clarity:

1. The material properties do not vary along the $Z$-axis in the twisted coordinate system;
2. The coefficients of the differential operators are independent on the axial variable $Z$;
3. The cross-section does not varies along the $Z$-axis in the twisted coordinate system.

Conditions 1 and 3 have already been proved in Part 1. Condition 2 must be checked for the dynamics of prestressed waveguides. A closer look at Eq. (1) shows that $\nabla_0 \mathbf{u}$ and the Cauchy prestress tensor $\boldsymbol{\sigma}_0$ must be independent on $Z$.

With regard to the gradient operator, its coefficients do not depend on $Z$ in the twisted coordinate system (this is due to the independence on $Z$ of the Christoffel symbol, as already noticed in Part 1). As for $\boldsymbol{\sigma}_0$, we have to require that the prestressed state does not vary along the $Z$-axis. In practice, under axial loads applied at the end cross-sections of the helical structure, this condition is fulfilled far from the ends. Therefore, the static prestressed state is invariant along the axis.

As already examined in Section 3 of Part I, translational invariance in multi-layer wire ropes is also satisfied if the torsion of each wire remains identical (the numerical method proposed in this paper is still applicable). However, translational invariance is not fulfilled in cross-lay strands as well as double helical structures such as independent wire rope core.

### 4.2. SAFE formulation

Following the SAFE approach, the displacement vector and its test field are rewritten under the form (8) (Treyssède, 2008; Treyssède and Laguerre, 2010). The displacement fields dependence in $e^{ikZ}$ allows to replace the axial derivatives $\partial/\partial Z$ by $ik$. The variational formulation (7) then reduces to a 2D problem posed on the cross-section $S_0$. The SAFE variational formulation is:

$$\begin{aligned}
&\forall\{\delta u\},\ \int_{S_0}\{\delta u\}^T(\mathbf{L}_{xy}^T[C_0]\mathbf{L}_{xy}+\mathbf{G}_{xy}^T[\Sigma_0]\mathbf{G}_{xy})\{u\}dxdy\\
&+ik\int_{S_0}\{\delta u\}^T(\mathbf{L}_{xy}^T[C_0]\mathbf{L}_Z-\mathbf{L}_Z^T[C_0]\mathbf{L}_{xy}+\mathbf{G}_{xy}^T[\Sigma_0]\mathbf{G}_Z-\mathbf{G}_Z^T[\Sigma_0]\mathbf{G}_{xy})\{u\}dxdy\\
&+k^2\int_{S_0}\{\delta u\}^T(\mathbf{L}_Z^T[C_0]\mathbf{L}_Z+\mathbf{G}_Z^T[\Sigma_0]\mathbf{G}_Z)\{u\}dxdy\\
&-\omega^2\int_{S_0}\rho_0\{\delta u\}^T\{u\}dxdy=0.
\end{aligned}\tag{9}$$

The finite element approximation is defined by $\{u\}=[N^e]\{U^e\}$, where $[N^e]$ is the matrix of the shape functions and $\{U^e\}$ the vector of nodal displacements, with 3 degrees of freedom per node. The FE discretization of Eq. (9) leads to the following eigenvalue problem:

$$\{[K_{1\sigma}]-\omega^2[M]+ik([K_{2\sigma}]-[K_{2\sigma}]^T)+k^2[K_{3\sigma}]\}\{U\}=0,\tag{10}$$

where the element matrices are expressed as:

$$\begin{aligned}
[M^e]&=\int_{S_0^e}\rho_0[N^e]^T[N^e]dxdy,\\
[K_{1\sigma}^e]&=[K_1^e]+\int_{S_0^e}[N^e]^T\mathbf{G}_{xy}^T[\Sigma_0]\mathbf{G}_{xy}[N^e]dxdy,\\
[K_{2\sigma}^e]&=[K_2^e]+\int_{S_0^e}[N^e]^T\mathbf{G}_{xy}^T[\Sigma_0]\mathbf{G}_Z[N^e]dxdy,\\
[K_{3\sigma}^e]&=[K_3^e]+\int_{S_0^e}[N^e]^T\mathbf{G}_Z^T[\Sigma_0]\mathbf{G}_Z[N^e]dxdy,\\
[K_1^e]&=\int_{S_0^e}[N^e]^T\mathbf{L}_{xy}^T[C_0]\mathbf{L}_{xy}[N^e]dxdy,\\
[K_2^e]&=\int_{S_0^e}[N^e]^T\mathbf{L}_{xy}^T[C_0]\mathbf{L}_Z[N^e]dxdy,\\
[K_3^e]&=\int_{S_0^e}[N^e]^T\mathbf{L}_Z^T[C_0]\mathbf{L}_Z[N^e]dxdy.
\end{aligned}\tag{11}$$

The second term of the right hand side in the expressions of $[K_{1\sigma}^e],[K_{2\sigma}^e]$ and $[K_{3\sigma}^e]$ correspond to the so-called geometric stiffness effect (second term of formulation (1)), related to the presence of a prestress field ($\boldsymbol{\sigma}_0\neq\mathbf{0}$). Note that the SAFE formulation given by Eqs. (10) and (11) for prestressed helical structures degenerates to the unprestressed case (Treyssède and Laguerre, 2010) if $[\Sigma_0]=0$ and $S_0=S$.

The matrice $[K_1^e]$ is the same as the matrix $[K^e]$ defined in Part 1 for the static problem, except that the integration is now performed on the prestressed configuration $S_0$ (instead of $S$), accounting for the geometry deformation.

In practice, the cross-section mesh of the prestressed structure is obtained as follows. The cross-section of the structure without initial stress is first meshed. The prestressed state is computed based on this mesh. Then, the position of nodes is updated to provide the mesh of the cross-section $S_0$ in the prestressed configuration. The guided modes are computed on this updated mesh.

The solution of the eigensystem (10) yields the modes of propagation. It can be noticed that $[K_{1\sigma}],[K_{3\sigma}]$ and $[M]$ are symmetric. Hence for an eigenvalue $k,-k$ is also an eigenvalue. This problem has then two kinds of eigensolutions: $(k_i,U_i^+)$ and $(-k_i,U_i^-)$ for $i=1,\ldots,n$ ($n$ being the number of degrees of freedom), representing $n$ modes traveling in the positive direction and $n$ modes in the negative direction. For undamped materials, pure real and imaginary wavenumbers represent propagating and evanescent modes, respectively. Complex wavenumber are referred to as inhomogeneous modes (such modes are oscillatory but decay after a few oscillations). Pure real and imaginary solutions appear in pairs of opposite signs and complex solutions appear in quadruple of opposite signs and complex conjugates.

The eigensystem (10) can be solved by setting the wavenumber $k$ and finding the frequency $\omega$ or inversely. For propagating modes in undamped materials, the eigenvalue system can be solved by setting a real positive wavenumber $k$. The system is then linear in $\omega^2$. For non-propagating modes or for damped materials, wavenumbers become complex and the problem must be solved by setting $\omega$ and finding $k$. The eigensystem is then quadratic in $k$ and the system should be linearized (Tisseur and Meerbergen, 2001).

In this study our concern is propagating modes. Thereafter, eigensolutions are obtained by finding frequencies associated with real wavenumbers.

## 5. Modal velocities

The goal of this section is to formally derive group and energy modal velocities expressions in prestressed waveguides.

### 5.1. Group velocity

For a real wavenumber $k$, the phase and group velocities are defined by $V_\phi=\omega/k$ and $V_g=\partial\omega/\partial k$, respectively. For undamped materials and propagating modes, the SAFE expression of group velocity has been obtained for unprestressed structures in Bartoli et al. (2006) and Finnveden (2004). The method consists in differentiating with respect to $k$ the SAFE eigenproblem. In the presence of prestress, the eigenproblem (10) to be solved remains quadratic and keeps the same general form as its unprestressed counterpart. As a consequence, the expression derived in the above-mentioned references can be directly extended to the prestress case, which yields:

$$V_g=\frac{1}{2\omega}\frac{\{U\}^{T*}(i([K_{2\sigma}]-[K_{2\sigma}]^T)+2k[K_{3\sigma}])\{U\}}{\{U\}^{T*}[M]\{U\}},\tag{12}$$

where as shown in Section 4.2, matrices $[K_{2\sigma}^e]$ and $[K_{3\sigma}^e]$ account for geometric stiffness effects. The above expression has also been used in Loveday (2009) for straight waveguides subjected to axial loads.

### 5.2. Energy velocity

The energy velocity is defined as the ratio between the transmitted power and the stored energy, averaged in time and in the cross-section (see e.g. Achenbach, 1973):

$$V_e=\frac{\int_{S_0}\overline{\mathbf{P}}\cdot\mathbf{n}dS_0}{\int_{S_0}(\overline{E}_k+\overline{E}_p)dS_0},\tag{13}$$

where the bar denotes time average and $\mathbf{n}$ is the unit vector normal to the cross-section. $\mathbf{P},E_k$ and $E_p$ are the Poynting vector, the kinetic energy density and the potential energy density, respectively.

To the authors knowledge, the above definition has mainly been applied to structures without initial stress. Hence, one needs to properly define $\mathbf{P},E_k$ and $E_p$ in the presence of prestress.

For prestressed structures, the strong form corresponding to the variational formulation (1) is:

$$\nabla_0\cdot(\mathbf{C}_0:\boldsymbol{\epsilon}+\nabla_0\mathbf{u}\cdot\boldsymbol{\sigma}_0)=\rho_0\ddot{\mathbf{u}}.\tag{14}$$

It can be checked that this equilibrium equation indeed derives from a Lagrangian density $L$, where $L=E_k-E_p$ with:

$$E_k = \frac{1}{2}\rho_0 \dot{\mathbf{u}}\cdot\dot{\mathbf{u}}, \tag{15}$$

and:

$$E_p = \frac{1}{2}\boldsymbol{\epsilon} : \mathbf{C}_0 : \boldsymbol{\epsilon} + \frac{1}{2}\mathrm{tr}(\nabla_0\mathbf{u}\cdot\boldsymbol{\sigma}_0\cdot\nabla_0\mathbf{u}^T). \tag{16}$$

Concerning the Poynting vector (i.e. the power flow per unit area), it can be calculated thanks to the Lagrangian density from: $P_J = \dot{u}_I \partial L/\partial u_{I,J}$ (here, index notation is used in the Cartesian coordinate system with the Einstein summation convention). Calculations yield:

$$\mathbf{P} = -\dot{\mathbf{u}}\cdot(\mathbf{C}_0 : \boldsymbol{\epsilon} + \nabla_0\mathbf{u}\cdot\boldsymbol{\sigma}_0). \tag{17}$$

When $\boldsymbol{\sigma}_0 = \mathbf{0}$, Eqs. (16) and (17) degenerate to the well known energy and power flow expressions without prestress (see Achenbach (1973) for instance).

From SAFE matrices, it can be easily checked that:

$$\int_{S_0}\overline{E}_k dS_0 = \frac{\omega^2}{4}Re(\{U\}^{T*}[M]\{U\}), \quad \int_{S_0}\overline{E}_p dS_0 = \frac{1}{4}Re\Big(\{U\}^{T*}([K_{1\sigma}] + ik([K_{2\sigma}] - [K_{2\sigma}]^T) + k^2[K_{3\sigma}])\{U\}\Big). \tag{18}$$

The computation of the cross-section and time averaged Poynting vector requires further developments (Treyssède, 2008; Benmeddour et al., 2011). Replacing the normal vector $\mathbf{n}$ by $\mathbf{e}_Z$ and averaging the Poynting vector, we obtain:

$$\int_{S_0}\overline{\mathbf{P}}\cdot\mathbf{n}dS_0 = \frac{\omega}{2}Im\left(\int_{S_0} u^*_\alpha(\mathbf{C}_0 : \boldsymbol{\epsilon} + \nabla_0\mathbf{u}\cdot\boldsymbol{\sigma}_0)_{\alpha Z}dS_0\right), \tag{19}$$

where $\alpha = x, y, Z$. The integrand can be written as $u^*_\alpha(\mathbf{C}_0 : \boldsymbol{\epsilon} + \nabla_0\mathbf{u}\cdot\boldsymbol{\sigma}_0)_{\alpha Z} = \{u\}^{T*}(\mathbf{L}_Z^T[C_0](\mathbf{L}_{xy} + ik\mathbf{L}_Z) + \mathbf{G}_Z^T[\Sigma_0](\mathbf{G}_{xy} + ik\mathbf{G}_Z))\{u\}$. Eq. (19) becomes:

$$\int_{S_0}\overline{\mathbf{P}}\cdot\mathbf{n}dS_0 = \frac{\omega}{2}Im\Big(\{U\}^{T*}([K_{2\sigma}]^T + ik[K_{3\sigma}])\{U\}\Big). \tag{20}$$

Finally, Eqs. (18) and (20) yield a direct computation of energy velocity from SAFE matrices:

$$V_e = \frac{2\omega Im\Big(\{U\}^{T*}([K_{2\sigma}]^T + ik[K_{3\sigma}])\{U\}\Big)}{Re\Big(\{U\}^{T*}(\omega^2[M] + [K_{1\sigma}] + ik([K_{2\sigma}] - [K_{2\sigma}]^T) + k^2[K_{3\sigma}])\{U\}\Big)}. \tag{21}$$

This equation degenerates to the unprestressed case, for which $[K_{1\sigma}] = [K_1], [K_{2\sigma}] = [K_2]$ and $[K_{3\sigma}] = [K_3]$ becomes the SAFE matrices of non-prestressed structures found in Treyssède (2008) and Treyssède and Laguerre (2010).

Under prestress, the expression (21) is checked in the Appendix by showing the equality between the energy velocity and the group velocity for propagating modes in undamped materials.

## 6. Validation for a helical spring

The purpose of this section is to validate the SAFE model for prestressed helical springs.

The dispersion curves of prestressed helical waveguides obtained from the SAFE model will be compared to results obtained by the authors in Frikha et al. (2011), here used as a reference. In Frikha et al. (2011) the propagation modes in helical beams under axial loads are computed based on a Timoshenko model approximation. This model is limited to large helix radius of curvature $(1/\kappa)$ compared to the cross-section radius $a$. Moreover the static prestressed state is calculated from a non-linear analytical solution derived in Wahl (1963), which is valid only for large helix angle $\Phi$ ($\Phi \geqslant 65^\circ$) and large ratio $R/a$ ($R/a \geqslant 5$). The reader may refer to Frikha et al. (2011) for a detailed study of load effects for various angles and radii.

In this section, the following data are chosen: the initial parameters of the helix (without initial stress) are $R_i/a = 10$ and $\Phi_i = 75^\circ$. The prestress corresponds to a macroscopic axial deformation: $E^E = 40\%$ and $E^T = 0$. It is important to note that with these data both the effects of prestress and geometry deformation are important and thus need to be properly accounted for, as shown in Frikha et al. (2011).

The static analysis of a helical waveguide with these data has been presented in Section 6.1 of Part 1, where local displacements have been computed. The prestress matrix $[\sigma_0]$ is then determined from these local displacements. The geometry deformation is taken into account in the SAFE method by integration on the deformed cross-section $S_0$ (updating the node position, see Section 4.2). Fig. 1 illustrates the initial and the updated cross-sections FE mesh under $E^E = 40\%$ and $E^T = 0$, yielding an updated lay angle $\Phi = 68.8^\circ$ and helix radius $R/a = 9.71$.

In a low frequency range ($\omega a/c_s \in [0; 0.005]$), Fig. 2 shows the dimensionless dispersion curves, $\omega a/c_s$ vs. $ka$, obtained from the SAFE model, where $c_s = \sqrt{E/2\rho(1+\nu)}$ is the shear velocity with Poisson ratio $\nu$ equal to 0.3. Grey and black curves refer to

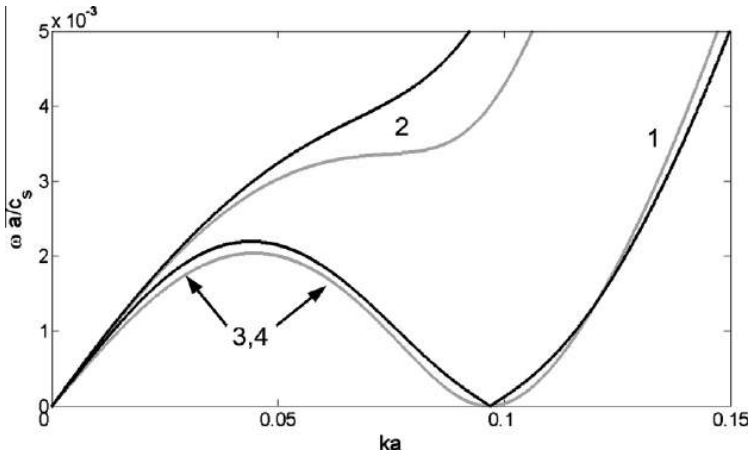


**Fig. 2.** Plot of dimensionless frequency $\omega a/c_s$ vs. wavenumber $ka$ for $R_i/a = 10, \Phi_i = 75^\circ, \omega a/c_s \in [0; 0.005], E^E = 0$ (grey) and $E^E = 40\%$ (black).

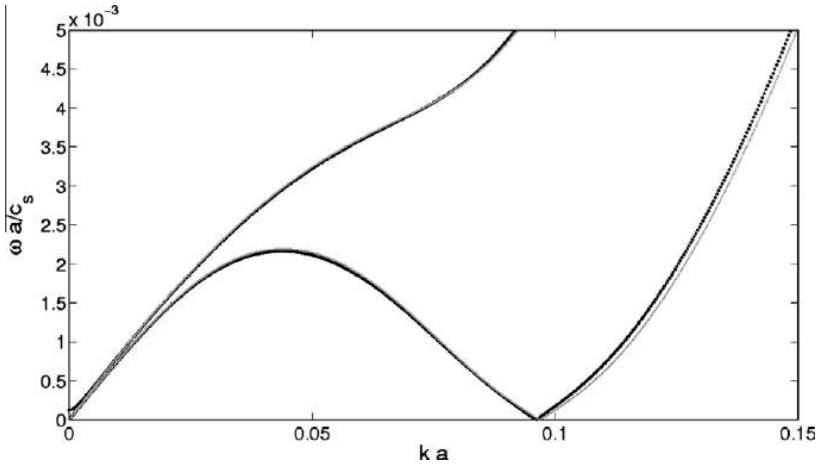


**Fig. 3.** Plot of dimensionless frequency $\omega a/c_s$ vs. wavenumber $ka$ for $R_l/a = 10, \Phi_l = 75^\circ, \omega a/c_s \in [0; 0.005], E^E = 40\%$. Grey: reference model, black: SAFE model.

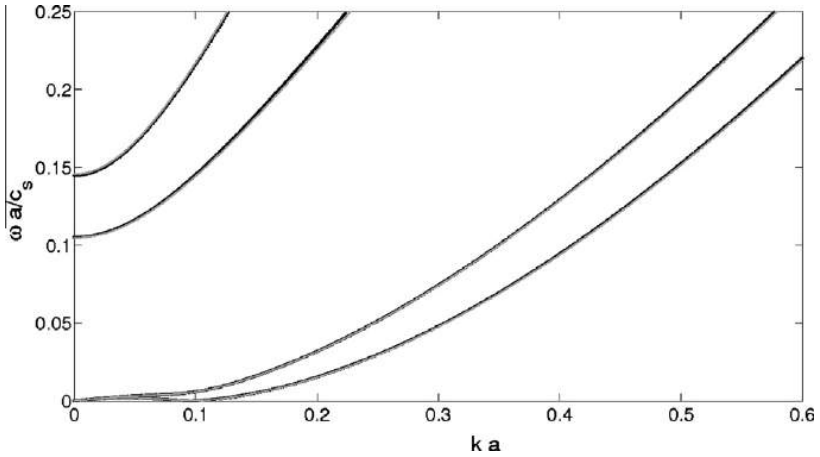


**Fig. 4.** Plot of dimensionless frequency vs. wavenumber for $R_l/a = 10, \Phi_l = 75^\circ, \omega a/c_s \in [0; 0.25], E^E = 40\%$. Grey: reference model, black: SAFE model.

unloaded ($E^E = 0$ and $E^T = 0$) and loaded ($E^E = 40\%$ and $E^T = 0$) cases, respectively. It can be observed that four modes are propagating in the frequency range considered. The tensile load has an effect on the four propagating modes. The load effect is found to be the most important for mode 2, its dispersion curve shifting to higher frequencies.

Figs. 3 and 4 compare the dispersion curves obtained from both SAFE method and the analytical model of Frikha et al. (2011) when the spring is loaded ($E^E = 40\%$ and $E^T = 0$). Good agreement is found between both models in the two frequency ranges $[0; 0.005]$ and $[0; 0.25]$. As shown in Frikha et al. (2011), the loading effect becomes smaller at higher frequencies. One points out that the wavenumber $k$ presented in Figs. 2–4 is measured with respect to the curved helical axis, instead of the straight axis. This means that the wavenumber computed in the twisting basis with the SAFE method has been transformed to the helical system by multiplying $ka$ with the ratio $L/l$ where $l = \sqrt{L^2 + 4\pi^2 R^2}$ (see Treyssède and Laguerre (2010) for more details). This allows a direct comparison with the results of Frikha et al. (2011), obtained in a helical coordinate system.

In Fig. 3, a slight difference for mode 1 and $ka \in [0.1; 0.15]$ is found between SAFE and analytical results. Note however that the static state is computed using a non-linear solution in the reference model while the SAFE model is linear. Moreover the analytical solution is based on a Timoshenko beam model while the SAFE method starts from a 3D formulation without beam assumption. Therefore, this difference is small for such a validation test, with a large load applied on a helical spring of large helix angle.

## 7. Dispersion analysis of seven-wire strands

In this section, results for guided wave propagation in multi-wire structures are presented. The study is restricted to seven-wire strands, with a central straight wire and one layer of six helical wires, for which some experimental data are available (Laguerre et al., 2002; Kwun et al., 1998). In Laguerre et al. (2002), the effect of axial load on a seven-wire strand was studied for different axial loads of 2%, 10% and 60% of the Ultimate Tensile Strength (UTS). Experimental results showed the existence of a frequency band ('notch frequency') for different axial loads, where the first compressional mode does not seem to propagate. For an unloaded strand with a nominal outer diameter 15.7 *mm*, the notch frequency is around 67 *kHz*. This frequency shifts to 88 *kHz* under

**Table 1**
Strand characteristics.

| Parameter | Strand 1 | Strand 2 |
|---|---|---|
| Nominal diameter (mm) | 15.7 | 12.7 |
| Core radius $a$ (mm) | 2.7 | 2.16 |
| Young's modulus (Pa) | 2.17e11 | 2.1e11 |

60% of the UTS. Also in the experiments of Kwun et al. (1998), the notch frequency of a seven-wire strand was found to vary linearly with $\log(T)$, where $T$ is the axial load.

Though numerical results will be presented in a dimensionless form, we focus on seven-wire strands with geometrical and material data experimented in the above-mentioned references. Thus in the following we will consider two strands which will be denoted Strand 1 and Strand 2. Characteristics are given in Table 1, the geometrical parameters corresponding to the initial configuration, without initial stress. For both strands, one will assume: $R_i/a = 1.967, \Phi_i = 7.9^\circ, \nu = 0.28$ and $\rho = 7800\ \mathrm{kg/m^3}$. As already explained in Part I, the contact between wires is modeled with perfect bonding conditions for simplicity (slip or friction effects are neglected).

### 7.1. Preliminary results for unprestressed strands

In order to make this paper self-contained, the main results presented in Treyssède and Laguerre (2010), for strands without initial stress, and obtained with a SAFE method are recalled in this section.

Strand 1 is considered. There is no contact between two peripheral helical wires, and the contact between central and peripheral wires is assumed to be perfectly stick, see Part 1.

Dispersion curves have been computed by fixing a real wavenumber $ka$ for the dimensionless frequency range $[0;2]$. Fig. 5 presents the energy velocity vs. frequency curves for this unloaded seven-wire strand. Due to inter-wire coupling, the dynamic behavior is quite complex compared to single-wire waveguides. Yet, a noticeable phenomenon can be observed: a veering frequency of the fastest mode occurs around $\omega a/c_s = 0.33$, corresponding to 65 *kHz* for Strand 1. This veering frequency leads to an abrupt velocity decrease and the fastest mode corresponds to the first compressional-like mode in the strand, as shown in Treyssède and Laguerre (2010). Therefore, this veering frequency can be actually identified as the notch frequency observed in experiments, i.e. 67 *kHz* (Laguerre et al., 2002; Treyssède and Laguerre, 2010).

Other experimental results are reported in Kwun et al. (1998) with a notch frequency found around 80 *kHz*. In that reference, the strand diameter is 12.7 *mm*. Using the SAFE approach with Strand 2, the dimensionless frequency $\omega a/c_s = 0.33$ yields a dimensional value of 79 *kHz*, which is again in good agreement with the experimental notch frequency.

In the following, the validation of the SAFE model proposed in this paper for loaded strands will be performed using the notch frequency as the quantity of interest, because experimental results are available.

### 7.2. Prestressed strand with line contact approximation

A seven-wire strand subjected to an axial tensile strain $E^E = 0.6\%$ ($E^T = 0$) is now considered. As a first step, one assumes that the contact area between the central and peripheral wires is a line, which is exact in the initial configuration (without any loading). This assumptions means a point-to-point contact for the 2D microscopic problem derived in the Part 1 of this paper. Moreover, this contact is supposed to be stick, see Part 1.

As in Section 6, the computation of modes of propagation in prestressed strands requires the computation of the static prestressed state, which is then used into the computation of propagation modes. Similarly to helical single wire waveguides, the static state has been already computed in Part 1, using the cross-section mesh of the unloaded strand (Fig. 6(a)). The nodes position is then updated to provide the mesh of the deformed cross-section $S_0$. Propagations modes are computed from this geometry.

The strand characteristics are those of Strand 1. Fig. 6(a) shows the superposition of the undeformed cross-section, in gray, and the updated mesh, in black. Differences between both meshes are negligible. In particular, Fig. 6(b) confirms that there is no contact between peripheral wires, even as a tensile load is applied.

Note that for better accuracy of numerical results, the mesh has been refined at contact points, yielding 17019 dofs. From the static solution given in Part 1, an axial strain of $E^E = 0.6\%$ (with $E^T = 0$) for this seven-wire strand corresponds to an axial force $T = 190.3\ kN$. This value provides a mean axial stress equal to 1260 *MPa*, corresponding to the mean stress applied in Laguerre et al. (2002) (i.e. 60% of the UTS).

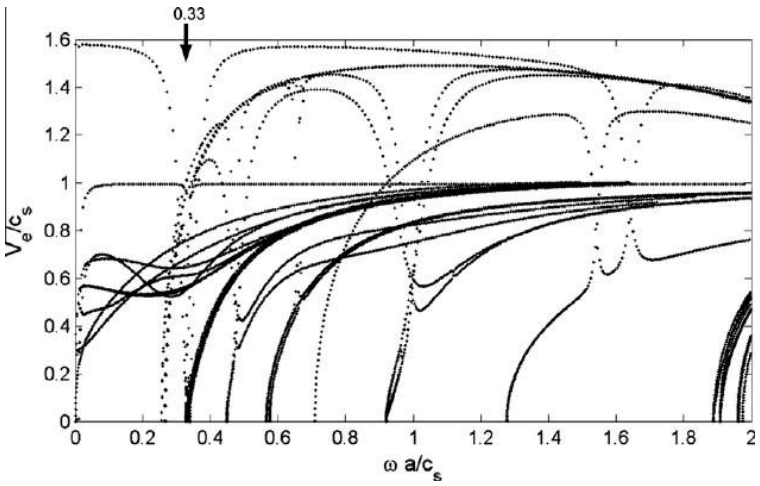


**Fig. 5.** Dimensionless energy velocity $V_e/c_s$ vs. frequency $\omega a/c_s$ for an unloaded seven-wire strand ($E^E = 0$).

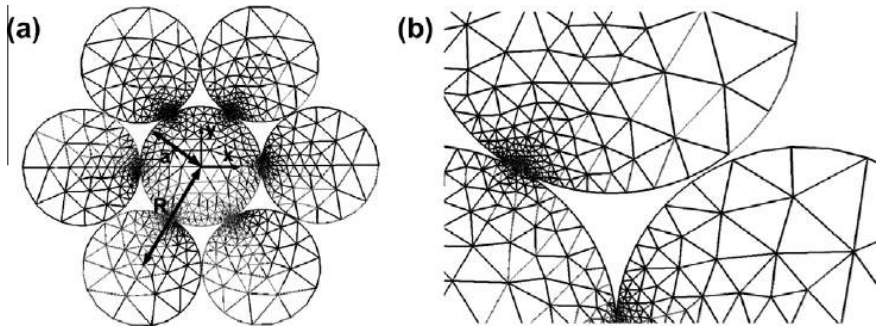


**Fig. 6.** Cross-section FE mesh of a seven-wire strand with $R_l/a = 1.967$ and $\Phi_l = 7.9°$. Grey: initial mesh ($E^E = 0$), black: updated mesh ($E^E = 0.6\%$), plotted in the initial and updated twisting coordinate system respectively. (a): overview, (b): interwire view.

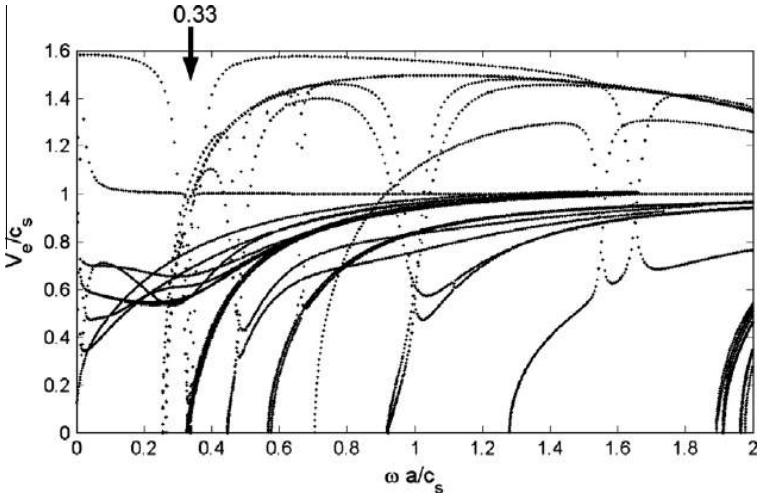


**Fig. 7.** Dimensionless energy velocity $V_e/c_s$ vs. frequency $\omega a/c_s$ for a seven-wire strand subjected to a tensile strain $E^E = 0.6\%$ with line contact approximation.

Fig. 7 shows the dispersion curves (energy velocity vs. frequency). Except at low frequencies (below 0.1), we note that there is no difference between these results and those obtained for unloaded strand (see Fig. 5). In particular, the notch frequency remains around the dimensionless frequency $\omega a/c_s = 0.33$, as opposed to experimental results.

However a closer analysis of the deformed configuration due to the static load in the wire-wire contact zone shows that the impenetrability condition is violated for the nodes in the vicinity of the contact points. This result is in line with Jiang et al. (2008) in which it is reported that contact area increases with the strand extension. Thus the line contact assumption is not valid and at this step it is suspected that this wrong assumption is responsible for the discrepancy between SAFE results and experimental data. Therefore hereafter a new model which properly takes into account the contact conditions will be used.

### 7.3. Surface Contact consideration

The new contact procedure is as follows. First, it has to be noticed that matching meshes are used for potentially contact lines of the central wire and each helical wire. This easily allows to address the line-to-line contact through individual node-to-node contacts for the 2D model. Thus contact pairs of nodes are formed on both sides of the initial point-to-point contact zone. Starting with the initial configuration from only one point-to-point contact between the core and each helical wire, the axial strain value gradually increases and the nodes position is updated. When the distance between the nodes of the same pair vanishes, the stick contact condition is imposed through the continuity of the displacement between these two nodes. Finally, when $E^E = 0.6\%$, we have obtained an updated geometry with eleven pairs of nodes in contact between the central wire and each peripheral wire.

With this contact procedure, note that a tensile strain $E^E = 0.6\%$ applied on a seven-wire strand with nominal diameter 15.7 *mm* (Strand 1) yields a resultant force $T = 189.4$ *kN* and moment $M = 116.9$ *Nm*. These values are quite close to those obtained in Part 1 from a point-to-point contact approximation: $T = 190.3$ *kN* and $M = 118.1$ *Nm*. This is consistent with the results obtained in Ghoreishi et al. (2007), where it has been shown that the global static behavior is very little sensitive to contact assumptions.

Fig. 8 shows the energy velocity $V_e/c_s$ with respect to the dimensionless frequency $\omega a/c_s$. Under an applied tensile strain $E^E = 0.6\%$, the notch frequency now shifts around the dimensionless frequency $\omega a/c_s = 0.44$. This value corresponds to 86 *kHz* for a seven-wire strand with a nominal diameter 15.7 *mm*, which is in good agreement with experimental results (approximately 88 *kHz* in Laguerre et al. (2002)). If we compare these dispersion

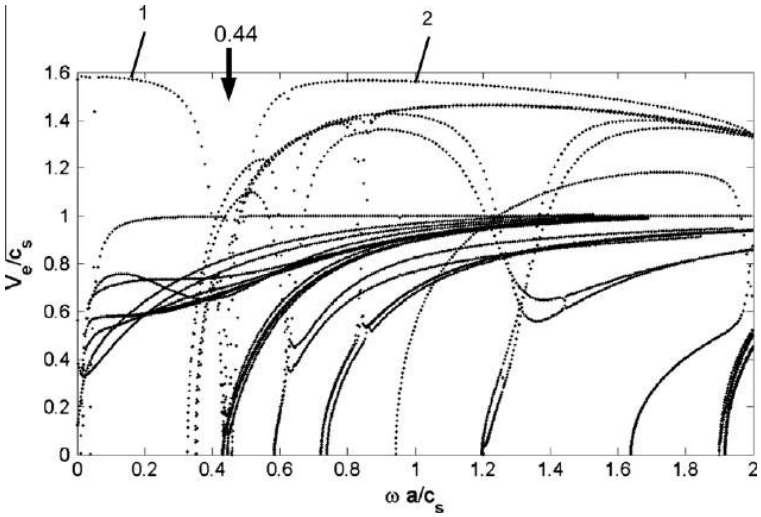


**Fig. 8.** Dimensionless energy velocity $V_e/c_s$ vs. frequency $\omega a/c_s$ of a seven-wire strand subjected to a tensile strain $E^E = 0.6\%$ with surface contact consideration (no interpenetration).

curves with those obtained in Fig. 7, we can conclude that the shift of the notch frequency is mainly due to contact effects, and more precisely to the increasing of the contact area.

As shown for unloaded strands in Treyssède and Laguerre (2010), the notch frequency phenomenon corresponds to a veering frequency between two extensional modes interchanging their behavior. Under axial loads, one can check that this phenomenon still occurs, as illustrated in Fig. 9 showing the mode shapes at points 1 and 2 (see Fig. 8), corresponding to solutions $(ka, \omega a/c_s, V_e/c_s) = (0.1, 0.16, 1.57)$ and $(0.60, 0.96, 1.56)$ respectively. These mode shapes are quite close to those found in Treyssède and Laguerre (2010). Indeed, modes 1 and 2 belong to two distinct branches. Their global axial motion confirms that they are compressional-like modes, which have interchanged their shapes (for more details, the reader may refer to Treyssède and Laguerre (2010)). However, these modes are not exactly similar because the real parts of their axial displacement have opposite signs.

Comparing the dispersion curves of a prestressed strand (Fig. 8) with the unprestressed ones (Fig. 5), at low frequencies ($\omega a/c_s < 0.1$), large differences are found for some fundamental branches. For instance, the torsional mode (which quickly tends to $V_e/c_s = 1$ at higher frequencies), is found to be very sensitive to the tensile

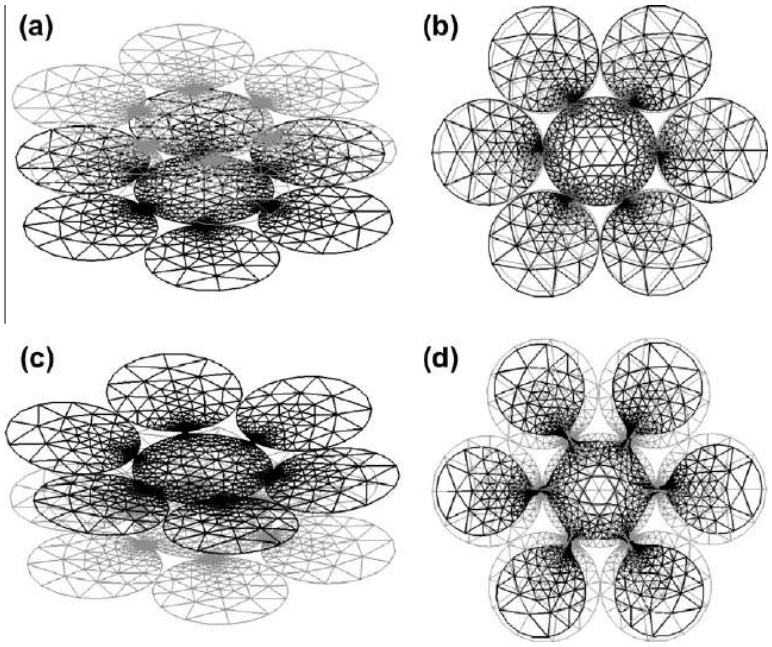


**Fig. 9.** Mode shapes of a seven-wire strand subjected to a tensile strain $E^E = 0.6\%$ calculated at points 1, real (a) and imaginary (b) parts, and at point 2, real (c) and imaginary (d) parts. Grey meshes refer to the cross-section in its static configuration.

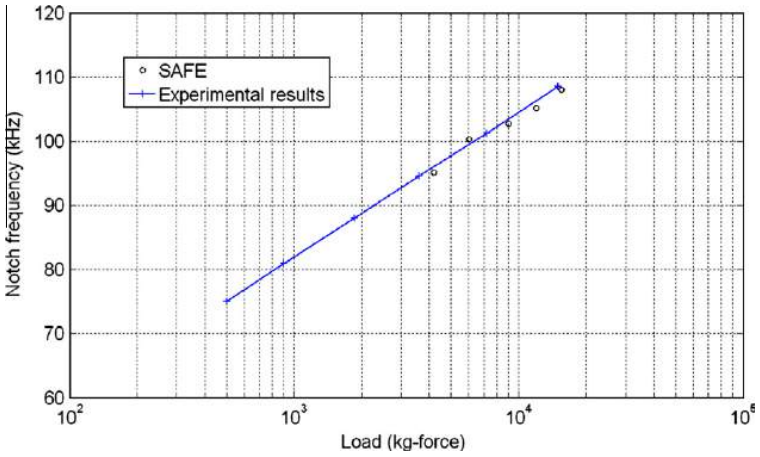


**Fig. 10.** Variation of the notch frequency (kHz) vs. the applied load (kg-force) for a seven-wire strand of nominal diameter 12.7*mm*. Circles: SAFE computation, crosses: experimental values of Kwun et al. (1998).

load. However, these results need to be confirmed by experiments, which is beyond the scope of this paper. We can observe also that dispersion curves shift to higher frequencies under the effect of tensile load, even at high frequencies. Due to contact effects, this contrasts with the results obtained for helical springs for which it was shown that the effects of axial load was significant only on low frequencies.

Finally, the SAFE results are now compared to other experimental results provided in Kwun et al. (1998), in which it has been found that the notch frequency varies linearly with $\log(T)$. Considering Strand 2, Fig. 10 shows the variation of the notch frequency as a function of the applied load computed from our SAFE model. The SAFE results have been obtained from the first node-to-node contacts formed on both side of initial contact points, yielding notch frequencies from 95 to 108 kHz in Fig. 10. Note that the low tension part of the experimental curve has not been explored with the numerical model because a much finer mesh would have been required around initial contact points. As it can be seen, the SAFE numerical results are in very good agreement with the experimental measurements of Kwun et al. (1998). The fact that the computed result for 100 kHz crosses the test result can be explained by simplifying assumptions used in the model (linear prestress state, frictionless contact).

Thus one can conclude to a validation of the SAFE approach with surface contact by comparison with the experimental results of Laguerre et al. (2002) and Kwun et al. (1998).

## 8. Conclusions

In this paper, elastic wave propagation in prestressed helical waveguides has been studied. The prestressed state is taken into account through the prestress (static Cauchy stress) and the deformed static geometry within an updated Lagrangian formulation. This prestressed static state, corresponding to axial loads, is computed thanks to the homogenization method proposed in Part 1 of this study. In Part 2, a SAFE formulation has been developed accounting for the translational invariance property, hence reducing the 3D elastodynamic equations of prestressed structures, written in the twisted coordinate system, to a 2D problem posed on the static deformed cross-section.

The present approach has been first applied to prestressed helical springs and the results have been compared to those obtained from an analytical solution based on a Timoshenko beam model. Good agreement has been found on dispersion curves. Moreover it was shown that the effect of the prestressed state was significant at low frequencies.

Next a seven-wire strand subjected to axial loads has been considered. In this case the important role of the contact area has been highlighted, which thus requires its updating. Including this feature, we have shown that the SAFE model can reproduce experimental results with respect to the notch frequency of the fundamental compressional-like mode, which increases with the tensile load. From a physical point of view, a complex behavior is observed due to interwire coupling. Moreover, numerical results show that over a wide spectrum of frequencies, dispersion curves shift to high frequencies under the effect of tensile loads.

## Appendix A. Equality between group and energy velocities

For propagating modes in undamped materials, group and energy velocities of guided modes must be equal, as opposed to damped cases (Bernard et al., 2001). Hence, let us assume that the material is undamped in order to show the equality between expressions (12) and (21).

Multiplying the eigenproblem (10) by $\{U\}^{T*}$, we get:

$$\{U\}^{T*}\Big([K_{1\sigma}]+ik([K_{2\sigma}]-[K_{2\sigma}]^T)+k^2[K_{3\sigma}]\Big)\{U\}=\omega^2\{U\}^{T*}[M]\{U\}. \tag{22}$$

This equation shows the equality between the kinetic and potential energies. Therefore, Eq. (18) becomes:

$$\int_{S_0}\overline{E}_k dS_0=\int_{S_0}\overline{E}_p dS_0=\frac{\omega^2}{4}Re(\{U\}^{T*}[M]\{U\}). \tag{23}$$

From Eqs. (20) and (23), the energy velocity expression (13) becomes:

$$V_e=\frac{Im\Big(\{U\}^{T*}([K_{2\sigma}]^T+ik[K_{3\sigma}])\{U\}\Big)}{\omega Re(\{U\}^{T*}[M]\{U\})}. \tag{24}$$

Besides, the imaginary part can be rewritten as:

$$Im\Big(\{U\}^{T*}([K_{2\sigma}]^T+ik[K_{3\sigma}])\{U\}\Big)$$
$$=\{U\}^{T*}\frac{1}{2i}([K_{2\sigma}]^T+ik[K_{3\sigma}])\{U\}-\{U\}^{T*}\frac{1}{2i}([K_{2\sigma}]^*-ik^*[K_{3\sigma}]^{T*})\{U\}. \tag{25}$$

For undamped materials, the matrix $[K_{3\sigma}]$ is real symmetric ($[K_{3\sigma}]^{T*} = [K_{3\sigma}]$ and the matrix $[K_{2\sigma}]$ is real ($[K_{2\sigma}]^{*} = [K_{2\sigma}]$). Then, Eq. (25) becomes:

$$Im\{\{U\}^{T*}([K_{2\sigma}]^{T} + ik[K_{3\sigma}])\{U\}\} = \frac{1}{2}\{U\}^{T*}(i([K_{2\sigma}] - [K_{2\sigma}]^{T}) + (k + k^{*})[K_{3\sigma}])\{U\}. \quad (26)$$

For propagating modes, wavenumbers are real ($k = k^{*}$) and Eq. (26) becomes equal to the numerator of the group velocity (12). Also, the denominator of Eq. (12) is always real because $[M]$ is real symmetric. Therefore, the energy velocity is equal to the group velocity.

## References


Achenbach, J.D., 1973. Wave Propagation in Elastic Solids. North-Holland, Amsterdam.

Bartoli, I., Marzani, A., di Scalea, F.L., Viola, E., 2006. Modeling wave propagation in damped waveguides of arbitrary cross-section. Journal of Sound and Vibration 295, 685–707.

Bathe, K.J., 1996. Finite Element Procedures. Prentice Hall, Englewood Cliffs, New Jersey.

Benmeddour, F., Treyssède, F., Laguerre, L., 2011. Numerical modeling of guided wave interaction with non-axisymmetric cracks in elastic cylinders. International Journal of Solids and Structures 48, 764–774.

Bernard, A., Lowe, M.J.S., Deschamps, M., 2001. Guided waves energy velocity in absorbing and non-absorbing plates. Journal of the Acoustical Society of America 110, 186–196.

Chapelle, D., Bathe, K.J., 2003. The Finite Element Analysis of Shells-Fundamentals. Springer.

Chen, F., Wilcox, P.D., 2007. The effect of load on guided wave propagation. Ultrasonics 47, 111–122.

Damljanovic, V., Weaver, R.L., 2004. Propagating and evanescent elastic waves in cylindrical waveguides of arbitrary cross section. Journal of the Acoustical Society of America 115, 1572–1581.

Demma, A., Cawley, P., Lowe, M., Pavlakovic, B., 2005. The effect of bends on the propagation of guided waves in pipes. Journal of Pressure Vessel technology 127, 328–335.

Dong, S.B., Nelson, R.B., 1972. On natural vibrations and waves in laminated orthotropic plates. Journal of Applied Mechanics 39, 739–745.

Duhamel, D., Mace, B.R., Brennan, M.J., 2006. Finite element analysis of the vibrations of waveguides and periodic structures. Journal of Sound and Vibration 294, 205–220.

Finnveden, S., 2004. Evaluation of modal density and group velocity by a finite element method. Journal of Sound and Vibration 273, 51–75.

Finnveden, S., Fraggstedt, M., 2008. Waveguide finite elements for curved structures. Journal of Sound and Vibration 312, 644–671.

Frikha, A., Treyssède, F., Cartraud, P., 2011. Effect of axial load on the propagation of elastic waves in helical beams. Wave Motion 48, 83–92.

Gavric, L., 1995. Computation of propagative waves in free rail using a finite element technique. Journal of Sound and Vibration 185, 531–543.

Ghoreishi, S.R., Messager, T., Cartraud, P., Davies, P., 2007. Validity and limitations of linear analytical models for steel wire strands under axial loading, using a 3d fe model. International Journal of Mechanical Sciences 49, 1251–1261.

Gry, L., Gontier, C., 1997. Dynamic modelling of railway track: A periodic model based on a generalised beam formulation. Journal of Sound and Vibration 199, 531–558.

Hayashi, T., Tamayama, C., Murase, M., 2006. Wave structure analysis of guided waves in a bar with an arbitrary cross-section. Ultrasonics 41, 175–183.

Jezzine, K., 2006. Approche modale pour la simulation globale de contrôles non-destructifs par ondes élastiques guidées. Ph.D. thesis. Université de Bordeaux. (Modal approach for the full simulation of nondestructive tests by elastic guided waves, in French).

Jiang, W.G., Warby, M.K., Henshall, J.L., 2008. Statically indeterminate contacts in axially loaded wire strand. European Journal of Mechanics A/Solids 27, 69–78.

Kwun, H., Bartels, K.A., Hanley, J.J., 1998. Effects of tensile loading on the properties of elastic-wave propagation in a strand. Journal of the Acoustical Society of America 103, 3370–3375.

Laguerre, L., Brissaud, M., Aime, J.C., 2002. Low-frequency ultrasound reflectometry device based on magnetoelastic transducers for the non destructive evaluation of steel rods and cables. Bulletin des Laboratoires des Ponts et Chaussées 239, 7–27.

Loveday, P.W., 2009. Semi-analytical finite element analysis of elastic waveguides subjected to axial loads. Ultrasonics 49, 298–300.

Marzani, A., 2008. Time-transient response for ultrasonic guided waves propagating in damped cylinders. International Journal of Solids and Structures 45, 6347–6368.

Mencik, J.M., Ichchou, M.N., 2007. Wave finite elements in guided elastodynamics with internal fluid. International Journal of Solids and Structures 44, 2148–2167.

Nicolet, A., Movchan, A.B., Geuzaine, C., Zolla, F., Guenneau, S., 2007. High order asymptotic analysis of twisted electrostatic problems. Physica B: Condensed Matter 394, 335–338.

Nicolet, A., Zola, F., 2007. Finite element analysis of helicoidal waveguides. Measurement and Technology 28, 67–70.

Nicolet, A., Zola, F., Guenneau, S., 2004. Modeling of twisted optical waveguides with edge elements. The European Physical Journal Applied Physics 28, 153–157.

Onipede, O., Dong, S.B., 1996. Propagating waves and end modes in pretwisted beams. Journal of Sound and Vibration 195, 313–330.

Rattanawangcharoen, N., Shah, A.H., Datta, S.K., 1992. Wave propagation in laminated composite circular cylinders. International Journal of Solids and Structures 29, 767–781.

Synge, J.L., Schild, A., 1978. Tensor Calculus. Dover.

Tisseur, F., Meerbergen, K., 2001. The quadratic eigenvalue problem. SIAM Review 43, 235–286.

Treyssède, F., 2007. Numerical investigation of elastic modes of propagation in helical waveguides. Journal of the Acoustical Society of America 121, 3398–3408.

Treyssède, F., 2008. Elastic waves in helical waveguides. Wave Motion 45, 457–470.

Treyssède, F., 2011. Mode propagation in curved waveguides and scattering by inhomogeneities: application to the elastodynamics of helical structures. Journal of the Acoustical Society of America 129, 1857–1868.

Treyssède, F., Laguerre, L., 2010. Investigation of elastic modes propagating in multi-wire helical waveguides. Journal of Sound and Vibration 329, 1702–1716.

Wahl, A.M., 1963. Mechanical Springs, second ed. Mc Graw-Hill, Inc., New York.

Wempner, G., 1981. Mechanics of Solids with Applications to Thin Bodies. Sijthoff and Noordhoff, The Netherlands.

Yang, Y.B., Kuo, S.R., 1994. Nonlinear Framed Structures. Simon and Schuster, Asia Pte Ltd.

Zhuang, W., Shah, A.H., Dong, S.B., 1999. Elastodynamic green's function for laminated anisotropic circular cylinders. Journal of Applied Mechanics 66, 665–674.

Journal of Sound and Vibration 344 (2015) 158–178

Contents lists available at ScienceDirect

Journal of Sound and Vibration

journal homepage: www.elsevier.com/locate/jsvi

# Numerical modeling of three-dimensional open elastic waveguides combining semi-analytical finite element and perfectly matched layer methods

K.L. Nguyen [a,*], F. Treyssède [a], C. Hazard [b]

[a] LUNAM Université, IFSTTAR, GERS, F-44344 Bouguenais, France
[b] ENSTA-UMA, POEMS, 828 Boulevard des Maréchaux, 91120 Palaiseau, France

ARTICLE INFO

*Article history:*
Received 27 May 2014
Received in revised form
23 November 2014
Accepted 22 December 2014
Handling Editor: G. Degrande
Available online 10 February 2015

ABSTRACT

Among the numerous techniques of non-destructive evaluation, elastic guided waves are of particular interest to evaluate defects inside industrial and civil elongated structures owing to their ability to propagate over long distances. However for guiding structures buried in large solid media, waves can be strongly attenuated along the guide axis due to the energy radiation into the surrounding medium, usually considered as unbounded. Hence, searching the less attenuated modes becomes necessary in order to maximize the inspection distance. In the numerical modeling of embedded waveguides, the main difficulty is to account for the unbounded section. This paper presents a numerical approach combining a semi-analytical finite element method and a perfectly matched layer (PML) technique to compute the so-called trapped and leaky modes in three-dimensional embedded elastic waveguides of arbitrary cross-section. Two kinds of PML, namely the Cartesian PML and the radial PML, are considered. In order to understand the various spectral objects obtained by the method, the PML parameters effects upon the eigenvalue spectrum are highlighted through analytical studies and numerical experiments. Then, dispersion curves are computed for test cases taken from the literature in order to validate the approach.



## 1. Introduction

Among the numerous techniques of non-destructive evaluation (NDE), elastic guided waves are of particular interest to evaluate defects inside industrial and civil elongated structures due to their ability to propagate over long distances. Two categories of waveguides can be distinguished: closed waveguides (guides in vacuum) and open waveguides (embedded waveguides).

In closed waveguides, waves can propagate along the guide axis without attenuation. However in practice, guides are often embedded in large solid media that can be considered as unbounded. In this case, waveguides are called open because of the energy radiation into the surrounding medium. Three kinds of wave modes can occur in open waveguides: radiation modes, trapped modes and leaky ones. Their characteristics are briefly recalled in the following paragraphs. These modes

* Corresponding author.
*E-mail address:* khac-long.nguyen@ifsttar.fr (K.L. Nguyen).

http://dx.doi.org/10.1016/j.jsv.2014.12.032
0022-460X/

are obtained by assuming a dependence of wave fields in $e^{i(kz-\omega t)}$, where $k$ is the axial wavenumber, $\omega$ is the angular frequency and $z$ is the coordinate along the waveguide axis. The following dispersion relations hold: $k^2+k_{l/s}^2=\omega^2/c_{l/s}^2$, where $c_l$ and $c_s$ are the longitudinal and shear wave speeds, $k_l$ and $k_s$ denote the longitudinal and shear transverse wavenumbers of the unbounded medium respectively.

Radiation modes are standing waves in the transverse directions and can be either oscillating or evanescent in the longitudinal direction, *i.e.* $k_{l/s}\in\mathbb{R}$ and $k$ is real or pure imaginary. They constitute a continuous spectrum [1,2], resulting from the unbounded nature of the problem. Resonating mainly in the surrounding medium, radiation modes are of little interest for the NDE of elongated structures.

Conversely, trapped modes are of particular interest. These modes exponentially decay in the transverse directions ($k_{l/s}\in i\mathbb{R}$) and propagate along the axis without attenuation ($k\in\mathbb{R}$) in non-dissipative waveguides. Their energy is confined into the core of waveguides without energy leakage into the surrounding medium allowing long inspection distances. Nevertheless, trapped modes do not always occur. For scalar open waveguides (characterized by a scalar field such as the acoustic pressure or the SH wave displacement), trapped modes exist only if the bulk velocity in the core is lower than in the surrounding medium [3]. In the elastic case, both compressional and shear bulk waves occur and, unless Stoneley waves are allowed on the interface between materials, no trapped modes are present when the shear velocity is faster in the core [4,5]. Unfortunately, such a configuration is often encountered in civil structures because the guiding structures are usually embedded in soft solid media such as concrete, cement or grout for instance.

As opposed to trapped modes, leaky modes always exist in open waveguides. Their energy leakage into the surrounding medium yields attenuation along the guide axis ($k\in\mathbb{C}/\mathbb{R}$, $\mathrm{Im}(k)$ being positive for positive-going modes and negative for negative-going ones), which can strongly limit their propagation distance. An unusual behavior of leaky modes is that, while decaying along the axis, their amplitudes increase in the transverse directions. This feature is well-known in electromagnetism [3,6] and has sometimes been mentioned in elastodynamics [7–11].

From a mathematical point of view, leaky modes are not spectral objects because they belong to the forbidden Riemann sheet [3,12]. They constitute a discrete set which is not part of the complete set constituted by the continuum of radiation modes and the discrete set of trapped modes [1,2]. The mathematical characterization of leaky modes requires a complicated analytical continuation [13] which is out of scope here. From a physical point of view, leaky modes can constitute a good approximation of the continuum of radiation modes in the excited field over a restricted area, near the core region [6]. Through the imaginary part of their axial wavenumbers, leaky modes allow to directly evaluate the ability of waves to propagate far away along the axis. With radiation modes, such an information is hidden into the continuum. Therefore, an accurate determination of leaky modes is essential for the NDE of embedded waveguides in order to find modes and frequencies of lowest attenuation.

In the literature, many researches have been conducted on embedded waveguides based on analytical approaches [14,15]. Analytical models are mainly based on transfer matrix or global matrix methods [14,15] and allow to plot the dispersion curves of solid embedded waveguides. Methods based on Debye series have also been proposed in Ref. [16]. Yet, these techniques are limited to simple geometries such as plates and cylinders [17–19].

The modeling of more complex geometries usually relies on numerical approaches. A powerful technique is the so-called Semi-Analytical Finite Element (SAFE) method [20–23], which restricts the FE discretization on transverse directions only. The SAFE method has been mainly used for the simulation of closed waveguides. The numerical modeling of open waveguides encounters two difficulties: the cross-section is unbounded and the amplitude of leaky modes transversely increases. In order to overcome these difficulties, the SAFE method must be associated with other techniques.

A simple numerical procedure is the absorbing layer (AL) method proposed in Refs. [24,25], which consists in creating artificial viscoelastic layers in the surrounding medium for absorbing waves. Instead of using artificial layers, Mazzotti et al. have recently combined the boundary element method (BEM) with the SAFE method to model three-dimensional elastic waveguides embedded in a solid [26] or in a fluid [27]. The BEM expresses the solution in the exterior domain by integral formula on the core boundary. Analogously to the SAFE–BEM method, Hayashi and Inoue [28] have proposed a formulation for open plate waveguides. An alternative technique is the perfectly matched layer (PML) method, which consists in analytically extending real coordinates of physical equations into the complex ones. The SAFE–PML method has already been applied to scalar wave problems [29–31]. More recently, the authors have presented this method to model open solid plate waveguides [32,33] (one-dimensional modal problems).

Among these three techniques, the SAFE-AL method is the simplest to implement as it does not require specific programming in existing codes. However, the AL artificial viscoelasticity must be slowly growing in order to minimize reflection so that large layers can be required in practice, hence increasing the computational cost. Compared to AL, the PML thickness is expected to be significantly reduced. Theoretically, the PML can strongly attenuate waves without artificial reflection thanks to the analytical extension of coordinates (perfectly matched property). Contrary to SAFE-AL and SAFE–PML methods, the SAFE–BEM method avoids the discretization of the unbounded medium, which significantly reduces the computational domain. Yet, the SAFE–BEM eigenproblem is highly nonlinear and difficult to solve. To avoid the eigenproblem nonlinearity with SAFE–BEM methods, some modified formulations have been proposed. Hayashi and Inoue [28] have successfully transformed the nonlinear eigenproblem into a linear one for the special case of a surrounding fluid (scalar waves). Gravenkamp et al. [34] have proposed a simplified boundary condition, namely dashpot boundary condition, which amounts to neglect transverse wavenumbers in the exact radiation condition. This dashpot condition is usually no longer accurate for low frequency or for low contrast of acoustic impedance. Unlike the SAFE–BEM approach, both the SAFE-AL and SAFE–PML methods yield a linear eigenvalue problem.

In this paper, the SAFE–PML technique is proposed as an alternative to SAFE-AL and SAFE–BEM methods to compute modes in three-dimensional elastic waveguides of arbitrary cross-section embedded in an unbounded solid matrix. Two kinds of PML, Cartesian and radial, are considered. This yields two formulations referred to as the SAFE–Cartesian PML (SAFE–CPML) method and the SAFE–radial PML (SAFE–RPML) method. It is pointed out that both kinds of PML have been analyzed mathematically for computing the acoustic resonances of open cavities [35,36], which constitutes a problem close to that of the present paper. Note also that the SAFE–CPML formulation of this paper is indeed similar to the 2.5D displacement-based PML formulation recently proposed in Ref. [37] (yet in this reference, the discretized problem was not considered as an eigenvalue problem, but rather inverted by considering a source term for fixed transverse wavenumbers).

This paper focuses on the implementation and the validation of the SAFE–PML method. The comparative study between this technique and other techniques such as SAFE-AL or SAFE–BEM methods is out of scope of this paper and left for further studies.

The SAFE–CPML and SAFE–RPML formulations are presented in Sections 2 and 3 respectively. In order to understand the various spectral objects obtained from these formulations and to clarify the effects of PML parameters, the eigenvalue spectrum is analyzed for each formulation based on analytical studies and numerical experiments. In Section 4, the computation of modal properties (group velocity, energy velocity and kinetic energy) is introduced and dispersion curves are computed for several test cases taken from the literature to validate both formulations.

## 2. SAFE–CPML method

### 2.1. Initial formulation of 3D elastodynamics

One considers a three-dimensional waveguide $\widetilde{\Omega}=\widetilde{S}\times]-\infty,+\infty[$. Linear elastic materials are assumed. The waveguide cross-section $\widetilde{S}$ lies in the $(\widetilde{x},\widetilde{y})$ plane. The tilde notation will be explained through the introduction of PML in Section 2.2. The time harmonic dependence is chosen as $e^{-i\omega t}$. The study is focused on eigenmodes. Acoustic sources and external forces are then discarded.

The variational formulation of the elastodynamic problem for the displacement field $\mathbf{u}$ is given by

$$\int_{\widetilde{\Omega}}\delta\widetilde{\boldsymbol{\epsilon}}^{T}\widetilde{\boldsymbol{\sigma}}\,\mathrm{d}\widetilde{\Omega}-\omega^{2}\int_{\widetilde{\Omega}}\widetilde{\rho}\,\delta\widetilde{\mathbf{u}}^{T}\widetilde{\mathbf{u}}\,\mathrm{d}\widetilde{\Omega}=0 \tag{1}$$

where $\mathrm{d}\widetilde{\Omega}=\mathrm{d}\widetilde{x}\,\mathrm{d}\widetilde{y}\,\mathrm{d}z$. This formulation holds for any kinematically admissible displacement $\delta\widetilde{\mathbf{u}}=[\delta\widetilde{u}_x\delta\widetilde{u}_y\delta\widetilde{u}_z]^T$. The notation $\delta\widetilde{\boldsymbol{\epsilon}}=[\delta\widetilde{\epsilon}_{xx}\delta\widetilde{\epsilon}_{yy}\delta\widetilde{\epsilon}_{zz}\ 2\delta\widetilde{\epsilon}_{xy}2\delta\widetilde{\epsilon}_{xz}2\delta\epsilon_{yz}]^T$ is the virtual strain vector, $\widetilde{\boldsymbol{\sigma}}=[\widetilde{\sigma}_{xx}\widetilde{\sigma}_{yy}\widetilde{\sigma}_{zz}\widetilde{\sigma}_{xy}\widetilde{\sigma}_{xz}\widetilde{\sigma}_{yz}]^T$ denotes the stress vector. The stress–strain relation is given by $\widetilde{\boldsymbol{\sigma}}=\widetilde{\mathbf{C}}\widetilde{\boldsymbol{\epsilon}}$, where $\widetilde{\mathbf{C}}$ is the matrix of material properties. $\widetilde{\rho}$ is the material mass density. The superscript $T$ denotes the matrix transpose. We assume that $\widetilde{\mathbf{C}}$ and $\widetilde{\rho}$ depend only on the transverse coordinates $(\widetilde{x},\widetilde{y})$, which means that we consider translationally invariant waveguides along the $z$-axis. Moreover we assume that the medium is homogeneous outside a bounded region which represents the core of the waveguide.

Separating transverse from axial derivatives, the strain–displacement relation can be written as follows:

$$\widetilde{\boldsymbol{\epsilon}}=\left(\mathbf{L}_{\widetilde{S}}+\mathbf{L}_z\frac{\partial}{\partial z}\right)\widetilde{\mathbf{u}} \tag{2}$$

where $\mathbf{L}_{\widetilde{S}}=\mathbf{L}_x(\partial/\partial\widetilde{x})+\mathbf{L}_y(\partial/\partial\widetilde{y})$ and

$$\mathbf{L}_x=\begin{bmatrix}1&0&0\\0&0&0\\0&0&0\\0&1&0\\0&0&1\\0&0&0\end{bmatrix},\quad \mathbf{L}_y=\begin{bmatrix}0&0&0\\0&1&0\\0&0&0\\1&0&0\\0&0&0\\0&0&1\end{bmatrix},\quad \mathbf{L}_z=\begin{bmatrix}0&0&0\\0&0&0\\0&0&1\\0&0&0\\1&0&0\\0&1&0\end{bmatrix}. \tag{3}$$

$\mathbf{L}_{\widetilde{S}}$ and $\mathbf{L}_z\partial/\partial z$ are the operators of derivatives with respect to the transverse directions $(\widetilde{x},\widetilde{y})$ and the $z$-axis respectively.

### 2.2. Combining SAFE and Cartesian PML techniques

The SAFE method consists in assuming a harmonic axial dependence of fields and applying the FE method to the transverse directions. The problem is then reduced from three dimensions to the two dimensions of the waveguide cross-section. The SAFE method has been widely used for modeling closed waveguides (guides in vacuum), for which the cross-section is bounded (see for instance [20–23]).

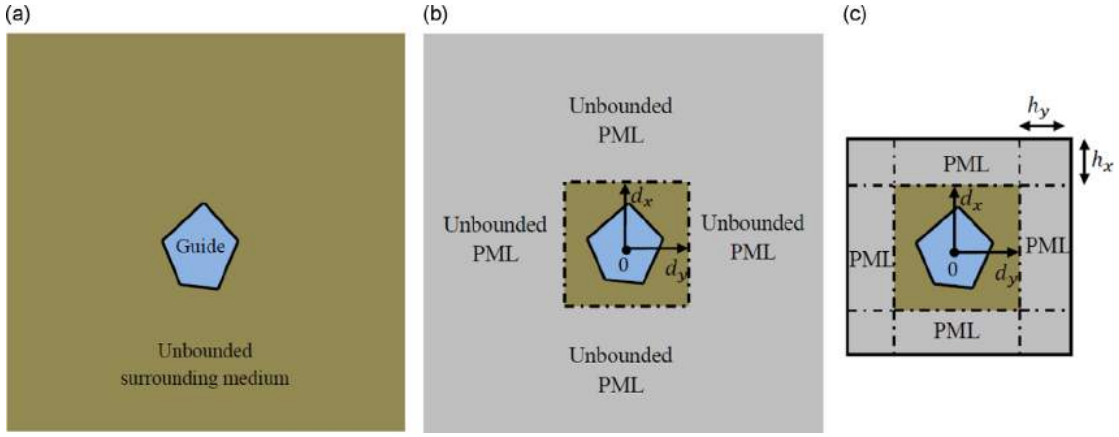


**Fig. 1.** (a) Arbitrary cross-section of an open waveguide, (b) introduction of Cartesian PML in the surrounding medium and (c) PML truncation.

The modeling of open waveguides requires to combine the SAFE method with another technique due to the unbounded nature of the section. We assume that outside a possibly inhomogeneous region representing the core of the waveguide, the medium is homogeneous. The basic idea consists in closing the waveguide section by replacing the unbounded homogeneous region with a PML of finite thickness. As shown in Fig. 1, a PML is introduced along the Cartesian transverse coordinates in order to attenuate waves in the surrounding medium. By truncating the cross-section to a sufficiently large distance, the problem becomes closed and the SAFE method can be applied. In this case, $\widetilde{S}$ denotes the truncated section including the PML.

The basic principle of PML can be readily understood in a one-dimensional situation. Consider for instance the case of a longitudinal wave traveling in the positive $\widetilde{x}$ direction. Such a wave can be expressed as an exponential function $\exp(ik_l\widetilde{x})$, which extends to an entire function for complex values of $\widetilde{x}$. Hence, instead of considering real $\widetilde{x}$, one can choose a particular path $\widetilde{x}(x)$ in the complex plane parametrized by a real variable $x$ such that $\exp(ik_l\widetilde{x}(x))$ decays exponentially as $x$ tends to $+\infty$. The same considerations apply in the $\widetilde{y}$ direction or for a shear wave. The Cartesian PML method consists in extending the initial equilibrium equations to complex coordinates $\widetilde{x}$ and $\widetilde{y}$, properly parametrized to attenuate waves (the PML parametrization will be discussed in Section 2.4). Here we define

$$\widetilde{x}(x)=\int_0^x \gamma_x(\xi)\,\mathrm{d}\xi,\ \widetilde{y}(y)=\int_0^y \gamma_y(\xi)\,\mathrm{d}\xi \tag{4}$$

where $\gamma_x(x)$, $\gamma_y(y)$ are complex functions satisfying

- $\gamma_x(x)=1$ for $|x|\le d_x$ ; $\gamma_y(y)=1$ for $|y|\le d_y$,
- Im $\{\gamma_x\}>0$ for $|x|>d_x$ ; Im $\{\gamma_y\}>0$ for $|y|>d_y$.

$d_x$ and $d_y$ are positive parameters chosen such that the rectangle $[-d_x,+d_x]\times[-d_y,+d_y]$ contains the inhomogeneous part of the medium. Thus $\widetilde{x}$ and $\widetilde{y}$ become non-real in the homogeneous surrounding medium.

Since waves are attenuated, the PML can be truncated at a finite distance. We denote by $h_x$ and $h_y$ the PML thicknesses in the $x$ and $y$ directions respectively (see Fig. 1c). Thus, in the $(x,y)$ plane, the truncated cross-section including the PML is the rectangle of half-thicknesses $d_x+h_x$ and $d_y+h_y$. On the exterior boundary of the PML, the boundary condition can be arbitrarily chosen (usually of Dirichlet type).

From Eq. (4), the change of variables $\widetilde{x}\mapsto x$, $\widetilde{y}\mapsto y$ yields for any function $\widetilde{f}$:

$$\frac{\partial\widetilde{f}}{\partial\widetilde{x}}=\frac{1}{\gamma_x}\frac{\partial f}{\partial x},\ \frac{\partial\widetilde{f}}{\partial\widetilde{y}}=\frac{1}{\gamma_y}\frac{\partial f}{\partial y},\ \mathrm{d}\widetilde{x}=\gamma_x\mathrm{d}x,\ \mathrm{d}\widetilde{y}=\gamma_y\mathrm{d}y \tag{5}$$

where $\widetilde{f}(\widetilde{x}(x),\widetilde{y}(y),z)=f(x,y,z)$.

Applying this change of variable to Eq. (2) leaves the operator $\mathbf{L}_z$ unchanged while the operator $\mathbf{L}_{\widetilde{S}}$ has to be replaced with

$$\mathbf{L}_S=\frac{1}{\gamma_x}\mathbf{L}_x\frac{\partial}{\partial x}+\frac{1}{\gamma_y}\mathbf{L}_y\frac{\partial}{\partial y}. \tag{6}$$

Now applying the SAFE method, the displacement $\mathbf{u}$ and the virtual displacement $\delta\mathbf{u}$ are expressed on one element $e$ as follows:

$$\mathbf{u}(x,y,z)=\mathbf{N}^e(x,y)\mathbf{U}^e\mathrm{e}^{\mathrm{i}kz},\ \delta\mathbf{u}(x,y,z)=\mathbf{N}^e(x,y)\delta\mathbf{U}^e\mathrm{e}^{-\mathrm{i}kz} \tag{7}$$

where $k$ is the axial wavenumber, $\mathbf{U}^e$ is the displacement vector and $\mathbf{N}^e$ is the matrix of interpolating functions on the element $e$.

Replacing the axial derivative $\partial/\partial z$ of the trial and test functions with products by $+ik$ and $-ik$ respectively, the formulation (1) is reduced from three dimensions $(x,y,z)$ to a bidimensional problem written in the transverse directions $(x, y)$. The strain–displacement relation becomes

$$\boldsymbol{\epsilon} = (\mathbf{L}_S + ik\mathbf{L}_z)\mathbf{N}^e\mathbf{U}^e e^{ikz}. \tag{8}$$

The FE discretization of the truncated cross-section finally yields

$$\{\mathbf{K}_1 - \omega^2\mathbf{M} + ik(\mathbf{K}_2 - \mathbf{K}_2^T) + k^2\mathbf{K}_3\}\mathbf{U} = \mathbf{0} \tag{9}$$

with the elementary matrices:

$$\mathbf{K}_1^e = \int_e \mathbf{N}^{eT}\mathbf{L}_S^T\mathbf{C}\mathbf{L}_S\mathbf{N}^e\gamma_x\gamma_y \,dx\,dy, \mathbf{K}_2^e = \int_e \mathbf{N}^{eT}\mathbf{L}_S^T\mathbf{C}\mathbf{L}_z\mathbf{N}^e\gamma_x\gamma_y \,dx\,dy$$
$$\mathbf{K}_3^e = \int_e \mathbf{N}^{eT}\mathbf{L}_z^T\mathbf{C}\mathbf{L}_z\mathbf{N}^e\gamma_x\gamma_y \,dx\,dy, \mathbf{M}^e = \int_e \rho\mathbf{N}^{eT}\mathbf{N}^e\gamma_x\gamma_y \,dx\,dy.$$

Note that the SAFE–CPML matrices are complex due to the functions $\gamma_x$ and $\gamma_y$ in the integrands.

### 2.3. Linear eigenvalue problem

Given the frequency $\omega$, the formulation (9) is quadratic with respect to $k$, which can be linearized as [33,38]

$$(\mathbf{A} - k\mathbf{B})\hat{\mathbf{U}} = 0 \tag{10}$$

with

$$\mathbf{A} = \begin{bmatrix} \mathbf{0} & \mathbf{I} \\ -(\mathbf{K}_1 - \omega^2\mathbf{M}) & -i(\mathbf{K}_2 - \mathbf{K}_2^T) \end{bmatrix}, \quad \mathbf{B} = \begin{bmatrix} \mathbf{I} & \mathbf{0} \\ \mathbf{0} & \mathbf{K}_3 \end{bmatrix}, \quad \hat{\mathbf{U}} = \begin{bmatrix} \mathbf{U} \\ k\mathbf{U} \end{bmatrix}. \tag{11}$$

The symmetry of $\mathbf{K}_1$, $\mathbf{K}_3$ and $\mathbf{M}$ implies that if $k$ is an eigenvalue of (9), then $-k$ is also an eigenvalue. Thus, the eigenspectrum includes two families of solutions, $(k_j, \mathbf{U}_j^+)$ and $(-k_j, \mathbf{U}_j^-)$, $(j=1,\ldots,n)$ representing $n$ positive-going and $n$ negative-going waves.

In the presence of PML, $\mathbf{K}_1$, $\mathbf{K}_2$, $\mathbf{K}_3$ and $\mathbf{M}$ are complex. $\mathbf{A}$ and $\mathbf{B}$ are not Hermitian, which somewhat complicates the numerical treatment of the eigensystem (10). As outlined in Ref. [35,30], the non-hermitian character of matrices may yield spurious eigenvalues which are associated with large values of the norm of resolvent. This problem can be reduced by setting the PML not too far from the core.

In this paper, the ARPACK library [39] is used for solving the eigensystem (10). This library is based on the implicitly restarted Arnoldi method. For each frequency, a specified number of eigenvalues is looked for around a user-defined shift.

### 2.4. PML absorbing functions

In each direction $x$ and $y$, the PML depends on three user-defined parameters: the position of the interface $(d_x, d_y)$, the thickness $(h_x, h_y)$ and the absorbing function $(\gamma_x, \gamma_y)$. For a given interface position and PML thickness, the optimal choice of absorbing functions is crucial for maximizing the attenuation of waves with minimal reflections.

In scattering problems (source problems), the PML function is usually frequency dependent [40,41] and chosen as: $\gamma_x(x) = 1 + i\sigma_x(x)/\omega$ where $\sigma_x(x)$ is a continuous function, parabolic inside the PML region (a similar expression holds for $\gamma_y(y)$). In modal problems, the proper choice of PML functions is slightly different.

As mentioned in the preceding section, if we consider a longitudinal or shear wave $\exp(ik_{l/s}\tilde{x})$ for real $\tilde{x}$ (where $k_l$ and $k_s$ denote the transverse longitudinal and shear wavenumbers respectively), the effect of an infinite PML in the positive $x$ direction is to transform this function into an exponentially decaying function $\exp(ik_{l/s}\tilde{x}(x))$ as $x$ tends to $+\infty$. From (4), it is easily seen that the total attenuation across a layer of finite thickness $h_x$ is given by

$$\exp(-\mathrm{Im}(k_{l/s}\hat{\gamma}_x h_x)) = \exp(-|k_{l/s}||\hat{\gamma}_x|h_x \sin(\arg k_{l/s} + \arg\hat{\gamma}_x)) \tag{12}$$

where $\hat{\gamma}_x$ denotes the average values of $\gamma_x$ in the layer :

$$\hat{\gamma}_x = \frac{1}{h_x}\int_{d_x}^{d_x+h_x} \gamma_x(\xi)\,d\xi. \tag{13}$$

One recalls that leaky modes decay along the axial direction $z$ ($\mathrm{Im}\,k > 0$) but grow in the transverse direction, *i.e.* $\mathrm{Im}\,k_{l/s} < 0$ or equivalently $\arg k_{l/s} < 0$. From Eq. (12), leaky waves can be attenuated by the PML if $\hat{\gamma}_x$ is such that $\arg k_{l/s} > -\arg\hat{\gamma}_x$ (in this paper, arg denotes the principal argument and lies in the interval $]-\pi, +\pi]$). Hence, increasing $\arg\hat{\gamma}_x$ will enlarge the region of the complex plane where leaky modes can be computed. Increasing $|\hat{\gamma}_x|h_x$ will increase the PML absorption.

For trapped modes, waves propagate without axial attenuation ($\mathrm{Im}\, k = 0$) and exponentially decay in the transverse direction so that: $\mathrm{Re} k_{l/s} = 0$ and $\mathrm{Im}\, k_{l/s} > 0$, or equivalently $\arg k_{l/s} = \pi/2$. In the presence of PML, trapped waves will thus remain decaying if $\arg \hat{\gamma}_x < \pi/2$. The PML will be able to enhance the natural decay of trapped modes if $\mathrm{Im}(k_{l/s}\hat{\gamma}_x) > \mathrm{Im}\, k_{l/s}$, or equivalently $\mathrm{Re}\, \hat{\gamma}_x > 1$.

Note that $|\hat{\gamma}_x|$ cannot be too high in practice for a given $h_x$, otherwise waves will attenuate too fast to be well approximated by the FE discretization. This phenomenon is well-known in the PML literature [40].

For a PML introduced in the $y$-direction, the above considerations also holds with $\hat{\gamma}_y$ defined by

$$\hat{\gamma}_y = \frac{1}{h_y}\int_{d_y}^{d_y+h_y} \gamma_y(\xi)\, \mathrm{d}\xi. \tag{14}$$

For open waveguide modal problems, the PML functions have been usually set to a constant complex value [30,42–44], yielding a discontinuity at the PML interface. However a smooth profile can improve the accuracy of modes, as recently shown in Refs. [32,33]. In this paper, a parabolic function is set for both the real and the imaginary parts of $\gamma_x$ and $\gamma_y$:

$$\gamma_x(x) = \begin{cases} 1 & \text{if } |x| \le d_x \\ 1 + 3(\hat{\gamma}_x - 1)\left(\frac{|x|-d_x}{h_x}\right)^2 & \text{if } |x| > d_x \end{cases}, \quad \gamma_y(y) = \begin{cases} 1 & \text{if } |y| \le d_y \\ 1 + 3\left(\hat{\gamma}_y - 1\right)\left(\frac{|y|-d_y}{h_y}\right)^2 & \text{if } |y| > d_y \end{cases}. \tag{15}$$

$\hat{\gamma}_x$ and $\hat{\gamma}_y$ quantify the PML absorption. Note that the PML functions $\gamma_x$ and $\gamma_y$ are independent of $\omega$, which avoids the calculation of SAFE–CPML matrices at each frequency.

### 2.5. Eigenspectrum

The goal of this subsection is to get a better understanding of the influence of each PML parameter upon each type of modes. First, the analytical solution of a homogeneous medium is derived and compared with numerical results obtained with the SAFE–CPML method. Second, a more complex case corresponding to a steel cylinder buried in a solid medium is considered. Numerical experiments are performed to understand how the Cartesian PML acts on the eigenspectrum.

#### 2.5.1. Homogeneous medium

An isotropic elastic homogeneous medium in three dimensions can be viewed as an open homogeneous waveguide of unbounded section in the $(x, y)$ plane ($z$ being the axial direction). Introducing a PML of finite thickness in both directions $x$ and $y$, the problem becomes closed. A boundary condition, defined later, must be applied at the PML ends. Let us denote $\ell_x$ and $\ell_y$ the half thicknesses of the whole cross-section ($\ell_x = d_x + h_x$, $\ell_y = d_y + h_y$). $\tilde{\ell}_x$ and $\tilde{\ell}_y$ are the complex half thicknesses, defined as follows:

$$\tilde{\ell}_x = \int_0^{\ell_x} \gamma_x(\xi)\, \mathrm{d}\xi = d_x + \hat{\gamma}_x h_x, \quad \tilde{\ell}_y = \int_0^{\ell_y} \gamma_y(\xi)\, \mathrm{d}\xi = d_y + \hat{\gamma}_y h_y. \tag{16}$$

*Analytical solution*: Applying the Helmholtz decomposition [45], the displacement vector $\tilde{\mathbf{u}}$ is written as $\tilde{\mathbf{u}} = \tilde{\nabla}\tilde{\phi} + \tilde{\nabla} \wedge \tilde{\boldsymbol{\psi}}$ (with $\tilde{\nabla} \cdot \tilde{\boldsymbol{\psi}} = 0$), where $\phi$ and $\tilde{\boldsymbol{\psi}} = [\tilde{\psi}_x\ \tilde{\psi}_y\ \tilde{\psi}_z]^T$ are scalar and vector potentials corresponding to longitudinal ($l$) and shear ($s$) waves respectively. The equilibrium equations of elastodynamics yield the uncoupled differential equations for potentials:

$$\frac{\partial^2\tilde{\phi}}{\partial\tilde{x}^2} + \frac{\partial^2\tilde{\phi}}{\partial\tilde{y}^2} + \left(\frac{\omega^2}{c_l^2} + \lambda\right)\tilde{\phi} = 0 \quad \text{and} \quad \frac{\partial^2\tilde{\boldsymbol{\psi}}}{\partial\tilde{x}^2} + \frac{\partial^2\tilde{\boldsymbol{\psi}}}{\partial\tilde{y}^2} + \left(\frac{\omega^2}{c_s^2} + \lambda\right)\tilde{\boldsymbol{\psi}} = 0, \tag{17}$$

where $\lambda = -k^2$. $c_l$ and $c_s$ are the bulk velocities of longitudinal and shear waves respectively.

Free or Dirichlet boundary conditions couple the potentials $\tilde{\phi}$ and $\tilde{\boldsymbol{\psi}}$ so that fully analytical solutions are not achievable. Instead, the following mixed boundary conditions are considered:

$$\tilde{u}_x = 0,\ \tilde{\sigma}_{xy} = 0,\ \tilde{\sigma}_{xz} = 0 \text{ at } \tilde{x} = \pm\tilde{\ell}_x \quad \text{and} \quad \tilde{u}_y = 0,\ \tilde{\sigma}_{xy} = 0,\ \tilde{\sigma}_{yz} = 0 \text{ at } \tilde{y} = \pm\tilde{\ell}_y. \tag{18}$$

It can be shown that such boundary conditions yield uncoupled boundary conditions for $\tilde{\phi}$ and $\tilde{\boldsymbol{\psi}}$:

$$\begin{cases} \frac{\partial\tilde{\phi}}{\partial\tilde{x}} = 0 & \text{at } \tilde{x} = \pm\tilde{\ell}_x \\ \frac{\partial\tilde{\phi}}{\partial\tilde{y}} = 0 & \text{at } \tilde{y} = \pm\tilde{\ell}_y \end{cases} \quad \begin{cases} \frac{\partial\tilde{\psi}_x}{\partial\tilde{x}} = 0 & \text{at } \tilde{x} = \pm\tilde{\ell}_x \\ \tilde{\psi}_x = 0 & \text{at } \tilde{y} = \pm\tilde{\ell}_y \end{cases} \quad \begin{cases} \tilde{\psi}_y = 0 & \text{at } \tilde{x} = \pm\tilde{\ell}_x \\ \frac{\partial\tilde{\psi}_y}{\partial\tilde{y}} = 0 & \text{at } \tilde{y} = \pm\tilde{\ell}_y \end{cases} \quad \begin{cases} \tilde{\psi}_z = 0 \text{at } \tilde{x} = \pm\tilde{\ell}_x \\ \tilde{\psi}_z = 0 \text{at } \tilde{y} = \pm\tilde{\ell}_y \end{cases}. \tag{19}$$

By separating the variables $\tilde{x}$ and $\tilde{y}$, the eigenvalues of the problem (17) and (19) are given by

$$\lambda_l^{(p,q)} = -\frac{\omega^2}{c_l^2} + \left(\frac{p\pi}{2\tilde{\ell}_x}\right)^2 + \left(\frac{q\pi}{2\tilde{\ell}_y}\right)^2, \quad \lambda_s^{(m,n)} = -\frac{\omega^2}{c_s^2} + \left(\frac{m\pi}{2\tilde{\ell}_x}\right)^2 + \left(\frac{n\pi}{2\tilde{\ell}_y}\right)^2 \tag{20}$$

where $m, n, p, q$ are integers. These apparently formal calculations can be easily justified following the same ideas as in [33].

From Eq. (20), it can be seen that two spectra occur instead of one with scalar waveguides [30,43]. These two spectra correspond to compressional and shear waves respectively.

Without PML, the eigenvalues are real ($\widetilde{\ell}_x=\ell_x, \widetilde{\ell}_y=\ell_y$). In the initial unbounded problem, $\ell_x$ and $\ell_y$ tend to infinity: the spectra in terms of $\lambda=-k^2$ tend to two real continuous half-lines $[-\omega^2/c_l^2, +\infty[$ and $[-\omega^2/c_s^2, +\infty[$. These continua of eigenmodes are the so-called radiation modes, which are standing waves oscillating in the transverse directions. As simply shown by Eq. (20), each continuum is discretized by the truncation of cross-section at some finite distance.

With PML, the eigenvalues $\lambda$ are no longer real. The associated modes are still referred to as radiation modes since they are oscillating inside the PML. In the complex $\lambda$-plane, the eigenvalues of Eq. (20) belong to two angular sectors of origins $-\omega^2/c_l^2$ and $-\omega^2/c_s^2$. Each sector is limited by two half-lines of rotation angles $-2\arg\widetilde{\ell}_x$ and $-2\arg\widetilde{\ell}_y$. For clarity, these half-lines are denoted as

$$\left(\Delta_x^{l/s}\right): -\omega^2/c_{l/s}^2+\mathbb{R}^+/\widetilde{\ell}_x^2, \quad \left(\Delta_y^{l/s}\right): -\omega^2/c_{l/s}^2+\mathbb{R}^+/\widetilde{\ell}_y^2. \tag{21}$$

Each sector reduces to half-lines if $\arg\widetilde{\ell}_x=\arg\widetilde{\ell}_y$. When $|\widetilde{\ell}_x|$ and $|\widetilde{\ell}_y|$ increase, each spectrum of radiation modes gets denser and becomes continuous when $|\widetilde{\ell}_x|$ and $|\widetilde{\ell}_y|$ tend to $\infty$.

From Eq. (16), the rotation angles of $\left(\Delta_x^{l/s}\right)$ and $\left(\Delta_y^{l/s}\right)$ are respectively

$$-2\arg\widetilde{\ell}_x=-2\arg(d_x+\hat{\gamma}_x h_x), \quad -2\arg\widetilde{\ell}_y=-2\arg(d_y+\hat{\gamma}_y h_y). \tag{22}$$

This shows that each angle does not depend on the PML function profile itself (only its average value has an effect). It is noteworthy that the result given by Eq. (22) agrees with that obtained in Ref. [46] from a mathematical study of the scalar acoustic PML problem.

*Numerical example*: A concrete medium is considered. The material characteristics are given in Table 1. The PML interface positions are chosen as $d_x=d_y=d$ and the PML thicknesses are set to $h_x=h_y=3d$. The whole section is a square of half-thicknesses $\ell_x=\ell_y=4d$.

Fig. 2 shows the dimensionless spectrum $\lambda d^2$ at the dimensionless angular frequency $\Omega=\omega d/c_s=1$ with different values of $\hat{\gamma}_x$ and $\hat{\gamma}_y$.

As shown in Fig. 2a and c, the analytical eigenvalues given by Eq. (20) belong to two angular sectors. They are limited by two half-lines $\left(\Delta_x^{l/s}\right)$ and $\left(\Delta_y^{l/s}\right)$ defined in Eq. (21), rotated from the real axis by angles of $-74^\circ$ and $-113^\circ$ respectively, in agreement with Eq. (22). As can be seen from Fig. 2b and d, the angular sectors are reduced to half-lines when PML parameters are identical in both directions.

Numerical eigenvalues computed by the SAFE–CPML method are also shown in Fig. 2 (crosses). The finite elements are six-node triangles, whose average length is denoted by $l_e$. The PML functions $\gamma_x$ and $\gamma_y$ are parabolic, as defined in Eq. (15).

Numerical results are in agreement with the analytical ones, except for poles that are far from the real axis. Such poles indeed correspond to higher order modes (higher values of $p$, $q$, $m$, $n$ in Eq. (20)), which have high transverse wavenumbers, *i.e.* small transverse wavelengths. As in conventional eigenvalue FE problems, these modes are not well approximation due to the FE discretization. Refining the mesh allows to improve numerical results, as confirmed by Fig. 2c and d.

### 2.5.2. Embedded cylindrical elastic waveguides

In this subsection, numerical experiments are conducted on a cylindrical waveguide embedded into a softer solid matrix (the bulk velocities of the core are greater than in the surrounding medium). The test case is taken from the paper of Castaings and Lowe [24]. It consists of a steel cylinder of 10 mm radius buried in concrete. The material characteristics are given in Table 1. The steel is considered as elastic in this test ($\beta_l=\beta_s=0$, where $\beta_l$ and $\beta_s$ denote the longitudinal and shear bulk wave attenuations in Neper per wavelength).

Contrary to the previous subsection, the eigenspectrum now includes leaky modes in addition to radiation modes (note that no trapped modes occur in this test case).

*Numerical parameters*: The radius of the circular core section is denoted by $a$. A Dirichlet condition is applied at the exterior boundary of the truncated section. As shown in Fig. 3, finite elements are six-node triangles. PML functions are parabolic. The PML parameters in the $x$ and $y$ directions are identical: $d_x=d_y$, $h_x=h_y$, $\hat{\gamma}_x=\hat{\gamma}_y$. The PML thicknesses are equal to $0.9a$.

*Numerical eigenspectrum*: Fig. 4 represents the dimensionless numerical spectrum $\lambda a^2$ for various PML parameters at the dimensionless frequency $\Omega=\omega a/c_{s_0}=3.86$ (where $c_{s_0}$ is the shear wave velocity of the core). Two kinds of modes can be distinguished.

The first kind corresponds to radiation modes, yielding two spectra of origins $(-\omega^2/c_l^2, 0)$ and $(-\omega^2/c_s^2, 0)$, where $c_l$ and $c_s$ denote the bulk longitudinal and shear wave velocities of the embedding medium (concrete). Similarly to Section 2.5.1,

**Table 1**
Material characteristics.

| Material | $c_l$ (m/s) | $c_s$ (m/s) | $\rho$ (kg/m$^3$) | $\beta_l$ (Np/wavelength) | $\beta_s$ (Np/wavelength) |
|---|---|---|---|---|---|
| Steel | 5960 | 3260 | 7932 | 0.003 | 0.008 |
| Concrete | 4222.1 | 2637.5 | 2300 | 0.0 | 0.0 |
| Stiff stone | 5720 | 3300 | 2200 | 0.0 | 0.0 |
| Grout | 2810 | 1700 | 1600 | 0.043 | 0.100 |

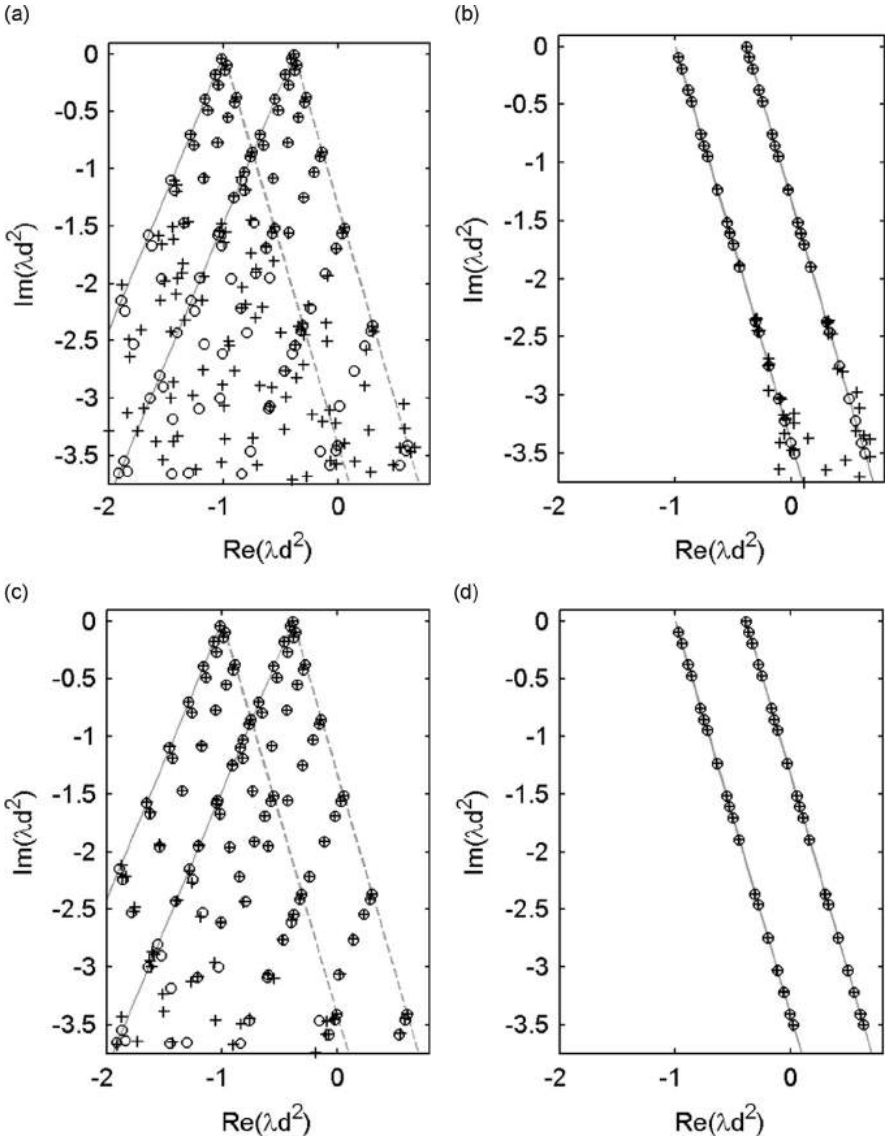


**Fig. 2.** Spectrum of homogeneous concrete medium with section truncated by Cartesian PML at $\Omega = 1$ ($d_x = d_y = d$, $h_x = h_y = 3d$) for (a) $\hat{\gamma}_x = 1+\mathrm{i}$, $\hat{\gamma}_y = 1+2\mathrm{i}$, $l_e = 0.4d$, (b) $\hat{\gamma}_x = \hat{\gamma}_y = 1+\mathrm{i}$, $l_e = 0.4d$, (c) $\hat{\gamma}_x = 1+\mathrm{i}$, $\hat{\gamma}_y = 1+2\mathrm{i}$, $l_e = 0.2d$ and (d) $\hat{\gamma}_x = \hat{\gamma}_y = 1+\mathrm{i}$, $l_e = 0.2d$. Crosses: SAFE–CPML results, circles: analytical results. Dashed lines: ($\Delta_x^{l/s}$), continuous lines: ($\Delta_y^{l/s}$).

these spectra correspond to the discretized continua of longitudinal and shear waves. Modes near the origins approximately form straight lines rotated from the real axis with angles equal to 107° in Fig. 4a and 61° in Fig. 4b. These angles are in agreement with the analytical formula given by Eq. (22). Far from their origins, radiation modes deviate from straight lines. Such modes are high order modes which the FE mesh can no longer approximate. This is confirmed by Fig. 4d, obtained with a refined mesh (the deviation occurs at a greater distance from the origins).

The rotation of radiation modes indeed allows to discover a second kind of modes, hidden in the original problem without PML. These modes are leaky modes. As observed in Fig. 4, the number of discovered leaky modes grows as the rotation angle is increased: compared to Fig. 4a ($\hat{\gamma}_x = \hat{\gamma}_y = 2+4\mathrm{i}$), two leaky modes are not present in Fig. 4b ($\hat{\gamma}_x = \hat{\gamma}_y = 5+4\mathrm{i}$). As expected from Section 2.4, more leaky modes can be found by increasing the argument of $\hat{\gamma}_x$ and $\hat{\gamma}_y$.

The rotation angles can also be modified by adjusting the PML interface position $d_x$ and $d_y$. Comparing Fig. 4c with a shows that high values of $d_x$ and $d_y$ reduce the rotation angles, in agreement with Eq. (22). In Fig. 4c, note that two leaky modes are spoiled by the deviation of high order radiation modes.

In practice for computing leaky modes, the PML interface should be set close to the core as suggested in Refs. [33,30,35]. From a physical point of view, a PML interface too far from the core allows leaky modes to significantly grow before entering

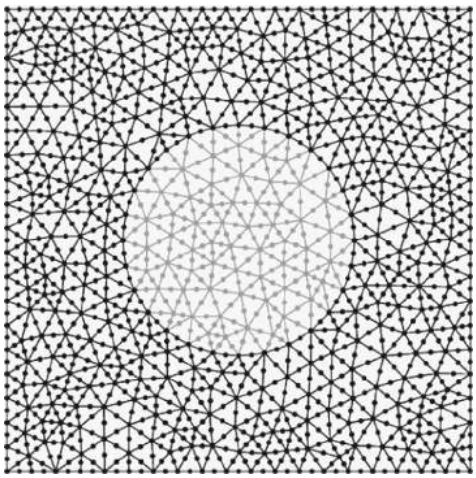

**Fig. 3.** Cross-section mesh of an embedded cylindrical bar using Cartesian PML ($l_e = 0.2a$).

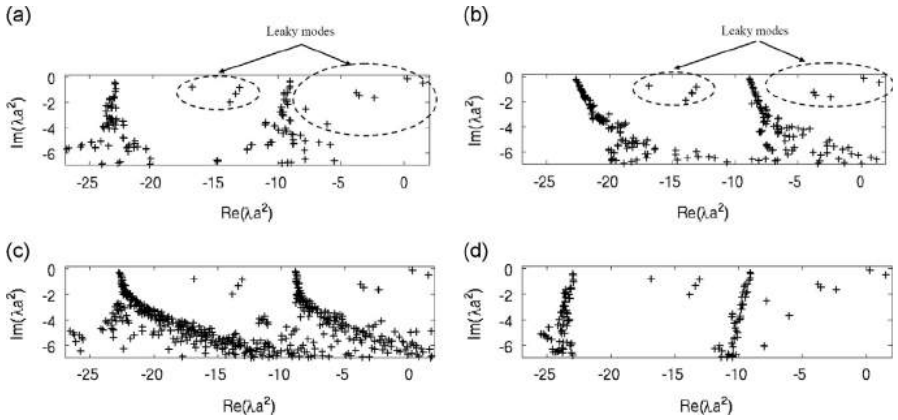


**Fig. 4.** Numerical spectrum of steel-concrete waveguide obtained at $\Omega = \omega a/c_{s_0} = 3.86$ by the SAFE–CPML method ($h_x = h_y = 0.9a$) for (a) $\hat{\gamma}_x = \hat{\gamma}_y = 2+4\mathrm{i}$, $d_x = d_y = 1.1a$, $l_e = 0.2a$, (b) $\hat{\gamma}_x = \hat{\gamma}_y = 5+4\mathrm{i}$, $d_x = d_y = 1.1a$, $l_e = 0.2a$, (c) $\hat{\gamma}_x = \hat{\gamma}_y = 2+4\mathrm{i}$, $d_x = d_y = 3a$, $l_e = 0.2a$, (d) $\hat{\gamma}_x = \hat{\gamma}_y = 2+4\mathrm{i}$, $d_x = d_y = 1.1a$, $l_e = 0.1a$.

the PML, which can deteriorate their computation. This has been mathematically justified by the increase of the norm of the resolvent of the eigenproblem [30,35].

The spectra of radiation modes can be densified by choosing higher values of PML parameters $(d_x, d_y)$, $(h_x, h_y)$ or $(\hat{\gamma}_x, \hat{\gamma}_y)$, which increases the complex half-thicknesses $|\widetilde{\ell}_x|$ and $|\widetilde{\ell}_y|$ as explained in Section 2.5.1. As an example, compared to Fig. 4a, these spectra get denser in Fig. 4b and c, for which the parameters $\mathrm{Re}\,\hat{\gamma}_x = \mathrm{Re}\,\hat{\gamma}_y$ and $d_x = d_y$ have been increased respectively.

## 3. SAFE–RPML method

In this section, the SAFE–RPML formulation is introduced. Following the same approach as in Section 2, the associated eigenspectrum is briefly studied through analytical and numerical experiments.

### 3.1. Combining SAFE and radial PML techniques

The formulation (1) is rewritten in cylindrical coordinates as follows:

$$\int_{\widetilde{\Omega}} \delta\widetilde{\boldsymbol{\epsilon}}^T \widetilde{\boldsymbol{\sigma}}\, \widetilde{r}\, \mathrm{d}\widetilde{r}\, \mathrm{d}\theta\, \mathrm{d}z - \omega^2 \int_{\widetilde{\Omega}} \widetilde{\rho}\, \delta\widetilde{\mathbf{u}}^T \widetilde{\mathbf{u}}\, \widetilde{r}\, \mathrm{d}\widetilde{r}\, \mathrm{d}\theta\, \mathrm{d}z = 0 \tag{23}$$

where $\widetilde{x} = \widetilde{r}\cos\theta$, $\widetilde{y} = \widetilde{r}\sin\theta$. The tilde notation represents the introduction of a PML along the radial direction. Note that in the above formulation, vectors and tensors are written in cylindrical coordinates but still expressed in the Cartesian basis.

In cylindrical coordinates, the operator $\mathbf{L}_{\widetilde{S}}$ of the strain–displacement relation (2) is

$$\mathbf{L}_{\widetilde{S}} = \mathbf{L}_x\left(\cos\theta\frac{\partial}{\partial\widetilde{r}} - \frac{\sin\theta}{\widetilde{r}}\frac{\partial}{\partial\theta}\right) + \mathbf{L}_y\left(\sin\theta\frac{\partial}{\partial\widetilde{r}} + \frac{\cos\theta}{\widetilde{r}}\frac{\partial}{\partial\theta}\right). \tag{24}$$

Applying the PML technique in the radial direction, the formulation (23) can be interpreted as the analytical continuation of the equilibrium equations into the complex radial coordinate $\widetilde{r}$, with

$$\widetilde{r}(r) = \int_0^r \gamma(\xi)\,\mathrm{d}\xi \tag{25}$$

where $\gamma(r)$ is a complex function satisfying

- $\gamma(r) = 1$ for $r \le d$
- $\mathrm{Im}\{\gamma\} > 0$ for $r > d$.

$d$ is the position of the PML interface. As shown in Fig. 5, the cross-section of a SAFE–RPML problem is typically a circle of radius $d+h$, $h$ denoting the PML thickness. Similarly to Cartesian PML, the boundary condition applied at the PML exterior boundary can be arbitrarily chosen.

From Eq. (25), the change of variable $\widetilde{r}\mapsto r$ yields for any function $\widetilde{f}$:

$$\frac{\partial\widetilde{f}}{\partial\widetilde{r}} = \frac{1}{\gamma}\frac{\partial f}{\partial r},\ \mathrm{d}\widetilde{r} = \gamma\,\mathrm{d}r \tag{26}$$

where $\widetilde{f}(\widetilde{r},\theta,z) = f(r,\theta,z)$. Applying this change of variable and the SAFE method to Eq. (24) leads to an expression identical to Eq. (8), with

$$\mathbf{L}_S = \mathbf{L}_x\left(\frac{\cos\theta}{\gamma}\frac{\partial}{\partial r} - \frac{\sin\theta}{\widetilde{r}}\frac{\partial}{\partial\theta}\right) + \mathbf{L}_y\left(\frac{\sin\theta}{\gamma}\frac{\partial}{\partial r} + \frac{\cos\theta}{\widetilde{r}}\frac{\partial}{\partial\theta}\right). \tag{27}$$

Before FE discretization, the formulation must be transformed back to Cartesian coordinates. The operator $\mathbf{L}_S$ then becomes

$$\mathbf{L}_S = \mathbf{L}_x\left[\left(\frac{x^2}{\gamma r^2} + \frac{y^2}{\widetilde{r}r}\right)\frac{\partial}{\partial x} + \left(\frac{1}{\gamma r^2} - \frac{1}{\widetilde{r}r}\right)xy\frac{\partial}{\partial y}\right] + \mathbf{L}_y\left[\left(\frac{1}{\gamma r^2} - \frac{1}{\widetilde{r}r}\right)xy\frac{\partial}{\partial x} + \left(\frac{y^2}{\gamma r^2} + \frac{x^2}{\widetilde{r}r}\right)\frac{\partial}{\partial y}\right]. \tag{28}$$

Finally, the FE discretization of the formulation along the cross-section yields the same form of eigenproblem as Eq. (9), but with the following elementary matrices:

$$\mathbf{K}_1^e = \int_e \mathbf{N}^{eT}\mathbf{L}_S^T\mathbf{C}\mathbf{L}_S\mathbf{N}^e\frac{\widetilde{r}\gamma}{r}\,\mathrm{d}x\,\mathrm{d}y,\ \mathbf{K}_2^e = \int_e \mathbf{N}^{eT}\mathbf{L}_S^T\mathbf{C}\mathbf{L}_z\mathbf{N}^e\frac{\widetilde{r}\gamma}{r}\,\mathrm{d}x\,\mathrm{d}y$$
$$\mathbf{K}_3^e = \int_e \mathbf{N}^{eT}\mathbf{L}_z^T\mathbf{C}\mathbf{L}_z\mathbf{N}^e\frac{\widetilde{r}\gamma}{r}\,\mathrm{d}x\,\mathrm{d}y,\ \mathbf{M}^e = \int_e \rho\mathbf{N}^{eT}\mathbf{N}^e\frac{\widetilde{r}\gamma}{r}\,\mathrm{d}x\,\mathrm{d}y.$$

### 3.2. PML absorbing function

As suggested for Cartesian PML, a parabolic profile independent of frequency is chosen for the radial PML function $\gamma$, expressed as follows:

$$\gamma(r) = \begin{cases} 1 & \text{if } r \le d \\ 1 + 3(\hat{\gamma}-1)\left(\frac{r-d}{h}\right)^2 & \text{if } r > d \end{cases} \tag{29}$$

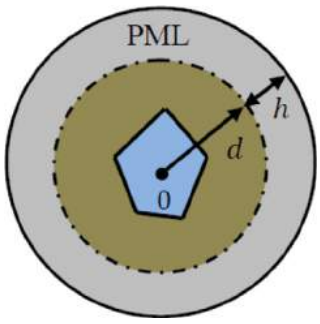


**Fig. 5.** Open waveguide with cross-section truncated by radial PML.

where $\hat{\gamma}$ is the average value of $\gamma$ in the radial PML region:

$$\hat{\gamma} = \frac{1}{h}\int_d^{d+h} \gamma(\xi)\, \mathrm{d}\xi \tag{30}$$

For radial PML, the influence of $\hat{\gamma}$ on wave absorption can be illustrated by considering wave solutions in cylindrical coordinates. In the PML region ($r > d$), the wave fields can be expressed by a combination of Hankel functions. Assuming negligible refection from the PML exterior boundary ($r = \ell_r = d+h$), the radial dependence of wave fields is written as $H_n^{(1)}(k_{l/s}\tilde{r})$, where $H_n^{(1)}$ is the Hankel function of first kind and $k_{l/s}$ denotes the radial wavenumber (shear or longitudinal).

Let us denote the complex radius $\tilde{\ell}_r$ by

$$\tilde{\ell}_r = \int_0^{\ell_r} \gamma(\xi)\, \mathrm{d}\xi. \tag{31}$$

For simplicity, we assume that the radial wavelength is small enough compared to $d$ and $|\tilde{\ell}_r|$ (*i.e.* $|k_{l/s}d| \gg 1$ and $|k_{l/s}\tilde{\ell}_r| \gg 1$). Then, the wave solutions at the PML interface and at the PML end, written in terms of $H_n^{(1)}(k_{l/s}d)$ and $H_n^{(1)}(k_{l/s}\tilde{\ell}_r)$ respectively, asymptotically behave like $\mathrm{e}^{\mathrm{i}k_{l/s}d}/\sqrt{k_{l/s}d}$ and $\mathrm{e}^{\mathrm{i}k_{l/s}\tilde{\ell}_r}/\sqrt{k_{l/s}\tilde{\ell}_r} = \left(\mathrm{e}^{\mathrm{i}k_{l/s}d}/\sqrt{k_{l/s}\tilde{\ell}_r}\right)\mathrm{e}^{\mathrm{i}k_{l/s}\hat{\gamma}h}$ respectively. Therefore, the total attenuation from the interface to the PML end can then be approximated by

$$\frac{|H_n^{(1)}(k_{l/s}\tilde{\ell}_r)|}{|H_n^{(1)}(k_{l/s}d)|} \simeq \frac{\exp(-|k_{l/s}||\hat{\gamma}|h\sin(\arg k_{l/s} + \arg\hat{\gamma}))}{\sqrt{\left|1+\dfrac{\hat{\gamma}h}{d}\right|}}. \tag{32}$$

Concerning the numerator (exponential term), it can be noticed that the radial wavenumber $k_{l/s}$ plays the same role as in Eq. (12). Therefore, the influence of $\hat{\gamma}$ is similar to the effect of $\hat{\gamma}_x$ and $\hat{\gamma}_y$ with the Cartesian PML method, already described in Section 2.4.

The slight difference with radial PML is that this exponential term is modulated by an attenuation factor given by $1/\sqrt{|1+\hat{\gamma}h/d|}$. Without PML ($\hat{\gamma} = 1$), this attenuation factor corresponds to the geometrical attenuation of cylindrical waves and is equal to $1/\sqrt{1+h/d}$. A radial PML enhances this attenuation factor as $|\hat{\gamma}|$ increases.

### 3.3. Eigenspectrum (homogeneous medium)

The SAFE–RPML eigenspectrum is now briefly analyzed in order to understand how a radial PML acts on the eigenspectrum. The analytical solution of a homogeneous medium is derived. Compared to Cartesian coordinates, it is difficult with cylindrical coordinates to find appropriate boundary conditions leading to fully analytical solutions of the elastic problem. Therefore, the analytical solution of this section is obtained for the scalar wave equation of acoustics. The elastic problem will be handled through numerical experiments. For conciseness, this section is limited to the case of a homogeneous medium. The reader is referred to Appendix A for the analysis of a cylindrical core waveguide embedded into an infinite medium, where similarly to the homogeneous case, the analytical solution for an acoustic waveguide is first studied and numerical experiments in the elastic case are then performed.

A homogeneous medium can be considered as an open homogeneous waveguide of unbounded cross-section. Introducing a radial PML of finite thickness $h$ and of position $d$, the cross-section becomes bounded and of radius $\ell_r = d+h$.

*Analytical solution for a scalar problem*: The acoustic wave equation written in cylindrical coordinates is

$$\frac{\mathrm{d}^2\tilde{\phi}}{\mathrm{d}\tilde{r}^2} + \frac{1}{\tilde{r}}\frac{\mathrm{d}\tilde{\phi}}{\mathrm{d}\tilde{r}} - \frac{n^2}{\tilde{r}^2}\tilde{\phi} + \left(\frac{\omega^2}{c^2} - k^2\right)\tilde{\phi} = 0 \tag{33}$$

where $\tilde{\phi}$ denotes the acoustic variable, $n$ is the circumferential order and $c$ is the acoustic wave velocity.

The solution of Eq. (33) is $\tilde{\phi}(\tilde{r}) = AJ_n(k_r\tilde{r}) + BY_n(k_r\tilde{r})$, where $k_r$ is the radial wavenumber satisfying the relation $k_r^2 + k^2 = \omega^2/c^2$. $J_n$ and $Y_n$ are Bessel functions of the first kind and of the second kind respectively. Since $Y_n(k_r\tilde{r})$ tends to infinity when $|\tilde{r}|$ tends to 0, $B$ must vanish. A Dirichlet condition $\tilde{\phi}(\tilde{\ell}_r) = 0$ is applied at the PML exterior boundary, yielding the characteristic equation: $J_n(k_r\tilde{\ell}_r) = 0$. The eigenvalues are hence

$$\lambda_{nm} = -k_{nm}^2 = -\frac{\omega^2}{c^2} + \left(\frac{\chi_{nm}}{\tilde{\ell}_r}\right)^2 \tag{34}$$

where $\chi_{nm}$ denotes the $m$th zero of $J_n(x)$.

Without PML ($\tilde{\ell}_r = \ell_r$), the eigenvalues are real. In the initial problem of infinite section, $R$ tends to infinity and the $\lambda$ spectrum becomes a real continuous half-line $[-\omega^2/c^2, +\infty[$. This continuum can be referred to as the essential spectrum of radiation modes [30,35].

With a radial PML, the eigenvalues $\lambda$ of radiation modes become complex. In the complex plane, they belong to a discretized half-line of rotation angle

$$-2\arg\tilde{\ell}_r = -2\arg(d+\hat{\gamma}h). \tag{35}$$

This coincides with the result obtained in Ref. [35] for the computation of acoustic resonances with a radial PML method. Similarly to the Cartesian PML (see Section 2.5.1), the discretized half-line gets denser when $|\widetilde{\ell}_r|$ increases and the rotation angle is independent of the radial PML function profile.

*Numerical solution for an elastic problem*: The radiation modes of a homogeneous elastic problem are now computed by the SAFE–RPML method. A concrete medium is considered. Finite elements are six-node triangles, whose average length $l_e$ is chosen as $0.1d$. The PML function $\gamma$ is parabolic, as defined by Eq. (29). The PML thickness is set to $h=3d$. The radius of the whole cross-section is $\ell_r=4d$.

Fig. 6 shows the spectrum at the dimensionless frequency $\Omega=\omega d/c_s=1$ with $\hat{\gamma}=2+4\mathrm{i}$. Instead of one half-line with the scalar problem, the eigenvalues belong to two discretized half-lines starting from $-\omega^2/c_l^2$ and $-\omega^2/c_s^2$. As already found in Section 2.5.1, these two spectra of radiation modes correspond to longitudinal and shear waves respectively (their deviation from straight lines being due to the poor FE approximation of higher order modes).

The half-lines are rotated from the real axis with equal rotation angles, approximately equal to 118°. This angle is in agreement with the acoustic formula (35).

## 4. Dispersion curves

In this section, the dispersion curves of leaky and trapped modes are computed by both the SAFE–CPML and the SAFE–RPML methods for three test cases taken from the literature. The calculation of modal properties in open waveguides is presented first (kinetic energy, energy velocity and group velocity).

### 4.1. Kinetic energy

By analytical continuation into complex coordinates, the cross-section and time averaged kinetic energy can be defined as $\overline{E}_k=\frac{1}{2}\int_{\widetilde{S}}\widetilde{\rho}\widetilde{\mathbf{v}}\cdot\widetilde{\mathbf{v}}\,\mathrm{d}\widetilde{S}$, where $\widetilde{\mathbf{v}}=\mathrm{d}\widetilde{\mathbf{u}}/\mathrm{d}t$ is the velocity vector and bars denote time averaging over one period. As already mentioned in Section 2.2, $\widetilde{S}$ denotes the waveguide cross-section including the truncated PML.

This definition is rewritten by using the change of variables from complex to real coordinates as

$$\overline{E}_k=\frac{1}{4}\int_S\rho\,\mathrm{Re}\left(\mathbf{v}^*\cdot\mathbf{v}\right)\,\mathrm{d}\widetilde{S}=\frac{\omega^2}{4}\int_S\rho\,\mathrm{Re}\left(\mathbf{u}^*\cdot\mathbf{u}\right)\,\mathrm{d}\widetilde{S}=\frac{\omega^2}{4}\int_S\rho\mathbf{u}^*\cdot\mathbf{u}\,\mathrm{d}\widetilde{S}\tag{36}$$

where $\mathrm{d}\widetilde{S}=\gamma_x\gamma_y\,\mathrm{d}x\,\mathrm{d}y$ for the SAFE–CPML method and $\mathrm{d}\widetilde{S}=\widetilde{r}\gamma/r\,\mathrm{d}x\,\mathrm{d}y$ for the SAFE–RPML method. The superscript $*$ refers to the complex conjugate transpose.

The FE expression of kinetic energy is given by

$$\overline{E}_k=\frac{\omega^2}{4}\sum_e\int_{S^e}\rho\mathbf{u}^{e*}\cdot\mathbf{u}^e\,\mathrm{d}\widetilde{S}=\frac{\omega^2}{4}\sum_e\mathbf{U}^{e*}\left(\int_{S^e}\rho\mathbf{N}^{eT}\mathbf{N}^e\,\mathrm{d}\widetilde{S}\right)\mathbf{U}^e=\frac{\omega^2}{4}\mathbf{U}^*\mathbf{M}\mathbf{U}.\tag{37}$$

This result is the same as for closed waveguides (without PML) [21,47]. In the presence of PML, the slight difference is that $\mathbf{M}$ is no longer real and the kinetic energy becomes complex.

### 4.2. Energy velocity

For closed waveguides, the energy velocity is defined as follows [45]:

$$v_e=\frac{\mathrm{Re}\left(\int_S\overline{\mathbf{P}}\cdot\mathbf{n}\,\mathrm{d}S\right)}{\mathrm{Re}(\overline{E}_k)+\mathrm{Re}(\overline{E}_p)}\tag{38}$$

where $\mathbf{P}$ is the complex Poynting vector given by $P_j=-\frac{1}{2}v_i^*\sigma_{ij}$. $\overline{E}_p$ denotes the cross-section and time averaged potential energy, given by $\overline{E}_p=\frac{1}{2}\int_S\overline{\boldsymbol{\epsilon}^*\boldsymbol{\sigma}}\,\mathrm{d}S$. $\mathbf{n}$ is the unit vector normal to the cross section (in the $z$ direction). The potential energy $\overline{E}_p$ and the complex power flow $\int_S\overline{\mathbf{P}}\cdot\mathbf{n}\,\mathrm{d}S$ can be post-processed from SAFE matrices thanks to the following formula [47], here

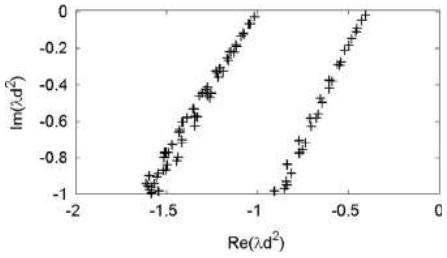


**Fig. 6.** Dimensionless spectrum of homogeneous concrete medium computed with the SAFE–RPML method at $\omega d/c_s=1$. PML parameters are $h=3d$, $\hat{\gamma}=2+4\mathrm{i}$ ($l_e=0.2d$).

modified for complex wavenumbers:

$$\int_S \overline{\mathbf{P}} \cdot \mathbf{n}\, ds = -\frac{i\omega}{2}\mathbf{U}_c^*(\mathbf{K}_2 + ik\mathbf{K}_3)\mathbf{U}, \quad \overline{E}_k = \frac{\omega^2}{4}\mathbf{U}^*\mathbf{M}\mathbf{U}, \quad \overline{E}_p = \frac{1}{4}\mathbf{U}^*\left(\mathbf{K}_1 + ik\mathbf{K}_2 - ik^*\mathbf{K}_2^T + k^*k\mathbf{K}_3\right)\mathbf{U}. \tag{39}$$

For open waveguides, the definition of $v_e$ is similar to Eq. (38). However the integrals on the cross-section are usually restricted to the core region [48,49], which avoids the transverse growth of leaky modes at infinity. Hence, Eqs. (38) and (39) still apply for open waveguides but $S$ must be replaced with $S_0$, which denotes the cross-section of the core.

### 4.3. Group velocity

The group velocity is usually defined by $v_g = \partial\omega/\partial k$. The calculation of $v_g$ can be achieved from the derivative of the SAFE eigensystem with respect to $k$, as done in Refs. [21,50]. However, the definition $v_g = \partial\omega/\partial k$ only applies when the axial wavenumber $k$ is real. In open waveguides, the axial wavenumber of leaky modes is complex. The proper definition of group velocity for damped modes is [48,51]

$$v_g = \frac{d\omega}{d\,\mathrm{Re}(k)} = \left[\mathrm{Re}\left(\frac{dk}{d\omega}\right)\right]^{-1}. \tag{40}$$

Let $(k_j, \mathbf{U}_j^+)$ denote an eigensolution of Eq. (9):

$$\left(\mathbf{K}_1 - \omega^2\mathbf{M} + ik_j(\mathbf{K}_2 - \mathbf{K}_2^T) + k_j^2\mathbf{K}_3\right)\mathbf{U}_j^+ = \mathbf{0}. \tag{41}$$

Taking the derivative of Eq. (41) with respect to $\omega$ yields

$$\left(-2\omega\mathbf{M} + i\frac{dk_j}{d\omega}\left(\mathbf{K}_2 - \mathbf{K}_2^T\right) + 2k_j\frac{dk_j}{d\omega}\mathbf{K}_3\right)\mathbf{U}_j^+ = -\left(\mathbf{K}_1 - \omega^2\mathbf{M} + ik_j(\mathbf{K}_2 - \mathbf{K}_2^T) + k_j^2\mathbf{K}_3\right)\frac{d\mathbf{U}_j^+}{d\omega}. \tag{42}$$

As mentioned in Section 2.2, $(-k_j, \mathbf{U}_j^-)$ is also a solution of Eq. (9). Left-multiplying Eq. (42) by the transpose of $\mathbf{U}_j^-$ allows the right-hand term to vanish, which leads to the group velocity of the $j$th mode:

$$v_{g_j} = \left[\mathrm{Re}\left\{\frac{2\omega\mathbf{U}_j^{-T}\mathbf{M}\mathbf{U}_j^+}{\mathbf{U}_j^{-T}\left(i(\mathbf{K}_2 - \mathbf{K}_2^T) + 2k_j\mathbf{K}_3\right)\mathbf{U}_j^+}\right\}\right]^{-1}. \tag{43}$$

The calculation of $v_g$ for a given mode hence requires its opposite-going counterpart.

As opposed to the energy velocity, it should be noticed that the group velocity may generally be not appropriate for attenuated waves [48] (including leaky waves). Yet, the group velocity still applies for trapped modes, which are non-attenuated (in non-dissipative media).

### 4.4. Modal filtering

According to Sections 2.5, 3.3 and Appendix A, the SAFE–PML methods provide many radiation modes in addition to the modes of interest (leaky or trapped). Since radiation modes mainly oscillate inside the PML, they are dependent on the choice of PML parameters and cannot be considered as intrinsic to the physics. A large number of radiation modes perturbs the visualization of dispersion curves of trapped and leaky modes. A modal filtering must be processed to identify and remove these radiation modes. The filtering criterion proposed in this paper is based on the ratio of kinetic energy in the PML region over the kinetic energy of the whole cross-section. Physical modes are then identified if this criterion is smaller than a user-defined value $\eta_{\max}$:

$$\frac{|\overline{E}_{k_{PML}}|}{|\overline{E}_k|} < \eta_{max} \tag{44}$$

where $\overline{E}_{k_{PML}}$ is defined from Eq. (36) by replacing $S$ with $S_{PML}$, which denotes the cross-section restricted to the PML region. Note that the modulus must be used in Eq. (44) since the kinetic energy is complex in the presence of PML. Note that $\eta_{max}$ is independent of frequency in this paper. For a given FE mesh, the appropriate value of $\eta_{max}$ essentially depends on the PML parameters, which have been assumed as constant with frequency (see Sections 2.4 and 3.2).

### 4.5. Results

Three examples of open waveguides are considered. The first one has already been described in Sections 2.5.2 and Appendix A (steel cylinder in concrete). The second test case is taken from the work of Pavlakovic [19] and is a 1 mm radius steel cylinder in stiff stone. This case is of interest due to the existence of one trapped mode. The third example, taken from Ref. [26], is a steel square bar buried in a viscoelastic grout, for which no analytical solution is available. Material characteristics are given in Table 1. The steel is considered as elastic for the first two examples ($\beta_l = \beta_s = 0$) and as viscoelastic in the last one ($\beta_l = 0.003$, $\beta_s = 0.008$).

The PML position and thickness are set to $h_x = h_y = h = 0.9a$ and $d_x = d_y = d = 1.1a$, where $a$ denotes the radius of the cylindrical core for the first two test cases and the half-thickness of the squared core for the third case. Note that with the SAFE–RPML formulation, the PML could be set to $d = a$ when the core is cylindrical. A Dirichlet condition is applied at the PML exterior boundaries (numerical tests have shown that other boundary conditions yield small differences on trapped and leaky modes). The finite elements are six-node triangles whose length satisfies the following meshing criterion: $l_e \leq \lambda_m/5$, where $\lambda_m = \min(c_s)/\max(f)$ ($\min(c_s)$ is the lowest shear velocity of the problem). The SAFE–PML dispersion curves are shown after modal filtering, the parameter $\eta_{max}$ being specified for each example.

Let us consider the first test case. The FE meshes are shown in Figs. 3 and 7. According to the eigenspectrum analyses in Sections 2.5.2 and Appendix A, the eigenvalues of leaky modes are located around $|\omega/c_l|$ in the complex plane. The computation has been centered around $+\omega/c_l$ in order to reduce the number of eigenvalues to solve. In this way, only positive-going modes are calculated. 300 modes have been computed at each frequency with the SAFE–CPML method, against 150 modes with the SAFE–RPML method. Actually, the SAFE–RPML method appears more advantageous from a computational point of view for this example because the core is of circular shape: the PML region can be smaller, which also decreases the number of radiation modes to solve. Besides, 5139 dofs (degrees of freedom) are generated with the SAFE–CPML method against 3975 dofs with the SAFE–RPML method.

In order to illustrate the efficiency of the filtering criterion proposed in Section 4.4, Fig. 8 shows the phase velocity dispersion curves obtained by both SAFE–PML methods without modal filtering. Clearly, the presence of many radiation modes in the dispersion curves prevents the identification of leaky modes.

Fig. 9 represents the kinetic energy ratio of modes obtained by the SAFE–RPML method at 200 kHz. It can be observed that radiation modes yield a ratio approximatively equal to 1 because they mainly oscillate in the PML region, as opposed to leaky modes. Fig. 9 shows that the energy kinetic ratio allows to well distinguish the radiation modes from the others and that an appropriate value of the threshold $\eta_{max}$ is rather easy to choose (here, a threshold value of 0.75 turns out to be satisfying).

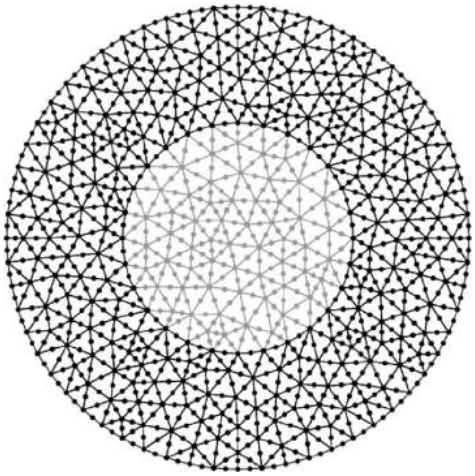

**Fig. 7.** Cross-section mesh of an embedded cylindrical bar using radial PML ($l_e = 0.2a$).

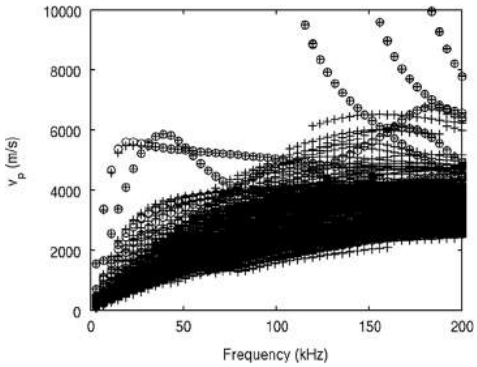


**Fig. 8.** Phase velocity dispersion curves of steel-concrete cylindrical waveguide without filter ($\eta_{max} = 1$). Crosses: SAFE–CPML results, circles: SAFE–RPML results. PML parameters are $\hat{\gamma}_x = \hat{\gamma}_y = \hat{\gamma} = 2+4\mathrm{i}$, $d_x = d_y = d = 1.1a$, $h_x = h_y = h = 0.9a$.

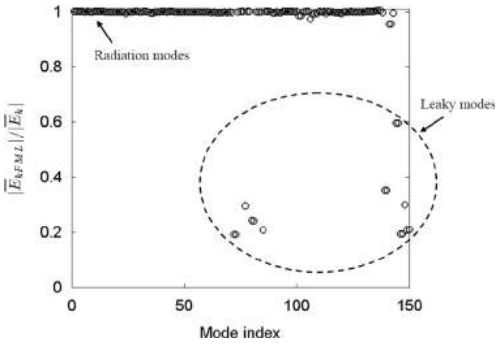


**Fig. 9.** Kinetic energy ratio of modes in steel-concrete cylindrical waveguide obtained by the SAFE–RPML method at 200 kHz. PML parameters are $\hat{\gamma}=2+4\mathrm{i}$, $d=1.1a$, $h=0.9a$.

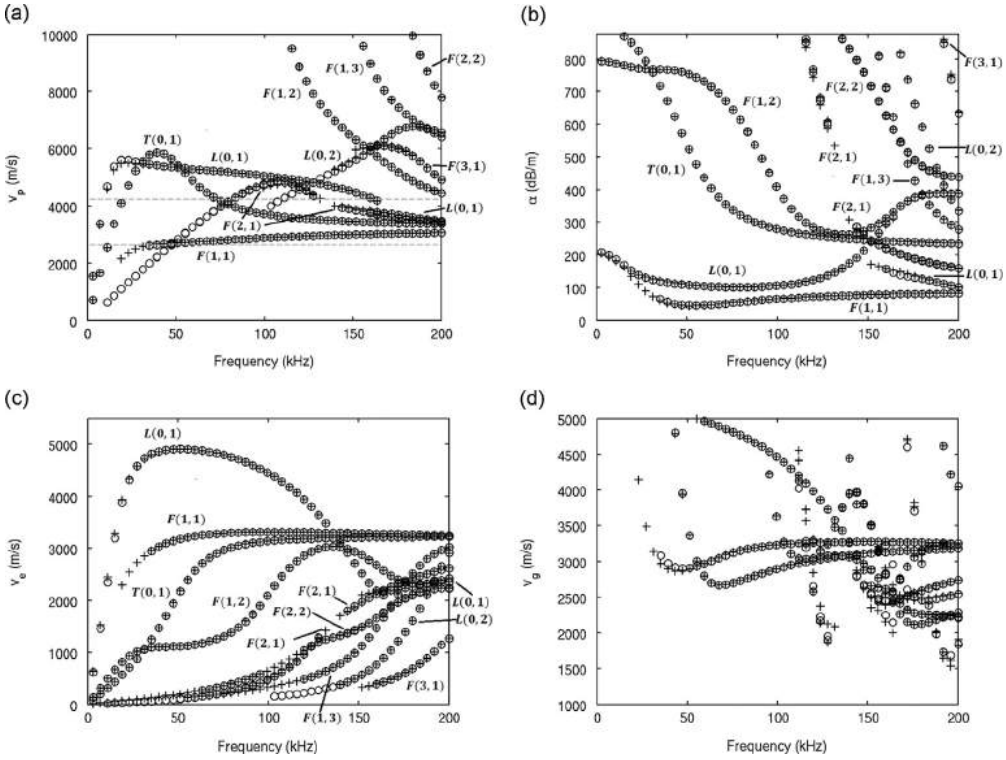


**Fig. 10.** Dispersion curves of steel-concrete cylindrical waveguide for (a) phase velocity, (b) axial attenuation, (c) energy velocity and (d) group velocity. Crosses: SAFE–CPML results ($\eta_{max}=0.9$), circles: SAFE–RPML results ($\eta_{max}=0.75$). PML parameters are $\hat{\gamma}_x=\hat{\gamma}_y=\hat{\gamma}=2+4\mathrm{i}$, $d_x=d_y=d=1.1a$, $h_x=h_y=h=0.9a$.

Fig. 10 represents the dispersion curves with modal filtering. The curves of leaky modes are now clearly observed (compare Figs. 10a and 8). We point out that other energy ratio, based on Poynting vector or potential energy, have been experimented. However, our numerical tests have not shown any improvement in the filtering of radiation modes (results not shown for paper conciseness). Therefore, the kinetic energy based ratio is preferred owing to its simpler post-processing.

The axial attenuation expressed in dB/m (Fig. 10b) is defined by $\alpha=8.686\,\mathrm{Im}\,k$. Note that for calculating the group velocity (Fig. 10d), it was also necessary to compute the negative-going modes by searching eigenvalues around $-\omega/c_l$.

The dispersion curves obtained with the SAFE–CPML and the SAFE–RPML methods are superimposed, which tends to show that both methods yield the same order of accuracy. The curves shown in Fig. 10a–c are in good agreement with the results obtained by the SAFE-AL technique [24] or the SAFE–BEM method [26]. This validates the SAFE–PML approaches proposed in this paper. Note that the AL thickness used in Ref. [24] is 16 times larger than the core radius, so approximately 16 times larger than the PML used in this paper, yielding dispersion curves that are not so accurate as those obtained by the PML method.

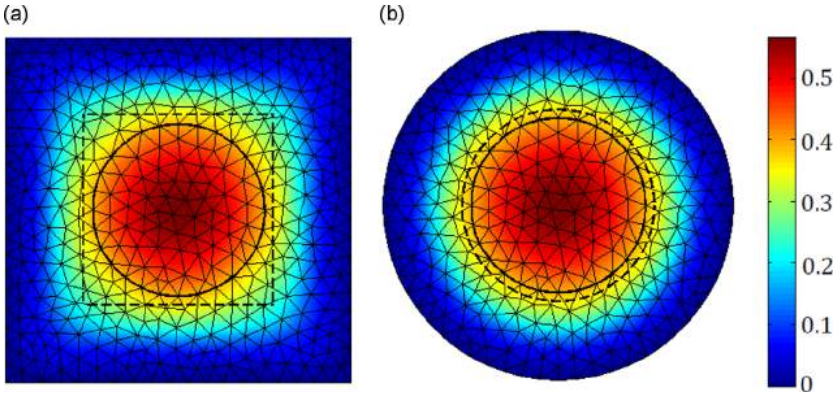


**Fig. 11.** Modulus of axial displacement of the L(0,1) mode at 103.8 kHz (steel-concrete cylindrical waveguide) obtained by (a) SAFE–CPML and (b) SAFE–RPML methods. Dashed line: PML interface, continuous line: material interface.

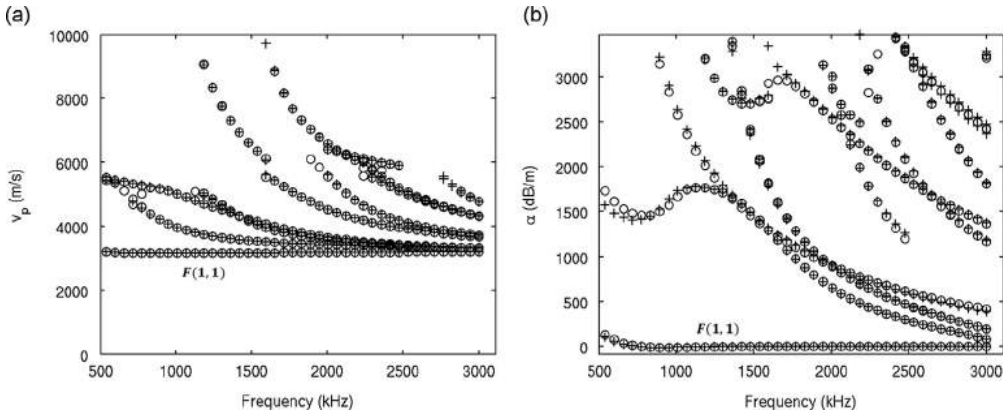


**Fig. 12.** Dispersion curves of steel-stiff stone cylindrical waveguide for (a) phase velocity and (b) axial attenuation. Crosses: SAFE–CPML results ($\eta_{max} = 0.75$), circles: SAFE–RPML results ($\eta_{max} = 0.7$). PML parameters are $\hat{\gamma}_x = \hat{\gamma}_y = \hat{\gamma} = 4+4\mathrm{i}$, $d_x = d_y = d = 1.1a$, $h_x = h_y = h = 0.9a$.

It can be observed that the group velocity curves differ quite significantly from the energy velocity (compare Fig. 10c and d). One recalls that Bernard et al. [48] have shown that this difference disappears for modes with no attenuation but always exists for attenuated modes (such as leaky modes).

Fig. 11 shows the axial displacement field of a given mode, here the leaky compressional $L(0,1)$ mode, obtained with each method at 103.8 kHz. In the PML region, it can be observed that the CPML absorption strength is non-axially symmetric, as opposed to the RPML method. However, the modeshapes are found to be identical in the physical region (*i.e.* excluding the PML zone).

From a physical point of view, it can be noticed that the $L(0,1)$ and $F(2,1)$ curves are discontinuous around 163 kHz and 135 kHz respectively. These discontinuities are physical and occur when the phase velocity $v_p$ crosses the bulk wave velocities $c_l$ or $c_s$ of the surrounding medium (concrete) – see Fig. 10a for instance. For a given mode, the partial longitudinal (or shear) wave actually changes from leaky to trapped when $v_p$ becomes lower than $c_l$ (or $c_s$) [19].

In practice, the calculation of modes having a phase velocity at the vicinity of $c_l$ and $c_s$ can be difficult due to the undefined nature of partial waves (Fig. 10) [19,24,26]. This problem is also encountered with SAFE–PML methods because the transverse wavenumbers become small when $v_p$ is close to $c_l$ or $c_s$. According to Eqs. (12) and (32), large values of PML thickness or PML function would be required to sufficiently attenuate waves.

The same problem is also encountered for the computation of modes at low frequencies. For instance, in Fig. 10, leaky modes are still found to exist for phase velocities of a given mode smaller than the bulk shear velocity of the surrounding media, which does not seem physically correct. These low frequency modes are indeed not properly computed. Restricting the analysis to a low frequency range, one remedy would be to enhance the PML absorption strength by increasing the PML thickness or the average value of PML functions.

Fig. 12 represents the phase velocity and the attenuation for the second test case (steel-stiff stone waveguide). The FE meshes used with Cartesian and radial PML methods are the same as in the first test case. In this example, the $F(1,1)$ mode is trapped ($\mathrm{Im}\, k = 0$) while the other modes are leaky. In the initial problem without PML, trapped modes are located on the

real axis of the complex plane. Their wavenumber in absolute value is larger than $\omega/c_s$ [4,52]. Hence in this test case, the computation has been centered around $\omega/c_s$ instead of $\omega/c_l$. For each frequency, 265 and 180 modes have been solved for the SAFE–CPML and the SAFE–RPML methods respectively.

Since both trapped and leaky modes exist, the real and imaginary parts of $\hat{\gamma}_x$, $\hat{\gamma}_y$ and $\hat{\gamma}$ have been set to a sufficiently large value ($\hat{\gamma}_x = \hat{\gamma}_y = \hat{\gamma} = 4+4\mathrm{i}$) in order to attenuate both kinds of modes. Results are in agreement with those of Ref. [19] calculated by an analytical approach. In particular, the trapped mode is well approximated by SAFE–PML methods (except for lowest frequencies, for the same reason as mentioned in the previous test case).

For the third test case (viscoelastic steel-grout squared waveguide), the SAFE–CPML method has been preferred because the cross-section of the core is of rectangular shape. The FE mesh is shown in Fig. 13, generating 5127 dofs. 600 modes have been solved, centered round $\omega/c_l$. Fig. 14 shows the dispersion curves in phase velocity and attenuation. The modes have been labeled as in Ref. [26]. Here again, numerical results are in good agreement with the literature results, obtained in Ref. [26] with a SAFE–BEM technique. Note that a poor approximation of lowest frequency modes possibly occurs for the same reasons as in the previous test case.

## 5. Conclusion

In this work, SAFE–PML methods have been applied to compute the eigenmodes of three-dimensional open elastic waveguides. Two kinds of PML, Cartesian and radial, have been implemented.

The spectral objects obtained from the proposed numerical approach have been clarified and the effects of PML parameters on radiation and leaky modes have been highlighted through analytical solutions and numerical experiments. The radiation modes of open elastic waveguides are shown to belong to two continua corresponding to longitudinal and shear waves respectively. The PML rotates these continua in the complex plane. The truncation of the PML discretizes them,

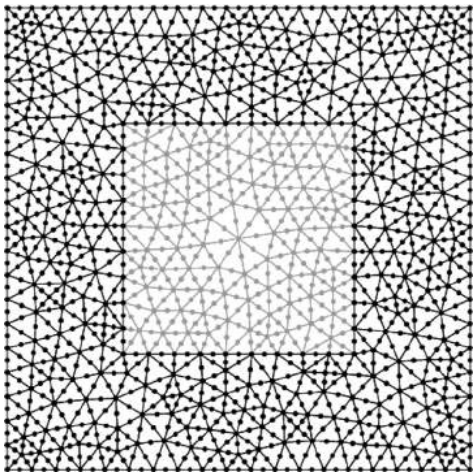

**Fig. 13.** Cross-section mesh of an embedded square bar using Cartesian PML ($l_e = 0.2a$).

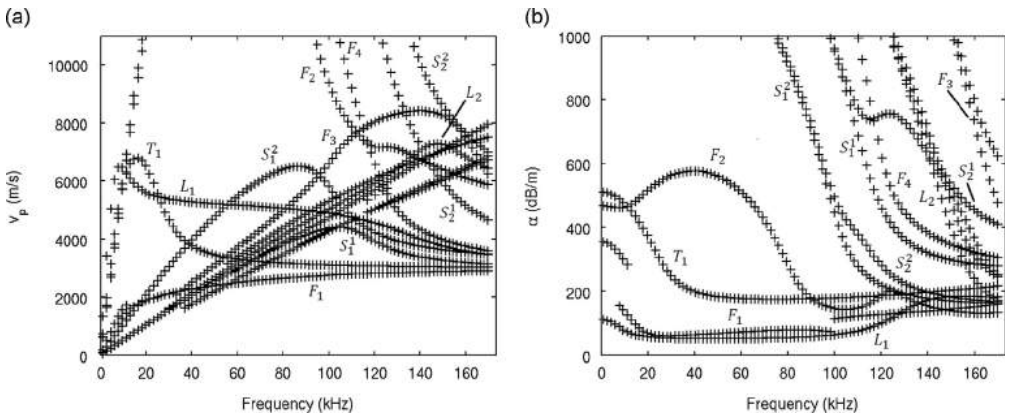


**Fig. 14.** Dispersion curves of a viscoelastic rectangular steel bar buried in grout computed by the SAFE–CPML method for (a) phase velocity and (b) axial attenuation. PML parameters are $\hat{\gamma}_x = \hat{\gamma}_y = \hat{\gamma} = 2+4\mathrm{i}$, $d_x = d_y = d = 1.1a$, $h_x = h_y = h = 0.9a$ ($\eta_{max} = 0.9$).

with a densification by increasing the so-called complex thickness (or radius). The rotation angle of radiation modes are shown to be independent of PML function profiles and must be large enough to discover the leaky modes of interest.

For three test cases taken from the literature, the dispersion curves computed by both SAFE–CPML and SAFE–RPML methods provide satisfying results, for leaky modes as well as trapped modes. A modal filtering criterion has been proposed. This criterion is based on the ratio of kinetic energy in the PML region over the whole section and allows to efficiently remove the radiation modes in the visualization of dispersion curves. As far as the computational time is concerned, the SAFE–RPML appears to be more suitable for modeling open waveguides of circular cross-section. Conversely, the Cartesian PML should be preferred when the cross-section of the core is rectangular.

The main drawback of the approach is the presence of many radiation modes, which significantly increases the computational time. These modes are not intrinsic to the physics (since they depend on PML parameters) and are not of interest for NDE. Another drawback is the appropriate choice of PML parameters. Such a drawback is inherent to any problem involving PML and is also encountered with the AL technique. When the reference results are not known *a priori*, a convergence study is necessary. For instance for a given profile of PML function, the convergence of numerical results can be investigated by refining the finite element size and increasing the PML thickness. Note that the appropriate PML interface position is rather straightforward to choose as the PML should be set as close as possible to the core in order to limit the transverse growth of leaky waves.

**Acknowledgments**

This work has been partially funded by the French Agence Nationale de la Recherche in frame of the Programme Inter Carnot Fraunhofer PICF of the Franco-German FilameNDT project.

## Appendix A. Eigenspectrum of embedded cylindrical waveguides with radial PML

*Analytical solution of scalar problem*: In this analytical study, one considers a cylindrical acoustic waveguide of radius $a$ embedded into an infinite medium. A radial PML of finite thickness $h$ is introduced at the position $d \geq a$. The total radius of cross-section including PML is $\ell_r = d+h$.

The system of equations in radial complex coordinates is given by two Helmholtz equations (one for each medium). Continuity conditions are applied at the interface $r=a$ between both media and a Dirichlet condition is applied at the PML exterior boundary:

$$\phi_0(a) = \tilde{\phi}(a), \quad \frac{1}{\rho_0}\frac{\mathrm{d}\phi_0}{\mathrm{dr}}(a) = \frac{1}{\rho}\frac{\mathrm{d}\tilde{\phi}}{\mathrm{d}\tilde{r}}(a), \quad \tilde{\phi}\left(\tilde{\ell}_r\right) = 0. \tag{A.1}$$

$\phi_0$ and $\tilde{\phi}$ denote the acoustic variables in the core and in the surrounding medium respectively. $\rho_0$ and $\rho$ are the mass densities of the core and of the exterior medium. We assume that the core and the surrounding medium are homogeneous: fluid properties are constant (the tilde has been dropped for conciseness).

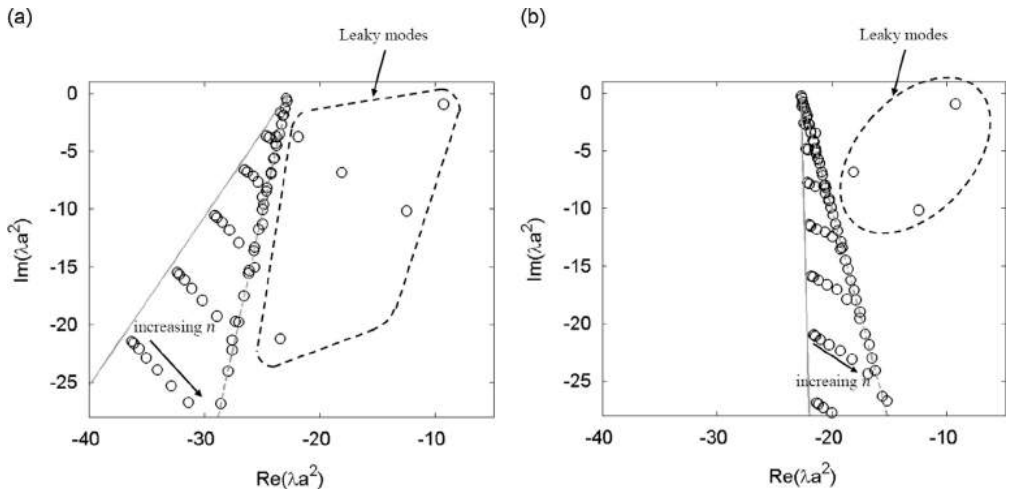


**Fig. 15.** Analytical spectrum of an embedded cylindrical acoustic waveguide at $\Omega = \omega a/c_0 = 3.86$ ($\rho = 0.29\rho_0$, $c = 0.81c_0$) with $d = 1.1a$, $h = 0.9a$ for (a) $\hat{\gamma} = 2+4\mathrm{i}$ and (b) $\hat{\gamma} = 4+4\mathrm{i}$. Dashed line: ($\Delta_1$) and continuous line: ($\Delta_2$).

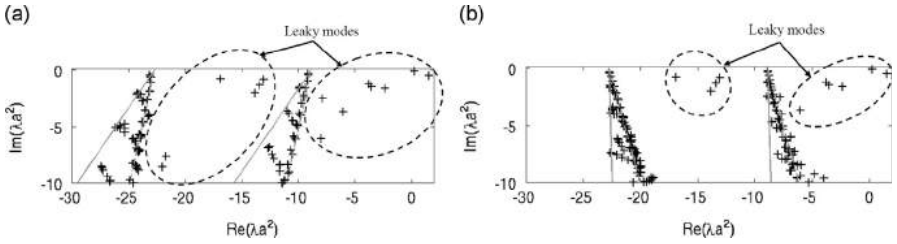


**Fig. 16.** Numerical spectrum of steel-concrete waveguide obtained by the SAFE–RPML method at $\Omega=3.86$ with $d=1.1a$, $h=0.9a$ ($l_e=0.1a$) for (a) $\hat{\gamma}=2+4$i and (b) $\hat{\gamma}=4+4$i. Dashed line: $(\Delta_1^{l/s})$ and continuous line: $(\Delta_2^{l/s})$.

It can be readily shown that the dispersion relation associated to this problem is

$$J_n'(k_{r_0}a)\left[Y_n(k_ra)J_n(k_r\widetilde{\ell}_r)-Y_n(k_r\widetilde{\ell}_r)J_n(k_ra)\right]\frac{k_{r_0}}{\rho_0}-J_n(k_{r_0}a)\left[Y_n'(k_ra)J_n(k_r\widetilde{\ell}_r)-Y_n(k_r\widetilde{\ell}_r)J_n'(k_ra)\right]\frac{k_r}{\rho}=0 \tag{A.2}$$

where $k_{r_0}=\sqrt{\omega^2/c_0^2-k^2}$ and $k_r=\sqrt{\omega^2/c^2-k^2}$ are the transverse wavenumbers in each medium ($c_0$ and $c$ denote the velocities of the core and of the exterior medium respectively).

The above equation cannot be solved analytically. Concerning radiation modes, further insight can be gained from an asymptotic point of view. Assuming a large complex radius ($|\widetilde{\ell}_r/a|\ll 1$), the transverse wavelength of low order radiation modes can be considered as sufficiently large to neglect the influence of the core: such modes almost satisfy the homogeneous medium equation derived in Section 3.3, *i.e.* $J_n(k_r\widetilde{\ell}_r)\simeq 0$, yielding a first asymptote $(\Delta_1)$:

$$(\Delta_1):\ -\omega^2/c^2+\mathbb{R}^+/\widetilde{\ell}_r^2 \tag{A.3}$$

which is a half-line of origin $-\omega^2/c^2$ rotated by $-2\arg\widetilde{\ell}_r$ in the complex plane.

Conversely, it can be shown that for a given $n$, the eigenvalues $\lambda$ of high order radiation modes (low transverse wavelength) tend toward a second asymptote $(\Delta_2)$ defined by

$$(\Delta_2):\ -\omega^2/c^2+\mathbb{R}^+/(\widetilde{\ell}_r-a)^2 \tag{A.4}$$

yielding a half-line of origin $-\omega^2/c^2$ rotated by $-2\arg(\widetilde{\ell}_r-a)$. Details are not shown for paper conciseness. Similar asymptotic developments can be found in Ref. [30].

Fig. 15 shows an example of eigensolutions of Eq. (A.2) for $d=1.1a$, $h=0.9a$ and different values of $\hat{\gamma}$. In this example, $(\rho_0,c_0)$ and $(\rho,c)$ are the mass densities and the shear velocities of steel and concrete respectively (see Table 1). The circumferential order $n$ varies from 0 to 10. As expected, the eigenspectrum contains both leaky modes and radiation modes. It can be observed that the radiation modes appear to be included inside a sector delimited by $(\Delta_1)$ and $(\Delta_2)$. More precisely, radiation modes are found to be located on one branch asymptotic to $(\Delta_1)$ and sub-branches. In each sub-branch, the radiation modes get closer to $(\Delta_1)$ as the circumferential order $n$ increases.

Note that the rotation angles of $(\Delta_1)$ and $(\Delta_2)$ are also independent of the PML function profile $\gamma$ because one has

$$-2\arg\widetilde{\ell}_r=-2\arg(d+\hat{\gamma}h),\quad -2\arg(\widetilde{\ell}_r-a)=-2\arg(d+\hat{\gamma}h-a). \tag{A.5}$$

Compared to Fig. 15a, the angular sector of radiation modes is reduced in Fig. 15b. This is due to the fact that increasing $\mathrm{Re}\,\hat{\gamma}$ increases $\mathrm{Re}\,\widetilde{\ell}_r$, which reduces the difference between the rotation angles of $(\Delta_1)$ and $(\Delta_2)$ (this can be readily shown from Eq. (A.5)). Given that leaky modes are discovered in the region where $\arg\lambda<-2\arg\widetilde{\ell}_r$, more leaky modes are found in Fig. 15a than in Fig. 15b thanks to a greater rotation angle of $(\Delta_1)$.

Without core ($a=0$), note that Eqs. (A.3) and (A.4) yield equal rotation angles for $(\Delta_1)$ and $(\Delta_2)$: the radiation modes sector is reduced to one discretized half-line rotated by $-2\arg\widetilde{\ell}_r$, which coincides with the result of Section 3.3.

*Numerical experiments on an elastic waveguide*: The same test case as in Section 2.5.2 is considered (elastic steel-concrete waveguide). Fig. 7 shows the example of a cross-section mesh used with the SAFE–RPML method ($l_e=0.2a$). Note that the effects of radial PML interface position and mesh size on eigenspectrum are identical to Cartesian PML (see Section 2.5.2). Therefore this subsection focuses on the effects of $\hat{\gamma}$ specific to the SAFE–RPML method.

Fig. 16 represents the eigenspectrum computed by the SAFE–RPML method at the dimensionless frequency $\Omega=3.86$. As suggested for Cartesian PML, the radial PML interface is set close to the core ($d=1.1a$). The average length of finite elements is $l_e=0.1a$.

As shown for the scalar problem in the previous subsection, it can be noticed that the radiation elastic modes are included in sectors. Instead of one, the elastic problem yields two sectors, associated with longitudinal and shear waves respectively. Each sector is limited by two half-lines, denoted as $(\Delta_1^{l/s})$ and $(\Delta_2^{l/s})$, of rotation angles approximately equal to 100° and 120° in Fig. 16a (73° and 88° in Fig. 16b). These angles are closed to the acoustic formula (A.5). Similarly to the acoustic case, each sector is formed by one branch asymptotic to $(\Delta_1^{l/s})$ and sub-branches and angular sectors are reduced as $\mathrm{Re}\hat{\gamma}$ increases (compare Fig. 16b with Fig. 16a). Similarly to the SAFE–CPML method, increasing $|\hat{\gamma}|$ densifies the spectrum of radiation modes.

Concerning leaky modes, only those of arguments lower than the angle of ($\Delta_1^{l/s}$) can be discovered (*i.e.* arg $\lambda < -2$ arg $\widetilde{\epsilon}_r$), which explains why less leaky modes are found in Fig. 16b than in Fig. 16a.

To conclude this section, it is worth noting that the leaky modes shown in Fig. 16 are in agreement with those of Fig. 4, obtained the SAFE–RPML method.

## References


[1] V. Maupin, The radiation modes of a vertically varying half-space: *a new representation of the complete Green's function in terms of modes*, *Geophysical Journal International* 126 (3) (1996) 762–780.
[2] L. Margerin, Generalized eigenfunctions of layered elastic media and application to diffuse fields, *Journal of the Acoustical Society of America* 125 (1) (2009) 164–174.
[3] R.E. Collin, *Field Theory of Guided Waves*, 2nd ed. IEEE Press, New York, 1991.
[4] R.N. Thurston, Elastic-waves in rods and clad rods, *Journal of the Acoustical Society of America* 64 (1) (1978) 1–37.
[5] A. Bamberger, Y. Dermenjian, P. Joly, Mathematical analysis of the propagation of elastic guided waves in heterogeneous media, *Journal of Differential Equations* 88 (1) (1990) 113–154.
[6] J. Hu, C.R. Menyuk, Understanding leaky modes: *slab waveguide revisited*, *Advances in Optics and Photonics* 1 (1) (2009) 58–106.
[7] J.A. Simmons, E. Drescher-Krasicka, H.N.G. Wadley, Leaky axisymmetric modes in infinite clad rods I, *Journal of the Acoustical Society of America* 92 (2) (1992) 1061–1090.
[8] L.E. Alsop, A.S. Goodman, S. Gregersen, Reflection and transmission of inhomogeneous waves with particular application to Rayleigh waves, *Bulletin of the Seismological Society of America* 64 (6) (1974) 1635–1652.
[9] A.C. Hladky-Hennion, P. Langlet, M. de Billy, Conical radiating waves from immersed wedges, *Journal of the Acoustical Society of America* 108 (6) (2000) 3079–3083.
[10] T. Vogt, M. Lowe, P. Cawley, The scattering of guided waves in partly embedded cylindrical structures, *Journal of the Acoustical Society of America* 113 (3) (2003) 1258–1272.
[11] G. Cavigilia, A. Morro, *Inhomogeneous Waves in Solids and Fluids*, World Scientific Publishing Co. Pte. Ltd., Farrer Road, Singapore, 1992.
[12] C.H. Chapman, Lamb's problem and comments on the paper "On leaking modes" by Usha Gupta, *Pure and Applied Geophysics* 94 (1) (1972) 233–247.
[13] P.D. Hislop, I.M. Sigal, *Introduction to Spectral Theory. With Applications to Schrödinger Operators, Applied Mathematical Sciences*, Springer-Verlag, New York, 1996, p. 113.
[14] M.J.S. Lowe, Plate Waves for the NDT of Diffusion Bonded Titanium, PhD Thesis, Mechanical Engineering Department, Imperial College London, 1992.
[15] M.D. Beard, M.J.S. Lowe, Non-destructive testing of rock bolts using guided ultrasonic waves, *International Journal of Rock Mechanics and Mining Sciences* 40 (4) (2003) 527–536.
[16] L. Laguerre, A. Grimault, M. Deschamps, Ultrasonic transient bounded-beam propagation in a solid cylinder waveguide embedded in a solid medium, *Journal of the Acoustical Society of America* 121 (4) (2007) 1924–1934.
[17] M.J.S. Lowe, P. Cawley, Comparison of the modal properties of a stiff layer embedded in a solid medium with the minima of the plane-wave reflection coefficient, *Journal of the Acoustical Society of America* 97 (3) (1995) 1625–1637.
[18] M.J.S. Lowe, P. Cawley, The influence of the modal properties of a stiff layer embedded in a solid medium on the field generated in the layer by a finite-sized transducer, *Journal of the Acoustical Society of America* 97 (3) (1995) 1638–1649.
[19] B.N. Pavlakovic, Leaky Guided Ultrasonic Waves in NDT, PhD Thesis, Mechanical Engineering Department, Imperial College London, 1998.
[20] L. Gavric, Computation of propagative waves in free rail using a finite element technique, *Journal of Sound and Vibration* 185 (3) (1995) 531–543.
[21] I. Bartoli, A. Marzani, F. Lanza di Scalea, E. Viola, Modeling wave propagation in damped waveguides of arbitrary cross-section, *Journal of Sound and Vibration* 295 (2006) 685–707.
[22] T. Hayashi, W.-J. Song, J.L. Rose, Guided wave dispersion curves for a bar with an arbitrary cross-section, a rod and rail example, *Ultrasonics* 41 (3) (2003) 175–183.
[23] P.W. Loveday, Semi-analytical finite element analysis of elastic waveguides subjected to axial loads, *Ultrasonics* 49 (2009) 298–300.
[24] M. Castaings, M. Lowe, Finite element model for waves guided along solid systems of arbitrary section coupled to infinite solid media, *Journal of the Acoustical Society of America* 123 (2) (2008) 696–708.
[25] Z. Fan, M.J.S. Lowe, M. Castaings, C. Bacon, Torsional waves propagation along a waveguide of arbitrary cross section immersed in a perfect fluid, *Journal of the Acoustical Society of America* 124 (4) (2008) 2002–2010.
[26] M. Mazzotti, I. Bartoli, A. Marzani, E. Viola, A coupled SAFE–2.5D BEM approach for the dispersion analysis of damped leaky guided waves in embedded waveguides of arbitrary cross-section, *Ultrasonics* 53 (7) (2013) 1227–1241.
[27] M. Mazzotti, I. Bartoli, A. Marzani, Ultrasonic leaky guided waves in fluid-coupled generic waveguides: *hybrid finite-boundary element dispersion analysis and experimental validation*, *Journal of Applied Physics* 115 (2014) 143–512.
[28] T. Hayashi, D. Inoue, Calculation of leaky lamb waves with a semi-analytical finite element method, *Ultrasonics* 54 (6) (2014) 1460–1469.
[29] A. Pelat, S. Felix, V. Pagneux, On the use of leaky modes in open waveguides for the sound propagation modeling in street canyons, *Journal of the Acoustical Society of America* 126 (6) (2009) 2864–2872.
[30] B. Goursaud, Étude mathématique et numérique de guides d'ondes ouverts non uniformes, par approche modale (Mathematical and numerical study of non uniform open waveguides, modal approach, in French), PhD Thesis, École Polytechnique, 2010.
[31] A.-S. Bonnet-BenDhia, B. Goursaud, C. Hazard, A. Prieto, Finite element computation of leaky modes in stratified waveguides, in: 5th Meeting of the Anglo-French-Research-Group, vol. 128, 2009, pp. 73–86.
[32] F. Treyssède, K. L. Nguyen, A.-S. Bonnet-BenDhia, C. Hazard, On the use of a SAFE–PML technique for modeling two-dimensional open elastic waveguides, in: Acoustics 2012, France, April 23–27, 2012, pp. 673–678.
[33] F. Treyssède, K.L. Nguyen, A.-S. Bonnet-BenDhia, C. Hazard, Finite element computation of trapped and leaky elastic waves in open stratified waveguides, *Wave Motion* 51 (2014) 1093–1107.
[34] H. Gravenkamp, C. Birk, C. Song, Computational of dispersion curves for embedded waveguides using dashpot boundary condition, *Journal of the Acoustical Society of America* 135 (3) (2014) 1127–1138.
[35] S. Kim, J.E. Pasciak, The computation of resonances in open systems using a perfectly matched layer, *Mathematics of Computation* 78 (267) (2009) 1375–1398.
[36] S. Kim, Cartesian PML approximation to resonances in open systems in $\mathbb{R}^2$, *Applied Numerical Mathematics* 81 (2014) 50–75.
[37] S. François, M. Schevenels, G. Lombaert, G. Degrande, A two-and-a-half-dimensional displacement-based PML for elastodynamic wave propagation, *International Journal for Numerical Methods in Engineering* 90 (7) (2012) 819–837.
[38] F. Tisseur, K. Meerbergen, The quadratic eigenvalue problem, *SIAM Review* 43 (2) (2001) 235–286.
[39] R. Lehoucq, D.C. Sorensen, C. Yang, *ARPACK User's Guide: Solution of Large Scale Eigenvalue Problems with Implicitly Restarted Arnoldi Methods*, SIAM, Philadelphia, PA, 1998.
[40] A. Bermúdez, L. Hervella-Nieto, A. Prieto, R. Rodríguez, An optimal perfectly matched layer with unbounded absorbing function for time-harmonic acoustic scattering problems, *Journal of Computational Physics* 223 (2) (2007) 469–488.
[41] E.A. Skelton, S.D.M. Adams, R.V. Craster, Guided elastic waves and perfectly matched layers, *Wave Motion* 44 (2007) 573–592.

[42] A. Pelat, S. Felix, V. Pagneux, A coupled modal-finite element method for the wave propagation modeling in irregular open waveguides, *Journal of the Acoustical Society of America* 129 (3) (2011) 1240–1249.
[43] A.-S. Bonnet-BenDhia, B. Goursaud, C. Hazard, A. Prieto, Finite element computation of leaky modes in stratified waveguides, *Ultrasonic Wave Propagation in Non Homogeneous Media*, Springer Proceedings in Physics, vol. 128, 2009, pp. 73–86.
[44] Y. OuldAgha, F. Zolla, A. Nicolet, S. Guenneau, On the use of PML for the computation of leaky modes. An application to microstructured optical fibres, *The International Journal for Computation and Mathematics in Electrical and Electronic Engineering* 27 (1) (2008) 95–109.
[45] J.D. Achenbach, *Wave Propagation in Elastic Solids*, North-Holland, Amsterdam, 1973.
[46] S. Kim, J.E. Pasciak, Analysis of the spectrum of a Cartesian perfectly matched layer (PML) approximation to acoustic scattering problems, *Journal of Mathematical Analysis and Applications* 361 (2) (2010) 420–430.
[47] F. Treyssède, Mode propagation in curved waveguides and scattering by inhomogeneities: *application to the elastodynamics of helical structures*, *Journal of the Acoustical Society of America* 129 (4) (2011) 1857–1868.
[48] A. Bernard, M.J.S. Lowe, M. Deschamps, Guided waves energy velocity in absorbing and non-absorbing plates, *Journal of the Acoustical Society of America* 110 (2001) 186–196.
[49] B. Pavlakovic, M. Lowe, Disperse User's Manual, Version 2.0.11, 2001, p. 131.
[50] S. Finneveden, Evaluation of modal density and group velocity by a finite element method, *Journal of Sound and Vibration* 273 (2004) 51–75.
[51] J.M. Carcione, D. Gei, S. Treitel, The velocity of energy through a dissipative medium, *Geophysics* 75 (2) (2010) 37–47.
[52] H. Cui, B. Zhang, S. Ji, Propagation characteristics of guided waves in a rod surrounded by an infinite solid medium, *Acoustical Physics* 56 (4) (2010) 412–421.

Gallezot *et al.*: JASA Express Letters [http://dx.doi.org/10.1121/1.4973313] Published Online 6 January 2017

# Contribution of leaky modes in the modal analysis of unbounded problems with perfectly matched layers

**Matthieu Gallezot, Fabien Treyssède, and Laurent Laguerre**
*IFSTTAR, GERS, GeoEND, F-44344 Bouguenais, France*
*matthieu.gallezot@ifsttar.fr, fabien.treyssede@ifsttar.fr, laurent.laguerre@ifsttar.fr*

**Abstract:** The modal analysis of wave problems of unbounded type involves a continuous sum of radiation modes. This continuum is difficult to handle mathematically and physically. It can be approximated by a discrete set of leaky modes, corresponding to improper modes growing to infinity. Perfectly matched layers (PMLs) have been widely applied in numerical methods to efficiently simulate infinite media, most often without considering a modal approach. This letter aims to bring insight into the modal basis computed with PMLs. PMLs actually enable to reveal of the contribution of leaky modes by redefining the continua (two for elastodynamics), discretized after PML truncation.


[OAG]
**Date Received:** October 20, 2016 **Date Accepted:** December 7, 2016

## 1. Introduction

Modal analysis is a powerful tool for treating bounded wave problems, for which modes provide a discrete basis that allows in-depth physical analysis. For unbounded problems, the modal basis is yet more complicated because it involves a continuous sum of modes (radiation modes) in addition to a discrete set (trapped modes, if any).[1] This contribution of the continuum is usually quite difficult to calculate and interpret from a physical point of view. Based on steepest descent techniques, for example, it can be approximated by a discrete set of another class of modes, the so-called leaky modes.[2] These modes behave like attenuated modes and reveal some interesting physical features. For instance, they can give the leakage attenuation of wave packets in open waveguides, which is of particular interest in the field of nondestructive evaluation (NDE).[3] However, leaky modes correspond to improper modes that spatially grow to infinity in the unbounded direction of the problem (they are not part of the modal basis). Their use in modal analysis hence requires special care.

As for numerical methods, perfectly matched layers (PMLs) have been widely employed to efficiently simulate infinite media. More particularly, they have been successfully applied to compute modes in open systems.[4,5] It has been shown that PMLs allow getting both trapped and leaky modes as well as a third type of mode sometimes called PML modes.[6] PML modes mainly resonate inside the PML region (their fields strongly depend on PML parameters). However, the contribution of these different kinds of modes in a modal analysis may still be unclear. This letter aims to bring insight into the modal basis computed with PMLs and to justify its use for the analysis of excitation and scattering problems using a modal approach. Without loss of generality, two-dimensional waveguides are considered. For simplicity, the analysis starts from the scalar wave equation and is then extended to elastodynamics, where two continua occur instead of one.

## 2. Background

This section briefly recalls some theoretical results[1,2,7] taking the example of a two-dimensional bilayer waveguide, homogeneous and infinite in the axial direction $z$ as shown in Fig. 1. In the transverse direction, the bottom layer is labelled 0 and extends from $x=-h$ to $x=0$. The top layer is infinite and labelled $\infty$. The wave field solution to the problem satisfies the Helmholtz equation in both layers and is denoted in the angular frequency-wavenumber domain by $\psi(x,\beta,\omega)$, where $\beta$ and $\omega$ are the axial wavenumber and the angular frequency. A convention in $e^{j(\beta z-\omega t)}$ is adopted for the harmonic dependence of wave fields. The transverse wavenumbers in the two layers are given by $\alpha_{0,\infty}^2=k_{0,\infty}^2-\beta^2$, with $k_{0,\infty}=\omega/c_{0,\infty}$. In this paper, $'$ or Re and $''$ or Im will denote, respectively, the real part and the imaginary part of a complex number. As an example, let us assume that the waveguide in Fig. 1 is excited by an out-of-plane

 

Gallezot *et al.*: JASA Express Letters [http://dx.doi.org/10.1121/1.4973313] Published Online 6 January 2017

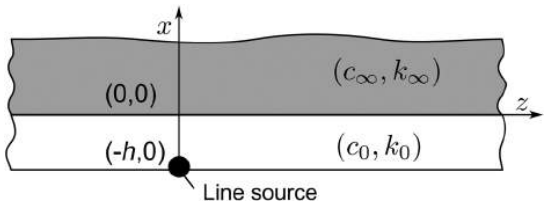


Fig. 1. Example of a two-dimensional bilayer open waveguide.

line source located at $(x,z)=(-h,0)$ through the Neumann boundary condition $d\psi(-h,z,\omega)/dx = s(\omega)\delta(z)$.

The solution must also satisfy continuity conditions at the interface ($x=0$) and must be bounded and outwards at infinity[2] ($x\to\infty$). The spatial inverse Fourier transform of the solution leads to an expression of the following form:

$$\psi(x,z,\omega)=\begin{cases}\dfrac{s(\omega)}{2\pi}\displaystyle\int_{\mathbb{R}}\frac{\alpha_0\cos(\alpha_0 x)+jC_m\alpha_\infty\sin(\alpha_0 x)}{\alpha_0[\alpha_0\sin(\alpha_0 h)+jC_m\alpha_\infty\cos(\alpha_0 h)]}e^{j\beta z}d\beta & \text{if } -h\le x\le 0,\\ \dfrac{s(\omega)}{2\pi}\displaystyle\int_{\mathbb{R}}\frac{1}{\alpha_0\sin(\alpha_0 h)+jC_m\alpha_\infty\cos(\alpha_0 h)}e^{j\alpha_\infty x}e^{j\beta z}d\beta & \text{if } x>0,\end{cases} \tag{1}$$

where $C_m$ is a ratio of material properties which depends on the problem type (i.e., dielectric, acoustic, or SH-elastic). First, a lossy outer medium is assumed (i.e., $k''_\infty>0$). The key point is the value of $\alpha_\infty$, which depends on the sign of the square root of $k_\infty^2-\beta^2$ and hence defines a two-sheeted Riemann surface.[2] Let us consider the two sheets defined by $\alpha''_\infty>0$ and $\alpha''_\infty<0$, respectively. The corresponding branch cut is given by $\alpha''_\infty=0$ and is a portion of hyperbola[1] in the $(\beta',\beta'')$ plane beginning at branch point $(k'_\infty, k''_\infty)$, as shown in Fig. 2(a). The remaining portion of the hyperbola satisfies the equation $\alpha'_\infty=0$.

The integrals in Eq. (1) can be evaluated thanks to Cauchy's residue theorem. The path $\mathbb{R}$ is conveniently closed by a semi-infinite circle along which the integrals vanish. This implies that the exponentials $e^{j\alpha_\infty x}$ and $e^{j\beta z}$ must tend to zero at infinity. For clarity, let us focus on the solution in the region $z>0$, where waves are positive-going and decreasing ($\beta''>0$). In this case, the integration must be carried out on the upper semi-circle $\mathcal{C}^+$, defined by $\beta''>0$ and located on the proper sheet, which is $\alpha''_\infty>0$ (the improper sheet being $\alpha''_\infty<0$). Furthermore, the branch cut is a discontinuity that cannot be crossed. It must be circumvented by the path $\Gamma^+$ [see Fig. 2(a)]. Finally, on the contour $\mathbb{R}+\Gamma^++\mathcal{C}^+$, the application of the residue theorem leads to $\int_{\mathbb{R}}=2\pi j\sum\text{residues}-\int_{\Gamma^+}$. The residues are calculated from the poles [zeros of denominators of Eq. (1)] that lie on the proper Riemann sheet $\alpha''_\infty>0$, that is to say, the trapped modes. Thus, two parts contribute to $\psi(x,z,\omega)$. The first one is a discrete sum of positive going trapped modes. The second part is a continuous sum and stands for the continuum of radiation modes.

Together, trapped modes and radiation modes form the modal basis of an open waveguide:[1]

$$\psi(x,z,\omega)=\sum\text{trapped}+\int_{\Gamma^+}\text{radiation modes}. \tag{2}$$

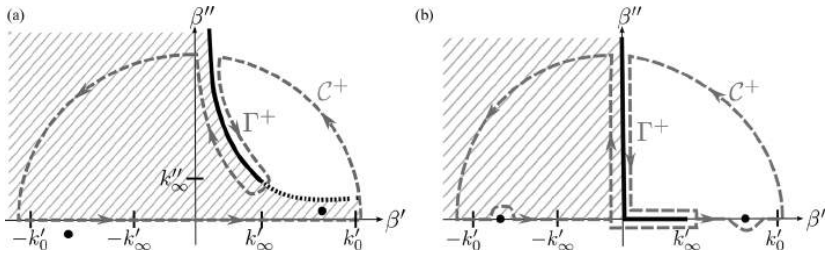


Fig. 2. Representation of the proper sheet $\alpha''_\infty>0$ in the upper complex plane $\beta''>0$: (a) lossy medium, (b) lossless. Branch cut $\alpha''_\infty=0$ (thick line), curve $\alpha'_\infty=0$ (dotted line), trapped modes (•), and integration contour (dashed line). Hatched region: $\alpha'_\infty>0$. White region: $\alpha'_\infty<0$.

As mentioned previously, the continuum is difficult to handle. Its contribution can be approximated by a discrete sum of a third class of modes, the so-called leaky modes (e.g., using the steepest descent method[8]). It has to be emphasised that leaky modes are also poles of Eq. (1). However, they do not belong to the modal basis because they are improper poles that lie in the negative Riemann sheet[2] $\alpha''_\infty < 0$. Hence, leaky modes grow to infinity in the transverse direction. They can approximate the wave field only in a strictly delimited spatial region.[9] From a physical point of view, leaky modes might be seen in the bottom layer as imperfect guided waves that suffer from leakage attenuation, while trapped modes are guided waves that propagate without leakage attenuation. Radiation modes form standing waves in the transverse direction and can be propagative or evanescent in the axial direction.[7]

The lossless case ($k''_\infty = 0$), not considered so far, can be readily deduced asymptotically and is shown in Fig. 2(b). If the medium is lossless, trapped modes have purely real wavenumbers[2] and exist only if $k_\infty < \beta < k_0$.

Note that the problem given by Eq. (1) has been introduced in this section for illustrative purposes only. The main results of this letter will apply to more complex open waveguides (e.g., multilayered or excited by other types of source), since the analysis in the remainder essentially lies in the definition of the branch cut of the square root, which is intrinsic to the halfspace.

### 3. Modal basis with a PML

A PML is now applied in the infinite top layer. This amounts to perform an analytical extension[10] for $x > 0$ with the change of variable $\tilde{x} = \int_0^x \gamma(\zeta) d\zeta$, where $\gamma(x)$ is a complex function such that $\arg\gamma \in [0; \pi/2[$. For simplicity, let us consider a constant function inside the whole top layer [$\gamma(x) = \gamma$]. In this case, $\tilde{x} = \gamma x$ in the top layer. It can be readily checked that solving the Helmholtz equation in both layers yields the same solution as Eq. (1) except that the term $e^{j\alpha_\infty x}$ is now replaced with $e^{j\tilde{\alpha}_\infty x}$, where $\tilde{\alpha}_\infty = \gamma\alpha_\infty$. The poles of the denominators (trapped and leaky modes) are left unchanged by the PML.

Following the same approach as in Sec. 2, the application of the residue theorem requires considering a new proper Riemann sheet, defined by $\tilde{\alpha}''_\infty > 0$. Consequently, the branch cut is now given by $\tilde{\alpha}''_\infty = 0$ and defines a new integration path denoted by $\tilde{\Gamma}^+$. To understand the effect of the PML on the modal basis, it is necessary to look further into the branch cut transformation induced by the PML, namely, from $\Gamma^+$ to $\tilde{\Gamma}^+$.

The branch cut $\tilde{\alpha}''_\infty = 0 = \pm\mathrm{Im}\sqrt{\mathrm{Re}\,\tilde{\alpha}^2_\infty + j\mathrm{Im}\,\tilde{\alpha}^2_\infty}$ in the $(\beta', \beta'')$ plane can be unequivocally determined by the following conditions: $\mathrm{Im}\,\tilde{\alpha}^2_\infty = 0$ and $\mathrm{Re}\,\tilde{\alpha}^2_\infty > 0$ (see Ref. 1, pp. 180 and 181 for the case without PML). Then, from the expansion $\tilde{\alpha}^2_\infty = (\gamma' + j\gamma'')(k'^2_\infty - k''^2_\infty - \beta'^2 + \beta''^2 + 2j(k'_\infty k''_\infty - \beta'\beta''))$, the equation $\mathrm{Im}\,\tilde{\alpha}^2_\infty = 2\tilde{\alpha}'_\infty\tilde{\alpha}''_\infty = 0$ becomes

$$A\beta'^2 + B\beta'\beta'' + C\beta''^2 + D = 0, \tag{3}$$

with $C = -A = \gamma'\gamma''$, $B = \gamma''^2 - \gamma'^2$, $D = \gamma'\gamma''(k'^2_\infty - k''^2_\infty) + (\gamma'^2 - \gamma''^2)k'_\infty k''_\infty$. Equation (3) represents a hyperbola in the frame $(\beta', \beta'')$. The principal axes of this hyperbola make an angle $\theta$ with the axes of the frame given by the formula $\cot 2\theta = (A - C)/B$, which leads to

$$\theta = \frac{\pi}{4} - \arg\gamma. \tag{4}$$

From the study of the sign of $\mathrm{Re}\,\tilde{\alpha}^2_\infty$, it can be checked that the branch cut $\tilde{\alpha}''_\infty = 0$ is on the upper part of the hyperbola and that the lowest part corresponds to the curve $\tilde{\alpha}'_\infty = 0$. Both parts are delimited by the branch point $(k'_\infty, k''_\infty)$, analogously to the case without PML.

Without PML, $\arg\gamma = 0$ and $\theta = \pi/4$: the asymptotes of the hyperbola coincide with the real and imaginary axes [as already shown in Fig. 2(a)]. With PML, the angle becomes $(\pi/4) - \arg\gamma$: the asymptotes are rotated by $-\arg\gamma$. Hence, the branch cut transformation from $\Gamma^+$ to $\tilde{\Gamma}^+$ is a rotation of an angle equal to $-\arg\gamma$ [see Fig. 3(a)]. In the lossless case [Fig. 3(b)], note that the PML branch cut is still a hyperbola.

As shown hereafter, this branch cut rotation has an important consequence. With PML, the proper Riemann sheet satisfies $\tilde{\alpha}''_\infty > 0$ (i.e., $0 < \arg\tilde{\alpha}_\infty < \pi$) or, equivalently, by using the equality $\arg\tilde{\alpha}_\infty = \arg\gamma + \arg\alpha_\infty$:

$$-\arg\gamma < \arg\alpha_\infty < \pi - \arg\gamma. \tag{5}$$

Gallezot *et al.*: JASA Express Letters [http://dx.doi.org/10.1121/1.4973313] Published Online 6 January 2017

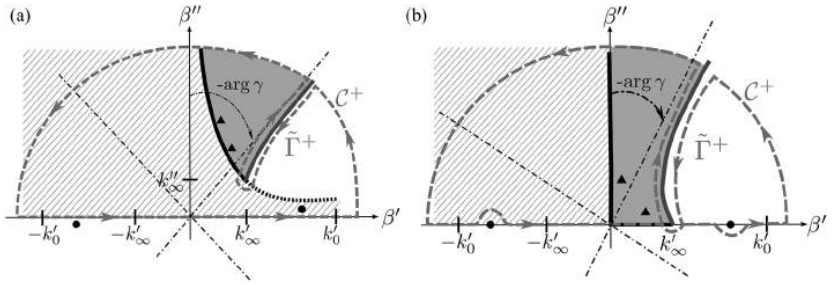


Fig. 3. Representation of the proper sheet with PML $\tilde{\alpha}''_\infty > 0$ in the upper complex plane $\beta'' > 0$: (a) lossy medium, (b) lossless. Same legend as Fig. 2 and PML branch cut $\tilde{\alpha}''_\infty = 0$ (thick gray line) with its asymptotes (dashed dotted), leaky modes (▲), revealed part of the improper sheet $\alpha''_\infty < 0$ (gray shaded region, satisfying $\alpha'_\infty > 0$).

In particular, the PML gives access to the region $-\arg\gamma < \arg\alpha_\infty < 0$ (shaded region in Fig. 3), which belongs to the initial improper sheet $\alpha''_\infty < 0$ where leaky modes occur. In other words, the rotation induced by the PML enables to reveal of the contribution of the leaky modes satisfying $\arg\alpha_\infty > -\arg\gamma$. These revealed leaky modes are proper poles of the problem with PML. Note that Eq. (5) coincides with the condition found for a PML to cancel the transverse exponential growth of a leaky mode.[4,5]

To summarize, the integration contour with PML is $\mathbb{R} + \mathcal{C}^+ + \tilde{\Gamma}^+$ as shown in Fig. 3. Applying Cauchy's residue theorem on this contour yields

$$\psi(x,z,\omega) = \sum \text{trapped} + \sum \text{revealed leaky} + \int_{\tilde{\Gamma}^+} \text{PML modes}. \tag{6}$$

The PML hence defines a new modal basis which properly includes some leaky modes. This modal basis still involves a continuum of modes, which mainly resonate inside the PML (PML modes). One must yet keep in mind that the field inside the PML is not physical: Eq. (6) coincides with the physical solution (2) only in the region out of the PML.

Inside the accessible region of the sheet $\alpha''_\infty < 0$ (i.e., the shaded region in Fig. 3) the sign of $\alpha'_\infty$ is single-valued and can be determined as follows. In the case without PML, the hyperbola given by Eq. (3) delimits two regions in the complex plane, $\alpha'_\infty \alpha''_\infty > 0$ (hatched region) and $\alpha'_\infty \alpha''_\infty < 0$ (white region)—see Fig. 2. The former and the latter are hence such that $\alpha'_\infty > 0$ and $\alpha'_\infty < 0$ in the proper Riemann sheet (i.e., $\alpha''_\infty > 0$), and conversely in the improper one ($\alpha''_\infty < 0$). Consequently, the revealed part of the sheet $\alpha''_\infty < 0$ is such that $\alpha'_\infty > 0$. As expected leaky waves are outgoing in the transverse direction.

## 4. The elastodynamic problem

In the elastodynamic case, two transverse wavenumbers must be considered: one for the longitudinal transverse wavenumber, $\alpha_{l\infty}$, and one for the shear transverse wavenumber, $\alpha_{s\infty}$. These are defined from $\alpha^2_{l\infty} = k^2_{l\infty} - \beta^2$ and $\alpha^2_{s\infty} = k^2_{s\infty} - \beta^2$, with $k_{l\infty} = \omega/c_{l\infty}$ and $k_{s\infty} = \omega/c_{s\infty}$. As a consequence, two branch cuts now occur (one for each square root).[11] Following Sec. 3, the branch cuts to consider correspond to zero imaginary parts, $\alpha''_{l\infty} = 0$ and $\alpha''_{s\infty} = 0$. This yields four Riemann sheets, labelled **1** for ($\alpha''_{l\infty} > 0$, $\alpha''_{s\infty} > 0$), **2** for ($\alpha''_{l\infty} > 0$, $\alpha''_{s\infty} < 0$), **3** for ($\alpha''_{l\infty} < 0$, $\alpha''_{s\infty} < 0$), and **4** for ($\alpha''_{l\infty} < 0$, $\alpha''_{s\infty} > 0$).

Applying the residue theorem, the elastodynamic solution without PML can then be expressed as a discrete sum of trapped modes and two continuous sums of radiation modes, instead of one in the scalar case. Trapped modes lie on the proper sheet **1** (on the real axis in the lossless case). Extending the results of Sec. 3, the PML rotates both branch cuts by $-\arg\gamma$. As shown in Fig. 4(a) (lossy case), this rotation reveals parts of the initial improper sheets **2**, **3**, and **4**, containing leaky modes. The solution then becomes expressed as a discrete sum of trapped modes, a discrete sum of revealed leaky modes and two continua of PML modes.

Similarly to Sec. 3, the sign of $\alpha'_{l\infty}$ and $\alpha'_{s\infty}$ can be determined in the accessible regions of sheets **2**, **3**, and **4**. This yields the following results:

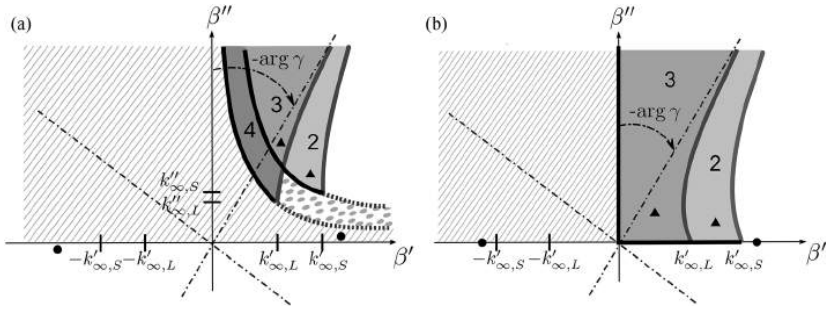


Fig. 4. Representation in the elastodynamic case of the proper sheet with PML ($\tilde{\alpha}''_{l\infty} > 0$, $\tilde{\alpha}''_{s\infty} > 0$): (a) lossy medium, (b) lossless. Same legend as in Fig. 3, except that sheet **1** ($\alpha''_{l\infty} > 0$, $\alpha''_{s\infty} > 0$) is now decomposed into hatched ($\alpha'_{l\infty} > 0$, $\alpha'_{s\infty} > 0$), white ($\alpha'_{l\infty} < 0$, $\alpha'_{s\infty} < 0$) and pea ($\alpha'_{l\infty} < 0$, $\alpha'_{s\infty} > 0$) regions. Shaded regions: revealed parts of the initial improper sheets **2**, **3**, and **4**.

$$\begin{aligned}
&\text{Region } \mathbf{2} : \alpha'_{l\infty} < 0, \alpha'_{s\infty} > 0\ (\alpha''_{l\infty} > 0, \alpha''_{s\infty} < 0),\\
&\text{Region } \mathbf{3} : \alpha'_{l\infty} > 0, \alpha'_{s\infty} > 0\ (\alpha''_{l\infty} < 0, \alpha''_{s\infty} < 0),\\
&\text{Region } \mathbf{4} : \alpha'_{l\infty} > 0, \alpha'_{s\infty} > 0\ (\alpha''_{l\infty} < 0, \alpha''_{s\infty} > 0).
\end{aligned} \tag{7}$$

Furthermore, sheet **1** can be decomposed into three regions, as shown in Fig. 4(a). Note that the transverse longitudinal wavenumbers of leaky modes revealed in sheet **2** have a positive imaginary part together with a negative real part. This partial wave hence behaves like a transverse backward wave decaying at infinity. This does not change the nature of the modes in region **2**, which are of leaky type owing to the transverse behavior of the partial shear wave (forward and growing at infinity).

In the lossless case [Fig. 4(b)], the sheet **4** cannot be accessible by the PML. In Fig. 4(a), the revealed region of sheet **4** is located between the two hyperbolas. In Fig. 4(b), these hyperbolas collapse with the axes of the frame, and so does the revealed part of **4**. Nevertheless, it is pointed out that the contribution of this particular sheet is usually neglected with other approaches regardless PMLs.[12,13]

## 5. Discussion

In addition to trapped modes, a second class of proper modes is likely to occur depending on material properties.[8] These modes lie on the proper sheet but are complex even in the lossless case, as opposed to trapped ones. Hence, the discrete sum of trapped modes in Eqs. (2) and (6) should also include these complex proper modes (when they exist). Furthermore, trapped modes of backwards type may occur. Such modes have opposite sign of phase and group velocity and have not been represented in the figures of this paper for simplicity (backwards modes lie on the negative real axis while propagating in the positive direction, and conversely).

Only infinite PMLs have been considered here. Yet for numerical implementation, PMLs must be truncated at some finite distance. Both trapped and leaky modes can be accurately computed, even after PML truncation, provided that the PML is properly parametrized.[4,5] However, the PML truncation transforms the continuous sum of PML modes into a discrete one.[6] At first sight, the role of this discrete sum in the convergence of solutions might be questionable owing to the fact that discrete PML modes strongly depend on the boundary conditions arbitrarily set at the end of the truncated PML. Nevertheless, it has been proved for homogeneous scalar problems that the continuum of PML modes can be truly approximated by a sum over discrete PML modes.[14] The convergence of the discrete sum towards the continuous sum can be achieved depending on the thickness of the PML, its attenuation, and the number of PML modes. Such a convergence cannot be necessarily achieved with absorbing layers of non-perfectly matched type.[9]

To conclude, the PML technique may significantly simplify the modal analysis of unbounded problems: this tool, easy to implement from a computational point of view, enables to naturally reveal of the contribution of leaky modes. Furthermore, the discretized sum of PML modes can be included in the modal basis in order to improve the accuracy of numerical solutions, which may be necessary when the contribution of leaky modes is not sufficient for a desired accuracy. This fully justifies from a numerical point of view the use of the PML technique for the modal analysis of unbounded problems. Numerical results will be left for a separate publication. It must be yet recalled that the PML technique is known to fail in elastodynamics for some specific

properties of anisotropy of the PML medium.[15] Such situations are beyond the scope of this paper, in which isotropic materials have been implicitly assumed.

**Acknowledgments**

The authors wish to thank Région Pays de la Loire for their financial support.

**References and links**

[1]P. Malischewsky, *Surface Waves and Discontinuities* (Elsevier, Amsterdam, 1987).
[2]R. E. Collin, *Field Theory of Guided Waves* (IEEE Press, Wiley, New York, 1991).
[3]B. N. Pavlakovic, M. J. S. Lowe, and P. Cawley, "High-frequency low-loss ultrasonic modes in imbedded bars," J. Appl. Mech. **68**, 67–75 (2001).
[4]S. Kim and J. E. Pasciak, "The computation of resonances in open systems using a perfectly matched layer," Math. Comput. **78**, 1375–1398 (2009).
[5]F. Treyssède, K. L. Nguyen, A.-S. Bonnet-BenDhia, and C. Hazard, "Finite element computation of trapped and leaky elastic waves in open stratified waveguides," Wave Motion **51**, 1093–1107 (2014).
[6]H. Derudder, F. Olyslager, D. De Zutter, and S. Van den Berghe, "Efficient mode-matching analysis of discontinuities in finite planar substrates using perfectly matched layers," IEEE Trans. Ant. Propag. **49**, 185–195 (2001).
[7]D. Marcuse, *Theory of Dielectric Optical Waveguides* (Academic Press, New York, 1991).
[8]T. Tamir and A. A. Oliner, "Guided complex waves. Part 1: Fields at an interface," Proc. Inst. Electr. Eng. **110**, 310–324 (1963).
[9]J. Hu and C. R. Menyuk, "Understanding leaky modes: Slab waveguide revisited," Adv. Opt. Photon. **1**, 58–106 (2009).
[10]W. C. Chew and W. H. Weedon, "A 3D perfectly matched medium from modified Maxwell's equations with stretched coordinates," Microwave Opt. Technol. Lett. **7**, 599–604 (1994).
[11]V. Maupin, "The radiation modes of a vertically varying half-space: A new representation of the complete Green's function in terms of modes," Geophys. J. Int. **126**, 762–870 (1996).
[12]M. Mazzotti, I. Bartoli, A. Marzani, and E. Viola, "A coupled SAFE-2.5D BEM approach for the dispersion analysis of damped leaky guided waves in embedded waveguides of arbitrary cross-section," Ultrasonics **53**, 1227–1241 (2013).
[13]A. L. Kurkjian, "Numerical computation of individual far-field arrivals excited by an acoustic source in a borehole," Geophysics **50**, 852–866 (1985).
[14]F. Olyslager, "Discretization of continuous spectra based on perfectly matched layers," SIAM J. Appl. Math. **64**, 1408–1433 (2004).
[15]E. Becache, S. Fauqueux, and P. Joly, "Stability of perfectly matched layers, group velocities and anisotropic waves," J. Comput. Phys. **188**, 399–433 (2003).

Journal of Computational Physics 356 (2018) 391–409

Contents lists available at ScienceDirect

Journal of Computational Physics

www.elsevier.com/locate/jcp

# A modal approach based on perfectly matched layers for the forced response of elastic open waveguides

M. Gallezot, F. Treyssède *, L. Laguerre

*IFSTTAR, GERS, GeoEND, F-44344, Bouguenais, France*

ARTICLE INFO

*Article history:*
Received 21 July 2017
Received in revised form 8 December 2017
Accepted 10 December 2017
Available online 14 December 2017

*Keywords:*
Open waveguide
Forced response
Perfectly matched layer
Orthogonality
PML modes
Leaky modes

ABSTRACT

This paper investigates the computation of the forced response of elastic open waveguides with a numerical modal approach based on perfectly matched layers (PML). With a PML of infinite thickness, the solution can theoretically be expanded as a discrete sum of trapped modes, a discrete sum of leaky modes and a continuous sum of radiation modes related to the PML branch cuts. Yet with numerical methods (*e.g.* finite elements), the waveguide cross-section is discretized and the PML must be truncated to a finite thickness. This truncation transforms the continuous sum into a discrete set of PML modes. To guarantee the uniqueness of the numerical solution of the forced response problem, an orthogonality relationship is proposed. This relationship is applicable to any type of modes (trapped, leaky and PML modes) and hence allows the numerical solution to be expanded on a discrete sum in a convenient manner. This also leads to an expression for the modal excitability valid for leaky modes. The physical relevance of each type of mode for the solution is clarified through two numerical test cases, a homogeneous medium and a circular bar waveguide example, excited by a point source. The former is favourably compared to a transient analytical solution, showing that PML modes reassemble the bulk wave contribution in a homogeneous medium. The latter shows that the PML mode contribution yields the long-term diffraction phenomenon whereas the leaky mode contribution prevails closer to the source. The leaky mode contribution is shown to remain accurate even with a relatively small PML thickness, hence reducing the computational cost. This is of particular interest for solving three-dimensional waveguide problems, involving two-dimensional cross-sections of arbitrary shapes. Such a problem is handled in a third numerical example by considering a buried square bar.



## 1. Introduction

### 1.1. Context and state-of-the-art

Elastic guided waves are interesting for many applications involving elongated structures (*e.g.* non-destructive evaluation (NDE), structural health monitoring (SHM), exploration geophysics...), because of their ability to propagate over large distances. When the structure (the core) is embedded into a large solid matrix, it can be considered as an open waveguide (unbounded in the transverse direction). Such a configuration typically occurs in civil engineering and in geophysics for

* Corresponding author.
*E-mail addresses:* matthieu.gallezot@ifsttar.fr (M. Gallezot), fabien.treyssede@ifsttar.fr (F. Treyssède), laurent.laguerre@ifsttar.fr (L. Laguerre).

https://doi.org/10.1016/j.jcp.2017.12.017
0021-9991/

example. Contrary to waveguides in vacuum (closed waveguides), most of the waves in open waveguides are attenuated by leakage in the surrounding medium as they propagate. Moreover, the underlying physics is deeply transformed.

Indeed, in open waveguides, three main kinds of modes are distinguished: trapped modes, radiation modes, and leaky modes. Trapped modes propagate without leakage attenuation along the waveguide axis and decay exponentially in the transverse direction. These waves are confined in the core of the waveguide or at the interface. Their existence depends on material contrasts between the core and the surrounding medium [1]. Radiation modes are standing waves in the transverse direction, which are propagative or evanescent in the axis direction [2,3]. Finally, leaky modes propagate with leakage attenuation along the waveguide axis. These modes dramatically grow exponentially in the transverse direction [2,4,5].

Modes are computed by considering the source-free problem. This can be done by analytical methods (*e.g.* the Thomson–Haskell [6,7], the stiffness matrix [8] or the global matrix [9] methods), which are yet limited to canonical waveguide geometries. Numerical methods are well-suited for more complex geometries. The idea is then to discretize only the cross-section of the waveguide while describing analytically the direction of the wave propagation. In closed waveguides, this approach yields a linear eigenvalue problem. It has been applied under various names in the literature, such as the extended Ritz technique [10,11]; the thin layer method (TLM) for stratified waveguides in geophysics [12,13]; the strip-element method [14], the Semi-Analytical Finite Element method (SAFE) [15,16] or more recently the Scaled Boundary Finite Element Method (SBFEM) [17,18] in ultrasonics. In this paper, this approach will be referred to as *waveguide formulation* to avoid the use of acronyms.

Extending the waveguide formulation to open waveguides is not straightforward because of the unbounded nature of the problem in the transverse direction. This difficulty is enhanced by the transverse growth of leaky modes. Therefore, the waveguide formulation must be coupled to other techniques to numerically compute the modes of open waveguides.

The first class of methods avoids the discretization of the embedding medium by using appropriate boundary conditions. The waveguide formulation has been combined with the boundary element method to model three-dimensional waveguides immersed in fluids [19,20] or embedded in solids [21]. Similarly, exact boundary conditions have been proposed for two-dimensional waveguides (plates and cylinders) immersed in fluids [22]. All of these boundary conditions lead to a highly non-linear eigenproblem that is difficult to solve. The latter can be linearized in the case of two-dimensional plates immersed in perfect fluids [23,24]. In the case of high-contrast solid waveguides, the waveguide formulation can also be coupled to an approximate condition (the so-called dashpot boundary condition) [25]. With this approximation, the eigenproblem remains linear.

The second class of methods requires a discretization of the surrounding medium, which must be truncated. The eigenproblem remains linear. To avoid spurious reflections due to truncation, the waveguide formulation have been combined with non-reflecting [26] and continued-fraction absorbing [27] boundary conditions in fluids, or paraxial approximation in solids [13,28]. Absorbing layers of artificially growing damping can also be used to simulate fluid [29] or solid [30] infinite media. Another technique consists in using a Perfectly Matched Layer (PML) to model the infinite surrounding medium (solid or fluid) [31–36]. Contrary to absorbing layers, the PML avoids most spurious reflections from the layer, which allows its thickness to be greatly reduced. Moreover, it have been shown that the computation of leaky modes with a PML is mathematically relevant (see Ref. [37] for scalar wave problems).

As far as the forced response problem is concerned, modal expansion methods have been widely applied in closed waveguides [38]. However, their application to open elastic waveguides is more intricate and has been barely considered in the literature. With a numerical approach, the particular case of two-dimensional plates immersed in fluids has recently been handled by a waveguide formulation with exact boundary conditions [24]. The case of a stratified plate over or between half-spaces has been treated using a PML in Ref. [36].

Theoretically, the forced response of an open waveguide can be expanded on trapped modes and radiation modes [2,3,39], such that the displacement field can be symbolically written as:

$$u(\mathbf{r},\omega) = \sum \text{trapped} + \int \text{radiation modes} \tag{1}$$

where, in addition to trapped modes, complex poles of backward type are also likely to occur depending on the problem type [40,41]. Let us briefly recall the origin of Eq. (1). In the wavenumber domain, the solution of the problem is a multivalued function owing its dependence on the transverse wavenumber of the unbounded medium. The transverse wavenumber is indeed the square root of a complex number on a two-sheeted Riemann surface. To evaluate analytically the inverse spatial Fourier transform of the solution, a branch cut is defined separating the proper Riemann sheet (where trapped modes occur) from the improper Riemann sheet (where leaky modes occur). Hence, the inverse transform integration is performed only on the proper sheet and gives rise [see Eq. (1)] to the discrete sum of trapped modes and to the continuum of radiation modes, which represents the branch cut contribution. This continuum is characteristic of the unboundedness of the modal problem and is difficult to manipulate from a mathematical point of view. In elastodynamics, there are two continua instead of one because two transverse wavenumbers occur (longitudinal and shear waves) [42,43]. The continua can actually be approximated with a convenient discrete set of leaky modes, *e.g.* using the steepest descent method [39,40]. This approximation is valid in a zone restricted near the core, in which leaky modes can provide useful practical information such as axial attenuation and travelling velocity of waves packets [44].

In a recent work [45], the authors have shown that when the surrounding medium is modified by an infinite PML, the forced response can theoretically be obtained with a modal expansion on trapped modes, revealed leaky modes and two

continua of radiation modes related to the PML branch cuts. With numerical methods, the PML must yet be truncated to a finite thickness. The continua are then transformed into discrete sets of PML modes. It remains necessary to investigate the use of the so-obtained numerical modes to compute the forced response, based on an appropriate orthogonality relationship to guarantee the uniqueness of the solution. It is of particular interest to derive a general orthogonality relationship that remains applicable for a wide class of problems, including viscoelastic materials, full anisotropy and 3D waveguides of arbitrary cross-section. Moreover, it is necessary to clarify the contribution and the physical relevance of leaky and PML modes in the solution of the problem.

The aim of this article is to compute the forced response of elastic open waveguides with a modal approach based on a waveguide formulation combined with a PML. This approach will be termed PML waveguide formulation in this paper. It is briefly recalled in Sec. 1.2. Then, the modal approach used to compute the forced response is presented in Sec. 2. A general biorthogonality relationship is derived for the modes of the PML waveguide formulation. A validation test case is presented by considering a fully homogeneous medium in Sec. 3. Results are compared with an analytic solution, which allows understanding how the PML parameters act on PML modes together with the accuracy of the solution. Section 4 shows numerical results obtained for a circular bar waveguide (widely encountered in civil engineering). Time-domain results are obtained, which enables to clearly identify the distinctive role of PML modes and leaky modes and their ability to approximate the total field. An open square bar example is finally considered, in order to show the ability of the approach to handle three-dimensional waveguide problems.

### *1.2. PML waveguide formulation for mode computation*

This section briefly recalls the PML waveguide formulation to compute the eigenmodes of an open waveguide [31,32]. One considers an elastic open waveguide, where $z$ is the propagation axis of the waveguide. The core of the waveguide has an arbitrary cross-section. It is embedded in an infinite medium. Small strains and displacements are assumed. A time-harmonic dependence $\mathrm{e}^{-\mathrm{j}\omega t}$ is chosen. The elastodynamic equilibrium equations are written as:

$$\tilde{\nabla}.\tilde{\sigma}(\tilde{\mathbf{u}}) + \tilde{\rho}\omega^2\tilde{\mathbf{u}} = \tilde{\mathbf{f}}, \tag{2}$$

where $\tilde{\mathbf{u}}$ is the displacement vector field. The tilde notation is explained in the following with the PML introduction. $\tilde{\sigma}(\tilde{\mathbf{u}})$ is the stress tensor. The stress-strain relation is $\tilde{\sigma}(\tilde{\mathbf{u}}) = \tilde{C} : \tilde{\epsilon}(\tilde{\mathbf{u}})$, where $\tilde{C}$ is the stiffness tensor (complex for viscoelastic materials). The strain-displacement relation is $\tilde{\epsilon}(\tilde{\mathbf{u}}) = (\nabla\tilde{\mathbf{u}} + (\nabla\tilde{\mathbf{u}})^{\mathrm{T}})/2$. The superscript T denotes the transpose. $\tilde{\mathbf{f}}$ is the vector of volumic forces.

For numerical purpose, the infinite surrounding medium is truncated by a finite PML of thickness $h$. A radial PML is introduced by analytic continuation [46] of the elastodynamic equations (2) into the complex transverse coordinate $\tilde{r}$:

$$\tilde{r}(r) = \int_0^r \gamma(\xi)\mathrm{d}\xi. \tag{3}$$

Note that a Cartesian PML could be used instead of a radial PML [32], as done in Sec. 4.5. The function $\gamma(r)$ is a user-defined complex-valued function for absorbing outgoing waves in the surrounding medium, such that:

- $\gamma(r) = 1$ outside the PML region ($r < d$),
- $\mathrm{Im}(\gamma(r)) > 0$ inside the PML region ($d < r < d + h$).

$d$ is the position of the PML interface. A boundary condition is arbitrarily applied at the end of the PML. In this paper, a Dirichlet condition is used. Eq. (2) must be transformed to go back to the real radial direction $r$. The change of variable $\tilde{r} \mapsto r$ for any function $\tilde{g}(\tilde{r})$ gives:

$$\tilde{g}(\tilde{r}) = g(r), \quad \mathrm{d}\tilde{r} = \gamma(r)\mathrm{d}r, \quad \frac{\partial\tilde{g}}{\partial\tilde{r}} = \frac{\partial g}{\partial r}\frac{1}{\gamma(r)}. \tag{4}$$

Following the waveguide formulation in closed waveguides [31,32], the strain-displacement relation can be written as:

$$\boldsymbol{\epsilon} = (\mathbf{L}_S + \mathbf{L}_z\frac{\partial}{\partial z})\mathbf{u}, \tag{5}$$

where $\boldsymbol{\epsilon}$ is the strain vector and $\mathbf{u}$ the displacement vector. $\mathbf{L}_S$ is the operator containing all terms but derivatives with respect to the $z$-axis, and $\mathbf{L}_z$ is the operator of $z$-derivatives. The operator $\mathbf{L}_S$ includes derivatives with respect to $r$ and hence it depends on $\gamma(r)$ and $\tilde{r}$ [32]. A FE discretization is then applied to the cross-section (spectral elements can be equally used [33]). The displacement on each element can be written $\mathbf{u}^e(x, y, z, \omega) = \mathbf{N}^e(x, y)\mathbf{U}^e(z, \omega)$, where $\mathbf{N}^e(x, y)$ is the matrix of two-dimensional interpolation functions and $\mathbf{U}^e(z, \omega)$ is the vector of nodal displacements. The derivation of the weak formulation of Eq. (2) yields the global matrix system:

$$(\mathbf{K}_1 - \omega^2\mathbf{M})\mathbf{U} + (\mathbf{K}_2 - \mathbf{K}_2^{\mathrm{T}})\mathbf{U}_{,z} - \mathbf{K}_3\mathbf{U}_{,zz} = \mathbf{F}, \tag{6}$$

with the element matrices:

$$\mathbf{K}_1^e = \int \mathbf{L}_S^{\mathrm{T}}\mathbf{C}\mathbf{L}_z \frac{\tilde{r}\gamma}{r}\mathrm{d}S, \quad \mathbf{K}_2^e = \int \mathbf{L}_S^{\mathrm{T}}\mathbf{C}\mathbf{L}_z \frac{\tilde{r}\gamma}{r}\mathrm{d}S, \quad \mathbf{K}_3^e = \int \mathbf{L}_z^{\mathrm{T}}\mathbf{C}\mathbf{L}_z \frac{\tilde{r}\gamma}{r}\mathrm{d}S,$$
$$\mathbf{M}^e = \int \rho \mathbf{N}^{e\mathrm{T}}\mathbf{N}^e \frac{\tilde{r}\gamma}{r}\mathrm{d}S, \quad \mathbf{F}^e = \int \mathbf{N}^{e\mathrm{T}}\mathbf{f}\frac{\tilde{r}\gamma}{r}\mathrm{d}S, \tag{7}$$

where $\mathbf{C}$ is the stiffness matrix defined from Voigt notation of the tensor $C$.

A spatial Fourier transform in the $z$-direction is applied to Eq. (6), which leads to the PML waveguide formulation [31,32]:

$$\left(\mathbf{K}_1 - \omega^2\mathbf{M} + \mathrm{j}k(\mathbf{K}_2 - \mathbf{K}_2^{\mathrm{T}}) + k^2\mathbf{K}_3\right)\hat{\mathbf{U}} = \hat{\mathbf{F}}, \tag{8}$$

where $\hat{\mathbf{U}}(k,\omega)$ is the vector of nodal displacements, $\hat{\mathbf{F}}$ is the vector of nodal forces and $k$ is the axial wavenumber with the following notation for any function $g(z)$:

$$\hat{g}(k) = \int_{-\infty}^{+\infty} g(z)\mathrm{e}^{-\mathrm{j}kz}\mathrm{d}z. \tag{9}$$

Further details of the derivation can be found in Refs. [31,32]. For paper self-containedness, additional steps are given in Appendix A for an axisymmetric open waveguide, which will be used for most of the numerical results presented in Secs. 3 and 4.

The source term in Eq. (8) is dropped (*i.e.* $\hat{\mathbf{F}} = 0$). The source-free problem gives a quadratic eigenvalue problem in terms of $k$. The eigenproblem is linearized (see Appendix B) and solved for each angular frequency $\omega$. The matrices $\mathbf{K}_1$, $\mathbf{K}_3$ and $\mathbf{M}$ are symmetric. From this property, it can be shown that the eigenspectrum is made of symmetric pairs of eigenvalues and eigenvectors, $(k_m, \mathbf{U}_m)$ and $(-k_m, \mathbf{U}_m^-)$, $(m = 1, \ldots, M)$, representing $M$ positive-going modes and $M$ negative-going modes respectively. In the following, the negative-going modes will be denoted $(k_{-m}, \mathbf{U}_{-m})$.

As recalled in Sec. 1.1, the PML waveguide formulation gives three kinds of eigenmodes: trapped modes (if any), leaky modes and the so-called PML modes. PML parameters have a strong influence on the accuracy of trapped and leaky modes. Theoretically (see *e.g.* Refs. [31,32]), leaky modes are attenuated by the PML if:

$$\arg(k_{l/s}) > -\arg(\hat{\gamma}), \tag{10}$$

where $k_{l/s}$ is the longitudinal or shear transverse wavenumber and $\hat{\gamma}$ is the average value of $\gamma(r)$ inside the PML region. When the condition (10) is fulfilled, only small reflections occur at the end of a thick enough PML. As usual with PML, the attenuation rate should not be too high to be properly approximated by the FE discretization. Concerning trapped modes, the PML can accentuate their natural transverse decay if $\mathrm{Re}(\hat{\gamma}) > 1$ [31,32]. As for PML modes, these modes mainly resonate inside the PML and fully depend on PML parameters.

## 2. Forced response of an elastic open waveguide

Any arbitrary field in a waveguide can be expanded on a unique set of modes, provided that these modes are orthogonal [38]. In elastic open waveguides, orthogonality relationships theoretically hold between trapped modes and radiation modes, see *e.g.* Ref. [3,42]. However, the continua of radiation modes are difficult to manipulate. Conversely, leaky modes form a discrete set, which may approximate the radiation field [47–49] and which is easier to handle. However, they cannot satisfy orthogonality relationships [5,47], as they theoretically grow to infinity in the transverse direction (as recalled in Eq. (1), leaky modes do not belong to the theoretical modal basis). In this section, a general orthogonality relationship is derived when a finite PML is introduced to close the open problem.

### 2.1. Effects of a PML on the modal basis

In a recent work, the authors have studied the modal basis of an elastic open waveguide when the surrounding medium is replaced by an infinite PML [45]. It has been shown that the introduction of an infinite PML of constant attenuation profile $\gamma$ modifies the transverse wavenumbers and yields a rotation of branch cuts by an angle of $-\arg(\gamma)$ [45]. The rotation of the branch cuts induces a partial access to the initial improper sheets where leaky modes occur. Therefore with a PML, a discrete set of revealed leaky modes must be included in the modal basis. The set of trapped modes is left unchanged and the solution field with an infinite PML can hence be written:

$$\mathbf{u}(\mathbf{r},\omega) = \sum \text{trapped modes} + \sum \text{revealed leaky modes} + \int \text{PML branch cuts}. \tag{11}$$

The solution field described by Eq. (11) remains physically valid only in the region out of the PML ($r < d$).

With numerical methods, the PML must be truncated to a finite thickness. The continuous sums related to the PML branch cuts are then discretized [31,32,50]. These discretized sets are PML modes, non-intrinsic to the physics since they fully depend on the parameters of the truncated PML and on the boundary condition applied at the end of the PML. Therefore, the role of these sets in the convergence of the modal expansion might be questionable at first sight. This topic will be addressed in Sec. 3 through numerical results.

### 2.2. Derivation of a biorthogonality relationship

Let us start from the linear eigenvalue problem (see Appendix B), written for a mode $m$:

$$(\mathbf{A} - k_m \mathbf{B})\mathbf{x}_m = \mathbf{0}, \tag{12}$$

with $\mathbf{x}_m^{\mathrm{T}} = [\mathbf{U}_m^{\mathrm{T}} \; k_m \mathbf{U}_m^{\mathrm{T}}]^{\mathrm{T}}$. $\mathbf{A}$ is not symmetric, and then left eigenvectors must be considered [51]. The left eigenvector $\mathbf{y}_n$ satisfies the eigensystem:

$$\mathbf{y}_n^{\mathrm{T}}(\mathbf{A} - k_n \mathbf{B}) = \mathbf{0}. \tag{13}$$

The left and right eigenvectors are related by the following general biorthogonality relationships:

$$\mathbf{y}_n^{\mathrm{T}}\mathbf{B}\mathbf{x}_m = b_m \delta_{mn}, \quad \mathbf{y}_n^{\mathrm{T}}\mathbf{A}\mathbf{x}_m = k_m b_m \delta_{mn}, \tag{14}$$

where $b_m$ is a normalization factor and $\delta_{mn}$ is the Kronecker' symbol. $\mathbf{B}$ is symmetric, and from Eq. (13), the left eigenvector $\mathbf{y}_m$ satisfies:

$$(\mathbf{A}^{\mathrm{T}} - k_m \mathbf{B})\mathbf{y}_m = \mathbf{0}. \tag{15}$$

It can be checked that the above eigensystem is satisfied with:

$$\mathbf{y}_m^{\mathrm{T}} = [\mathbf{U}_{-m}^{\mathrm{T}} \; k_m \mathbf{U}_{-m}^{\mathrm{T}}]^{\mathrm{T}}. \tag{16}$$

The left eigenvectors can then be directly related to the right eigenvectors. This avoids to solve the left eigenproblem. Hence, from Eq. (B.2) the biorthogonality relationship $\mathbf{y}_n^{\mathrm{T}}\mathbf{B}\mathbf{x}_m = b_m \delta_{mn}$ can be expanded as:

$$\mathbf{U}_{-n}^{\mathrm{T}}(\mathbf{K}_1 - \omega^2 \mathbf{M})\mathbf{U}_m + k_n k_m \mathbf{U}_{-n}^{\mathrm{T}} \mathbf{K}_3 \mathbf{U}_m = b_m \delta_{mn}. \tag{17}$$

From Eq. (B.3) written for a given mode $m$, one gets $(\mathbf{K}_1 - \omega^2 \mathbf{M})\mathbf{U}_m = -\mathrm{j}k_m(\mathbf{K}_2 - \mathbf{K}_2^{\mathrm{T}})\mathbf{U}_m - k_m^2 \mathbf{K}_3 \mathbf{U}_m$. Eq. (17) can then be rewritten as:

$$\mathrm{j}k_m \mathbf{U}_{-n}^{\mathrm{T}}(\mathbf{K}_2^{\mathrm{T}} + \mathrm{j}k_m \mathbf{K}_3)\mathbf{U}_m - \mathrm{j}k_m \mathbf{U}_{-n}^{\mathrm{T}}(\mathbf{K}_2 - \mathrm{j}k_n \mathbf{K}_3)\mathbf{U}_m = b_m \delta_{mn}. \tag{18}$$

In Eq. (18), one can identify the so-called modal forces [52]:

$$\mathbf{F}_m = (\mathbf{K}_2^{\mathrm{T}} + \mathrm{j}k_m \mathbf{K}_3)\mathbf{U}_m, \tag{19}$$

such that after rearrangement, Eq. (18) yields:

$$\frac{\mathrm{j}\omega}{4}(\mathbf{U}_m^{\mathrm{T}}\mathbf{F}_{-n} - \mathbf{U}_{-n}^{\mathrm{T}}\mathbf{F}_m) = Q_{m,-m}\delta_{mn}, \tag{20}$$

with $Q_{m,-m} = -\omega b_m / 4k_m$. Eq. (20) provides a general orthogonality relationship involving the whole cross-section of the waveguide (*i.e.* including the finite PML). It is applicable to any kind of modes without distinction (trapped, leaky and PML modes).

This orthogonality relationship is identical to the orthogonality relationship derived for lossy closed waveguides in [52]. It remains valid for 3D waveguides of arbitrary cross-section, as well as for fully anisotropic and viscoelastic materials (it is noteworthy that Eq. (20) is also applicable with absorbing viscoelastic layers, see e.g. results in Ref. [52]). As shown in this reference, Eq. (20) can be readily expressed in an analytical form:

$$Q_{m,-n} = \frac{\mathrm{j}\omega}{4}\int_S (\mathbf{u}_m.\mathbf{t}_{-n} - \mathbf{u}_{-n}.\mathbf{t}_m)\mathrm{d}S = 0 \quad \text{if} \quad m \neq n, \tag{21}$$

where for each mode, $\mathbf{t}_m$ is the traction vector applied on the section $S$. Actually, Eq. (21) corresponds to Auld's real orthogonality relationship [38], which could therefore be used for the analytical modelling of open waveguides truncated by a finite PML. Note that except for real wavenumber modes (perfectly guided modes or trapped modes), $Q_{m,-m}$ differs from the averaged power flow $P_m$ [52]. The averaged power flow can yet be computed from the Poynting vector of each mode from Eq. (29).

As a side remark, a mathematically exact orthogonality relationship has been proposed in Ref. [47] for leaky modes in dielectric waveguides by deforming the radial coordinate into the complex plane. The approach of the present paper, applied to elastodynamics, is quite similar.

### 2.3. Modal solution of the problem

Let us consider the excitation of the waveguide by a force. The linear formulation [see Eq. (B.1)] is premultiplied by $\mathbf{y}_n^{\mathrm{T}}$ and the vector $\mathbf{x}$ is decomposed on $2M$ modes as follows: $\mathbf{x} = \sum_{-M}^{M} \alpha_m \mathbf{x}_m$ ($m \neq 0$). The system is then expanded and, thanks to the biorthogonality relation (20), it can be checked that the modal coefficients are given by $\alpha_m = -\omega \mathbf{U}_{-m}^{\mathrm{T}} \hat{\mathbf{F}} / [4 Q_{m,-m}(k_m - k)]$. Hence, the displacement solution to the forced response problem is:

$$\hat{\mathbf{U}} = -\sum_{\substack{m=-M \\ m\neq 0}}^{+M} \frac{\omega \mathbf{U}_{-m}^{\mathrm{T}} \hat{\mathbf{F}}}{4 Q_{m,-m}(k_m - k)} \mathbf{U}_m. \tag{22}$$

Then, the inverse Fourier transform $\mathbf{U}(z,\omega) = 1/(2\pi) \int_{\infty}^{+\infty} \hat{\mathbf{U}}(k,\omega) \mathrm{e}^{\mathrm{j}kz} \mathrm{d}k$ is used to go back to the real space $(z,\omega)$. With the help of Cauchy residue theorem, it can be shown that the field outside the source region going towards the positive $z$ direction is [52]:

$$\mathbf{U}(z,\omega) = \sum_{m=1}^{M} \mathbf{E}_m \hat{\mathbf{F}}(k_m) \mathrm{e}^{\mathrm{j}k_m z} \tag{23}$$

where $\mathbf{E}_m$ is the generalized modal excitability matrix:

$$\mathbf{E}_m = \frac{\mathrm{j}\omega}{4 Q_{m,-m}} \mathbf{U}_m \mathbf{U}_{-m}^{\mathrm{T}}. \tag{24}$$

$(\mathbf{E}_m)_{ij}$ is the displacement amplitude of mode $m$ at degree of freedom (dof) $i$ when excited by a unit force at dof $j$. If one is interested in the field going towards the negative $z$ direction, then the summation in Eq. (23) must be performed on negative-going modes. The $+\mathrm{j}$ factor in Eq. (24) is replaced by $-\mathrm{j}$ and the subscripts $m$ and $-m$ are switched.

Finally, the time-transient displacement is obtained by the inverse Fourier transform $1/(2\pi) \int_{\infty}^{+\infty} \mathbf{U}(z,\omega) \mathrm{e}^{-\mathrm{j}\omega t} \mathrm{d}\omega$.

### 2.4. Determination of the travelling direction

The solution given by Eq. (23) requires to determine the travelling direction of each mode. Modal characteristics can be computed straightforwardly from the eigensolutions $(k_m, \mathbf{U}_m)$ and the finite element matrices [32]. The phase velocity of a mode $m$ is:

$$v_{p_m} = \frac{\omega}{\mathrm{Re}(k_m)}. \tag{25}$$

Its attenuation in dB/m is:

$$\eta_m = 8,686 \mathrm{Im}(k_m). \tag{26}$$

The group velocity $v_{g_m} = \partial\omega/\partial k_m$ is computed as follows:

$$v_{g_m} = \mathrm{Re}\left[ \left( \frac{2\omega \mathbf{U}_{-m}^{\mathrm{T}} \mathbf{M} \mathbf{U}_m}{\mathbf{U}_{-m}^{\mathrm{T}} (\mathrm{j}(\mathbf{K}_2 - \mathbf{K}_2^{\mathrm{T}}) + 2k_m \mathbf{K}_3) \mathbf{U}_m} \right)^{-1} \right]. \tag{27}$$

The phase velocity does not necessarily give the travelling direction owing to the existence of backward modes, which have phase and group velocities of opposite sign [38]. The direction of propagation of the modes can be properly determined according to the following criterion:

- the sign of $\mathrm{Im}(k_m)$ if $\mathrm{Im}(k_m) \neq 0$, such that if $\mathrm{Im}(k_m) > 0$, the mode is a positive-going mode, and if $\mathrm{Im}(k_m) < 0$ the mode is negative-going,
- the sign of $v_{g_m}$ if $k_m \in \mathbb{R}$ (that is for trapped modes, when they exist).

The case of trapped modes is somehow particular. The case of purely trapped modes never occurs in viscoelastic media since the wavenumbers always have a non zero imaginary part. In purely elastic waveguides, trapped waves exist only if the shear velocity is greater in the core, unless longitudinal and shear waves couple into interface trapped waves, called Stoneley waves [1].

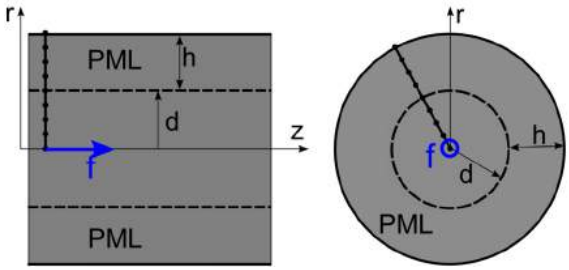


**Fig. 1.** (Colour online) Sketch of the excited homogeneous medium truncated by a finite PML.

### 2.5. Remarks on the energy velocity

In lossy waveguides, it has been shown that the group velocity can yield non-physical values [53], so that the energy velocity is usually preferred in closed waveguides. However, the energy velocity must be averaged on the whole cross-section, which is theoretically unbounded considering open waveguides.

For trapped modes, which are non-attenuated waves that exponentially decay in the transverse direction, the group velocity is equal to the energy velocity. Hence, the criterion proposed in Section 2.4 to determine their travelling direction is consistent (it does not matter whether the group velocity or the energy velocity is used).

For leaky modes, the energy velocity cannot be theoretically defined because these modes grow to infinity in the transverse directions. In practice, the energy velocity integration of leaky modes is usually restricted to the core, which can give a reasonable approximation of the velocity of wave packets [44,53]. The energy velocity restricted to the core cross-section can be calculated as follows:

$$v_{e_m} = \frac{\mathrm{Re}(P_m)}{\mathrm{Re}(T_m) + \mathrm{Re}(V_m)}, \tag{28}$$

where for each mode $m$, $P_m$ is the normal component of the Poynting vector integrated on the core cross-section, $T_m$ is the core cross-section and time-averaged kinetic energy, and $V_m$ is the core cross-section and time-averaged potential energy. These quantities can be post-processed from [32]:

$$P_m = \frac{-\mathrm{j}\omega}{2}\overline{\mathbf{U}}_m^*(\overline{\mathbf{K}}_2^{\mathrm{T}} + \mathrm{j}k_m\overline{\mathbf{K}}_3)\overline{\mathbf{U}}_m\ , \tag{29}$$

$$T_m = \frac{\omega^2}{4}\overline{\mathbf{U}}_m^*\overline{\mathbf{M}}\overline{\mathbf{U}}_m\ , \tag{30}$$

$$V_m = \frac{1}{4}\overline{\mathbf{U}}_m^*(\overline{\mathbf{K}}_1 + \mathrm{j}k_m\overline{\mathbf{K}}_2 - \mathrm{j}k_m^*\overline{\mathbf{K}}_2^{\mathrm{T}} + k_m^*k_m\overline{\mathbf{K}}_3)\overline{\mathbf{U}}_m\ , \tag{31}$$

where the $^*$ superscript denotes conjugate transpose and the overbar stands for the dof restriction to the core cross-section.

It is noteworthy that the integration restriction to the core is quite arbitrary. Therefore, the so-defined energy velocity cannot be considered as a general indicator to determine the travelling direction of any type of modes (of PML modes, in particular). In the following of this paper, the above-defined energy velocity will be only used for the post-processing of dispersion curves of leaky modes and their comparison with literature results.

## 3. The homogeneous test case

In this section, the forced response of a homogeneous medium excited by a point load is computed by the numerical method and compared to an analytical solution. A homogeneous medium can be viewed as an open waveguide without a core. This test case is actually the worst scenario for the numerical modal approach since there is no contrast of impedance: only the discrete set of PML modes occurs (there is neither trapped nor leaky modes). As outlined in Section 2.1, the contribution of PML modes to the solution has to be clarified because these modes are not intrinsic to the physics (they mainly oscillate in the PML region, which mainly depends on user-defined parameters).

### 3.1. Description

Let us assume a homogeneous, isotropic and unbounded medium, made of cement grout material (see Fig. 1). Material properties are given in Table 1. In this section, the medium is pure elastic ($\eta_l = \eta_s = 0$). The medium is excited by a point force in the $z$-direction at the origin: $\mathbf{f} = F(t)\delta(\mathbf{x})\mathbf{e_z}$ ($\mathbf{f} = \frac{F(t)}{2\pi r}\delta(r)\delta(z)\mathbf{e_z}$ in cylindrical coordinates). The signal $F(t)$ is a sinus of centre frequency $f_c = 60$ kHz with an amplitude of 1 N, modulated over 5 cycles by a Hanning window.

**Table 1**
Material properties.

| Material | $\rho$ (kg/m$^3$) | $c_l$ (m/s) | $c_s$ (m/s) | $\eta_l$ (Np/wavelength) | $\eta_s$ (Np/wavelength) |
|---|---|---|---|---|---|
| Cement grout | 1600 | 2810 | 1700 | 0.043 | 0.1 |
| Steel | 7932 | 5960 | 3260 | 0.003 | 0.008 |

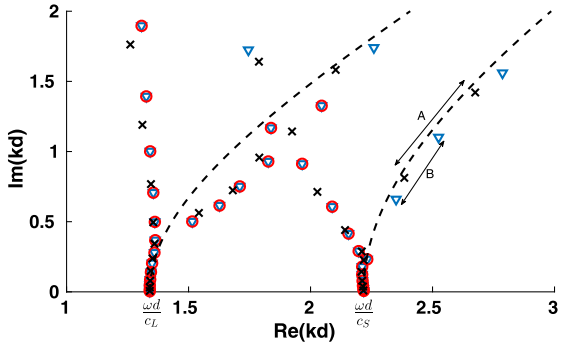


**Fig. 2.** (Colour online) Wavenumber spectrum of an elastic homogeneous medium computed with the PML waveguide formulation at $f = f_c$. PML parameters: $\hat{\gamma} = 4 + 4\mathrm{j}$; blue triangle: $h = 4d$, $M = 50$; red circle: $h = 4d$, $M = 30$; black cross: $h = 3d$, $M = 50$. Dashed black line: theoretical branch cut rotated by $-\arg(d + h\hat{\gamma})$ with $h = 4d$.

The transient axial displacement along the $z$-axis (*i.e.* at $r = 0$) at a distance $z$ to the source is given by the following analytical solution (see *e.g.* Ref. [54]):

$$u_z^{\mathrm{ref}}(z,t) = \frac{1}{2\pi\rho z^3}\int_{z/c_l}^{z/c_s} \tau F(t-\tau)\mathrm{d}\tau + \frac{1}{4\pi\rho c_l^2 z}F(t-\frac{z}{c_l}). \tag{32}$$

The first term of Eq. (32) is a near-field contribution. The second term is the far-field contribution of the P-wave (along the $z$-axis, there is no far-field contribution of the S-wave [54]).

The problem is solved with an axisymmetrical PML waveguide formulation (see Appendix A). The PML starts at $r = d =$ 10 mm. Following Refs. [31,32], the attenuation function of the PML is chosen as parabolic and is given by

$$\gamma(r) = \begin{cases} 1 & \text{if} \quad r \leq d \\ 1 + 3(\hat{\gamma} - 1)\left(\frac{r-d}{h}\right)^2 & \text{if} \quad r > d, \end{cases} \tag{33}$$

where $\hat{\gamma} = \frac{1}{h}\int_d^{d+h}\gamma(\xi)d\xi$ is the average value of $\gamma(r)$ inside the PML region. $\hat{\gamma}$ and $h$ are user-defined parameters. The solution is computed in the frequency range $[0, f_{\max}]$, with $f_{\max} = 120$ kHz, divided into 176 frequency steps. The cross-section is discretized with three-nodes line elements of length $\Delta r = 0.25d \approx \lambda_{min}/5$, where $\lambda_{\min} = c_s/f_{\max}$. The eigenproblem (B.4) is solved with the ARPACK library [55]. Based on an implicit restarted Arnoldi method, this library enables to compute a user-defined number of eigenvalues (denoted as $2M$) that are the closest in absolute value to a user-defined shift, set to 0 in this paper (except in Sec. 4.5). The displacement at the FE node located at $r = 0$ is then computed from Eq. (23) and denoted as $u_z^{\mathrm{num}}(z,\omega)$. The modal expansion (23) contains PML modes only.

The accuracy of the numerical solution is assessed as a function of the distance $z$ with the following relative error in the L2-norm:

$$e(z) = \sqrt{\frac{\int |u_z^{\mathrm{ref}}(z,\omega) - u_z^{\mathrm{num}}(z,\omega)|^2\mathrm{d}\omega}{\int |u_z^{\mathrm{ref}}(z,\omega)|^2\mathrm{d}\omega}}, \tag{34}$$

where $u_z^{\mathrm{ref}}(z,\omega)$ is obtained from the analytic Fourier transform of Eq. (32), given in Appendix C (from Parseval's equality, the relative error has the same value both in frequency and time domains).

### 3.2. Results

Fig. 2 represents the discrete modal spectrum in the complex wavenumber $kd$-plane ($\mathrm{Re}(kd) > 0, \mathrm{Im}(kd) > 0$) at the centre frequency, computed for $\hat{\gamma} = 4 + 4\mathrm{j}$ and the following three cases: ($h = 4d, M = 50$), ($h = 4d, M = 30$) and ($h = 3d$, $M = 50$). This enables to study the influence of two key features on the relative error of the forced response:

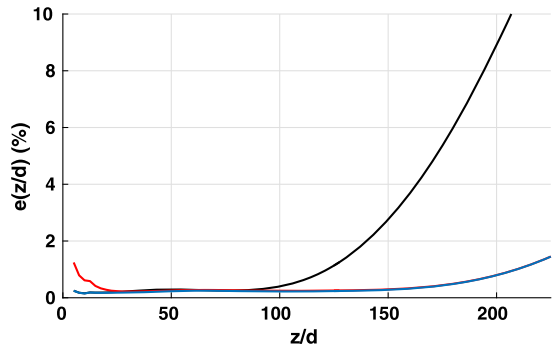


**Fig. 3.** (Colour online) Relative error as a function of the distance $z$ between PML waveguide formulation and analytical solutions. Same parameters and colour legend as in Fig. 2.

- the complex thickness $d + \hat{\gamma} h$,
- the number of modes $M$ retained in the modal expansion.

The number of dofs of the quadratic eigenvalue problem is equal to 68 dofs for $h = 3d$ and 84 dofs for $h = 4d$. These values must be multiplied by two for the linearized eigenvalue problem (see Appendix B).

As observed in Fig. 2, the poles close to the real axis ($\mathrm{Im}(kd) = 0$) lie along two hyperbolas, corresponding to the branch cuts rotated by the PML. As briefly recalled in Sec. 2.1, these branch cuts are rotated by an angle equal to $-\arg(\gamma)$ in the case of an infinite PML (for further details, see Ref. [45]). For a PML of finite thickness, this angle becomes equal to $-\arg(d + h\hat{\gamma})$ as shown in Ref. [32]. Note that the deviation from the theoretical hyperbolas observed here for high order poles is explained by the FE approximation: this deviation can be moved further away from the real axis by reducing the size of elements (see Ref. [31]).

The relative error of the forced response is plotted in Fig. 3 as a function of the distance $z$. It can be observed that a good accuracy is reached for the three cases in the range $z \in [20d, 90d]$, with a relative error lower than 0.5%. This shows the ability of PML modes, when the PML is properly parametrized, to reconstruct the analytical solution. In particular, the geometrical decay of the field is well recovered by the superposition of PML modes, which are by nature exponentially decaying.

Further away from the source ($z > 90d$), it turns out that the error gets lower by increasing the complex thickness (compare red and blue results with the black ones). As shown in previous studies [31,32], the discretization of the continua gets denser as the complex thickness increases. This effect can be observed in Fig. 2 (see *e.g.* the distance labelled A and B between two poles for two different complex thicknesses). Indeed, only modes with low $|\mathrm{Im}(kd)|$ can significantly contribute to the forced response at far distances. It is then necessary to have a denser spectrum to reassemble a geometrically decaying solution.

Yet in the near field ($z < 20d$), even highly attenuated PML modes (with high $|\mathrm{Im}(kd)|$) can significantly contribute to the solution. For a given modal density (*i.e.* a given complex thickness), the error can then be reduced by increasing the maximum imaginary part of the computed spectrum, that is to say, the number of modes $M$ retained in the modal expansion (compare blue with red results). Conversely, for a fixed number of modes $M$, the error in the near field could also be reduced by decreasing the complex thickness.

It has to be mentioned that the numerical results of Fig. 3, obtained in this paper for the elastodynamic problem, are consistent with the theoretical proof of convergence of the PML mode expansion derived in Ref. [50] for the Helmholtz equation.

As an example, Fig. 4 compares the transient numerical and analytical solutions calculated at the distance $z = 175d$. Good agreement is found, which confirms the ability of the numerical approach to accurately compute the forced response even in the fully homogeneous configuration (worst scenario). Note that the distance $z = 175d$ will be of interest when considering a core waveguide example as discussed later in Sec. 4.

The argument of the complex thickness, denoted as $\theta$ ($\theta \in ]0, \pi/2[$), also plays a role on the accuracy of the numerical results. Fig. 5 shows the relative error for different values of $\theta$ by keeping constant the modulus of the complex thickness, set to $|d + h\hat{\gamma}| = 25$ ($h = 4d$, $M = 50$). This means that $\hat{\gamma}$ now varies as a function of $\theta$, such that $\mathrm{Im}(\hat{\gamma})$ increases as $\theta$ increases and conversely.

Not too far from the source, the error remains low regardless of the value of $\theta$ (less than 1.2% for $z/d \in [0, 150d]$). For greater distances, the error increases with a rate depending on $\theta$. The error remains small (below 2%) in a wide range of values ($\theta \in [30, 60]$ deg), with a minimum reached around $\theta = 45$ deg. Outside this range, the accuracy of the solution decreases because the PML attenuation is not strong enough. More precisely, when the argument is small (*e.g.* $\theta = 20$ deg), waves are reflected at the end of the PML ($\mathrm{Im}(\hat{\gamma})$ is too low), which deteriorates the solution. Equivalently, $\theta$ must not be too close to $\pi/2$ either (see *e.g.* $\theta = 70$ deg), otherwise the rotated branch cuts become too close to the real axis. In this

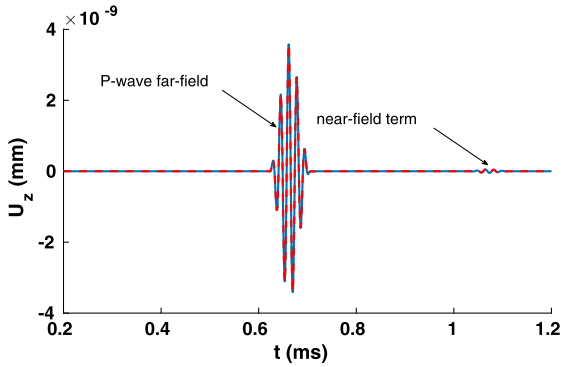


**Fig. 4.** (Colour online) Transient axial displacement calculated at a distance $z = 175d$ with the PML waveguide formulation (dashed red line) and the analytical solution (blue line). Parameters: cement grout, $\hat{\gamma} = 4 + 4\mathrm{j}$, $h = 4d$, $M = 50$.

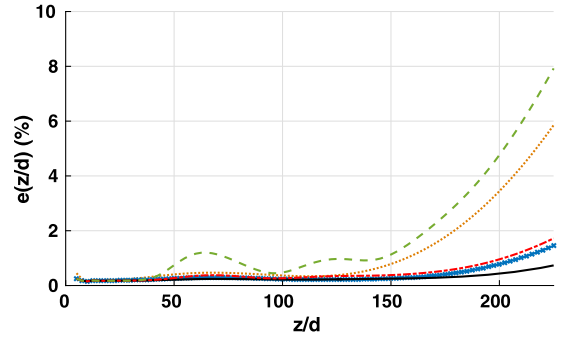


**Fig. 5.** (Colour online) Relative error as a function of distance between PML waveguide formulation and analytical solutions for a complex thickness $25e^{i\theta}$. Dotted orange line: $\theta = 20$ deg; crossed blue line: $\theta = 30$ deg; black line: $\theta = 45$ deg; dashed-dotted red line: $\theta = 60$ deg; dashed green line: $\theta = 70$ deg.

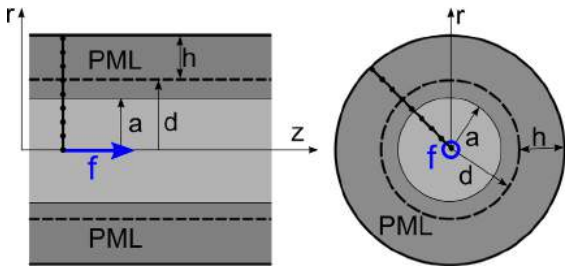


**Fig. 6.** (Colour online) Sketch of the excited steel circular bar embedded into cement grout truncated by a finite PML.

case, the problem becomes equivalent to the computation of trapped modes (these modes occur along the real axis also), and as shown in Ref. [31], a proper transverse attenuation of such modes requires to increase $\mathrm{Re}(\hat{\gamma})$ instead of $\mathrm{Im}(\hat{\gamma})$.

## 4. Application

A steel core is now included in the homogeneous medium previously studied (see Fig. 6). First, the core has a circular cross-section. This configuration enables to highlight the contribution of leaky modes, compared to that of PML modes, as a function of the distance to the source. As before, this open waveguide is modelled with the axisymmetrical PML waveguide formulation. Then, a square cross-section is considered as an example of three-dimensional waveguide.

### *4.1. Circular bar test case description*

The material properties are given in Table 1. The shear wave velocity in the core (steel) is greater than in the embedding medium (cement grout). For this configuration, there is no trapped modes [1,44], so that only leaky modes and PML modes occur. The core has a radius $a = 10$ mm. Both the elastic and viscoelastic cases will be considered. The embedding medium

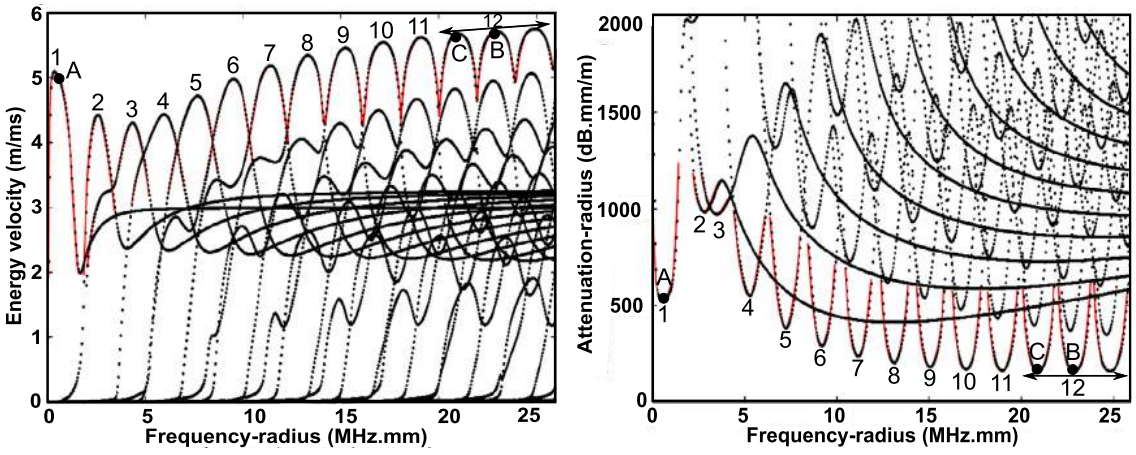


(a) (b)

**Fig. 7.** (Colour online) PML waveguide formulation results (black dots) and results of Ref. [44] (red line) for (a) the energy velocity and (b) the attenuation (steel circular bar embedded into cement grout, viscoelastic case). The PML parameters are: $h = a$, $\hat{\gamma} = 1 + 2\mathrm{j}$. Filtering criterion: $\eta_{\min} = 0.6$. Point A: $f = 0.60$ MHz mm; Point B: $f = 22.84$ MHz mm; Point C: $f = 20.92$ MHz mm.

is truncated by a PML of thickness $h$ starting at a distance $r = d$ with the same attenuation profile as Eq. (33). In order to avoid spurious eigenvalues and limit the transverse growth of leaky modes, it is preferable to set the PML close to the core [37] ($d - a$ should be small). The PML interface has been set to $d = a$.

#### 4.1.1. Dispersion curves

For the visualisation of dispersion curves, only the modes intrinsic to the physics are of interest (leaky and trapped modes). It is then necessary to filter out PML modes. A filtering criterion has been proposed in previous studies [31,32] to identify and remove PML modes. A slightly modified version is presented here. The proposed filtering criterion is based on the ratio of the imaginary part over the modulus of the kinetic energy, defined from Eq. (30) but integrating the whole cross-section (*i.e.* including the PML, so that the overbar has to be discarded in Eq. (30)). The modes are retained in the visualisation if they fulfil the following criterion:

$$1 - \frac{\mathrm{Im}(T_m)}{|T_m|} > \eta_{\min} \tag{35}$$

where $0 < \eta_{\min} < 1$ is a user-defined parameter.

The filtered dispersion curves obtained for the viscoelastic case are shown in Fig. 7. The figure shows 12 modes, of leaky type, corresponding to longitudinal modes (these modes are usually labelled $\mathrm{L}(0, n)$ in the literature). Also shown are the results of Ref. [44], which confirms the ability of the PML waveguide formulation to accurately compute leaky modes [31–33].

#### 4.1.2. Excitation parameters

The forced response of the open waveguide is computed with the same type of force as in Sec. 3, with an amplitude of 1 N, considering the following two signals:

- $f_c = 60$ kHz with a 5 cycles Hanning window. At this frequency, only one leaky mode propagates (see point A in Fig. 7). This low-frequency excitation allows a direct comparison with the results of Sec. 3 and aims to clarify the influence of leaky modes on the solution compared to that of PML modes. The problem is solved on the frequency range $[f_{\min}, f_{\max}]$, with $f_{\min} = 12$ kHz and $f_{\max} = 120$ kHz, divided into 323 frequency steps. The size of finite elements is set to $\Delta r = 0.25a$, yielding 84 dofs for the quadratic eigenvalue problem ($84 \times 2$ for the linearized one).
- $f_c = 2.284$ MHz with a 10 cycles Hanning window. This high-frequency excitation involves several leaky modes and is of interest for NDE because the mode of lowest attenuation is excited (see point B in Fig. 7). For this high-frequency excitation, the problem is solved for $[f_{\min}, f_{\max}]$, with $f_{\min} = 1.14$ MHz and $f_{\max} = 3.42$ MHz, divided into 1823 steps. The size of finite elements is set to $\Delta r = 0.019a$, yielding 240 dofs for the quadratic eigenvalue problem ($240 \times 2$ for the linearized one).

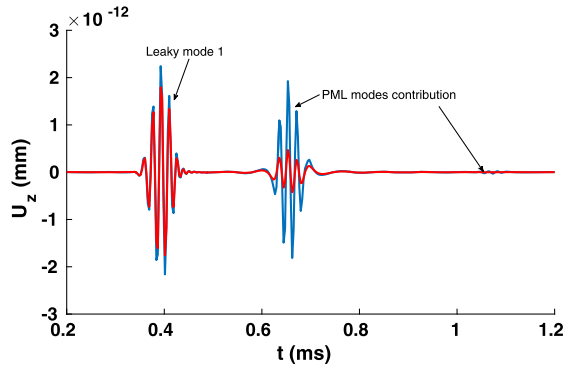


**Fig. 8.** (Colour online) Transient axial displacement $u_z(r=0, z=175a, t)$ in a steel-cement grout circular bar open waveguide, in the pure elastic case (blue line) and in the viscoelastic case (red line), for a low-frequency excitation ($f_c = 60$ kHz). PML parameters: $\hat{\gamma} = 4 + 4\mathrm{j}$, $h = 4a$, $M = 51$.

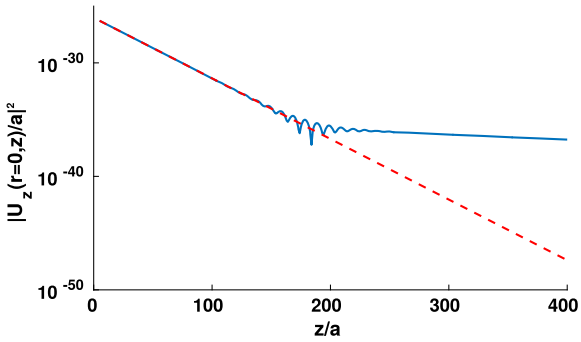


**Fig. 9.** (Colour online) Energy as a function of distance in a steel-cement grout circular bar open waveguide (elastic case). PML parameters: $\hat{\gamma} = 4 + 4\mathrm{j}$, $h = 4a$. Blue line: modal superposition over 50 PML modes and 1 leaky mode ($M = 51$); dashed red line: contribution of the leaky mode only (exponential decay).

### *4.2. Low frequency response*

For the low-frequency excitation ($f_c = 60$ kHz), the PML parameters are set according to the results of Sec. 3 in order to ensure a good accuracy of the PML mode contribution ($h = 4a$, $\hat{\gamma} = 4 + 4\mathrm{j}$). As in Sec. 3, the axial component $u_z$ of the forced response is computed along the $z$-axis. 50 PML modes and 1 leaky mode are now included in the modal superposition.

Fig. 8 shows the transient response at $z/a = 175$ both for the elastic and the viscoelastic cases. As expected, the amplitude of the response is reduced in the viscoelastic case (but the times of flight are nearly unchanged). Three wave packets can be observed. The first one is the contribution of the leaky mode. The second and third packets are the contribution of PML modes (it has been checked that these packets disappear if PML modes are not retained in the modal expansion). Interestingly, the second and third packets can be compared to the results of Fig. 4 obtained for the homogeneous test case (*i.e.* without steel core): it can be noticed that the times of flight coincide each other. Therefore, the contribution of PML modes observed in Fig. 8, inside the steel core, can be interpreted as the trace of the field radiated into the surrounding medium.

To confirm this interpretation, Fig. 9 plots the quantity proportional to the energy, $|u_z(r=0, z)|^2$, as a function of the distance $z$ computed at the centre frequency (elastic case). Up to a certain distance ($z/a = 170$), the leaky mode contribution prevails: the energy decreases exponentially. But further away from the source, the leaky mode contribution becomes negligible and the PML mode contribution prevails: the energy decreases with a geometrical decay. In between, there is a transition zone (around $z/a = 175$) where both types of modes contribute nearly equally as can be observed in Fig. 8.

Similar results have been obtained analytically in the case of optical scalar waveguides [49], showing that radiation modes first reassemble the leaky mode contribution (exponentially decaying) and then yields the long-term diffraction (geometrically decaying). Provided that the PML parameters are set properly, Fig. 8 and 9 show that the PML technique enables to compute the long-term diffraction phenomenon. This is not the case with absorbing viscoelastic layers [49].

### *4.3. High frequency response*

The NDE of open waveguides requires that enough energy remains inside the core. At high frequencies, the energy can be concentrated into the core and the leakage attenuation reduced [44]. In Fig. 7, the lowest attenuation is reached for

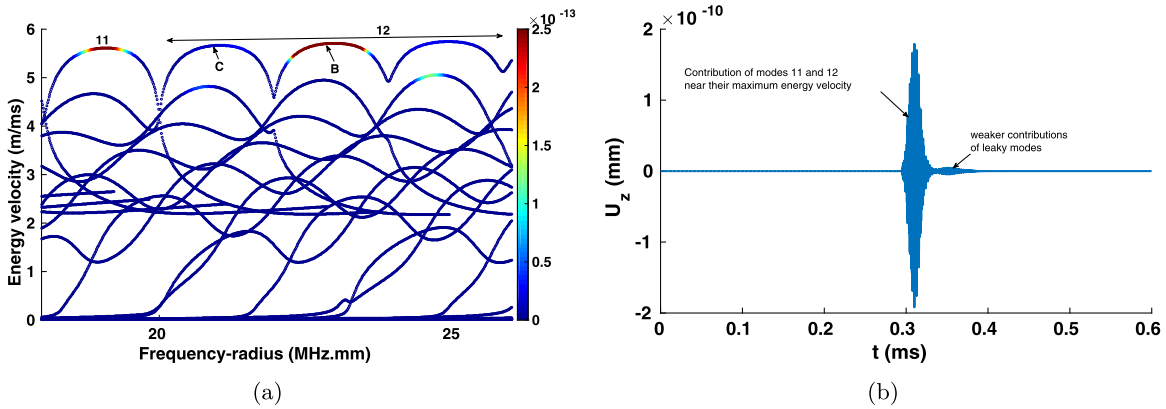


**Fig. 10.** (Colour online) (a) Energy velocity curves with the modal contribution of axial displacement at $r = 0$ and $z = 175a$ at each frequency (colourmap) and (b) transient axial displacement $u_z(r = 0, z = 175a, t)$ in a steel-cement grout circular bar open waveguide (viscoelastic case) for a high-frequency excitation ($f_c = 2.284$ MHz). PML parameters: $\hat{\gamma} = 1 + 2\mathrm{j}$, $h = 0.1a$, $M = 20$.

the 12th leaky mode, with a characteristic series of lobes above 20 MHz mm (the minimum attenuation is reached for the second lobe, at point B, and equals 159 dB mm/m). At higher frequencies, the attenuation of higher order modes increases because of greater losses due to viscoelasticity than to leakage [44]. Since it can propagate over greater distances than the others, the 12th mode is hence quite attractive.

In the context of NDE, only leaky modes are of interest. The contribution of PML modes (long-term diffraction, geometrically decaying) does not need to be considered because it occurs when a lot of energy has been already lost from the core (that is to say, when the problem can somehow no longer be considered as a waveguide problem). The computational cost can then be reduced here because, for the high-frequency excitation ($f_c = 2.284$ MHz), an acceptable convergence of leaky modes can actually be reached with a thin PML. After numerical tests, the PML thickness has been reduced to $h = 0.1a$ with $\hat{\gamma} = 1 + 2\mathrm{j}$.

Fig. 10b shows the transient solution at $z/a = 175$. $M = 20$ leaky modes have been used to compute the forced response. Thanks to the modal approach used in this paper, the contribution of each mode $m$ to the total forced response at a given distance of propagation can be computed. This modal contribution is given by the vector $\mathbf{E}_m \hat{\mathbf{F}}(k_m) \mathrm{e}^{\mathrm{j}k_m z}$ (see Sec. 2.3). The so-obtained values are plotted in Fig. 10a for the dof corresponding to the axial displacement at $r = 0$, over the energy velocity curves. It shows that the first wave packet is mainly due to the 12th mode with a smaller contribution of the 11th mode. The wave packet of the second arrival is composed of weaker modal contributions, corresponding to parts of dispersion curves having higher attenuation and slower velocity. As expected, the energy is essentially contained in the first arrival because the centre frequency of the excitation coincides with the maximum energy velocity and the minimum attenuation of the 12th mode (point B in Fig. 7).

### *4.4. Excitability of leaky modes*

In the analysis of elastic waveguides, the excitability of a given mode is an important feature, defined by the displacement-force ratio, which typically enables to optimise the type and location of sensors to be used [56]. The expression of excitability arises from the orthogonality of modes. Yet from a theoretical point of view and as mentioned earlier, leaky modes cannot satisfy an orthogonality relationship because the wave fields of such modes do not vanish at infinity in the transverse direction. To circumvent this problem, some authors have proposed to restrict the integration over the core [5].

However, the PML technique used in this paper enables to calculate the excitability, as defined from Eq. (24), by integrating over the whole cross-section including the PML. Like the biorthogonality relation (20), the so-defined excitability is applicable to any type of modes, and in particular to leaky modes.

Fig. 11 represents the modulus of the excitability over a wide frequency range for an axial point force applied at the centre of the core. For clarity of the figure, the excitability of each mode is shown only in a frequency range where their maximum energy velocity and their minimum attenuation occur (these regions are of low modal dispersion).

The excitability is found to be strong for odd modes (modes 1, 3, 5, 7, 9, 11) and weak for even modes up to the 12th mode. As previously mentioned, the 12th mode is somehow specific as it is composed of a series of lobes. These lobes also exhibit a strong variation of excitability (contrary to the energy velocity and the attenuation). For instance, the excitability of the second lobe (point B) is much higher than the excitability of the first lobe (point C), by an amount of $20 \log_{10} |E_B / E_C| = 42$ dB.

These differences of excitability can be explained by inspecting the mode shapes. As an example, Fig. 12 shows the mode shapes of the first two lobes of the 12th mode. The modal displacement of the first lobe is significantly lower at the centre of the core (*i.e.* where the point force is applied), hence reducing the excitability at this point.

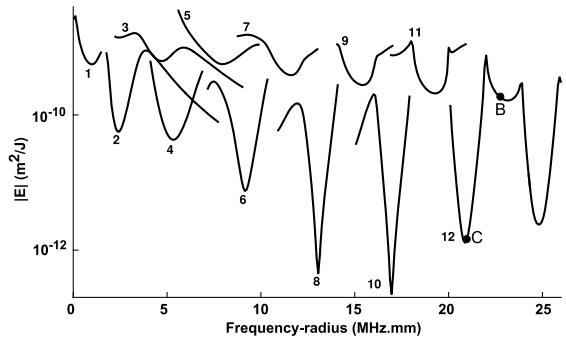


**Fig. 11.** Excitability in a steel-cement grout circular bar open waveguide (viscoelastic case) for a point-force excitation at the core centre oriented in the axial direction. PML parameters: $h = a$, $\hat{\gamma} = 1 + 2\mathrm{j}$.

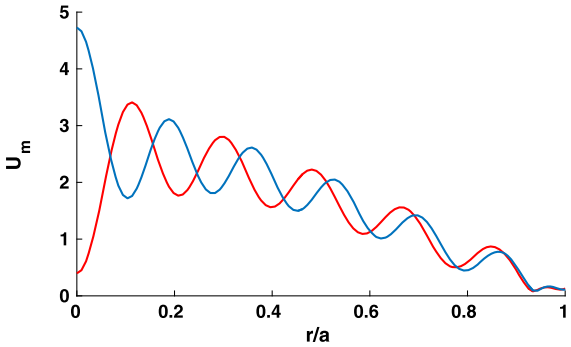


**Fig. 12.** (Colour online) Mode shape $\mathbf{U}_m$ in the $z$ direction of the 12th leaky mode for the first lobe (point C, $f = 20.92$ MHz mm, red line) and for the second lobe (point B, $f = 22.84$ MHz mm, blue line) in a steel-cement grout circular bar open waveguide (viscoelastic case). PML parameters: $\hat{\gamma} = 1 + 2\mathrm{j}$, $h = a$.

### 4.5. A square bar example

A three-dimensional waveguide with a core cross-section of square shape is now considered. As previously mentioned, the theory of Sec. 2 remains fully applicable. However, the computational cost significantly increases because the cross-section is now two-dimensional (instead of one-dimensional in the previous test cases). Furthermore, the eigenspectrum contains flexural and torsional leaky modes (in addition to longitudinal modes) and much more PML modes as well. In the following, the forced response of the square bar is computed in a high-frequency range and compared to the circular case.

#### 4.5.1. Square bar test case description

The dispersion curves of a square bar open waveguide have already been obtained with a Cartesian PML waveguide formulation discretized with spectral elements in Ref. [33]. The square bar is made of viscoelastic steel and is embedded into viscoelastic cement grout. Materials are given in Table 1. The half-width of the square is given by $a = 10$ mm. The Cartesian PML is introduced by an analytic continuation of the elastodynamic equations (2) into the complex plane $(\tilde{x}, \tilde{y})$. As in the circular bar case, its attenuation is chosen parabolic. The PML parameters are then given in both directions $x$ and $y$ by the mean attenuations $\hat{\gamma}_x$ and $\hat{\gamma}_y$, the thickness $h_x$ and $h_y$ and the distances $d_x$ and $d_y$. In the following, $d_x = d_y = a$. Details about the implementation of a Cartesian PML can be found in Ref. [32] and are not recalled in this paper for conciseness. As for spectral elements discretization, the specific element matrices and details about the convergence of the method can be found in Ref. [33]. To reduce the number of computed modes, the eigensolver shift is set to $k_0 = \omega/c_{l0}$, where $c_{l0}$ is the longitudinal bulk velocity in the core. This enables to compute mainly longitudinal modes, while avoiding the computation of PML modes or highly attenuated leaky modes of minor interest [33]. Note that opposite-going modes also have to be computed (using a $-k_0$ shift) to obtain the forced response.

The waveguide is excited by a unit force of 1 N applied at the centre of the square shape in $z$ direction. The excitation signal is a 10 Hanning window with $f_c = 2.247$ MHz. At this frequency, the mode with the lowest attenuation is excited. The problem is then solved for $[f_{\min}, f_{\max}]$, with $f_{\min} = 1.797$ MHz and $f_{\max} = 2.697$ MHz, divided into 542 steps. The half-width of the square is meshed with 4 spectral elements of order 8 (see Fig. 13), yielding 20 451 dofs for the quadratic eigenvalue problem ($20\,451 \times 2$ for the linearized one).

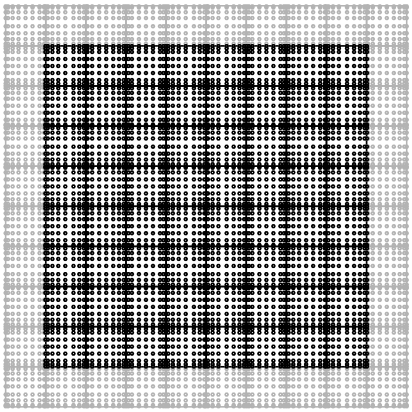

**Fig. 13.** Spectral element mesh (8th order elements) of a square bar (viscoelastic steel) embedded into viscoelastic cement grout. Black: square bar; gray: embedding medium (PML).

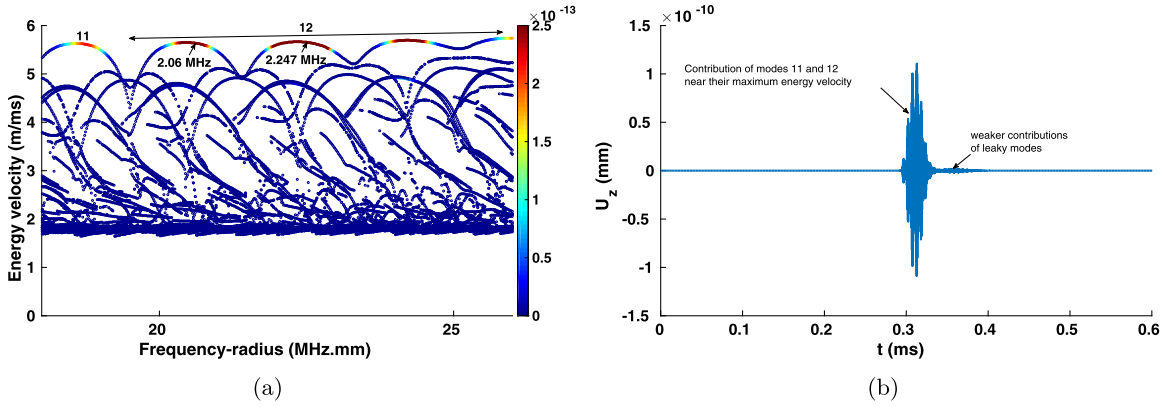


**Fig. 14.** (Colour online) (a) Energy velocity curves with the modal contribution of axial displacement at $r = 0$ and $z = 175a$ at each frequency (colourmap) and (b) transient axial displacement $u_z(r = 0, z = 175a, t)$ in a steel-cement grout square open waveguide (viscoelastic case) for a high-frequency excitation ($f_c = 2.247$ MHz). PML parameters: $\hat{\gamma}_x = \hat{\gamma}_y = 1 + 2\mathrm{j}$, $h_x = h_y = 0.25a$, $M = 50$.

*4.5.2. High-frequency response*

As shown in Ref. [33], low-leakage longitudinal modes also occurs in square bars at high frequencies. Herein, the lowest attenuation is reached for the second lobe of the 12th longitudinal mode at $f = 2.247$ MHz and equals 147 dB mm/m. These values are in good agreement with the results of Ref. [33]. They have been obtained with the following PML parameters: $h_x = h_y = 0.25a$ and $\hat{\gamma}_x = \hat{\gamma}_y = 1 + 2\mathrm{j}$.

Fig. 14b shows the transient axial displacement at $z/a = 175$ and the modal contribution are displayed in Fig. 14a. $M = 50$ modes have been used to compute the forced response. Because of the symmetry of the source, only longitudinal modes are excited. As in the circular case (Fig. 10b), two wave packets propagate in the square bar. The first wave packet is due to the arrivals of the 11th and 12th leaky modes, which are the fastest and the less attenuated ones. The second wave packet contains weaker modal contributions of slower velocities.

Note that the wave packets are of slightly smaller amplitudes than in the circular bar. Although the attenuation of the modes is a bit smaller in the square bar, the energy spreads over a wider cross-section area. Moreover, the energy repartition among the modes is also modified. Contrary to the circular case, each lobe of the 12th mode significantly contributes to the response (see Fig. 14a). These differences can be explained by the mode shapes of the square bar. The latter are displayed in Fig. 15a and Fig. 15b for the first two lobes at their lowest attenuation. At the centre of the circular bar, the modal displacement is roughly ten times smaller for the first lobe than for the second lobe (Fig. 12). In the square bar, the modal displacement at the centre ($x = y = 0$) is only twice smaller for the first lobe than for the second lobe, hence increasing the modal contribution of the first lobe in the response.

## 5. Conclusion

A modal approach based on PML has been proposed to compute the forced response of elastic open waveguides. Solving the eigenproblem of the PML waveguide formulation leads to three discrete sets of modes: trapped modes, revealed leaky

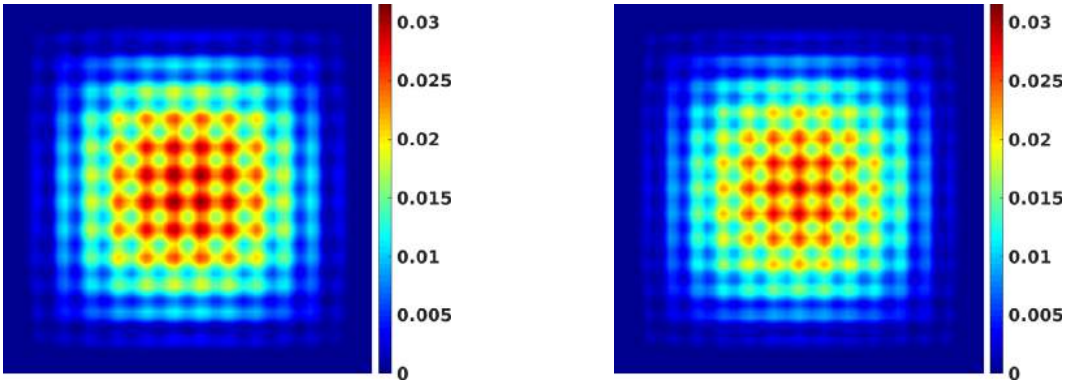


(a) (b)

**Fig. 15.** (Colour online) Mode shape $\mathbf{U}_m$ in the $z$ direction of the 12th longitudinal leaky mode for (a) the first lobe ($f = 2.06$ MHz), (b) the second lobe ($f = 2.247$ MHz) in a steel-cement grout square open waveguide.

modes and PML modes. The latter comes from a continuous set of modes, discretized by the truncation of the PML, and fully depends on the PML parameters. A biorthogonality relationship has been derived, applicable to any types of modes, which enables to obtain the forced response with a unique modal superposition, as well as to define the excitability of leaky modes.

A numerical study in a homogeneous elastic medium has shown that, despite their dependence on PML parameters and their exponential decay, the contribution of the discrete set of PML modes enables to reassemble the exact solution (geometrically decaying).

In a waveguide, the PML modes enable to obtain the long-term diffraction phenomenon, which occurs at great distances to the source when most energy has leaked into the surrounding medium. However, leaky modes dominate over a wide range of distance inside the core. In this range, leaky modes are sufficient to obtain a good approximation of the solution. Furthermore, the leaky mode contribution remains accurate even with a small PML thickness, hence reducing the computational cost.

**Acknowledgement**

This work was supported by the Région Pays de la Loire.

**Appendix A. Axisymmetrical PML waveguide formulation**

Let us go back to Eq. (2) written in the cylindrical coordinate system $(\tilde{r}, \theta, z)$. The waveguide is axisymmetric, and then the cross-section is reduced to the radial direction $\tilde{r}$. The core of the waveguide has a radius $\tilde{r} = a$, and is made of one or several layers. Only axisymmetric solutions are considered, so that $\partial(.)/\partial\theta = 0$ and $\tilde{u}_\theta = 0$. Hence the displacement field in Eq. (2) is expressed as $\tilde{\mathbf{u}} = [\tilde{u}_r \ \tilde{u}_z]^{\mathrm{T}}$, and only depends on the variables $\tilde{r}$ and $z$.

Based on Eq. (3), the change of variable (4) is applied to Eq. (2). In the strain-displacement relation (5), the operators $\mathbf{L}_S$ and $\mathbf{L}_z$ are given by:

$$\mathbf{L}_S = \left( \frac{1}{\gamma} \begin{bmatrix} 1 & 0 \\ 0 & 0 \\ 0 & 0 \\ 0 & 1 \end{bmatrix} \frac{\partial}{\partial r} + \begin{bmatrix} 0 & 0 \\ 1 & 0 \\ 0 & 0 \\ 0 & 0 \end{bmatrix} \frac{1}{\tilde{r}} \right), \quad \mathbf{L}_z = \begin{bmatrix} 0 & 0 \\ 0 & 0 \\ 0 & 1 \\ 1 & 0 \end{bmatrix}. \tag{A.1}$$

Then, a one-dimensional finite element discretization is applied along the radial direction, yielding the following interpolation on each element:

$$\mathbf{u}^e(r, z, \omega) = \mathbf{N}^e(r)\mathbf{U}^e(z, \omega). \tag{A.2}$$

$\mathbf{N}^e(r)$ is the matrix of interpolation one-dimensional functions. $\mathbf{U}^e(z, \omega)$ is the vector of nodal displacements. The weak formulation is established by integrating by parts the second order derivatives with respect to $r$ in Eq. (2). Regardless of the presence of a PML, detailed steps of the integration can be found in the literature (see [15] for instance) and are not repeated here. It yields Eq. (6), where the element matrices are given by Eq. (7) with $\mathrm{d}S = 2\pi r dr$. Under the assumption used in this appendix, $\mathbf{C}$ is reduced to a four-by-four matrix. For instance, the matrix $\mathbf{C}$ for an isotropic material is:

$$\mathbf{C} = \begin{bmatrix} \lambda+2\mu & \lambda & \lambda & 0 \\ \lambda & \lambda+2\mu & \lambda & 0 \\ \lambda & \lambda & \lambda+2\mu & 0 \\ 0 & 0 & 0 & \mu \end{bmatrix}. \tag{A.3}$$

## Appendix B. Linearization of the quadratic eigenvalue problem

The system (8) can be linearized [15,51,52], and yields for instance:

$$(\mathbf{A} - k\mathbf{B})\mathbf{x} = \mathbf{q}, \tag{B.1}$$

with:

$$\mathbf{A} = \begin{bmatrix} \mathbf{0} & \mathbf{K}_1 - \omega^2\mathbf{M} \\ \mathbf{K}_1 - \omega^2\mathbf{M} & \mathrm{j}(\mathbf{K}_2 - \mathbf{K}_2^{\mathrm{T}}) \end{bmatrix}, \mathbf{B} = \begin{bmatrix} \mathbf{K}_1 - \omega^2\mathbf{M} & \mathbf{0} \\ \mathbf{0} & -\mathbf{K}_3 \end{bmatrix}, \mathbf{x} = \begin{bmatrix} \hat{\mathbf{U}} \\ k\hat{\mathbf{U}} \end{bmatrix}, \mathbf{q} = \begin{bmatrix} \mathbf{0} \\ \hat{\mathbf{F}} \end{bmatrix}. \tag{B.2}$$

The free response problem is considered by dropping the source term:

$$\left(\mathbf{K}_1 - \omega^2\mathbf{M} + \mathrm{j}k(\mathbf{K}_2 - \mathbf{K}_2^{\mathrm{T}}) + k^2\mathbf{K}_3\right)\hat{\mathbf{U}} = \mathbf{0}, \tag{B.3}$$

and yields the generalized eigenvalue problem:

$$(\mathbf{A} - k\mathbf{B})\mathbf{x} = \mathbf{0}. \tag{B.4}$$

Because of the PML, the matrices are complex. **A** and **B** are not Hermitian.

## Appendix C. Fourier transform of Eq. (32)

This appendix gives the analytic Fourier transform $u_z^{\mathrm{ref}}(z,\omega) = \int_{-\infty}^{+\infty} u_z^{\mathrm{ref}}(z,t)\mathrm{e}^{+\mathrm{j}\omega t}\mathrm{d}t$ of Eq. (32).
First, the near-field term is written as a convolution product:

$$\int_{z/c_l}^{z/c_s} \tau F(t-\tau)\mathrm{d}\tau = a(t) * F(t) \tag{C.1}$$

with

$$a(t) = \begin{cases} t & \text{if} \quad t \in [z/c_l; z/c_s] \\ 0 & \text{otherwise.} \end{cases} \tag{C.2}$$

The Fourier transform of $a(t) * F(t)$ is equal to $A(\omega)F(\omega)$, where $F(\omega)$ is the spectrum of the excitation force, and $A(\omega)$ is obtained from an integration by parts, yielding:

$$A(\omega) = \frac{1}{\omega^2}(\mathrm{e}^{\mathrm{j}\omega\frac{z}{c_s}} - \mathrm{e}^{\mathrm{j}\omega\frac{z}{c_l}}) + \frac{z}{\mathrm{j}\omega}\left(\frac{\mathrm{e}^{\mathrm{j}\omega\frac{z}{c_s}}}{c_s} - \frac{\mathrm{e}^{\mathrm{j}\omega\frac{z}{c_l}}}{c_l}\right). \tag{C.3}$$

Finally, the Fourier transform of Eq. (32) is:

$$u_z^{\mathrm{ref}}(z,\omega) = \frac{1}{2\pi\rho z^3}A(\omega)F(\omega) + \frac{1}{4\pi\rho c_l^2 z}F(\omega)\mathrm{e}^{\mathrm{j}\omega\frac{z}{c_l}}. \tag{C.4}$$

## References


[1] R. Thurston, Elastic waves in rods and clad rods, J. Acoust. Soc. Am. 64 (1978) 1–37, https://doi.org/10.1121/1.381962.
[2] D. Marcuse, Theory of Dielectric Optical Waveguides, 1st edn., Academic Press, New York, 1974.
[3] P. Malischewsky, Surface Waves and Discontinuities, Elsevier, Amsterdam, 1987.
[4] A. Hladky-Hennion, P. Langlet, M. de Billy, Conical radiating waves from immersed wedges, J. Acoust. Soc. Am. 108 (2000) 3079–3083, https://doi.org/10.1121/1.1322569.
[5] T. Vogt, M. Lowe, P. Cawley, The scattering of guided waves in partly embedded cylindrical structures, J. Acoust. Soc. Am. 113 (2003) 1258–1272, https://doi.org/10.1121/1.1553463.
[6] W.T. Thomson, Transmission of elastic waves through a stratified solid medium, J. Appl. Phys. 21 (1950) 89–93.
[7] N.A. Haskell, The dispersion of surface waves on multilayered media, Bull. Seismol. Soc. Am. 43 (1953) 17–34.
[8] E. Kausel, J. Roësset, Stiffness matrices for layered soils, Bull. Seismol. Soc. Am. 71 (1981) 1743–1761.
[9] B. Pavlakovic, M. Lowe, D. Alleyne, P. Cawley, Disperse: a general purpose program for creating dispersion curves, in: Review of Progress in Quantitative Nondestructive Evaluation, vol. 16, Springer, US, 1997, pp. 185–192.
[10] R. Nelson, S. Dong, R. Kalra, Vibrations and waves in laminated orthotropic circular cylinders, J. Sound Vib. 18 (1971) 429–444.

[11] B. Aalami, Waves in prismatic guides of arbitrary cross section, J. Appl. Mech. 40 (1973) 1067–1072.
[12] E. Kausel, An Explicit Solution for the Green Functions for Dynamic Loads in Layered Media, MIT Research Report R81-13, Department of Civil Engineering, School of Engineering, Massachusetts Institute of Technology, 1981.
[13] J. Park, Wave Motion in Finite and Infinite Media Using the Thin-Layer Method, Ph.D. thesis, Massachusetts Institute of Technology, 2002.
[14] G. Liu, J. Achenbach, Strip element method to analyze wave scattering by cracks in anisotropic laminated plates, J. Appl. Mech. 62 (1995) 607.
[15] A. Marzani, Time-transient analysis response for ultrasonic guided waves propagating in damped cylinders, Int. J. Solids Struct. 45 (2008) 6347–6368, https://doi.org/10.1016/j.ijsolstr.2008.07.028.
[16] V. Damljanovic, R. Weaver, Forced response of a cylindrical waveguide with simulation of the wavenumber extraction problem, J. Acoust. Soc. Am. 115 (2004) 1582–1591, https://doi.org/10.1121/1.1675818.
[17] H. Gravenkamp, C. Song, J. Prager, A numerical approach for the computation of dispersion relations for plate structures using the Scaled Boundary Finite Element Method, J. Sound Vib. 331 (2012) 2543–2557, https://doi.org/10.1016/j.jsv.2012.01.029.
[18] H. Gravenkamp, H. Man, C. Song, J. Prager, The computation of dispersion relations for three-dimensional elastic waveguides using the scaled boundary finite element method, J. Sound Vib. 332 (2013) 3756–3771, https://doi.org/10.1016/j.jsv.2013.02.007.
[19] M. Mazzotti, A. Marzani, I. Bartoli, Dispersion analysis of leaky guided waves in fluid-loaded waveguides of generic shape, Ultrasonics 54 (2014) 408–418, https://doi.org/10.1016/j.ultras.2013.06.011.
[20] M. Mazzotti, I. Bartoli, A. Marzani, Ultrasonic leaky guided waves in fluid-coupled generic waveguides: hybrid finite-boundary element dispersion analysis and experimental validation, J. Appl. Phys. 115 (14) (2014) 143512, https://doi.org/10.1063/1.4870857.
[21] M. Mazzotti, I. Bartoli, A. Marzani, E. Viola, A coupled SAFE-2.5D BEM approach for the dispersion analysis of damped leaky guided waves in embedded waveguides of arbitrary cross-section, Ultrasonics 53 (2013) 1227–1241, https://doi.org/10.1016/j.ultras.2013.03.003.
[22] H. Gravenkamp, C. Birk, C. Song, Numerical modeling of elastic waveguides coupled to infinite fluid media using exact boundary conditions, Comput. Struct. 141 (2014) 36–45, https://doi.org/10.1016/j.compstruc.2014.05.010.
[23] T. Hayashi, D. Inoue, Calculation of leaky Lamb waves with a semi-analytical finite element method, Ultrasonics 54 (2014) 1460–1469, https://doi.org/10.1016/j.ultras.2014.04.021.
[24] D. Inoue, T. Hayashi, Transient analysis of leaky Lamb waves with a semi-analytical finite element method, Ultrasonics 62 (2015) 80–88, https://doi.org/10.1016/j.ultras.2015.05.004.
[25] H. Gravenkamp, C. Birk, C. Song, Computation of dispersion curves for embedded waveguides using a dashpot boundary condition, J. Acoust. Soc. Am. 135 (2014) 1127–1138, https://doi.org/10.1121/1.4864303.
[26] A. Hladky-Hennion, P. Langlet, R. Bossut, M. De Billy, Finite element modelling of radiating waves in immersed wedges, J. Sound Vib. 212 (1998) 265–274, https://doi.org/10.1006/jsvi.1997.1408.
[27] A. Astaneh, M. Guddati, Dispersion analysis of composite acousto-elastic waveguides, Composites Part B, Engineering 130 (2017) 200–216, https://doi.org/10.1016/j.compositesb.2017.07.040.
[28] E. Kausel, Physical interpretation and stability of paraxial boundary conditions, Bull. Seismol. Soc. Am. 82 (1992) 898–913.
[29] Z. Fan, M.J.S. Lowe, M. Castaings, C. Bacon, Torsional waves propagation along a waveguide of arbitrary cross section immersed in a perfect fluid, J. Acoust. Soc. Am. 124 (2008) 2002–2010, https://doi.org/10.1121/1.2968677.
[30] M. Castaings, M. Lowe, Finite element model for waves guided along solid systems of arbitrary section coupled to infinite solid media, J. Acoust. Soc. Am. 123 (2008) 696–708, https://doi.org/10.1121/1.2821973.
[31] F. Treyssède, K. Nguyen, A.-S. Bonnet-BenDhia, C. Hazard, Finite element computation of trapped and leaky elastic waves in open stratified waveguides, Wave Motion 51 (2014) 1093–1107, https://doi.org/10.1016/j.wavemoti.2014.05.003.
[32] K. Nguyen, F. Treyssède, C. Hazard, Numerical modeling of three-dimensional open elastic waveguides combining semi-analytical finite element and perfectly matched layer methods, J. Sound Vib. 344 (2015) 158–178, https://doi.org/10.1016/j.jsv.2014.12.032.
[33] F. Treyssède, Spectral element computation of high-frequency leaky modes in three-dimensional solid waveguides, J. Comput. Phys. 314 (2016) 341–354, https://doi.org/10.1016/j.jcp.2016.03.029.
[34] P. Zuo, X. Yu, Z. Fan, Numerical modeling of embedded solid waveguides using SAFE-PML approach using a commercially available finite element package, NDT E Int. 90 (2017) 11–23, https://doi.org/10.1016/j.ndteint.2017.04.003.
[35] P. Zuo, Z. Fan, SAFE-PML approach for modal study of waveguides with arbitrary cross sections immersed in inviscid fluid, J. Sound Vib. 406 (2017) 181–196, https://doi.org/10.1016/j.jsv.2017.06.001.
[36] J.M. de Oliveira Barbosa, J. Park, E. Kausel, Perfectly matched layers in the thin layer method, Comput. Methods Appl. Mech. Eng. 217 (2012) 262–274, https://doi.org/10.1016/j.cma.2011.12.006.
[37] S. Kim, J. Pasciak, The computation of resonances in open systems using a perfectly matched layer, Math. Comput. 78 (2009) 1375–1398.
[38] B. Auld, Acoustic Fields and Waves in Solids, vol. 2, Wiley, New York, 1973.
[39] R. Collin, Field Theory of Guided Waves, 2nd edn., IEEE Press, Wiley, New York, 1991.
[40] T. Tamir, A. Oliner, Guided complex waves. Part 1: fields at an interface, Proc. Inst. Electr. Eng. 110 (1963) 310–324, https://doi.org/10.1049/piee.1963.0044.
[41] I.A. Nedospasov, V.G. Mozhaev, I.E. Kuznetsova, Unusual energy properties of leaky backward Lamb waves in a submerged plate, Ultrasonics 77 (2017) 95–99, https://doi.org/10.1016/j.ultras.2017.01.025.
[42] V. Maupin, The radiation modes of a vertically varying half-space: a new representation of the complete Green's function in terms of modes, Geophys. J. Int. 126 (1996) 762–780, https://doi.org/10.1111/j.1365-246X.1996.tb04701.x.
[43] L. Margerin, Generalized eigenfunctions of layered elastic media and application to diffuse fields, J. Acoust. Soc. Am. 125 (2009) 164–174, https://doi.org/10.1121/1.3021312.
[44] B. Pavlakovic, M.J.S. Lowe, P. Cawley, High-frequency low-loss ultrasonic modes in imbedded bars, J. Appl. Mech. 68 (2001) 67–75, https://doi.org/10.1115/1.1347995.
[45] M. Gallezot, F. Treyssède, L. Laguerre, Contribution of leaky modes in the modal analysis of unbounded problems with perfectly matched layers, J. Acoust. Soc. Am. 141 (2017) EL16–EL21, https://doi.org/10.1121/1.4973313.
[46] W. Chew, W. Weedon, A 3D perfectly matched medium from modified Maxwells equations with stretched coordinates, Microw. Opt. Technol. Lett. 7 (1994) 599–604, https://doi.org/10.1002/mop.4650071304.
[47] R. Sammut, A. Snyder, Leaky modes on a dielectric waveguide: orthogonality and excitation, Appl. Opt. 15 (1976) 1040–1044, https://doi.org/10.1364/AO.15.001040.
[48] S.-L. Lee, Y. Chung, L. Coldren, N. Dagli, On leaky mode approximations for modal expansion in multilayer open waveguides, IEEE J. Quantum Electron. 31 (1995) 1790–1802, https://doi.org/10.1109/3.466054.
[49] J. Hu, C. Menyuk, Understanding leaky modes: slab waveguide revisited, Adv. Opt. Photonics 1 (2009) 58–106, https://doi.org/10.1364/AOP.1.000058.
[50] F. Olyslager, Discretization of continuous spectra based on perfectly matched layers, SIAM J. Appl. Math. 64 (2004) 1408–1433, https://doi.org/10.1137/S0036139903430197.
[51] F. Tisseur, K. Meerbergen, The quadratic eigenvalue problem, SIAM Rev. 43 (2001) 235–286.
[52] F. Treyssède, L. Laguerre, Numerical and analytical calculation of modal excitability for elastic wave generation in lossy waveguides, J. Acoust. Soc. Am. 133 (2013) 3287–3837.

[53] A. Bernard, M. Lowe, M. Deschamps, Guided waves energy velocity in absorbing and non-absorbing plates, J. Acoust. Soc. Am. 110 (2001) 186–196, https://doi.org/10.1121/1.1375845.
[54] K. Aki, P. Richards, Quantitative Seismology, Theory and Methods, vol. 1, 2nd edn., Freeman, 1980.
[55] R. Lehoucq, D. Sorensen, C. Yang, ARPACK Users' Guide: Solution of Large-Scale Eigenvalue Problems with Implicitly Restarted Arnoldi Methods, vol. 6, SIAM, 1998.
[56] P. Wilcox, M. Lowe, P. Cawley, Mode and transducer selection for long range lamb wave inspection, J. Intell. Mater. Syst. Struct. 12 (2001) 553–565.

Wave Motion 87 (2019) 75–91

Contents lists available at ScienceDirect

Wave Motion

journal homepage: www.elsevier.com/locate/wamot

# Free and forced response of three-dimensional waveguides with rotationally symmetric cross-sections

Fabien Treyssède

*IFSTTAR, GERS, GeoEND, F-44344, Bouguenais, France*

## HIGHLIGHTS

- A numerical method is presented for 3D waveguides involving two kinds of symmetry.
- The continuous translational invariance along the axis is described analytically.
- The discrete rotational symmetry of the cross-section is described by Floquet theory.
- The forced response is calculated thanks to a specific biorthogonality relationship.
- The forced solution remains applicable with anisotropy and loss.

## ARTICLE INFO

*Article history:*
Received 22 February 2018
Received in revised form 9 July 2018
Accepted 2 August 2018
Available online 3 August 2018

*Keywords:*
Wave
Finite element
Rotational symmetry
Mode
Response
Cable

## ABSTRACT

The analysis of high-frequency wave propagation in waveguides of arbitrarily shaped cross-sections requires specific numerical methods. A rather common technique consists in discretizing the cross-section with finite elements while describing analytically the axis direction of the waveguide. This technique enables to account for the continuous translational invariance of a waveguide and leads to a modal problem written on the cross-section. Although two-dimensional, solving the so-obtained eigensystem can yet become computationally costly with the increase of the size of the problem. In most applications involving waveguides, the cross-section itself often obeys rules of symmetry, which could also be exploited in order to further reduce the size of the modal problem. A widely encountered type of symmetry is rotational symmetry. Typical examples are bars of polygon-shaped cross-section or multi-wire cables. The goal of this paper is to propose a numerical method that exploits the discrete rotational symmetry of the waveguide cross-section. Bloch–Floquet conditions are applied in the circumferential direction while the continuous translational invariance of the waveguide along its axis is still described analytically. Both the free and the forced response problems are considered. A biorthogonality relationship specific to the rotationally symmetric formulation is derived. Numerical results are computed and validated for the simple example of a cylinder and for the more complex test case of a multi-wire structure. In addition to reducing the computational effort, the rotationally symmetric formulation naturally provides a classification of modes in terms of their circumferential order, which can be of great help for the dynamic analysis of complex structures.



## 1. Introduction

Elastic guided waves are of great interest for the dynamic analysis of elongated structures and provide the theoretical background necessary for many applications (nondestructive evaluation, vibration and noise reduction, statistical energy

*E-mail address:* fabien.treyssede@ifsttar.fr.

https://doi.org/10.1016/j.wavemoti.2018.08.001
0165-2125/

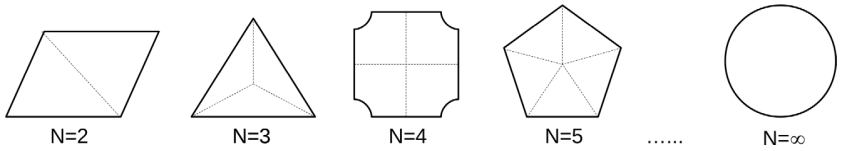


**Fig. 1.** Examples of rotationally symmetric cross-sections ($N$ denotes the order of rotational symmetry).

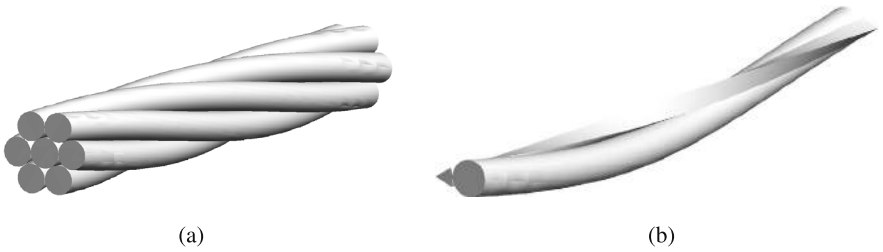


**Fig. 2.** Example of a multi-wire cable: (a) three-dimensional geometry of a seven-wire strand, (b) unit cell view ($N = 6$).

analysis...). Guided waves are yet multimodal and dispersive. Modeling tools are required to further understand the mechanism of their propagation. Dispersion curves of phase and group velocities as functions of frequency typically enable to identify modes that propagate in a frequency range of interest. Such curves represent modal properties obtained regardless excitation (free response). It is also essential to determine and control the amplitudes of each guided modes excited by a given source (forced response). This can be investigated with the help of modal excitabilities [1,2] (for a given frequency, the excitability of a mode is defined as the ratio of the displacement of that mode to a point force applied in a given direction).

Canonical geometries (plates, cylinders) can be modeled thanks to analytical methods, such as the Thomson–Haskell [3,4], the stiffness matrix [5] or the global matrix [6] methods. However, the analysis of arbitrarily shaped three-dimensional waveguides requires numerical methods.

Based on the theory of wave propagation in periodic structures, a first numerical approach consists in applying boundary conditions based on Floquet's principle in the finite element (FE) model of a single repetitive cell of the problem (see Refs. [7–10] for instance). This first approach leads to a modal problem, three-dimensional but reduced on the unit cell. When the translational invariance of the waveguide is continuous, another technique consists in discretizing only the cross-section of the waveguide while describing analytically the direction of wave propagation. Compared to the first approach, this second method also leads to a modal problem but the problem is reduced on the cross-section (two-dimensional), which further reduces the computational cost. This second approach, which will be termed as *waveguide formulation* in this paper, has been applied under various names in the literature: the extended Ritz technique, the thin layer method for stratified waveguides in geophysics, the strip-element method, the semi-analytical finite element method or the scaled boundary finite element method in ultrasonics (see *e.g.* Refs. [11–16]).

Although two-dimensional, the eigenproblem of the waveguide formulation can still be computationally costly when the FE mesh has to be refined and/or the modal density increases (*e.g.* at high frequency [17]). It is hence desirable to further reduce the size of the modal problem. The goal of this paper is to propose a waveguide formulation that accounts for the rotational symmetry of cross-sections. With a modal approach, accounting for rotational symmetry has indeed two computational benefits: the reduction of the problem size in terms of degrees of freedom and the reduction of the number of modes to compute.

Rotationally symmetric cross-sections are often encountered in practical applications (for instance, regular polygons). Simple examples are given by Fig. 1 for various orders of rotational symmetry, denoted by $N$ in this paper. Another example is that of multi-wire cables, for which the modeling is of particular interest in the context of nondestructive evaluation. Cables are usually made of individual helical wires, which are coupled through contact conditions. As an example widely employed in civil engineering cables, Fig. 2 depicts a seven-wire strand, constituted by a central cylindrical wire surrounded by six helical wires (here, the order of rotational symmetry is hence equal to 6). Such a structure yields large size problems involving mesh refinements in the contact regions [18].

Investigating the free response of three-dimensional waveguides, the first approach has been applied in Ref. [19] by revising the Bloch–Floquet conditions in order to consider discrete symmetries that are not purely translational, including screw and rotational symmetries. The particular case of continuous rotational symmetry, *i.e.* axisymmetric waveguides (pipes and cylinders), has been treated in the literature using both the first approach [20,21] and the second approach [22,23]. Among these references, the forced response has been investigated in Refs. [21,22] only. Regardless waveguides, the structural modeling of discrete rotational symmetry has also been explored in the context of vibration analysis [24,25]. In Refs. [20,21,19], it is noteworthy that Bloch–Floquet periodic boundary conditions are applied both in the axial and in the

circumferential directions. Since the rotational symmetry of interest in this paper is of discrete type, the cross-section of the waveguide has to be viewed as a periodic medium along the circumferential direction. Hence, the circumferential periodic conditions used in the present paper are of Bloch–Floquet type also. However, the propagation along the waveguide axis is still described analytically in order to fully exploit the continuous translational symmetry of the waveguide along its axis.

Section 2 briefly recalls the waveguide formulation for arbitrarily shaped cross-sections. The rotationally symmetric formulation is presented in Section 3 by treating both the free and the forced response problems. The forced response is solved by expanding the excited field as a sum of the guided modes determined from the free response. One difficulty is that the introduction of rotational symmetry in the waveguide formulation breaks the symmetry property of the eigenproblem. A specific biorthogonality relationship between eigenmodes is hence derived to determine the contribution of each mode explicitly as a function of the excitation. Sections 4 and 5 are devoted to numerical results. In Section 4, a cylindrical waveguide of circular cross-section is considered to validate the approach. Section 5 shows results obtained for a seven-wire strand and demonstrates the potentiality of the method.

## 2. Background: waveguide formulation

The waveguide formulation is a FE method dedicated to waveguides that aims to account for the translational invariance of the geometry to reduce the size of the problem. The initial fully three-dimensional problem is reduced to a two-dimensional modal problem so that one only needs to mesh with FE the cross-section of the waveguide. This section briefly recalls the waveguide formulation. Details can be found in the literature (see *e.g.* [14,15]).

Let us denote $(x, y)$ the cross-section coordinates and $z$ the axis coordinate of the waveguide. First, the strain–displacement relation is written as:

$$\boldsymbol{\epsilon} = (\mathbf{L}_{xy} + \mathbf{L}_z \partial/\partial z)\mathbf{u} \tag{1}$$

where $\mathbf{u}$ denotes the displacement field, $\mathbf{L}_{xy}$ is the operator containing all terms but derivatives with respect to the $z$-axis and $\mathbf{L}_z$ is the operator of $z$-derivatives:

$$\mathbf{L}_{xy} = \begin{bmatrix} \partial/\partial x & 0 & 0 \\ 0 & \partial/\partial y & 0 \\ 0 & 0 & 0 \\ \partial/\partial y & \partial/\partial x & 0 \\ 0 & 0 & \partial/\partial x \\ 0 & 0 & \partial/\partial y \end{bmatrix}, \quad \mathbf{L}_z = \begin{bmatrix} 0 & 0 & 0 \\ 0 & 0 & 0 \\ 0 & 0 & 1 \\ 0 & 0 & 0 \\ 1 & 0 & 0 \\ 0 & 1 & 0 \end{bmatrix}. \tag{2}$$

After applying a time Fourier transform, the approach consists in discretizing only the cross-section $(x, y)$ by a FE method while describing analytically the direction of wave propagation $z$. Inside one finite element $e$, the displacement field can thus be expressed as follows:

$$\mathbf{u}(x, y, z, t) = \mathbf{N}^e(x, y)\mathbf{U}^e(z)e^{-\mathrm{i}\omega t} \tag{3}$$

where $\mathbf{U}^e$ is the nodal displacement vector, $\mathbf{N}^e$ is the matrix of nodal interpolating functions of the element $e$ and $\omega$ is the angular frequency.

Following a waveguide formulation approach (see *e.g.* Refs. [22,26] for details), the variational formulation of three-dimensional elastodynamics yields from Eqs. (1)–(3):

$$(\mathbf{K}_1 - \omega^2\mathbf{M})\mathbf{U} + (\mathbf{K}_2 - \mathbf{K}_2^{\mathrm{T}})\mathbf{U}_{,z} - \mathbf{K}_3\mathbf{U}_{,zz} = \mathbf{F} \tag{4}$$

with the elementary matrices:

$$\begin{aligned} \mathbf{K}_1^e &= \int_{S^e} \mathbf{N}^{e\mathrm{T}}\mathbf{L}_{xy}^{\mathrm{T}}\mathbf{C}\mathbf{L}_{xy}\mathbf{N}^e \mathrm{d}S, \quad \mathbf{K}_2^e = \int_{S^e} \mathbf{N}^{e\mathrm{T}}\mathbf{L}_{xy}^{\mathrm{T}}\mathbf{C}\mathbf{L}_z\mathbf{N}^e \mathrm{d}S, \\ \mathbf{K}_3^e &= \int_{S^e} \mathbf{N}^{e\mathrm{T}}\mathbf{L}_z^{\mathrm{T}}\mathbf{C}\mathbf{L}_z\mathbf{N}^e \mathrm{d}S, \quad \mathbf{M}^e = \int_{S^e} \rho\mathbf{N}^{e\mathrm{T}}\mathbf{N}^e \mathrm{d}S \end{aligned} \tag{5}$$

where $(\cdot)_{,z}$ denotes partial derivatives with respect to $z$, $\mathrm{d}S = \mathrm{d}x\mathrm{d}y$, $\mathbf{C}$ is the matrix of material properties and $\rho$ is the mass density. For clarity, $\mathbf{U} = \mathbf{U}(z, \omega)$ is the column vector containing cross-section nodal displacements in the space–frequency domain. $\mathbf{F} = \mathbf{F}(z, \omega)$ represents the excitation vector in the space–frequency domain. For later use, it is also convenient to introduce the following vector:

$$\mathbf{T} = \mathbf{K}_2^{\mathrm{T}}\mathbf{U} + \mathbf{K}_3\mathbf{U}_{,z} \tag{6}$$

which can be interpreted as the nodal traction vector applied on the cross-section surface $S$ of unit normal $\mathbf{e}_z$ [26].

Setting $\mathbf{F} = \mathbf{0}$ (no elastodynamic source) and performing a Fourier transform in the $z$ direction (which is equivalent to introduce a space harmonic dependence $\mathrm{e}^{\mathrm{i}kz}$), Eq. (4) is a quadratic eigenvalue problem whose eigensolutions $\{k_m, \mathbf{U}_m\}$ are the guided modes propagating in the translationally invariant structure. Quadratic eigenproblems are more difficult to handle with standard numerical eigensolvers. A rather well-known procedure consists in recasting the quadratic eigenproblem as

a linear one (see Refs. [27,17] for instance). In this paper, the linear eigensystem is solved with the ARPACK library [28], appropriate for large sparse matrices and based on the implicitly restarted Arnoldi method.

One emphasizes that the matrices $\mathbf{K}_1$, $\mathbf{K}_3$ and $\mathbf{M}$ in Eq. (4) are symmetric and the matrix $(\mathbf{K}_2 - \mathbf{K}_2^{\mathrm{T}})$ is skew-symmetric. One consequence of these properties is that guides modes occur in pairs of opposite-going modes, denoted as $\{k_m, \mathbf{U}_m\}$ and $\{-k_m, \mathbf{U}_{-m}\}$. In this case, a biorthogonality relation involving opposite-going modes can be derived in order to calculate the forced response as a modal expansion on the guided modes. For waves travelling toward the positive $z$-direction and $z$ outside the source region (one assumes that the excitation is zero outside a finite interval along $z$), the forced response can be expressed as follows [26]:

$$\mathbf{U} = \sum_{m>0} \mathbf{E}_m \hat{\mathbf{F}}(k_m) \mathrm{e}^{\mathrm{i}k_m z} \tag{7}$$

where $\mathbf{E}_m$ is the so-called modal excitability matrix:

$$\mathbf{E}_m = \frac{\mathrm{i}\omega}{4Q_{m,-m}} \mathbf{U}_m \mathbf{U}^{\mathrm{T}}_{-m} \tag{8}$$

In Eq. (7), the summation is performed on positive-going waves only (denoted by positive values of $m$) and the vector $\hat{\mathbf{F}}(k)$ denotes the space Fourier transform of $\mathbf{F}(z)$: $\hat{\mathbf{F}}(k) = \int_{-\infty}^{+\infty} \mathbf{F}(z)\mathrm{e}^{-\mathrm{i}kz}\mathrm{d}z$.

As proved in Ref. [26], the solution given by Eqs. (7) and (8) is actually based on the so-called Auld's real biorthogonality relationship [29] and remains applicable for non-propagating modes, fully anisotropic materials and lossy waveguides (in particular, the matrix of material properties $\mathbf{C}$ can be complex to handle viscoelastic materials). The normalization factor in Eq. (8) is given by $Q_{m,-m} = \mathrm{i}\frac{\omega}{4}\left(\mathbf{T}^{\mathrm{T}}_{-m}\mathbf{U}_m - \mathbf{U}^{\mathrm{T}}_{-m}\mathbf{T}_m\right)$ and usually differs from the averaged power flow of a mode. In the particular case of propagating modes in lossless waveguides ($k_m \in \mathbb{R}$), the solution can be simplified thanks to the so-called Auld's complex biorthogonality relationship [29] and $Q_{m,-m}$ becomes equal to the modal averaged power flow. The reader may refer to [26] for more details on this topic.

However as shown further, the introduction of rotational symmetry in the waveguide formulation breaks the skew-symmetry of the matrix in Eq. (4) so that Eqs. (7) and (8) are no longer applicable.

## 3. Formulation with rotational symmetry

Let us denote $N$ the order of the rotational symmetry of the problem. As shown in Fig. 3, the structure is divided into $N$ rotationally periodic cells. In the following, the left superscript $s$ will be used to identify the cell index of elastodynamic fields ($s = 0, 1, \ldots, N-1$). The vectors ${}^s\mathbf{U}$ and ${}^s\mathbf{F}$ will denote the displacement vector of the cell $s$ and the external force vector applied to the cell $s$ respectively. The cell $s = 0$ will be considered as the reference cell, that is to say, the unique cell that needs to be discretized by finite elements. For conciseness of notations, one will drop out the superscript $s = 0$ for the reference cell: $\mathbf{U} = {}^0\mathbf{U}$, $\mathbf{F} = {}^0\mathbf{F}$.

### 3.1. Free response

Let us consider the equilibrium equation for the reference cell. This equation is given by Eq. (4). The displacement and force vectors are partitioned as follows:

$$\mathbf{U} = \begin{bmatrix} \mathbf{U}_l \\ \mathbf{U}_i \\ \mathbf{U}_r \end{bmatrix}, \quad \mathbf{F} = \begin{bmatrix} \mathbf{F}_l \\ \mathbf{F}_i \\ \mathbf{F}_r \end{bmatrix} \tag{9}$$

where the subscripts $l$ and $r$ stand for the left and right degrees of freedom (dofs), associated with the left and right boundaries of the rotationally periodic cell of the cross-section – see Fig. 3 (see also Figs. 4 and 9 for examples). The subscript $i$ is left for the remaining dofs (internal dofs).

Since the free response is considered here, there is no external force and the vector $\mathbf{F}$ must be understood as the internal force vector acting on the reference cell ($\mathbf{F} = \mathbf{F}_{\mathrm{int}}$). These internal forces correspond to the forces acting on the left and right boundaries, which are connected to the adjacent cells. Hence, there is no force acting on internal dofs ($\mathbf{F}_i = \mathbf{0}$).

The Bloch–Floquet boundary conditions for a given field $\phi$ and its dual variable $\psi$ are $\phi_r = \lambda\phi_l$ and $\psi_r = -\lambda\psi_l$ [30,31], where $\lambda = \mathrm{e}^{\mathrm{i}\mu}$ and $\mathrm{i}\mu$ is called the propagation constant. However, the periodicity to be applied in this paper is of rotational type and concerns a nonscalar field (the displacement vector). The Bloch–Floquet conditions must then be expressed along the circumferential direction in an appropriate frame, namely the cylindrical coordinate system.

Since the displacement components $\mathbf{U}_l$ and $\mathbf{U}_r$ are initially expressed in a $(x, y, z)$ Cartesian frame, they must be transformed to the $(r, \theta, z)$ cylindrical frame. Cartesian and cylindrical coordinates are related by $(x, y) = (r\cos\theta, r\sin\theta)$ ($r = 0$ corresponding to the center of rotational symmetry). Let us denote $\mathbf{Q}_l$ and $\mathbf{Q}_r$ the transformation matrices of $\mathbf{U}_l$ and $\mathbf{U}_r$ from the Cartesian to the cylindrical frames. The rotationally periodic conditions for the displacement and force vector fields are then:

$$\mathbf{Q}_r\mathbf{U}_r = \lambda\mathbf{Q}_l\mathbf{U}_l \tag{10a}$$

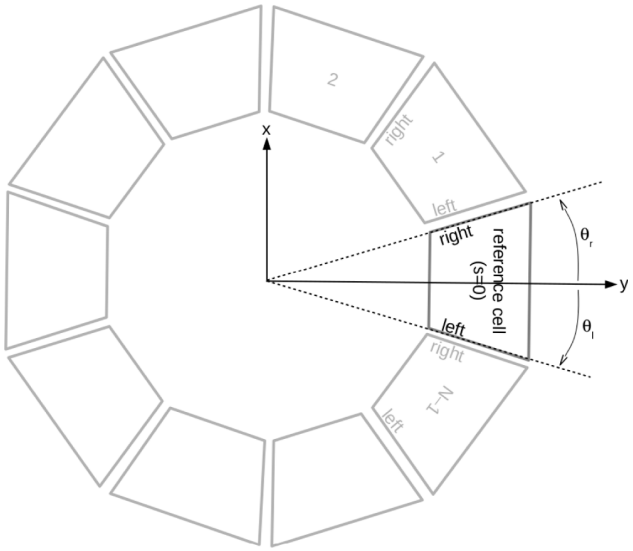


**Fig. 3.** Sketch of a rotationally symmetric cross-section of order $N$ with its reference unit cell. $\theta_l$ and $\theta_r$ denote the angles of the left and right boundaries of the reference cell respectively.

$$\mathbf{Q}_r\mathbf{F}_r = -\lambda\mathbf{Q}_l\mathbf{F}_l \tag{10b}$$

The transformation matrices $\mathbf{Q}_{l,r}$ are block diagonal and comprise three-by-three sub-matrices $\mathbf{q}_{l,r}$ (for the three components of the displacement vector at every node) defined as:

$$\mathbf{q}_{l,r} = \begin{bmatrix} \cos\theta_{l,r} & \sin\theta_{l,r} & 0 \\ -\sin\theta_{l,r} & \cos\theta_{l,r} & 0 \\ 0 & 0 & 1 \end{bmatrix} \tag{11}$$

where $\theta_l$ and $\theta_r$ are the angles of the left and right boundaries respectively (see Fig. 3). These sub-matrices are rotation matrices and are hence orthogonal. Therefore, the following properties hold: $\mathbf{Q}_{l,r}^{-1} = \mathbf{Q}_{l,r}^{\mathrm{T}}$.

As depicted by Fig. 3, the wave fields at the right boundary of the last cell ($s = N-1$) should be equal to the fields at the left boundary of the reference cell ($s = 0$). This leads to the equation $\lambda^N = 1$, or equivalently: $\mu = 2n\pi/N$, where $n = 0, 1, \ldots, N-1$. Therefore, $\lambda$ is a function of the integer $n$ and can be viewed as a fixed user-defined parameter written as follows:

$$\lambda(n) = \mathrm{e}^{\mathrm{i}2n\pi/N} \tag{12}$$

Instead of numbering the circumferential order $n$ from 0 to $N-1$, it is convenient to adopt the following numbering:

$$n = \begin{cases} -\dfrac{N}{2}+1, \ldots, 0, \ldots, \dfrac{N}{2} & \text{for } N \text{ even} \\ -\dfrac{N-1}{2}, \ldots, 0, \ldots, \dfrac{N-1}{2} & \text{for } N \text{ odd} \end{cases} \tag{13}$$

Such a numbering will be of particular interest in Section 3.2 and enables to pair right-handed modes (rotating anti-clockwise around the $z$-axis) with left-handed modes (rotating clockwise). Owing to the $\mathrm{e}^{\mathrm{i}(\mu(n)-\omega t)}$ convention used in this paper, right-handed modes are such that $n > 0$ while left-handed modes are such that $n < 0$. The modes $n = 0$ are rotationally symmetric.

From Eq. (10a) written for a given $n$, the displacement dofs can be related by:

$$\mathbf{U} = \mathbf{R}(n)\tilde{\mathbf{U}}, \quad \mathbf{R}(n) = \begin{bmatrix} \mathbf{I} & \mathbf{0} \\ \mathbf{0} & \mathbf{I} \\ \lambda(n)\mathbf{Q}_r^{-1}\mathbf{Q}_l & \mathbf{0} \end{bmatrix}, \quad \tilde{\mathbf{U}} = \begin{bmatrix} \mathbf{U}_l \\ \mathbf{U}_i \end{bmatrix}. \tag{14}$$

It is noteworthy that the matrix $\mathbf{R}(n)$ has the following property:

$$\overline{\mathbf{R}(n)} = \mathbf{R}(-n) \tag{15}$$

where the overbar denotes complex conjugate. From this property, the following equality holds: $\mathbf{R}(n)^{\mathrm{H}}\mathbf{K}_2^{\mathrm{T}}\mathbf{R}(n) = \left(\mathbf{R}(-n)^{\mathrm{H}}\mathbf{K}_2\mathbf{R}(-n)\right)^{\mathrm{T}}$. Based on the reduced displacement vector $\tilde{\mathbf{U}}$ and setting a space harmonic dependence $\mathrm{e}^{\mathrm{i}kz}$, Eq. (4) can then be

rewritten as:

$$\left\{\tilde{\mathbf{K}}_1(n) - \omega^2\tilde{\mathbf{M}}(n) + \mathrm{i}k\left(\tilde{\mathbf{K}}_2(n) - \tilde{\mathbf{K}}_2(-n)^{\mathrm{T}}\right) + k^2\tilde{\mathbf{K}}_3(n)\right\}\tilde{\mathbf{U}} = \mathbf{R}(n)^{\mathrm{H}}\mathbf{F} \tag{16}$$

where $\tilde{\mathbf{K}}_i(n) = \mathbf{R}(n)^{\mathrm{H}}\mathbf{K}_i\mathbf{R}(n)$ $(i = 1, 2, 3)$, $\tilde{\mathbf{M}}(n) = \mathbf{R}(n)^{\mathrm{H}}\mathbf{M}\mathbf{R}(n)$ (the superscript H denotes complex conjugate transpose).

Accounting for the orthogonality of $\mathbf{Q}_{l,r}$, the expansion of the right hand side of Eq. (16) leads to:

$$\mathbf{R}(n)^{\mathrm{H}}\mathbf{F} = \begin{bmatrix} \mathbf{F}_l + \overline{\lambda(n)}\mathbf{Q}_l^{-1}\mathbf{Q}_r\mathbf{F}_r \\ \mathbf{0} \end{bmatrix} \tag{17}$$

From Eq. (10b), one has: $\mathbf{F}_l + \overline{\lambda(n)}\mathbf{Q}_l^{-1}\mathbf{Q}_r\mathbf{F}_r = (1 - |\lambda(n)|^2)\mathbf{F}_l$. This expression indeed vanishes because $|\lambda(n)| = |\mathrm{e}^{\mathrm{i}2n\pi/N}| = 1$, so that:

$$\mathbf{R}(n)^{\mathrm{H}}\mathbf{F} = \mathbf{0} \tag{18}$$

Therefore, Eq. (16) is a homogeneous equation, corresponding to the eigensystem that accounts both for the continuous translational invariance along the axis (using the waveguide formulation) and for the discrete rotational symmetry of the cross-section (thanks to the application of Bloch–Floquet conditions).

Compared to the eigenvalue problem (4), it can be noticed that the matrix $\left(\tilde{\mathbf{K}}_2(n) - \tilde{\mathbf{K}}_2(-n)^{\mathrm{T}}\right)$ is not skew-symmetric for $n \neq 0$ and $n \neq N/2$ (the particular cases $n = 0$ and $n = N/2$ yield $\lambda = 1$ and $\lambda = -1$ respectively, which preserves the skew-symmetry property of the matrix). Note that left multiplying by the transpose of $\mathbf{R}(n)$, instead of the complex transpose, does not enable to cancel the right hand side of Eq. (16) (the product $\mathbf{R}(n)^{\mathrm{T}}\mathbf{F}$ leads to the factor $(1 - \lambda^2)$, which does not vanish except for $n = 0$ and $n = N/2$). This break of symmetry means that modes computed with the rotationally symmetric formulation for a given circumferential order $n$ do not necessarily occur in pairs of opposite wavenumbers. As a consequence, the forced response calculation as given in Ref. [26] and recalled by Eqs. (7) and (8) is no longer applicable. A specific biorthogonality relation is required as derived in the next subsection.

Throughout this paper, the $m$th eigensolution obtained for a given circumferential order $n$ will be denoted as follows:

$$\{k_m^{(n)}, \tilde{\mathbf{U}}_m^{(n)}\} \tag{19}$$

Left-multiplying both sides of Eq. (6) by $\mathbf{R}(n)^{\mathrm{H}}$, the modal traction associated with the eigendisplacement $\tilde{\mathbf{U}}_m^{(n)}$ is therefore:

$$\tilde{\mathbf{T}}_m^{(n)} = \left(\tilde{\mathbf{K}}_2(-n)^{\mathrm{T}} + ik_m^{(n)}\tilde{\mathbf{K}}_3(n)\right)\tilde{\mathbf{U}}_m^{(n)} \tag{20}$$

where $\tilde{\mathbf{T}}_m^{(n)} = \mathbf{R}(n)^{\mathrm{H}}\mathbf{T}_m^{(n)}$ and $\mathbf{U}_m^{(n)} = \mathbf{R}(n)\tilde{\mathbf{U}}_m^{(n)}$.

### 3.2. Biorthogonality relationship

The eigenproblem (16) is unsymmetric. Left and right eigenvectors are different from each other. The right eigensolution $\{k_m^{(n)}, \tilde{\mathbf{U}}_m^{(n)}\}$ satisfies:

$$\left\{\tilde{\mathbf{K}}_1(n) - \omega^2\tilde{\mathbf{M}}(n) + \mathrm{i}k_m^{(n)}\left(\tilde{\mathbf{K}}_2(n) - \tilde{\mathbf{K}}_2(-n)^{\mathrm{T}}\right) + k_m^{(n)2}\tilde{\mathbf{K}}_3(n)\right\}\tilde{\mathbf{U}}_m^{(n)} = \mathbf{0} \tag{21}$$

The left eigensolution $\{k_m^{(n)}, \tilde{\mathbf{V}}_m^{(n)}\}$ satisfies:

$$\tilde{\mathbf{V}}_m^{(n)\mathrm{T}}\left\{\tilde{\mathbf{K}}_1(n) - \omega^2\tilde{\mathbf{M}}(n) + \mathrm{i}k_m^{(n)}\left(\tilde{\mathbf{K}}_2(n) - \tilde{\mathbf{K}}_2(-n)^{\mathrm{T}}\right) + k_m^{(n)2}\tilde{\mathbf{K}}_3(n)\right\} = \mathbf{0} \tag{22}$$

Noticing the properties that result from Eq. (15):

$$\tilde{\mathbf{K}}_1^{(n)\mathrm{T}} = \tilde{\mathbf{K}}_1(-n), \quad \tilde{\mathbf{K}}_3^{(n)\mathrm{T}} = \tilde{\mathbf{K}}_3(-n), \quad \tilde{\mathbf{M}}^{(n)\mathrm{T}} = \tilde{\mathbf{M}}(-n) \tag{23}$$

and taking the transpose of Eq. (22), one gets:

$$\left\{\tilde{\mathbf{K}}_1(-n) - \omega^2\tilde{\mathbf{M}}(-n) - \mathrm{i}k_m^{(n)}\left(\tilde{\mathbf{K}}_2(-n) - \tilde{\mathbf{K}}_2(n)^{\mathrm{T}}\right) + k_m^{(n)2}\tilde{\mathbf{K}}_3(-n)\right\}\tilde{\mathbf{V}}_m^{(n)} = \mathbf{0} \tag{24}$$

which shows that $\{-k_m^{(n)}, \tilde{\mathbf{V}}_m^{(n)}\}$ is a right eigensolution for the opposite circumferential order $-n$. For this solution, the following notation will be adopted:

$$\{-k_m^{(n)}, \tilde{\mathbf{V}}_m^{(n)}\} = \{k_{-m}^{(-n)}, \tilde{\mathbf{U}}_{-m}^{(-n)}\} \tag{25}$$

What Eq. (24) means is that if $k_m^{(n)}$ is an eigenvalue for the order $n$, then $-k_m^{(n)} = k_{-m}^{(-n)}$ is an eigenvalue for the order $-n$. Hence, the eigenproblem has two subsets of eigensolutions, $(k_m^{(n)}, \tilde{\mathbf{U}}_m^{(n)})$ and $(k_{-m}^{(-n)}, \tilde{\mathbf{U}}_{-m}^{(-n)})$ $(m = 1, \ldots, M)$ representing $M$ pairs of opposite-going modes, traveling in the opposite $z$-direction and also rotating in the opposite direction.

Eq. (22) is rewritten with the notation (25) for a given mode $m'$ and then right-multiplied by the eigenvector $\tilde{\mathbf{U}}_m^{(n)}$:

$$\tilde{\mathbf{U}}_{-m'}^{(-n)\mathrm{T}}\left\{\tilde{\mathbf{K}}_1(n) - \omega^2\tilde{\mathbf{M}}(n) - \mathrm{i}k_{-m'}^{(-n)}\left(\tilde{\mathbf{K}}_2(n) - \tilde{\mathbf{K}}_2(-n)^{\mathrm{T}}\right) + k_{-m'}^{(-n)2}\tilde{\mathbf{K}}_3(n)\right\}\tilde{\mathbf{U}}_m^{(n)} = \mathbf{0} \tag{26}$$

The above equation is then subtracted from Eq. (21) left-multiplied by $\mathbf{U}_{-m'}^{(-n)\mathrm{T}}$, which leads to the following equation:

$$\mathrm{i}\left(k_m^{(n)}+k_{-m'}^{(-n)}\right)\tilde{\mathbf{U}}_{-m'}^{(-n)\mathrm{T}}\left\{\tilde{\mathbf{K}}_2(n)-\tilde{\mathbf{K}}_2(-n)^{\mathrm{T}}-\mathrm{i}\left(k_m^{(n)}-k_{-m'}^{(-n)}\right)\tilde{\mathbf{K}}_3(n)\right\}\tilde{\mathbf{U}}_m^{(n)}=\mathbf{0} \tag{27}$$

Introducing the modal traction expression (20), the above equation can be rewritten as the biorthogonality relationship:

$$\mathrm{i}\frac{\omega}{4}\left(\tilde{\mathbf{T}}_{-m'}^{(-n)\mathrm{T}}\tilde{\mathbf{U}}_m^{(n)}-\tilde{\mathbf{U}}_{-m'}^{(-n)\mathrm{T}}\tilde{\mathbf{T}}_m^{(n)}\right)=Q_{m,-m'}^{(n,-n)}\delta_{mm'} \tag{28}$$

where $\delta_{mm'}$ denotes Kronecker's symbol. This relation can actually be viewed as a discrete version of Auld's real biorthogonality relationship [29], specific to the rotationally symmetric formulation. No specific assumption is needed in the nature of modes and materials so that this relationship remains applicable for non-propagating modes, fully anisotropic materials and lossy waveguides.

### 3.3. Equilibrium equation for the forced response

Starting from Eq. (4) written for the cell $s$, the forced response problem of this cell is given by the following equation:

$$(\mathbf{K}_1-\omega^2\mathbf{M})^s\mathbf{U}+(\mathbf{K}_2-\mathbf{K}_2^{\mathrm{T}})^s\mathbf{U}_{,z}-\mathbf{K}_3{}^s\mathbf{U}_{,zz}={}^s\mathbf{F}={}^s\mathbf{F}_{\mathrm{ext}}+{}^s\mathbf{F}_{\mathrm{int}} \tag{29}$$

where the force vector has been split into external forces and internal forces. Note that the matrices on the left-hand side are independent on $s$ because the geometry is rotationally symmetric, which implies that the displacement and force components in ${}^s\mathbf{U}$ and ${}^s\mathbf{F}$ must be understood as written in a local frame rotated by an angle $2\pi s/N$ with respect to the frame of the reference cell.

The following circumferential order decomposition is adopted (see Appendix):

$${}^s\mathbf{U}=\sum_n\mathbf{U}^{(n)}\mathrm{e}^{\mathrm{i}2\pi ns/N},\quad {}^s\mathbf{F}_{\mathrm{ext}}=\sum_n\mathbf{F}_{\mathrm{ext}}^{(n)}\mathrm{e}^{\mathrm{i}2\pi ns/N},\quad {}^s\mathbf{F}_{\mathrm{int}}=\sum_n\mathbf{F}_{\mathrm{int}}^{(n)}\mathrm{e}^{\mathrm{i}2\pi ns/N}, \tag{30}$$

where it is recalled that the left superscripts for the reference cell have been dropped out ($\mathbf{U}^{(n)}={}^0\mathbf{U}^{(n)}$, $\mathbf{F}_{\mathrm{ext}}^{(n)}={}^0\mathbf{F}_{\mathrm{ext}}^{(n)}$ and $\mathbf{F}_{\mathrm{int}}^{(n)}={}^0\mathbf{F}_{\mathrm{int}}^{(n)}$). In the above expansions, the $n$th coefficient is actually uniquely determined thanks to the formula (A.5).

Let us multiply Eq. (29) by the factor $\mathrm{e}^{-\mathrm{i}2\pi n's/N}$ and sum the equation for every cell $s$:

$$\left\{\mathbf{K}_1-\omega^2\mathbf{M}+(\mathbf{K}_2-\mathbf{K}_2^{\mathrm{T}})\frac{\partial}{\partial z}-\mathbf{K}_3\frac{\partial^2}{\partial z^2}\right\}\left(\frac{1}{N}\sum_{s=0}^{N-1}{}^s\mathbf{U}\mathrm{e}^{-\mathrm{i}2\pi n's/N}\right)=\frac{1}{N}\sum_{s=0}^{N-1}({}^s\mathbf{F}_{\mathrm{ext}}+{}^s\mathbf{F}_{\mathrm{int}})\mathrm{e}^{-\mathrm{i}2\pi n's/N} \tag{31}$$

Using Eq. (30) into (31) together with the formula (A.2), one gets an equilibrium equation written on the reference cell only:

$$(\mathbf{K}_1-\omega^2\mathbf{M})\mathbf{U}^{(n)}+(\mathbf{K}_2-\mathbf{K}_2^{\mathrm{T}})\mathbf{U}_{,z}^{(n)}-\mathbf{K}_3\mathbf{U}_{,zz}^{(n)}=\mathbf{F}_{\mathrm{ext}}^{(n)}+\mathbf{F}_{\mathrm{int}}^{(n)} \tag{32}$$

The vectors $\mathbf{U}^{(n)}$ and $\mathbf{F}_{\mathrm{int}}^{(n)}$ obey the Bloch–Floquet conditions (10). Hence, following the same steps as in Section 3.1, the application of these periodicity conditions to Eq. (32) leads to:

$$\left(\tilde{\mathbf{K}}_1(n)-\omega^2\tilde{\mathbf{M}}(n)\right)\tilde{\mathbf{U}}^{(n)}+\left(\tilde{\mathbf{K}}_2(n)-\tilde{\mathbf{K}}_2(-n)^{\mathrm{T}}\right)\tilde{\mathbf{U}}_{,z}^{(n)}-\tilde{\mathbf{K}}_3(n)\tilde{\mathbf{U}}_{,zz}^{(n)}=\tilde{\mathbf{F}}_{\mathrm{ext}}^{(n)} \tag{33}$$

where:

$$\tilde{\mathbf{F}}_{\mathrm{ext}}^{(n)}=\mathbf{R}(n)^{\mathrm{H}}\,\mathbf{F}_{\mathrm{ext}}^{(n)} \tag{34}$$

Eq. (33) is the forced response problem accounting for rotational symmetry. The equation has to be solved for each circumferential order $n$. The decomposition for ${}^s\mathbf{U}$ in Eq. (30) shows that the response in an arbitrary cell $s$ can be obtained once the response for the reference cell $\mathbf{U}^{(n)}$ has been solved for each $n$.

As shown by Eq. (A.5), the coefficients $\mathbf{F}_{\mathrm{ext}}^{(n)}$ can be determined from the applied external forces ${}^s\mathbf{F}_{\mathrm{ext}}$ ($s=0,\ldots,N-1$) as follows:

$$\mathbf{F}_{\mathrm{ext}}^{(n)}=\frac{1}{N}\sum_{s=0}^{N-1}{}^s\mathbf{F}_{\mathrm{ext}}\mathrm{e}^{-\mathrm{i}2\pi ns/N} \tag{35}$$

For clarity, let us consider two excitation examples. First, if the excitation is rotationally symmetric (${}^s\mathbf{F}_{\mathrm{ext}}={}^0\mathbf{F}_{\mathrm{ext}}=\mathbf{F}_{\mathrm{ext}}$ for any $s$), then Eq. (35) yields:

$$\mathbf{F}_{\mathrm{ext}}^{(n)}=\frac{1}{N}\mathbf{F}_{\mathrm{ext}}\sum_{s=0}^{N-1}\mathrm{e}^{-\mathrm{i}2\pi ns/N}=\begin{cases}\mathbf{F}_{\mathrm{ext}} & \text{for } n=0\\ 0 & \text{for } n\neq 0\end{cases} \tag{36}$$

Second, if the excitation is localized on a single cell (the reference cell $s=0$ for convenience), then Eq. (35) yields:

$$\mathbf{F}_{\mathrm{ext}}^{(n)}=\frac{1}{N}\mathbf{F}_{\mathrm{ext}}\quad \text{for any } n \tag{37}$$

### 3.4. Solution of the forced response

The solution to Eq. (33) is expanded on the eigenmodes:

$$\tilde{\mathbf{U}}^{(n)}(z) = \sum_m \alpha_m^{(n)}(z)\tilde{\mathbf{U}}_m^{(n)} \tag{38}$$

where the $\alpha_m^{(n)}(z)$ are the modal coefficients to be determined. As done analytically in Refs. [29,32], an elegant way of determining the forced response is to start from a reciprocity relationship.

Let us consider two states $A$ and $B$, with displacements denoted as $\tilde{\mathbf{U}}_A^{(n)}$ and $\tilde{\mathbf{U}}_B^{(-n)}$, satisfying Eq. (33) for the circumferential order $n$ with an external force $\tilde{\mathbf{F}}_A^{(n)}$ and for the order $-n$ with a force $\tilde{\mathbf{F}}_B^{(-n)}$ respectively. One can write:

$$\tilde{\mathbf{U}}_B^{(-n)\mathrm{T}}\left\{\left(\tilde{\mathbf{K}}_1(n)-\omega^2\tilde{\mathbf{M}}(n)\right)\tilde{\mathbf{U}}_A^{(n)}+\left(\tilde{\mathbf{K}}_2(n)-\tilde{\mathbf{K}}_2(-n)^{\mathrm{T}}\right)\tilde{\mathbf{U}}_{A,z}^{(n)}-\tilde{\mathbf{K}}_3(n)\tilde{\mathbf{U}}_{A,zz}^{(n)}\right\}=\tilde{\mathbf{U}}_B^{(-n)\mathrm{T}}\tilde{\mathbf{F}}_A^{(n)}, \tag{39a}$$

$$\tilde{\mathbf{U}}_A^{(n)\mathrm{T}}\left\{\left(\tilde{\mathbf{K}}_1(-n)-\omega^2\tilde{\mathbf{M}}(-n)\right)\tilde{\mathbf{U}}_B^{(-n)}+\left(\tilde{\mathbf{K}}_2(-n)-\tilde{\mathbf{K}}_2(n)^{\mathrm{T}}\right)\tilde{\mathbf{U}}_{B,z}^{(-n)}-\tilde{\mathbf{K}}_3(-n)\tilde{\mathbf{U}}_{B,zz}^{(-n)}\right\}=\tilde{\mathbf{U}}_A^{(n)\mathrm{T}}\tilde{\mathbf{F}}_B^{(-n)} \tag{39b}$$

Taking the transpose of (39b) and subtracting it from Eq. (39a) yields thanks to the properties (23):

$$\frac{\partial}{\partial z}\left\{\tilde{\mathbf{U}}_B^{(-n)\mathrm{T}}\left(\tilde{\mathbf{K}}_2(n)-\tilde{\mathbf{K}}_2(-n)^{\mathrm{T}}\right)\tilde{\mathbf{U}}_A^{(n)}-\tilde{\mathbf{U}}_B^{(-n)\mathrm{T}}\tilde{\mathbf{K}}_3(n)\tilde{\mathbf{U}}_{A,z}^{(n)}+\tilde{\mathbf{U}}_{B,z}^{(-n)\mathrm{T}}\tilde{\mathbf{K}}_3(n)\tilde{\mathbf{U}}_A^{(n)}\right\}=\tilde{\mathbf{U}}_B^{(-n)\mathrm{T}}\tilde{\mathbf{F}}_A^{(n)}-\tilde{\mathbf{U}}_A^{(n)\mathrm{T}}\tilde{\mathbf{F}}_B^{(-n)} \tag{40}$$

Introducing the traction vector as defined from Eq. (6), the above equation can be rewritten as:

$$\frac{\partial}{\partial z}\left\{\tilde{\mathbf{T}}_B^{(-n)\mathrm{T}}\tilde{\mathbf{U}}_A^{(n)}-\tilde{\mathbf{U}}_B^{(-n)\mathrm{T}}\tilde{\mathbf{T}}_A^{(n)}\right\}=\tilde{\mathbf{U}}_B^{(-n)\mathrm{T}}\tilde{\mathbf{F}}_A^{(n)}-\tilde{\mathbf{U}}_A^{(n)\mathrm{T}}\tilde{\mathbf{F}}_B^{(-n)} \tag{41}$$

Note that this identity can be interpreted as a discrete version of Auld's real reciprocity relation [29]. In order to obtain the modal coefficients $\alpha_m^{(n)}(z)$, state $A$ is chosen as the forced response we are looking for and state $B$ is set to the virtual propagation state of a single mode $-m'$. Therefore, we set:

$$\tilde{\mathbf{U}}_A^{(n)}=\sum_m \alpha_m^{(n)}(z)\tilde{\mathbf{U}}_m^{(n)},\quad \tilde{\mathbf{T}}_A^{(n)}=\sum_m \alpha_m^{(n)}(z)\tilde{\mathbf{T}}_m^{(n)},\quad \tilde{\mathbf{F}}_A^{(n)}=\tilde{\mathbf{F}}_{\mathrm{ext}}^{(n)}(z), \tag{42a}$$

$$\tilde{\mathbf{U}}_B^{(-n)}=\tilde{\mathbf{U}}_{-m'}^{(-n)}\exp\left(\mathrm{i}k_{-m'}^{(-n)}z\right),\quad \tilde{\mathbf{T}}_B^{(-n)}=\tilde{\mathbf{T}}_{-m'}^{(-n)}\exp\left(\mathrm{i}k_{-m'}^{(-n)}z\right),\quad \tilde{\mathbf{F}}_B^{(-n)}=\mathbf{0} \tag{42b}$$

Using Eq. (42b) into Eq. (41) and exploiting the biorthogonality relationship (28), the summation on the left-hand side has only a single nonzero term, yielding an uncoupled ordinary differential equation for each $\alpha_m^{(n)}(z)$:

$$\frac{\mathrm{d}}{\mathrm{d}z}\left\{\alpha_m^{(n)}(z)\exp\left(-\mathrm{i}k_m^{(n)}z\right)\right\}=\frac{\mathrm{i}\omega}{4Q_{m,-m}^{(n,-n)}}\tilde{\mathbf{U}}_{-m}^{(-n)\mathrm{T}}\tilde{\mathbf{F}}_{\mathrm{ext}}^{(n)}(z)\exp\left(-\mathrm{i}k_m^{(n)}z\right) \tag{43}$$

Solving this equation for waves traveling toward the positive $z$-direction and $z$ outside the source region (one assumes that the excitation is zero outside a finite interval along $z$) finally leads to the forced solution:

$$\tilde{\mathbf{U}}^{(n)}=\sum_{m>0}\mathbf{E}_m^{(n)}\hat{\tilde{\mathbf{F}}}_{\mathrm{ext}}^{(n)}(k_m^{(n)})\mathrm{e}^{\mathrm{i}k_m^{(n)}z} \tag{44}$$

where $\mathbf{E}_m^{(n)}$ is the excitability matrix defined by:

$$\mathbf{E}_m^{(n)}=\frac{\mathrm{i}\omega}{4Q_{m,-m}^{(n,-n)}}\tilde{\mathbf{U}}_m^{(n)}\tilde{\mathbf{U}}_{-m}^{(-n)\mathrm{T}} \tag{45}$$

Note that the summation in Eq. (44) is performed on positive-going waves only (denoted by positive values of $m$). The solution outside the source region for waves traveling toward the negative $z$-direction is identical to Eq. (44) but with a minus sign and a summation on negative-going modes ($m<0$). The vector $\hat{\tilde{\mathbf{F}}}_{\mathrm{ext}}^{(n)}(k)$ is defined as the space Fourier transform of $\tilde{\mathbf{F}}_{\mathrm{ext}}^{(n)}(z)$: $\hat{\tilde{\mathbf{F}}}_{\mathrm{ext}}^{(n)}(k)=\int_{-\infty}^{+\infty}\tilde{\mathbf{F}}_{\mathrm{ext}}^{(n)}(z)\mathrm{e}^{-\mathrm{i}kz}\mathrm{d}z$. In the excitability matrix, the term $\left(\mathbf{E}_m^{(n)}\right)_{ij}$ represents the displacement amplitude for the order $n$ of the single wavemode $m$ at dof $i$ when a unit force acts at dof $j$.

Compared to Eqs. (7) and (8), the solution given by Eqs. (44) and (45) requires two computations, one for the circumferential order $+n$ and another one for the opposite order $-n$. However, note that solving the left eigenproblem (22) is not needed.

Finally, the response in any cell $s$ can be recovered thanks to Eq. (30), which gives:

$${}^s\tilde{\mathbf{U}}=\sum_n\sum_{m>0}\mathbf{E}_m^{(n)}\tilde{\mathbf{F}}_{\mathrm{ext}}^{(n)}(k_m^{(n)})\mathrm{e}^{\mathrm{i}k_m^{(n)}z}\mathrm{e}^{\mathrm{i}2\pi ns/N} \tag{46}$$

and the solution in the space–time domain $(z,t)$ is obtained from the inverse time Fourier transform of ${}^s\tilde{\mathbf{U}}$, given by $\frac{1}{2\pi}\int_{-\infty}^{+\infty}{}^s\tilde{\mathbf{U}}\mathrm{e}^{-\mathrm{i}\omega t}\mathrm{d}\omega$.

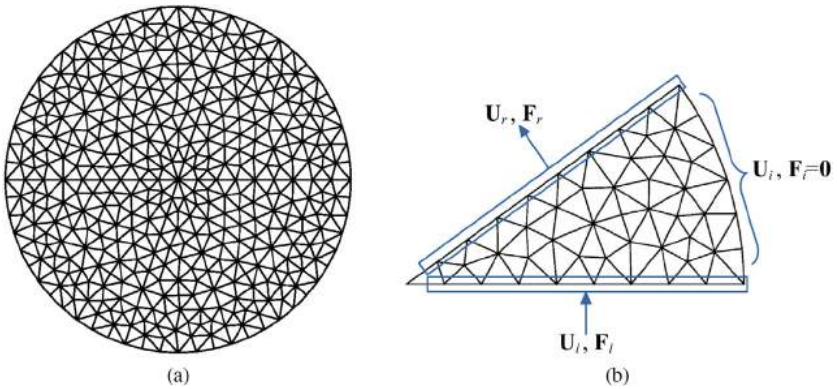


**Fig. 4.** FE mesh of the cross-section of a cylindrical waveguide: (a) complete model (4743 dofs), (b) reduced model of a rotationally symmetric cell with $N = 10$ (531 dofs).

As a side remark, the traveling direction in elastic waveguides of a given mode has to be determined from the sign of energy velocity for purely propagating modes ($k_m^{(n)} \in \mathbb{R}$) and from the sign of Im $k_m^{(n)}$ otherwise. The real part of wavenumbers cannot be used because backward modes may occur (the energy and phase velocities of such modes have opposite signs).

## 4. The cylindrical test case

In this section, the method is validated for a cylindrical waveguide by comparing results with those obtained from the waveguide formulation of a complete cross-section (*i.e.* formulation recalled in Section 2). Both the free response and the forced response are computed.

Assuming an isotropic material, results for the free response are given as dispersion curves for the normalized energy velocity $v_e/c_s$ as a function of the normalized frequency $\omega a/c_s$, where $c_s = \sqrt{E/2\rho(1+\nu)}$ denotes the shear wave velocity and $a$ is the radius of the cylinder ($E$, $\rho$ and $\nu$ denote Young's modulus, mass density and Poisson's ratio respectively). The energy velocity $v_e$ of a given mode $\mathbf{U}_m^{(n)}$ can be post-processed as follows (see Ref. [33] for instance):

$$v_e = \frac{2\omega \mathrm{Im}\left\{\mathbf{U}_m^{(n)\mathrm{H}}(\mathbf{K}_2^{\mathrm{T}} + ik_m^{(n)}\mathbf{K}_3)\mathbf{U}_m^{(n)}\right\}}{\mathrm{Re}\left\{\mathbf{U}_m^{(n)\mathrm{H}}(\mathbf{K}_1 + \omega^2\mathbf{M} + ik_m^{(n)}(\mathbf{K}_2 - \mathbf{K}_2^{\mathrm{T}}) + k_m^{(n)2}\mathbf{K}_3)\mathbf{U}_m^{(n)}\right\}} \tag{47}$$

where $\mathbf{U}_m^{(n)} = \mathbf{R}(n)\tilde{\mathbf{U}}_m^{(n)}$. The Poisson coefficient of the isotropic material is set to $\nu = 0.28$.

The FE discretization of the rotationally periodic cell is generated so that left and right boundaries have a compatible mesh that allows a direct connection between left and right nodes. Six-node triangles are used (*i.e.* quadratic interpolating functions). The FE meshes of this paper have been built from the free software Gmsh [34]. Fig. 4 shows the FE meshes used for the discretization of the complete cross-section and for the unit cell. Owing to the circular cross-section, the angular sector of the unit cell can be arbitrarily thin. In this example, $N$ is set to 10 (the rotationally symmetric model is hence reduced to a sector of angle $2\pi/10$). The full cross-section mesh has been built from the reduced one in order to get rid of the FE discretization error between both models. The finite elements are six-node triangles whose length $l_e$ satisfies the following meshing criterion: $l_e < \lambda/5$, where $\lambda = 2\pi c_s/\omega_{\max}$ is the smallest wavelength of the problem. Note that the node located at the center of rotational symmetry ($r = 0$) constitutes a special case: Bloch–Floquet conditions are not applied at this point. Instead, a zero displacement has to be enforced in the transverse directions if $n = 0$ or in the axial direction otherwise.

### 4.1. Free response

Fig. 5 plots the normalized energy velocity dispersion curves computed with the complete model and with the reduced model for $n = 0$ and $n = \pm 1$. Both models give identical results. For $n = 0$, the reduced model gives axisymmetric propagation modes, which can be of the torsional or compressional type in a cylinder. The modes $n \neq 0$, not axisymmetric, are of the flexural type. Compressional modes have been labeled as L(0,p) in the figure. The missing dispersion curves in Fig. 5b correspond to modes of circumferential order $|n| > 1$, which have been omitted for the clarity of the figure (although not shown, it has been checked that these higher order modes also coincide with those computed with the complete model).

In this example, taking into account the rotational symmetry of the problem has allowed reducing the number of dofs by a factor approximately equal to 10 (531 dofs against 4743) as well as reducing the number of modes to compute by roughly the same factor (30 modes per frequency step for a given $n$ against 300 modes with the complete model). The computation time for a given order $n$ of the reduced model has been found about 80 times faster than with the complete model.

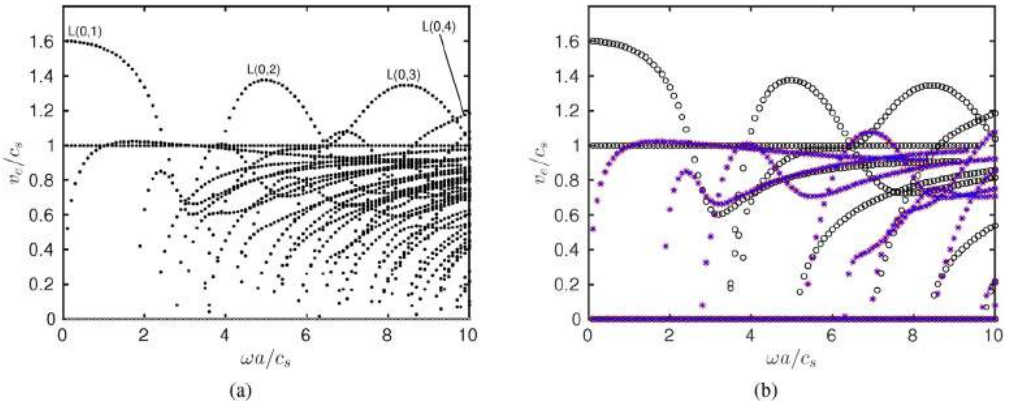


**Fig. 5.** Energy velocity dispersion curves in a cylindrical waveguide computed with: (a) the complete model, (b) the reduced model for $n = 0$ (∘), $n = +1$ (red $+$ ) and $n = -1$ (blue $\times$). (For interpretation of the references to colour in this figure legend, the reader is referred to the web version of this article.)

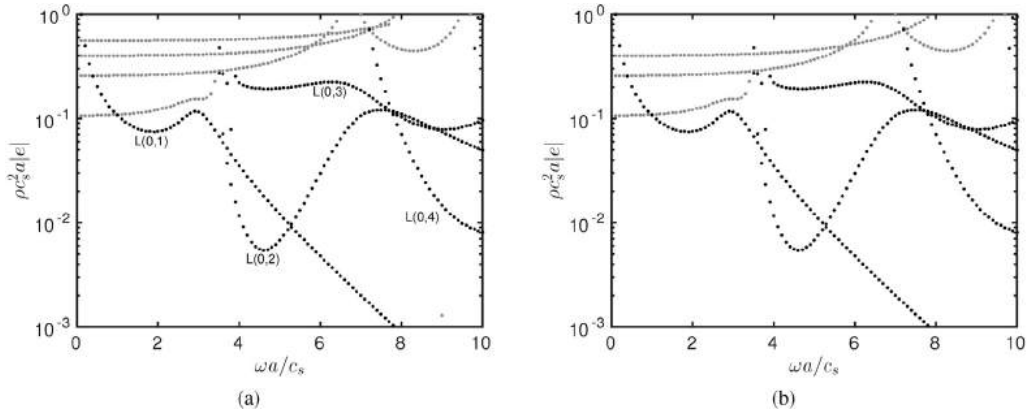


**Fig. 6.** Excitability dispersion curves in a cylindrical waveguide excited by a centered point force oriented in the $z$-direction, computed with: (a) the complete model (Eq. (8)), (b) the reduced model for $n = 0$ (Eq. (45)). Gray color is used to identify non-propagating modes (Im $k_z \neq 0$).

### 4.2. Forced response

Let us consider a point force excitation located at the center of the circular cross-section ($x = y = z = 0$) with a unit amplitude ($F$=1 Newton). Two orientation cases are considered.

The first case corresponds to an orientation of the point force in the $z$-direction (waveguide axis) so that the excitation is rotationally symmetric (Eq. (36) applies) and only the L(0,p) modes are excited. Fig. 6 plots the modulus of modal excitability $e = (\mathbf{E}_m^{(0)})_{ii}$ post-processed at the center and in the $z$-direction with the reduced model (the index $i$ here corresponds to the $z$-displacement degree of freedom of the center node). Fig. 6 also plots the excitability calculated from Eq. (8) with the complete model. As expected, the results obtained with both models agree since Eq. (45) degenerates to Eq. (8) for the particular case $n = 0$ (in this particular case, the skew-symmetry property is not broken by the rotationally symmetric formulation). A curve is missing in the results of the reduced model, which is merely due to the limited number of modes (set to 30 modes per frequency, as previously mentioned) – see upper curve in Fig. 6a (this curve yet corresponds to a non-propagating mode and is of less interest). As can be observed, the excitabilities of L(0,1) and L(0,3) modes near their respective maximum of energy velocity are significantly greater than the excitabilities of L(0,2) and L(0,4) modes. This phenomenon is explained by their mode shapes (not shown for paper conciseness), greater at center for L(0,1) and L(0,3) modes.

The second orientation case corresponds to a point force in the $x$-direction (perpendicular to the waveguide axis). In this case, the excitation is no longer rotationally symmetric and can be considered as localized in the reference cell (Eq. (37) now applies). As opposed to the previous example, a direct comparison of individual modal excitabilities is difficult for non-axisymmetric modes (*i.e.* flexural modes) because, in the complete model, these modes occur in pairs of equal eigenvalues so that their mode shapes are combined by the eigensolver in an arbitrary way. Instead, one compares an example of response calculated at center in the $x$-direction and at the distance $z = 5a$ from the source. Fig. 7 plots the normalized response calculated with the complete model (Eq. (7)) and with the reduced model (Eq. (44)). In the latter case, it has been decided to

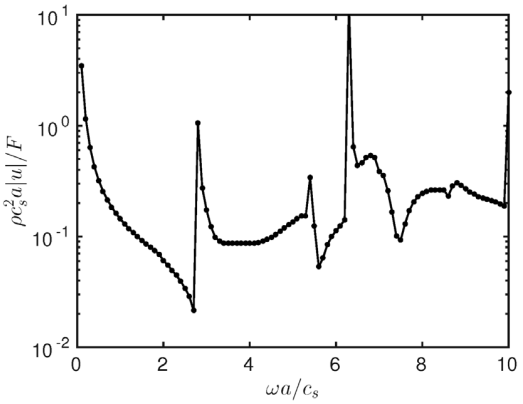


**Fig. 7.** Response at $z = 5a$ in a cylindrical waveguide excited by a centered point force oriented in the $x$-direction, computed by Eq. (7) for the complete model (•) and by Eq. (44) for the reduced model (continuous line). In the reduced model, only the contribution of modes $n = \pm 1$ has been retained.

retain only the contribution of modes $n = \pm 1$ in the response. Despite this, a very good agreement can be observed between both models (the modes $n \neq \pm 1$ have hence a negligible contribution in this example), which validates the forced response calculation proposed in this paper.

### 4.3. Remarks about anisotropy

It can be noticed in Fig. 5 that the energy velocity curves obtained for the left-handed modes are equal to the right-handed ones (compare $n = +1$ vs. $n = -1$). This property is due to the isotropy of the material. In this case, the eigenvalue spectrum computed for the order $-n$ is identical to the order $+n$, as illustrated in Fig. 8a for $n = \pm 1$ at $\omega a/c_s = 6$.

Let us now consider a particular case of transversely isotropic material, made of unidirectional fiber composite lamina where all fibers are parallel to the $z$-axis, and such that the matrix of material properties is of the following form:

$$\mathbf{C} = \begin{bmatrix} C_{11} & C_{12} & C_{12} & 0 & 0 & 0 \\ C_{12} & C_{11} & C_{12} & 0 & 0 & 0 \\ C_{12} & C_{12} & C_{33} & 0 & 0 & 0 \\ 0 & 0 & 0 & C_{66} & 0 & 0 \\ 0 & 0 & 0 & 0 & C_{66} & 0 \\ 0 & 0 & 0 & 0 & 0 & C_{66} \end{bmatrix} \quad \text{with:} \quad \begin{cases} C_{11} = \dfrac{(1-\nu)E}{(1+\nu)(1-2\nu)} \\ C_{12} = \dfrac{\nu E}{(1+\nu)(1-2\nu)} \\ C_{66} = \dfrac{E}{2(1+\nu)} \end{cases} \tag{48}$$

Although this example is somehow artificial, the material is transversely isotropic if $C_{33} \neq C_{11}$ (and fully isotropic otherwise). We set $C_{33} = 2C_{11}$. As shown in Fig. 8b, the eigenvalues still occur in opposite pairs.

Now, the axis of fibers are rotated by an angle $\theta = 25°$ around the $x$-axis. The matrix of material properties becomes:

$$\mathbf{C}' = \mathbf{G}(\theta)^{\mathrm{T}} \mathbf{C} \mathbf{G}(\theta) \tag{49}$$

where $\mathbf{G}(\theta)$ is the transformation matrix corresponding to a rotation $\theta$ around the $x$-axis:

$$\mathbf{G}(\theta) = \begin{bmatrix} 1 & 0 & 0 & 0 & 0 & 0 \\ 0 & c^2 & s^2 & 0 & 0 & cs \\ 0 & s^2 & c^2 & 0 & 0 & -cs \\ 0 & 0 & 0 & c & s & 0 \\ 0 & 0 & 0 & -s & c & 0 \\ 0 & -2cs & 2cs & 0 & 0 & c^2 - s^2 \end{bmatrix} \tag{50}$$

with $c = \cos\theta$ and $s = \sin\theta$. As shown in Fig. 8c, the left-handed wavenumbers are no longer equal to the right-handed ones. This means that the modes propagating in a given $z$-direction behave differently depending on whether they are right- or left-handed. This loss of symmetry is due to the fact that the direction of rotation of modes is sensitive to the inclination of fibers. Yet for all cases (Fig. 8a–c), note that each wavenumber $k_m^{(n)}$ has always an opposite value $k_{-m}^{(-n)} = -k_m^{(n)}$, in agreement with the property shown by Eq. (25).

In the isotropic case (Fig. 8a) and in the transversely isotropic $\theta = 0°$ case (Fig. 8b), one can observe that the eigenvalues for a given order $n$ appear in opposite pairs, $k_m^{(n)}$ and $-k_m^{(n)}$. This suggests that the excitability (45) could be simplified by using an explicit relation between these pairs (see for instance [35]), leading to a degeneracy of the general biorthogonality (28) to a Frazer type biorthogonality [36,37]. The latter is yet of less interest in this paper because it cannot be applied to the

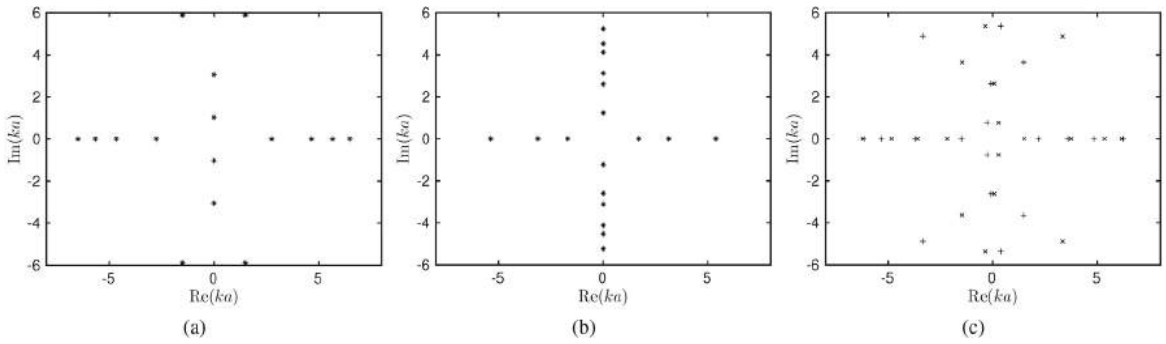


**Fig. 8.** Spectrum computed at $\omega a/c_s = 6$ for $n = +1$ (+) and $n = -1$ (×) in case of: (a) isotropy, (b) transverse isotropy with $\theta = 0°$, (c) transverse isotropy with $\theta = 25°$.

example considered in the next section, involving a form of anisotropy that breaks the symmetry of the spectrum (similarly to Fig. 8c).

## 5. Application to a multi-wire structure

In this section, the method is applied to a more complex structure by considering a seven-wire strand as shown in Fig. 2. The number of peripheral wires of the strand yields a rotational symmetry of order 6. The material is isotropic ($\nu = 0.28$). The characteristic length $a$ is chosen as the radius of the central wire. Because peripheral wires are not straight but helical, the analysis of guided waves requires a specific curvilinear coordinate system, called twisting coordinate system. A twisting system is a particular case of helical system, with zero curvature and a torsion $\tau = 2\pi/L$ (with $L$ denoting the helix pitch of peripheral wires). In this twisting system, the cross-section of the whole structure remains continuously translationally invariant so that guided waves truly exist [33]. The elastodynamic operators must be rewritten in the twisting coordinate system yielding expressions for $\mathbf{L}_{xy}$ and $\mathbf{L}_z$ that are different from Eq. (1) and depend on $\tau$. Furthermore, the strand is prestressed with a 0.6% elongation, which further modifies the operators.

The reader may refer to [38,39,18] for details about the modeling of prestressed seven-wire strands. Although more involved than that described in Section 2, the formulation leads to an eigensystem which keeps the same form as Eq. (4). Therefore, the whole procedure described in Section 3 remains applicable. Similarly to the previous section, results obtained with the proposed method are compared with those obtained with a complete model, which has been thoroughly studied in Refs. [18,40]. Fig. 9 shows the FE meshes used for the discretization of the complete cross-section and for the unit cell. As in Section 4, the full cross-section mesh has been built from the reduced one in order to get rid of the FE discretization error. The finite elements are six-node triangles obeying the same meshing criterion as before ($l_e < \lambda/5$), but the meshes are refined near interwire regions in order to accurately account for contact phenomena [18]. In this paper, the radius of peripheral wires is set to $0.967a$ and $\tau a = 0.0705$.

It is noteworthy that the diameter of peripheral wires (smaller than the central wire) is such that they do not contact each other. This is a widespread design criterion to minimize friction effects [41]. The gap between peripheral wires is indeed small and not visible in Fig. 9a. It remains nonzero in the prestressed case also [39]. Since no contact occurs between peripheral wires, Bloch–Floquet conditions are only applied in the central wire (as depicted in Fig. 9b). Hence, contact occurs only between the central wire and the peripheral ones. Infinite friction is assumed in the model (i.e. perfectly stick contact conditions). As thoroughly discussed in Ref. [40], this assumption has shown to give satisfying agreement with available experimental results (further experimental works are out-of-the-scope of the present paper).

### 5.1. Free response

Fig. 10 plots the normalized energy velocity dispersion curves obtained with the complete model and the reduced model for $n = 0$ and $n = \pm 1$. Results coincide with each other (modes calculated for $n = \pm 2, 3$ are not shown for conciseness). As can be observed, seven-wire strands are complex structures involving many dispersion curves owing to the interwire coupling. By analogy with a cylinder, modes can be classified into three categories: longitudinal, torsional and flexural (labeled as L(0,1), T(0,1) and F(1,1) respectively). A detailed description of these curves is out of the scope of this paper but can be found in Ref. [40]. It is yet noteworthy that the modal energy velocities computed for $n = -1$ are different from the order $n = +1$ even though the material is isotropic. Indeed, left-handed ($-n$) and right-handed modes ($+n$) behave differently due to the twist of the structure, which induces an anisotropy of geometric kind. This can be intuitively understood from the three-dimensional rotationally symmetric cell given by Fig. 2b: the twist, right-handed in this example, makes right-handed and left-handed modes have different wave speeds. In Fig. 10b for $n \neq 0$, the fastest modes are right-handed, that is to say co-rotating with the twist (these modes are of longitudinal type, as identified later in Fig. 12).

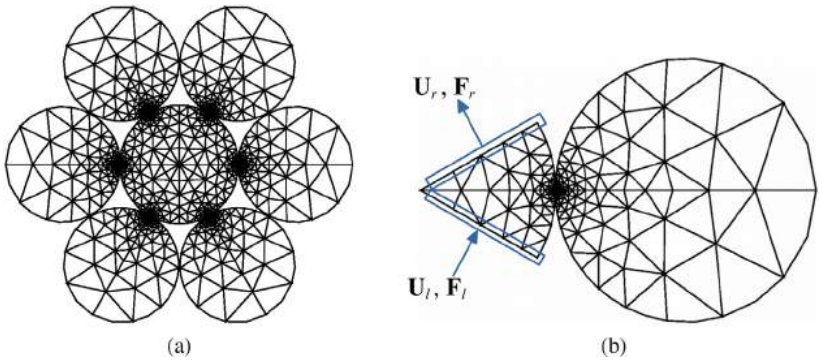


**Fig. 9.** FE mesh of the cross-section of a seven-wire strand: (a) complete model (12 369 dofs), (b) reduced model with $N = 6$ of a rotationally symmetric cell (2094 dofs).

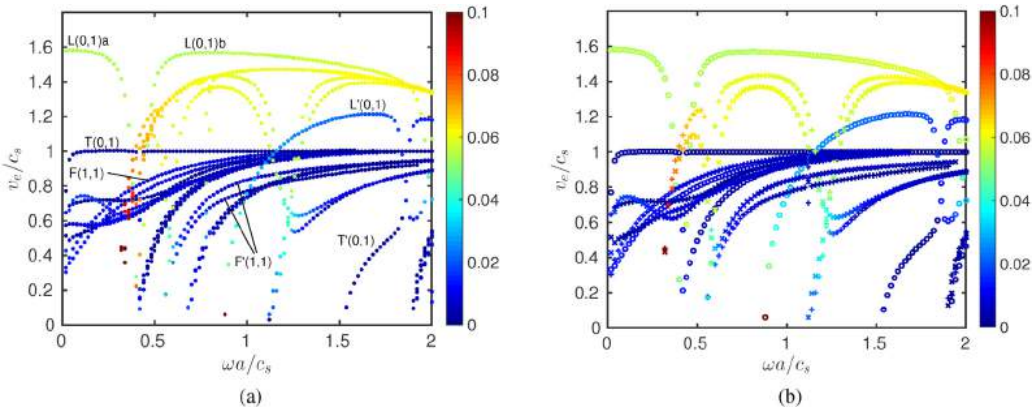


**Fig. 10.** Energy velocity dispersion curves in a seven-wire strand computed with: (a) the complete model, (b) the reduced model for $n = 0$ (∘), $n = +1$ (+) and $n = -1$ (×). Colors represent the modal amplitude $|\alpha|$ for an excitation localized inside a peripheral wire. For comparison with the complete model, the coefficient $\alpha$ calculated by the reduced model has been multiplied by $\sqrt{N}$ (color online).

In this example, the rotationally symmetric formulation has allowed reducing the number of dofs by a factor 6 as well as the number of computed modes by roughly the same factor (20 modes per frequency step against 120 with the complete model). The computation time for a given order $n$ of the reduced model has been found about 10 times faster than with the complete model.

Another advantage of the formulation is the intrinsic classification of modes in terms of their circumferential order $n$, which can help the analysis of the dynamic behavior of complex structures. This observation coincides with the findings of Refs. [42,19] dealing with different periodic structures, for which dispersion curves turn out to be much easier to interpret when a reduced unit cell is used.

### 5.2. Forced response

As done in Ref. [40], one considers an excitation localized inside the central wire. Peripheral wires are not excited. The excitation is oriented along the $z$-direction in order to mainly excite compressional-like mode. The excitation is therefore rotationally symmetric and Eq. (36) applies. The excitation profile is distributed over the cross-section of the central wire as a radial cosine function vanishing at its boundary. One assumes that the excitation is constant with frequency and concentrated at $z = 0$ (the $z$-dependence of the excitation is the Dirac function so that the space Fourier transform of the excitation does not depend on $k$).

Fig. 11 plots the modal coefficient modulus $|\alpha|$ computed both with the complete model and the reduced one. The modal coefficient $\alpha$ of the reduced model is defined as associated with the normalized displacement mode shapes $\tilde{\mathbf{U}}_m^{(n)}/\sqrt{Q_{m,-m}^{(n,-n)}}$

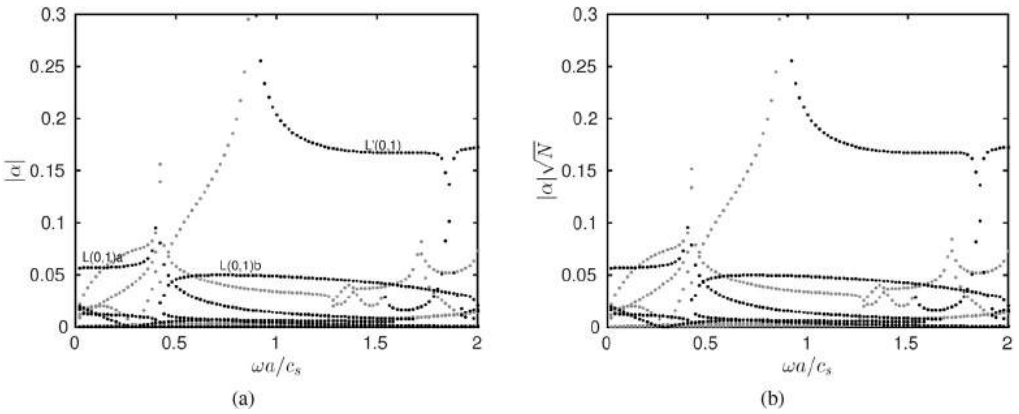


**Fig. 11.** Modulus of modal coefficients $|\alpha|$ as a function of the normalized frequency for a seven-wire strand excited by a longitudinal force localized inside the central wire, computed with: (a) the complete model, (b) the reduced model for $n = 0$. Gray color is used to identify non-propagating modes ($\mathrm{Im}\, k_z \neq 0$).

and is hence defined from Eq. (44) by:

$$\alpha = \frac{\sqrt{\rho a^2 c_s}}{F} \frac{\mathrm{i}\omega}{4\sqrt{Q^{(n,-n)}_{m,-m}}} \tilde{\mathbf{U}}^{(-n)\mathrm{T}}_{-m} \hat{\tilde{\mathbf{F}}}^{(n)}_{\mathrm{ext}}(k^{(n)}_m) \tag{51}$$

where the factor $\sqrt{\rho a^2 c_s}/F$ has been introduced to provide dimensionless results ($F$ denotes the amplitude in Newton of the cosine distribution of the force). Similarly, the modal coefficient $\alpha$ of the complete model is given by the same equation but without the superscripts related to the circumferential orders. The normalized mode shapes of the complete model are given by $\mathbf{U}_m/\sqrt{Q_{m,-m}}$ but it has to be noticed that $Q_{m,-m} = NQ^{(n,-n)}_{m,-m}$. Therefore, the modal coefficient of the reduced model has been multiplied by $\sqrt{N}$ for a direct comparison with the complete one.

As seen in Fig. 11, very good agreement is achieved between both models. From a physical point of view, one can observe that the amplitude of the L'(0,1) mode after its cut-on is greater than the other modes. As explained in Ref. [40], this mode could be of interest for nondestructive applications because it is localized inside the central wire as opposed to the global motion of the compressional-like L(0,1)a,b modes.

Let us now consider the same excitation as before but now localized inside a single peripheral wire. Eq. (37) now applies. Because the modal behavior of the structure for a peripheral excitation is more complex than for a central excitation [40], a convenient and compact way of showing the contribution of individual modes to the response is to plot color dispersion curves indicating modal amplitudes $|\alpha|$ – see Fig. 10. Once again, it can be seen that the reduced model is in good agreement with the complete model. Up to a normalized frequency roughly equal to 0.3, the excited mode is mainly the L(0,1)a mode (the motion is of global type). Above this frequency, the motion changes due to the cut-on of several modes (these modes are mainly localized in peripheral wires and combine each other in a complex manner – see Ref. [40] for further details).

### 5.3. High-frequency results

Although the modal density significantly increases with frequency and complicates the analysis, the rotationally symmetric formulation enables to explore a higher frequency range than the complete model. Fig. 12 shows the dispersion curves for $n = 0, \pm 1$ computed with the reduced model up to a normalized frequency $\omega a/c_s = 10$ (100 modes computed per frequency step). Compared to Fig. 9b, the FE mesh has been refined to improve the accuracy of results yielding 18 876 dofs. In order to further demonstrate the potentiality of the approach, some material damping has also been included by choosing a frequency independent hysteretic model with longitudinal and shear bulk wave attenuations set to $\beta_l$=0.003 and $\beta_s$=0.043 Np/wavelength respectively (typical properties for steel, see [43] for instance). The viscoelastic Young's modulus and Poisson's ratio are then complex.

The compressional-like modes, labeled 1 to 4 in the figures, still emerge as the fastest modes although these modes suffer from multiple velocity drops due to veering phenomena. A typical example of veering occurs for the 1st low-frequency mode around $\omega a/c_s = 0.4$ (it can be clearly observed in Fig. 10, where the curve splits into two modes labeled L(0,1)a and L(0,1)b). This veering phenomenon has been thoroughly investigated in Ref. [18] and is due to the radial displacement constraint imposed between wires in the contact regions. The results in Fig. 12 suggest that similar veering phenomena may also occur for higher-order longitudinal modes.

Fig. 12 also shows the modal coefficient color plots for the same excitation as used for Fig. 10 (excitation localized inside a single peripheral wire and oriented in the axis direction to mainly excite longitudinal modes). Similarly to the cylinder

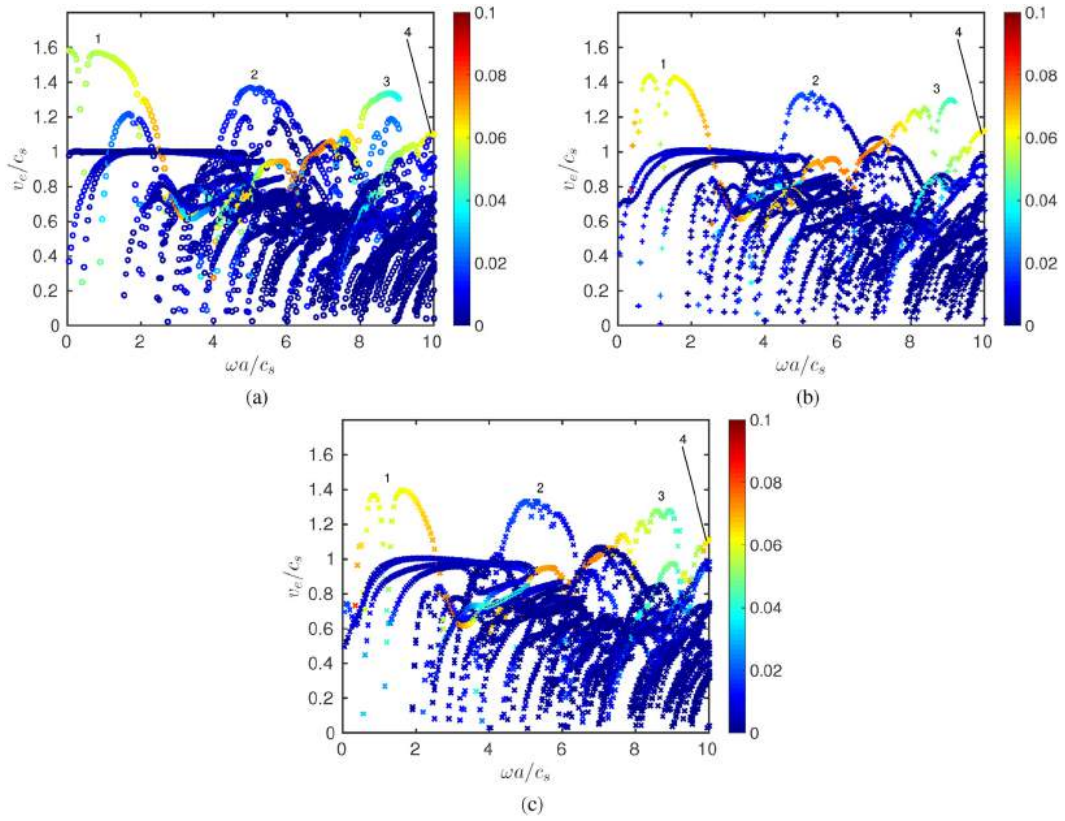


**Fig. 12.** High-frequency energy velocity dispersion curves for a seven-wire strand with material damping computed with the reduced model: (a) $n = 0$, (b) $n = +1$, (c) $n = -1$. Color: modal amplitude $\sqrt{N}|\alpha|$ for an excitation localized inside a peripheral wire (color online).

(Fig. 6), the first and third compressional-like modes turn out to be more excitable than the second one. Besides, the modal characteristics as the frequency increases tend to become identical whatever the order $n$ is, which suggests that the coupling between wires tends to decrease.

## 6. Conclusion

In this paper, a waveguide formulation has been presented to account for the discrete rotational symmetry of the cross-section of elastic waveguides. Both the free and the forced response problems have been considered. To circumvent a loss of symmetry in the eigenproblem, a specific biorthogonality relationship has been derived. This relation can be interpreted as a discrete version of Auld's real biorthogonality relationship. It allows an explicit calculation of modal coefficients of the forced response written as a modal expansion, without solving left eigenproblems. The solution remains applicable to non-propagating modes, fully anisotropic materials and lossy waveguides.

The method has been tested for the simple example of a cylinder and for the more complex test case of a seven-wire strand. Both reductions in terms of dofs and modes significantly contribute to diminishing the computational effort. Besides, the rotationally symmetric formulation naturally provides a classification of modes in terms of their circumferential order, which can be of great help for the dynamic analysis of complex structures. This formulation opens new possibilities for the numerical analysis of complex waveguides in high-frequency regime. For instance, it could facilitate the analysis of cables having a more complex architecture than seven-wire strands and involving rotational symmetry of higher order.

## Acknowledgments

The author wishes to thank Région Pays de la Loire and the West Atlantic Marine Energy Center for their financial support.

## Appendix. Circumferential order decomposition of elastodynamic fields

The sum of the first $N$ terms of a geometric series is:

$$\sum_{s=0}^{N-1} r^s = \begin{cases} \dfrac{1-r^N}{1-r} & \text{if } r \neq 1 \\ N & \text{if } r = 1 \end{cases} \tag{A.1}$$

where $r$ denotes the common ratio. Setting $r = \mathrm{e}^{\mathrm{i}2\pi(s'-s)/N}$, one gets the following useful formula:

$$\frac{1}{N}\sum_{s=0}^{N-1} \mathrm{e}^{\mathrm{i}2\pi(n-n')s/N} = \begin{cases} 0 & \text{if } n' \neq n \\ 1 & \text{if } n' = n \end{cases} \tag{A.2}$$

where $n'$ belongs to the same integer space as $n$ (see Eq. (13)).

Let us now consider the elastodynamic field of cell $s$, denoted by ${}^s\phi$. We can write the following decomposition:

$${}^s\phi = \sum_n \phi^{(n)} \mathrm{e}^{\mathrm{i}2\pi ns/N} \tag{A.3}$$

Multiplying both sides by $\mathrm{e}^{-\mathrm{i}2\pi n's/N}$ and summing over every cell $s$ yields:

$$\sum_{s=0}^{N-1} {}^s\phi \mathrm{e}^{-\mathrm{i}2\pi n's/N} = \sum_n \left( \phi^{(n)} \sum_{s=0}^{N-1} \mathrm{e}^{\mathrm{i}2\pi(n-n')s/N} \right) \tag{A.4}$$

Using the formula (A.2), one finally gets the $n$th coefficient of the decomposition:

$$\phi^{(n)} = \frac{1}{N}\sum_{s=0}^{N-1} {}^s\phi \mathrm{e}^{-\mathrm{i}2\pi ns/N} \tag{A.5}$$

Noticing that $\frac{2\pi s}{N} \xrightarrow{N\to\infty} \theta$, the degeneracy of Eqs. (A.3) and (A.5) as the number of cells goes to infinity yields:

$${}^s\phi \xrightarrow{N\to\infty} \phi(\theta) = \sum_{n=-\infty}^{+\infty} \phi^{(n)} \mathrm{e}^{\mathrm{i}n\theta}, \quad \phi^{(n)} \xrightarrow{N\to\infty} \frac{1}{2\pi}\int_{-\pi}^{+\pi} \phi(\theta)\mathrm{e}^{-\mathrm{i}n\theta}\mathrm{d}\theta \tag{A.6}$$

which are the well-known Fourier series formula. The results presented in this paper actually degenerate to the axisymmetry case (*i.e.* continuous rotational symmetry). It can be checked that the biorthogonality (28) and the solution given by Eqs. (46) and (45) remain applicable to a fully axisymmetric waveguide formulation (although the expressions of the elementary matrices (5) are different in this case — see for instance Ref. [22] for these expressions).

## References


[1] P. Wilcox, M. Evans, O. Diligent, P. Cawley, Dispersion and excitability of guided acoustic waves in isotropic beams with arbitrary cross-section, in: D.O. Thompson, D.E. Chimenti (Eds.), Review of Progress in Quantitative NDE, vol. 615, AIP Conference Proceedings, New York, 2002, pp. 203–210.
[2] A. Velichko, P.D. Wilcox, Modeling the excitation of guided waves in generally anisotropic multilayered media, J. Acoust. Soc. Am. 121 (2007) 60–69.
[3] W.T. Thomson, Transmission of elastic waves through a stratified solid medium, J. Appl. Phys. 21 (1950) 89–93.
[4] N.A. Haskell, The dispersion of surface waves on multilayered media, Bull. Seismol. Soc. Am. 43 (1953) 17–34.
[5] E. Kausel, J. Roësset, Stiffness matrices for layered soils, Bull. Seismol. Soc. Am. 71 (1981) 1743–1761.
[6] B.N. Pavlakovic, M.J.S. Lowe, D.N. Alleyne, P. Cawley, Disperse: a general purpose program for creating dispersion curves, in: Review of Progress in Quantitative NDE, vol. 16, 1997, pp. 185–192.
[7] L. Gry, C. Gontier, Dynamic modelling of railway track : a periodic model base on a generalized beam formulation, J. Sound Vib. 199 (1997) 531–558.
[8] B.R. Mace, D. Duhamel, M.J. Brennan, L. Hinke, Finite element prediction of wave motion in structural waveguides, J. Acoust. Soc. Am. 117 (2005) 2835–2843.
[9] D. Duhamel, B.R. Mace, M.J. Brennan, Finite element analysis of the vibrations of waveguides and periodic structures, J. Sound Vib. 294 (2006) 205–220.
[10] F. Treysséde, Numerical investigation of elastic modes of propagation in helical waveguides, J. Acoust. Soc. Am. 121 (2007) 3398–3408.
[11] R. Nelson, S. Dong, R. Kalra, Vibrations and waves in laminated orthotropic circular cylinders, J. Sound Vib. 18 (1971) 429–444.
[12] E. Kausel, An Explicit Solution for the Green Functions for Dynamic Loads in Layered Media, MIT Research Report R81-13, Department of Civil Engineering, School of Engineering, Massachusetts Institute of Technology, 1981.
[13] G. Liu, J. Achenbach, Strip element method to analyze wave scattering by cracks in anisotropic laminated plates, J. Appl. Mech. 62 (1995) 607–607.
[14] T. Hayashi, W.J. Song, J.L. Rose, Guided wave dispersion curves for a bar with an arbitrary cross-section, a rod and rail example, Ultrasonics 41 (2003) 175–183.
[15] I. Bartoli, A. Marzani, F. Lanza di Scalea, E. Viola, Modeling wave propagation in damped waveguides of arbitrary cross-section, J. Sound Vib. 295 (2006) 685–707.
[16] H. Gravenkamp, H. Man, C. Song, J. Prager, The computation of dispersion relations for three-dimensional elastic waveguides using the scaled boundary finite element method, J. Sound Vib. 332 (2013) 3756–3771.
[17] F. Treyssède, Spectral element computation of high frequency leaky modes in three-dimensional solid waveguides, J. Comput. Phys. 314 (2016) 341–354.

[18] F. Treyssède, Dispersion curve veering of longitudinal guided waves propagating inside prestressed seven-wire strands, J. Sound Vib. 367 (2016) 56–68.
[19] F. Maurin, C. Claeys, L. Van Belle, W. Desmet, Bloch theorem with revised boundary conditions applied to glide, screw and rotational symmetric structures, Comput. Methods Appl. Mech. Engrg. 318 (2017) 497–513.
[20] E. Manconi, B.R. Mace, Wave characterization of cylindrical and curved panels using a finite element method, J. Acoust. Soc. Am. 125 (2009) 154–163.
[21] J.M. Renno, B.R. Mace, Calculating the forced response of cylinders and cylindrical shells using the wave and finite element method, J. Sound Vib. 333 (2014) 5340–5355.
[22] A. Marzani, Time-transient response for ultrasonic guided waves propagating in damped cylinders, Int. J. Solids Struct. 45 (2008) 6347–6368.
[23] H. Gravenkamp, C. Birk, C. Song, The computation of dispersion relations for axisymmetric waveguides using the scaled boundary finite element method, Ultrasonics 54 (2014) 1373–1385.
[24] D.L. Thomas, Dynamics of rotationally periodic structures, Internat. J. Numer. Methods Engrg. 14 (1979) 81–102.
[25] M. Petyt, Introduction to Finite Element Vibration Analysis, Cambridge University Press, 1990.
[26] F. Treyssède, L. Laguerre, Numerical and analytical calculation of modal excitability for elastic wave generation in lossy waveguides, J. Acoust. Soc. Am. 133 (2013) 3287–3837.
[27] F. Tisseur, K. Meerbergen, The quadratic eigenvalue problem, SIAM Rev. 43 (2001) 235–286.
[28] R. Lehoucq, D. Sorensen, C. Yang, ARPACK User's Guide: Solution of Large Scale Eigenvalue Problems with Implicitly Restarted Arnoldi Methods, SIAM, Philadelphia, PA, 1998, pp. 1–142.
[29] B.A. Auld, Acoustic Fields and Waves in Solids, vol. II, second ed., Krieger, Malabar, FL, 1990, p. 432.
[30] D.J. Mead, A general theory of harmonic wave propagation in linear periodic systems with multiple coupling, J. Sound Vib. 27 (1973) 235–260.
[31] R.S. Langley, A variational principle for periodic structures, J. Sound Vib. 135 (1989) 135–142.
[32] J.D. Achenbach, Reciprocity in Elastodynamics, Cambridge University Press, Cambridge, UK, 2003, p. 255.
[33] F. Treyssède, L. Laguerre, Investigation of elastic modes propagating in multi-wire helical waveguides, J. Sound Vib. 329 (10) (2010) 1702–1716.
[34] C. Geuzaine, J.F. Remacle, Gmsh: a three-dimensional finite element mesh generator with built-in pre- and post-processing facilities, Internat. J. Numer. Methods Engrg. 79 (2009) 1309–1331.
[35] F. Treyssède, Three-dimensional modeling of elastic guided waves excited by arbitrary sources in viscoelastic multilayered plates, Wave Motion 52 (2015) 33–53.
[36] W.B. Fraser, Othogonality relation for Rayleigh-Lamb modes of vibration of a plate, J. Acoust. Soc. Am. 59 (1976) 215–216.
[37] V. Pagneux, A. Maurel, Lamb wave propagation in elastic waveguides with variable thickness, Proc. R. Soc. Lond. Ser. A Math. Phys. Eng. Sci. 462 (2006) 1315–1339.
[38] A. Frikha, P. Cartraud, F. Treyssède, Mechanical modeling of helical structures accounting for translational invariance. Part 1: Static behavior, Int. J. Solids Struct. 50 (2013) 1373–1382.
[39] F. Treyssède, A. Frikha, P. Cartraud, Mechanical modeling of helical structures accounting for translational invariance. part 2: Guided wave propagation under axial loads, Int. J. Solids Struct. 50 (2013) 1383–1393.
[40] F. Treyssède, Investigation of the interwire energy transfer of elastic guided waves inside prestressed cables, J. Acoust. Soc. Am. 140 (2016) 498–509.
[41] A. Nawrocki, M. Labrosse, A finite element model for simple straight wire rope strands, Comput. Struct. 77 (2000) 345–359.
[42] F. Maurin, Bloch theorem with revised boundary conditions applied to glide and screw symmetric, quasi-one dimensional structures, Wave Motion 61 (2016) 20–39.
[43] B.N. Pavlakovic, M.J.S. Lowe, P. Cawley, High-frequency low-loss ultrasonic modes in imbedded bars, J. Appl. Mech. 68 (2001) 67.